Aeroelastic Model Identification

of Winglet Loads
from Flight Test Data

Marianne J. Reijerkerk

Aeroelastic Model Identification

of Winglet Loads from Flight Test Data

Aeroelastic Model Identification

of Winglet Loads from Flight Test Data

PROEFSCHRIFT

ter verkrijging van de graad van doctor
aan de Technische Universiteit Delft,
op gezag van de Rector Magnificus Prof. dr. ir. J.T. Fokkema,
voorzitter van het College voor Promoties,
in het openbaar te verdedigen op
maandag 8 september 2008 om 12.30 uur
door

Marianne Jacoba REIJERKERK

ingenieur luchtvaart en ruimtevaart
geboren te Hanau, Duitsland.

Dit proefschrift is goedgekeurd door de promotor:

Prof. dr. ir. J.A. Mulder

Copromotor: Dr. Q.P. Chu

Samenstelling promotiecommissie:

Rector Magnificus	voorzitter
Prof. dr. ir. J.A. Mulder	Technische Universiteit Delft, promotor
Dr. Q.P. Chu	Technische Universiteit Delft, copromotor
Prof. dr.-ing. J. Ballmann	Rheinisch-Westfälische Technische Hochschule Aachen, Aachen, Duitsland
Dr.-ing. J. Bals	Deutsches Zentrum für Luft- und Raumfahrt, Oberpfaffenhofen, Duitsland
Prof. dr. ir. drs. H. Bijl	Technische Universiteit Delft
Dr.-ing. T. Heintsch	Airbus S.A.S., Hamburg, Duitsland
Prof. dr. ir. M.H.G. Verhaegen	Technische Universiteit Delft
Prof. dr. ir. M.J.L. van Tooren	Technische Universiteit Delft, reservelid

DISCLAIMER

The purpose of this thesis is to present an approach to the validation of flight loads models based on a comparison of experimental data with their theoretical predictions. In the case of significant model discrepancies the model can be adapted through parametric adaptation and if called for, structural extension. Although every effort has been made to verify that the numerical information in this thesis is consistent with industrial standards and processes, it is not part of official industrial policy or processes, and should not be construed as such.

Acknowledgements

To finish a thesis, requires a lot of endurance and confidence. When things are going well, this is not a real effort. Surviving the hard phases is essential. I would not be at the point, where I am today, without the help and support from many people for which I am truly grateful.

I would like express my gratitude to Prof.dr.ir. J.A. (Bob) Mulder, head of the Control and Simulation Department of the Delft University of Technology, for his scientific support, his limitless enthusiasm and for being my promotor. I would like to thank Dr. Q.P. (Ping) Chu, Associate Professor at the Control and Simulation Department of the Delft University of Technology, for his scientific support and for being my copromotor. I very much appreciated the technical and editorial advices of Bob and Ping in the fruitful discussions we had on this work.

The present work has become possible through a cooperation between the Institute of Robotics and Mechatronics at the German Aerospace Center (DLR) in Oberpfaffenhofen and the Department for Loads and Aeroelastics of Airbus S.A.S. in Hamburg. This constellation enabled me to gain experience with numerous aspects of research and development from the scientific as well as from the industrial perspective.
I would like to thank Dr. J. Bals, head of the System Dynamics and Control Department at the DLR Institute of Robotics and Mechatronics, for making this work possible at the Institute and Dr. T. Heintsch, Dr. M. Kordt for their support and for enabling me to do this work within the industrial context.

I would like to express my gratitude to Dr. J. Riedel for his coaching and for the numerous inspiring discussions.

I would like to thank B. König from the Institute for Aerodynamics and Gasdynamics from the University of Stuttgart for the good and pleasant cooperation.

I would like to thank all colleagues of the Institute of Robotics and Mechatronics and

Oberpfaffenhofen, July 2008   *Marion Reijerkerk*

Abstract

Numerical computational methods are getting more and more sophisticated every day, enabling more accurate aircraft load predictions. In the structural design of aircraft higher levels of flexibility can be tolerated to arrive at a substantial weight reduction. The result is that aircraft of the future can be bigger, have better performance and less mass. The performance of an aircraft can be even further enhanced by the use of winglets or other wing tip devices.

A more flexible structure in combination with larger dimensions can lead to substantial structural deflections. Due to these larger deflections, the interaction between the aerodynamics and structural mechanics is of increasing importance. Due to their outboard position, the aerodynamic performance of wing tip devices is obviously significantly influenced by the deformation of the flexible wing.

Off course, a safe and reliable operational life of the aircraft has to be guaranteed and proven with adequate design calculations. This is controlled by regulations drawn up by the aviation authorities. For the certification of transport category aircraft compliance of the design with these airworthiness requirements is mandatory. The Certification Specifications (CS) from the European Aviation Safety Agency (EASA) state in this respect that:

'if deflections under load would significantly change the distribution of external or internal loads, this redistribution must be taken into account' [1].

The goal of this thesis is to develop an algorithm to enable the identification of flexibility effects on the outer wing within a manoeuvre loads context based on the Maximum Likelihood Method. The main difference with approaches of existing publications is that the models considered here are based on distributed local data rather than on the net effect on aircraft performance. While this requires the size of the specific models to be much larger, the identified models allow a much more detailed physical interpretation of the observed performance benefits or penalties of winglets or wing tip devices.

---

[1] See CS 25.301(c)

First, it was investigated how a winglet or wing tip device works. There are many references that address the topic of aerodynamic performance of wing tip devices and also of winglets in particular. These studies mostly involve addressing the drag benefit due to a wing tip device compared to other devices and/or to a clean wing. These studies are all based on either wind tunnel measurements or pure aerodynamic (CFD) analysis, thus valid for rigid aircraft. These studies are very important in understanding the complicated flow condition at the wing tip in order to arrive quicker at even more efficient designs. However, flight test measurements have shown that flexibility of the airframe has to be taken into account when predicting the (aerodynamic) loads on the winglet.

As a second step, the manoeuvre loads model has been build up. An algorithm was developed that is able to identify the parameters in such a nonlinear coupled aero-elastic loads model. The algorithm is based on the Maximum Likelihood method which is capable of solving even rank-deficient problems. The algorithm is tested by using a simple 2 degree-of-freedom example first. Secondly, the algorithm is tested using simulated measurement data from a slightly adjusted flight loads monitoring model. In both of these cases, the 'real' system is actually known, thus the efficiency and correctness of the algorithm could be verified. Last but not least, the identification procedure is applied for a loads relevant industrial case using real flight test data. The identification procedure is performed five times using these in-flight measurements with modifications in the aerodynamic modelling on the wings and winglets.

The success of the identification of a specific model strongly depends on the structure of the model and the assumed initial values. The model must be sophisticated enough to capture/describe the phenomena contained in the measurements, however simple/small enough to enable its identification with the available computational resources. Due to the very high computational effort involved, it was found to be impossible at this moment to identify *nonlinear* aerodynamic *flexibility* effects on a model of this size and complexity. The identification of just linear flexibility effects, however, shows significant differences between the estimated model and the measurement data. This can be the result of errors in the apriori fixed parameters and/or because of physical phenomena not captured by the model. This linear model could not explain the high load increase observed on the outer wing and winglet as a function of the load factor. Further investigation of the phenomenon on the outer wing proved to be necessary.

Steady Reynolds-Averaged Navier-Stokes simulations of the trimmed flexible aircraft showed pretty good correspondence in the chordwise pressure distributions compared with flight test measurements. The lift coefficient derived from flight test pressure measurements is lower for the two winglet stations compared with the CFD-CSD[2] simulations. The pressure measurement for the winglet stations also show a higher after loading (higher nose down pitch) compared to the simulation. On the other hand, the integral values of the measured pressure distributions at the winglet have limited accuracy, because of the relatively small number of data points.

CFD simulations were used next to investigate loads distributions along the wings equipped

---

[2]CFD-CSM: Computational Fluid Dynamics - Computational Structural Mechanics

with winglets in more detail for the case of an alpha sweep of a rigid airframe.

One model was developed (called 'NL-rigid') that describes the nonlinear rigid behavior and could be optimised in an identification for a best fit to the flight test measurements. It was found that especially the local alpha-gradients on the winglet are much larger in this model as predicted by the corresponding results derived from the original aerodynamic database. These identified gradients were compared with the gradients determined from the CFD-simulations and it was shown that they correspond very well.

The flight loads model was also directly fed with the CFD-derived aerodynamic input data (called 'RANS-model'). The initial model showed good correspondence with flight test measurements. Further optimisation of this model was not possible without getting aerodynamic distributions which were physically improbable.

Two hybrid identifications were performed next. These were based on the same hybrid model (combination of baseline aerodynamics and CFD-data) developed to correct the RANS-model for the flight-to-jig-discrepancy present in the input data. The difference between these two hybrid identifications is only the choice of free parameters. The hybrid model improved the overall loads level, as desired, when compared with the results from the RANS-model. Further optimisation was not found to be possible without getting aerodynamic distributions, which are physically improbable, on the wings and winglets.

The identification algorithm from this thesis was shown to be a very good means to quantify model improvements during model development. Secondly, it can obviously be used to identify the most optimal values for the free model parameters.

M.J. Reijerkerk,
Oberpfaffenhofen, July 2008

Notation

Roman symbols

$\mathbf{A}$	=	State space system matrix
$\mathbf{A}_{JJ}$	=	Aerodynamic influence coefficient matrix
$\mathbf{B}$	=	State space system matrix
$\mathbf{B}$	=	Matrix that is an array of derivatives of the shape functions ($\mathbf{N}$)
b	=	Wing span
$\mathbf{b}$	=	Measurement bias
$\mathbf{b}_f$	=	Parameters of shape functions for correction factor
$\mathbf{b}_{f0}$	=	Parameters of shape functions for initial downwash field
$\mathbf{C}$	=	Damping matrix
$\mathbf{C}$	=	Linear differential operator matrix
$\mathbf{C}_f$	=	Matrix of Shape functions for correction factor
$\mathbf{C}_{f0}$	=	Matrix of Shape functions for initial downwash field
C_L	=	Global lift coefficient
C_{L_0}	=	Lift coefficient at reference condition
C_Z	=	Total wing lift coefficient in stability axis
C_M	=	Total wing moment coefficient in stability axis
c_Z	=	Local lift coefficient in stability axis
$\mathbf{C}$	=	Structural damping matrix
c_l	=	Local lift coefficient
c_m	=	Local pitching moment coefficient
c_p	=	Pressure coefficient
$\mathbf{D}$	=	Diagonal scaling matrix
$\mathbf{D}_{JK}$	=	Differentiation matrix
$\mathbf{d}$	=	Deformation vector
dV	=	Volume element in current configuration

$\mathbf{E}$	=	Stress-strain matrix
E	=	Young's modulus of elasticity
F_Z	=	Total force on wing in z-direction of the stability frame
$\mathbf{F}$	=	Nodal force vector
$\mathbf{F}_{aero}$	=	Vector with aerodynamic forces and moments
$\mathbf{F}_{elas}$	=	Elastic forces due to structural deformation
$\mathbf{F}_{grav}$	=	Gravitational forces
$\mathbf{F}_{ground}$	=	Vector with ground forces and moments
$\mathbf{F}_{inertial}$	=	Vector with forces and moments from inertia effects
$\mathbf{F}_{NK}$	=	Corrected net thrust
$\mathbf{F}_{N}$	=	Actual net thrust
$\mathbf{F}_{thrust}$	=	Vector with forces and moments from propulsion
$\mathbf{F}_{struc}$	=	Aerodynamic forces due to structural deformation
$\mathbf{F}_{x_R}$	=	Vector with aerodynamic forces and moments due to rigid body motion
$\mathbf{F}_{x_F}$	=	Vector with aerodynamic forces and moments due to deformation
$\mathbf{F}_{\delta}$	=	Vector with aerodynamic forces and moments due to control surface deflection
$\mathbf{f}$	=	Nodal force vector for an element
f	=	Eigenfrequency
$\mathbf{f}_J$	=	Panel pressures
$\mathbf{f}_0$	=	Initial pressures distribution
$\mathbf{G}$	=	Spline matrix
G	=	Shear modulus of elasticity
g	=	Gravitational acceleration
$\mathbf{H}$	=	Frequency response function
h	=	Altitude
h	=	Step size
$\mathbf{I}$	=	Unity matrix
$\mathbf{I}$	=	Inertia tensor
J	=	Likelihood function
$\mathbf{K}$	=	Stiffness matrix
k	=	Reduced frequency
l	=	Local chord
l_g	=	Geometric chord
$\mathbf{M}$	=	Mass matrix
$\mathbf{M}$	=	Fisher information matrix
$\mathbf{M}$	=	Moment
M	=	Mach number
M	=	Mass
M_X	=	Integrated moment in X-direction
M_Y	=	Integrated moment in Y-direction
M_Z	=	Integrated moment in Z-direction
$\mathbf{N}$	=	Matrix of displacement shape functions

N	=	Number of data points being analysed
N_E	=	Total number of finite elements
N_N	=	Total number of nodes
N_1	=	Fan speed
N_{1K}	=	Corrected fan speed
n	=	Load factor
n	=	Number of degrees of freedom of the full model
n_n	=	Number of nodes of a finite element
$\mathbf{n}_{panel}$	=	Normal vector of panel
n_E	=	Number of elements
$\mathbf{P}$	=	Distributed surface pressures
$\mathbf{P}$	=	Parameter error covariance matrix
$\mathbf{p}$	=	Position vector
p_0	=	Static pressure
$\mathbf{Q}_{JJ}$	=	Aerodynamic influence coefficient matrix, $\mathbf{Q}_{jj} = \mathbf{A}_{jj}^{-1}$
$\mathbf{Q}_B$	=	Body forces acting on the structure
$\mathbf{Q}_C$	=	Concentrated forces acting on the structure
$\mathbf{Q}_S$	=	Surface forces acting on the structure
Q_i	=	Generalised forces
$\mathbf{q}$	=	Modal coordinate vector
$\mathbf{q}_B$	=	Body forces acting on an element of the structure
$\mathbf{q}_C$	=	Concentrated forces acting on an element of the structure
$\mathbf{q}_S$	=	Surface forces acting on an element of the structure
q	=	Dynamic pressure
q_i	=	Generalised coordinates
$\underline{R}$	=	Position vector of a point in the reference configuration with respect to the global reference frame
$\mathbf{R}$	=	Condensation matrix
$\mathcal{R}$	=	Diagonal matrix with vector of correction factors on its main diagonal
R	=	Electric resistance
S	=	Surface of a general three dimensional solid
S	=	Wing surface
$\mathbf{S}_{KJ}$	=	Integration matrix
$\mathbf{s}$	=	Undeformed position vector
s	=	Surface of a finite element
$\mathbf{S}_{LM}$	=	Summation matrix
$\mathbf{T}$	=	Transformation matrix
$\mathbf{T}$	=	Kinetic energy
T_X	=	Integrated shear loads in x-direction
T_Y	=	Integrated shear loads in y-direction
T_Z	=	Integrated shear loads in z-direction
T_0	=	Static temperature
t	=	Time

U	=	Potential energy
U	=	Displacement vector at any point of the structure due to external forces
U_A	=	Output voltage
U_B	=	Feeding voltage
u	=	Translation vector
u	=	Displacement vector at any point within an element
u	=	Input vector
$\mathbf{u}_F$	=	Deformation of the structure
$\mathbf{u}_K$	=	Deformation of the structure in the aerodynamic degrees of freedom
V	=	Volume of a general three dimensional body
V_0^e	=	Volume of the element in the reference configuration
v	=	Measurement noise
υ	=	Volume of a finite element
W	=	Total work
w	=	Downwash
$\mathbf{w}_j$	=	Panel downwash
$\mathbf{w}_{j0}$	=	Panel downwash due to prescribed angle of attack
$\mathbf{w}_0$	=	Initial downwash
X	=	Nodal displacement vector
x	=	Nodal displacement vector of an element
x	=	Position vector in reference frame of element
x	=	State vector
$\mathbf{x}_R$	=	State vector
x	=	Displacement in x-direction of global reference frame
x_N	=	Center of pressure
Y	=	State vector
y	=	Displacement in y-direction of global reference frame
z	=	Displacement in z-direction of global reference frame
z	=	Observation vector
$\mathbf{z}_F$	=	Nodal coordinates of complete structure

Greek symbols

α	=	Angle of attack
α	=	Index showing the direction in the reference frame
α_0	=	Angle of attack at zero lift ($C_L = 0$)
β	=	Angle of sideslip
β	=	Index showing the direction in the reference frame
Γ	=	Wing dihedral
γ	=	Shear strain
γ	=	Index showing the direction in the reference frame
Δ	=	Small increment
$\Delta\alpha_{elas}$	=	Change in angle of attack due to elastic deformation
$\Delta\mathbf{w}_{Je}$	=	Deformation induced downwash
$\boldsymbol{\varepsilon}$	=	Strain vector
ε	=	Normal strain
ε	=	Computing precision
ε_0	=	Initial strain
$\boldsymbol{\eta}$	=	Innovation
η	=	Dimensionless spanwise coordinate
$\boldsymbol{\theta}$	=	Parameters
θ	=	Rotation
θ	=	Pitch angle
Λ	=	Diagonal matrix with the eigenvalues on its main diagonal (Spectral matrix)
λ	=	Eigenvalue
μ	=	Singular value
ν	=	Poisson ratio
ξ	=	Chordwise position coordinate
$\tilde{\xi}$	=	Modal damping ratio
ρ	=	Material mass density
$\boldsymbol{\sigma}$	=	Stress vector
σ	=	Normal stress
$\boldsymbol{\Sigma}$	=	First Piola stress tensor or Lagrangian stress tensor
τ	=	Shear stress
$\boldsymbol{\phi}$	=	Eigenvector
ϕ	=	Roll angle
ϕ_x	=	Rotation in x-direction of global reference frame
ϕ_y	=	Rotation in y-direction of global reference frame
ϕ_z	=	Rotation in z-direction of global reference frame
Ψ	=	Harmonic acceleration potential
ψ	=	Phase angle
ψ	=	Azimuth angle
$\boldsymbol{\omega}$	=	Angular velocity
ω	=	Circular frequency

Abbreviations

AIC	=	Aerodynamic Influence Coefficient
CFD	=	Computational Fluid Dynamics
CSM	=	Computational Structural Mechanics
DLM	=	Doublet Lattice Method
EPR	=	Engine Pressure Variation
FDAMS	=	Flight Data Acquisition and Management System
GPS	=	Global Positioning System
IAS	=	Indicated Airspeed
IMU	=	Inertial Measuring Unit
INS	=	Inertial Navigation System
ITT	=	Inter-Turbine Temperature
ML	=	Maximum Likelihood
RANS	=	Reynolds Averaged Navier Stokes
TAS	=	True airspeed
WBL	=	Integrated bending moment on the left wing
WBR	=	Integrated bending moment on the right wing
WLT	=	Winglet
WSL	=	Integrated shear force on the left wing
WSR	=	Integrated shear force on the right wing
WTL	=	Integrated torsional moment on the left wing
WTR	=	Integrated torsional moment on the right wing

Contents

Chapter 1

Introduction

The calculation methods for aircraft load predictions are becoming more and more sophisticated, allowing more accurate predictions of the design loads. This means future aircraft can be designed to be bigger, lighter and have better performance. The performance of an aircraft can be even further enhanced by the use of winglets or other wing tip devices.

More accurate engineering predictions imply an increase in the aircraft flexibility as lighter structures can be achieved. A more flexible structure in combination with large dimensions will lead to larger structural deflections. As structural deformations lead to a modified aerodynamic form, the interaction between aerodynamics and structural mechanics is of ever-increasing importance. The aerodynamic performance of wing tip devices for example, will obviously be significantly influenced by the deformation of a flexible wing.

A safe and reliable operational life of the aircraft has to be guaranteed and proven with adequate design calculations. The underlying models must be based on reliable input data and have to be validated by ground and flight tests. This is controlled by regulations drawn up by aviation authorities. For the certification of transport category aircraft compliance of the design with airworthiness requirements is mandatory. The Federal Aviation Regulations (FAR) state in this respect that: *if deflections under load would significantly change the distribution of external or internal loads, this redistribution must be taken into account.*

1.1 Winglets

A big focus in aircraft design is on minimization of total airframe drag. Reneaux presents in [Ren04] hybrid laminar flow (HLF) technology, which means suction of the boundary layer to reduce the skin friction drag, a major drag component (in the order of one half of the total drag). The second major drag component (in the order of one third of the total

drag) is the lift-induced drag for which innovative wing tip devices, like winglets, offer the greatest potential for drag reduction. Techniques to reduce the third component, the transonic wave drag, are presented in [Ren04].

Winglets are upward swept extensions or small lifting surfaces, attached to the outboard end of an aircraft wing. The initial work on winglets was done by Richard Whitcomb at NASA in 1976, see reference [Whi76]. He presented a design approach for winglets that involved the use of vortex lattice methods along with parametric experimentation in the wind tunnel. Kichio Ishimitsu from Boeing wrote also in 1976 an AIAA paper on the design and analysis of winglets, see reference [Ish76]. This paper comprises theoretical and experimental results on a KC-135 aircraft. In 1979 to 1981, NASA Dryden Flight Research Center was involved with general aviation research with the KC-135 aircraft. A winglet concept, developed by Richard Whitcomb of Langley Research Center, was tested on a KC-135A tanker. It was a joint NASA/USAF program to develop and flight test winglets on this aircraft. The results of this program were published in 1981 in reference [Bar81]. The research showed that the winglets could increase an aircraft's range by as much as 7% at cruise speeds.

Many references exist that address the topic of aerodynamic performance of wing tip devices in general and more specifically of winglets. These studies mostly involve addressing the drag benefit due to a wing tip device compared to other devices and/or to a clean wing. Also many publications exist that study specific parameters of a certain wing tip device, such as aerodynamic and geometric twist, installation angle (cant and toe angles). These studies are very important in understanding the complicated flow condition at the wing tip in order to arrive quicker at even more efficient designs. See further section 3.2 where the performance of wing tip devices on a rigid aircraft are discussed.
To meaningfully compare wing tip devices the wing root bending moment (WRBM) is introduced as a means to quantify the influence of a tip device with respect to loads. For the trade-off between alternative designs this is a good parameter to predict the structural (weight) impact of these devices. However, when the design decision is made, a more detailed analysis is required to address the loads along the whole span to enable a safe and efficient wing design. Some references exist that compare in-flight measurements although only on aircraft with relatively rigid wings. For example reference [Dam83] has compared with in-flight test measurements on an agricultural aircraft. Reference [Coi00] describes an experimental study on wing tip devices also for agricultural aircraft. Such aircraft have a relatively small span and thus quite rigid wings.
Furthermore, if flight test measurements are considered, these concentrate on the performance aspects of the wing tip devices (drag, local pressures) and if loads are considered then only in terms of the WRBM. Running loads (loads along the aircraft components) are very rarely addressed.

A recent publication [HG06] has addressed for the first time the aspect of winglets on a flexible airframe of a large transport aircraft. This paper is unique as it considers the influence of a winglet in a multidisciplinary way (combination of an aerodynamic and structural analysis). It is the first known publication that addresses the influence of a

flexible airframe on the winglet performance and it presents the influence on the wing running loads. It considers the transonic cruise condition for which the addition of a winglet to a wing does not simply consist in reducing the induced drag.

Within the Loads field, the focus lies on covering the complete flight envelope, where the cruise condition is not a critical design case for the wing. The flight envelope that is prescribed by the airworthiness requirements, to be interpreted as minimum requirements, is bounded with manoeuvres ranging from -1g to +2.5g. Obviously, for the bookcase of a 2.5g pull-up manoeuvre the largest deformations of the wing will occur. Therefore for loads, accounting for flexibility effects and their consequent effects on aerodynamic behavior is essential for the accurate prediction of the correct outer wing and winglet loads. To arrive at the most efficient wing-winglet design, these should be considered in their combination right from the start of the design process. However, at least in the past, the design and research studies carried out on the winglet topic often consider the aerodynamics separately from the structural aspects, thus basically for a rigid aircraft. In spite of the fact that the flexibility of the airframe and more specific the twist of the wing has a strong influence on the performance of the device. Depending on the shape of the winglet the wing deformation with the winglet on may even spoil the aerodynamic efficiency of the wing and the required structural strengthening may even cancel or overcome the aerodynamic gains in the rigid case. This is all the more true for large devices with significant loading. The global effectiveness of a winglet is rarely established in a comprehensive manner leading to conservative wing plus winglet designs with moderate winglet sizes.

Comparison with flight test measurements showed that structural flexibility has to be taken into account when predicting the (aerodynamic) loads on the winglet. Therefore for loads, accounting for flexibility effects and the possible consequent changes in the aerodynamic behavior is essential for the accurate prediction of the correct outer wing and winglet loads. This obviously explains the special treatment of these devices within this loads investigation.

In [HG06] a Reynolds Averaged Navier-Stokes based method combined with an aeroelastic model was used. They arrived at accurate predictions of the wing deformations and performance although they report that some discrepancy remains in the aerodynamic simulation of the tip of the wing. They also investigated the influence of the different devices on drag and its physical breakdown (wave drag, viscous drag and induced drag). The large winglet configuration is shown to have great drag benefits but also large structural implications. The purpose of this thesis is to improve the loads prediction methods, such that the structural reinforcement and thus additional weight for a wing with large winglet can be reduced such that the large winglet configuration can fully exploit its potential.

1.2   Flexible aircraft modelling

Multi-disciplinary flight dynamics models for rigid and flexible aircraft are used in various areas and stages of the aircraft design process, like for example flight loads analysis

and flight control law design. These models must be sufficiently accurate, but also allow for thousands of simulations in a reasonable amount of time (i.e. be loop-capable). Depending on the application, flight dynamics models need to be available in various forms, like ODEs for nonlinear simulation, linear state space models for control analysis, etc. A major challenge in development of multi-disciplinary flight dynamics models is the handling and integration of data from various sources, removing overlaps, and filling in gaps in case specific data is missing.

During the last decade, the DLR Institute of Robotics and Mechatronics has developed methods and tools for these tasks, as well as for model implementation in various forms suitable for aircraft design analysis. Recently, these aspects have been integrated in a standardized efficient model integration process, called DAMIP (Dynamic Aircraft Model Integration Process).

Also at the DLR Institute of Robotics and Mechatronics an interactive 3D Simulation of the flexible aircraft in realtime is realised. The underlying simulation environment has mainly been developed for the design of flight control algorithms. For the development of the corresponding multidisciplinary aircraft models a flight dynamics library was designed based on the object-oriented modelling language Modelica, see references [Loo08], [Loo99] and [Loo05] for further information.

The previously mentioned DAMIP process uses the data structure of VarLoads, which is developed in cooperation with Airbus, and is backed by appropriate methods and tools. In reference [Kie07] an overview of DAMIP is given, as well as some recent application examples. In reference [Hof03] the VarLoads simulation environment is presented that was developed for special structural dynamics investigations. This environment is characterised by a modular software structure and an object-oriented data structure. The aircraft model and equations of motion can easily be adapted to the required level of detail. The data structure generated by the pre-process of Varloads was also used in this investigation. Some adjustments were made to this pre-process to allow for the modelling variants that are presented later in this thesis.

For the present investigation, it is desired to exclude possible integration errors from the time simulation. Therefore, the simulating part of VarLoads was not used here. Instead, a software-script is developed for the integrated fully flexible aircraft model that is directly fed with the measured aircraft states. For the present application, taking into account the quality of the specific flight test instrumentation, the states of the aircraft can be considered to be measured with sufficient accuracy.

The derivation of the nonlinear equations of motion for an elastic airplane was presented by Waszak in 1986 and again in 1988, see respectively references [Was86] and [Was88]. For airframes with sufficient rigidity or stiffness, wide frequency separation results between those natural modes of the aircraft dominated by the rigid body degrees of freedom and the remaining modes dominated by the elastic degrees of freedom. Therefore, aircraft dynamic modelling, analysis and synthesis activities frequently address either the rigid body dynamics or the structural dynamics.

With the development of larger aircraft and the desire for lighter structures for improved fuel economy, by the use of new materials (e.g., composites), etc., there is an increased potential for significant contributions from aero-elastic effects in the dynamic response

of flight vehicles of the future to pilot input and/or atmospheric turbulence. Not only can the dynamic response due to aero-elastic modes themselves become significant, but coupling between the aero-elastic and the rigid-body degrees of freedom can noticeably alter the rigid body dynamics of the vehicle. Consequently, it is not always justified to decouple between rigid body dynamics and structural dynamics. The model that accounts for the coupling between flight mechanics and aero-elasticity is called the integral model. Schuler presents in reference [Sch97] the integral modelling approach (in the frequency as well as in the time domain) and control law design for a large highly flexible aircraft. In [Teu03] Teufel investigated the effect of 2D gusts on aero-elasticity and flight mechanics using the integral model.

In [Was87] a simulation experiment is described that addresses the effects of structural flexibility on the dynamic characteristics of a generic family of aircraft. The simulation was performed using the NASA Langley Visual/Motion Simulator facility and the results comprised complete response data together with pilot ratings and comments. It is observed that increased flexibility can lead to increased tracking errors, degrading handling qualities and changes in the frequency content of the pilot inputs. Damveld presented in reference [Dam05] the influence of unsteady aerodynamics and trimming on the dynamics of an aero-elastic aircraft, also based on the equations derived by Waszak and Schmidt in [Was88]. Buttrill derived in reference [But87] the equations of motion while accounting for inertial coupling. Reschke presented in reference [Res05] a dynamic simulation of a large transport aircraft to show the influence of inertial coupling terms on the simulation and loads computation.

The focus in this thesis is on the field of static aero-elasticity. In static aero-elasticity, the effect of the structural deformation on the aerodynamic coefficients and on the related pressure distributions is studied. It differs from the more general aero-elastic problem by the fact that the elastic displacements are supposed slow enough to neglect the structural inertia and damping forces. The external forces are therefore in static balance with the elastic forces, these external forces depending themselves on the elastic displacement. The static aero-elastic forces have a strong impact on the handling qualities of the aircraft.

Different methodologies exist to deal with the loads computation of the 'statically flexible' aircraft. One method is based on the direct coupling of the aero and elastic forces (direct solution of the aircraft equilibrium equations imbedding the relationship between the elastic and aerodynamic forces). The merit of this approach is that it is extremely straightforward since it allows a 'one-shot' computation of the loads.

This one-shot computation of the loads computation refers to the fact that the loads computation process can be seen as a two step procedure. The two steps would be the following: The first step is the solution of the global balance, requiring global data. The second step is typical for the loads problem, that is the computation of the local loads on each point of the structure, requiring load distribution data. There is, however, a coupling between the two due to the elastic deformation of the aircraft, therefore this direct coupling of the two is the more accurate approach.

A second method to deal with the loads computation of the 'statically flexible' aircraft is based on the pre-computation of the elastic forces due to each flight mechanics parame-

ter (angle of attack, control surface deflections, load factors, angular accelerations, etc.).
These forces are computed by constraining the Finite Element model in an empirical but
physical manner, i.e. no displacements for two points at the wing root. These forces
when integrated provide a kind of corrective term due to the flexibility to be added to the
basic 'rigid' aerodynamic coefficient. For example the global lift slope will be the sum of
the 'rigid' derivative measurable in the wind tunnel, plus this elastic part. In this thesis,
the first method will be used, that directly couples the aerodynamic and elastic forces.
A general overview of the field of aircraft aero-elasticity can be found in reference
[Liv03]. Emerging trends, as well as challenges and needs in the field of aircraft aero-
elasticity are surveyed and discussed, completed with an extensive bibliography.

There are certain regions within the possible range of angle of attack (both in positive
as in negative direction), where the aerodynamics gets more and more nonlinear. In this
thesis, a method is presented that accounts for nonlinear aerodynamics in combination
with a flexible airframe. The linear model will not give accurate results, if there are some
regions on the aircraft, where the effects of nonlinear aerodynamics get significant. This
might be because of wing stall, which is a pure aerodynamic nonlinearity. Furthermore,
the wing structure can be deformed so much that the outer wing 'sees' an angle of attack
that significantly differs from that in the rigid case. This change of effective local angle
of attack can also interact with the local nonlinear aerodynamics. Consequently, a more
advanced procedure is needed to account for local airframe deformation in combination
with aerodynamic nonlinearities.

1.3   Loads measurement

Knowledge on the mechanical stress inside the material of the structure is important to
evaluate the exposure of the material to loading. Direct measurement of mechanical
stresses is practically impossible during operating conditions. A practical method to de-
termine the material stresses experimentally is based on the discovery done by Robert
Hooke in 1678. He discovered a relationship between material stress and the resulting
deformation. This deformation, called 'strain', appears at the surface of the object. Con-
sequently, it is accessible for measurement.
In the beginning, these measurements were performed mechanically using complicated
constructions. These measuring devices had only limited application, see further [Hof87].

From about 1935, people got aware in this context of the effect published already in
1843 by Charles Wheatstone. The effect that is meant is that of the change in the resis-
tance of an electric conductor through the influence of mechanic loading. It took over 80
years until this phenomenon was used technically. One of its reasons is that the change
in resistance of a wire loaded by tension is very small. The development of amplifiers
first established the necessary premises.
Around 1938, two people, Edward E. Simmons and Arthur Claude Ruge, independently
developed the idea further to use this effect for measuring purposes, see reference [Hof87].

The actual 'electric resistance-strain gauge with bonded grid' as it is known now, was invented by Arthur Claude Ruge of the Institute for Seismology from the Massachusetts Institute of Technology. Here, only such electric resistance strain gauges will be considered. For more information on other types of strain gauges one is referred to [Hof87].

Environmental circumstances like high pressures or magnetic fields, temperature and humidity have an influence on the behavior of strain gauges. A description of these influences can be found in reference [Kli06]. Changes in temperature affect mostly the point of origin of the measurement value of the strain gauge. This error can be limited to an acceptable amount by selecting self-compensating strain gauges or by applying an adequate compensation method. An example of such a compensation method is presented in reference [Wel80].
The compensation principle of the Wheatstone bridge is that disturbances that influence both neighboring branches of the Wheatstone bridge, have a different sign and thus diminish or even cancel each other in the output voltage.

In the present investigation, structural loads, such as shear force[1], bending moment and torsion along structural components, are measured using strain gauges. Such a structural load can generally not be measured by a single strain gauge, but should be determined from a combination of multiple strain gauges. The optimal number of strain gauges and their positions can be determined from a loads calibration procedure.
Contrarily to the measurement of local stresses, the selection and calibration of the strain gauges gets more complicated or less straightforward. Although the use of a strain gauge for loads measurement is in some respect similar to its use in stress determination, a somewhat different approach is required since now strain is to be used as a means of obtaining information about the loads.
In one loads calibration method, a series of point loads is applied to the structure. The loads equations are then derived via a least squares curve fitting algorithm using the strain gauge responses to the applied loads. An example of such a method that is used often in praxis, is the method developed by T.H. Skopinski, W.S. Aiken and W.B. Huston in 1954, see reference [Sko54]. In this method the parameters of the so-called Skopinski-equations (loads equations) are determined. However, the structure is usually highly instrumented with strain gauges and the number and selection of gauges used in the loads equation can be problematic. In reference [Nel94] an improved technique is presented that uses a genetic algorithm to choose the strain gauges used in the loads equations. The performance of this genetic algorithm is also compared with that of the so-called T-value technique and the Best Step Down technique, see [Nel94] for more information on these methods.

Another difficulty in the measurement of structural loads stems from the fact that the aircraft structure is not loaded under one discrete force/moment, but by distributed gravitational loads, external pressure distributions, etc. There are many possible loading conditions. Each of these loading conditions have a contribution to the stress as measured

---

[1] These shear forces are not to be confused with the shear stress τ

locally. These stresses are the sum of stresses from torsional loads, bending loads, et cetera. It is very difficult to determine which portion was caused by which load.

In reference [Lok04] a parametric study is presented of various aircraft wing-load test features that affect the quality of the resultant derived shear force, bending moment and torque strain gauge load equations. The effect on the accuracy of the derived strain gauge equation has been compared for: single point loading compared with distributed loading, variation in applied test load magnitude and number of applied load cases. The object of study in reference [Lok04] has been an extensive wing-load calibration test of the (Active Aeroelastic Wing) F/A-18 aircraft. It was shown that the distributed-loading approach generally yields superior results when compared to those derived from a single-point loading approach. This can mainly be explained by the much higher total net load produced in the distributed loading cases than in the single-point loading cases. In the single-point loading cases, only a small amount of the load envelope can be exercised by the loading. This is a typical limiting factor of single-point loading. When loads are introduced to the test structure through surface-contact load pads, there is often a surface peak pressure limit, as imposed by local skin bending or substructure-crushing considerations.

The effect of load magnitude was also studied separately in reference [Lok04] and was found to be significant. However, in the test a peak of 70% design limit load was applied, where it was found that already 50% of design limit loads would have given similar results. Although two dozen of distributed-load cases were available, it was also shown that only 6 diverse distributed-load cases would already lead to satisfactory equations.

Pressure distribution methods permit the determination of aerodynamic loads in flight without corrections for inertia effects. The pressure measurement installations must however be very complete in order to obtain accurate load data. The time of installation and data reduction might be very lengthly. Therefore, the general use of pressure distribution methods in the measurement of loads on aircraft in flight is avoided, except when specific detailed load-distribution data are desired. A comparison of wing loads measured in flight on a fighter-type aircraft by strain gauge and pressure distribution methods has been performed in reference [Aik49].

In this thesis, the comparison with the pressure measurements can be seen as spot checking the CFD-CSD results. If the comparison is good for those checks, the detailed distributed data from the CFD-CSD results can then be used to determine the complete load distributions. These results can then again be checked with the loads measurements that used strain gauges. The information contained in the pressure and loads measurements only is too little such that they can be combined straight away. The CFD-CSD calculations might provide the missing link between the two. However, it is obvious that the CFD-CSD calculations must be of high quality to describe the real phenomenon accurate enough.

1.4   System identification

System identification is the process of determining an adequate mathematical model with unknown parameters, where the parameters have to be determined indirectly from measurement data. In case the model structure is kept fixed, this process is called parameter estimation. The theory and practice of aircraft system identification can be found in references [Kle06] and [Jat06].

Traditionally, aircraft parameter identification is the process of extracting numerical values for the aerodynamic stability and control derivatives and other subsidiary parameters (sensor errors, wind gusts, etc.) from a set of flight test data. Accurate knowledge on the stability and control derivatives is needed to arrive at accurate mathematical models that these coefficients provide. These mathematical models are used to provide input to simulators or to provide a basis for the design of flight control systems. This has been a field of investigation since about 1948.

The stability and control derivatives have been identified for all kind of aircraft, but have been restricted to values for the total aircraft (integrated values). However, the loads model is a distributed model, where knowledge of the distributed loads and thus the aerodynamic *distributions* are needed. Today, due to the large increase in computational power it has become possible (at least for research projects) to use the distributed aeroelastic models even for real-time flight simulators as well. Therefore, the extension of this procedure to the type of model as it is used in the loads departments of aircraft manufacturers, is a natural step and it will be of increasing importance.

The focus here will lie on a parameter estimation method that is suitable for a phenomenological model based on physical insight. Developing such a model, which is usually preferred, because it leads to better understanding of the underlying physics, can be highly demanding. Alternatively one could make use of neural networks that are used for pattern recognition. They provide a general framework for nonlinear functional mapping of the input-output subspace. They provide less physical insight, but are very capable methods in cases that are highly nonlinear. More information on the procedure with neural networks can be found in [Jat06].

The principal elements of the aircraft identification process are:

- the identification algorithm,

- the flight control input,

- the instrumentation.

The success of the identification process is totally dependent on all three of these elements. This thesis is focussed on the first aspect, the development of an identification technique for the loads model based on the Maximum Likelihood criterion.

In reference [Mul86] a technique is described for the optimization of control input signals. Information on the general arrangement of a flight test instrumentation system can also be found in this reference.

Furthermore, the parameter-state estimation problem of dynamic flight tests is discussed in detail in reference [Mul86]. It is shown that under certain conditions the parameter-state estimation problem can be solved in two consecutive steps pertaining to the reconstruction of the state and the estimation of the aerodynamic model parameters respectively. This technique is called the two-step method (TSM). In reference [Mul99] it is focussed on the first step of the TSM, often referred to as 'flight path reconstruction'. Requirements with respect to type and quality of flight test transducers are also discussed in this reference. In [Mul99] an overview is also presented of different approaches to the solution of the flight path reconstruction problem with emphasis on Kalman filter/smoother and Maximum Likelihood methods.

The Maximum Likelihood (ML) identification technique has originally been developed by Systems Control, Inc. (SCI) in 1970 to reduce data from flight tests where gusts were present. In such cases both the measurement noise and process noise statistics were identified. In [Gro72], an output error method based on the ML method is described for a rigid body aircraft model.

There have been many methods proposed and tried for extracting stability and control derivatives from flight data. It is described in reference [Ste73] that most of these have proved to be successful only under idealized conditions such as in the absence of wind gusts or modelling errors and known instrumentation accuracies. Often a significant amount of flight test data has to be discarded, because there is no technique general enough to process it under less than ideal conditions. The development of the ML identification technique has given rise to the realization that much of the previously discarded data can be successfully processed. The limitations of the instrumentation system, flight control input and inadequate aerodynamic model are recognized and compensated for. Furthermore, the presence of wind gusts can be included in the model structure and can be accounted for in the identification algorithm. These aspects make that the best set of identified values for the stability and control derivatives can be obtained.

In reference [Ste73], four different approaches to identifiability problems are presented:

- Fixing parameters,

- A priori weighting,

- Constrained optimization,

- Rank deficient solutions.

The usual remedy for parameter dependencies has often been to fix some of the dependent parameters during identification. This generally improves the numerical convergence. The basic reasons why the parameter fixing technique does not always work are the following. The correlation is usually not simply between pairs of parameters, but may involve the entire set of unknown parameters. Secondly, the choice of a particular parameter to fix and the value at which it is fixed are generally not clear.

If a range of allowable values or relationships between the parameters can be specified, from practical or theoretical considerations, they can be used as constraints on the parameter estimates. Such a procedure would require a constrained optimization technique. Including such parameter value constraints will most probably also reduce the convergence rate.

Without any of the above shortly described remedies, the parameter identifiability problems will usually appear as a difficulty with inverting the information matrix and obtaining accurate parameter estimates and error covariances. In such a case, a rank deficient solution for the inverse rather than a full rank solution might be better.

In reference [Ste73] a comparison of results is presented between the rank deficient solution, the fixing parameters and the a priori weighting technique for a three state model. It is shown there that the rank deficient solution gives the best estimates.

The optimisation algorithm will be based on the Gauss-Newton method. The Gauss-Newton method (or alternatively Levenberg-Marquardt method) delivers information on the statistical accuracy of the estimates as a by-product. This is, besides the fast convergence, one of the advantages of this method when compared with other optimisation methods such as Powell's, Jacob's, simplex or subplex, see further reference [Jat06].

The Levenberg-Marquardt method augments the information matrix ($\mathbf{M}^{-1} = (\mathbf{M}_0 + k\mathbf{A})^{-1}$, where the matrix $\mathbf{M}_0$ is the original information matrix) to improve its conditioning and thereby produce a more reasonable inverse. More information on this method can be found in references [Kle06], [Lou05] and [Nie99].

The Bayes-like method improves the conditioning of the information matrix by combining the measured data with prior estimates of some or all of the unknown parameters in the model. A weighting technique is performed using the confidence of certain parameters. More details on this method can be found in [Kle06].

A good reference that deals with the most common numerical difficulties encountered when implementing the Newton Method on a digital system is [Den96]. It deals with numerical methods for unconstrained optimization and nonlinear equations for algorithms that are all based on Newton's method. Many real problems are poorly scaled, meaning that the sizes of the variables differ greatly. For example, one variable may always be in the range 10^6 to 10^7 and another in the range 1 to 10. It is stated in reference [Den96] that most of the work in this field did not pay attention to the problem of scaling.

1.5   Goal of the thesis

The goal of this thesis is to develop an algorithm to enable the identification of flexibility effects on the outer wing within a manoeuvre loads context based on the Maximum Likelihood Method. The main difference with approaches of existing publications is that the models considered here are based on distributed local data rather than on the net effect on aircraft performance. While this requires the size of the specific models to be much larger, the identified models allow a much more detailed physical interpretation of the

observed performance benefits or penalties of winglets or wing tip devices.

First, it will be investigated how a winglet or wing tip device works. Secondly, the manoeuvre loads model will be build up. Then an algorithm will be developed that is able to identify parameters for a nonlinear coupled aero-elastic loads model. The algorithm will be tested using a simple example first. Furthermore, the algorithm will be tested using simulated measurement data from a slightly adjusted flight loads monitoring model. In these cases, the 'real' system will be actually known, thus the efficiency and correctness of the algorithm can be verified. Last but not least, the identification procedure is applied for a loads relevant industrial case using real flight test data. The identification procedure is performed five times using these in-flight measurements with modifications in the aerodynamic modelling on the wings and winglets.

1.6   Outline of the thesis

The structure of this thesis is as follows. In **chapter 2** the requirements and necessary background information of the manoeuvre loads context in aircraft design are presented. It is shown that within the complete loads context, the subject addressed here falls within the field of static aero-elastics.

The loads model concerned with the determination of the loads due to in-flight manoeuvres is called the Manoeuvre Loads Model. Loads models must be developed to simulate the design manoeuvres prescribed by the airworthiness requirements (FAR/CS). These models must be based on reliable input data and should be validated by ground and flight tests.

The Manoeuvre Loads Model is also necessary to monitor the loads on the aircraft during flight tests. In flight test, it is used to anticipate the load level expected during particular manoeuvres required for the flight test program. This model is usually the same as that used for the assessment of the design loads. However, this flight test model may additionally imbed several realistic features that are important to reconstruct the exact detailed conditions for arbitrary flight test manoeuvres. The model presented in this report is an example of such a 'flight test manoeuvre loads model'. The model presented in this report will not be used to perform typical manoeuvre loads computations as prescribed by the rule, such as a Rolling Manoeuvre, a One-engine-out case, etc. The model presented in this report is used to reconstruct specific flight test manoeuvres, performed to address specific static aero-elastic effects.

Chapter 3 presents design aspects of wing tip devices in general and of winglets in particular. An overview is given of the possible alternatives in wing tip devices. The advantages and drawbacks of one of these devices in specific, the winglet, are described, as well as its implications on aircraft design.

The airflow around winglets is complicated and winglets have to be carefully designed and tested for each aircraft. The manufacturer who wants to install a winglet has to

balance the aerodynamic gains with the structural impact. The design and research studies carried out on the winglet topic often consider the aerodynamics separately from the structural aspects, thus basically for a rigid aircraft. However, the flexibility of the airframe and more specific the twist of the wing has a strong influence on the performance of the device. Flight test measurements have also shown that the flexibility of the airframe has to be taken into account when predicting the (aerodynamic) loads on the winglet. Therefore for loads, accounting for flexibility effects and the possible consequent changes in the aerodynamic behavior is essential for the accurate prediction of the correct outer wing and winglet loads.

In **chapter 4** all necessary modelling aspects and calculation techniques can be found that are of importance for the loads model used here. The first section of this chapter presents some of the basic and important aspects of the theoretical background of finite element modelling. The finite element method is the most convenient and accurate method for the analysis of large-scale structural systems with complex geometry, load conditions, material combinations, boundary conditions and geometrical and material nonlinearities.

In loads analysis, a large amount of flight conditions and loading conditions must be covered. This necessitates a reduction of the degrees of freedom of the complex, highly detailed finite element model in order to have a cost and time efficient model. The number of degrees of freedom can be reduced in several ways. Section 4.2 presents some methods of model reduction. The oldest and most popular one is the static or Guyan reduction.

In section 4.3 the equations of motion of an unconstrained elastic aircraft are derived, that builds the flight dynamics model for an aero-elastic vehicle. Section 4.4 presents the aspects of importance for the aerodynamic model. It describes how the aerodynamic load distributions can be determined from experimental data, derived for example from wind tunnel tests, complemented with CFD-analysis. It gives a short overview of the theoretical models and describes the doublet/vortex lattice method in more detail. It is also presented how the vortex lattice model can be corrected for nonlinear aerodynamics. The aerodynamic loads due to aircraft deformation are the topic of section 4.5. In order to determine the correct deformation of a wing that has wing mounted engines, it is important to have a detailed thrust model. Such a thrust model is presented in section 4.6. One of the last topics of this chapter are the spline techniques. The interconnection of the structure with the aerodynamics is modelled by a spline matrix. This interconnection is a very important aspect of an aeroelastic analysis. The derivation of the integrated loads vector from the nodal force vector is the topic of section 4.8.

Chapter 5 presents the theory for the flight test identification based on the Maximum Likelihood Method, together with some practical applications of the algorithm for a simple 2 degree-of-freedom example.

The focus here will lie on a parameter estimation method that is suitable for a phenomenological model based on physical insight. Developing such a model, which is usually preferred, because it leads to better understanding of the underlying physics, can be highly demanding.

The Maximum Likelihood Method is presented in section 5.3, where the Likelihood function is derived and the optimization algorithm is presented. Section 5.4 discusses the symptoms and causes of identifiability and uniqueness problems and presents a rank deficient solution procedure. In section 5.5 some important numerical aspects are addressed, such as line searching, scaling, the calculation of a sensitivity matrix, etc. Finally, some practical applications are presented of the algorithm for a simple 2 degree-of-freedom example. One that has a nonsingular information matrix and one that has a singular information matrix.

Chapter 6 presents the industrial application of the flight test identification technique using different aerodynamic models.
First, a general description of the flight test instrumentation system is given in section 6.1. In the present investigation, structural loads, such as bending moment and torsion along structural components, are measured using strain gauges. Section 6.2 therefore gives a thorough description of the loads measurement by strain gauges. Contrarily to the measurement of local stresses, the selection and calibration of the strain gauges gets more complicated or less straightforward.
Section 6.3 presents the flight loads monitoring model. For the specific identification examples, the part that describes the aerodynamic modelling for the flight loads monitoring model, is varied. The identification of a theoretical model is used to check the algorithm from chapter 5 where the 'real' system is still exactly known. The remaining part of the chapter is devoted to the actual identification using the real flight test measurements for alternative aerodynamic models.
The first approach assumes correct rigid body aerodynamics and modifies only aspects of the model that describe the aerodynamic loads due to deformation of the airframe. In section 6.6 it is investigated, using steady Reynolds-Averaged Navier-Stokes (RANS) simulations, whether dropping the assumption of correct rigid aerodynamics could improve the correspondence with the flight test measurements. Section 6.7 presents and optimizes an aerodynamic model that describes the rigid aerodynamic effects on the wings and winglets as second order functions of the angle of attack. Section 6.8 presents and optimizes the models that are based on aerodynamic input data derived from CFD calculations. In section 6.9 a summary of the proposed methods is given. Model validation is the topic of section 6.10, where it will be dealt with issues related to the process of determining the correctness, accuracy, adequacy and applicability of the identified model.

Finally, the conclusions will be drawn in **chapter 7** and the recommendations are presented in **chapter 8**.

Chapter 2

Design loads requirements

This chapter gives an introduction in the main aspects of the design loads determination that are of concern in the present investigation. It is by no means a complete overview of this field. The field of loads analysis is very large and each subject has, apart from the general aspects, its very own special rules from the airworthiness requirements for example, such that a detailed description goes beyond the scope of this report. See also reference [Squ05] for a more extensive treatment of loads requirements and computations.

An overview of the subjects that have to be addressed during the loads analysis in aircraft design:

- Static aero-elasticity.

- Loads due to in flight manoeuvres.

- Loads due to atmospheric turbulence.

- Ground loads.

- Interaction between structural loads and the Electronic Flight Control System (EFCS).

- Interaction between the landing gear design and the structural loads.

- Fatigue loads.

- Loads in system failure conditions.

- Primary control system and control system loads.

- High lift devices loads.

- Engine and engine strut loads.

- Special Loads analysis:

  - Pressurisation loads.

  - Emergency landing.

  - Heavy landing.

  - Crash.

  - Ditching.

  - Sustained engine imbalance - wind milling

Notice that also combinations of these topics have to be addressed, for example: engine and engine strut fatigue loads, etc.

The investigation of this report can be seen as a research topic within the combined field of the first two bullet points: static aero-elasticity and loads due to in flight manoeuvres. The general aspects of loads analysis and special topics that are of importance in this investigation will be presented in this chapter.

2.1   Aviation authorities

In 1970, the National Civil Aviation Authorities of the European Union member countries, plus those of some other countries in Europe formed an association. This association was called the Joint Aviation Authorities, or JAA. One of the main objectives was to develop and implement common rules and procedures governing safety in civil aviation. These common rules and procedures developed by the JAA were published in a set of documents called Joint Aviation requirements or JARs. However, the JAA was an association or 'club' with no authority over the member countries. This gradually produced multiple variants of the JARs, due to national interpretations of the common rules and procedures. The need for a real European Aviation Authority emerged. Europe needed an Authority that was the equivalent of the Federal Aviation Administration (FAA) in the United States. On September 28th, 2003 the European Union set up a transnational Civil Aviation Authority. This authority is called the European Aviation Safety Agency or EASA. The old JAA will be referred to as the EASA - meaning the European Aviation Authorities - from this point forward. The previously named Joint Aviation Requirements or JARs are now called Certification Specifications or CSs.

2.2   Loads basic principles

The external loads are a fundamental input to structure designers and to stress specialists throughout the aircraft design process. This design process starts from the establishment of the design principles and ends with the certification of the aircraft through the delivery of the manufacturing drawings of the airframe structures. There are four steps in aircraft development that must be supported by suitable loads information: Pre-design phase (identification of design solutions and assessment of component weight objectives), Design phase (final sizing and detail drawings), Check stress (sizing verification)

and Certification (final validation).

There are several different types of loads classifications. Loads can be classified into the three categories: static strength loads, fatigue strength loads and residual strength loads, depending on the type of structural analysis they are aimed for.
Depending on the phase in which they can be met, the loads can also be classified as flight loads and ground loads. Here, the focus lies mainly on the flight loads. Depending on the type of aeroplane model necessary for their calculation, the loads can be classified as: static or quasi-static loads and dynamic loads.

The loads model is the crossing point of several disciplines. The loads specialist can therefore be seen as one of the main integrators in the design office of an aircraft manufacturer. Many synergies exist between the loads activities and other design and development processes. This can be explained by the fact that in order to determine reliable loads, the movement of the aircraft in flight and on the ground has to be accurately described.

Civil aircraft have to comply with the FAR (Federal Aviation Requirements) rules in the USA, or with the almost equivalent EASA CS rules in Europe. These rules give minimum requirements for structure design and qualification/certification according to the usage of the aeroplane (military or civil), the category of the airplane, etc.
The FAR/CS 25 is applicable to transport category aircraft, where most of the loads requirements are defined FAR/CS in subpart C (Structure). Other side requirements are also defined in the subparts: B (Flight), D (Design and Construction), E (Powerplant), F (Equipment) and G (Operating Limitations and Information).

The basic CS 25.301 Loads Requirement:

(a) Strength requirements are specified in terms of **limit loads** (the maximum loads expected in service) and **ultimate loads** (limit loads multiplied by prescribed factors of safety). Unless otherwise provided, prescribed loads are limit loads.

(b) Unless otherwise provided, the specified air, ground and water loads must be placed in equilibrium with inertia forces, considering each item of mass in the aeroplane. These loads must be distributed to conservatively approximate or closely represent actual conditions. Methods used to determine loads intensities and distribution must be **validated by flight load measurement** unless the methods used for determining those loading conditions are shown to be reliable.

(c) If **deflections** under load would significantly change the distribution of external or internal loads, this redistribution must be taken into account.

2.2.1 Static strength loads

In this report it will be concentrated on the static strength loads. The static strength loads are the loads to be used for static strength assessment. They ensure the structure to have

adequate strength to withstand extreme and very rare events implying the highest stress. The scenarios (manoeuvres, gust encountering, etc.) to be considered for static strength loads are defined in:

- the relevant basic regulation (FAR/CS).

- special conditions issued by the Airworthiness Authorities. Special Conditions take into account particular features of the aircraft not captured in the existing rules.

- in-house rules, describing loads scenarios derived from the experience of the manufacturer.

The loads evaluated for each prescribed scenario by the appropriate aircraft model provide a loading condition called limit loads. The limit loads must be factored by a coefficient, called the safety factor, to obtain ultimate loads.

The value of the safety factor is prescribed by the regulation:

CS 25.303 Factor of safety:

- Unless otherwise specified, a factor of safety of 1.5 must be applied to the prescribed limit load which are considered external loads on the structure. When a loading condition is prescribed in terms of ultimate loads, a factor of safety need not be applied unless otherwise specified.

In general the factor of safety is thus equal to 1.5. Lower values may be prescribed for more rare events. For example, extreme loads conditions due to rare events (manoeuvres, gust,..), experienced by an aircraft with failure of a system that can interact with the load level itself, call for a safety factor ranging between 1 and 1.5 according to the probability of the failure.
Other extremely rare events, such as fan blade failure or a landing impact with one or more landing gear retracted, are considered ultimate loads conditions. Thus according to the above regulation on the safety factor, a safety factor of 1 is prescribed for these conditions.
The safety factor was not initially intended to account for the probability of the event. It was intended to cover uncertainties on the definition of the load condition, the approximation in the loads model, the uncertainties in the material properties, the manufacturing tolerances, the approximation in stress analysis and/or on test execution. More recently the regulation trend is to include in some extent the safety factor in the frame of an overall objective in terms of 'tolerated' risk. This is similar to the approach widely applied in the system safety assessment.
Limit loads are the maximum loads anticipated on the aircraft structure during its lifetime. It must be demonstrated that the structure, when submitted to limit load conditions, does not suffer permanent detrimental deformation. Moreover, it must not loose its operating capability. It must be possible, for example, to deflect a control surface under limit loads. The limit loads ensure an adequate level of protection against local damages

due to extreme (about once per lifetime) events. The airworthiness of the airframe is
also ensured by the ability in detecting these events on each individual aircraft in service
to trigger the necessary maintenance actions. Obviously, the means for detecting such
events are relatively limited. Nevertheless, the design limit loads level, together with the
existing detection techniques can be considered adequate to ensure satisfactory continu-
ous airworthiness.

Furthermore, each aircraft structure must be able to sustain the ultimate loads without
rupture. Generally, the demonstration of the capability of the structure to sustain ulti-
mate loads is based on theoretical analyses and validated by static tests. During such a
test the structure must sustain ultimate loads during at least three seconds without col-
lapsing. The ultimate loads prescribed by the rule ensure adequate strength to withstand
loads arising from extremely rare events. A fundamental role is played by the safety fac-
tor applied to the limit loads. This has the effect of lowering the probability of structural
failures well below the probability of meeting limit loads conditions.

The load conditions requiring the highest static strength are fortunately rather rare events,
far from the events experienced in normal daily operation. When these events occur, they
present an array of different features. It is therefore quite difficult to prescribe a complete
set of detailed scenarios capturing all possible events. Even if the rules prescribe more
or less complex assumptions and modelling, these conditions still remain more or less
arbitrary. However, the past has shown that these simplified cases are able to provide a
satisfactory safety level.

Flight envelope
The analysed flight conditions (speed and altitude), must cover in an exhaustive manner
the flight envelope defined by the certified range of operational altitudes and by the struc-
tural design speeds and the minimum/maximum load factor prescribed by the rule, see
figure (2.1).

It is impossible to analyse all potential manoeuvres the aircraft may be faced to. There-
fore, a limited set of manoeuvres have to be defined that provide an adequate level of
strength.

2.2.2   Static aero-elasticity

In principle the classical aerodynamic data refer to a 'rigid' aircraft. The wind tunnel
tests are in general performed using a quite rigid model with the targeted cruise distorted
shape.

The static aero-elastic methodologies give the knowledge of the aerodynamic behavior
of the flexible aircraft. The flexible aircraft aerodynamic derivatives are a function of the
Mach number and the dynamic pressure, whereas the rigid aircraft derivatives depend
only on the Mach number.

In static aero-elasticity, the effect of the structural deformation on the aerodynamic co-
efficients and on the related pressure distributions is studied. It differs from the more
general aero-elastic problem by the fact that the elastic displacements are supposed slow
enough to neglect the inertia and damping forces. The external forces are therefore in
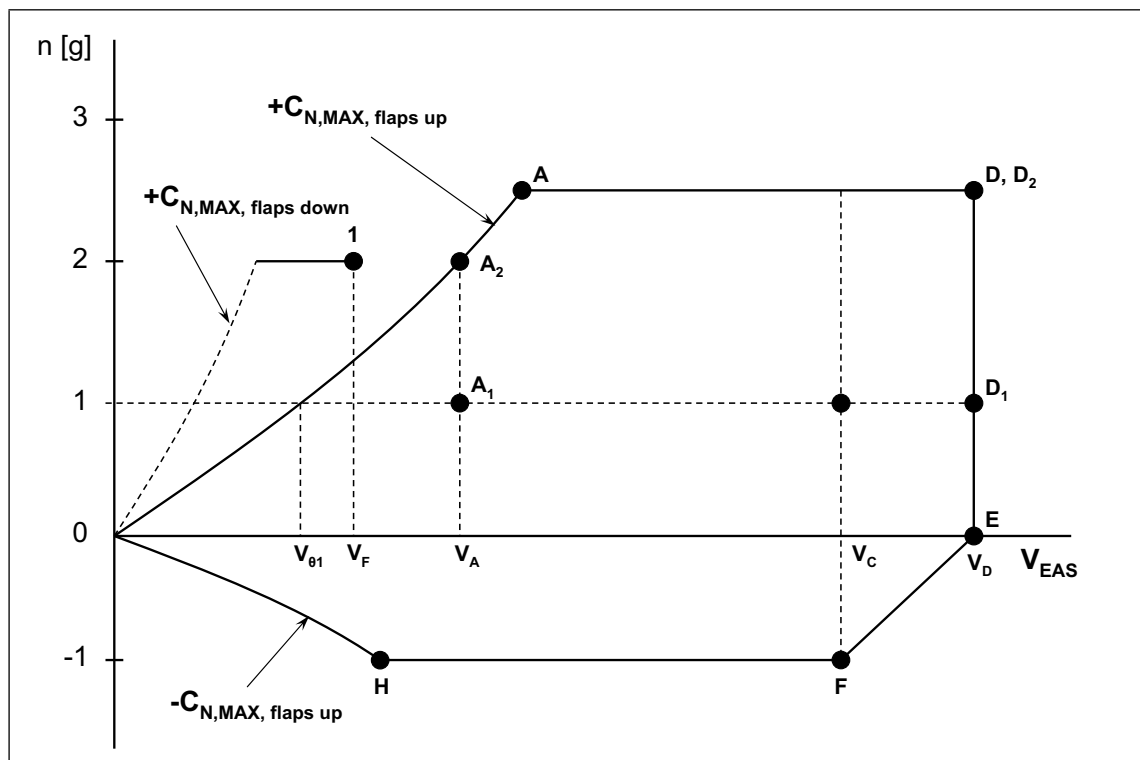
Figure 2.1: *Flight envelope, image according to FAR 25 Subpart C Section 25.333 (http://www.airweb.faa.gov/). Plotted is the Load factor n versus the equivalent airspeed V_{EAS}.*

static balance with the elastic forces, these external forces depending themselves on the elastic displacement.

The static aero-elastic forces have a strong impact on the handling qualities of the aircraft.

The FAR/CS rules explicitly require in 25.301(c), as was shown before, that the effect of the aero-elastic distortion on the loads is taken into account.

There are two effects of the aero-elastic distortion on the loads. First, it modifies the aircraft response to a pilot input. Secondly, it modifies the aerodynamic loads distribution for a given aircraft response.

Different methodologies exist to deal with the loads computation of the 'statically flexible' aircraft. One method is based on the direct coupling of the aero and elastic forces (direct solution of the aircraft equilibrium equations imbedding the relationship between the elastic and aerodynamic forces). The merit of this approach is that it is extremely straightforward since it allows a 'one-shot' computation of the loads.

This one-shot computation of the loads computation refers to the fact that the loads computation process can be seen as a two step procedure. However, often the problem is solved in a single step of which this static aero-elastic method would be an example. The two steps would be the following: The first step is the solution of the global balance, requiring global data. The second step is typical for the loads problem, that is the computation of the local loads on each point of the structure, requiring load distribution data. There is however a coupling between the two due to the elastic deformation of the

aircraft, therefore this direct coupling of the two is the more accurate approach.

A second method to deal with the loads computation of the 'statically flexible' aircraft is based on the pre-computation of the elastic forces due to each flight mechanics parameter (angle of attack, control surface deflections, load factors, angular accelerations, etc.). These forces are computed by constraining the Finite Element model in an empirical but physical manner, i.e. no displacements for two points at the wing root. These forces when integrated provide a kind of corrective term due to the flexibility to be added to the basic 'rigid' aerodynamic coefficient. For example the global lift slope will be the sum of the 'rigid' derivative measurable in the wind tunnel, plus this elastic part.

In this report, the first method will be used, that directly couples the aerodynamic and elastic forces.

The flexible static aero-elastic effects play a very important role in aircraft design:

- for the structural design, since they dramatically change the aerodynamic total loads and the loads distribution,

- for the handling quality design, since they dramatically modify the aerodynamic derivatives and therefore also the needed size of the empennages.

- for the flight control system design, since they dramatically influence the control surfaces effectiveness and therefore they are an important driver on the number and of the position of the control surfaces,

- for the aircraft performance, since the optimum cruise shape of the aircraft will be achieved only by means of a good prediction of the aero-elastic twist.

2.2.3   Loads due to in-flight manoeuvres

The loads model concerned with the determination of the loads due to in-flight manoeuvres is called the manoeuvre loads model. Loads models must be developed to simulate the design manoeuvres prescribed by the rule (FAR/CS). These models must be based on reliable input data and should be validated by ground and flight tests.

The manoeuvre loads model is intended to cover the loads on the aircraft due to pilot actions. Furthermore, it should cover the static loads from exceptional manoeuvres having a probability of about once per aircraft life. Last but not least, it has to cover fatigue loads, from operational manoeuvres, occurring at each flight, but at lower frequency for more severe pilot input.

The Manoeuvre Loads Model is also necessary to monitor the loads on the flight test aircraft. In flight test, it is used to anticipate the load level expected during particular manoeuvres required for the flight test program. This model is usually the same as that used for the assessment of the design loads. However, this flight test model may additionally imbed several realistic features that are important to reconstruct the exact detailed conditions for arbitrary flight test manoeuvres. The model presented in this report is an example of such a 'flight test manoeuvre loads model'. The model presented in this report will not be used to perform typical manoeuvre loads computations as prescribed

by the rule, such as a Rolling Manoeuvre, a One-engine-out case, etc. Therefore, these topics will not be described in further detail. The model presented in this report is used to reconstruct specific flight test manoeuvres, performed to address specific static aero-elastic effects.

The airframe flexibility must be considered to take into account the effect of the aero-elastic distortion of the structure. Either a simple beam model can be used or a complete aircraft finite element model condensed in a suitable number of points can be used. The finite element modelling technique and its condensation is described in detail in section 4.1. For the certification exercise, the stiffness data may be validated on Ground Vibration Test, or on static test. Also, a global validation of the aerodynamics plus structural properties may be performed by flight tests.

The aerodynamic data (derivatives and pressure distributions) for the steady part have to be established for all aircraft configurations throughout the relevant Mach range. They can be determined based on wind tunnel testing and/or by application of appropriate CFD-methods. For the certification exercise, adjustments of the model based on the measurements during the flight test campaign can be undertaken, if necessary, in order to validate or to refine the loads assessed by means of the pre-flight model.

The mass data should be established to cover all of the weight-CG diagram. This means that mass distributions must be derived for the whole range of weight, from zero fuel conditions to full fuel conditions and from low payload to maximum zero fuel weight (MZFW). Furthermore, mass distributions must be derived for the whole range of center of gravity as well as for the whole range (from minimum to maximum) of the fuel density. The fuel mass distribution should cover the refuel and the fuel usage sequences as defined in the fuel management system in a realistic or conservative manner. The payload distributions used in building the design mass cases must also adequately cover the loading requirements of the different airlines. Otherwise the operators would face unacceptable loadability limitations.
A last remark concerning the mass distributions is very important in the light of the present investigation. The fuel distribution along the wing plays a very important role in the wing bending and thus in the static aero-elastic case. The fuel alleviates the effect in upward bending conditions, dominated by the aerodynamic loads. The fuel also has a penalising effect for the downward bending. The structural optimisation may therefore sometimes rely on the optimisation or compromises with the fuel management system.

In case an electronic flight control system (EFCS) is fitted onboard of the aircraft, this has to be modelled where the control law features are relevant for loads. Often Special Conditions adapted to the particular EFCS-philosophy are issued by the Certification Authorities. Particular care must be put in the definition of the EFCS in failure conditions, where the behavior is degraded with potential effect on the loads. The EFCS will not be further considered here.

2.3   External loads

The external loads are loads due to:

- aerodynamic action acting on the external contour of the aircraft,

- propulsion loads,

- loads introduced by the ground.

    - ground loads introduced directly by the ground on the landing gear
    - ground loads introduced on the landing gear or on other parts of the airframe by handling or maintenance devices such as towing vehicles, jacking devices, tie-down devices.

- gravitational loads

- inertial loads, which is the aircraft reaction to balance all the loads above.

Therefore the forces acting on each point of the loads model grid can be written in the most general manner as:

$$\mathbf{F} = \mathbf{F}_{aero} + \mathbf{F}_{thrust} + \mathbf{F}_{ground} + \mathbf{F}_{inertial} \tag{2.1}$$

The determination of these force contributions will be described in detail in chapter 4. The ground forces are not described because in this report only flight loads are considered.

Generally, each loads effect has its own loading grid in the loads model. That is, the aerodynamic forces are applied on the aerodynamic grid. The inertia loads on the mass grid, which is the grid on which the masses are concentrated. More information on the mass modelling can be found in section 4.2.4. The thrust effects are applied to points representative of the point of application of the propulsive forces and torque. The ground loads if present would be applied to the landing gear at points such as the jacking and tie-down points. Because all effects are defined at their own grids, techniques are necessary to describe the interaction between these grids. This technique is called splining and the transformation matrices between the grids are called spline-matrices. The splining technique is described in section 4.7.

The six integrated loads $(T_X, T_Y, T_Z, M_X, M_Y, M_Z)$ for each of the N_s aircraft sections on which the integrated loads vector $\mathbf{S}$ is computed can be written as:

$$\mathbf{S} = \mathbf{TF}, \tag{2.2}$$

where $\mathbf{T}$ is a rectangular transformation matrix composed by distances between the point representative of the computing section and the point on the loading grid or by 1. The vector $\mathbf{F}$ is the nodal force vector containing in general 6 degrees of freedom (forces and moments) for each node. This is further described in section 4.8.

The integrated loads along the component axis are called running loads, for example integrated wing loads along the span. These running loads are used for defining the loads spectrum for the component design.

2.4   Loads validation

The loads are in general calculated and monitored several times in so-called loads loops. Each loads loop takes benefit of the improved knowledge of the data gathered by the progress of the models provided by the other disciplines. At the end of the process, before the certification, a final analysis is necessary to validate the loads information and therefore to validate the adequacy of the structure.
The final analysis is based on a number of tests:

- Landing gear drop test: validates the landing gear model at the impact.

- Ground vibration test: validates the structure dynamic model used for the dynamic tests.

- Flight test: validates the overall loads model.

- Other flight and ground tests, even if out of the responsibility of the loads domain, contribute to the validation of the loads model.

The flight test campaign is performed on the flight test aircraft equipped with calibrated strain gauges allowing measurement of the loads on a selected number of representative sections (wing, fuselage, empennages) or on elements such as the engine attachments, the landing gear, the control surfaces, etc. The programm consists in performing flight or ground manoeuvres close to those required by the rule. Often these are performed at a reasonably lower level in order to avoid damaging the structure. Other manoeuvres are also performed that are useful to the identification of parts of the loads model. Other unplanned events leading to high loads level, such as hard landing, relatively frequent in the early flights, are very useful for the validation process.

Chapter 3

Wing tip design aspects

In aircraft design it is, in general, always sought for maximum performance and efficiency. One way of improving the aerodynamic efficiency of the airframe is by adding devices at the wing tips, the so-called wing tip devices. First, an overview is given of the possible alternatives in wing tip devices. After that, one of those wing tip devices will be described in more detail, i.e. the winglet.

Winglets can significantly improve the aerodynamic efficiency of the airframe. But adding winglets also significantly increases the wing's dynamic and static flight loads. Flight test measurements also showed that the flexibility of the airframe has to be accounted for, when predicting the (aerodynamic) loads on the winglet. This obviously explains the special treatment of these devices within this loads investigation.

A big focus in aircraft design is on minimization of total airframe drag. Reneaux presents in [Ren04] hybrid laminar flow (HLF) technology, which means suction of the boundary layer to reduce the skin friction drag, a major drag component (in the order of one half of the total drag). The second major drag component (in the order of one third of the total drag) is the lift-induced drag for which innovative wing tip devices offer the greatest potential for drag reduction. Techniques to reduce the third component, the transonic wave drag, are also presented in [Ren04].

This chapter should provide background information on the advantages and drawbacks of wing tip devices in general and especially of winglets. Furthermore, it should provide insight into the working principle of the winglet and into the difficult flow conditions at the wing tip.

Before being able to implement a proper winglet model into the loads model, one has to understand how a winglet works and what the driving design parameters are.

3.1   Wing tip devices

Wake vortices are generated whenever an aircraft produces lift, see figure (3.1) for an impression of the wake behind an aircraft. Figure (3.2), shows the wake roll-up calculated using CFD (Navier-Stokes) analysis. A vortex, in general terms, is the rotational motion of fluid, often comprising a strong low-pressure region in its core. The principal structure of the wake downstream from a wing comprises a trailing vortex pair, each vortex being formed in the vicinity of the wing tip. The two vortices are formed by the difference between pressure on the upper surface of an airplane's wing and that on the lower surface. High pressure on the lower surface creates a natural airflow that makes its way to the wing tip and curls upward around it. When flow around the wing tips streams out behind the aircraft, a vortex is formed. The complicated vortex wake produced by aircraft may produce unforeseen turbulence in the air. Such flow structures play an important role in flight safety, since they can induce large rolling moments on neighboring aircraft and have been known to cause loss of control and occasionally fatalities.

The strength of the vortex is governed by the weight, speed and shape of the wing of the generating aircraft. The vortex characteristics can also be changed by extension of flaps or other wing-configuring devices. However as the basic factor is weight, the vortex strength increases proportionally with an increase in aircraft operating weight. Peak vortex tangential speeds up to almost 100 m/s have been recorded.

The wing tip can be considered as a dead-zone in regards to aerodynamic efficiency, as it generates a lot of drag and no significant lift. The induced drag represents 30-40% of the total drag of a transport aircraft in the cruise condition. Therefore it has a large impact onto the fuel consumption. The induced drag is proportional to the square of the lift coefficient. Therefore, at take-off, climbing, long-range cruise and during holding phases, most benefits can be achieved with devices reducing the induced drag.

The idea behind all the devices described below is to diffuse the strong vortices released at the tip and optimize the spanwise lift distribution, while maintaining the additional moments on the wing within certain limits.

Swept, tapered and crescent planform extensions have been proposed since the 1920's. Benefits have been claimed either due to the nonplanar wake behind the wing at incidence or a thrust force component on the leading edges of a swept tip. If the sweep of the tip is larger than the wing flexural axis sweep then the device may also impact aero-elastic behavior at high loads. The raked tip patents claim benefits through this mechanism, demonstrating the multidisciplinary nature of the tip design problem.

Lower outboard loading reduces the effectiveness of a tip device, which operates at a lower load due to the reduced cross flow at the tip. It is worth noting that whilst a tip device may give large increases in pitching moment the potential trim penalties are usually more than compensated for by the change in the wing drag polar.

Possible alternatives in wing tip devices:

- **conventional winglet** (long range A330, A340 and B747-400), see figure (3.7) and section 3.2.

- span increase in the form of a **raked tip** (B767-400, see figure (3.8))

- **blended winglet** (BBJ and B737-800; Patented and designed by Dr. L.B. Gratzer of Aviation Partners, Inc. API, Seattle, Washington), see figure (3.13). The blended winglets differ from most other winglets in that they are joined to the wing tip in a large radius curve rather than a smaller one. The smooth curve appearance, according to the Boeing company reduces the shock interference between winglet and the wing near the tip, thus allowing the winglet chord to be extended forward of the point of maximum thickness at the tip. However, proper design of the contours adjacent to the attachment can produce the same effect as providing a large radius of curvature and are very much simpler to design. The last thing any structural engineer wants, is a beam which has a complex curvature built into it. This because it would end up having to be substantially stronger than it would otherwise be if it were a straight or simple beam.

- **wing tip fence** (A319, A320, A380; Patent 1987 J.Jupp and P. Rees), see figure (3.10). The wing tip fence generates non-planar lift using stable vortical flow from a small delta wing at the wing tip. This device will not suffer stall as readily as an attached flow winglet and the impact on wing bending moment is extremely small. They prove particularly useful for retrofits since the impact on wing load is small. For the A380 wing design there was a constraint on the wing span in view of its future integration in the airport infrastructure. In this frame the wing tip fence devices proves to be the solution providing drag reduction both at high and low speed conditions.

- **Tip tanks**, see figure (3.6): Tip tanks are devices that extend beyond the physical range of the wings and protrude from both the leading edge and the trailing edge. They are generally cylindrical bodies that modify the tip vortex structure and work as endplates, although they are not as effective. On fighter aircraft they can be disposable bodies.

- **multi-winglets**: multiple winglets like a bird wing, also called **Tip sails**: Tip sails are more complicated devices consisting of several tapered fins (or smaller winglets), placed radially with an axial gap between two elements, see figure (3.5). They also have the leading edge protuberance similar to the tip tanks. For best performance it is suggested that the number of vanes be no more than 4 at angles 15-20 degrees between 2 vanes. Each vane should have a chord no larger than 30% of the tip tank chord.

- **split wing loop**, see figure (3.3) - comparable: **spiroid-tipped wing** (USA) - **Möbius-wing** (Russian). The spiroid tip is a spiral loop obtained when joining by their tip a vertical winglet and a horizontal one. This unconventional device seems promising to reduce the tip vortex intensity but has a complex geometry difficult to optimize.
  Spiroid Winglets[1], which look like a large loop of rigid ribbon material attached to each wing tip, cut fuel consumption by 6% - 10% in cruise flight. The Spiroid eliminates concentrated wing tip vortices, which represent nearly half the induced

---

[1]http://www.aviationpartners.com/spiroids.html

drag generated during cruise.

The Spiroid-Tipped Wing introduces a substantial change in design direction for wing tip devices that control vortices generated by lifting surfaces. As with any wing tip device, the objectives are to minimize airplane drag and improve performance throughout the flight envelope. Concentrated tip vortices in the wake of conventional planar wings produce high cross stream velocities and wasted energy which is associated with lift induced drag. Winglets are wing-like tip devices which reduce the vorticity strength and concentration thereby reducing drag. The Spiroid concept, featuring a closed contour, carries this trend to its logical conclusion, eliminating concentrated vorticity and further reducing drag.

Minimum induced drag for any lifting system requires an optimum aerodynamic surface loading and the Spiroid-Tipped wing is no exception. To accomplish this, appropriately matched airfoils for the twisted and cambered Spiroid surface are essential. Furthermore, to minimize friction drag, the Spiroid chord distribution must be held to lower limits but matched to the loading, while maintaining buffet margins. However, if this is carried too far, the resulting flexible structure may distort excessively under load thereby causing performance loss or dynamic problems. Adverse high speed effects which are associated with shock waves and flow separation can be avoided by appropriate airfoil selection and placement of the Spiroid segments in relation to themselves and also, to the wing. The Spiroid must also be appropriately sized for the intended application. The added weight and skin friction drag, which is the price that must be paid for induced drag reduction, are closely tied to geometry, structural load and design approach. For a given wing, there is an optimum Spiroid geometry which will minimize drag without exceeding wing structural capability. Normally, this will result in an overall span reduction which may also be seen as a benefit. However, if the wing has structural capability not currently being utilized, the ultimate drag benefit can be even greater but with somewhat increased span. Obviously there are many ways to exploit the tradeoff between drag, span, structural margins and wing weight; the designer's role being to select the appropriate combination for a specific application. Flight testing of Spiroids on a Gulfstream II aircraft within the normal flight envelope has shown impressive performance gains (e.g., more than 10% drag reduction) relative to the basic aircraft. Also, preliminary exploration of the vortex wake behind the Spiroid from a chase aircraft has indicated the potential for large decreases in wake intensity. This could substantially alter requirements for separation distances between lead and following aircraft in airport traffic patterns.

- **Wing endplates**: The endplates are vertical surfaces (generally rectangular) added to a wing to redistribute the lift along the span. The lift coefficient is strongly increased, the drag coefficient is decreased by a tiny amount. The resulting efficiency L/D is generally greatly improved. The effect of the endplates can be described as an increase in wing aspect ratio that is proved to be effective. Endplates are considered a more simple engineering solution than the winglets. Typical applications
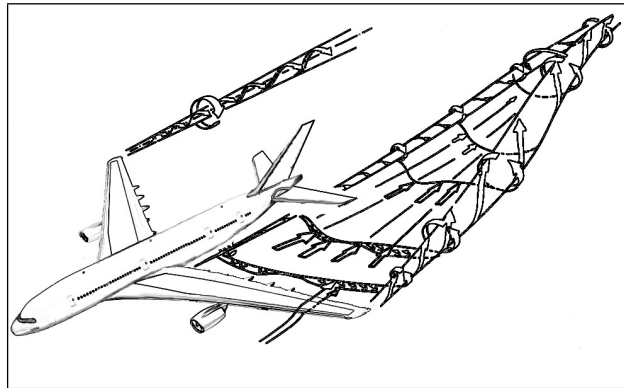
Figure 3.1: *Artist impression of the typical wake with tip vortices behind an aircraft.*

of endplates are in racing cars, where the aspect ratios are necessary small and enormous efforts are made by the engineers to produce a few percent of extra lift, while not penalizing the drag.

- **Hoerner tips**, see figure (3.4): Hoerner tips are crescent-shaped geometries with a slight upward feathering. They are proved to be slightly better than conventional round tips, since they promote a better diffusion of the tip vortex.

- **Shark fin** (Patent G. Heller 2004), see figure (3.9). The shark fin is in reality a highly blended non-planar wing tip span extension gaining additional advantage from conical sweep

- **Wing grid**

- **Wing tip turbine**

Selection of the wing tip device depends on the specific situation and the airplane model. The potential of wing tip devices has greatly expanded for fixed-wing aircraft. Also, it is expected this new technology development will ultimately provide superior performance gains as well as operational benefits (e.g., increased safety, less noise, smaller space needs) in many applications where lifting surfaces are employed.

3.2 Winglets

Winglets are upward swept extensions or small lifting surfaces, attached to the outboard end of an aircraft wing. Usually they are mounted at, or near to, a vertical angle from the wing structure. The main purpose and direct benefit of winglets are reduced airplane drag. This reduction in drag provides a substantial improvement in fuel efficiency, which can be translated into greater payload or longer range for a given fuel load. The airflow around winglets is complicated and winglets have to be carefully designed and tested for each aircraft. The magnitude and orientation of the lift force generated by the winglet itself are determined by the cant angle and the toe angle. The cant angle is the angle to which the winglet is bent from the vertical. The toe angle is the angle at which the
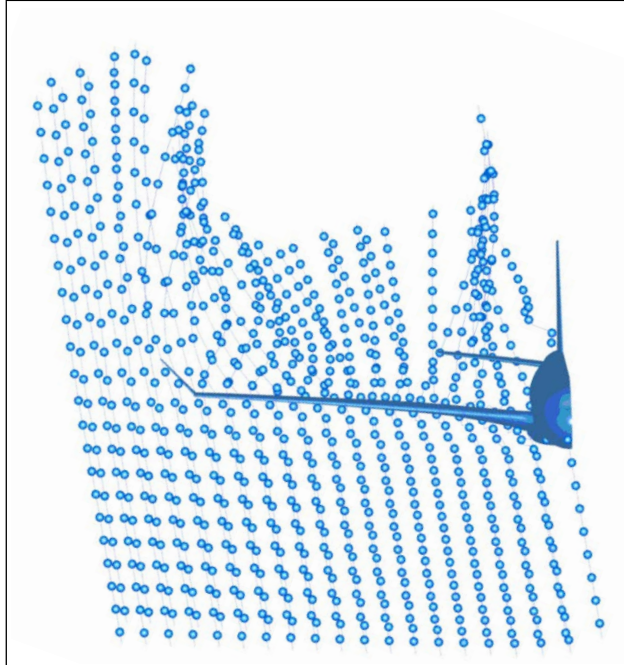
Figure 3.2: Visualization of the flow around an aircraft from CFD (Navier-Stokes) analysis, showing the typical wake roll-up at the wing tip, see also section 6.6.1.

Figure 3.3: Spiroid wing tip. Picture by courtesy of Aviation Partners, Inc.
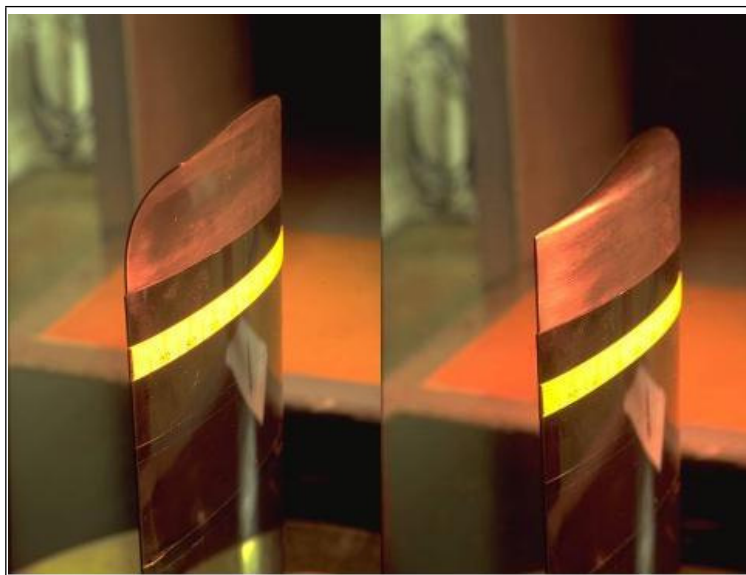
Figure 3.4: *A wind tunnel model of a wing with a Hoerner tip on the left. For comparison, the same wing with a round tip on the right. Photo by Antonio Filippone. See figure (D.1) in the appendix for the full color image.*
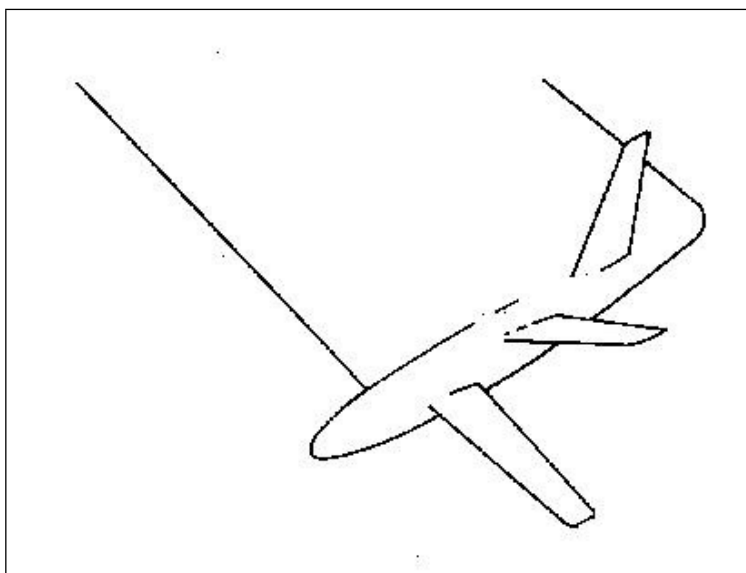
Figure 3.5: *Example of a wing tip sail, here with three tapered fins. Drawing by Antonio Filippone.*
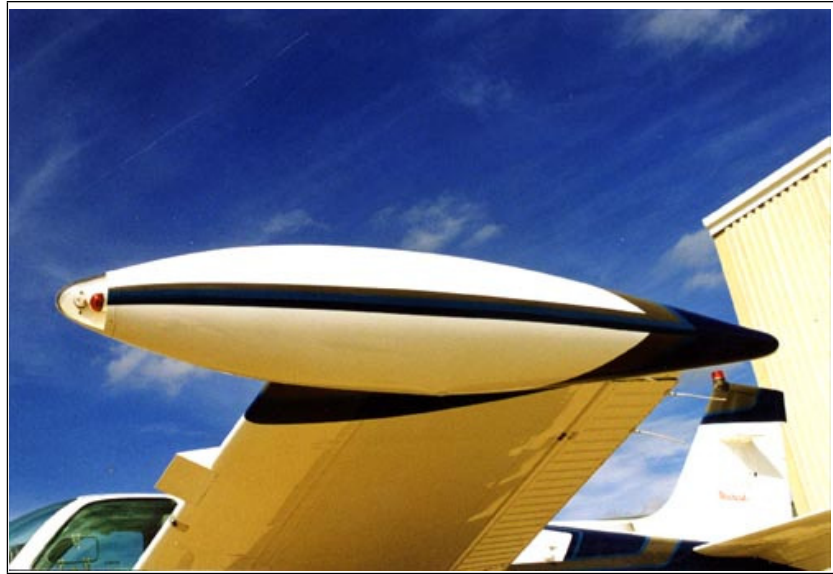
Figure 3.6: Example of a wing tip tank. Photo by Dave Biggerstaff.

Figure 3.7: Conventional winglet of an Airbus A340-541. Photo by Fabian Gysel. See figure (D.2) in the appendix for the full color image.

Figure 3.8: *Raked tip on a Boeing 767-400ER. Picture by courtesy of the Boeing Company*

Figure 3.9: *Shark fin tip on a HPH 304 S sailplane. Photo by Tim Mara. See figure (D.3) in the appendix for the full color image.*

Figure 3.10: *Wing Tip Fences on the Airbus A380. Photo by Thomas Wirtenberger. See figure (D.4) in the appendix for the full color image.*

winglet's airfoils diverge from the relative wind direction. Due to the local flow field at a wing tip, the lift vector on a winglet will point forward creating a negative drag force, i.e. thrust, that more than compensates for the additional wetted surface.

On top of the aerodynamic performance matters, a winglet influences the flight mechanics, the flutter characteristics and the low speed performance. An existing wing can be retrofitted or a new wing can be designed to fit the winglet. The manufacturer who wants to install a winglet has to balance the aerodynamic gains with the structural impact. Nevertheless, the design and research studies carried out on the winglet topic often consider the aerodynamics separately from the structure. The influence of a flexible airframe on the aerodynamic performance is the topic of section 3.3.

3.2.1   Historical overview

The initial work on winglets was done by Richard Whitcomb at NASA in 1976, see reference [Whi76]. He presented a design approach for winglets that involved the use of vortex lattice methods along with parametric experimentation in the wind tunnel. Kichio Ishimitsu from Boeing wrote also in 1976 an AIAA paper on the design and analysis of winglets, see reference [Ish76]. This paper comprises theoretical and experimental results on a KC-135 aircraft. In 1979 to 1981, NASA Dryden Flight Research Center was involved with general aviation research with the KC-135 aircraft. A winglet concept,

developed by Richard Whitcomb of Langley Research Center, was tested on a KC-135A tanker. It was a joint NASA/USAF program to develop and flight test winglets on this aircraft. The results of this program were published in 1981 in reference [Bar81]. The research showed that the winglets could increase an aircraft's range by as much as 7% at cruise speeds.

3.2.2   Advantages and drawbacks

A winglet accelerates the airflow at the tip in such a way that it generates lift and improves the wing loading distribution, which is related to the induced drag. The aircraft will fly at a slightly lower angle of attack for the same lift coefficient.

A key advantage of winglets is that they increase performance at the cost of a smaller increase in wing root bending moment compared to an equivalent wing span extension. The winglets must be mounted on the rear part of the wing to minimize interference effects. Winglets can increase the aerodynamic efficiency. For a given amount of lift, drag can be reduced. These improvements create direct economic benefits to aircraft operators in various combinations: lower operating costs by a decrease in fuel burn, increased payload or range, improved takeoff performance, reduced engine maintenance and lower airport noise levels. The winglet-block-fuel-burn improvement increases with cruise range. Block fuel can be reduced by 3.5 to 4% on missions greater than 1000 nautical miles. Furthermore, aircraft equipped with winglets can have lower emissions through a lower cruise thrust. Alternatively stated, winglet equipped aircraft have a more efficient climb profile. They are able to climb to initial altitude faster and save fuel compared to those not equipped. The profile also allows the aircraft to take-off at lower thrust settings, leading to a smaller noise footprint and extending engine life. In case of some business jets, the winglets can enable the aircraft to reach maximum cruising altitude without having to step-climb while fuel is burnt.

Aircraft take-off weight is sometimes limited by the second climb segment, which occurs after the landing gear is retracted. The reduction in take-off flap drag during the second segment of climb allows increased payload capability at take-off-limited airports. In some situations, there is enough field length but some passengers are left behind because the aircraft cannot fulfill the climb requirements, especially on hot days. In many cases winglets help to minimize this kind of problem or they can even solve it.

An additional benefit of winglets is increased wing buffet margin. Wing buffet occurs when lift on a wing is so great that it causes flow separation and wing stall. Any increase in buffet margin allows the aircraft to fly at higher altitudes where fuel mileage is increased. In general, the longer the range, the higher the cruising altitude and Mach number, the greater the fuel savings. Another benefit that plays a key role in the decision of airlines for a particular type of aircraft or the desire to retrofit the existing fleet, is that of the high tech visual appearance. The winglets bring a modern look and feel to the aircraft and improve customers'perceptions of the reliability and modernity of the airline. Environmental benefits include a reduction in noise levels (6.5% for the B737) around airports on take-off and a reduction of nitrogen dioxide emissions (4% on a 2000nmi flight for the B737).

Despite the benefits of winglets, there are some drawbacks. The wing root bending moment is higher and may require additional structural wing reinforcements. Winglets could also contribute to a slightly worsening of the aircraft Dutch Roll and flutter characteristics. The flutter characteristics of an aircraft are evident at high speed when the combined structural and aerodynamic interaction can produce a destabilizing or divergent condition. Under such circumstance, an aircraft with winglets is sensitive to the weight and center of gravity of the winglets and associated structural wing changes. Additional weight near the wing tip, either higher than or aft of the wing structural neutral axis, will adversely affect flutter.

Winglets also generate viscous and induced drag that should be minimized and obviously not offset the induced drag reduction caused by the winglets itself on the configuration.

The design of a winglet airfoil imposes a great challenge to the aerodynamics department because the winglet surface is usually highly loaded and works under a large range of Mach numbers and lift coefficients. Apart from the airfoil, other parameters that must be taken into account to optimize the winglet design include cant angle, toe angle, root incidence angle, twist distribution, sweepback, taper ratio and aspect ratio.

Other design considerations not directly related to the drag include the winglet possibly having to house anti-collision and navigation lights. Winglets also require protection against lightning, considering they exert some attraction for it. Although winglets frequently cause an increase in maximum lift coefficient, the final configuration must keep, at the very least, the maximum lift coefficient of the wing not fitted with winglets.

Many designers still argue that one should design a wing to meet all customer performance goals at entry into service with a conventional and simpler-to-design straight wing. Had the B777 been designed with a winglet-equipped shorter span wing, then it is doubtful that the reduced wing area (and hence increased wing loading) would have been able to support the new high-gross weight long-range derivatives, let alone accommodate the necessary fuel tankage.

The efficient wing of the A320 was also designed without winglets. It was only after entry into service, when additional range was sought, that its distinctive wing-tip devices were added.

From the perspective of loads and dynamics, the three areas that affect structural change are static loads, dynamic flight loads and flutter.

Winglets's influence on static loads

Static loads are determined by the aircraft manufacturer, the FAA and EASA design requirements, such as a symmetric 2.5g manoeuvre, a roll manoeuvre, or an abrupt rudder input that results in a sideslip manoeuvre. Although these maneuvers all contribute to the wingbox design, most of the wingbox is designed for 2.5g maneuvers. The highest loads on the mid- to outboard part of the wing occur when speed brakes are extended. The inboard portion of the wing reaches its highest loads in the clean wing configuration (i.e., with speed brakes retracted).

The outboard tip of the wing generally is designed for roll manoeuvres. However, after the addition of winglets, the high loads on the winglets during sideslip manoeuvres cause the wing tip area to be more highly loaded. Consequently, sideslip manoeuvres become the design case for the wing tip and winglet.

Winglet's influence on dynamic flight loads

Dynamic flight loads also contribute to the maximum load envelope of the outboard wing. The response of the airframe to gusts or turbulence creates dynamic flight loads on the wing and winglet. During turbulence, the airframe responds at different frequencies depending on its aerodynamics, inertia and stiffness. Modifications to these parameters change how the airframe responds to turbulence, which in turn changes the loads. In addition to the winglet-induced increase in air load, the weight of the winglet itself and its extreme outboard location also increase the loads for the outboard wing. The heavier the winglets are, the higher the dynamic loads. For the production winglets on the Boeing 737, the winglet weighs about 60 kilograms. The increased weight to the aircraft for modifying wing and installing winglets is about 218 kilograms.

Winglet's influence on flutter

The flutter characteristics of an airplane are evident at high speed when the combined structural and aerodynamic interaction can produce a destabilizing or divergent condition. Under such circumstances, an aircraft with winglets is sensitive to the weight and center of gravity of the winglets and associated structural wing changes. Additional weight near the wing tip, either higher than or aft of the wing structural neutral axis, will adversely affect flutter.

The Boeing design team gathered technical data on aerodynamics, loads and flutter through wind tunnel and flight tests. Boeing analyzed the loads on a 737-600/-700/-800/-900 aircraft with winglets through wind tunnel testing using a standard model constructed in the 1g cruise shape and a unique model. The unique wing model was built in the deflected shape for the 2.5g design manoeuvre condition, see figure (3.11). The test data from this configuration were used to determine the change in air load distribution on the wing in the deflected shape. This information was used to refine the analysis and helped minimize the adverse effects of the higher loads that resulted from the winglets. Flight tests were conducted to determine the cruise drag reduction of the winglets and provide data on loads, handling qualities and aerodynamic performance. Strain gauges and rows of pressure taps placed on the winglet and outboard wing were used to indicate the changes in bending moment on the outboard wing resulting from the winglet. Data from these flight tests were used to adjust and validate the aerodynamic database derived from the wind tunnel tests.

Aerodynamic flight test results on the prototype winglet on the B737 reported by Boeing:

- **Performance**:

    - 4-5% cruise drag reduction

    - No change to initial buffet boundary

    - No change to stall speeds

    - No pilot-perceived buffet before stick shaker

Figure 3.11: *Image of the Boeing 737 wind tunnel model constructed in the shape of the 2.5g deflected wing superimposed over an image of the wing in the nominal 1g cruise shape. Picture by courtesy of the Boeing Company*

- Flaps-down lift increase
- Significant drag reduction for take-off flaps

- **Handling Qualities**:

  - Improved Mach tuck
  - Improved directional stability
  - Improved longitudinal and lateral trim stability
  - Increased pitch stability
  - No degradation of stall characteristics and stall identification
  - Unchanged rudder crossover speed
  - Unchanged Dutch roll damping

The gross fuel mileage improvement with winglets was recorded in the range of 4-5%. Taking into account the weight of the winglet and the related wing structural modifications, the net performance improvement was approximately 4% for long-range flights. Low speed testing showed a significant reduction in take-off and landing drag and a significant benefit in payload capability for certain operations.

Five major issues were addressed in Boeing's development of the optimal winglet configuration:

- Toe angle

- Speed brake angle

- Structural changes

- Weight and CG control

- Damage tolerance and fatigue

Toe angle

The initial winglet design for the B737 was at a 0 degree toe angle. It was designed to minimize the induced drag, but resulted in high wing loads. Therefore, the winglet was toed out at 2 degrees to reduce wing bending loads. While reducing the loads it did not compromise the cruise drag. The increase in induced drag from unloading the winglet was offset by the reduction in trim, profile and wave drag. A performance flight test showed equivalent drag for a 0 degree toe angle and a 2 degree toe-out angle.

The toe-out angle did slightly reduce the winglet induced lift when the flaps were down. Induced drag is much greater during during flaps down operation than at cruise due to the higher lift of the wing. This loss in improved performance during flap down operation was considered an acceptable trade off for reduced structural modifications.

Speed brake angle

The loads on the mid and outboard portion of the wing can be lowered by reducing the in-flight speed-brake angle. The reduction in acceptable speed-brake angle depends on the aircraft utilization by the operators. The B737-800 commercial aircraft required full use of the speed brakes to the in-flight detent position for emergency descent certification requirements, where the angle of the BBJ (Boeing Business Jet) could be reduced by 50%. For the B737-800 retrofits, a load alleviation system was developed to reduce the speed-brake angle automatically at heavy weights and high speed for critical design load conditions.

Structural changes

After the studies of the toe angle and the speed brake angle, the adverse effects of the wing structural modifications on flutter had to be minimized. To this end, the mid to outboard wing's torsional stiffness was maximized in relation to bending stiffness. The inboard wing had sufficient strength margins, such that structural modifications to that area were minimal or unnecessary.

Weight and CG control

The weight and CG control of the B737 winglet were considered to address the effects of both flutter and dynamic load. This included the location of the winglet lights and specifications for the painting and possible repair of the winglet. To meet flutter requirements with minimal structural changes, additional wing tip ballast was mounted on the front spar to counteract the incremental weight of the winglet located aft on the wing. The use of wing tip ballast depended on the structural configuration of the wing. In some cases, ballast was simpler and more cost effective than structural modification of the wing box.

Damage tolerance and fatigue

The winglet and wing modifications have to be designed to meet the aircraft manufacturer, the FAA and the EASA criteria for damage tolerance and fatigue. Any unchanged structure affected by the increased loads must be analyzed to ensure that all requirements are met. No additional rework was required on the BBJ, whereas some wing panel fastener holes required rework for fatigue considerations on the retrofitted B737-800 commercial airplane. This can be explained by the higher cycles of aircraft utilization and

take-off weights. The winglet structure and systems fit within the current airplane main-tenance intervals and life cycles. The winglets on the B737 thus have a minimal effect on aircraft maintenance.

3.2.3   Winglet development at Embraer

Winglet development at Embraer began in 1989, when it conducted subsonic wind-tunnel tests at Centro Técnico Aerospacial, a Brazilian Research agency for Aeronautics and Astronautics. The test results indicated potential benefits of fitting winglets with a smooth transition onto the tips of existing aircraft wings. A prototype of the twin-pusher CBA-123 was flown equipped with a preliminary design in February 1991 to gather flight test data. The engineers at Embraer used Computational Fluid Dynamics (CFD) analysis to clearly visualize the flow patterns around the wings and winglets at low- and high-speed regimes. Using simulation results as a guide they fine-tuned winglet geometry to reduce induced drag, while improving both fuel consumption and field performance. The results of the CFD simulations on the first winglet design of the ERJ-145 showed transonic shock waves at the junction of the wing and winglet at Mach 0.78. The designers had created a smooth transition rather than a right angle to prevent the formation of a vortex that could produce drag and negate the winglet's benefit. The analysis revealed that the smooth transition was the right idea. The shape just needed to be modified to eliminate the shock waves. When the new design was implemented on the aircraft, several important performance advantages were documented. The aircraft had an considerable increase in weight capacity at take-off via the winglets, increasing the lift to drag ratio during the climb stage. The test pilots reported faster climbing. Also drag at maximum cruise condition was reduced by 4.5%.

3.2.4   Retrofitting the Boeing 737-800 with winglets

The information in this section has mainly been extracted from the Boeing website[2]. Blended winglets were developed for improved airplane performance. The Boeing 737-800 wing was originally designed and certified without winglets. Flight testing of the Boeing Business Jet (BBJ), a derivative of the Next Generation 737-700, showed that the expected gains in aerodynamic efficiency from winglets to be real, as were increases in flight loads. The technical challenge then became to add winglets to the existing 737 wing design, improving aerodynamic efficiency but with minimal structural weight penalty and system changes. The program involved integrating winglets into both existing fleet 737 aircraft and new production aircraft.
Retrofitting winglets creates different challenges than installing them on the production line. Another program challenge was minimizing cost of flight test and certification for several distinct wing configurations, preferably using a common winglet design. The winglets on the 737-800 are 8ft ($\approx$ 2.44m) tall blended winglets, with a tip chord of approximately 2ft and a root chord of 4ft.

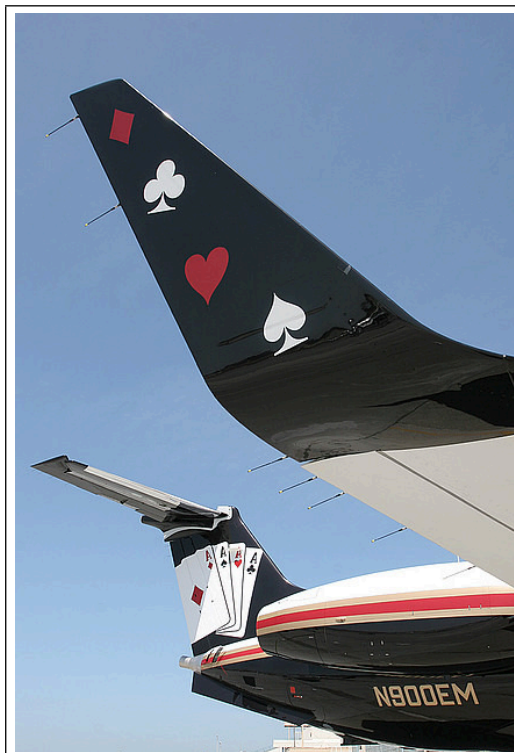[2]http://www.boeing.com/commercial/aeromagazine/aero_17/winglets.pdf

Figure 3.12: Blendet winglet on an Embraer 135BJ legacy. Photo by Keith Wahamaki.

The construction of the winglets is made out of approximately 70% graphite-epoxy by weight. A blended winglet configuration was selected because it required fewer changes to the wing structure. The aerodynamic advantage of a blended winglet is in the transition from the existing wing tip to the vertical winglet. The blended winglet allows for the chord distribution to change smoothly from the wing tip to the winglet, which optimizes the distribution of the span load lift and minimizes any aerodynamic interference or airflow separation.

The changes necessary to the aircraft to enable the retrofit of winglets are changes in: stabilizer trim setting, auto-throttle, flight management computer data, structural changes. Adding winglets increases the wing's dynamic and static flight loads significantly. An economical retrofit program minimizes the recurring costs of the installation, which is difficult because the retrofit modification is limited by existing parameters in the basic aircraft. For example increasing skin thickness may be the most efficient means of increasing the wing bending strength, but skin replacement is not cost-effective. For the retrofit, wing strength was increased by adding straps and angles to the stringers inside the wing box. Development of a speed-brake load-alleviation system minimized modifications to the wing. This system changes the angle of the in-flight speed-brakes in critical flight conditions to reduce wing loading. Wing service life goals were achieved by reworking existing fasteners in the lower wing skin. The fasteners were removed and replaced with interference-fit fasteners to improve fatigue life.

The increased pitch inertia at the wing tips caused by the addition of winglets aggravated

critical flutter modes. Adding 41 kilograms of ballast per wing in the outboard leading edge avoided a reduction in the low-altitude operating speed. Also, replacement of the removable outer, two-bay skin panels improved flutter tip modes.
An absolute seal is installed to prevent any flammable fuel vapors in the inboard wing from reaching any potential ignition sources in the winglet.

Aircraft system changes were also required for the addition of winglets in production. For production installations, additional bending and torsional stiffness must be carefully designed into the wing. The structural provisions have to be designed to lessen the weight impact on aircraft not equipped with the optional winglets. The structural changes also must be designed to minimize the effects of winglets on the company's final assembly lines. For the B737-800, flutter considerations drove a significant effort to control wing torsional stiffness and winglet weight and center of gravity. To reduce the weight penalty for customers who did not opt for winglets, the outboard (2/3 of the wing) structural wing enhancements stop at rib 25. This configuration is known as partial provisions, which includes new ribs 25-27 with additional reinforcement as needed. Some minor strengthening was also required in the center wing.
Since the winglets improve cruise performance, a new 737-800 winglet model engine database for the flight mission computer was required.

Five different 737 aircraft were flight tested from 1998 to 2001 to confirm and certify the winglet installations. The first flight with certified 737-800 winglets was by Hapag-Lloyd on May 8th, 2001. Since completion of certification, a significant interest in winglets has been confirmed in the passenger and freighter market.

3.3   The influence of airframe flexibility on winglet performance

Many references exist that address the topic of aerodynamic performance of wing tip devices in general and more specifically of winglets. These studies mostly involve addressing the drag benefit due to a wing tip device compared to other devices and/or to a clean wing. Also many publications exist that study specific parameters of a certain wing tip device, such as aerodynamic and geometric twist, installation angle (cant and toe angles). These studies are very important in understanding the complicated flow condition at the wing tip in order to arrive quicker at even more efficient designs. See also section 3.2 where the performance of wing tip devices on a rigid aircraft were discussed. These studies are all based on either wind tunnel measurements or pure aerodynamic (CFD) analysis. However flight test measurements have shown that the flexibility of the airframe has to be taken into account when predicting the (aerodynamic) loads on the winglet. Obviously, the largest contribution stems from the flexibility of the wing.
The loads level on the complete wing depends on the loads level on the outer wing, as the loads of the wing integrate from the tip to the root. A more outboard loading of the wing (at the same C_L) is closer to the theoretical elliptic lift distribution for which Prandtl showed that this leads to the smallest lift-induced drag for a planar wing. These higher outer wing loads however will lead to higher loads along the complete span of the
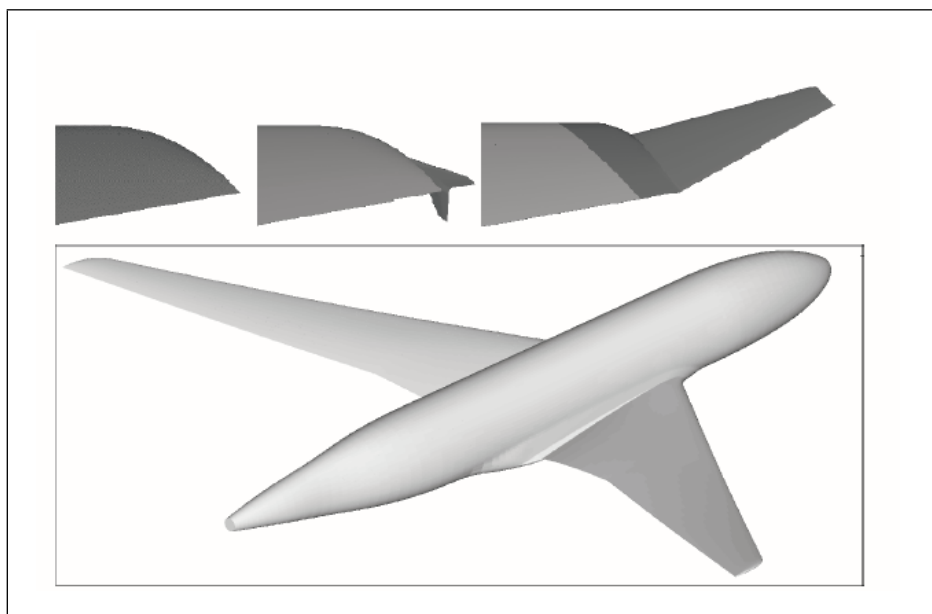
Figure 3.13: *Generic large civil transport aircraft with several tip devices (Küchemann tip, tip fence and large winglet). Image by Jean-Luc Hantrais-Gervois, see also reference [HG06].*

wing. Today's aircraft have a span loading with a roughly triangular shape, which is a compromise between low lift-induced drag and structural weight.

To meaningfully compare wing tip devices the wing root bending moment (WRBM) is introduced as a means to quantify the influence of a tip device with respect to loads. For the trade-off between alternative designs this is a good parameter to predict the structural (weight) impact of these devices. However, when the design decision is made, a more detailed analysis is required to address the loads along the whole span to enable a safe and efficient wing design. Some references exist that compare in-flight measurements although only on aircraft with relatively rigid wings. For example reference [Dam83] has compared in-flight test measurements on an agricultural aircraft. Reference [Coi00] describes an experimental study on wing tip devices also for agricultural aircraft. Such aircraft have a relatively small span and thus quite rigid wings.

 Furthermore, if flight test measurements are considered, these concentrate on the performance aspects of the wing tip devices (drag, local pressures) and if loads are considered then only in terms of the WRBM. Running loads (loads along the aircraft components) are very rarely addressed.

A recent publication [HG06] has addressed for the first time the aspect of winglets on a flexible airframe of a large transport aircraft. This paper is unique as it considers the influence of a winglet in a multidisciplinary way (combination of an aerodynamic and structural analysis). It is the first known publication that addresses the influence of a flexible airframe on the winglet performance and it presents the influence on the wing running loads. It considers the transonic cruise condition for which the addition of a winglet to a wing does not simply consist in reducing the induced drag.

Within the Loads field, the focus lies on covering the complete flight envelope, where the cruise condition is not a critical design case for the wing. The flight envelope that
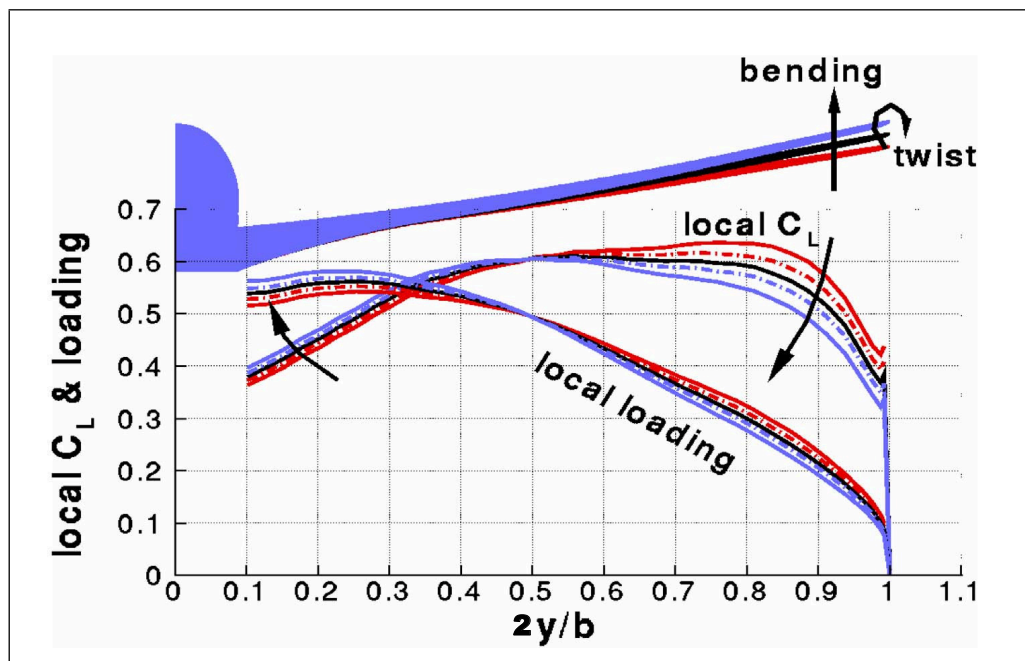
Figure 3.14: *Clean wing - Loads variations along the span at cruise as a function of twist. Arrows indicate nose down twist. The wing tip variation is ± 1 degree in comparison to the reference. Black = reference, blue = nose down and red = nose up. Image by Jean-Luc Hantrais-Gervois, see also reference [HG06]. See figure (D.5) in the appendix for the full color image.*

is prescribed by the airworthiness requirements, to be interpreted as minimum requirements, is bounded with manoeuvres ranging from -1g to +2.5g, see again figure (2.1). Obviously, for the bookcase of a 2.5g pull-up manoeuvre the largest deformations of the wing will occur. Therefore for loads, accounting for flexibility effects and their consequent changes effects on aerodynamic behavior is essential for the accurate prediction of the correct outer wing and winglet loads.

To arrive at the most efficient wing-winglet design, these should be considered in their combination right from the start of the design process. However, at least in the past, the design and assessment process often looked as follows. After a wing shape in flight was designed, the winglet was designed independently to provide aerodynamic gains on this wing shape. The first step consisted of a rigid aerodynamic assessment. In a second step the structural behavior of the wing plus winglet assembly was analysed. In this step the wing twist and bending and the required structural strengthening were determined. Depending on the shape of the winglet the wing deformation with the winglet on may even spoil the aerodynamic efficiency of the wing and the required structural strengthening may even cancel or overcome the aerodynamic gains in the rigid case. This is all the more true for large devices with significant loading. The global effectiveness of a winglet is rarely established in a comprehensive manner leading to conservative wing plus winglet designs with moderate winglet sizes.

3.3.1   Aerodynamic and structural behavior of a wing equipped with winglets at cruise

The information of this section is extracted from reference [HG06]. This reference presents the results from aero-elastic computations on a real aircraft equipped with large and standard winglets at cruise condition, see figure (3.13). The influence of the different devices on drag and its physical breakdown (wave drag, viscous drag and induced drag) is presented. They have made the same observation that for configurations with a large device there is a large sensitivity of drag and wing root bending moment to twist compared to a clean wing. In reference [HG06] it was looked at multiple cruise conditions, by weight and altitude variations and the simulated results are compared with flight test. By application of a state-of-the-art method, they arrived at accurate predictions of the wing deformations and performance although they report that some discrepancy remains in the aerodynamic simulation of the tip of the wing.

The non-planar winglets are known to improve the drag performance by increasing the outboard loading without offsetting the gains by a too important wing root bending moment as a simple wing extension would do. These principles considering only the lift-induced drag for a rigid wing are not sufficient to model transonic cases where the wing flexibility and other drag components play important roles.

The computations of reference [HG06] were Reynolds Averaged Navier-Stokes (elsA) computations combined with an aero-elastic model. The drag contributions were calculated in the postprocessing of the data using the far field technique. The one equation Spalart-Allmaras turbulence model was used together with an implicit LU scheme with relaxation. A second order central difference is used for the spatial discretisation of the mean flow (Jameson scheme with second and fourth order dissipation terms). A first order central discretisation is used for the turbulent quantities. The first order backward-Euler time scheme is used. The multi-grid technique is used to speed up the convergence process. The computed fluid around the geometry is discretised in structured blocks. A high level of similarity between the meshes was used to limit the mesh effects between the configurations. The fluid structure coupling is embedded in elsA and can resort to several mesh deformation techniques and is able to handle large displacements. The structure was modelled by a reduced stiffness matrix extracted from the full finite element model by a static analysis of MSC.NASTRAN.

The principle of the drag calculation with the far field technique used in reference [HG06] is to replace the integration of drag at the skin of the aircraft by the integration in the whole volume of the computed field. Each cell can be analysed according to its drag contents. One of the advantages of this method is that areas are identified where drag arises and separated according to their physical origin: wave drag, lift-induced drag and viscous drag. Another advantage is that computational errors, occurring in the classical surface integration due to strong gradients at the leading edge, can be accounted for. This also decreases the mesh dependency of the results.
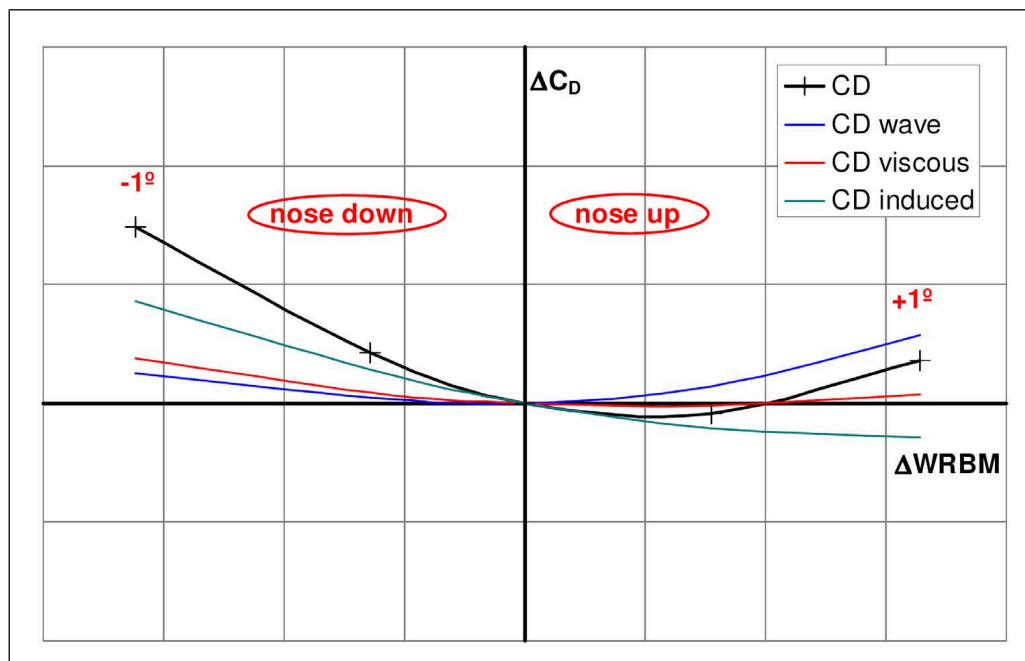
Figure 3.15: *Clean wing - Drag and WRBM increments to the reference flight shape at cruise as a function of twist. The wing tip variation is ± 1 degree in comparison to the reference. Image by Jean-Luc Hantrais-Gervois, see also reference [HG06]. See figure (D.6) in the appendix for the full color image.*

Theoretical twist effect on a clean wing with Küchemann tip

The influence of a range of realistic wing shape twists have been studied for a wing with Küchemann tip in cruise conditions. Compared are the results carried out at a fixed lift coefficient. The deformation levels considered were +/- 1 degree of twist at the wing tip compared to a reference shape close to target flight shape. When the nose down twist increases, the outboard loading decreases and inboard loading increases, see figure (3.14). Due to this inboard shift of the wing loading, the wing root bending moment decreases but the lift-induced drag increases with nose down twist, see also figure (3.15). The induced drag is thus affected by the wing shape. Viscous drag is only marginally affected by the wing shape. For nose up twist, the wave drag counteracts the lift-induced drag gains. The tip region is responsible for the important wave drag increase for nose up twist, see also figure (3.16). The resulting total drag curve is a complex combination of these drag components. The total aerodynamic drag exhibits a convex shape with moderate variations in both wing root bending moment and drag.

Theoretical twist effect on a wing plus large winglet

The same kind of comparison has been made for the wing equipped with a large winglet, see figure (3.18). Due to the presence of the winglet, there is now 0.3 degrees more nose down twist at the tip. The impact of twist on the wing loading is similar to what was observed for the clean wing, see figure (3.19). Nevertheless, the order of magnitude of the variations in both wing root bending moment and in drag is very different compared
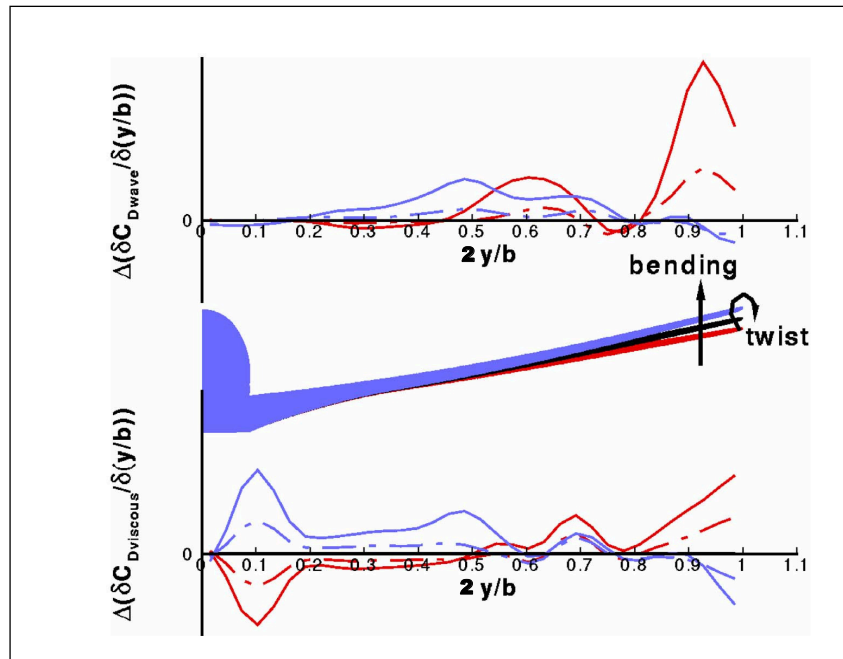
Figure 3.16: *Clean wing - Drag increments to the reference flight shape at cruise over span as a function of twist.The wing tip variation is $\pm$ 1 degree in comparison to the reference. Blue = nose down and red = nose up. Image by Jean-Luc Hantrais-Gervois, see also reference [HG06]. See figure (D.7) in the appendix for the full color image.*
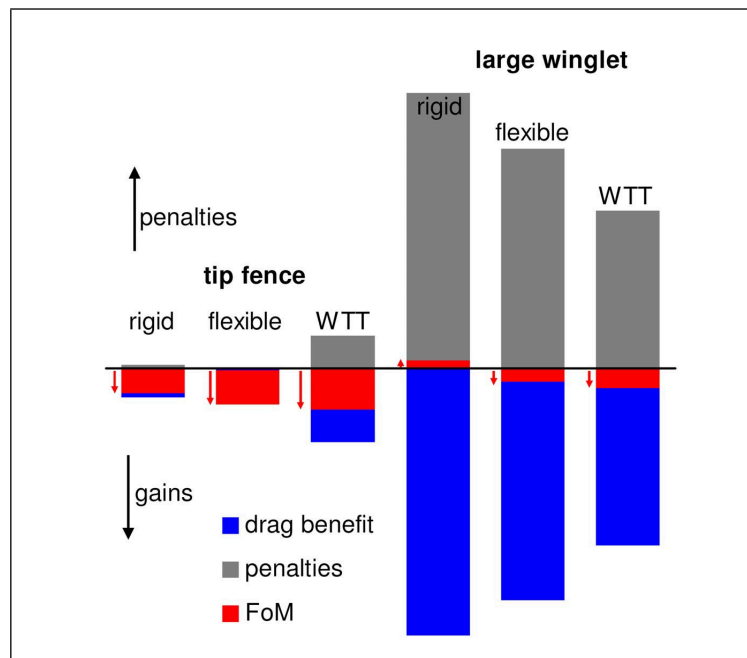
Figure 3.17: *Comparison of the rigid and flexible assessments of a tip fence and a large winglet in comparison with a reference Küchemann tip. The penalties include structural, weight and industrial trade-off considerations. Image by Jean-Luc Hantrais-Gervois, see also reference [HG06]. See figure (D.8) in the appendix for the full color image.*
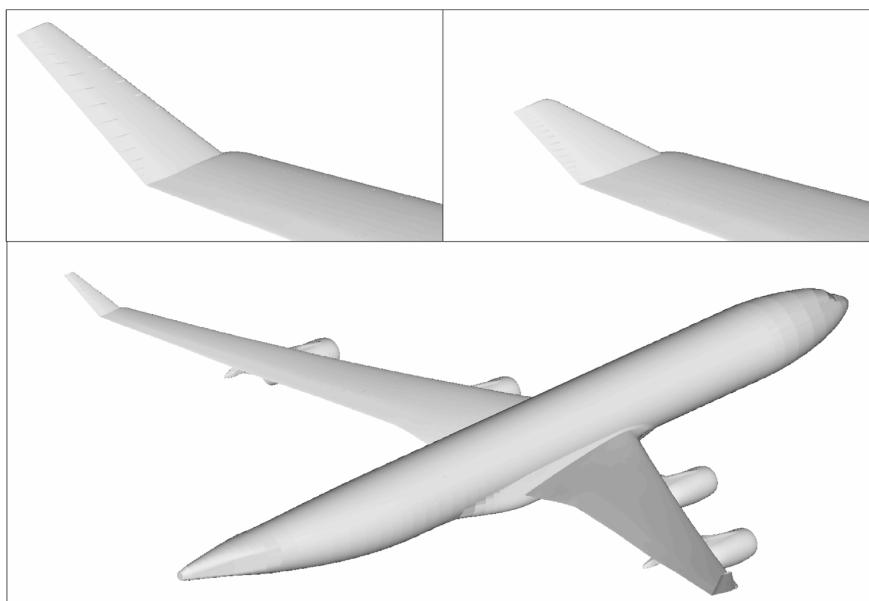
Figure 3.18: *Aircraft configuration with the large and standard winglets. Image by Jean-Luc Hantrais-Gervois, see also reference [HG06].*

to the clean configuration, see figure (3.20). The shape of the curves is similar but the amplitude differs. When a large winglet is fitted on a wing, the links between the twist law on the one hand and wing root bending moment and drag on the other hand are significantly modified.

The wave drag and viscous drag evolutions are comparable but the induced drag sensitivity to twist is stronger. Consequently, the wave drag begins to compensate the induced drag at higher nose up twist values (1.5 degrees instead of 1 degree).

If the variation of wave drag and viscous drag are considered along the span for the different twist settings, the same conclusions can be drawn as for the clean configuration, except that the variations at the tip are damped, see figure (3.21).

In reference [HG06] the drag benefits and the penalties are compared for the tip fence and for the large winglet. For each of these two devices, these effects are also compared for the device from a rigid assessment, from wind tunnel measurements and from a flexible assessment at exactly the deformations measured in the wind tunnel. It is shown that the drag benefits of the tip fence are much smaller, but also the (structural) penalties (WRBM) are much smaller compared to the large winglet configuration, see also figure (3.17). The large winglet configuration is shown to have great drag benefits but also large structural implications. The purpose of this thesis is to improve the loads prediction methods, such that the structural reinforcement and thus additional weight for a wing with large winglet can be reduced such that the large winglet configuration can fully exploit its potential. In reference [HG06] it is further shown that their numerical prediction, especially the flexible one, compares correctly to the experimental deltas, but some differences remain. They argue that the discrepancy stems from some loss of accu-

Figure 3.19: *Wing plus large winglet - Loads variations along the span at cruise as a function of twist. Arrows indicate nose down twist. The wing tip variation is ± 1 degree in comparison to the reference. Black = reference, blue = nose down and red = nose up. Image by Jean-Luc Hantrais-Gervois, see also reference [HG06]. See figure (D.9) in the appendix for the full color image.*
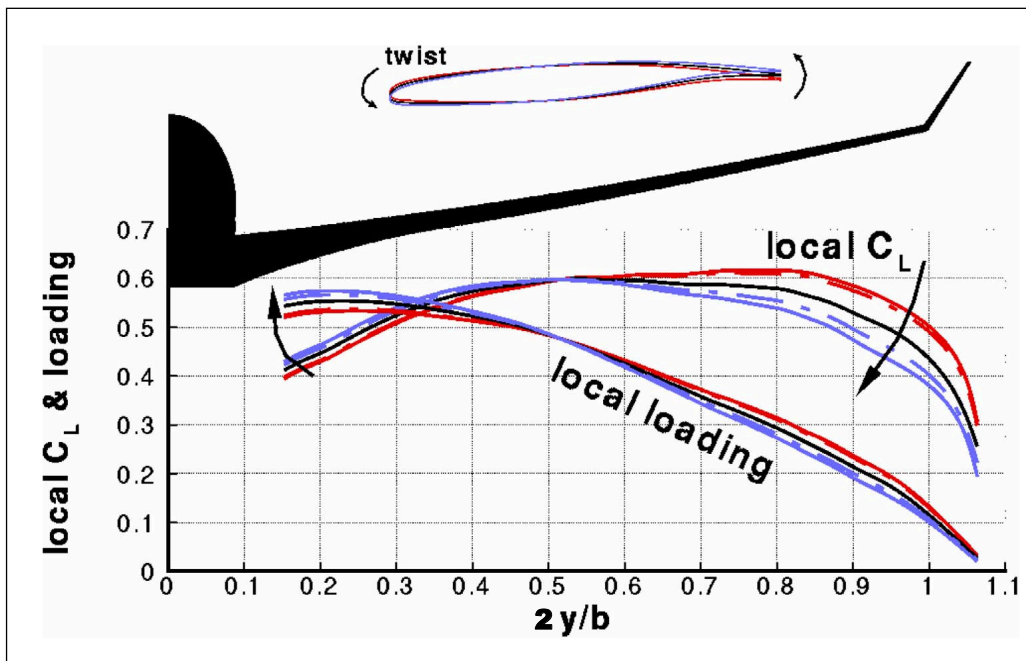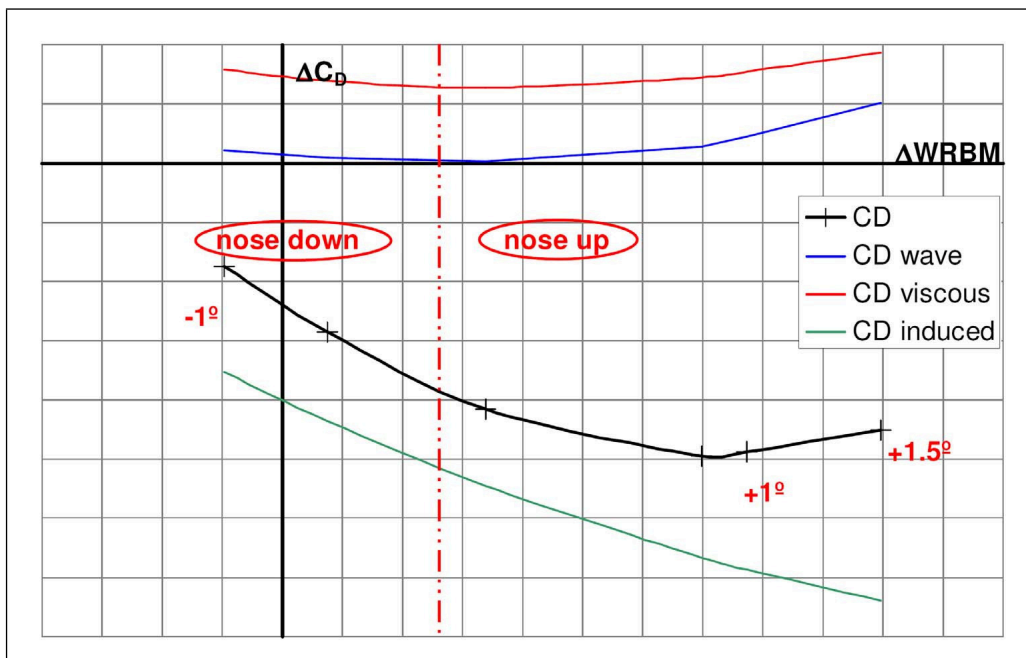

Figure 3.20: *Wing plus large winglet - Drag and WRBM increments to the reference clean flight shape at cruise as a function of twist. The wing tip variation is +1.5/-1 degree in comparison to the reference equipped with the large winglet (dash-dot red line). Image by Jean-Luc Hantrais-Gervois, see also reference [HG06]. See figure (D.10) in the appendix for the full color image.*

Figure 3.21: *Wing plus large winglet - Drag increments to the reference flight shape at cruise over span as a function of twist. The wing tip variation is ± 1 degree in comparison to the reference equipped with the large winglet. Blue = nose down and red = nose up. Image by Jean-Luc Hantrais-Gervois, see also reference [HG06]. See figure (D.11) in the appendix for the full color image.*
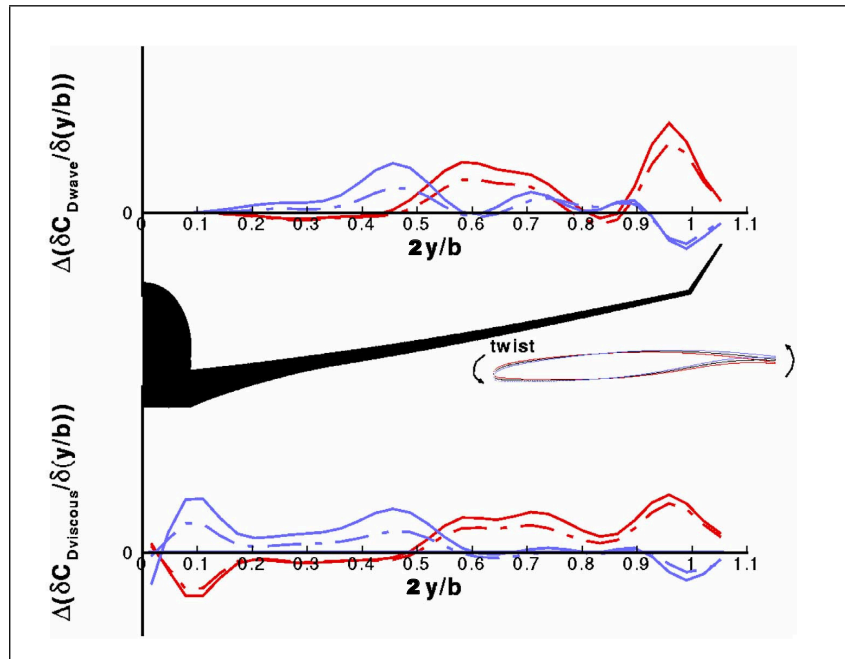
racy in the computations around the tip of the wing.

Due to the low bending moment impact of the wing tip fence, its rigid assessment is only refined with the flexible assessment (very small differences between the two). The large winglet assessment is more impacted. For this device, the drag gains diminish and the root bending moment is alleviated. This can be explained by the increase in the nose down twist in the outer wing due to the important aerodynamic load on the winglet (more than 0.3 degrees at the wing tip). The effect is a decrease in the outer wing loading in comparison to the rigid case and consequently alleviation of the wing loads.

The trade-off (quantified by a figure of merit: FoM, see further [HG06]) for the large winglet was shown to be negative in the rigid assessment. Saying that the weighted benefits were smaller than the weighted drawbacks. However when flexibility is taken into account, the FoM becomes beneficial. For the large devices, the global gains (FoM) are a difference between large aerodynamic gains and large structural losses. Both of these are strongly impacted by the wing twist law. Eventually the remaining gains or losses are subject to the accuracy of the method used.

In reference [HG06] comparisons are made of the aero-elastic behavior of the standard and large winglet configurations on a real aircraft. The aerodynamic model includes wings, engines, pylons, standard/large winglets, fuselage and the thrust is modelled. The tailplanes and flap track fairings were not modelled for these comparisons of reference [HG06]. It is remarked that these features have a small impact on the deltas between the standard and large winglet configurations.

As expected, the bending deformation and nose down twist increase with lift and the simulated results comply quite good with flight test measurements of the deformation and pressures for the cruise condition (M = 0.82, h = 36000 ft, C_L = 0.5). The suction peaks are correctly predicted, the rear loading and the lower wing part match the test too. The shock location over the wing is close to the experimental one. For the winglet, the pressure distribution exhibits a discrepancy, too much loading predicted by the simulation, see figure (3.27).

The behavior of both winglets is also compared for the same weight evolution, figures (3.22) and (3.23). Comparing light and heavy configurations, the wing has practically the same tendency in twist (wing tip difference of 0.9 degrees) and vertical deformation (wing tip difference of 0.4m) whatever the winglet is. Whereas bending is only slightly affected, the twist deformation is largely influenced by the tip device with a difference of 0.6 degrees to 0.65 degrees at the winglet root. This is clearly the effect of a redistribution of the spanwise aerodynamic loading of the wing.

Weight evolution at a fixed lift coefficient implies a change of altitude to operate the aircraft. This results in both a dynamic pressure effect and a Reynolds number effect. The impact of weight and flight level on the wing loading is presented in figure (3.24). The elastic impact makes the loading change between the inner and the outer wing around the mid wing (η = 0.6). The lighter the aircraft is, the more loading is located on the outboard wing (more nose up twist). The standard winglet is heavily loaded in comparison to the large winglet. The local load decreases for the large winglet in comparison to the standard winglet on the outboard wing before the winglet ($0.8 < \eta < 1.0$), which is directly related to the tip twist difference. It was shown that the twist deformation at the winglet root was largely influenced by the large winglet. At the same weight condition the large winglet configuration had significantly more nose down twist compared to the standard winglet configuration. The difference between the WRBM is small between the two winglets, see figure (3.24).

Drag comparison for the large and standard winglets

Figure (3.25) shows the drag evolution over weight for the large and standard winglets configuration. The loading shift induces a lift-induced drag increase with weight as the outboard loading decreases (higher weight, consequently more nose down twist, more inboard loading, increase in lift-induced drag). The wave drag is marginally impacted. The wing deformation effect due to weight is marginal for viscous drag, but the Reynolds number effect is important. A decrease in viscous drag occurs from the light to the heavy cruise. This effect is more pronounced than the induced drag variation. The total drag variation is limited for both winglets.

Figure (3.26) shows a direct drag comparison between the large and the standard winglet. The large winglet improves the lift induced drag over the whole weight range, due to the more outer wing loading. The drag directly provided by the aerodynamic software is too optimistic (integration of drag on the aircraft skin) compared to flight test results. These predictions are improved through the use of the drag analysis by the far field technique
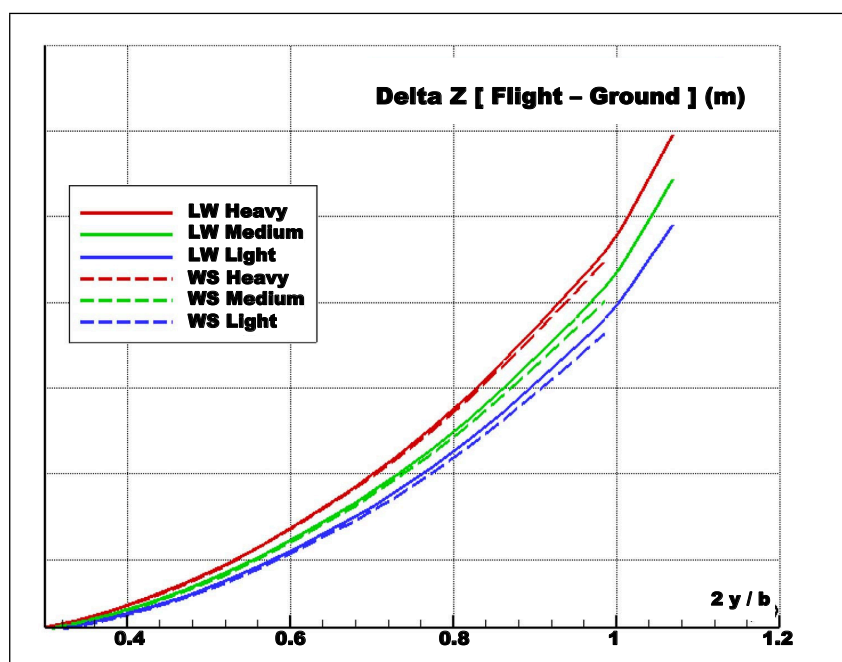
Figure 3.22: *Comparison of vertical bending deformations with a weight evolution for both winglets. Image by Jean-Luc Hantrais-Gervois, see also reference [HG06]. See figure (D.12) in the appendix for the full color image.*
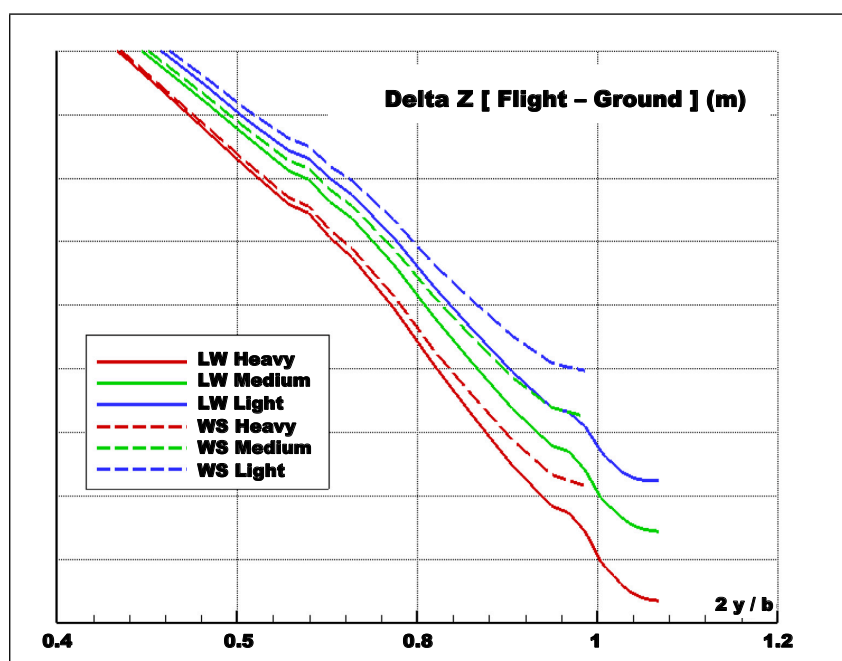
Figure 3.23: *Comparison of twist deformations with a weight evolution for both winglets. Image by Jean-Luc Hantrais-Gervois, see also reference [HG06]. See figure (D.13) in the appendix for the full color image.*
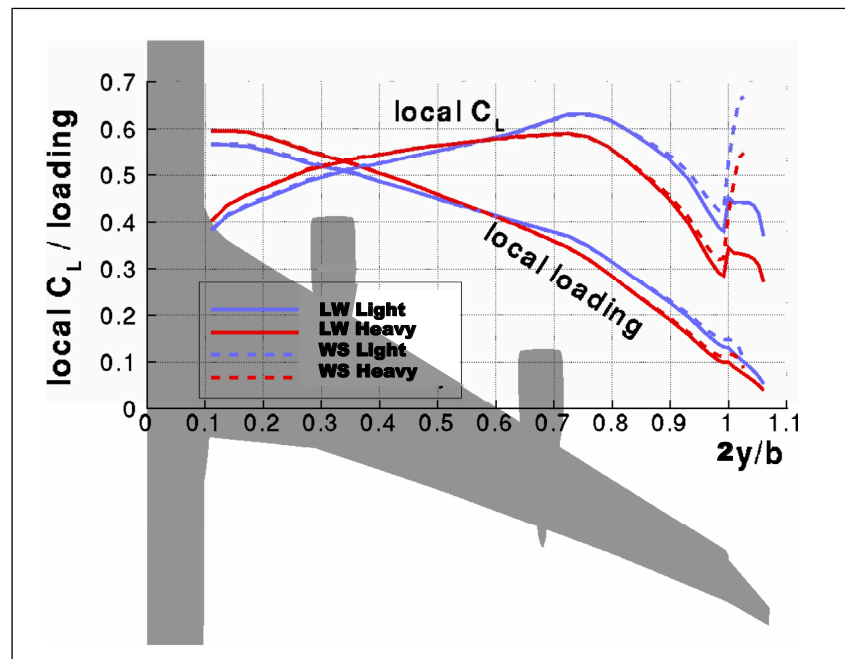
Figure 3.24: *Large winglet and standard winglet span loadings for two weights. Image by Jean-Luc Hantrais-Gervois, see also reference [HG06]. See figure (D.14) in the appendix for the full color image.*
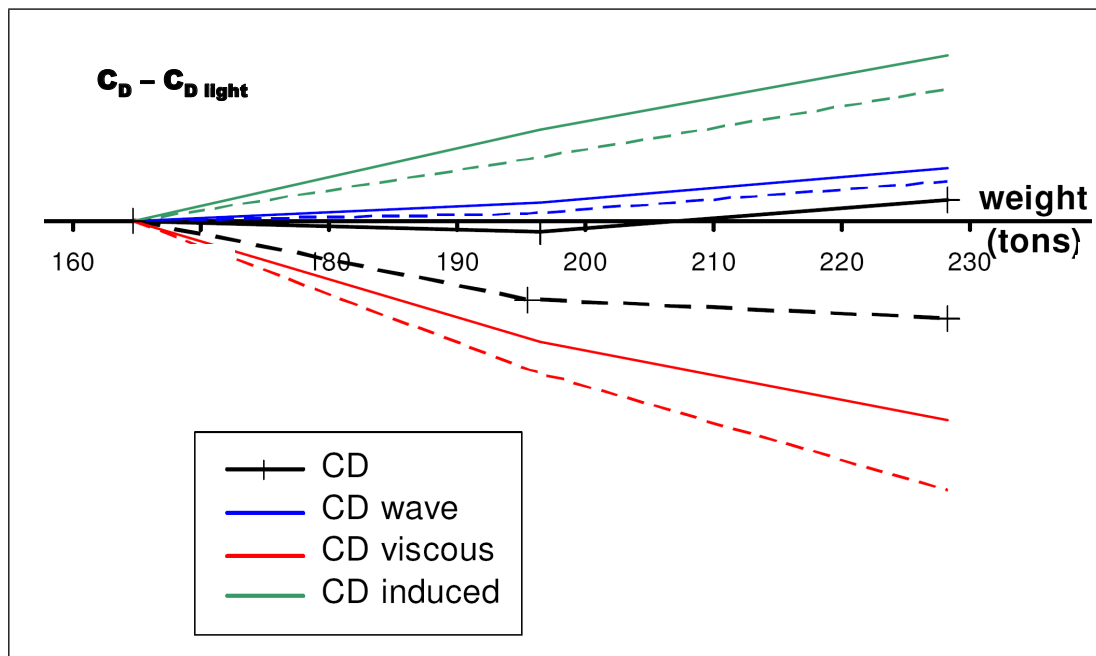
Figure 3.25: *Large winglet (solid lines) and standard winglet (dashed lines) drag evolutions over weight. Image by Jean-Luc Hantrais-Gervois, see also reference [HG06]. See figure (D.15) in the appendix for the full color image.*

by removing some numerical spurious drag. The far field predictions are closer to flight test measurements and the gradient of the drag gains over weight is accurate. The predictions here seem less precise because here the deltas between the standard and large winglet are very small. Previous comparison was performed between a clean wing and one with large winglets, where the deltas are significantly larger. Flight tests are also more difficult to handle than wind tunnel tests according to reference [HG06].

The large winglet total drag gains diminish with the weight of the aircraft, linked to both induced drag and viscous contributions. Due to its size, the large winglet is more affected by the twist variations than the standard winglet (induced drag). On the contrary, the decrease in viscous drag from the light to the heavy cruise condition is less pronounced for the large winglet due to its lower loading. At low weights it can be seen that the viscous drag on the large winglet configuration is even lower than on the standard winglet configuration.

Summary

Reference [HG06] concludes that some discrepancies between the tests and the computations remain on the complex wing tip pressure field. The aircraft weight and the flight level have a significant impact on the winglet performance over a cruise range. It is shown that it is difficult to assess a tip device in detail. When performing a wind tunnel test to assess tip devices, the clean wing jig shape is fixed and several tip devices are attached to it. However, it is shown that the flexibility of the airframe, and more specific the twist of the wing has a strong influence on the performance of the device. A fully numerical approach would be beneficial to develop adequate less conservative wing plus tip device assemblies.
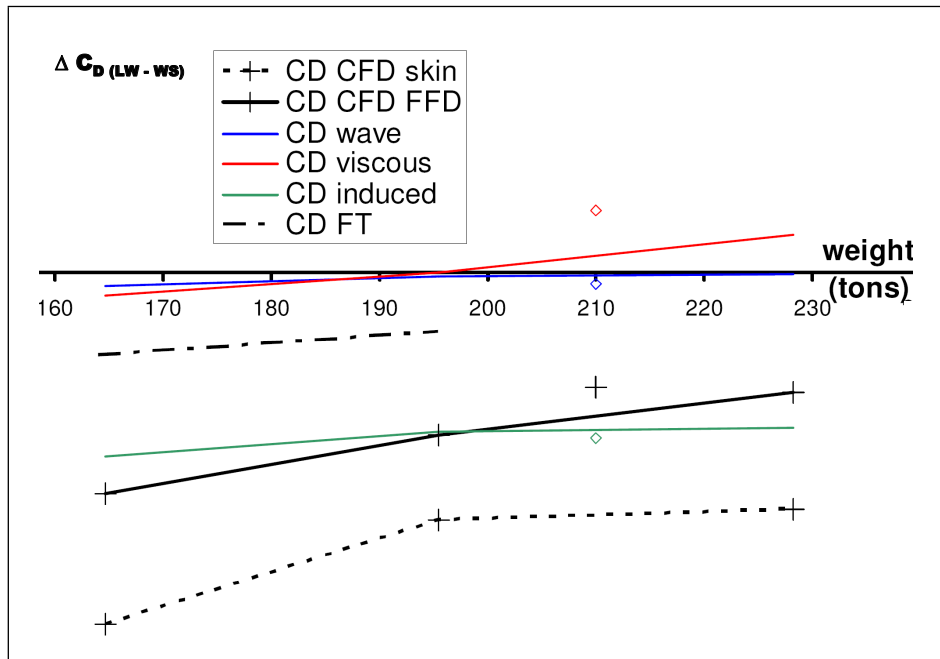
Figure 3.26: *Large winglet drag gains in comparison to the standard winglet as a function of weight. The rigid predictions are indicated in empty symbols. Image by Jean-Luc Hantrais-Gervois, see also reference [HG06]. See figure (D.16) in the appendix for the full color image.*
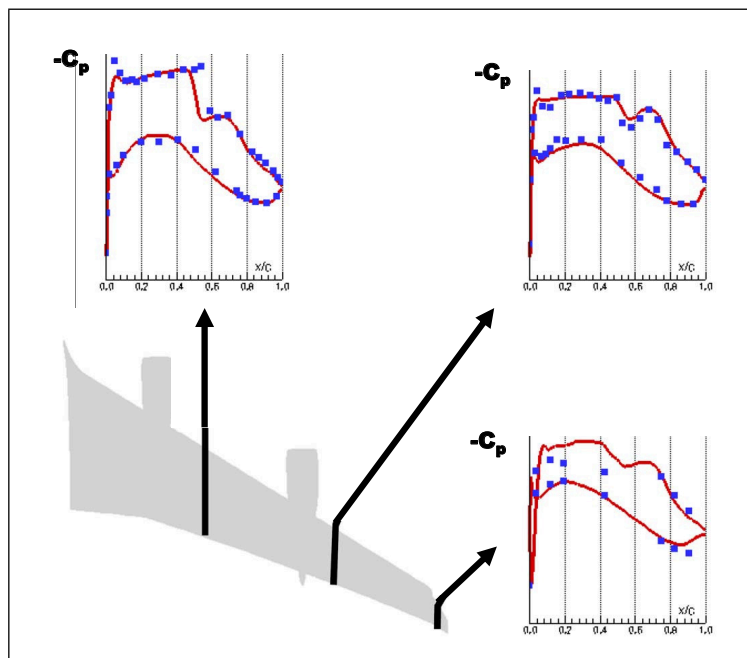
***Figure 3.27:*** *Computed pressure distributions for the large winglet configuration (lines) compared to the flight tests (symbols). Image by Jean-Luc Hantrais-Gervois, see also reference [HG06].*
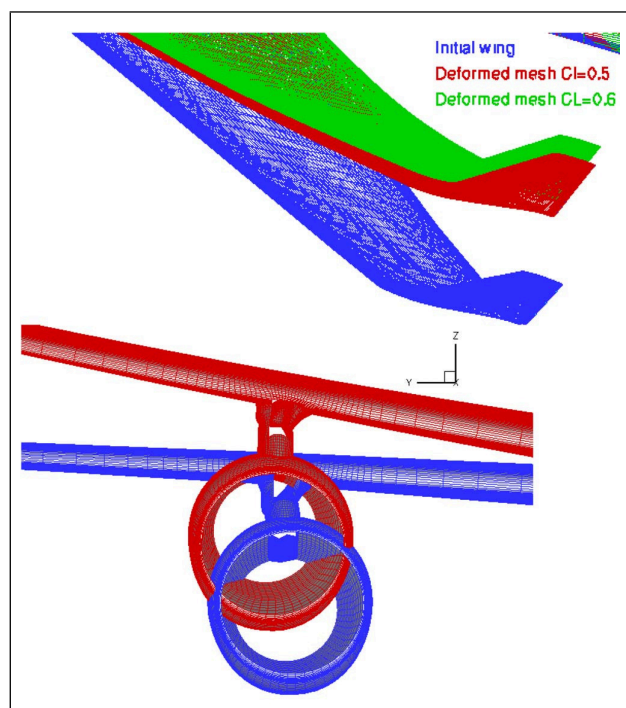
Figure 3.28: Examples of mesh deformation. Image by Jean-Luc Hantrais-Gervois, see also reference [HG06]. See figure (D.17) in the appendix for the full color image.

Chapter 4

Predictive modelling & calculation techniques

4.1 Finite Element Modelling

This section presents some of the basic and important aspects of the theoretical background of finite element modelling. In this section it is not described how to generate a finite element model starting from a continuous structure. It is assumed that a finite element model is already available for the specific structure. More information on the general steps of finite element modelling can be found in reference [Qu04]. For example the following items can be found in this reference in more detail:

- the discretization and selection of element types,

- the selection of displacement functions,

- the determination of relationships between stresses, strains and nodal displacements,

- the derivation of element matrices and equations,

- Assemblage of element equations.

4.1.1 Introduction

Numerical analysis is generally used to analyse structures that are of practical importance. These structures are usually too complex to be analysed by classical, analytical techniques. The numerical technique that is most widely used for structural and system analyses is the finite element method.

In the finite element method, a continuum is divided into a series but finite number of smaller regions, the finite elements. These finite elements should neither overlap nor have

Figure 4.1: General three dimensional solid or structure.

a gap between each other. Each element has so-called nodes, a number of key points that control the behavior of the element. These elements usually have simpler geometries, load conditions, boundary conditions, etc. than the original problem. This ensures that the stresses and displacement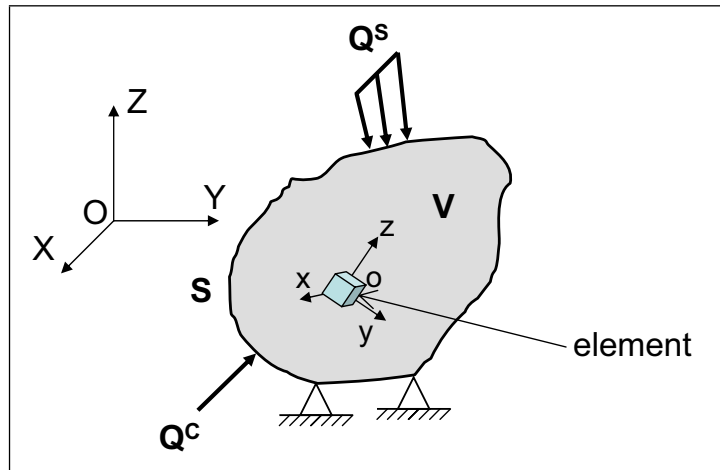s within each element vary monotonically. Consequently, the deformation within each element can be approximated by displacement functions. The stresses at any point in an element can be made dependant on those at the nodes. A finite number of differential equations of motion for such nodes must only be determined. This approach enables the conversion of a problem with an infinite number of degrees of freedom to one with a finite number. The solution process is heavily simplified.

The finite element method is the most convenient and accurate method for the analysis of large-scale structural systems with complex geometry, load conditions, material combinations, boundary conditions and geometrical and material nonlinearities. The finite element method was initially used for structural analysis, but it has been adapted to many other disciplines in engineering and mathematical physics, for example in fluid flow, heat transfer, diffusion, soil mechanics and many other phenomena.

4.1.2 Definitions

Consider a general three dimensional solid or structure of volume V enclosed by the surface S, see figure (4.1). The reference frame $OXYZ$ is the global reference frame, where XYZ are the global coordinates, also called structural coordinates, or system coordinates. The structure as a whole is referred to the global reference frame. There is only one global coordinate system in a particular analysis. Usually, it is aligned with the supports of the structure. The external forces acting on the structure can be categorized into body forces, surface forces and concentrated forces. These forces have the general form:

$$\mathbf{Q}^B = \begin{bmatrix} Q_x^B \\ Q_y^B \\ Q_z^B \end{bmatrix}, \quad \mathbf{Q}^S = \begin{bmatrix} Q_x^S \\ Q_y^S \\ Q_z^S \end{bmatrix}, \quad \mathbf{Q}^C = \begin{bmatrix} Q_x^C \\ Q_y^C \\ Q_z^C \end{bmatrix}, \tag{4.1}$$

The displacements at any point of the structure resulting from the external forces are defined in the global coordinates and denoted by:

$$\mathbf{U} = \begin{bmatrix} U \\ V \\ W \end{bmatrix}, \tag{4.2}$$

where U, V and W represent the displacements in the X, Y and Z directions respectively. Suppose the three dimensional structure is divided into N_E elements and N_N nodes. Each element has one set of local coordinates $oxyz$, see also figure (4.1). The local reference frame is aligned with the geometry of the finite element. The local coordinates are also called element coordinates. The external forces can be replaced by an equivalent nodal force vector that has the form:

$$\mathbf{F} = \begin{bmatrix} \mathbf{F}_1 \\ \mathbf{F}_2 \\ \vdots \\ \mathbf{F}_{N_N} \end{bmatrix}, \tag{4.3}$$

The nodal displacement vector $\mathbf{X}$ of the structure is similarly given by:

$$\mathbf{X} = \begin{bmatrix} \mathbf{X}_1 \\ \mathbf{X}_2 \\ \vdots \\ \mathbf{X}_{N_N} \end{bmatrix}, \tag{4.4}$$

Notice, that in equations (4.3) and (4.4) $\mathbf{F}_i$ and $\mathbf{X}_i$ are vectors whose sizes depend on the number of degrees of freedom at each node.

Consider an element in the structure. The external forces acting on this element can be written as:

$$\mathbf{q}^B = \begin{bmatrix} q_x^B \\ q_y^B \\ q_z^B \end{bmatrix}, \quad \mathbf{q}^S = \begin{bmatrix} q_x^S \\ q_y^S \\ q_z^S \end{bmatrix}, \quad \mathbf{q}^C = \begin{bmatrix} q_x^C \\ q_y^C \\ q_z^C \end{bmatrix}, \tag{4.5}$$

The displacements at any point within the three dimensional element can be represented by the vector:

$$\mathbf{u} = \begin{bmatrix} u \\ v \\ w \end{bmatrix}, \tag{4.6}$$

where u, v and w represent the displacements in the local coordinate directions x, y and z respectively.

If this element has n_n nodes, the equivalent nodal force vector $\mathbf{f}$ can be written as:

$$\mathbf{f} = \begin{bmatrix} \mathbf{f}_1 \\ \mathbf{f}_2 \\ \vdots \\ \mathbf{f}_{n_n} \end{bmatrix}, \tag{4.7}$$

Notice, that if all translational and rotational degrees of freedom are present for the nodes, the force vector at each node has the general form:

$$\mathbf{f}_i = \begin{bmatrix} f_{ix} \\ f_{iy} \\ f_{iz} \\ m_{ix} \\ m_{iy} \\ m_{iz} \end{bmatrix}, \tag{4.8}$$

for i = 1,2,..., n_n, where m denotes the moment. Similarly, the nodal displacement vector $\mathbf{x}$ of this element has the form:

$$\mathbf{x} = \begin{bmatrix} \mathbf{x}_1 \\ \mathbf{x}_2 \\ \vdots \\ \mathbf{x}_{n_n} \end{bmatrix}, \tag{4.9}$$

where:

$$\mathbf{x}_i = \begin{bmatrix} x_{ix} \\ x_{iy} \\ x_{iz} \\ \theta_{ix} \\ \theta_{iy} \\ \theta_{iz} \end{bmatrix}, \tag{4.10}$$

for i = 1,2,..., n_n, where θ denotes rotation.

4.1.3 Stress and strain

In this section the stress-strain relationships, together with the strain- and stress-displacement relationships, will be derived for linear elastic isotropic material.

As a reaction to the external loads excitation, various types of internal stresses and strains occur, depending on the nature of the problem. Consider an infinitesimal element $(dx \times dy \times dz)$ within a three dimensional solid, see figure (4.2).

Stress

There are three components of normal stresses (σ_x, σ_y and σ_z, where the subscript indicates the coordinate directions) and six components of shear stresses ($\tau_{xy}, \tau_{yz}, \tau_{xz}$, etc.). The first subscript of the shear stresses indicate the face of the element on which it acts, the second subscript indicates the coordinate direction. There are only three independent shear stresses, due to the following relations:

$$\tau_{xy} = \tau_{yx}, \quad \tau_{yz} = \tau_{zy}, \quad \tau_{zx} = \tau_{xz}. \tag{4.11}$$
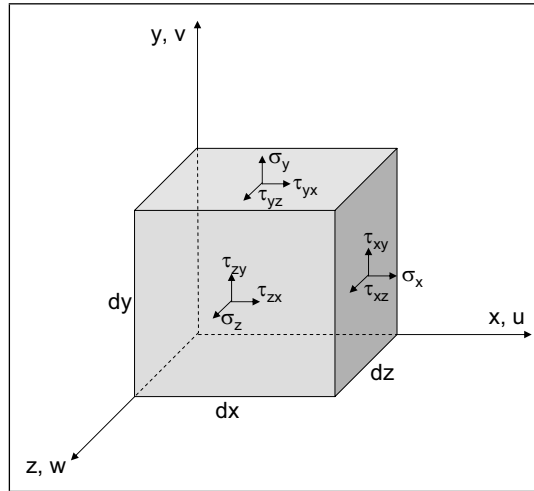
Figure 4.2: *Stresses on an infinitesimal element.*

Consequently, there are only six independent components of stress to be considered, that can be represented by the column vector:

$$\boldsymbol{\sigma} = \begin{bmatrix} \sigma_x \\ \sigma_y \\ \sigma_z \\ \tau_{xy} \\ \tau_{yz} \\ \tau_{zx} \end{bmatrix}. \tag{4.12}$$

Strain

There are three normal strains (ε_x, ε_y and ε_z) corresponding to the normal stresses. These normal strains are defined as:

$$\varepsilon_x = \frac{\partial u}{\partial x}, \quad \varepsilon_y = \frac{\partial v}{\partial y}, \quad \varepsilon_z = \frac{\partial w}{\partial z}. \tag{4.13}$$

Furthermore, there are three independent shear strains (γ_{xy}, γ_{yz} and γ_{zx}) corresponding to the three independent shear stresses. These independent shear strains are defined in terms of the derivatives of the translational displacements as:

$$\gamma_{xy} = \gamma_{yx} = \frac{\partial u}{\partial y} + \frac{\partial v}{\partial x}, \tag{4.14}$$

$$\gamma_{yz} = \gamma_{zy} = \frac{\partial v}{\partial z} + \frac{\partial w}{\partial y}, \tag{4.15}$$

$$\gamma_{zx} = \gamma_{xz} = \frac{\partial w}{\partial x} + \frac{\partial u}{\partial z}. \tag{4.16}$$

The six independent strains can be represented in a column vector, similar to the stress vector in equation (4.12), as:

$$\varepsilon = \begin{bmatrix} \varepsilon_x \\ \varepsilon_y \\ \varepsilon_z \\ \gamma_{xy} \\ \gamma_{yz} \\ \gamma_{zx} \end{bmatrix}. \tag{4.17}$$

Strain-stress relationships

The stress and strain vectors of equations (4.12) and (4.17) and their associated coordinate axes constitute a complete description of the state of stress and strain at any point in a three dimensional structure.

For linear elastic isotropic material, the strain-stress relationships can be written as:

$$\varepsilon_x = \frac{1}{E}(\sigma_x - \nu\sigma_y - \nu\sigma_z), \qquad \gamma_{xy} = \frac{\tau_{xy}}{G}, \tag{4.18}$$

$$\varepsilon_y = \frac{1}{E}(\sigma_y - \nu\sigma_z - \nu\sigma_x), \qquad \gamma_{yz} = \frac{\tau_{yz}}{G}, \tag{4.19}$$

$$\varepsilon_z = \frac{1}{E}(\sigma_z - \nu\sigma_x - \nu\sigma_y), \qquad \gamma_{zx} = \frac{\tau_{zx}}{G}, \tag{4.20}$$

where ν is Poisson's ratio, the constant E denotes Young's modulus of elasticity and the constant G is the shear modulus of elasticity, given by:

$$G = \frac{E}{2(1+\nu)}. \tag{4.21}$$

Hook's law, $\sigma = E\varepsilon$, is valid for linear elastic material or Hookean material. It practically states that the amount by which a material body is deformed (the strain) is linearly related to the force causing the deformation (the stress). If the equations (4.18) are now explicitly written in terms of the stress vectors of equations (4.12), the following strain-stress relationship (called generalised Hooke's Law) results:

$$\boldsymbol{\sigma} = \mathbf{E}\boldsymbol{\varepsilon}, \tag{4.22}$$

where $\mathbf{E}$ is called the stress-strain matrix, defined as:

$$\mathbf{E} = \frac{E}{(1+\nu)(1-2\nu)} \begin{bmatrix} 1-\nu & \nu & \nu & 0 & 0 & 0 \\ \nu & 1-\nu & \nu & 0 & 0 & 0 \\ \nu & \nu & 1-\nu & 0 & 0 & 0 \\ 0 & 0 & 0 & \frac{1-2\nu}{2} & 0 & 0 \\ 0 & 0 & 0 & 0 & \frac{1-2\nu}{2} & 0 \\ 0 & 0 & 0 & 0 & 0 & \frac{1-2\nu}{2} \end{bmatrix}. \tag{4.23}$$

The stresses must be related to the strains through the stress-strain law, generally called the constitutive law. The ability to define the material behavior accurately is most important in obtaining acceptable results. The simplest of stress-strain laws, Hooke's law is

often used in stress analysis.

Strain-displacement relationships
The displacements $\mathbf{u}$ at any point of an element in the finite element method are usually described in terms of the nodal displacements $\mathbf{x}$ using the displacement shape functions contained in the rectangular Matrix $\mathbf{N}$:

$$\mathbf{u} = \mathbf{Nx}. \tag{4.24}$$

The displacement function is generally approximate and the accuracy of the final result depends to a great extent on these functions. Two common types of displacement functions are simple polynomial and interpolation functions.

The strain-displacement relationships can now be derived introducing equation (4.24) into equations (4.13) to (4.16), such that:

$$\varepsilon = \mathbf{Cu}, \tag{4.25}$$

where matrix $\mathbf{C}$ is a linear differential operator matrix that expresses the strains in terms of the displacements $\mathbf{u}$:

$$\mathbf{C} = \begin{bmatrix} \frac{\partial}{\partial x} & 0 & 0 \\ 0 & \frac{\partial}{\partial x} & 0 \\ 0 & 0 & \frac{\partial}{\partial z} \\ \frac{\partial}{\partial y} & \frac{\partial}{\partial x} & 0 \\ 0 & \frac{\partial}{\partial z} & \frac{\partial}{\partial y} \\ \frac{\partial}{\partial z} & 0 & \frac{\partial}{\partial x} \end{bmatrix} \tag{4.26}$$

Substitution of equation (4.24) into (4.25) gives the strain displacement relationships, in terms of the nodal displacements $\mathbf{x}$:

$$\varepsilon = \mathbf{CNx} = \mathbf{Bx}, \tag{4.27}$$

where the matrix $\mathbf{B}$ is an array of derivatives of the shape functions.

Stress-displacement relationships
The derivation of the stress-displacement relationships in terms of the nodal displacements $\mathbf{x}$ is very straightforward. Substitution of equation (4.27) into equation (4.22), directly gives:

$$\sigma = \mathbf{EBx}, \tag{4.28}$$

where the matrix product $\mathbf{EB}$ gives the stresses at any point within the element due to unit values of nodal displacements.

4.1.4   Principle of Virtual Work

In this section, expressions will be derived for the mass and stiffness matrices and for the external force vector, using the Principle of Virtual Work. This principle plays a vital

role in the analysis of discretized continua using finite elements. The Principle of Virtual Work (using virtual displacements) is applicable for any material behavior, whereas Castigliano's theorem and the principle of minimum potential energy are only applicable to elastic materials. These are two other methods frequently used for derivation of element equations. All three principles yield identical element equations for linear-elastic materials. The choice for one of these methods for this kind of material in structural analysis is a matter of convenience and personal preference.

After derivation of the individual element equations, these can be assembled using a method of superposition (the direct stiffness method) to get the global equations for the whole structure. The basic assumption in this method is nodal equilibrium, and the concept of continuity or compatibility, requiring that the structure remains together and no tears occur anywhere in the structure.

According to the Principle of Virtual Work, the total work done by the internal (stresses) and external forces on any compatible, infinitesimal virtual displacement $\delta\mathbf{U}$ is zero:

$$\delta W = \delta W_{int} - \delta W_{ext} = 0. \tag{4.29}$$

The external work is equal to the actual body forces $\mathbf{Q}^B dV$, surface forces $\mathbf{Q}^S dS$, concentrated forces $\mathbf{Q}^C$ and inertia body forces $-\rho\ddot{\mathbf{U}}dV$ going through the virtual displacement $\delta\mathbf{U}$:

$$\delta W_{ext} = \int_V \delta\mathbf{U}^T\mathbf{Q}^B dV + \int_S \delta\mathbf{U}_S^T\mathbf{Q}^S dS + \sum_i \delta\mathbf{U}_i^T\mathbf{Q}_i^C - \int_V \delta\mathbf{U}^T\rho\ddot{\mathbf{U}}dV \tag{4.30}$$

where V is the volume of the solid with surface S. Notice that the virtual surface displacements where the surface forces act are denoted by the subscript S. The subscript i denotes the virtual displacement at the position where the concentrated force $\mathbf{Q}_i^C$ is applied.

The internal work is equal to the actual stresses $\boldsymbol{\sigma}$ going through the virtual strains $\delta\varepsilon$ (corresponding to the imposed virtual displacements $\delta\mathbf{U}$) and is given by:

$$\delta W_{int} = \int_V \delta\varepsilon^T\boldsymbol{\sigma}dV \tag{4.31}$$

Due to its complexity, the damping effect in the structure are temporarily ignored. Equations (4.30) and (4.31) can be rewritten as a sum integration over the volume and surface of all finite elements (N_E):

$$\delta W_{ext} = \sum_{m=1}^{N_E} \delta w_{ext} \tag{4.32}$$

$$= \sum_{m=1}^{N_E} \left[\int_v \delta\mathbf{u}^T\mathbf{q}^B dv + \int_s \delta\mathbf{u}_S^T\mathbf{q}^S ds + \sum_i \delta\mathbf{u}_i^T\mathbf{q}_i^C - \int_v \delta\mathbf{u}^T\rho\ddot{\mathbf{u}}dv \right]$$

$$\delta W_{int} = \sum_{m=1}^{N_E} \delta w_{int} = \sum_{m=1}^{N_E} \int_v \delta\varepsilon^T\boldsymbol{\sigma}dv \tag{4.33}$$

In the above equations m denotes the mth element. Furthermore, it is important to note that the integration in the upper equations are performed over the element volumes v and surfaces s for each element separately. Consequently, it is allowed to use different element coordinate systems in the calculations not only for reasons of convenience but it also makes the evaluation of the integrals of the general element assemblage very effectively.

The upper expression for the internal work can be rewritten in terms of the nodal displacements by substitution of equations (4.27) and (4.28):

$$\delta W_{int} = \sum_{m=1}^{N_E} \left[\int_v \delta\mathbf{x}^T \mathbf{B}^T \mathbf{E} \mathbf{B} \mathbf{x} \, dv \right] \tag{4.34}$$

The expression for the external work can similarly be rewritten in terms of the nodal displacements by substitution of equation (4.24):

$$\delta W_{ext} = \sum_{m=1}^{N_E} \left[\int_v \delta\mathbf{x}^T \mathbf{N}^T \mathbf{q}^B dv + \int_s \delta\mathbf{x}^T \mathbf{N}^T \mathbf{q}^S ds + \sum_i \delta\mathbf{x}^T \mathbf{N}_i^T \mathbf{q}_i^C - \int_v \delta\mathbf{x}^T \mathbf{N}^T \rho \mathbf{N} \ddot{\mathbf{x}} dv \right] \tag{4.35}$$

Substitution of the equations (4.34) and (4.35) into the Principle of Virtual Work, as stated in equation (4.29) and rearranging terms, leads to:

$$\sum_{m=1}^{N_E} \delta\mathbf{x}^T \left[\int_v \mathbf{B}^T \mathbf{E} \mathbf{B} \mathbf{x} \, dv + \int_v \mathbf{N}^T \rho \mathbf{N} \ddot{\mathbf{x}} dv \right] =$$

$$= \sum_{m=1}^{N_E} \delta\mathbf{x}^T \left[\int_v \mathbf{N}^T \mathbf{q}^B dv + \int_s \delta\mathbf{N}^T \mathbf{q}^S ds + \sum_i \mathbf{N}_i^T \mathbf{q}_i^C \right] \tag{4.36}$$

Considering the virtual displacements'characteristic and the relationships between the element displacements and structural displacements, the above expression can be written as:

$$\delta\mathbf{X}^T \left[\sum_{m=1}^{N_E} \left[\int_v \mathbf{B}^T \mathbf{E} \mathbf{B} \, dv \right] \mathbf{X} + \sum_{m=1}^{N_E} \left[\int_v \mathbf{N}^T \rho \mathbf{N} dv \right] \ddot{\mathbf{X}} \right] =$$

$$\delta\mathbf{X}^T \sum_{m=1}^{N_E} \left[\int_v \mathbf{N}^T \mathbf{q}^B dv + \int_s \delta\mathbf{N}^T \mathbf{q}^S ds + \sum_i \mathbf{N}_i^T \mathbf{q}_i^C \right] \tag{4.37}$$

This expression can be further simplified to:

$$\sum_{m=1}^{N_E} \left[\int_v \mathbf{B}^T \mathbf{E} \mathbf{B} \, dv \right] \mathbf{X} + \sum_{m=1}^{N_E} \left[\int_v \mathbf{N}^T \rho \mathbf{N} dv \right] \ddot{\mathbf{X}} = \tag{4.38}$$

$$\sum_{m=1}^{N_E} \left[\int_v \mathbf{N}^T \mathbf{q}^B dv + \int_s \delta\mathbf{N}^T \mathbf{q}^S ds + \sum_i \mathbf{N}_i^T \mathbf{q}_i^C \right]$$

Equation (4.38) are the equilibrium equations of the undamped structure written in terms of the nodal displacements. These equations can be written in the short and well-known form:

$$\mathbf{M\ddot{X}} + \mathbf{KX} = \mathbf{F}, \tag{4.39}$$

where $\mathbf{M}$ and $\mathbf{K}$ are respectively the mass and stiffness matrices of the structure. It can be seen from equation (4.38) that these have the form:

$$\mathbf{M} = \sum_{m=1}^{N_E} \left[\int_v \mathbf{N}^T \rho \mathbf{N} dv \right] = \sum_{m=1}^{N_E} \mathbf{M}_m, \tag{4.40}$$

$$\mathbf{K} = \sum_{m=1}^{N_E} \left[\int_v \mathbf{B}^T \mathbf{E} \mathbf{B}\, dv \right] = \sum_{m=1}^{N_E} \mathbf{K}_m, \tag{4.41}$$

where $\mathbf{M}_m$ and $\mathbf{K}_m$ are the element mass and stiffness matrices with respect to the global coordinates. In element or local coordinates, these element matrices are given by:

$$\mathbf{m}_m = \int_v \mathbf{N}^T \rho \mathbf{N} dv, \tag{4.42}$$

$$\mathbf{k}_m = \int_v \mathbf{B}^T \mathbf{E} \mathbf{B}\, dv. \tag{4.43}$$

The equivalent force vector contains the effects of element body forces, surface forces and concentrated forces:

$$\mathbf{F} = \mathbf{F}^B + \mathbf{F}^S + \mathbf{F}^C \tag{4.44}$$

defined as:

$$\mathbf{F}^B = \sum_{m=1}^{N_E} \left[\int_v \mathbf{N}^T \mathbf{q}^B dv \right] = \sum_{m=1}^{N_E} \mathbf{F}^B_m, \tag{4.45}$$

$$\mathbf{F}^S = \sum_{m=1}^{N_E} \left[\int_s \delta \mathbf{N}^T \mathbf{q}^S ds \right] = \sum_{m=1}^{N_E} \mathbf{F}^S_m, \tag{4.46}$$

$$\mathbf{F}^C = \sum_{m=1}^{N_E} \left[\sum_i \mathbf{N}_i^T \mathbf{q}_i^C \right] = \sum_{m=1}^{N_E} \mathbf{F}^C_m, \tag{4.47}$$

Notice that in the above derivation, stresses and strains were considered due to the nodal displacements only. If initial strains ε_0 exist, the stress vector can be expressed as:

$$\boldsymbol{\sigma} = \mathbf{E}(\boldsymbol{\varepsilon} - \boldsymbol{\varepsilon}_0) \tag{4.48}$$

This expression can be substituted for $\boldsymbol{\sigma}$ in equation (4.31) to get the contribution from initial strain $\mathbf{F}^\varepsilon$ to the equivalent force:

$$\mathbf{F} = \mathbf{F}^B + \mathbf{F}^S + \mathbf{F}^C + \mathbf{F}^\varepsilon. \tag{4.49}$$

The effect of the element initial strains is given by:

$$\mathbf{F}^\varepsilon = \sum_{m=1}^{N_E} \left[\int_v \mathbf{B}^T \mathbf{E} \boldsymbol{\varepsilon}_0 dv \right] = \sum_{m=1}^{N_E} \mathbf{F}_m^\varepsilon. \tag{4.50}$$

In the above derivation, the acceleration field (the inertia forces) was defined using the assumed displacement field of the element. In the finite element formulation, this is the most commonly used formulation for the mass matrix, the so-called consistent mass formulation. The resulting mass matrix is often nondiagonal and positive definite and is called the consistent mass matrix.
The lumped mass formulation is another commonly used mass formulation in the finite element method. The element mass matrix is obtained by lumping the element mass at the nodal points. One possibility of using the lumped mass approach is to describe the inertia of the element by concentrated masses that have zero moment of inertia about their centers. The resulting mass matrix is singular for the bending beam, plate, etc. because no inertia is assigned to the rotational degrees of freedom. The resulting mass matrix is called a lumped mass matrix.

4.1.5   Dynamic Equations of Motion

Recall, that damping effects were temporarily neglected in the derivation of the mass and stiffness matrices for the finite element model, see the previous section. Generally, the formulation of mathematical expressions for the energy dissipation is quite complicated. Therefore often simplified models are sought that give adequate results, that are fit for purpose. The main question is: under which circumstances can the effects of damping upon the dynamic responses be ignored?

- A typical example is the short time response of a structure that has very little damping and is excited by a short-duration shock.

- The damping effects on the steady state response can also be ignored when the frequency of a periodic excitation is far away from the resonance or eigenfrequencies of the system.

Damping should be included in the dynamic analysis when the exciting frequency is close to the natural frequency as damping effect become significant. There are three commonly used damping models:

- viscous damping: occurs when a structure is moving in a fluid medium. The damping force is a function of the velocity of the moving fluid. In the simplified viscous damping model, the damping force is assumed to be linearly proportional to the velocity of a particle moving in fluid.

- structural damping: is caused by relative motions between components in a structure that has common points of contact, joints or supports.

- internal damping or material damping: results from various microscopic and macroscopic processes in material.

If the damping is modelled with linear viscous damping, equation (4.39) can be modified as follows:

$$\mathbf{M\ddot{X}} + \mathbf{C\dot{X}} + \mathbf{KX} = \mathbf{F}, \tag{4.51}$$

This equation is the general form of the dynamic equilibrium equations of the structure with linear viscous damping. The matrix $\mathbf{C}$ is the damping matrix whose elements or damping coefficients, can be seen as the forces required by unit velocities. The vectors $\mathbf{\ddot{X}}$, $\mathbf{\dot{X}}$ and $\mathbf{X}$ are respectively the acceleration, velocity and displacement vector, of the full model with n degrees of freedom, defined as:

$$\mathbf{\ddot{X}}(t) = \begin{bmatrix} \ddot{x}_1(t) \\ \ddot{x}_2(t) \\ \vdots \\ \ddot{x}_n(t) \end{bmatrix}, \mathbf{\dot{X}}(t) = \begin{bmatrix} \dot{x}_1(t) \\ \dot{x}_2(t) \\ \vdots \\ \dot{x}_n(t) \end{bmatrix}, \mathbf{X}(t) = \begin{bmatrix} x_1(t) \\ x_2(t) \\ \vdots \\ x_n(t) \end{bmatrix}, \mathbf{F}(t) = \begin{bmatrix} f_1(t) \\ f_2(t) \\ \vdots \\ f_n(t) \end{bmatrix} \tag{4.52}$$

where $\mathbf{F}(t)$ is the vector of applied forces and the time t denotes that the acceleration, velocity, displacement responses and external forces are time dependent.

The mass, damping and stiffness matrices are symmetrical and highly banded. The mass matrix is usually positive definite, the damping matrix semi-positive definite. The stiffness matrix is positive definite for the system without a rigid mode and semi-positive definite for the system with a rigid model. The stiffness matrix is usually singular, its determinant is zero and it has one or more rigid degrees of freedom. To remove this singularity problem, certain boundary conditions must be invoked (or constraints or supports) such that the structure remains in place instead of moving as a rigid body.

Equation (4.51) represents in general a set of n simultaneous linear second-order ordinary differential equations with constant coefficients.

Fourier Transformation of the dynamic equilibrium equations

Suppose that all the components of the vectors $\mathbf{X}(t)$ and $\mathbf{F}(t)$ are Fourier transformable and their transformations are respectively $\mathbf{X}(\omega)$ and $\mathbf{F}(\omega)$, and the start condition holds that $\mathbf{\ddot{X}}(t) = \mathbf{X}(t) = \mathbf{0}$ for $t = 0$. Using the property of the Fourier transform that the Fourier transform of $\frac{dX}{dt}$ is equal to $i\omega X(\omega)$, the Fourier transformation of equation

(4.51) can be written as:

$$(-\omega^2\mathbf{M} + i\omega\mathbf{C} + \mathbf{K})\mathbf{X}(\omega) = \mathbf{F}(\omega), \tag{4.53}$$

where ω is the circular frequency of exciting forces and $i = \sqrt{-1}$. The vector $\mathbf{X}(\omega)$ is called the frequency response vector. Equation (4.53) can be rewritten using the frequency response function $\mathbf{H}(\omega)$ defined as:

$$\mathbf{H}(\omega) = (-\omega^2\mathbf{M} + i\omega\mathbf{C} + \mathbf{K})^{-1} \tag{4.54}$$

in the short notation:

$$\mathbf{X}(\omega) = \mathbf{H}(\omega)\mathbf{F}(\omega), \tag{4.55}$$

4.2   Model reduction

In loads analysis, a large amount of flight conditions and loading conditions must be covered. This necessitates a reduction of the degrees of freedom of the complex, highly detailed finite element model in order to have a cost and time efficient model.
The number of degrees of freedom can be reduced in several ways. The oldest and most popular one is the static or Guyan reduction. The Guyan reduction is only exact at zero frequency. For cases involving dynamic effects due to inertia forces in the structure, other methods will produce better results as presented in reference [Myk02]. In this reference the three methods are compared to each other statically and dynamically for a 15 degrees of freedom mass-spring system. It is stated that the differences between the three reduction methods are equally well illustrated with this simplified system. Although the three reduction methods considered here, are usually applied to finite element structures. The three reduction methods are:

- static or Guyan reduction

- Improved Reduced System (IRS) method

- Component Mode Synthesis (CMS) method

In the above methods, it is assumed that the mass and stiffness matrices are coupled and are simultaneously reduced. This is a natural procedure in case a structure is modelled with finite elements having stiffness and material (density) properties.
It is common practice however to model the structure by finite elements having stiffness properties but zero mass. The masses of the structure are modelled separately by a lumped mass model, already introduced in section 4.2.4. This modelling procedure allows that core competencies can be split up in structure and mass issues, that can be treated by two specialized groups of engineers. Traditionally by a structural and a mass department. The advantage of such a modelling procedure is that during the design loops of a specific airframe, updates in the mass model may occur, due to the better insight coming with each step in the design process. This mass update must not imply a change

in the mass bounds (see section 4.2.4). As long as the mass bounds remain the same, the mass model update does not require a new reduction of the stiffness model, the stiffness properties of the model do not change.
In case of the coupled model reduction, each change in either mass or stiffness model requires a new reduction of the full finite element model.

In this investigation, the structural model is reduced by a static Guyan reduction, which is exact statically, there is no error in the modes. In the case of this decoupled procedure, this is also called quasi-static reduction. This reduced stiffness matrix is then coupled with the lumped mass model. This mass model is a very good representation of the airframe. The engineers of the mass department can be assumed to know their job. Coupling of the lumped mass model with the reduced stiffness matrix results in good correspondence of the dynamic reaction of reduced model compared with that of the full model. In a dynamic analysis, as long as the lumped masses correctly represent the airframe, the correct inertia terms will be accounted for.

4.2.1   Overview of reduction methods

This information is taken from [Qu04]. Although the computer speed and memory capacity continue to double every eighteen months, the phenomenon that the demand of computer storage and speed exceeds existing capabilities has been consistently demonstrated in finite element analysis during the past half century. The development of increasing complex structures and mechanical systems demands sophisticated simulation techniques for design, control and optimization. These systems typically involve multiple coupled energy domains and media (mechanical, electrical, magnetically, etc.) and inherent nonlinearities of electrostatic actuation forces, geometric nonlinearities caused by large deformation, material nonlinearities and other nonlinearities exist. Due to the complex nature of these systems, the size of discrete models resulting from the finite element model is usually very large. Even though modern supercomputers might be able to handle that size of engineering problem, the simulations would be extremely computationally intensive and time-consuming if the full model is used directly.
The most important conclusion that can be drawn from these limitations on the hardware (computer storage and speed) and computational cost and time is: the computational technique is as important as the computer technique. Efficient computational techniques may significantly reduce the computer storage and time required.
The computational effort of finite element analysis is approximately proportional to the cubic of the size of a problem, see [Qu04]. The computational work could be reduced drastically if the size of the problem is reduced. Therefore, recently it has become a major goal of simulation and modelling research to develop efficient model reduction methods for creating accurate low-order dynamic models. This is one of the motivations of the development of model reduction technique.
Generally, the experimental results from a modal test are used to verify and modify a finite element model in the stage of design and analysis. Due to the complexity of practical structural systems and limitation of the testing technique, the measured data from a modal test are incomplete. The main incompleteness is the insufficiency of the mea-

sured degrees of freedom. The number of measured degrees of freedom is in general much smaller than that of the total degrees of freedom in the finite element model. This incompatibility between two models may be solved either by reducing the finite element model to the size of the test model or by expanding the test model to the size of the finite element model. Both necessitates the model reduction technique. This is the second motivation of using model reduction techniques.

Other motivation can be found in active control, interaction problems, etc. The reduced order model control is very popular in control engineering.

The size of a full model can be reduced significantly with the application of model reduction techniques. However, due to the truncated errors, the reduced model cannot retain all features of the full model. Therefore, there is a trade-off between the size of the model and its accuracy. The crux of model reduction is to pursue a smallest model that contains the highest degree of information of the full model.

There are many techniques of model reduction, for example: static condensation, exact condensation, dynamic condensation, SEREP and iterative dynamic condensation.

Dynamic Model Reduction techniques

Model order reduction techniques are common practice in the structural dynamics community. It is used in global-local analysis, reanalysis and structural dynamic optimisation, eigenvalue problem, structural vibration and buckling, model update, damage detection and sensitivity studies and control parameters design. Reduced order models have also been used to analyse different non-structural problems related to heat transfer, fluid-structure interaction, other linear and nonlinear steady-state boundary value problems.

In structural dynamic analyses, the dynamic equations of equilibrium are generally written as a set of linear second-order differential equations, see also equation (4.51):

$$\mathbf{M}\ddot{\mathbf{X}}(t) + \mathbf{C}\dot{\mathbf{X}}(t) + \mathbf{K}\mathbf{X}(t) = \mathbf{F}(t), \tag{4.56}$$

where $\mathbf{M}$ is the mass matrix, $\mathbf{C}$ is the damping matrix, $\mathbf{K}$ is the stiffness matrix, all $\epsilon\, R^{n \times n}$ of the full order model, simply called full model. $\ddot{\mathbf{X}}, \dot{\mathbf{X}}$, and $\mathbf{X} \; \epsilon \;\; R^n$ are the acceleration, velocity and displacement response vectors respectively, of the full model under the external loads $= \mathbf{F}\epsilon R^n$. This is also called the equivalent force vector acting on the model. The number of degrees of freedom of the full model is denoted by n. Since this number n is generally very large for a practical structural problem, dynamic analyses, simulations and design require very expensive computational efforts. The size of the full model is usually reduced by introducing a model reduction technique that leads to a reduced order model.

Many model reduction schemes involve the form of coordinate transformation:

$$\mathbf{X}(t) = \mathbf{T}\mathbf{Z}(t) \tag{4.57}$$

where $\mathbf{T}\epsilon R^{n \times m}$ is the coordinate transformation matrix, and $\mathbf{Z}\epsilon R^m$ are the reduced order coordinates. Generally, it is assumed that the transformation matrix $\mathbf{T}$ is time invariant, such that differentiation of equation (4.57) with respect to time gives:

$$\dot{\mathbf{X}}(t) = \mathbf{T}\dot{Z}(t) \tag{4.58}$$

$$\ddot{\mathbf{X}}(t) = \mathbf{T}\ddot{Z}(t) \tag{4.59}$$

Now these expressions can be substituted into equation (4.56). Together with a left-multiplication of the transpose of the transformation matrix $\mathbf{T}$ this leads to:

$$\mathbf{T}^T\mathbf{M}\mathbf{T}\ddot{\mathbf{Z}}(t) + \mathbf{T}^T\mathbf{C}\mathbf{T}\dot{\mathbf{Z}}(t) + \mathbf{T}^T\mathbf{K}\mathbf{T}\mathbf{Z}(t) = \mathbf{T}^T\mathbf{F}(t) \tag{4.60}$$

$$\mathbf{M}_R\ddot{\mathbf{Z}}(t) + \mathbf{C}_R\dot{\mathbf{Z}}(t) + \mathbf{K}_R\mathbf{Z}(t) = \mathbf{F}_R(t) \tag{4.61}$$

where the reduced mass, damping and stiffness matrices are introduced,by:

$$\mathbf{M}_R = \mathbf{T}^T\mathbf{M}\mathbf{T} \tag{4.62}$$

$$\mathbf{C}_R = \mathbf{T}^T\mathbf{C}\mathbf{T} \tag{4.63}$$

$$\mathbf{K}_R = \mathbf{T}^T\mathbf{K}\mathbf{T} \tag{4.64}$$

$\mathbf{M}_R, \mathbf{C}_R$ and $\mathbf{K}_R \epsilon R^{m \times m}$. Equation (4.61) are the reduced dynamic equations of equilibrium.The dynamic characteristics of the full model within the interested frequency range may be retained in the reduced model, although the size of the reduced model will be much smaller, $m << n$. The reduced model is therefore very useful in further dynamic analyses, especially when repeated computation is required.

Based on the type of coordinates retained as the reduced order coordinates, the existing model order reduction techniques fall into three basic categories:

- physical coordinate reduction,

- generalised coordinate reduction,

- hybrid coordinate reduction.

Physical coordinate reduction
It is called physical coordinate reduction, if the reduced model is obtained by removing part of the physical coordinates of the full model. The coordinates of the reduced model actually belong to a subset of the full model. Of the three categories of model reduction, this one is the most straightforward. The physical coordinate reduction is usually called dynamic condensation. Its coordinate transformation matrix takes the form

$$\mathbf{T} = \begin{bmatrix} \mathbf{I} \\ \mathbf{R} \end{bmatrix} \tag{4.65}$$

where $\mathbf{I}$ is the identity matrix of order m, $\mathbf{R}$ is called the dynamic condensation matrix.

Generalised coordinate reduction
All the coordinates that are not physical coordinates are generally referred to as generalised coordinates. The modal coordinate and the Ritz coordinate are two types of frequently used generalised coordinates. Modal coordinate reduction is one of the classical methods of the generalised coordinate reduction. The dynamic responses of an n degree of freedom model in the physical space $\mathbf{X}$ can be expressed in terms of the modal coordinates in the modal space $\mathbf{q}_m$:

$$\mathbf{X}(t) = \mathbf{\Phi}_m\mathbf{q}_m \tag{4.66}$$

where $\mathbf{\Phi}_m \epsilon R^{n \times m}$ is the eigenvector matrix of the full model. Each column of this matrix is an eigenvector or mode shape. The m modes may be taken from the lowest frequency range or any interested frequency range or any interested modes of the full model, depending on the frequency spectral of exciting forces. Substitution of equation (4.66) into (4.56) followed by a left multiplication with the transpose of the eigenvector matrix, leads to:

$$\mathbf{M}_r \ddot{\mathbf{q}}_m(t) + \mathbf{C}_r \dot{\mathbf{q}}_m(t) + \mathbf{K}_r \mathbf{q}_m(t) = \mathbf{F}_r(t) \tag{4.67}$$

where the modal mass, modal damping and modal stiffness matrices are defined as:

$$\mathbf{M}_r = \mathbf{\Phi}_m{}^T \mathbf{M} \mathbf{\Phi}_m \tag{4.68}$$

$$\mathbf{C}_r = \mathbf{\Phi}_m{}^T \mathbf{C} \mathbf{\Phi}_m \tag{4.69}$$

$$\mathbf{K}_r = \mathbf{\Phi}_m{}^T \mathbf{K} \mathbf{\Phi}_m \tag{4.70}$$

The modal mass and stiffness matrices are diagonal matrices for this linear model. Depending on the type of damping matrix, the modal damping matrix might be diagonal. The m equations of (4.66) can be uncoupled in the modal space by normalisation of the eigenvector matrix $\mathbf{\Phi}_m$ with respect to the mass matrix. The modal mass and stiffness matrices become the identity matrix and the eigenvalue matrix of the full model together with equation (4.66), can be seen as m single degree of freedom models. This procedure is known as mode superposition or modal superposition. A more detailed description on modal analysis can be found in section 4.2.2.

In the transformation from the physical coordinates to the generalised coordinates, it is not always necessary to determine the eigenvectors of the full model. If the loads are known, the approximation by Ritz vectors can be chosen as a good representation of the eigenvectors for example. The costly eigenvalue analysis may then be skipped and in some cases where the eigenvectors are not the best choice the accuracy might be increased. The Ritz vector methods can be seen as a generalised mode superposition approach in which the exact eigenvectors are replaced by more generally defined Ritz vectors. However, the dynamic equations of motion of the reduced model derived with the Ritz vector methods are generally coupled. In the modal coordinate reduction, they are usually uncoupled. The Ritz vector method has a similar coordinate transformation as given in equation (4.66). The generalised coordinates in the Ritz vector method are called Ritz coordinates. The construction of the Ritz vectors is generally more computationally efficient than the determination of the exact eigenvectors.

Hybrid reduction

There are many hybrid coordinate reduction schemes. A typical hybrid reduction is the fixed interface component mode synthesis. The coordinates of the reduced model consist of some physical coordinates of the full model and part of the modal coordinates of the model with the interface degrees of freedom fixed. The coordinate transformation has the form:

$$\mathbf{T}_{CMS} = \begin{bmatrix} \mathbf{\Phi}_N & \mathbf{R}_{Guyan} \\ \mathbf{0} & \mathbf{I} \end{bmatrix} \tag{4.71}$$

4.2.2   Modal analysis

The dynamic characteristics (dynamic responses, strains, stresses, etc.) of the system can be obtained by solving the differential equations of the finite element model, equation (4.51), using direct integration methods in the time domain. For example with the finite difference method, or with the Newmark method. Alternatively, these coupled equations of motion may be solved by transforming them into a set of independent uncoupled equations by means of a modal matrix. This procedure is the classical meaning of modal analysis. Actually, the procedure of determining the system's modal parameters, including the natural frequency, natural mode, damping factor, modal scaling, etc., is also referred to as modal analysis. The determination of these modal parameters may be of either a theoretical (analytical or numerical) approach and called theoretical modal analysis, or may be an experimental approach, called experimental modal analysis.

Modal theory of undamped systems

In the absence of damping and external forces, the dynamic equations (4.51) reduce to:

$$\mathbf{M}\ddot{\mathbf{X}}(t) + \mathbf{K}\mathbf{X}(t) = \mathbf{0}, \tag{4.72}$$

referred to as undamped free vibration. These are n simultaneous homogeneous differential equations. Generally, the solution of this equation has the form:

$$\mathbf{X}(t) = \boldsymbol{\phi}\sin(\omega t + \psi), \tag{4.73}$$

where $\boldsymbol{\phi}$ is the vector of amplitudes or mode shapes, ω is the frequency of harmonic response or natural frequency and ψ is the phase angle. Differentiation of equation (4.73) twice with respect to time gives:

$$\ddot{\mathbf{X}}(t) = -\omega^2\boldsymbol{\phi}\sin(\omega t + \psi). \tag{4.74}$$

Substitution of these expressions for $\ddot{\mathbf{X}}$ and $\mathbf{X}$ into equation (4.72) leads to a set of n algebraic equations:

$$(\mathbf{K} - \omega^2\mathbf{M})\boldsymbol{\phi} = \mathbf{0}, \tag{4.75}$$

which has the form of an algebraic eigenvalue problem. Nontrivial solutions only exist if the determinant of the coefficient matrix is equal to zero:

$$|\mathbf{K} - \omega^2\mathbf{M}| = 0. \tag{4.76}$$

This equation leads to a polynomial of the order n in ω^2 that generally possesses n distinct roots, called the eigenvalues denoted by $\omega_i^2 = \lambda_i$. Associated with each eigenvalue ω_i^2 there is a n-dimensional vector ϕ_i whose elements are real numbers, therefore these are also called real modes. This vector ϕ_i (for $i = 1, 2, ..., n$) is known as an eigenvector or modal vector and has the form:

$$\phi_i = \begin{bmatrix} \phi_{1i} \\ \phi_{2i} \\ \vdots \\ \phi_{ni} \end{bmatrix} \tag{4.77}$$

The eigenvector represents the shape of vibration and is therefore referred to as mode shape or natural mode. There are many solution procedures available for the eigenvalue problem of equation (4.75). The phase relationships are either in phase or out of phase in 180 degrees. All points on the structure pass through their equilibrium positions simultaneously. Therefore, undamped modes have well-defined modal points or lines.

Modal orthogonality and normal modes

It can be shown, see reference [Qu04], that the mode shapes are orthogonal with respect to the mass matrix $\mathbf{M}$ and stiffness matrix $\mathbf{K}$. This orthogonality indicates that all the eigenvectors are linearly independent. Due to this property, the modal vectors can be used as a vector basis, the modal basis. The space spanned by these modal vectors is called the principal space. The corresponding coordinates are called the principal coordinates.

The eigenvectors may be scaled arbitrarily. However, it is often convenient to choose the magnitude of the eigenvector so as to reduce the modal mass to unity and consequently the modal stiffness to the eigenvalue, see also reference [Qu04]. This process is known as the normalization of eigenvectors with respect to the mass matrix. Using this process, the rth eigenvector (of the rth mode) can be scaled such that it is orthonormal with respect to the mass matrix:

$$\phi_r^n = \frac{\phi_r}{\sqrt{m_r}} = \frac{\phi_r}{\sqrt{\phi_r^T \mathbf{M} \phi_r^T}}, \tag{4.78}$$

where m_r is referred to as the rth modal mass. The corresponding mode is called the normal mode. The superscript n will be omitted in the following.

An $n \times n$ eigenvector matrix or normal mode matrix can be formed by placing all the normalised eigenvectors columnwise in this matrix:

$$\mathbf{\Phi} = \begin{bmatrix} \phi_1 \phi_2 \ldots \phi_n \end{bmatrix} \tag{4.79}$$

Furthermore, the eigenvalue matrix or spectral matrix $\mathbf{\Lambda}$ can be defined as:

$$\mathbf{\Lambda} = diag(\lambda_1, \lambda_2, \ldots, \lambda_n). \tag{4.80}$$

This is an $n \times n$ diagonal matrix whose diagonal elements are the eigenvalues of the model. With these matrices, the eigenproblem from equation (4.75) can be formulated as:

$$\mathbf{K}\mathbf{\Phi} = \mathbf{M}\mathbf{\Phi}\mathbf{\Lambda}, \tag{4.81}$$

where the orthogonal conditions of the eigenvector matrix with respect to the mass and stiffness matrices are given by:

$$\mathbf{\Phi}^T \mathbf{M} \mathbf{\Phi} = \mathbf{I}, \tag{4.82}$$

$$\mathbf{\Phi}^T \mathbf{K} \mathbf{\Phi} = \mathbf{\Lambda}. \tag{4.83}$$

The space and coordinates associated with the normal modal matrix are called normal space or modal space and normal coordinates or modal coordinates.

Modal superposition
If the system is time invariant, the responses may be expressed as a linear combination of all the responses in the normal space. This procedure is called mode superposition or modal superposition. The response on the lth degree of freedom may be given by:

$$x_l(t) = \phi_{l1}q_1(t) + \phi_{l2}q_2(t) + \ldots + \phi_{ln}q_n(t) = \sum_{r=1}^{n} \phi_{lr}q_r(t), \qquad (4.84)$$

where ϕ_{lr} is the lth component of the rth eigenvector. The response for all degrees of freedom can be written as:

$$\mathbf{X}(t) = \mathbf{\Phi}\mathbf{q}(t) = \sum_{r=1}^{n} \phi_r q_r(t), \qquad (4.85)$$

where the vector $\mathbf{q}(t)$ are the normal coordinates or modal coordinates of the model, defined as:

$$\mathbf{q}(t) = \begin{bmatrix} \mathbf{q_1(t)} \\ \mathbf{q_2(t)} \\ \vdots \\ \mathbf{q_n(t)}, \end{bmatrix} \qquad (4.86)$$

representing the responses in the normal space.

Substitution of (4.85) into the undamped equations (4.39) and left-multiplication with the transpose of the eigenvector, leads to:

$$\mathbf{\Phi}^T\mathbf{M}\mathbf{\Phi}\ddot{\mathbf{q}}(t) + \mathbf{\Phi}^T\mathbf{K}\mathbf{\Phi}\mathbf{q}(t) = \mathbf{\Phi}^T\mathbf{F}(t), \qquad (4.87)$$

Using the orthogonality conditions of equation (4.82) and (4.83) leads to the expression:

$$\ddot{\mathbf{q}}(t) + \mathbf{\Lambda}\mathbf{q}(t) = \mathbf{\Phi}^T\mathbf{F}(t), \qquad (4.88)$$

Recall that the eigenvalue matrix is a diagonal matrix, thus the dynamic equilibrium equation (4.88) is uncoupled in the modal space. Consequently, the n differential equations can be solved separately in the modal space.
From equation (4.85) it can be seen that all the modes are included to compute the responses and there are as many eigenmodes as there are degrees of freedom (n) in the finite element model. The finite element model of a practical structure usually has thousands through millions of degrees of freedom. First of all, it is practically impossible to calculate all the modes of such a size of a model. Secondly, the higher order modes, the five thousandth and higher of a ten thousand degree of freedom finite element model, usually have very large errors with respect to the real modes.

This does not really pose a problem, as the contribution of each mode to the response is different, due to the large dependency on the frequency content (frequency or spectral) of the exciting forces and the natural frequency of the model. If the exciting forces have a frequency close to a natural frequency, the corresponding mode of vibration will be excited and will have a significant effect on the dynamic responses of the model. The frequency content of exciting forces furthermore often has an upper limit. Consequently, the modes whose frequencies are much higher than this upper limit will not be well excited and will have a very small contribution to the responses. Therefore generally, these contributions are ignored without much loss of accuracy. Only a small part of the modes is retained in the modal superposition, a procedure called modal truncation.

Which modes should be retained depends highly on the frequency content of the exciting forces that are to be analysed. The lowest modes can be included in the modal superposition: meaning modes 1 to $L < n$ are retained. This is called middle-high modal truncation. For some applications, the frequency spectral of the exciting forces falls in the middle frequency range of the model. For these cases, the low modes have low contribution to the responses and hence can be ignored. This procedure is called low-high modal truncation, where the modes L_1 to L_2 are retained ($1 < L_1 < L_2 < n$). A large amount of work can be saved using modal truncation.

Modal theory of proportionally damped systems

In the previous section, damping was not included in the modal analysis, but there is some form of damping in any dynamic system. Proper modelling of that damping is sometimes very important for a dynamic system. However, if the damping is included, the matrix $\mathbf{\Phi}^T \mathbf{C} \mathbf{\Phi}$ is generally not a diagonal matrix. The use of the undamped modal coordinates will not lead to a system of independent differential equations. A special case of equivalent damping is widely used in the structural system community to still use the advantage of the undamped modal coordinates. In this special case of equivalent damping, the damping matrix is proportional to the mass and stiffness matrices. Under this condition, a system of uncoupled differential equations expressed in terms of modal coordinates can be obtained.

If the transformed damping matrix $\mathbf{\Phi}^T \mathbf{C} \mathbf{\Phi}$ is a diagonal matrix, the corresponding viscous damping is called proportional damping (or classical damping). The damping matrix in the proportionally damped model is assumed to be a linear combination of the stiffness and mass matrices:

$$\mathbf{C} = \alpha \mathbf{M} + \beta \mathbf{K}, \tag{4.89}$$

where α and β are constants. This is the special case of equivalent damping that leads to uncoupled equations. Left and right multiplication of this expression with the eigenvector matrix gives:

$$\mathbf{\Phi}^T \mathbf{C} \mathbf{\Phi} = \mathbf{\Phi}^T (\alpha \mathbf{M} + \beta \mathbf{K}) \mathbf{\Phi} = \alpha \mathbf{I} + \beta \mathbf{\Lambda}, \tag{4.90}$$

which is a diagonal matrix by the definition of diagonal matrices $\mathbf{I}$ and $\mathbf{\Lambda}$.

Expression (4.89) can be substituted into equation (4.51) to get the dynamic equations of

motion in the physical space:

$$\mathbf{M}\ddot{\mathbf{X}}(t) + (\alpha\mathbf{M} + \beta\mathbf{K})\dot{\mathbf{X}}(t) + \mathbf{K}\mathbf{X}(t) = \mathbf{F}(t). \tag{4.91}$$

The corresponding equations in the modal space can be written as:

$$\ddot{\mathbf{q}}(t) + (\alpha\mathbf{I} + \beta\mathbf{\Lambda})\dot{\mathbf{q}}(t) + \mathbf{\Lambda}\mathbf{q}(t) = \mathbf{\Phi}^T\mathbf{F}(t). \tag{4.92}$$

Therefore, in the modal space the ith equation of motion is expressed as:

$$\ddot{q}(t) + c_i\dot{q}(t) + \omega_i^2 q(t) = f_i(t), \tag{4.93}$$

where c_i is the modal damping for the ith mode and is given by:

$$c_i = 2\omega_i\xi_i = \alpha + \beta\omega_i^2, \tag{4.94}$$

with the natural frequency of the undamped model indicated by ω_i. The corresponding modal damping ratio is represented by ξ_i. Clearly, the proportionally damped dynamic equations of motion are uncoupled in the undamped modal space. Each of these uncoupled equations can be treated as a viscously damped single degree of freedom system.

Modal theory of nonclassically damped systems

Most real structures and mechanical systems have locally concentrated damping sources such as dampers, vibration absorbers, jointing damping, etc. These damping sources are not as continuously distributed as the mass and stiffness. Consequently, the assumption of proportional damping is invalid. Therefore, for the systems with general viscous damping (also called nonclassical damping), the damping matrix cannot be diagonalized simultaneously with the mass and stiffness matrices. Commonly, the state space description is used for such systems, where a $2n$-dimensional state vector $\mathbf{Y}$ is introduced:

$$\mathbf{Y} = \begin{bmatrix} \mathbf{X} \\ \dot{\mathbf{X}} \end{bmatrix}. \tag{4.95}$$

This vector contains both the displacement and the velocity and thus represents the state of the system. The n-dimensional space spanned by the state vector is called state space. Using this definition of the state vector, the dynamic equations of motion of the structure can be written as a state equation:

$$\mathbf{A}\mathbf{Y} + \mathbf{B}\dot{\mathbf{Y}} = \mathbf{F}, \tag{4.96}$$

where the system matrices $\mathbf{A}$ and $\mathbf{B} \in R^{2n \times 2n}$ and the force vector $\mathbf{F} \in R^{2n}$ in the state space are given by:

$$\mathbf{A} = \begin{bmatrix} \mathbf{K} & \mathbf{0} \\ \mathbf{0} & -\mathbf{M} \end{bmatrix}, \qquad \mathbf{B} = \begin{bmatrix} \mathbf{C} & \mathbf{M} \\ \mathbf{M} & \mathbf{0} \end{bmatrix}, \qquad \mathbf{F} = \begin{bmatrix} \mathbf{f} \\ \mathbf{0} \end{bmatrix}, \tag{4.97}$$

or alternatively by:

$$\mathbf{A} = \begin{bmatrix} \mathbf{0} & \mathbf{K} \\ \mathbf{K} & \mathbf{C} \end{bmatrix}, \qquad \mathbf{B} = \begin{bmatrix} -\mathbf{K} & \mathbf{0} \\ \mathbf{0} & \mathbf{M} \end{bmatrix}, \qquad \mathbf{F} = \begin{bmatrix} \mathbf{0} \\ \mathbf{f} \end{bmatrix}. \tag{4.98}$$

The system matrices $\mathbf{A}$ and $\mathbf{B}$ are real symmetric if the mass, damping and stiffness matrices are.

Free vibration and eigenvalue problem
Recall from equation (4.56) that the dynamic equations of equilibrium of the damped model can be written as:

$$\mathbf{M}\ddot{\mathbf{X}}(t) + \mathbf{C}\dot{\mathbf{X}}(t) + \mathbf{K}\mathbf{X}(t) = \mathbf{F}(t). \qquad (4.99)$$

The solution of these equations has the form:

$$\mathbf{X} = \psi e^{\lambda t}, \qquad (4.100)$$

where ψ is the n-dimensional vector of amplitudes and λ is the complex frequency of the response. The complex frequency has the general form $\lambda_j = \alpha_j + i\beta_j$, where α_j and β_j are real numbers. Depending upon the values of α_j and β_j, the system may have different types of responses. The most common type in practice is where $\alpha_j < 0$ and β_j are conjugate pairs, for which the modal response is exponentially decaying oscillatory motion. Differentiation of equation (4.100) with respect to time twice gives:

$$\dot{\mathbf{X}} = \psi\lambda e^{\lambda t}, \qquad \ddot{\mathbf{X}} = \psi\lambda^2 e^{\lambda t} \qquad (4.101)$$

Substitute these expressions into equation (4.99) for free vibration to get the eigenvalue problem of the damped model:

$$(\lambda^2 \mathbf{M} + \lambda \mathbf{C} + \mathbf{K})\psi = \mathbf{0}. \qquad (4.102)$$

It is a quadratic eigenproblem or nonlinear eigenproblem defined in the displacement space, the n-dimensional space spanned by the displacement vector $\mathbf{X}$.
It is quite difficult to solve this equation in the displacement space. The commonly used scheme is to transform it from the displacement space into the state space.
Using the form for $\mathbf{X}$ from equation (4.100), the state vector can be written as:

$$\mathbf{Y} = \begin{bmatrix} \mathbf{X} \\ \dot{\mathbf{X}} \end{bmatrix} = \begin{bmatrix} \psi \\ \psi\lambda \end{bmatrix} e^{\lambda t}. \qquad (4.103)$$

The time derivative of the state vector can then be written as:

$$\dot{\mathbf{Y}} = \begin{bmatrix} \dot{\mathbf{X}} \\ \ddot{\mathbf{X}} \end{bmatrix} = \lambda \begin{bmatrix} \psi \\ \psi\lambda \end{bmatrix} e^{\lambda t} = \lambda \mathbf{Y}. \qquad (4.104)$$

Consider equation (4.96), for damped free vibration, the equations of motion now become:

$$\mathbf{A}\mathbf{Y} + \mathbf{B}\dot{\mathbf{Y}} = \mathbf{0}, \qquad (4.105)$$
$$(\mathbf{A} + \lambda\mathbf{B})\mathbf{Y} = \mathbf{0}, \qquad (4.106)$$
$$(\mathbf{A} + \lambda\mathbf{B})\tilde{\psi} = \mathbf{0}, \qquad (4.107)$$

where:

$$\tilde{\psi} = \begin{bmatrix} \psi \\ \psi\lambda \end{bmatrix}$$

(4.108)

Equation (4.107) is referred to as the eigenvalue problem of the nonclassically damped model in the state space. Notice that it doubles the size of the matrix. For the non-classically underdamped models, the solutions of the eigenvalue problem consist of $2n$ complex eigenvalues (in complex conjugate pairs). Each complex eigenvalue has a complex eigenvector (or complex conjugate eigenvectors respectively) with both real and imaginary parts. The complex eigenvector has arbitrary amplitude and arbitrary phase angle scaling. The difference of phase angle may be any angle between 0 and 180°.

It can also be shown, see reference [Qu04], that the complex eigenvectors $\tilde{\psi}$ are orthogonal with respect to the matrices $\mathbf{A}$ and $\mathbf{B}$. The real and imaginary parts of an arbitrary eigenvector are both parallel-orthogonal with respect to the matrix $\mathbf{A}$, as well as cross-orthogonal with respect to the matrix $\mathbf{A}$. Therefore the real and imaginary parts of the eigenvectors of a nonclassically damped model are all orthogonal with respect to the system matrix $\mathbf{A}$ in the state space. Similarly this feature is also true for the matrix $\mathbf{B}$. Because all the eigenvectors are linearly independent, the eigenvector matrix is fully ranked

Again the eigenvectors can be normalised, in this case with respect to the $\mathbf{B}$ matrix, leading to the following orthogonality conditions:

$$\tilde{\mathbf{\Psi}}^T \mathbf{B} \tilde{\mathbf{\Psi}} = \mathbf{I},$$

(4.109)

$$\tilde{\mathbf{\Psi}}^T \mathbf{A} \tilde{\mathbf{\Psi}} = \tilde{\mathbf{\Omega}},$$

(4.110)

where the eigenvector matrix $\tilde{\mathbf{\Psi}} \epsilon R^{2n\times 2n}$ and the complex eigenvalue matrix or complex frequency matrix $\tilde{\mathbf{\Omega}} \epsilon R^{2n\times 2n}$ are defined as:

$$\tilde{\mathbf{\Psi}} = \begin{bmatrix} \tilde{\psi}_1 & \tilde{\psi}_2 & \ldots & \tilde{\psi}_n & \tilde{\psi}_1^* & \tilde{\psi}_2^* & \ldots & \tilde{\psi}_n^* \end{bmatrix},$$

(4.111)

$$\tilde{\mathbf{\Omega}} = diag(\lambda_1, \lambda_2, \ldots, \lambda_n, \lambda_1^*, \lambda_2^*, \ldots \lambda_n^*).$$

(4.112)

The superscript * denotes the complex conjugate. These matrices can also be written as follows, see also reference [Qu04]:

$$\tilde{\mathbf{\Omega}} = \begin{bmatrix} \mathbf{\Omega} & \mathbf{0} \\ \mathbf{0} & \mathbf{\Omega}^* \end{bmatrix}, \qquad \tilde{\mathbf{\Psi}} = \begin{bmatrix} \mathbf{\Psi} & \mathbf{\Psi}^* \\ \mathbf{\Psi\Omega} & \mathbf{\Psi}^*\mathbf{\Omega}^* \end{bmatrix},$$

(4.113)

where $\mathbf{0} \epsilon R^{n\times n}$ is the null matrix. Using the above definitions, the eigenvalue problem can be written as:

$$\mathbf{A}\tilde{\mathbf{\Psi}} = \mathbf{B}\tilde{\mathbf{\Psi}}\tilde{\mathbf{\Omega}}$$

(4.114)

The undamped natural frequency $\tilde{\omega}_i$, the modal damping ratio $\tilde{\xi}_i$ and the damped fre-

quency ω_d are defined as:

$$\tilde{\omega}_i \quad = \quad \sqrt{\alpha_i^2 + \beta_i^2} \tag{4.115}$$

$$\xi_i \quad = \quad \frac{-\alpha_i}{\sqrt{\alpha_i^2 + \beta_i^2}} = \frac{-\alpha_i}{\tilde{\omega}_i} \tag{4.116}$$

$$\omega_d \quad = \quad \tilde{\omega}_i\sqrt{1 - \xi_i^2} \tag{4.117}$$

The undamped frequency defined in equation (4.115) is not equal to that obtained from the corresponding undamped model ($\mathbf{C} = \mathbf{0}$).

Complex mode superposition
Using equation (4.96), combined with equations (4.109) and (4.110), the dynamic equilibrium equations in the complex modal space can be derived, given by:

$$\dot{\tilde{\mathbf{q}}}(t) + \tilde{\mathbf{\Omega}}\tilde{\mathbf{q}}(t) = \tilde{\mathbf{\Psi}}^T\mathbf{F}(t) \tag{4.118}$$

where the coordinate transformation for the state vector is given as:

$$\mathbf{Y}(t) = \tilde{\mathbf{\Psi}}\tilde{\mathbf{q}}(t). \tag{4.119}$$

in which $\tilde{\mathbf{q}}(t)$ are the complex modal coordinates. Because the eigenvalue matrix is a diagonal matrix, the dynamic equilibrium equations (4.118) are uncoupled in the complex modal space. Thus, the $2n$ differential equations can be solved separately in the modal space.

There is an essential difference between the real modal analysis and the complex modal analysis. In the mode vibration of the complex model, the phase angles are different at different points while the difference is 0 or π in the real mode. Consequently, the shape of the complex mode is meaningless.

4.2.3   Guyan Reduction

In this section, the most popular condensation method will be described. This method is usually referred to as static condensation, because in the condensation the dynamic effect is ignored. Since the late 1960s, this technique has been widely used in many static and dynamic problems. This condensation technique for the deletion of unwanted degrees of freedom was first proposed by Guyan and Irons both in 1965.
This static condensation technique is described in detail in this section. Because inertia effects are ignored in this condensation, the accuracy of the resulting reduced model is generally very low for dynamic problems. To achieve reasonably accurate results, the master degrees of freedom must be chosen with great care and the number of masters should be greater than the number of modes interested. To alleviate the limitations, the inertia effects can be partially or fully included in the condensation. The corresponding condensation approaches are generally called dynamic condensation. Dynamic condensation techniques will not be described here. For detailed information on these techniques, one is referred to [Qu04].

The Guyan condensation matrix will be derived here from the static response problem, dynamic response problem and eigenproblem, respectively.

There are two modifications to improve the accuracy of Guyan condensation. One is the generalised Guyan condensation, which is Guyan condensation combined with the generalised inverse of the stiffness matrix. The other is the quasi-static condensation, which is a combination of Guyan condensation and the eigenvalue or frequency shifted technique. A detailed description of these two modifications can be found as well in reference [Qu04].

Guyan Condensation for static problems

The derivation of Guyan condensation uses the static equilibrium equations, that is:

$$\mathbf{K}\mathbf{X} = \mathbf{F} \tag{4.120}$$

The discrete model without using condensation is called the full order model or just full model. The total degrees of freedom of the full model can be categorized as the master degrees of freedom (primary degrees of freedom, or kept degrees of freedom) and the slave degrees of freedom (secondary degrees of freedom, or deleted degrees of freedom). They are simply referred to as the masters (m) and slaves (s) respectively. Using this arrangement, the static equation (4.120) can be partitioned as:

$$\begin{bmatrix} \mathbf{K}_{mm} & \mathbf{K}_{ms} \\ \mathbf{K}_{sm} & \mathbf{K}_{ss} \end{bmatrix} \begin{Bmatrix} \mathbf{X}_m \\ \mathbf{X}_s \end{Bmatrix} = \begin{Bmatrix} \mathbf{F}_m \\ \mathbf{F}_s \end{Bmatrix}. \tag{4.121}$$

The displacement vector $\mathbf{X}_m \in R^m$ corresponds to the masters, which are to be retained. The vector $\mathbf{X}_s \in R^s$ corresponds to the slaves, which are to be condensed. If the multiplication of the matrices in equation (4.121) is performed, the following two equations result:

$$\mathbf{K}_{mm}\mathbf{X}_m + \mathbf{K}_{ms}\mathbf{X}_s = \mathbf{F}_m \tag{4.122}$$

$$\mathbf{K}_{sm}\mathbf{X}_m + \mathbf{K}_{ss}\mathbf{X}_s = \mathbf{F}_s. \tag{4.123}$$

Using equation (4.123), the vector $\mathbf{X}_s$ can be expressed in terms of $\mathbf{X}_m$ as:

$$\mathbf{X}_s = -\mathbf{K}_{ss}^{-1}\mathbf{K}_{sm}\mathbf{X}_m + \mathbf{K}_{ss}^{-1}\mathbf{F}_s. \tag{4.124}$$

Due to the linearity of this model, the displacements at the slaves consist of two parts. One part results from the displacements at the masters and is called attached displacements. Another part results from the external forces acting on the slaves and is called relative displacements. Substitution of equation (4.124) into (4.122) results in:

$$\mathbf{K}_R\mathbf{X}_m = \mathbf{F}_R, \tag{4.125}$$

where the stiffness matrix $\mathbf{K}_R \in R^{m \times m}$ corresponds to the masters. The equivalent force vector $\mathbf{F}_R \in R^m$ acts on the masters. These are both defined by:

$$\mathbf{K}_R = \mathbf{K}_{mm} - \mathbf{K}_{ms}\mathbf{K}_{ss}^{-1}\mathbf{K}_{sm}, \tag{4.126}$$

$$\mathbf{F}_R = \mathbf{F}_m - \mathbf{K}_{ms}\mathbf{K}_{ss}^{-1}\mathbf{F}_s. \tag{4.127}$$

Equation (4.125) are the static equilibrium equations corresponding to the masters. Guyan assumed in 1965 in the derivation that the external forces at the slaves are zero: $\mathbf{F}_s = \mathbf{0}$. This assumption is actually only necessary for deriving the relation of the displacements between the masters and the slaves. Letting $\mathbf{F}_s = \mathbf{0}$ on the right-hand side of equation (4.124) gives:

$$\mathbf{X}_s = \mathbf{R}_G \mathbf{X}_m. \tag{4.128}$$

The matrix $\mathbf{R}_G \in R^{s \times m}$ is called the condensation matrix and is defined as:

$$\mathbf{R}_G = -\mathbf{K}_{ss}^{-1} \mathbf{K}_{sm}. \tag{4.129}$$

Equation (4.128) describes the relations of displacements between the masters and slaves. Because the external forces at the slaves were ignored in the derivation, the corresponding condensation matrix is a load-independent matrix. This condensation method was first proposed by Guyan and is usually referred to as Guyan condensation. The condensation matrix in equation (4.129) is called the Guyan condensation matrix. Due to the ignorance of dynamic effects in the condensation matrix, Guyan condensation is also referred to as static condensation. The Guyan condensation matrix provides the means to reduce the stiffness matrix. This condensation is usually used in the static problem to eliminate unwanted degrees of freedom such as the internal degrees of freedom of an element used in the finite element method. Using the condensation matrix from equation (4.128), the displacement vector $\mathbf{X}$ can be expressed as follows:

$$\mathbf{X} = \begin{Bmatrix} \mathbf{X}_m \\ \mathbf{X}_s \end{Bmatrix} = \mathbf{T}_G \mathbf{X}_m, \tag{4.130}$$

where the coordinate transformation matrix or global mapping matrix $\mathbf{T}_G \in R^{n \times m}$ relates the responses at all the degrees of freedom to those at the masters. This coordinate transformation matrix is defined as:

$$\mathbf{T}_G = \begin{bmatrix} \mathbf{I} \\ \mathbf{R}_G \end{bmatrix}, \tag{4.131}$$

where $\mathbf{I}$ is an $m \times m$ identity matrix. Equation (4.130) can be substituted into equation (4.120). Pre-multiplication of both sides of the resulting equation by the transpose of $\mathbf{T}_G$, gives:

$$\mathbf{K}_G \mathbf{X}_m = \mathbf{F}_G. \tag{4.132}$$

This equation represents the static equilibrium equations of the reduced order model or simply reduced model, which denotes the model after condensation. The stiffness matrix $\mathbf{K}_G \in R^{m \times m}$ is the stiffness matrix of the reduced model and is referred to as the reduced stiffness matrix. $\mathbf{F}_G \in R^m$ is the equivalent force vector acting at the masters. They are defined as:

$$\mathbf{K}_G = \mathbf{T}_G^T \mathbf{K} \mathbf{T}_G, \tag{4.133}$$

$$\mathbf{F}_G = \mathbf{T}_G^T \mathbf{F}. \tag{4.134}$$

These equations can also be rewritten using the submatrices of the stiffness matrix and the subvectors of the force vector:

$$\mathbf{K}_G = \mathbf{K}_{mm} - \mathbf{K}_{ms}\mathbf{K}_{ss}^{-1}\mathbf{K}_{sm}, \tag{4.135}$$

$$\mathbf{F}_G = \mathbf{F}_m + \mathbf{R}_G^T\mathbf{F}_s = \mathbf{F}_m - \mathbf{K}_{ms}\mathbf{K}_{ss}^{-1}\mathbf{F}_s. \tag{4.136}$$

Notice that they are the same as the definitions in respectively equations (4.126) and (4.127). The static equilibrium equations were given in equation (4.132). Clearly, the reduced model has m degrees of freedom, which are usually much less than those of the full model. The coordinates used to define the full model and reduced model are, for convenience, referred to as full order coordinates and reduced order coordinates respectively. After the displacements at the masters are obtained, equation (4.124) rather than equation (4.128) is used to calculate the displacements at the slaves.

As shown in equations (4.129), (4.135) and (4.136), the calculation of the condensation matrix, the stiffness matrix and the equivalent force vector of the reduced model requires the inconvenient calculation of the inverse matrix $\mathbf{K}_{ss}^{-1}$. This inverse procedure is not mandatory. These matrices and vector may be directly obtained if the standard Gauss-Jordan elimination process is applied systematically on the static equilibrium equations of the full model. More details on this Gauss-Jordan elimination process can be found in reference [Qu04].

A simple numerical example to demonstrate the static Guyan condensation can also be found in [Qu04]. It is demonstrated that the calculated displacements at the masters and slaves of the reduced model are exactly the same as those from the full model.

Guyan Condensation for dynamic problems

Recall from equation (4.39) that the dynamic equilibrium equations of the full model without damping are given by:

$$\mathbf{M}\ddot{\mathbf{X}}(t) + \mathbf{K}\mathbf{X}(t) = \mathbf{F}(t), \tag{4.137}$$

where the mass matrix of the full model is $\mathbf{M} \in R^{n \times n}$ and this matrix is positive definite. $\ddot{\mathbf{X}}(t)$ is the acceleration vector. This equation can also be written in a partitioned form as:

$$\begin{bmatrix} \mathbf{M}_{mm} & \mathbf{M}_{ms} \\ \mathbf{M}_{sm} & \mathbf{M}_{ss} \end{bmatrix} \begin{Bmatrix} \ddot{\mathbf{X}}_m(t) \\ \ddot{\mathbf{X}}_s(t) \end{Bmatrix} + \begin{bmatrix} \mathbf{K}_{mm} & \mathbf{K}_{ms} \\ \mathbf{K}_{sm} & \mathbf{K}_{ss} \end{bmatrix} \begin{Bmatrix} \mathbf{X}_m(t) \\ \mathbf{X}_s(t) \end{Bmatrix} = \begin{Bmatrix} \mathbf{F}_m(t) \\ \mathbf{F}_s(t) \end{Bmatrix}. \tag{4.138}$$

Similar to the static case, assume that the external forces at the slaves are zero: $\mathbf{F}_s = \mathbf{0}$. Then the second equation of equation (4.138) can be expressed as:

$$\mathbf{M}_{sm}\ddot{\mathbf{X}}_m(t) + \mathbf{M}_{ss}\ddot{\mathbf{X}}_s(t) + \mathbf{K}_{sm}\mathbf{X}_m(t) + \mathbf{K}_{ss}\mathbf{X}_s(t) = \mathbf{0}. \tag{4.139}$$

The derivation of the relation of displacements between the masters and slaves is done by the assumption of $\ddot{\mathbf{X}}_m(t) = \ddot{\mathbf{X}}_s(t) = \mathbf{0}$ in equation (4.139). The equation that results

is exactly that of equation (4.128).

The displacement vector $\mathbf{X}$ can therefore also be expressed as:

$$\mathbf{X} = \left\{ \begin{matrix} \mathbf{X}_m \\ \mathbf{X}_s \end{matrix} \right\} = \mathbf{T}_G \mathbf{X}_m, \tag{4.140}$$

see equation (4.130). Because the coordinate transformation matrix $\mathbf{T}_G$ is independent of time, differentiation twice with respect to time t of this equation leads to:

$$\ddot{\mathbf{X}}(t) = \mathbf{T}_G \ddot{\mathbf{X}}_m(t), \tag{4.141}$$

Substitute equations (4.140) and (4.141) into equation (4.138). After pre-multiplication of it by the transpose of the matrix $\mathbf{T}_G$ the dynamic equilibrium equations of the reduced model result:

$$\mathbf{M}_G \ddot{\mathbf{X}}_m(t) + \mathbf{K}_G \mathbf{X}_m(t) = \mathbf{F}_G(t). \tag{4.142}$$

In this equation, the mass and stiffness matrices of the reduced model are called respectively the reduced mass matrix and the reduced stiffness matrix. These matrices and the equivalent force vector are defined as:

$$\mathbf{M}_G = \mathbf{T}_G^T \mathbf{M} \mathbf{T}_G, \tag{4.143}$$

$$\mathbf{K}_G = \mathbf{T}_G^T \mathbf{K} \mathbf{T}_G, \tag{4.144}$$

$$\mathbf{F}_G = \mathbf{T}_G^T \mathbf{F}(t). \tag{4.145}$$

These may be rewritten in terms of the submatrices of the mass and stiffness matrices and subvectors of the force vector as:

$$\mathbf{M}_G = \mathbf{M}_{mm} + \mathbf{K}_{ms} \mathbf{K}_{ss}^{-1} \mathbf{M}_{ss} \mathbf{K}_{ss}^{-1} \mathbf{K}_{sm} +$$
$$- \mathbf{K}_{ms} \mathbf{K}_{ss}^{-1} \mathbf{M}_{sm} - \mathbf{M}_{ms} \mathbf{K}_{ss}^{-1} \mathbf{K}_{sm}, \tag{4.146}$$

$$\mathbf{K}_G = \mathbf{K}_{mm} - \mathbf{K}_{ms} \mathbf{K}_{ss}^{-1} \mathbf{K}_{sm}, \tag{4.147}$$

$$\mathbf{F}_G(t) = \mathbf{F}_m(t) + \mathbf{R}_G^T \mathbf{F}_s(t) = \mathbf{F}_m(t) - \mathbf{K}_{ms} \mathbf{K}_{ss}^{-1} \mathbf{F}_s(t). \tag{4.148}$$

It is a little bit difficult to anticipate the acceleration responses at the slaves from those at the masters if the force vector on the slaves is not zero. Therefore, usually the degrees of freedom at which the responses are of interest are kept in the set of masters.

Notice that the Guyan condensation matrix is obtained from the dynamic equations when the dynamic effects are ignored. Recall that in the derivation of equation (4.140) it was assumed that $\ddot{\mathbf{X}}_m(t) = \ddot{\mathbf{X}}_s(t) = \mathbf{0}$. Hence, error is introduced when the dynamic problem is considered. The magnitude of these errors depends on the natural properties of the full model and how many and what degrees of freedom are selected as the masters.

The potential elastic energy U and the kinetic energy K of the full model may be written as:

$$U = \frac{1}{2} \mathbf{X}^T \mathbf{K} \mathbf{X} \tag{4.149}$$

$$K = \frac{1}{2} \dot{\mathbf{X}}^T \mathbf{M} \dot{\mathbf{X}} \tag{4.150}$$

Substitution of equation (4.140) into the above expressions leads to:

$$U = \frac{1}{2} \, \mathbf{X}_m^T \mathbf{T}_G^T \mathbf{K} \mathbf{T}_G \mathbf{X}_m \tag{4.151}$$

$$K = \frac{1}{2} \, \dot{\mathbf{X}}_m^T \mathbf{T}_G^T \mathbf{M} \mathbf{T}_G \dot{\mathbf{X}}_m \tag{4.152}$$

Using equations (4.143) and (4.144) this can also be written as:

$$U = \frac{1}{2} \, \mathbf{X}_m^T \mathbf{K}_G \mathbf{X}_m \tag{4.153}$$

$$K = \frac{1}{2} \, \dot{\mathbf{X}}_m^T \mathbf{M}_G \dot{\mathbf{X}}_m \tag{4.154}$$

Equations (4.153) and (4.154) express respectively the potential energy and kinetic energy in terms of the masters. Therefore, $\mathbf{K}_G$ and $\mathbf{M}_G$ are called the stiffness and mass matrices of the reduced model defined only by the masters. By this definition, the potential and kinetic energy of the full model will be fully retained in the reduced model.

A simple numerical example to demonstrate the dynamic Guyan condensation can be found in [Qu04]. Generally, the displacements obtained from the reduced model are close to those from the full model. However, there are some errors. The magnitude of the errors depends on the choice of master and slave degrees of freedom. Even at the same number of master degrees of freedom, the quality of the solution (correspondence with the full model) will depend on the selection of which degrees of freedom will be masters and which will be slaves.

Although Guyan condensation is exact for static problems, its accuracy is usually very low for dynamic problems. The accuracy highly depends on the selection of masters. Generally, the lower orders of frequencies have higher accuracy than the higher orders of frequencies. The explanation of this can be found in chapter 5 of [Qu04]. The optimal selection of masters may increase the accuracy of the reduced model. For given eigenpairs, increasing the number of masters can also increase their accuracy.

The way to slightly increase the number of masters is feasible in practice although the computational effort may be increased. Generally, a finite element model of a practical structure has a minimum of tens of thousands degrees of freedom. Obviously, the full model has tens of thousands of modes. However, substantially less already suffice for the dynamic analysis of the model. After the slight increase of the number of masters, the size of the reduced model is still much smaller than that of the full model, while the accuracy of the reduced model in that frequency range may be increased significantly.

Guyan Condensation for Eigenproblems

The full eigenproblem, which is the general eigenproblem of a full model, can be given by:

$$(\mathbf{K} - \lambda \mathbf{M})\phi = \mathbf{0}, \tag{4.155}$$

where λ and ϕ are respectively the eigenvalue (square of frequency) and the corresponding eigenvector (mode shape) of the full model, compare with equation (4.75). Using the

same division as before of the total degrees of freedom in master m and slave s degrees of freedom, this can be written in partitioned form as:

$$\left(\begin{bmatrix} \mathbf{K}_{mm} & \mathbf{K}_{ms} \\ \mathbf{K}_{sm} & \mathbf{K}_{ss} \end{bmatrix} - \lambda \begin{bmatrix} \mathbf{M}_{mm} & \mathbf{M}_{ms} \\ \mathbf{M}_{sm} & \mathbf{M}_{ss} \end{bmatrix} \right) \begin{Bmatrix} \phi_m \\ \phi_s \end{Bmatrix} = \begin{Bmatrix} \mathbf{0} \\ \mathbf{0} \end{Bmatrix}. \tag{4.156}$$

By performing these simple multiplications, this equation can be expanded into the following two equations:

$$\begin{aligned} (\mathbf{K}_{mm} - \lambda \mathbf{M}_{mm})\phi_m + (\mathbf{K}_{ms} - \lambda \mathbf{M}_{ms})\phi_s &= \mathbf{0}, & (4.157) \\ (\mathbf{K}_{sm} - \lambda \mathbf{M}_{sm})\phi_m + (\mathbf{K}_{ss} - \lambda \mathbf{M}_{ss})\phi_s &= \mathbf{0}. & (4.158) \end{aligned}$$

The relation of the eigenvector between the masters and slaves may be obtained from equation (4.158):

$$\phi_s = \mathbf{R}(\lambda)\phi_m. \tag{4.159}$$

The matrix $\mathbf{R}(\lambda) \, \epsilon \, R^{s \times m}$ is called the condensation matrix and is defined as:

$$\mathbf{R}(\lambda) = -(\mathbf{K}_{ss} - \lambda \mathbf{M}_{ss})^{-1}(\mathbf{K}_{sm} - \lambda \mathbf{M}_{sm}). \tag{4.160}$$

This expression for the computation of the condensation matrix is given explicitly, but it is a nonlinear function of the unknown eigenvalue λ. Letting $\lambda = 0$ in this equation leads to the Guyan condensation matrix as presented in equation (4.129). The eigenvector of the full model can therefore be expressed in terms of the eigenvector at the masters as:

$$\phi = \mathbf{T}_G \phi_m, \tag{4.161}$$

where $\mathbf{T}_G$ is the coordinate transformation matrix as defined in equation (4.131). Substitution of equation (4.161) into equation (4.156) and premultiplication with the transpose of $\mathbf{T}_G$ results in the eigenproblem of the reduced model:

$$(\mathbf{K}_G - \lambda \mathbf{M}_G)\phi_m = \mathbf{0}. \tag{4.162}$$

This equation is referred to as the reduced eigenproblem. The reduced stiffness matrix $\mathbf{K}_G$ and the reduced mass matrix $\mathbf{M}_G$ are as defined already in respectively equations (4.143) and (4.144). In the derivation of the Guyan condensation matrix, the eigenvalue is set to zero. Consequently, the dynamic effect is ignored in the condensation matrix. Therefore, Guyan condensation is a static condensation. As the eigenvalue increases, the ignored effects become more significant.

It is shown in [Qu04] that Guyan condensation is the first-order approximation of the exact reduced eigenproblem. Hence, the eigenvalue and corresponding eigenvector resulting from Guyan condensation are also the first-order approximation of the exact values. In that reference an equation is also presented describing the error in the (Guyan) condensation matrix. That equation shows that the valid eigenvalue (frequency) range of Guyan condensation is $\lambda < \lambda_c = \tilde{\lambda}_1$, where λ_c is usually called cut eigenvalue or cut frequency and $\tilde{\lambda}_1$ is the smallest eigenvalue of the slave model. To guarantee that the

condensation has enough accuracy, $\lambda < 0.3\lambda_c$, is usually selected.

Different masters results in different slave models as well as a different lowest eigenvalue. This means that the lowest eigenvalue of the slave model, that is the cut eigenvalue, depends on the choice of masters. Therefore, optimal selection of masters may increase the ratio $\frac{\lambda_c}{\lambda}$ and thus the accuracy of Guyan condensation. The lowest eigenvalue (cut eigenvalue) may also be increased significantly by increasing the number of masters (constraint degrees of freedom). Consequently, what and how many degrees of freedom are retained in the master set have significant influence on the accuracy of Guyan condensation.

Guyan condensation is generally valid in the lowest frequency range of the full model and the corresponding results have reasonable accuracy within that range. See further reference [Qu04] for the exact condensation method that does not ignore the inertia effects in the condensation matrix, that is for $\lambda \neq 0$. Let $\lambda = 0$ in the exact condensation and Guyan condensation results.

Assuming $\lambda = \omega_i^2$, leads to the so-called quasistatic condensation or classical dynamic condensation, which is exact only at the prescribed frequency ω_i. The corresponding reduced model exactly represents the full model at that frequency. Further information can be found in reference [Qu04].

4.2.4   Mass modelling

There are two common methods to model the mass of a structure for a finite element analysis. From a FE-perspective, the first one is the most obvious. Commercial FE-analysis codes are basically tailored for that option. The option to define additional to the geometry of the finite elements, properties and corresponding materials. For example: a (sub)structure is modelled by a collection of beams made of aluminium. So these beams get in addition to the definition of their geometric arrangement, the definition of their properties, in this case that of aluminium.

This modelling procedure can give a very good representation of static and dynamic behavior of the real structure. It is therefore extensively used in detailed studies of small substructures in a late design phase.

The focus of this report lies on the determination of flight loads, principally for the complete flight envelopes, throughout the whole design process. Besides the strict requirements on computational efficiency, this also implies a large variation of the amount of detail of the available models. Throughout the complete design process, including multiple design loops, the aircraft model undergoes multiple modifications and updates, due to product improvements (of the aircraft design) or because more knowledge has been gained through wind tunnel testing, structural testing, etc. Refer to chapter 2 for more information about loads analysis and its requirements.

The modifications or model updates can range from very low impact to very high impact on the loads envelopes. The loads determination process should be organized such that low to moderate model changes only involve small or moderate workload to recalculate part or all of the simulations.

These prerequisites imply the use of a loads model insensitive to small mass changes. Structural changes have an obvious pronounced influence on the loads envelope and re-

quire almost always a recalculation of the complete workflow in generating the loads envelope. The loads model gets less sensitive to small mass changes if the structural/elastic properties are decoupled from the mass properties. This is achieved by modelling the airframe with finite elements having structural properties but zero mass. The mass model is a separate model that is used in addition to the structural model.

Two separate models allows a decoupling of mass and structure. But, how can a mass model be generated independently from the structural model? The lumped mass model proves to be the solution of this problem. Furthermore, one should notice that the mass of an airframe is much more than just structural mass. The majority stems from cables and wiring and the wide variety of systems that are necessary for the safe and commercial operation of the aircraft. The details of these systems, etc. are neither available yet (preliminary design phase) nor do they have to be modelled in detail to address the loads.

The lumped mass model enables a good representation of the global properties of the structure and systems without the necessity to address all details yet in preliminary design phases. It is generated by dividing the continuous airframe into its components: right wing, left wing, fuselage (either as a whole or subdivided into cargo deck, first deck, etc.), engines, pylons, left and right horizontal stabilizer, fin, and whatever additional components are present. Each of these components have a defined main direction that can be described by a dimensionless coordinate. The main directions are: spanwise direction for the wing, running length along the fuselage, etc. Each component is then further subdivided along this main direction. These divisions are the so-called: mass bounds. Between each of two neighboring bounds, the mass properties are estimated/determined from the continuous airframe design. Between each pair of bounds a point mass is located, such that its mass exactly corresponds to the mass of the continuous subdivision. The point mass also has an offset, such that the moments of inertia are exactly met.

The less lumped masses are taken, the smaller the model gets. In the most extreme case, one could take one lumped mass, that would correspond with the center of gravity of the aircraft. Off course this would lead to shorter simulation times. This approach is the industrial standard in performance calculations. For loads calculations however, the amount of lumped masses should be chosen such that the resulting mass distribution of the components is detailed enough to calculate the running loads with sufficient accuracy.

A few comments with respect to condensation:
The mass matrix used in dynamic analyses is usually positive definite. However, the mass matrix formulation for many structural dynamic problems only includes inertia terms corresponding to translational degrees of freedom, while a more generalized formulation for the stiffness matrix including terms corresponding to rotational degrees of freedom is often employed. One popular example of the mass matrix resulting from these formulations is a lumped mass matrix with some zero diagonal elements. This kind of mass matrix is easy to be formulated and could save a lot of computer storage and time. However, this discretization of inertia leads to a number of massless degrees of freedom. Consequently, the mass matrix becomes nonpositive definite and it is very difficult to perform some dynamic analyses directly. Therefore, usually the condensation approach is necessary to delete those degrees of freedom at which the masses are zero.

Another popular example of the use of the mass matrix with massless coordinates can be found in the finite element modelling of structures with smart materials. Usually, both mechanical and electric degrees of freedom are used in solid and shell finite elements. The mass pertaining to the electric degrees of freedom is zero, therefore Guyan condensation may be used to condense these degrees of freedom from the dynamic equations. If the slave set contains all the degrees of freedom at which the inertia is not considered, then it holds that:

$$\mathbf{M}_{ms} = \mathbf{M}_{ms}^T = \mathbf{0} \qquad (4.163)$$
$$\mathbf{M}_{ss} = \mathbf{0} \qquad (4.164)$$

Consequently, the second equation of the dynamic equilibrium equations in partitioned form (4.138) is exactly the same as the second equation of that of the static equilibrium equations (4.123). The relation of displacements between the masters and slaves can be derived without having to assume that $\ddot{\mathbf{X}}_m(t) = \ddot{\mathbf{X}}_s(t) = \mathbf{0}$ and is expressed by the Guyan condensation matrix. Using the same transformation of the mass matrix from the full displacement space to the reduced displacement space, the reduced mass matrix is given by:

$$\mathbf{M}_R = \mathbf{M}_{mm} \qquad (4.165)$$

The reduced stiffness matrix and force vector are the same as derived in section 4.2.3 for the Guyan condensation for dynamic problems. Obviously, the reduced mass matrix in equation (4.165) is positive definite. Clearly the Guyan condensation method in this case does not alter the original problem. Therefore, no error is introduced to the reduced model.

4.3   Flight dynamics model of an aero-elastic vehicle

In this section the nonlinear equations of motion for an elastic airplane will be derived. The derivation of these equations was presented by Waszak in 1986 and again in 1988, see respectively references [Was86] and [Was88]. For airframes with sufficient rigidity or stiffness, wide frequency separation results between those natural modes of the aircraft dominated by the rigid body degrees of freedom and the remaining modes dominated by the elastic degrees of freedom. Therefore, aircraft dynamic modelling, analysis and synthesis activities frequently address either the rigid body dynamics or the structural dynamics.
With the development of larger aircraft and the desire for lighter structures for improved fuel economy, by the use of new materials (e.g., composites), etc., there is an increased potential for significant contributions from aero-elastic effects in the dynamic response of flight vehicles of the future to pilot input and/or atmospheric turbulence. Not only can the dynamic response due to aero-elastic modes themselves become significant, but coupling between the aero-elastic and the rigid-body degrees of freedom can noticeably alter the rigid body dynamics of the vehicle. Consequently, it is not always justified to decouple between rigid body dynamics and structural dynamics. The model that accounts for

the coupling between flight mechanics and aero-elasticity is called integral model. Schuler presents in reference [Sch97] the integral modelling approach (in the frequency as well as in the time domain) and control law design for a large highly flexible aircraft. In [Teu03] Teufel investigated the effect of 2D gusts on aero-elasticity and flight mechanics using the integral model.

In [Was87] a simulation experiment is described that addresses the effects of structural flexibility on the dynamic characteristics of a generic family of aircraft. The simulation was performed using the NASA Langley Visual/Motion Simulator facility and the results comprised complete response data together with pilot ratings and comments. It is observed that increased flexibility can lead to increased tracking errors, degrading handling qualities and changes in the frequency content of the pilot inputs. Damveld presented in reference [Dam05] the influence of unsteady aerodynamics and trimming on the dynamics of an aero-elastic aircraft, also based on the equations derived by Waszak and Schmidt in [Was88]. Buttrill derived in reference [But87] the equations of motion while accounting for inertial coupling. Reschke presented in reference [Res05] a dynamic simulation of a large transport aircraft to show the influence of inertial coupling terms on the simulation and loads computation.

Here, an integrated flexible aircraft model is presented, with particular attention paid to the assumptions made at the various stages of the modelling. The nonlinear equations of motion are derived from first principles, using the Lagrange equation together with the Principle of Virtual Work. The resulting model can then be used for example in real-time man-in-the-loop simulations, because the equations are expressed in terms of body-reference axes, rather than inertial axes. Large-amplitude displacements of the rigid-body degrees of freedom are modelled, leading to nonlinear equations of motion governing these degrees of freedom.

During derivation of the equations of motion, it is indicated when and where the following assumptions are needed:

1. The structural deformation should be sufficiently small to justify linear elastic theory.

2. A set of normal vibration modes (frequencies and mode shapes) are assumed to be available (from a finite-element analysis).

3. The body reference axes $oxyz$ are rotating relative to inertial space with angular velocity ω and each mass element is treated as a point mass.

4. The structural displacement is small or the displacement and displacement rate are colinear.

5. The mass density of each element is constant.

6. The inertia tensor is assumed to be constant.

Under the assumptions 1 and 2, the application of Lagrange's equations will lead directly to the scalar, ordinary differential equations of motion, expressed in terms of the generalised forces associated with the aerodynamic and propulsive forces. The elastic and
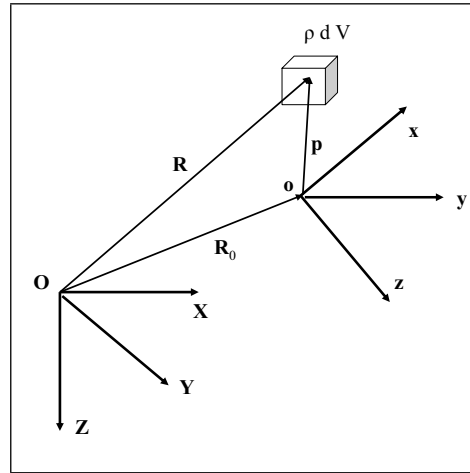
Figure 4.3: Position of mass element.

rigid body degrees of freedom are ultimately coupled via these forces. The modelling of the aerodynamic and propulsive forces is the topic of section 4.4 and 4.6 respectively.

4.3.1   Mean axes

In developing equations of motion of any unconstrained elastic system, the local body-reference coordinate system should be chosen appropriately. Otherwise inertial coupling can occur between the rigid body degrees of freedom and the elastic degrees of freedom. This noninertial reference system moves with the body but is not fixed to a material point in the body. Such a system is called a mean axis system.

The mean axes are defined such that at every instant, the relative linear and angular momenta due to elastic deformation are zero. The mean axes must be chosen such that the following equation holds:

$$\int_V \frac{\delta \mathbf{p}}{\delta t} \rho dV = \int_V \mathbf{p} \times \frac{\delta \mathbf{p}}{\delta t} \rho dV = 0, \tag{4.166}$$

where $\mathbf{p}$ is the position of a mass element relative to a local reference system $oxyz$, see also figure (4.3).

For this expression, a more practical constraint can be derived.

The position of a point of the body can be represented by its undeformed position $\mathbf{s}(x, y, z)$ plus its deformation $\mathbf{d}(x, y, z, t)$, thus for each mass element :

$$\mathbf{p} = \mathbf{s} + \mathbf{d}. \tag{4.167}$$

The undeformed position vector $\mathbf{s}$ is independent of time. Therefore equation (4.166) reduces to

$$\int_V \frac{\delta \mathbf{d}}{\delta t} \rho dV = \int_V (\mathbf{s} + \mathbf{d}) \times \frac{\delta \mathbf{d}}{\delta t} \rho dV = 0. \tag{4.168}$$

Now using assumption 4 and 5, this can be further simplified to arrive at the 'practical' mean axes constraints:

$$\frac{\delta}{\delta t} \int_V \mathbf{d}\rho dV = \frac{\delta}{\delta t} \int_V \mathbf{s} \times \mathbf{d}\rho dV = 0. \tag{4.169}$$

4.3.2   Equations of motion of an unconstrained elastic aircraft

The equations of motion will be derived using the equation of Lagrange:

$$\frac{d}{dt}\left[\frac{\partial T}{\partial \dot{q}_i}\right] - \frac{\partial T}{\partial q_i} + \frac{\partial U}{\partial q_i} = Q_i, \tag{4.170}$$

where T is the kinetic energy of the body, U the potential energy, Q_i are the generalised forces and q_i the generalised coordinates. First, the kinetic energy of the body will be derived.

Kinetic energy of the body

Consider a mass element ρdV of an elastic body, at the inertial position $\mathbf{R}$ relative to the inertial reference frame $OXYZ$, see figure (4.3). This inertial position can also be written in terms of its position relative to a local reference frame $oxyz$ and the position of this local reference frame relative to the inertial reference frame $OXYZ$ (i.e., $\mathbf{R} = \mathbf{R}_0 + \mathbf{p}$). The kinetic energy of the body can then be written:

$$T = \frac{1}{2} \int_V \frac{d\mathbf{R}}{dt} \cdot \frac{d\mathbf{R}}{dt} \rho dV \tag{4.171}$$

Using assumption 3, the derivative of the position vector can be written as:

$$\frac{d\mathbf{R}}{dt} = \frac{d\mathbf{R}_0}{dt} + \frac{\delta\mathbf{p}}{\delta t} + \boldsymbol{\omega} \times \mathbf{p}, \tag{4.172}$$

where $\frac{\delta(\cdot)}{\delta t}$ is the time derivative of $(\cdot)$ relative to the body reference frame. Substitute equation (4.172) into (4.171), to get the expression for the kinetic energy of the body:

$$T = \frac{1}{2} \int_V \{\frac{d\mathbf{R}_0}{dt} \cdot \frac{d\mathbf{R}_0}{dt} + 2\frac{d\mathbf{R}_0}{dt} \cdot \frac{\delta\mathbf{p}}{\delta t} + \frac{\delta\mathbf{p}}{\delta t} \cdot \frac{\delta\mathbf{p}}{\delta t} + \tag{4.173}$$

$$+2\frac{\delta\mathbf{p}}{\delta t} \cdot (\boldsymbol{\omega} \times \mathbf{p}) + (\boldsymbol{\omega} \times \mathbf{p}) \cdot (\boldsymbol{\omega} \times \mathbf{p}) + 2(\boldsymbol{\omega} \times \mathbf{p}) \cdot \frac{d\mathbf{R}_0}{dt}\}\rho dV.$$

This expression can be simplified by using the mean axes constraints from equation (4.166). Using equation (4.166), it can be shown that the second and fourth term in equation (4.173) are equal to zero:

$$\int_V \frac{d\mathbf{R}_0}{dt} \cdot \frac{\delta\mathbf{p}}{\delta t} \rho dV = \frac{d\mathbf{R}_0}{dt} \int_V \frac{\delta\mathbf{p}}{\delta t} \rho dV \equiv 0, \tag{4.174}$$

$$\int_V \frac{\delta\mathbf{p}}{\delta t} \cdot (\boldsymbol{\omega} \times \mathbf{p})\rho dV = \int_V \mathbf{p} \times \frac{\delta\mathbf{p}}{\delta t}\rho dV \cdot \boldsymbol{\omega} \equiv 0. \tag{4.175}$$

Locating the origin of the body-reference axes at the instantaneous center of mass requires that:

$$\mathbf{x}_{CG} = \frac{\int\limits_V \mathbf{p}\rho dV}{\int\limits_V \rho dV} = 0, \tag{4.176}$$

where $\mathbf{x}_{CG}$ is the position of the center of mass relative to the origin of the body-reference axes. Using expression (4.176), the last term in equation (4.173) for the kinetic energy is also equal to zero, because:

$$\int\limits_V (\boldsymbol{\omega} \times \mathbf{p}) \cdot \frac{d\mathbf{R}_0}{dt}\rho dV = \boldsymbol{\omega} \times \int\limits_V \mathbf{p}\rho dV \cdot \frac{d\mathbf{R}_0}{dt} \equiv 0. \tag{4.177}$$

Now the kinetic energy can be written as:

$$T = \frac{1}{2}\int\limits_V \{\frac{d\mathbf{R}_0}{dt} \cdot \frac{d\mathbf{R}_0}{dt} + \frac{\delta\mathbf{p}}{\delta t} \cdot \frac{\delta\mathbf{p}}{\delta t} + (\boldsymbol{\omega} \times \mathbf{p}) \cdot (\boldsymbol{\omega} \times \mathbf{p})\}\rho dV, \tag{4.178}$$

or equivalently:

$$T = \frac{1}{2}M\frac{d\mathbf{R}_0}{dt} \cdot \frac{d\mathbf{R}_0}{dt} + \frac{1}{2}\boldsymbol{\omega}^T[\mathbf{I}]\boldsymbol{\omega} + \frac{1}{2}\int\limits_V \frac{\delta\mathbf{p}}{\delta t} \cdot \frac{\delta\mathbf{p}}{\delta t}\rho dV, \tag{4.179}$$

where M is the mass of the body and $[\mathbf{I}]$ is the inertia tensor for the body. In general, the inertia tensor is a function of time due to the elastic deformation of the body. However, assuming small displacements (relative to the large rigid body displacements), the inertia tensor is usually assumed to be constant (see assumption 6).

The free vibration modes of an elastic body form a complete set of orthogonal functions that can be used to describe any forced motion of the body. The free vibration modes of an unconstrained elastic body can be used with the practical mean axes constraints to locate the origin and determine the orientation of the body-reference axes that decouple the kinetic energy expression.
Assume that the free vibration modes of the body are available (assumption 2). Then the relative displacements, for the body undergoing general elastic deformation, can be described in terms of the mode shapes $\phi_i(x, y, z)$ and generalised displacement coordinates $\eta_i(t)$:

$$\mathbf{d} = \sum_{i=1}^{\infty} \phi_i(x, y, z)\eta_i(t). \tag{4.180}$$

In terms of the mode shape and generalised coordinates, the practical mean axis constraints can be written as:

$$\sum_{i=1}^{\infty} \frac{d\eta_i}{dt}\int\limits_V \phi_i\rho dV = \sum_{i=1}^{\infty} \frac{d\eta_i}{dt}\int\limits_V \mathbf{s} \times \phi_i\rho dV = 0. \tag{4.181}$$

These expressions locate the mean body-reference axes. Furthermore, they can be interpreted as requiring the free vibration modes to be orthogonal to the rigid-body translational and rotational modes, respectively.

Applying equation (4.180) to the last term on the righthand side of expression (4.179) for the kinetic energy, leads to:

$$\int_V \frac{\delta \mathbf{p}}{\delta t} \cdot \frac{\delta \mathbf{p}}{\delta t} \rho dV = \int_V \frac{\delta \mathbf{d}}{\delta t} \cdot \frac{\delta \mathbf{d}}{\delta t} \rho dV = \tag{4.182}$$

$$= \int_V \{\sum_{i=1}^{\infty} \phi_i \frac{d\eta_i}{dt} \cdot \sum_{j=1}^{\infty} \phi_j \frac{d\eta_j}{dt}\} \rho dV = \tag{4.183}$$

$$= \sum_{i=1}^{\infty} M_i \dot{\eta}_i^2, \tag{4.184}$$

The last equation is derived using the orthogonality of the free vibration modes:

$$\int_V \phi_i \cdot \phi_j \, \rho dV \equiv 0, \qquad i \neq j \tag{4.185}$$

and after introducing the generalised mass of the ith mode, defined by:

$$M_i = \int_V \phi_i \cdot \phi_i \, \rho dV. \tag{4.186}$$

Now the kinetic energy from equation (4.179) can be written as:

$$T = \frac{1}{2} M \frac{d\mathbf{R}_0}{dt} \cdot \frac{d\mathbf{R}_0}{dt} + \frac{1}{2} \boldsymbol{\omega}^T [\mathbf{I}] \boldsymbol{\omega} + \frac{1}{2} \sum_{i=1}^{\infty} M_i \dot{\eta}_i^2. \tag{4.187}$$

Potential energy of the body

The potential energy of the body consists of gravitational potential energy and elastic strain energy. The gravitational potential energy can be written as:

$$U_g = -\int_V \mathbf{g} \cdot (\mathbf{R}_0 + \mathbf{p})\rho dV = \tag{4.188}$$

$$= -\int_V (\mathbf{R}_0 + \mathbf{p}) \cdot \mathbf{g}\rho dV = \tag{4.189}$$

$$= -\mathbf{R}_0 \cdot \mathbf{g} \int_V \rho dV - \int_V \mathbf{p}\rho dV \cdot \mathbf{g}, \tag{4.190}$$

where $\mathbf{g}$ is the gravitational acceleration vector. From equation (4.176) it follows that the second term on the righthand side of the above expression for the gravitational potential

energy is equal to zero. The expression for the gravitational potential energy can then be further simplified to:

$$U_g \;=\; -\mathbf{R}_0 \cdot \mathbf{g}M, \tag{4.191}$$

The elastic strain energy resulting from structural deformation is the work done on the structure in going from the undeformed reference shape to a deformed shape. The position of each mass element of the body can be written as:

$$\mathbf{p} = \mathbf{s} + \mathbf{d}, \tag{4.192}$$

where $\mathbf{s}(x, y, z)$ is the undeformed position and $\mathbf{d}(x, y, z, t)$ the deformation. Using the Principle of D'Alembert, then the strain energy can be written as:

$$U_e = -\frac{1}{2} \int_V \frac{\delta^2 \mathbf{d}}{\delta t^2} \cdot \mathbf{d} \rho dV \tag{4.193}$$

This expression can also be written in terms of the free vibrational modes from equation (4.180),as:

$$U_e = \frac{1}{2} \sum_{i=1}^{\infty} \omega_i^2 \eta_i^2 M_i, \tag{4.194}$$

where ω_i is the natural frequency of vibration for the ith mode. Notice that for a given deformation, the strain energy of a body undergoing arbitrary forced motion is the same as for the body undergoing free vibration.

The desired equations of motion are to be expressed in terms of quantities defined in the body-reference axes. The application of the equation of Lagrange necessitates the use of generalised coordinates describing motion relative to an inertial reference frame. Therefore define the inertial position of the origin of the body-reference mean axes (i.e., the instantaneous center of mass of the body) to be:

$$\mathbf{R}_0 = x\hat{\mathbf{i}} + y\hat{\mathbf{j}} + z\hat{\mathbf{k}}, \tag{4.195}$$

where $\hat{\mathbf{i}}, \hat{\mathbf{j}}, \hat{\mathbf{k}}$ are unit vectors in each of the coordinate directions of the body-reference axes. Also let:

$$\frac{d\mathbf{R}_0}{dt} = \frac{\delta \mathbf{R}_0}{\delta t} + \boldsymbol{\omega} \times \mathbf{R}_0 = U\hat{\mathbf{i}} + V\hat{\mathbf{j}} + W\hat{\mathbf{k}}. \tag{4.196}$$

The Euler angles (ϕ, θ, ψ) are used to define the inertial orientation of the body-reference axes, consistent with rigid aircraft analysis. The vector defining the inertial angular velocity of the body-reference axis is:

$$\boldsymbol{\omega} = p\hat{\mathbf{i}} + q\hat{\mathbf{j}} + r\hat{\mathbf{k}}, \tag{4.197}$$

where:

$$p = \dot{\phi} - \dot{\psi}\sin\theta, \tag{4.198}$$

$$q = \dot{\psi}\cos\theta\sin\phi + \dot{\theta}\cos\psi, \tag{4.199}$$

$$r = \dot{\psi}\cos\theta\cos\phi - \dot{\theta}\sin\phi \tag{4.200}$$

Then from equation (4.196) it follows that:

$$\begin{bmatrix} U \\ V \\ W \end{bmatrix} = \begin{bmatrix} \dot{x} \\ \dot{y} \\ \dot{z} \end{bmatrix} + \begin{bmatrix} p \\ q \\ r \end{bmatrix} \times \begin{bmatrix} x \\ y \\ z \end{bmatrix} = \begin{bmatrix} \dot{x} + qz - ry \\ \dot{y} + rx - pz \\ \dot{z} + py - qx \end{bmatrix} \tag{4.201}$$

Now the kinetic energy can be written as:

$$T = \frac{1}{2}M(U^2 + V^2 + W^2) + \frac{1}{2}[p\;q\;r]\,[\mathbf{I}]\begin{bmatrix} p \\ q \\ r \end{bmatrix} + \frac{1}{2}\sum_{i=1}^{\infty} M_i \dot{\eta}_i^2 \tag{4.202}$$

and the contributions of the potential energy can be written as:

$$U_g = -Mg(-x\sin\theta + y\sin\phi\cos\theta + z\cos\phi\cos\theta), \tag{4.203}$$

$$U_e = \frac{1}{2}\sum_{i=1}^{\infty} \omega_i^2 \eta_i^2 M_i. \tag{4.204}$$

Substitution of equations (4.198) to (4.201) into equation (4.202) gives the expression for kinetic energy in terms of the generalised coordinates $(x, y, z, \phi, \theta, \psi, \eta_i)$, where $i = 1, 2, ...$, and their time derivatives. This allows the direct application of the Equation of Lagrange (4.170). Here, the first equation of motion will be derived exemplarily by solving the Lagrange equation for the first generalised coordinate, i.e. x. The other six equations follow similarly by solving the Lagrange equation for respectively the generalised coordinates y, z, ϕ, θ, ψ and η_i. Recall the Lagrange equation from equation (4.170):

$$\frac{d}{dt}\left[\frac{\partial T}{\partial \dot{q}_i}\right] - \frac{\partial T}{\partial q_i} + \frac{\partial U}{\partial q_i} = Q_i,$$

where the total potential energy is given by:

$$U = U_g + U_e. \tag{4.205}$$

using the expressions from equations (4.203) and (4.204) for the gravitational potential energy and the elastic strain energy respectively.

For the first generalised coordinate (x), the Lagrange equation is given by:

$$\frac{d}{dt}\left[\frac{\partial T}{\partial \dot{x}}\right] - \frac{\partial T}{\partial x} + \frac{\partial U}{\partial x} = Q_X. \tag{4.206}$$

From the expression for the kinetic energy, equation (4.202), it can be derived that:

$$\frac{\partial T}{\partial \dot{x}} = M\dot{x} + M(qz - ry) = MU. \tag{4.207}$$

Take the time derivative of this expression to get the first term on the left hand side of equation (4.206):

$$\frac{d}{dt}\left[\frac{\partial T}{\partial \dot{x}}\right] = M\dot{U}. \tag{4.208}$$

The second term on the left hand side of equation (4.206) becomes:

$$\frac{\partial T}{\partial x} = \frac{1}{2}M\left(2r(\dot{y} + rx - pz) - 2q(\dot{z} + py - qx)\right) = M(rV - qW). \tag{4.209}$$

For the third term on the left hand side of equation (4.206), it can be derived that:

$$\frac{\partial U}{\partial x} = \frac{\partial U_g}{\partial x} = Mg\sin\theta. \tag{4.210}$$

The term on the right hand side of equation (4.206) is the generalised force Q_X. That is the force in the $\hat{\mathbf{i}}$-direction of the body reference mean axes. The exact expression of the generalised forces are determined at the end of this section.

Now equations (4.208) to (4.210) can be substituted into the Lagrange equation for the first generalised coordinate, i.e. equation (4.206). This gives the first equation of motion in the x-direction of the body reference mean axis frame:

$$M[\dot{U} - rV + qW + g\sin\theta] = Q_X. \tag{4.211}$$

It was already mentioned that the other six equations follow similarly by solving the Lagrange equation for respectively the generalised coordinates y, z, ϕ, θ, ψ and η_i. The resulting equations are again expressed in terms of U, V, W, p, q and r using equations (4.198) to (4.201). The equations of motion for an unconstrained elastic vehicle defined

in the body reference mean axes then get:

$$M[\dot{U} - rV + qW + g\sin\theta] = Q_X \quad (4.212)$$

$$M[\dot{V} - pW + rU - g\sin\phi\cos\theta] = Q_Y \quad (4.213)$$

$$M[\dot{W} - qU + pV - g\cos\phi\cos\theta] = Q_Z \quad (4.214)$$

$$I_{xx}\dot{p} - (I_{xy}\dot{q} + I_{xz}\dot{r}) + (I_{zz} - I_{yy}qr + (I_{xy}r - I_{xz}q)p +$$
$$+(r^2 - q^2)I_{yz} + M[-g\cos\theta(y\cos\phi - z\sin\phi) +$$
$$+(\dot{W} + Vp - Uq)y - (\dot{V} + Ur - Wp)z] = Q_\phi \quad (4.215)$$

$$I_{yy}\dot{q} - (I_{xy}\dot{p} + I_{yz}\dot{r}) + (I_{xx} - I_{zz}pr + (I_{xy}p - I_{yx}r)q +$$
$$+(p^2 - r^2)I_{xz} + M[g(x\cos\theta\cos\phi + z\sin\theta) +$$
$$+(\dot{U} + qW - rV)z - (\dot{W} + pV - qU)x] =$$
$$= [Q_\phi\cos\phi\sin\theta - Q_\theta\sin\phi\cos\theta + Q_\psi\sin\phi]\sec\theta \quad (4.216)$$

$$I_{zz}\dot{r} - (I_{xz}\dot{p} + I_{yz}\dot{q}) + (I_{yy} - I_{xx}pq + (I_{xz}q - I_{yz}p)r +$$
$$+(q^2 - p^2)I_{xy} + M[-g(x\cos\theta\sin\phi + y\sin\theta) +$$
$$+(\dot{V} + rU - pW)x - (\dot{U} + qW - rV)y] =$$
$$= [Q_\phi\sin\phi\sin\theta + Q_\theta\cos\phi\cos\theta + Q_\psi\sin\phi]\sec\theta \quad (4.217)$$

$$\ddot{\eta}_i + \omega_i^2\eta_i = \frac{Q_{\eta_i}}{M_i} \qquad i = 1, 2, ... \quad (4.218)$$

Generalised Forces

The generalised forces are determined using the Principle of Virtual Work. If δW is the work associated with arbitrary virtual displacements of the generalised coordinates, then:

$$Q_i = \frac{\partial}{\partial q_i}(\delta W). \quad (4.219)$$

Let the applied aerodynamic and propulsive forces and moments relative to the body reference axes be defined by:

$$\mathbf{F} = X\hat{\mathbf{i}} + Y\hat{\mathbf{j}} + Z\hat{\mathbf{k}}, \ \mathbf{M} = L\hat{\mathbf{i}} + M\hat{\mathbf{j}} + N\hat{\mathbf{k}}. \quad (4.220)$$

Here X, Y and Z are simply the total aerodynamic and propulsive forces along each of the body-reference-axes directions. Similarly, L, M, and N are the total aerodynamic and propulsive moments about each of the body-reference-axes directions.

The moment about the origin of the inertial axis is equal to $\mathbf{M} = \mathbf{R}_0 \times \mathbf{F}$. The virtual work relative to the inertial reference frame, done by the aerodynamic and propulsive forces and moments is:

$$\delta W = X\delta x + Y\delta y + Z\delta z + [L + (yZ - zY)]\delta\phi_B +$$
$$+ [M + (zX - xZ)]\delta\theta_B + [N + (xY - yX)]\delta\phi_B +$$
$$+ \int_S \mathbf{P}(x, y, z) \cdot \sum_{i=1}^{\infty} \phi_i\delta\eta_i dS, \quad (4.221)$$

where the last term is the work done by the distributed surface pressures $\mathbf{P}(x, y, z)$, due to the virtual displacements of each of the elastic generalised coordinates. The displacements $\delta\phi_B, \delta\theta_B$ and $\delta\psi_B$ are the virtual rotations about each of the body-reference coordinate directions. They are related to virtual rotations of the generalised coordinates (ϕ, θ and ψ) by the direction cosines relating the Euler-angle virtual rotations to the body-reference axes:

$$\delta\phi_B = \delta\phi - \delta\psi\sin\theta \tag{4.222}$$

$$\delta\theta_B = \delta\theta\cos\phi + \delta\psi\cos\theta\sin\phi \tag{4.223}$$

$$\delta\psi_B = -\delta\theta\sin\phi + \delta\psi\cos\theta\cos\phi \tag{4.224}$$

Now substitute equations (4.222) to (4.224) into equation (4.221) and that into equation (4.219) to get the expressions for the generalised forces. The equations (4.215) to (4.217) governing the rotational degrees of freedom can be simplified considerably, since they explicitly contain the 'translational' equations. Using furthermore that:

$$Q_x \equiv X, \quad Q_y \equiv Y, \quad Q_z \equiv Z \tag{4.225}$$

$$Q_{\phi_B} = L, \quad Q_{\theta_B} = M, \quad Q_{\psi_B} = N, \tag{4.226}$$

the simplified equations of motion become:

$$M[\dot{U} - rV + qW + g\sin\theta] = X \tag{4.227}$$

$$M[\dot{V} - pW + rU - g\sin\phi\cos\theta] = Y \tag{4.228}$$

$$M[\dot{W} - qU + pV - g\cos\phi\cos\theta] = Z \tag{4.229}$$

$$\begin{aligned} I_{xx}\dot{p} - (I_{xy}\dot{q} + I_{xz}\dot{r}) + (I_{zz} - I_{yy}qr + (I_{xy}r - I_{xz}q)p + \\ + (r^2 - q^2)I_{yz} = L \end{aligned} \tag{4.230}$$

$$\begin{aligned} I_{yy}\dot{q} - (I_{xy}\dot{p} + I_{yz}\dot{r}) + (I_{xx} - I_{zz}pr + (I_{xy}p - I_{yx}r)q + \\ + (p^2 - r^2)I_{xz} = M \end{aligned} \tag{4.231}$$

$$\begin{aligned} I_{zz}\dot{r} - (I_{xz}\dot{p} + I_{yz}\dot{q}) + (I_{yy} - I_{xx}pq + (I_{xz}q - I_{yz}p)r + \\ + (q^2 - p^2)I_{xy} = N \end{aligned} \tag{4.232}$$

$$\ddot{\eta}_i + \omega_i^2\eta_i = \frac{Q_{\eta_i}}{M_i} \qquad i = 1, 2, ... \tag{4.233}$$

The determination of the aerodynamic and propulsive forces and moments defined in body reference axes is the topic of respectively sections 4.4 and 4.6.

4.4 Aerodynamic modelling

In this section, the aerodynamic model will be described. The aerodynamic loads are distributed loads. They act as pressure loads on each part of the aircraft's external contour.

For a transonic jet aircraft, the difficulty lies in predicting and modelling the aerodynamic force at high Mach number and close to the C_L where buffet occurs. For such type of aircraft, the aerodynamic data must be provided:

- as a function of the Mach-number,

- taking into account the effects of non-linearities where needed,

- for each high lift configuration and with and without extended airbrakes,

- for landing gear retracted and extended, with ground effect when relevant.

For turboprop aircraft, usually having a cruise Mach number well below 0.6, the Mach-effect is much less critical. Even then, the aerodynamic forces must still be modelled as a function of Mach number. Turboprop aircraft and their specific topics are not further considered here.

Depending on their steady (or quasi-steady) or transient nature, the aerodynamic forces are computed by different techniques (tests and/or theoretical methods). Only those aerodynamic forces that are of importance in the quasi-steady manoeuvres investigated here, will be described. If needed, this model can also be extended to contain the aerodynamic forces due to gusts, etc.
The steady aerodynamic loads still rely in a large extent on wind tunnel tests, which can be complemented by Computational Fluid Dynamics (CFD) methodologies. The aerodynamic forces are to be modelled more or less complex into the loads model, depending on the type of the aircraft and on its flight envelope. The determination of the aerodynamic load distributions from for example wind tunnel test data, will be the topic of section 4.4.1.
For unsteady aerodynamics there is no or very little wind tunnel test support. Due to the inertia of the airflow, a finite time is necessary to reach the steady state conditions after a change of flight mechanics parameter, i.e. the angle of attack or a control surface position. The usual representation of the unsteady aerodynamics is in the frequency domain, instead of the time domain. The most frequently used technique is the Doublet Lattice Method (DLM), which is a three dimensional, small disturbance, thin plate, linear model. This methodology provides an aerodynamic influence coefficient (AIC) matrix that will be a complex matrix. This AIC-matrix gives the relationship between the pressure on each point of the aerodynamic grid for a harmonic unit variation of the angle of attack on another (or the same) point of the aerodynamic grid. These aerodynamic matrices are a function of the Mach number and of the non-dimensional frequency (reduced frequency $k = \frac{\omega c}{V_0}$). Notice that the steady (linear) aerodynamics corresponds to the (real) matrix for $k = 0$. If only the steady part of the Doublet Lattice Model is considered, this method is called Vortex Lattice Method (VLM). Unsteady aerodynamics are not further considered here.
However, it will be shown later, that the steady part of the DLM can be used to determine the deformation induced aerodynamic effects. Therefore the basic principles of the Doublet Lattice Method will be presented in section 4.4.3. The VLM model can either be used corrected or uncorrected. In section 4.4.4, the method for correcting the VLM-method based on empirical data (from wind tunnel tests and/or from CFD-analysis) is presented.
Here, it is assumed that the lift and moment distributions for the steady aerodynamic effects are available from wind tunnel measurements (complemented with CFD-analysis),

instead of estimating them completely by theoretical linear potential theory (i.e. the steady part of the Doublet Lattice Model).

The dynamic equations of motion for the flexible aircraft in generalized coordinates are, see also equation (4.67):

$$\mathbf{M}_{HH} \cdot \ddot{\mathbf{q}}_H + \mathbf{C}_{HH} \cdot \dot{\mathbf{q}}_H + \mathbf{K}_{HH} \cdot \mathbf{q}_H = \mathbf{F}_H = \mathbf{F}_{aero} + \mathbf{F}_{thrust}, \qquad (4.234)$$

where $\mathbf{q}_H$ are the modal coordinates, in this case after the modal reduction of the condensed model. The condensed model is generated by a static Guyan reduction of the full model. See further section 4.2 for more information on these model reduction techniques.
Equation (4.234) will be used to determine the deformation of the airframe, during a dynamic manoeuvre. In this section the focus lies on the description of $\mathbf{F}_{aero}$, the total aerodynamic loads. The determination of the thrust vector will be the topic of section 4.6.

The total aerodynamic loads can be split up into several separate contributions:

$$\mathbf{F}_{aero} = \mathbf{F}_{x_R} + \mathbf{F}_{\delta} + \mathbf{F}_{x_F}, \qquad (4.235)$$

where the load vector $\mathbf{F}_{x_R}$ is due to the rigid body motion of the aircraft, $\mathbf{F}_{\delta}$ are the aerodynamic loads induced by the deflection of the control surfaces and $\mathbf{F}_{x_F}$ are those induced by the deformation of the aircraft.
First, determination of the aerodynamic loads distributions due to rigid body motion and control surface deflections will be discussed.

4.4.1 Experimental database for the rigid aircraft

In this section, the aerodynamic load distributions will be determined from experimental data. This experimental data might stem from wind tunnel tests, complemented with CFD-analysis. These aerodynamic loads are distributed loads. They act as pressure loads on each part of the aircraft's external contour. They are considered as a local lift and moment coefficient acting on the aerodynamic center of each lifting surface section.

The distributions on all components of the aircraft have to be determined, i.e. on the fuselage, the wings, the tailplanes, winglets,...to get the complete aerodynamic load distribution on the aircraft. The determination of the distribution on such a component will be shown exemplarily for the wing. The distributions on the other components are determined similarly.

The load distribution on the wing can be build up using the following contributions:

- Spanwise wing loads due to incidence,
    - clean configuration,
    - high lift configuration (slats/flaps extended),

- Incremental spanwise wing loads due to sideslip,

- Incremental spanwise wing loads due to rate of roll,

- Incremental aerodynamic data due to

  - aileron deflection,
  - spoiler deflection,

- Incremental spanwise loads on the wing, airbrakes deployed, slats/flaps extended.

- Loads on the winglets,

- etc., ...Any additional effect specific for this aircraft.

As can be clearly seen from this list for the wing, there is a considerable number of effects that has to be accounted for. Each effect is again being build up from several contributions.

Similar lists can be written down for the other components. The aerodynamic database that is used here contains 1819 contributions, where most contributions are multidimensional functions of aircraft configuration, Mach number, dynamic pressure, etc. Obviously, describing all effects from all components for all kind of flight conditions and aircraft configurations definitely goes beyond the scope of this report. However, some aspects will be exemplarily described in more detail, such that the basic philosophy is clear to the reader.

Aerodynamic loads due to rigid body motion

The aerodynamic loads, i.e. the force and moment distributions due to the rigid body motion are described in this section. It is assumed that these load distributions are known for the rigid aircraft, either in jig-shape or in flight-shape, from wind tunnel measurements. These wind tunnel measurements can be combined with CFD-analysis to correct or analyze effects that are difficult or too expensive to measure in the wind tunnel.

The load distribution on the wing due to angle of attack in clean configuration, will now be described in more detail. All other effects can be described similarly. In the end, depending on the flight situation (clean, airbrakes out, flaps extended, etc.) and the kind of manoeuvre, all relevant load distributions are summed up to get the total distributed loads along all components of the aircraft.

In general, the separate effects can be divided into longitudinal and lateral effects. Notice at this point that, due to the measurement procedure of the separate effects in the wind tunnel, the longitudinal effects are usually given in stability axes, whereas the lateral effects are usually given in body axes. This should be accounted for, when adding these effects to arrive at the total distributions. Notice, that the transformation from stability to body axes depends on the current angle of attack of the aircraft. Because of computational considerations, one might already add some effects in the pre-processing phase of

the simulation, but remember that than care must be taken.

Furthermore, one has to pay attention, when dealing with additional devices. In practice, for example the loads on the winglets and their interference effects could be measured separately in the wind tunnel from a costs perspective. Consequently, their contribution can be given normal to the winglet surface instead of in stability or body axes. This is an additional transformation from the winglet axes to the body axes that has to be accounted for in that case. These transformations sound trivial, but due to the huge amount of data and effects, such transformations can be easily overseen.

local lift coefficient on the wing due to incidence

For a given angle of attack α using the global lift coefficient C_L, the local load on the wing can be written as:

$$\left[c_l \frac{l}{l_g}\right] = \left[c_l \frac{l}{l_g}\right]_0 + \left[\frac{\Delta c_l}{\Delta C_L} \frac{l}{l_g}\right]_\alpha \cdot \frac{\partial C_L}{\partial \alpha}(\alpha - \alpha_0) + \Delta \left[c_l \frac{l}{l_g}\right]_{R1} + \Delta \left[c_l \frac{l}{l_g}\right]_{R2}, \quad (4.236)$$

where c_l is the local lift coefficient. The terms between square brackets denote distributions along the wing span.

local pitching moment coefficient on the wing due to incidence

Similarly, the local pitching moment coefficient c_m relative to the leading edge of the local wing chord can be written as:

$$\left[c_m \frac{l}{l_g}\right] = \left[c_m\right]_0 \frac{l}{l_g} - \left[\frac{\Delta X_N}{l}\right]_\alpha \cdot \left[c_l \frac{l}{l_g}\right]_{Ref} + \Delta \left[c_m \frac{l}{l_g}\right]_{R1} + \Delta \left[c_m \frac{l}{l_g}\right]_{R2}, \quad (4.237)$$

where:

$$\left[c_l \frac{l}{l_g}\right]_{Ref} = \left[c_l \frac{l}{l_g}\right]_0 + \left[\frac{\Delta c_l}{\Delta C_L} \frac{l}{l_g}\right]_\alpha \cdot \frac{\partial C_L}{\partial \alpha}(\alpha - \alpha_0). \quad (4.238)$$

The above expressions for the load distributions on the wing can be written in matrix notation as follows:

$$\left[c_l \frac{l}{l_g}\right] = \left[\left[c_l \frac{l}{l_g}\right]_0 - \left[\frac{\Delta c_l}{\Delta C_L} \frac{l}{l_g}\right]_\alpha \cdot \frac{\partial C_L}{\partial \alpha} \cdot \alpha_0 \quad \left[\frac{\Delta c_l}{\Delta C_L} \frac{l}{l_g}\right]_\alpha \cdot \frac{\partial C_L}{\partial \alpha}\right] \begin{bmatrix} 1 \\ \alpha \end{bmatrix}, \quad (4.239)$$

Notice, that in this equation the nonlinear effects are neglected. A similar expression for the local pitching moment can also be derived.

This can be written all together in a short notation as:

$$\left[c_R \frac{l}{l_g}\right] = \mathbf{Q}_{kx_R} \mathbf{x}_R, \quad (4.240)$$

where:

$$\mathbf{Q}_{kx_R} = \left[\left[c_l \frac{l}{l_g}\right]_0 - \left[\frac{\Delta c_l}{\Delta C_L} \frac{l}{l_g}\right]_\alpha \cdot \frac{\partial C_L}{\partial \alpha} \cdot \alpha_0 \quad \left[\frac{\Delta c_l}{\Delta C_L} \frac{l}{l_g}\right]_\alpha \cdot \frac{\partial C_L}{\partial \alpha}\right], \quad (4.241)$$

$$\mathbf{x}_R = \begin{bmatrix} 1 \\ \alpha \end{bmatrix}, \quad (4.242)$$

and the local load (in this example: lift or moment) due to rigid body motion is indicated by $c_R \frac{l}{l_g}$.

Notice that the load distributions are described as a function of the state vector $\mathbf{x_R}$, where the state vector (and the aerodynamic influence matrix $\mathbf{Q}_{kx_R}$) can be easily extended to include the other effects:

$$\mathbf{x}_R = \begin{bmatrix} 1 \\ \alpha \\ \beta \\ p \\ q \\ r \end{bmatrix}. \tag{4.243}$$

Notice also that the local load due to rigid body motion that is indicated by $c_R \frac{l}{l_g}$ in equation (4.240) has to be multiplied with the dynamic pressure, the local stripwidth and local chord length, to get the specific grid (nodal) forces on the aerodynamic grid. It depends on the definition of the degrees of freedom and the local reference frames of the aerodynamic grid, indicated by subscript k, where (that is on which vector element) a specific force/moment appears in the load vector. Obviously, one has to make sure that the definition of the aerodynamic grid matches the definition of the aerodynamic distributions in $\mathbf{Q}_{kx_R}$, otherwise an adequate additional transformation becomes necessary when building this matrix.

Aerodynamic loads due to control surface deflections

Similar to the section describing the load distributions due to rigid body motion, the load distributions due to control surface deflections can be written as:

$$\left[c_\delta \frac{l}{l_g} \right] = \mathbf{Q}_{k\delta} \boldsymbol{\delta}, \tag{4.244}$$

Notice that the load distributions are described as a function of the control vector $\boldsymbol{\delta}$:

$$\boldsymbol{\delta} = \begin{bmatrix} i_H \\ \delta_e \\ \delta_{a1} \\ \delta_{a2} \\ \delta_{a3} \\ \delta_{a4} \\ \delta_r \\ \delta_{s1} \\ \delta_{s2} \end{bmatrix}. \tag{4.245}$$

Notice again that the local load due to control surface deflection that is indicated by $c_\delta \frac{l}{l_g}$ in equation (4.244) has to be multiplied with the dynamic pressure, the local stripwidth and local chord length, to get the specific grid (nodal) forces on the aerodynamic grid.

4.4.2   Overview of theoretical models

In the previous section, the empirical data from wind tunnel measurements were taken to determine the aerodynamic load distributions along the rigid aircraft. In this section, after a short overview of the available computational methods, the basic principles of the Doublet Lattice Method will be presented.

Solving the Reynolds-Averaged Navier-Stokes (RANS) equations gives the most accurate theoretical aerodynamic prediction for a practical problem. See Anderson [And91], for the derivation of the full Navier-Stokes equations. Solving these equations has a very large impact on the computational resources, because it involves the solution of a set of nonlinear partial differential equations in the complete flow domain. The Euler equations can be derived from the Navier-Stokes equations after neglecting the viscosity terms. The Full potential equations can be derived from these Euler equations if it is further assumed that the flow is isentropic and free of rotation. The flow field can then be completely described using a single quantity (the potential). If the steady and unsteady perturbations of the flow field are small, the perturbation equations can be derived from the full potential equations. For the transonic speed range, this leads to the Transonic Small Perturbation equations. For subsonic conditions, these can be further simplified to the Linear Potential Equations. Going from the Navier-Stokes equations to the Linear Potential Equations reduces the accuracy but also significantly the computational costs. In Schuler [Sch97] these methods are compared based on their relative computational time needed, see table 4.1

It can be easily seen from this table that the Navier-stokes method requires 10000 times more computational power than the Doublet Lattice Method. The Doublet Lattice Method will be discussed later and it is an example of Linear Potential Theory. Perturbation methods of potential theory is limited to thin airfoils and small oscillatory amplitudes (if unsteady). The solution of the flow field is also less accurate close to those areas with big changes in curvature of the wetted surface, for example at the leading edge of an airfoil or at deflected flaps.

Knowledge of the aerodynamic forces induced by rigid body motion and those induced by the deformation is a prerequisite for the build up of the present aerodynamic model. The rigid body motion of the aircraft relative to its stationary flight condition and the elastic deformation of the airframe in flight are described by the superposition of the modal shapes. The aerodynamic forces will be determined by the superposition of the contributions of these modal shapes.

The Doublet Lattice Method is the most frequently used method to calculate unsteady aerodynamic forces. The main reason for this are the relatively low computational costs at sufficient accuracy together with the ease of generating an aerodynamic model for a complex geometry. For the transonic speed regime, the influence of airfoil thickness on the unsteady pressure distribution gets significant. Viscosity then has to be taken into account, due to its influence on shock position and strength. Correction of the Doublet

Method:	Relative CPU-power:
Doublet Lattice	1
Full Potential	50
Euler	500
Navier-Stokes	10000

Table 4.1: Relative computational time needed for the specific theoretical aerodynamic methods

Lattice Method for the transonic influences is usually done by quasi-steady corrections of the unsteady aerodynamic forces. The pressure distribution according to the DLM is calculated for a quasi-steady reference condition (pitch, $\omega = 0$). These pressures are then modified, using two corrective distributions, such that their integral values correspond with the experimental data for lift increase and the position of the aerodynamic center. The corrective distributions are the first and the second Birnbaum distributions that stem from linear theory of lifting surfaces. This method is quite similar to the method to correct the steady part of the Doublet Lattice Method, which will be described in section 4.4.4.

4.4.3 Doublet/Vortex lattice method

The Doublet Lattice Method is a panel method for the calculation of steady and unsteady aerodynamic forces in the frequency domain. The complete theory and a detailed description of this method can be found in [Rod71].

The Doublet Lattice Method is a method based on potential theory in which the three dimensional lifting system is modelled by flat panels (small lifting surfaces). A three dimensional harmonically oscillating lifting surface system in inviscid and irrotational subsonic flow can be considered with this method. Every panel experiences an induced velocity from the perturbation of all the other panels. All these induced velocities on each panel have to satisfy the kinematic flow condition, or Kutta condition, i.e. flow at the trailing edge must be parallel to the surface. Using this Kutta condition and potential theory, the pressure difference between the upper and the lower surface can be determined. The pressure differences can then be integrated to steady and unsteady aerodynamic forces.

Assuming small harmonic perturbations, the following linear potential equation holds in the frequency domain:

$$(1 - M^2)\hat{\Psi}_{xx} + \hat{\Psi}_{yy} + \hat{\Psi}_{zz} - 2ikM^2\hat{\Psi}_x + k^2M^2\hat{\Psi} = 0, \qquad (4.246)$$

where respectively the harmonic acceleration potential Ψ and the reduced frequency k are defined as:

$$\Psi = \hat{\Psi}e^{ikt} \qquad (4.247)$$

$$k = \frac{\omega b}{2V_0}. \qquad (4.248)$$

Here b is the wing span and V_0 is the steady flight velocity. Equation (4.246) is a scalar equation of the complex amplitude $\hat{\Psi}$ of the acceleration potential. Multiple singularities
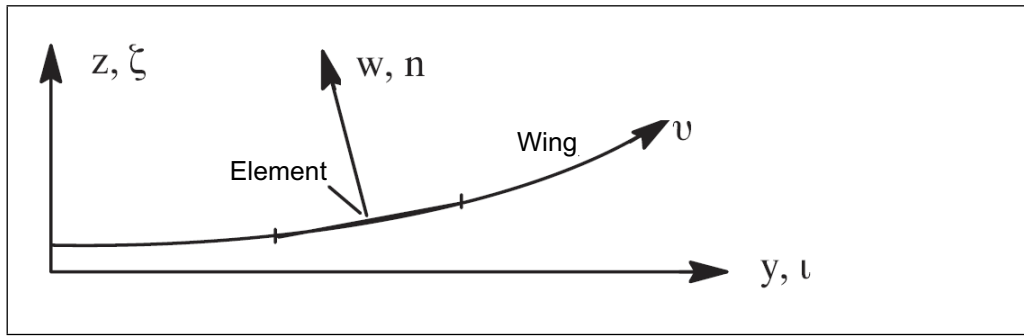
Figure 4.4: *Wing and element coordinates, where ζ: z-coordinate of lifting element and ι: y-coordinate of lifting element.*
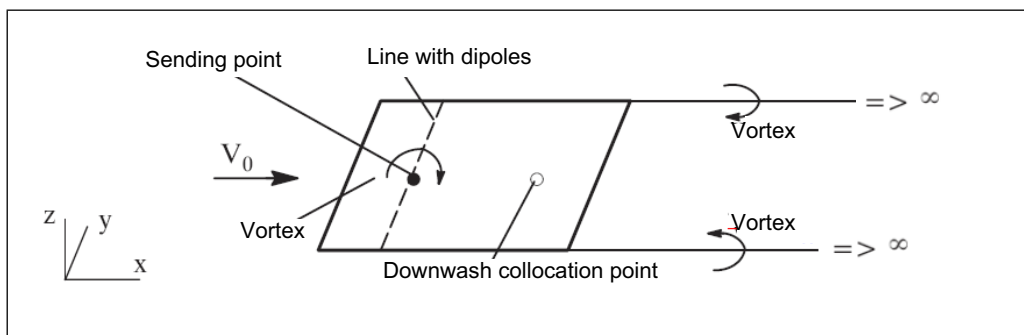

Figure 4.5: *Trapezoidal lifting element (panel).*

(sources, dipoles) are known as a single solution $\hat{\Psi}$ of the potential equation. For the Doublet Lattice Method, dipoles are placed along a line on the lifting surfaces to model the pressure jump Δc_p between the upper and lower side of the surfaces. The strengths of the dipoles can be expressed by the pressure jump, if the acceleration potential is used.

The downwash $w = \frac{\delta \hat{\Psi}}{\delta n}$ on a panel can be determined by the following integral equation:

$$ w(x, y, z) = \frac{1}{8\pi} \iint\limits_{S} K(x - \xi, y - \tau, z - \zeta, k, M) \Delta c_p d\xi d\nu, \qquad (4.249) $$

where K is the Kernelfunction that can be interpreted as aerodynamic influence function, giving the downwash due to a unity pressure jump c_p. ξ is the coordinate in streamwise direction and ν the tangential spanwise coordinate of an element, see also figure (4.4). The integration is to be performed over the complete surface S.

In subsonic flow conditions, the three dimensional lifting system can be idealised by harmonic oscillating thin surfaces. Wings and empennages are the most important lifting elements, having thin airfoils with little camber in general. Consequently, the calculations may be performed on flat surfaces that are aligned with the flow. Every lifting surface is divided into small trapezoidal elements, whose sides have to be parallel to the freestream, see also figure (4.5). Engines are usually modelled as 'pipes', see also figure
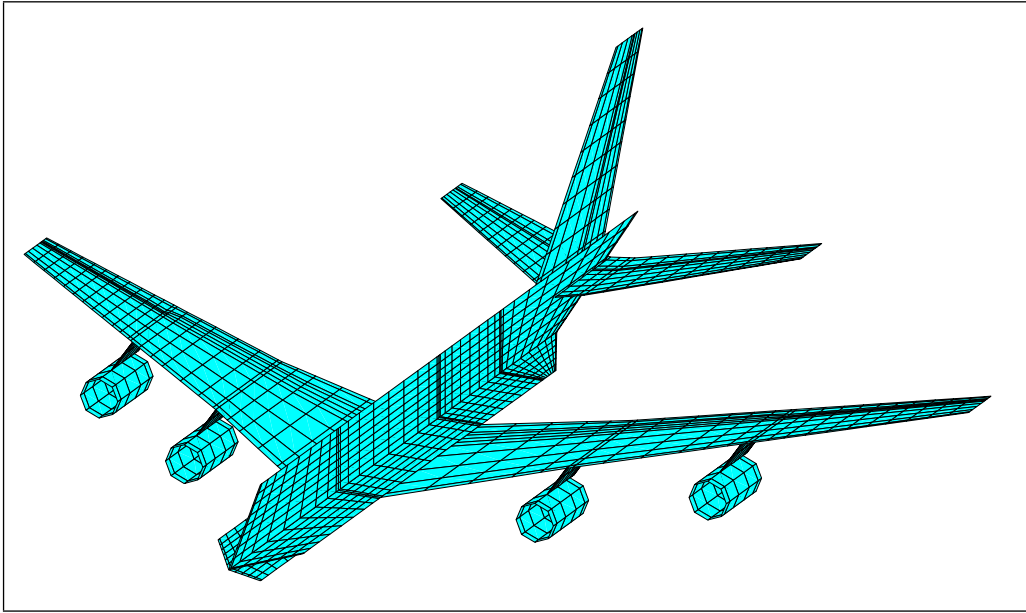
Figure 4.6: *Example of an aerodynamic model of a large transport aircraft for the Doublet Lattice Method.*

(4.6). The sides of the lifting surfaces and the rotational axes of the control surfaces are on the borders of the lifting surfaces. The pressure jump Δc_p is modelled by a dipole line-segment of constant strength at the quarter chord line of each panel, see also figure (4.5). This dipole line may have dihedral and sweep with respect to the freestream. In steady flow, every dipole line segment is equivalent to a horse shoe vortex whose bounded vortex line corresponds to the dipole line.

Panel methods using the acceleration potential do not require a special treatment of the sides of a lifting surface. The integral equation for the downwash, equation (4.249), can be transformed into an algebraic equation due to the dipole line segments with constant strength. The downwash on all panels j can be written in matrix form as:

$$\mathbf{w}_j = \mathbf{A}_{jj}\Delta\mathbf{c}_p, \qquad (4.250)$$

where $\mathbf{A}_{jj} \in R^{j \times j}$ is called the aerodynamic influence coefficient (AIC) matrix. This matrix contains all interferences between all the panels. For every element of the matrix, describing the interference of a lifting surface at the location of another lifting surface, the kernel function due to a unity pressure jump is calculated. The downwash $\mathbf{w}$ can be determined from the fact that the flow on the oscillating airfoil should be tangential to the surface. This kinematic flow condition is ascertained for both steady and unsteady flow at a collocation point in the middle of a panel at $\frac{3}{4}$ chord. The AIC matrix has to be calculated for every frequency and Mach number separately. For every steady deformation or every oscillation, the last equation can be solved for the unknown pressure jumps Δc_p:

$$\Delta\mathbf{c}_p = \mathbf{A}_{jj}^{-1}\mathbf{w}_j, \qquad (4.251)$$

In order to reduce computational time, the inverse of this matrix is usually saved directly. A more detailed description on the modelling of unsteady aerodynamic forces can be found in Schuler [Sch97].

4.4.4   Calculation of an initial downwash distribution

The aircraft model for Doublet Lattice is made up with trapezoidal boxes aligned in streamwise direction, see also figure (4.6). The pressure on each panel using the standard Vortex Lattice calculation can be calculated with:

$$\mathbf{f}_j = q \cdot \mathbf{Q}_{jj} \cdot \mathbf{w}_j. \tag{4.252}$$

Consequently, no lift is generated at zero angle of attack. Thus a method to consider zero incidence aerodynamics has to be adopted. In this section, it will be described how to calculate an initial downwash distribution based on prescribed local lift and moment distributions.

It is assumed that the local lift and moment distributions are known in the following form from an aerodynamic database, see also section 4.4.1:

$$c_z \frac{l}{l_g} = f(\eta, \alpha, M) \tag{4.253}$$

$$c_m \frac{l}{l_g} = f(\eta, \alpha, M). \tag{4.254}$$

These coefficients are needed in component axis (perpendicular to the panel surface) due to the properties of the panel model.

In preliminary design stages, some of this data for some components may still be unknown. It is obviously desired to use as much empirical data as early as possible in the design process. Therefore, all available data can and will be used here for the determination of the initial downwash field. For those components, where the data is not yet available, the initial downwash of the corresponding panels is zero. Notice that the pressure on those panels do not have to be zero, because of the influence from the other components.

For example, assume that there is only an initial downwash field on the wings. In that case, the fuselage panels in the proximity of the wings, will have nonzero pressures because of the interferences stemming from the full AIC matrix. The preservation of these effects is actually a desirable aspect of this method.

A more shorthand notation is now introduced for the local lift and moment distributions:

$$K_Z = c_z \frac{l}{l_g} \tag{4.255}$$

$$K_M = c_m \frac{l}{l_g}. \tag{4.256}$$

The distributions K_Z and K_M can be plotted as a function of spanwise position and angle of attack. This is shown in figure (4.7) for the local lift distribution on the left and
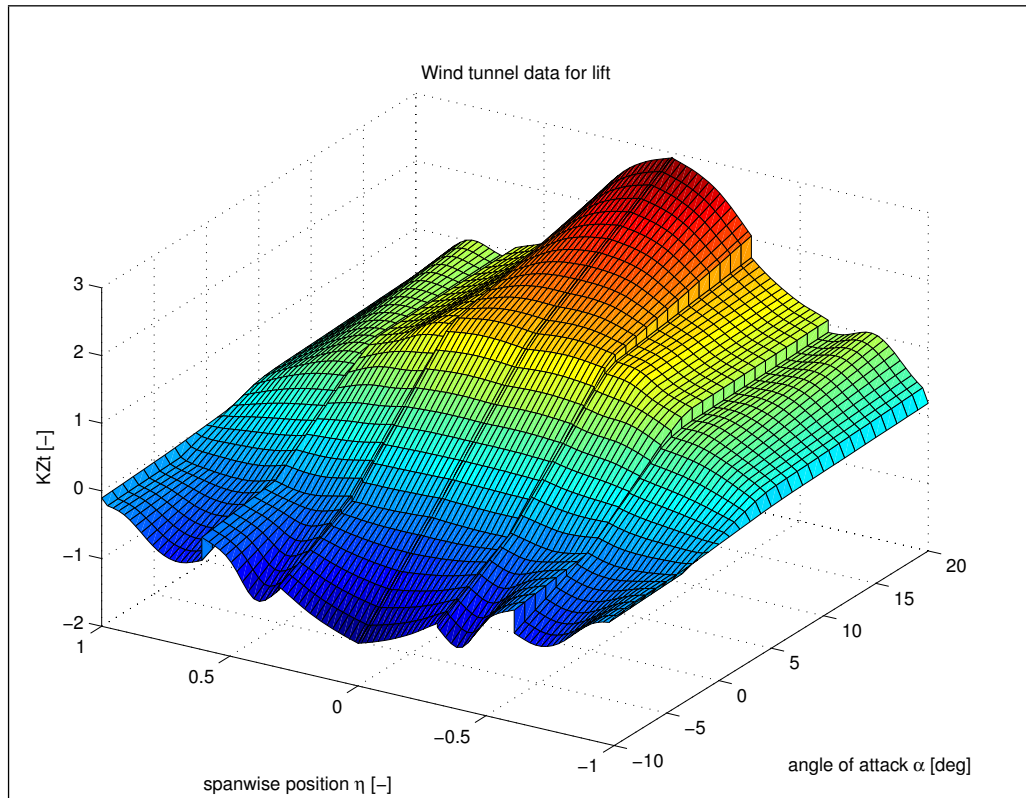
Figure 4.7: *Lift distribution (here* K_Z *is indicated by KZt) for a Mach number of 0.85. The values in this plot are scaled.*

right wing. There are two discontinuous jumps in the lift distribution, where the engines are mounted to the wing. The aerodynamic model of the aircraft is build up with trapezoidal elements as can be seen in figure (4.6). Therefore, the aerodynamic data has to be integrated over the strip-width of the aerodynamic elements. Due to the discretisation of the aircraft with the aerodynamic elements, discontinuities in the load distributions from the wind tunnel data (for example at the engines) cannot be exactly reproduced by the aerodynamic model.

The local load at each spanwise position for every angle of attack is known from the aerodynamic database. There are, however, only two values per spanwise position (two boundary conditions per strip), where there are in general more than two panels in chordwise direction. For every panel in a strip, an initial downwash has to be determined. So for every strip, the number of unknowns equals the number of panels in that strip. The system is therefore underdetermined.

A means to circumvent this is by assuming shape functions for the initial downwash field. A meaningful description of the form of the initial downwash field is that derived from thin airfoil theory. The downwash can then be thought of as a superposition of the distribution for a flat plate, plus that of a parabola and of a s-shaped profile. These contri-

butions are described by respectively the first, second and third Birnbaum distributions:

$$f_1 \quad = \quad 1 \tag{4.257}$$

$$f_2(\xi) \quad = \quad 1 - 2 \cdot \xi \tag{4.258}$$

$$f_3(\xi) \quad = \quad 1 + 8 \cdot \xi \cdot (\xi - 1) \tag{4.259}$$

Notice that a new variable ξ is introduced, that is the dimensionless chordwise position coordinate for each panel. This chordwise variable is defined as the distance of the control point of the panel with respect to the leading edge of the strip, divided by the local chord l. For panel j of strip i this can be written as:

$$\xi_j = \frac{x_j - x_{LEi}}{l_i} \tag{4.260}$$

Here the first (4.257) and second (4.258) Birnbaum distributions are chosen, because they have shown to give the best results. Using these shape functions, the initial downwash on a panel can be written as:

$$w_{j0}(\eta_i, \xi_j) = b_{f_1}(\eta_i) \cdot C_{f_1}(\xi_j) + b_{f_2}(\eta_i) \cdot C_{f_2}(\xi_j) \tag{4.261}$$

where each spanwise position or strip of panels has two unknown parameters b_1 and b_2. These parameters can be collected in the column vector $\mathbf{b}_0 \in R^{k2}$ and the shape functions can be written in a matrix $\mathbf{C}_{jk2} \in R^{j \times k2}$. Then the initial downwash can be written in matrix notation as:

$$\mathbf{w}_0 = \mathbf{C}_{jk2} \cdot \mathbf{b}_0 \tag{4.262}$$

The parameters of the shape functions $\mathbf{b}_0$ can now be calculated using the prescribed boundary conditions for lift and moment, as follows:

$$\mathbf{b}_0 = (q \cdot \mathbf{S}_{k2j} \cdot \mathbf{Q}_{jj} \cdot \mathbf{C}_{jk2})^{-1} \cdot \begin{bmatrix} \mathbf{K}_Z \\ \mathbf{K}_M \end{bmatrix} \tag{4.263}$$

After the determination of these parameters $\mathbf{b}_0$, the initial downwash can be calculated from equation (4.262).

4.4.5   Correcting the vortex lattice model for nonlinear aerodynamics

The lift curve slope of the standard vortex lattice model corresponds with the theoretical value of 2π. However, there are certain regions in the possible range of angle of attack (both in positive as in negative direction), where the aerodynamics gets more and more nonlinear. In this section a method is presented that accounts for nonlinear aerodynamics even for a flexible airframe. Meaning, that it is accounted for changes in the local angle of attack (or panel downwash) due to flexibility and the corresponding nonlinear effects.

The problem of accounting for nonlinear aerodynamics can be similarly accounted for as the determination of an initial downwash field, presented in section 4.4.4.
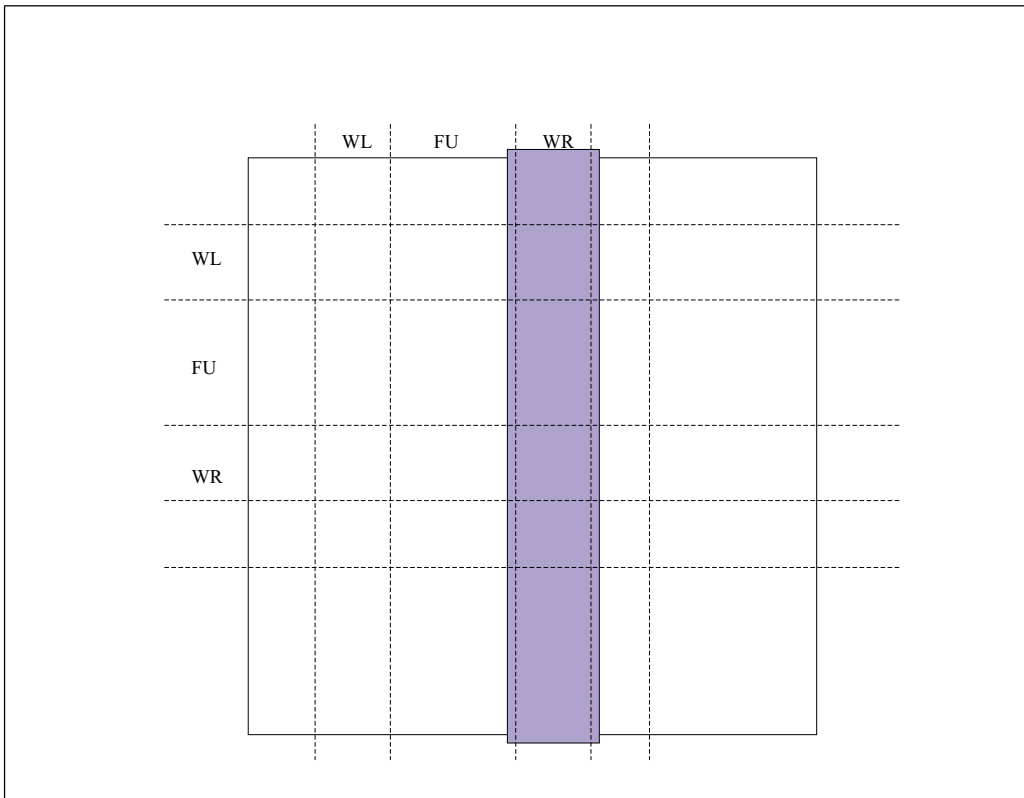
Figure 4.8: *Visualisation of the AIC-matrix. For clarity reasons the degrees of freedom of this matrix are sorted in this figure for the different components (FU=fuselage, WR=wing right, WL = wing left) which is not necessarily true. Also not all components are shown. The row that is indicated by the gray block shows the interaction of in this case the right wing onto all other components.*

The panel pressure using the standard Vortex Lattice calculation, based on a 2π lift curve slope was calculated as follows:

$$\mathbf{f}_{J,2\pi} = q \cdot \mathbf{Q}_{JJ} \cdot \mathbf{w}_J \qquad (4.264)$$

The fact that a panel does not behave according to the 2π lift curve slope can be accounted for using a 'correction factor' matrix $\mathcal{R}$:

$$\Delta\mathbf{f}_{J,2\pi} = q \cdot \mathbf{Q}_{JJ} \cdot \mathcal{R} \cdot \Delta\mathbf{w}_J \qquad (4.265)$$

This matrix $\mathcal{R}$ is a diagonal matrix. The correction factor of a specific panel is applied to all matrix elements in the column belonging to this panel to preserve its full influence, see also figure (4.8).

 Because the calculation with the 'Advanced VL-Method' calculates incremental differences with respect to a previous result, it suffices to determine 'lift curve slope correction factors'. A database is build of correction factors that are a function of panel-id, local angle of attack and Mach number.

It is again assumed that the local lift and moment distributions are known in the following form from an aerodynamic database:

$$c_z \frac{l}{l_g} = f(\eta, \alpha, M) = K_Z \qquad (4.266)$$

$$c_m \frac{l}{l_g} = f(\eta, \alpha, M) = K_M. \qquad (4.267)$$

The calculation of the 'correction factors' inside $\mathcal{R}$ is now based on the change in K_Z or K_M due to an increase in angle of attack with $\Delta\alpha$ at every geometric angle of attack. For a load calculation with correction, the change in load can be calculated with:

$$\begin{bmatrix} \Delta\mathbf{K}_Z \\ \Delta\mathbf{K}_M \end{bmatrix} = q \cdot S_{k2j} \cdot \mathbf{Q}_{jj} \cdot \mathcal{R} \cdot \Delta\mathbf{w}_j \qquad (4.268)$$

In this equation $\Delta\mathbf{w}_j$ is the increase in geometric angle of attack of each panel ($w_j = \alpha_{rad}$). This can be determined for every panel by the increase in the aircraft's geometric angle of attack in terms of downwash multiplied with the normal vector on each panel:

$$\Delta w_{j_i} = \begin{bmatrix} 0 \\ 0 \\ \Delta\alpha_{rad} \end{bmatrix} \cdot \mathbf{n}_{panel} \qquad (4.269)$$

Again the system of equations is underdetermined. Assuming shape functions is a proven approach in the determination of the initial downwash (see also section 4.4.4). There is however a difference. The shape functions describing the form of the initial downwash field can be physically interpreted. The downwash can for example be thought of as the superposition of the downwash on a flat plate, plus that of a parabola and that of a s-shaped profile. In case of the correction factor the form of the field of correction factors cannot be directly thought of as a superposition of some certain shapes, because the correction factor itself is not a physical quantity. A good choice of shape functions is to choose the same shape functions as for the initial downwash field. A point for further study could be to investigate the influence of the choice of different shape functions. A different choice of shape functions will lead to a different pressure distribution in chordwise direction, and therefore later in the elastic calculations to different deformations and deformation induced loads. This will also depend on the choice for a certain splining technique, see section 4.7.

The shape functions of the correction factor are chosen to be again the first and second Birnbaum distributions:

$$f_1 = 1 \qquad (4.270)$$
$$f_2(\xi) = 1 - 2 \cdot \xi \qquad (4.271)$$

With the shape functions from (4.270) and (4.271), the correction factor of the panel j can be written as function of the two unknowns b_1 and b_2 as:

$$
\begin{aligned}
R_j(\eta, \xi) &= b_1(\eta) \cdot C_1(\xi) + b_2(\eta) \cdot C_2(\xi) & (4.272)\\
\mathcal{R} &= diag(R_j) & (4.273)
\end{aligned}
$$

Notice that the correction factor for each panel can be seen as a correction for the 2d lift curve slope that differs from 2π. The boundary conditions are satisfied by simultaneously solving for the correction factors of all panels for the complete range of geometric angles of attack of the aircraft. This produces a database with correction factors for every panel at the rigid aircraft's geometric angle of attack. In order to be able to use this data in the elastic calculation, the accompanying local geometric angle of attack of the panel has also to be stored in the database. This effective angle of attack is calculated using the normal vector of the panel similar to equation (4.269).

4.5   Aerodynamic loads due to aircraft deformation

In section 4.5.1 it is described how the flexibility effect is accounted for based on linear aerodynamics. In section 4.5.2 the same is done accounting for nonlinear aerodynamics.

4.5.1   Flexibility effect based on linear aerodynamics

Correction of the matrix $\mathbf{Q}_{jj}$ for linear gradients is a well-established procedure in the industry. In this section, the calculation of the deformation induced aerodynamic forces and moments, based on linear (corrected) aerodynamics is presented. This corrected $\mathbf{Q}_{jj}$ matrix is indicated with the same symbol as the uncorrected matrix, because it will be clear from the context which matrix is meant. In those cases where it might be confusing, it will be mentioned explicitly.

As soon as the deformation of the aircraft is known, the load distribution due to deformations can be approximated with a vortex lattice model (panel code) by:

$$
\mathbf{F}_{flex} = q \cdot \mathbf{S}_{kj} \mathbf{Q}_{jj} w_{j\,f} \tag{4.274}
$$

$$
w_{j\,f} = \mathbf{D}_{jk} \mathbf{T}_{kg1} \mathbf{\Phi}_{g1F} \mathbf{q}_F, \tag{4.275}
$$

where $w_{j\,f}$ is the additional downwash induced by the flexible modes $\mathbf{q}_F$.
This equation is based on linear potential theory. The aerodynamic influence matrix $\mathbf{Q}_{jj}$ can be corrected based on empirical data, either from the wind tunnel or from CFD analysis.

4.5.2   Flexibility effect based on nonlinear aerodynamics

There are certain regions within the possible range of angle of attack (both in positive as in negative direction), where the aerodynamics gets more and more nonlinear. In this
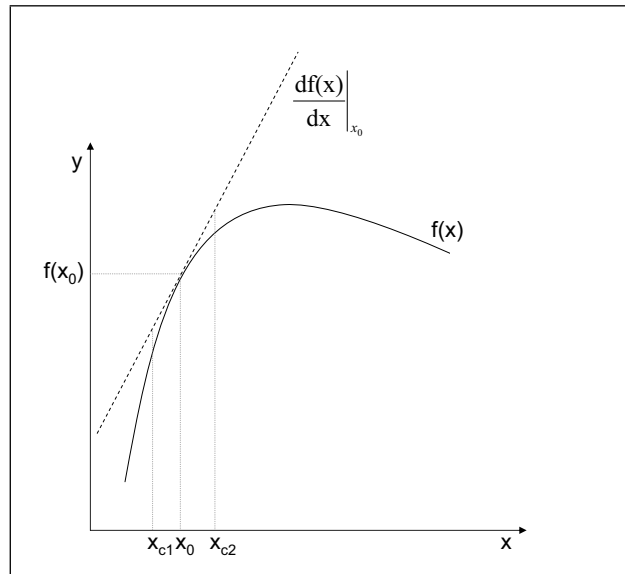
Figure 4.9: *The function $f(x)$ with its local derivative at x_0.*

section a method is presented that accounts for nonlinear aerodynamics in combination with a flexible airframe. The linear model will not give accurate results, if there are some regions on the aircraft, where the effects of nonlinear aerodynamics get significant. This might be because of wing stall, which is a pure aerodynamic nonlinearity. Furthermore, the wing structure can be deformed so much that the outer wing 'sees' an angle of attack that significantly differs from that in the rigid case. This change of effective local angle of attack can also interact with the local nonlinear aerodynamics. Consequently, a more advanced procedure is needed to account for local airframe deformation in combination with aerodynamic nonlinearities.

In mathematics, nonlinear systems represent systems whose behavior is not expressible as a sum of the behaviors of its descriptors. In particular, for nonlinear systems the principle of superposition may no longer be applied, as was the case for linear systems.

Linearity of a system allow certain mathematical assumptions and approximations, simplifying the computation of results. In nonlinear systems these assumptions cannot be made. Since nonlinear systems are not equal to the sum of their parts, they are often difficult (or impossible) to model, and their behavior with respect to a given variable (for example, time) is extremely difficult to predict. When modelling non-linear systems, therefore, it is common to approximate them by a linearisation around a nominal solution, see also figure (4.9).
For the nonlinear function:

$$y = f(x), \tag{4.276}$$

assume the nominal solution (x_0, y_0) and the first derivative $\frac{df}{dx}$ are known at the nominal condition. Then the function $f(x)$ can be locally approximated by:

$$\tilde{y} = y_0 + \left.\frac{df(x)}{dx}\right|_{x_0} (x - x_0). \tag{4.277}$$

Obviously, the closer x is taken to x_0, the smaller the error $y - y_0$ will be. Secondly, the smaller the changes in the derivative of $f(x)$ are, the larger $(x - x_0)$ is allowed to be for the same magnitude of the error. Call the smallest/largest value of x at which the maximum allowable absolute error occurs x_{c1}/x_{c2}. Corresponding to the lowest/highest bound in x where the linearisation is accurate enough.

This method can be used to calculate the deformation induced loads and in that context, it is called the linflex-method. This is exactly the method presented already in section 4.5.1. Notice that the curve $f(x)$ could be seen as a local lift curve. The variable x would then be the angle of attack, or the local angle of attack for the flexible aircraft.

Below, a method is presented that will lead on the one hand to more accurate results for $x_{c1} < x < x_{c2}$. On the other hand, it will will provide a means to get more accurate (accurate enough) results for $x < x_{c1}$ and for $x > x_{c2}$. It is basically an extension of the simple linearisation method from above.

The function $f(x)$ will now be approximated by multiple linear curves. Again, the solution is linearised around the nominal point (x_0, y_0). The next linearisation point is calculated similar to equation (4.277). Here this equation will be written for the more general case of calculating the (next) linearisation point i based on the previous $i - 1$:

$$\tilde{y}_i = \tilde{y}_{i-1} + \left.\frac{df(x)}{dx}\right|_{\tilde{x}_{i-1}} (x_i - \tilde{x}_{i-1}). \tag{4.278}$$

Obviously, the accuracy of this method depends on the chosen stepsize $(x_i - \tilde{x}_{i-1})$ and on the gradient of $f(x)$. In those regions of $f(x)$ where this function is either monotonically increasing or decreasing, the following holds:

$$\left| f(\tilde{x}_i) - \tilde{y}_i \right| > \left| f(\tilde{x}_{i-1}) - \tilde{y}_{i-1} \right|, \tag{4.279}$$

but this error will be smaller than that made in the linflex-method.

4.6   Thrust modelling

For aero-elastic calculations on aircraft with wing mounted engines, it is very important to know the amount of net thrust delivered by each engine. The amount of net thrust influences the wing bending and torsion and thus the aerodynamic flow condition along the whole wing. The geometric position of the winglet depends on the deformation of the complete wing. Therefore, especially for the determination of winglet loads and outer wing loads it is extremely important to determine the right shape of the wing.

In this section the thrust-model that is used in this investigation is described. This kind of model could also be used by a department that addresses the performance of the aircraft.

Two main factors in aircraft performance are the lift-to-drag ratio of the airframe and power and efficiency of the engines. In principle a customer buys a package of an aircraft without engines together with the desired engines. Within certain limitations you can get any type of engine on the aircraft you want. The performance of the engines are the responsibility of the engine manufacturer. The aircraft manufacturer will check whether the engines meet the requirements. This is one of the tasks of a performance department.

On the one hand, knowing the amount of net thrust of the engines for a certain flight condition, gives the opportunity to check whether the engines meet their performance requirements for that condition. On the other hand, it gives the opportunity to address the aerodynamic efficiency of the airframe in flight, because the thrust needed at a certain flight condition is directly related to the total amount of airframe drag. These two factors are very important for the total performance and efficiency of the aircraft and directly influence the direct operational costs (DOC) and thus the economical success of the aircraft. Only very small improvements in the performance of an aircraft can substantially decrease the DOC and thus increase the airlines'profit. Consequently, due to its importance and influence, the thrust models for cruise flight conditions are very accurate. For cruise conditions, this model predicts the net thrust with an accuracy of approximately 0.1%, which is absolutely accurate enough in the present investigation.

The model is based on tabulated data and gives the estimation of the amount of net thrust for given fan speed called N1 (given in %) of each engine and the corresponding flight condition (static temperature T_0 [K], Mach number M [-], static pressure p_0 [bar]). This model will now be described in more detail. Numbers or tabulated data cannot be provided, because this kind of information is generally concerned as highly proprietary data.

The corrected net thrust F_{NK} can be given in tabulated form as a function of Mach and N_{1K}. These tables have been extracted from the generalized curves of more detailed engine model for the specific engine bleed air condition and for the desired atmospheric conditions, consistently with the flight test conditions (Mach range of primary interest 0.65 - 0.85).

Now first N_{1K} has to be determined to be able to extract F_{NK} by table look-up.
The static pressure and static temperature are determined from the measured pressure altitude in combination with an atmospheric model based on the International Standard Atmosphere.

Using the measured fan speed N_1, Mach number and static temperature, the following

quantity can be determined:

$$N_{1K47} = \frac{N_1}{\left(\frac{T_0(1+0.2M^2)}{288.15}\right)^{0.47}} \tag{4.280}$$

as soon as this value is known, the coefficient α_L can be determined from table look-up:

$$\alpha_L = f(N_{1K47}) \tag{4.281}$$

If now the coefficient θ_1 is defined as:

$$\theta_1 = \frac{T_0(1+0.2M^2)}{288.15}, \tag{4.282}$$

the corrected fan speed N_{1K} can be determined from the relation:

$$N_{1K} = \frac{N_1}{\theta_1^{\alpha_L}}. \tag{4.283}$$

Now $F_{NK} = f(M, N_{1K})$ can be determined from table look-up. Having this value for F_{NK} enables the calculation of the actual net thrust of one engine with:

$$F_N = F_{NK}\delta_1, \tag{4.284}$$

where δ_1 is defined as:

$$\delta_1 = \frac{p_0 \cdot (1+0.2M^2)^{3.5}}{1.01325}. \tag{4.285}$$

4.7 Spline techniques

The crux of an aero-elastic analysis lies in the interconnection of the structure with the aerodynamics. This interdependency is modelled using a so-called spline matrix. This spline matrix defines the relationship between the structural and aerodynamic variables. The nodes of the structural grid are generally not similar to the nodes of the aerodynamic grid. The spline matrix enables the transfer of displacements and loads between these two domains. There are several splining techniques all based basically on interpolation. In the commercial finite element analysis code MSC.Nastran [Rod01] surface splines and linear splines are implemented. The theory involves the mathematical analysis of beams and plates. The linear spline is a generalisation of an infinite beam and allows torsional and bending degrees of freedom. The surface spline is based on infinite uniform plates.
It is possible with the linear beam spline to establish model interconnections based on beam interpolation elements and rigid connectors. These interpolation elements can be thought of as finite elements containing shape functions, but have neither stiffness nor mass. It does not require the explicit augmentation of the reduced model with rigid connectors as is the case for the surface spline in MSC.Nastran. In one model, several types of splines can be used.

Usually, the structural degrees of freedom are chosen as the independent degrees of freedom and the aerodynamic degrees of freedom as dependent. A matrix, the spline matrix, is derived that relates the dependent degrees of freedom to the independent ones. In principal, two transformations are required: the interpolation from the structural deflections to the aerodynamic deflections and the relationship between the aerodynamic forces and the structurally equivalent forces acting on the structural grid points.

The splining methods lead to an interpolation matrix $\mathbf{G}_{kg}$ relating the structural degrees of freedom to the aerodynamic ones:

$$\mathbf{u}_k = \mathbf{G}_{kg}\mathbf{u}_g \tag{4.286}$$

The derivation of the elements of the spline matrix can be found in reference [Rod01] for the surface and for the linear spline.

Application of the principle of virtual work shows that the transpose of $\mathbf{G}_{kg}$ is applicable to the loads transfer problem:

$$\mathbf{F}_g = \mathbf{G}_{kg}^T\mathbf{F}_k \tag{4.287}$$

In general, the spline matrix can be derived to transform between any two grids, which is very practical because the different loads effects (aerodynamic loads, propulsive loads, inertial loads) are in general described on their own grid.

4.8   Loads calculation

The equation to determine the integrated loads vector $\mathbf{S}$ from the nodal force vector $\mathbf{F}$ was already given by equation (2.2). The elements of the $\mathbf{T}$ matrix will be explained in this section using a very simple example to show the basic principle.

Assume there are three (structural) nodes having 3 degrees of freedom with known nodal force vectors and there are two loads stations ξ_1 and ξ_2, see also figure (4.10). For simplicity, assume further that everything is defined in the basic coordinate system $oxyz$. The loads stations are defined along the component loads axes (L.A.).

At the loads stations ξ_1 and ξ_2, the integrated (shear) forces and moments have to be determined from the nodal vectors. These can be written in vector form as:

$$\mathbf{S} = \begin{bmatrix} TX_{\xi 1} \\ TY_{\xi 1} \\ MZ_{\xi 1} \\ TX_{\xi 2} \\ TY_{\xi 2} \\ MZ_{\xi 2} \end{bmatrix} \tag{4.288}$$

At station ξ_1 the integrated shear loads and moment can be determined from the nodal force vector and its relative geometric position by:

$$TX_{\xi 1} = FX_a \tag{4.289}$$

$$TY_{\xi 1} = FY_a \tag{4.290}$$

$$MZ_{\xi 1} = MZ_a - FX_a dy_{a1} + FY_a dx_{a1} \tag{4.291}$$

Notice with this direction of integration node b has no influence on station ξ_1. The same can be done for loads station ξ_2, where the contributions from both nodes a and b have to be accounted for:

$$TX_{\xi 2} = FX_a + FX_b \tag{4.292}$$

$$TY_{\xi 2} = FY_a + FY_b \tag{4.293}$$

$$MZ_{\xi 2} = MZ_a - FX_a dy_{a2} + FY_a dx_{a2} +$$
$$+ MZ_b - FX_b dy_{a2} + FY_b dx_{a2} \tag{4.294}$$

This can be written in matrix form as:

$$
\begin{bmatrix} TX_{\xi 1} \\ TY_{\xi 1} \\ MZ_{\xi 1} \\ TX_{\xi 2} \\ TY_{\xi 2} \\ MZ_{\xi 2} \end{bmatrix}
=
\begin{bmatrix}
1 & 0 & 0 & 0 & 0 & 0 \\
0 & 1 & 0 & 0 & 0 & 0 \\
-dy_{a1} & dx_{a1} & 1 & 0 & 0 & 0 \\
1 & 0 & 0 & 1 & 0 & 0 \\
0 & 1 & 0 & 0 & 1 & 0 \\
-dy_{a2} & dx_{a2} & 1 & -dy_{b2} & dx_{b2} & 1
\end{bmatrix}
\begin{bmatrix} FX_a \\ FY_a \\ MZ_a \\ FX_b \\ FY_b \\ MZ_b \end{bmatrix},
\tag{4.295}
$$

thus giving the wanted relationship:

$$\mathbf{S} = \mathbf{TF}, \tag{4.296}$$

which can be easily extended to contain more node stations, degrees of freedom and loads stations.

Notice that in the derivation of the matrix $\mathbf{T}$ a vector with nodal forces was used. For example, the aerodynamic loads are usually given as force and moment distributions. This means that these have to be adequately integrated in the proximity of each node to transform the continuous distributions into discrete nodal forces and moments.
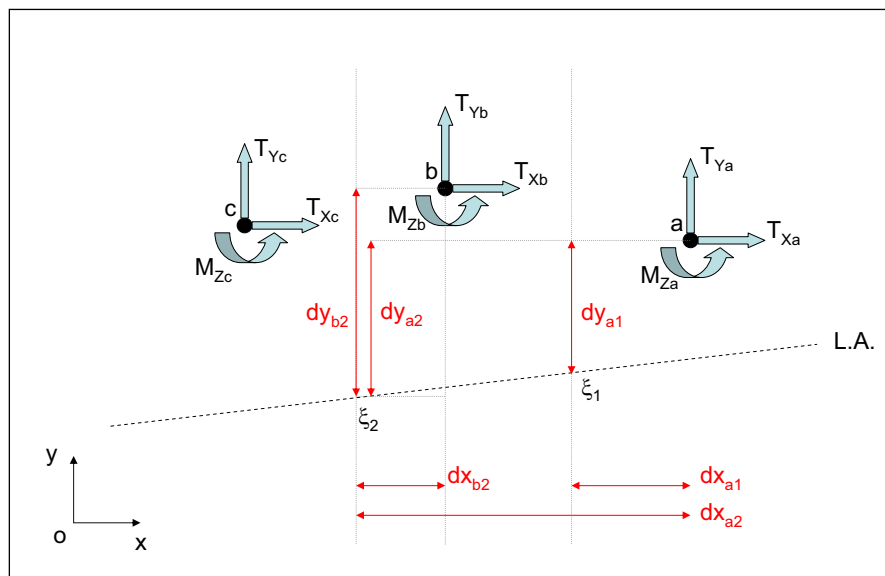
Figure 4.10: *Nodal loads and moments depicted at nodes a, b and c. Loads stations are indicated by ξ_i, here for two loads stations 1 and 2 along the component loads axis (L.A.).*

Chapter 5

Principles of Flight Test Identification

5.1 Introduction

Traditionally, aircraft parameter identification is the process of extracting numerical values for the aerodynamic stability and control derivatives and other subsidiary parameters (sensor errors, wind gusts, etc.) from a set of flight test data. This set of flight test data is a recorded time history of the flight control inputs and the resulting aircraft response variables. The field of identification has been pursued by diverse interests for many years.
The Maximum Likelihood (ML) identification technique has originally been developed by Systems Control, Inc. (SCI) in 1970 to reduce data from flight tests where gusts were present. In such cases both the measurement noise and process noise statistics were identified.

Accurate knowledge on the stability and control derivatives is needed to arrive at accurate mathematical models that these coefficients provide. These mathematical models are used to provide input to simulators or to provide a basis for the design of flight control systems. This has been a field of investigation since about 1948.
The stability and control derivatives have been identified for all kind of aircraft, but have been restricted to values for the total aircraft (integrated values). Remember from section 4.4 that the loads model is a distributed model, where knowledge of the distributed loads and thus the aerodynamic *distributions* are needed. Today, due to the large increase in computational power it has become possible (at least for research projects) to use the distributed aero-elastic models even for real-time flight simulators. Therefore, the extension of this procedure to the type of model as it is used in the loads departments of aircraft manufacturers, is a natural step and it will be of increasing importance.
The focus here will lie on a parameter estimation method that is suitable for a phenomenological model based on physical insight. Developing such a model, which is

usually preferred, because it leads to better understanding of the underlying physics, can be highly demanding. Alternatively one could make use of neural networks that are used for pattern recognition. They provide a general framework for nonlinear functional mapping of the input-output subspace. They provide less physical insight, but are very capable methods in cases that are highly nonlinear. More information on the procedure with neural networks and in general on flight vehicle system identification can be found in [Jat06].

The principal elements of the aircraft identification process are:

- the identification algorithm,

- the flight control input,

- the instrumentation.

The success of the identification process is totally dependent on all three of these elements. This study is focussed on the first aspect, the development of an identification technique for the loads model based on the Maximum Likelihood criterion. In reference [Mul86] a technique is described for the optimization of control input signals. Information on the general arrangement of a flight test instrumentation system can also be found in[Mul86].

In the most general case, the Maximum Likelihood identification technique is a combination of three steps:

- Kalman filtering to estimate the states and general residual or 'innovation' sequence,

- a modified Newton-Raphson algorithm for the parameter estimates,

- an algorithm to estimate the noise statistics (mean and variances of the measurement and process noise).

In addition, the Maximum Likelihood technique provides a lower bound on the variances of the parameter estimate and models for the measurement and process noise disturbances.

The parameter-state estimation problem of dynamic flight tests is discussed in detail in reference [Mul86]. It is shown that under certain conditions the parameter-state estimation problem can be solved in two consecutive steps pertaining to the reconstruction of the state and the estimation of the aerodynamic model parameters respectively. This technique is called the two-step method (TSM). In reference [Mul99] it is focussed on the first step of the TSM, often referred to as 'flight path reconstruction'. Requirements with respect to type and quality of flight test transducers are also discussed in this reference. Furthermore, an overview is presented in [Mul99] of different approaches to the solution of the flight path reconstruction problem with emphasis on Kalman filter/smoother and Maximum Likelihood methods.

There have been many methods proposed and tried for extracting stability and control derivatives from flight data. It is described in reference [Ste73] that most of these have proved to be successful only under idealized conditions such as in the absence of wind gusts or modelling errors and known instrumentation accuracies. Often a significant amount of flight test data has to be discarded, because there is no technique general enough to process it under less than ideal conditions. The development of the ML identification technique has given rise to the realization that much of the previously discarded data can be successfully processed. The limitations of the instrumentation system, flight control input and inadequate aerodynamic model are recognized and compensated for. Furthermore, the presence of wind gusts can be included in the model structure and can be accounted for in the identification algorithm. These aspects make that the best set of identified values for the stability and control derivatives can be obtained.

The identification techniques are classified in [Ste73] as either:

- Equation error methods,

- Output error methods,

- Advanced methods,

where these methods differ by

- the performance criterion that they are developed from,

- the kinds of estimates they produce,

- the problems to which they can be applied.

The Equation error method, Output error methods and Advanced methods will be described in section 5.2.

5.2   Identification methods

Equation error methods assume a performance criterion that minimizes the square of the equation error (process noise). All of these methods are basically least squares techniques. In general, it is necessary to measure all the response variables and their derivatives. The procedure is to express the stability and control derivatives as functions of the measured responses using the equations of motion. These methods do not allow for measurement errors (instrumentation errors). Therefore, when this type of error does exist, they will result in biased estimates. More information on equation error methods can be found in references [Kle06] and [Ste73].

Output error methods minimize the square of the error between the actual system output and the output of a model used to represent the actual system. This method assumes measurement noise but no process noise. Typical output error methods include

Newton-Raphson, Gradient methods, the Kalman filter (without process noise) and modified Newton-Raphson.
The modified Newton-Raphson method has been used extensively in flight test applications.

The advantages of Newton's method for systems of nonlinear equations are:

- It is q-quadratically convergent from a good starting guess if the Hessian matrix is nonsingular.

- An exact solution will be obtained in one iteration if the second order derivative actually is a quadratic function.

The disadvantages of the Newton's method are:

- It is not globally convergent for many problems.

- Each iteration requires the solution of a system of linear equations that may be singular or ill-conditioned.

- It requires the computation of the Hessian matrix at each iteration.

There are remedies to alleviate the first two disadvantages as will be shown later in this chapter. The last disadvantage implies a certain computational effort. This might be acceptable in the end, because of the good convergence rate of the method.
The principal disadvantage of the output error methods is that the results degrade when process noise (gusts, modelling errors) exists. This is because process noise is not included in their performance criterion. This may result in the computer program not converging or in estimates that have large variances or poor estimates. As long as these methods are applied to linear flight regions, or where the form of the equations is known, or where gusts do not exist, they work very well.

The most general identification problem is one of extracting stability and control derivatives for nonlinear aircraft models, from flight test data containing both measurement and process noise. The one advanced technique that has demonstrated the capability of extracting stability and control derivatives from flight data under these circumstances is an implementation of the Maximum Likelihood (ML) criterion.
The success of the ML technique can be attributed to several important properties of this method:

- no a priori knowledge is needed of the process noise covariance, measurement noise covariance or the initial parameter estimate covariance,

- in the absence of process noise, this method simplifies to the modified Newton-Raphson output error method (although with a specific weighing matrix),

- in the absence of measurement noise (an unlikely event) this method simplifies to the least squares equation error method,

- the Cramér-Rao lower bound on the covariance of the error in the stability and control derivative estimates are obtained as part of the algorithm,

- the minimum mean-square aircraft state variables (response variables) are obtained as an integral part of the algorithm. However, it is not required that initial state estimates are supplied.

See section 5.3 for a more detailed description of the Maximum Likelihood method.

5.3   Maximum Likelihood Identification

The idea of the Maximum Likelihood (ML) estimate was introduced into statistics by R.A. Fisher in 1906. It is based on a relatively simple thought. Assume that the outcome Z of an experiment depends on an unknown parameter θ. How can the best value of θ be derived from observation Z? One possible answer is to choose that value of θ which makes the observed value Z the most probable one to have occurred. This can be stated as: choose θ to maximize the conditional probability of Z, given a value of θ, i.e.:

$$\hat{\theta} = \max_{\theta} p(Z|\theta), \tag{5.1}$$

where $\hat{\theta}$ is the Maximum Likelihood estimate of θ and $p(Z|\theta)$ is the conditional probability of Z given θ. The same estimate is obtained by maximizing $\ln p(Z|\theta)$, which is known as the Likelihood function.

The above basic idea can be carried over to linear and nonlinear dynamic systems, with process and measurement noise. However, the details of the application become quite involved. In practice, there are two major problems in obtaining ML estimates for dynamic systems. These are:

- Deriving an expression for the Likelihood function,

- Maximizing the Likelihood function with respect to the unknown parameters.

The Likelihood function will be derived in section 5.3.1. In section 5.3.2 the optimization algorithm based on the Likelihood function will be presented.

5.3.1   Derivation of the Likelihood function

The Likelihood function is the logarithm of the joint probability density of the observations given the parameters.

ML estimation is a special case of Bayes' estimation. Bayes' estimation requires that the probability density $p(Z|\theta)$, $p(\theta)$ and knowledge of a cost function $C(\tilde{\theta})$, where the error of estimate is represented by $\tilde{\theta} = \theta - \hat{\theta}$, are available. The essence of the method is centered around Bayes'rule:

$$p(Z|\theta)p(\theta) = p(Z,\theta) = p(\theta|Z)p(Z), \tag{5.2}$$

If the observations are independent, it simplifies to:

$$p(Z, \theta) = p(\theta)p(Z). \tag{5.3}$$

The derivation of the Likelihood function becomes more difficult when the observations are correlated. This is necessarily the case for dynamic systems with random inputs, since the state at any time is correlated with the state at all previous times.
The ML method can be derived from Bayes' estimation method. For the ML method, less a priori knowledge is required. If the third assumption needed for the Bayes' estimation is dropped, the ML estimation procedure results. The third assumption in Bayes' estimation procedure is about a priori knowledge of a cost function $C(\tilde{\theta})$, which is thus no longer needed in the ML method.

The optimal estimate is the value of $\boldsymbol{\theta}$ that maximizes the conditional probability density $p(\boldsymbol{\theta}|\mathbf{z})$, see also equations (5.1) and (5.2). This estimate is called maximum a posteriori (MAP) estimate, $\hat{\boldsymbol{\theta}}_{MAP}$, which is defined by:

$$\left.\frac{\partial p(\boldsymbol{\theta}|\mathbf{z})}{\partial \boldsymbol{\theta}}\right|_{\boldsymbol{\theta}=\hat{\boldsymbol{\theta}}_{MAP}} = 0. \tag{5.4}$$

The estimate $\hat{\boldsymbol{\theta}}_{MAP}$ may also be obtained by maximizing the logarithm of $p(\boldsymbol{\theta}|\mathbf{z})$ with respect to $\boldsymbol{\theta}$. Using Bayes rule, equation (5.2), one gets:

$$p(\boldsymbol{\theta}|\mathbf{z}) = \frac{p(\mathbf{z}, \boldsymbol{\theta})}{p(\mathbf{z})} = \frac{p(\mathbf{z}|\boldsymbol{\theta})p(\boldsymbol{\theta})}{p(\mathbf{z})}. \tag{5.5}$$

Taking the logarithm of this expression gives:

$$\ln p(\boldsymbol{\theta}|\mathbf{z}) = \ln p(\mathbf{z}|\boldsymbol{\theta}) + \ln p(\boldsymbol{\theta}) - \ln p(\mathbf{z}). \tag{5.6}$$

Since $p(\mathbf{z})$ does not contain terms in $\boldsymbol{\theta}$, maximizing $p(\boldsymbol{\theta}|\mathbf{z})$ is equivalent to maximizing $p(\mathbf{z}, \boldsymbol{\theta})$. Thus the MAP estimate can be obtained from:

$$\left.\left[\frac{\partial \ln p(\mathbf{z}|\boldsymbol{\theta})}{\partial \boldsymbol{\theta}} + \frac{\partial \ln p(\boldsymbol{\theta})}{\partial \boldsymbol{\theta}}\right]\right|_{\boldsymbol{\theta}=\hat{\boldsymbol{\theta}}_{MAP}} = 0. \tag{5.7}$$

It is supposed here that there is no a priori knowledge of $\boldsymbol{\theta}$. In [Eyk79] this is expressed by assuming a uniform distribution $p(\boldsymbol{\theta}) = $ constant over the interval of consideration. The ignorance of a priori knowledge of $\boldsymbol{\theta}$ leads to:

$$\frac{\partial \ln p(\boldsymbol{\theta})}{\partial \boldsymbol{\theta}} = 0. \tag{5.8}$$

The resulting estimate is called the Maximum Likelihood estimate and is defined by:

$$\left.\frac{\partial \ln p(\mathbf{z}|\boldsymbol{\theta})}{\partial \boldsymbol{\theta}}\right|_{\boldsymbol{\theta}=\hat{\boldsymbol{\theta}}_{MLE}} = 0, \tag{5.9}$$

or equivalently:

$$\left.\frac{\partial p(\mathbf{z}|\boldsymbol{\theta})}{\partial \boldsymbol{\theta}}\right|_{\boldsymbol{\theta}=\hat{\boldsymbol{\theta}}_{MLE}} = 0, \tag{5.10}$$

where $p(\mathbf{z}|\boldsymbol{\theta})$ is the Likelihood function. The logarithm of the Likelihood function is indicated by J:

$$J = \ln p(\mathbf{z}|\boldsymbol{\theta}). \tag{5.11}$$

Maximizing this function, or equivalently minimizing its negative with respect to $\boldsymbol{\theta}$ results in optimal values of the parameters $\hat{\boldsymbol{\theta}}$. The negative logarithm is used since it conforms to optimization conventions that work with minimization rather than maximization, see [Chu87]. The ML estimate can thus be obtained by minimizing the negative of J. From here on, this function is called J:

$$J = -\ln p(\mathbf{z}|\boldsymbol{\theta}). \tag{5.12}$$

The ML estimate of the unknown parameter $\boldsymbol{\theta}$ is obtained by minimizing J:

$$\hat{\boldsymbol{\theta}} = \min_{\boldsymbol{\theta}} \ -\ln p(\mathbf{z}|\boldsymbol{\theta}), \tag{5.13}$$

In general, the dynamic behavior of a system can be described by:

$$\dot{\mathbf{x}}(t) \quad = \quad f\{\mathbf{x}(t), \mathbf{u}(t), \boldsymbol{\theta}\} + G\{\mathbf{x}(t)\}\mathbf{w}(t) \tag{5.14}$$

$$\mathbf{z}(t) \quad = \quad h\{\mathbf{x}(t), \mathbf{u}(t), \boldsymbol{\theta}\} + \mathbf{v}(t), \tag{5.15}$$

where $\mathbf{x}(t), \mathbf{u}(t), \mathbf{z}(t)$ are respectively the state, input and observation vector. The terms $\mathbf{w}(t), \mathbf{v}(t)$ represent respectively the state and measurement noise. The matrix G is the process noise input matrix. The process and measurement noises $\mathbf{w}(t)$ and $\mathbf{v}(t)$ are assumed to be zero mean, white and uncorrelated Gaussian noises with unknown covariance matrices:

$$E\{\mathbf{w}_i\mathbf{w}_i^{T}\} \quad = \quad V_{ww}(\boldsymbol{\theta}), \tag{5.16}$$

$$E\{\mathbf{v}_i\mathbf{v}_i^{T}\} \quad = \quad V_{vv}(\boldsymbol{\theta}), \tag{5.17}$$

$$E\{\mathbf{w}_i\mathbf{v}_i^{T}\} \quad = \quad 0. \tag{5.18}$$

The subscript i indicates that the data is sampled (discrete). The vector $\boldsymbol{\theta}$ is the parameter vector containing the m parameters that are to be identified based on the measured input and output of the system:

$$\hat{\boldsymbol{\theta}} = \hat{\boldsymbol{\theta}}\{\mathbf{u}^T(t), \mathbf{z}^T(t)\} = \left[\hat{\theta}_0, \cdots, \hat{\theta}_m\right]^T \tag{5.19}$$

The symbol $\hat{\boldsymbol{\theta}}$ indicates that it is an estimate of the process parameter $\boldsymbol{\theta}$.

The relative merits of one set of parameter estimates compared with another are usually measured by some objective criterion. In general, the criterion function can be a highly nonlinear function of the parameters. Its minimization requires off-line optimization techniques of an iterative nature. Criterion functions can be chosen arbitrarily. The use of the Likelihood criterion proves to be particularly useful as it directly provides information about the noise statistics. The corresponding optimization algorithm is known

as the iterative Maximum Likelihood method.

Define the innovation or prediction error vector as:

$$\hat{\boldsymbol{\eta}}_i(\boldsymbol{\theta}) \ = \ \mathbf{z}_{m,i} - \hat{\mathbf{z}}_i(\boldsymbol{\theta}), \tag{5.20}$$

$$\hat{\mathbf{z}}_i(\boldsymbol{\theta}) \ = \ h\{\tilde{\mathbf{x}}_i, \mathbf{u}_{m,i}(t), \boldsymbol{\theta}\}. \tag{5.21}$$

If $\mathbf{w}_i$ and $\mathbf{v}_i$ are independent and normally distributed, then $\mathbf{z}_i$ will also have these properties and the Likelihood function will be uniquely determined by the mean and covariance. It holds that:

$$E\left[\boldsymbol{\eta}_i \boldsymbol{\eta}_i^T\right] \equiv \mathcal{B}_i, \tag{5.22}$$

where $\mathcal{B}_i$ is the innovation covariance matrix. As the sampling rate increases, the probability density of the innovations approach a Gaussian distribution. Thus, for a sufficiently high sampling rate, the Likelihood function $p(\mathbf{z}|\boldsymbol{\theta})$ can be written as:

$$p(\mathbf{z}|\boldsymbol{\theta}) = (2\pi)^{-\frac{n_0}{2}} |\mathcal{B}_i|^{-\frac{1}{2}} \exp\left[-\tfrac{1}{2}\boldsymbol{\eta}_i^T \mathcal{B}_i^{-1} \boldsymbol{\eta}_i\right]. \tag{5.23}$$

The negative log-Likelihood function for all of the measured data is then equal to:

$$J = \frac{1}{2} \sum_{i=1}^N \left[\boldsymbol{\eta}_i^T \mathcal{B}_i^{-1} \boldsymbol{\eta}_i + \ln|\mathcal{B}_i|\right] + \frac{Nn_0}{2}\ln(2\pi), \tag{5.24}$$

where n_0 is the number of output variables. The term on the far right is a constant that has no effect on the optimization problem, so it can be dropped. This leaves:

$$J(\boldsymbol{\theta}) = \frac{1}{2} \sum_{i=1}^N \left[\boldsymbol{\eta}_i^T \mathcal{B}_i^{-1} \boldsymbol{\eta}_i + \ln|\mathcal{B}_i|\right]. \tag{5.25}$$

The problem of determining the negative log-Likelihood function is thus reduced to finding the mean and covariance of the innovations $\boldsymbol{\eta}_i$. These two statistics can be obtained from an extended Kalman filter. More information on the (extended) Kalman filter can be found in [Kle06], [Eyk79] and [Wel04].

5.3.2   Optimization algorithm

The second problem in obtaining ML estimates is a computational one. Generally, the Likelihood function is highly nonlinear in terms of the parameters. For finite data lengths, it is also known to have several local maxima. In the case of dynamic systems, certain differential equation constraints have to be satisfied. The choice of a suitable search algorithm is very important for the successful application of ML identification.

The best estimate of the parameter vector $\boldsymbol{\theta}$ is defined as the value that minimizes equation (5.25). There are several optimization techniques that could be applied to this nonlinear optimization problem, see also reference [Eyk79]. The Newton-Raphson scheme

has shown a very good convergence rate. This approach requires first and second order gradients of the cost function, which appear in the Taylor series expansion of $J(\boldsymbol{\theta})$. Assuming the vector $\boldsymbol{\theta}$ can be expressed as a small perturbation $\Delta\boldsymbol{\theta}$ from a nominal parameter estimate $\boldsymbol{\theta}_0$:

$$J(\boldsymbol{\theta}_0 + \Delta\boldsymbol{\theta}) = J(\boldsymbol{\theta}_0) + \Delta\boldsymbol{\theta}^T \frac{\partial J}{\partial \boldsymbol{\theta}}\bigg|_{\boldsymbol{\theta}=\boldsymbol{\theta}_0} + \Delta\boldsymbol{\theta}^T \frac{\partial^2 J}{\partial\boldsymbol{\theta}\partial\boldsymbol{\theta}^T}\bigg|_{\boldsymbol{\theta}=\boldsymbol{\theta}_0} \Delta\boldsymbol{\theta} + \ldots, \qquad (5.26)$$

where the vector of changes in $\boldsymbol{\theta}$ is denoted by $\Delta\boldsymbol{\theta}$, $\frac{\partial J}{\partial\boldsymbol{\theta}}$ is the vector of gradients $\frac{\partial J}{\partial\theta_j}$ for $j = 1, 2, \ldots, n_p$ and $\frac{\partial^2 J}{\partial\boldsymbol{\theta}\partial\boldsymbol{\theta}^T}$ is the second order gradient matrix, called the Hessian matrix, with elements $\frac{\partial^2 J}{\partial\theta_j\partial\theta_k^T}$, for $j, k = 1, 2, \ldots, n_p$.

Using the second order expansion in equation (5.26) as an approximation for $J(\boldsymbol{\theta}_0 + \Delta\boldsymbol{\theta})$,

$$J(\boldsymbol{\theta}_0 + \Delta\boldsymbol{\theta}) \approx J(\boldsymbol{\theta}_0) + \Delta\boldsymbol{\theta}^T \frac{\partial J}{\partial \boldsymbol{\theta}}\bigg|_{\boldsymbol{\theta}=\boldsymbol{\theta}_0} + \Delta\boldsymbol{\theta}^T \frac{\partial^2 J}{\partial\boldsymbol{\theta}\partial\boldsymbol{\theta}^T}\bigg|_{\boldsymbol{\theta}=\boldsymbol{\theta}_0} \Delta\boldsymbol{\theta}. \qquad (5.27)$$

The necessary condition for $J(\boldsymbol{\theta}_0 + \Delta\boldsymbol{\theta})$ to be a minimum is:

$$\frac{\partial}{\partial\boldsymbol{\theta}}\left[J(\boldsymbol{\theta}_0 + \Delta\boldsymbol{\theta})\right] = \mathbf{0}. \qquad (5.28)$$

Combining equations (5.27) and (5.28), gives:

$$\frac{\partial}{\partial\boldsymbol{\theta}}\left[J(\boldsymbol{\theta}_0 + \Delta\boldsymbol{\theta})\right] = \frac{\partial J}{\partial\boldsymbol{\theta}}\bigg|_{\boldsymbol{\theta}=\boldsymbol{\theta}_0} + \frac{\partial^2 J}{\partial\boldsymbol{\theta}\partial\boldsymbol{\theta}^T}\bigg|_{\boldsymbol{\theta}=\boldsymbol{\theta}_0} \Delta\boldsymbol{\theta} = \mathbf{0}. \qquad (5.29)$$

This equation can be rewritten to provide an estimate for the vector of parameter changes:

$$\Delta\hat{\boldsymbol{\theta}} = -\left[\frac{\partial^2 J}{\partial\boldsymbol{\theta}\partial\boldsymbol{\theta}^T}\bigg|_{\boldsymbol{\theta}=\boldsymbol{\theta}_0}\right]^{-1} \frac{\partial J}{\partial\boldsymbol{\theta}}\bigg|_{\boldsymbol{\theta}=\boldsymbol{\theta}_0}, \qquad (5.30)$$

assuming that the Hessian matrix is nonsingular. Since the first and second order gradients of the cost function are computed at a nominal value of the parameters ($\boldsymbol{\theta}_0$ for the first step), the updated parameter estimate is calculated from:

$$\hat{\boldsymbol{\theta}}^i = \hat{\boldsymbol{\theta}}^{i-1} + \alpha^{i-1}\Delta\hat{\boldsymbol{\theta}}^{i-1}, \qquad (5.31)$$

where the superscript i in $\hat{\boldsymbol{\theta}}^i$ denotes the parameter estimate at the ith iteration, the parameter update step $\Delta\hat{\boldsymbol{\theta}}^{i-1}$ is based on information about $J(\boldsymbol{\theta})$ acquired at previous iterations and the scalar α^{i-1} is chosen conveniently for a reduced value of $J(\boldsymbol{\theta})$, where $0 < \alpha^{i-1} < 1$. Due to the second order approximation to $J(\boldsymbol{\theta})$ in equation (5.27), it is necessary to repeat the estimation procedure. The reason for this iteration is that the output depends nonlinearly on the parameters, so the cost dependence on the parameters is more complicated than quadratic. In the present case, repeated quadratic approximations to the nonlinear dependence of the cost on the parameters are used to iteratively arrive at the solution. The iterative process is completed when selected convergence criteria are satisfied.

The Newton-Raphson iteration method is an often applied algorithm for the numerical minimization of the cost function. This method uses the values of the first and second order gradients of $J(\boldsymbol{\theta})$ with respect to the parameters $\boldsymbol{\theta}$. A difficulty with the Newton-Raphson method is that the Hessian matrix may not be positive definite and thus may not point in a 'downhill' direction. Furthermore, the second order gradients in the Hessian matrix are computationally expensive to obtain and are susceptible to numerical error. A good remedy is to apply the so-called Gauss-Newton method (also called Modified Newton-Raphson in literature), where the Hessian matrix is replaced by its expectation. This latter matrix is known as the Fisher information matrix. The Fisher information matrix can be shown to be non-negative definite.

It has been recognized that the extended Kalman filter is applied in the iterative Maximum Likelihood method to calculate the output prediction error vector. The calculation can be very time consuming. A simplification is that the system state equations can be assumed to be deterministic. This means that the system will be process noise free ($\mathbf{w}_i = 0$). The algorithm is then called the output error method. The output error vector is now calculated from directly integrating the nonlinear state equations. This significantly simplifies the algorithm. The state initial conditions from which the integration can be performed should still be estimated in this algorithm.

In the industrial application of the identification algorithm of chapter 6, the uncertainties in the states are much smaller than the uncertainties in the parameters. Therefore, it is assumed in this thesis that the state of the aircraft is known and only (a selection of) parameters are estimated.

Moreover, the assumptions of linearization that are valid for state estimation, are generally not valid for parameter estimation in the aircraft parameter identification problem.

In [Gro72], this output error method based on the ML method is described for a rigid body aircraft model.

In the absence of process noise, the dynamic system can be described by:

$$
\begin{aligned}
\dot{\mathbf{x}}(t) &= f\{\mathbf{x}(t), \mathbf{u}(t), \boldsymbol{\theta}\} & (5.32) \\
\mathbf{z}(t) &= h\{\mathbf{x}(t), \mathbf{u}(t), \boldsymbol{\theta}\} + \mathbf{v}(t),
\end{aligned}
$$

where $\mathbf{x}(t), \mathbf{u}(t), \mathbf{z}(t)$ are respectively the state, input and observation vector. The term $\mathbf{v}(t)$ represents the measurement noise. This measurement noise is assumed to be zero mean, white and uncorrelated Gaussian noise with unknown covariance matrix:

$$
E\{\mathbf{v}_i \mathbf{v}_j{}^T\} = \mathbf{R}\delta_{ij}. \tag{5.33}
$$

The state equations are deterministic and the Kalman gain is zero. The innovations become the output errors or residuals:

$$
\boldsymbol{\eta}_i = \mathbf{z}(t) - h\{\mathbf{x}(t), \mathbf{u}(t), \boldsymbol{\theta}\} = \mathbf{v}_i \tag{5.34}
$$

for $i = 1, \dots, N$. The negative Likelihood function now takes the form:

$$
J(\boldsymbol{\theta}) = \frac{1}{2}\sum_{i=1}^{N} \boldsymbol{\eta}_i^T \mathbf{R}^{-1} \boldsymbol{\eta}_i + \frac{N}{2}\ln|\mathbf{R}|. \tag{5.35}
$$

Recall at this point equation (5.25) that described the Likelihood function in the presence of process noise. For the dynamic system specified by equation (5.32), the unknown parameters can be elements of the functions f and h, $\mathbf{R}$ and the initial condition vector $\mathbf{x}_0$. Optimizing the right side of equation (5.35) with respect to $\mathbf{R}$ is done by differentiating with respect to $\mathbf{R}$. Setting the result equal to zero and solving for $\mathbf{R}$ gives:

$$\hat{\mathbf{R}} = \frac{1}{N} \sum_{i=1}^{N} \mathbf{v}_i \mathbf{v}_i^T. \tag{5.36}$$

From this equation, usually only the diagonal elements of the matrix $\mathbf{R}$ are estimated. This enforces the assumption that the measurement noise sequences for the n_0 measured outputs are uncorrelated with one another. In [Kle06] it is stated that this assumption is a good one in practice. A diagonal $\hat{\mathbf{R}}$ simplifies the calculations. Retaining the full matrix $\mathbf{R}$ can be done without conceptual difficulty, but the small difference in the results does not warrant the extra computation involved. For a given $\hat{\mathbf{R}}$, the negative log-Likelihood function cost function becomes:

$$J(\boldsymbol{\theta}) = \frac{1}{2} \sum_{i=1}^{N} \boldsymbol{\eta}_i^T \hat{\mathbf{R}}^{-1} \boldsymbol{\eta}_i, \tag{5.37}$$

where the last term in equation (5.35) is dropped because it does not depend on the unknown model parameters $\boldsymbol{\theta}$. Since the innovations $\boldsymbol{\eta}_i$ in the cost function are output errors, this approach is called the output error method.

The negative log-Likelihood function is minimized using a relaxation technique. The matrix $\hat{\mathbf{R}}$ is determined from equation (5.36) for a given fixed $\boldsymbol{\theta}$. Then the matrix $\mathbf{R} = \hat{\mathbf{R}}$ is fixed and the cost function in equation (5.37) is minimized with respect to $\boldsymbol{\theta}$. The idea is that optimization with respect to the complete set of unknown parameters in $\boldsymbol{\theta}$ and $\mathbf{R}$ is more well conditioned if $\boldsymbol{\theta}$ and $\mathbf{R}$ are adjusted alternately, with one being allowed to vary while the other is held constant. The two steps are repeated until convergence criteria are satisfied. There is no general proof that this sequence will converge. However, practical experience has shown that the sequence does in fact converge.

The gradient of the cost function is obtained as:

$$\nabla_{\boldsymbol{\theta}} J = \frac{\partial J(\boldsymbol{\theta})}{\partial \boldsymbol{\theta}} \quad = \quad \sum_{i=1}^{N} \frac{\partial \boldsymbol{\eta}_i^T}{\partial \boldsymbol{\theta}} \hat{\mathbf{R}}^{-1} \boldsymbol{\eta}_i \tag{5.38}$$

$$= \quad -\sum_{i=1}^{N} \frac{\partial \mathbf{y}_i^T}{\partial \boldsymbol{\theta}} \hat{\mathbf{R}}^{-1} \boldsymbol{\eta}_i, \tag{5.39}$$

which is a vector with elements:

$$\frac{\partial J(\boldsymbol{\theta})}{\partial \theta_j} = -\sum_{i=1}^{N} \frac{\partial \mathbf{y}_i^T}{\partial \theta_j} \hat{\mathbf{R}}^{-1} \boldsymbol{\eta}_i, \tag{5.40}$$

for $j = 1, 2, \ldots, n_p$.

The elements of the second order gradient matrix are:

$$\frac{\partial^2 J(\boldsymbol{\theta})}{\partial \theta_j \partial \theta_k} = \sum_{i=1}^{N} \frac{\partial \mathbf{y}_i^T}{\partial \theta_j} \hat{\mathbf{R}}^{-1} \frac{\partial \mathbf{y}_i^T}{\partial \theta_k} - \sum_{i=1}^{N} \frac{\partial^2 \mathbf{y}_i}{\partial \theta_j \partial \theta_k} \hat{\mathbf{R}}^{-1} \mathbf{v}_i, \tag{5.41}$$

for $j, k = 1, 2, \ldots, n_p$. The matrix that is formed by these elements is called Hessian matrix. It is stated in [Kle06], that if the second order partial derivative in the above equation is neglected, the resulting optimization algorithm is called Gauss-Newton or Modified Newton-Raphson. This simplification is made for practical reasons. The second order gradient is computationally expensive to obtain and susceptible to numerical error because of the higher order differentiation. Since the second order gradient term is multiplied by the residual $\mathbf{v}_i$, the approximation gets better as the estimated parameter vector approaches the solution and is very good near the solution. However, when the Fisher information matrix is used, instead of the Hessian matrix, the same result can be derived without having to neglect this term. The Fisher information matrix is defined as the expectation of the Hessian matrix, thus from equation (5.41):

$$E\left\{ \frac{\partial^2 J(\boldsymbol{\theta})}{\partial \theta_j \partial \theta_k} \right\} = E\left\{ \sum_{i=1}^{N} \frac{\partial \mathbf{y}_i^T}{\partial \theta_j} \hat{\mathbf{R}}^{-1} \frac{\partial \mathbf{y}_i^T}{\partial \theta_k} \right\} - E\left\{ \sum_{i=1}^{N} \frac{\partial^2 \mathbf{y}_i}{\partial \theta_j \partial \theta_k} \hat{\mathbf{R}}^{-1} \right\} E\left\{ \mathbf{v}_i \right\}. \tag{5.42}$$

The second term, contains the expectation of the gaussian noise $\mathbf{v}_i$, which is zero. The Gauss-Newton approximation to the Hessian is then:

$$M_{jk} = E\left\{ \frac{\partial^2 J(\boldsymbol{\theta})}{\partial \theta_j \partial \theta_k} \right\} = E\left\{ \sum_{i=1}^{N} \frac{\partial \mathbf{y}_i^T}{\partial \theta_j} \hat{\mathbf{R}}^{-1} \frac{\partial \mathbf{y}_i^T}{\partial \theta_k} \right\}. \tag{5.43}$$

Recall that this matrix is called the Fisher information matrix (the matrix $\mathbf{M}$ for short). The Hessian matrix rotates and scales the update from the negative gradient direction to produce single step convergence for quadratic cost functions. Errors in the Hessian matrix influence the path the algorithm takes to the minimum, but not the location of the minimum, since the gradient is calculated without error.
Far from convergence, the local estimate of the second gradient is not guaranteed to rotate the gradient in the best direction, nor optimally scale the length of the parameter vector change. In non-quadratic problems it is frequently better to make smaller parameter steps directed more in the negative gradient direction until the quadratic area near the minimum is reached.

Using the Fisher information matrix defined in equation (5.43), the parameter update can now be calculated by:

$$\hat{\boldsymbol{\theta}}^{i+1} = \hat{\boldsymbol{\theta}}^i - \alpha^i \, \mathbf{M}^{-1} \nabla_{\boldsymbol{\theta}} J \tag{5.44}$$

The elements of the $n_0 \times n_p$ matrix $\frac{\partial \mathbf{y}}{\partial \boldsymbol{\theta}}$ are called output sensitivities. The output sensitivities quantify the change in the outputs due to changes in the parameters. Because

the matrix $\hat{\mathbf{R}}^{-1}$ is typically diagonal, equation (5.43) shows that the output sensitivities must be linearly independent and nonzero for good matrix inversion and a reasonable $\Delta\hat{\boldsymbol{\theta}}$. When the output sensitivities are linearly independent and nonzero, each model parameter has a unique and significant impact on the model outputs. Minimizing the output error will be a well conditioned problem leading to accurate values for the unknown parameters. In section 5.4.2, the topic of a nearly singular Information matrix will be addressed.

The parameter covariance matrix satisfies:

$$cov(\hat{\boldsymbol{\theta}}) \geq \mathbf{M}^{-1}_{\boldsymbol{\theta}=\hat{\boldsymbol{\theta}}},\tag{5.45}$$

which is the Cramér-Rao inequality, indicating a lower bound for the parameter covariance matrix.

The dynamic model can be an arbitrary nonlinear function of the parameter vector. Consequently, the output error method can be used for arbitrary nonlinear models. In particular, the full nonlinear aircraft equations of motion can be used as the dynamic model equations, without any change to the output-error cost formulation or the nonlinear optimization.

5.4   Identifiability and uniqueness problems

There are some basic problems associated with extracting model parameters from flight test data. Most of these problems can be classified under the heading of 'identifiability', which is related to the degree of excitation for the particular modes of the system under investigation and the ability to identify associated parameters. Identifiability also relates to whether the parameters themselves can be identified or whether they can only be identified as part of a linear combination. In the following, some symptoms and causes of identifiability problems will be discussed.

5.4.1   Symptoms and causes of identifiability problems

The most obvious symptoms of identifiability problems are physically nonrealizable parameter estimates and large associated error covariances. Either of these symptoms may arise due to a number of different reasons. For example, if the input sequence does not adequately excite some of the modes, the associated parameters may not be identifiable. If the chosen model is inadequate, the parameters of that model may be forced to account for some major un-modelled effects. The estimated parameter values may thus be quite different from what aerodynamic theory and previous results may indicate. Also, additional factors such as too short a data length, local minima in the cost functional and poor initial parameter estimates may also result in nonphysical parameter values.

Large error covariances principally result from poor input sequences and attempts at identifying too many parameters. A poor input sequence reduces the sensitivity of the output to variations in some parameter values. The attempt of identifying too many parameters, causes linear dependencies between parameter estimates. An extraneous parameter does not, by definition, improve or degrade the fit to the observed data, its estimated value will be of no significance and the error covariance of the estimated value will be large.

Probably the most common identifiability problem encountered in processing flight data results from parameter dependencies. This may occur through a pair of parameters which always appear in the equations of motion together (for example C_{mq} and $C_{m\dot{\alpha}}$), or through a poor choice of inputs such that some of the aircraft response variables are linearly correlated, or it may occur through an overspecification of the number of parameters to be identified. In the last case, the information content in the data can be too low for the number of estimated parameters required. The estimator cannot produce results with sufficient accuracy, or the estimation process can fail completely.

Another cause is misspecification of the model. Changes in more than one model parameter produce nearly equivalent changes in the outputs, or perhaps one or more model parameters have little or no effect on the outputs. There can also be insufficient information content in the data. There is so little movement in the outputs that it appears that one or more parameters have little or no effect on the outputs. Consequently, the corresponding output sensitivities are near zero. Another form of this problem occurs when a model parameter is associated with a quantity that is constant or nearly constant. It causes the associated parameter to be confounded with the bias parameter. This could also be classified as model misspecification.

In each case, the result of the dependencies is a nearly singular information matrix. Inversion of this matrix to obtain the step size in the parameter estimates will cause numerical problems to occur.

More information on identifiability problems can be found in reference [Ste73].

5.4.2   Rank deficient solution procedure

In reference [Ste73], four different approaches to identifiability problems are presented:

- Fixing parameters,

- A priori weighting,

- Constrained optimization,

- Rank deficient solutions.

The first three approaches will only be shortly addressed. More information on these approaches can be found in reference [Ste73]. In this section the focus will lie on the last approach, the rank deficient solution.

The usual remedy for parameter dependencies has often been to fix some of the dependent parameters during identification. This generally improves the numerical convergence. The basic reasons why the parameter fixing technique does not always work are the following. The correlation is usually not simply between pairs of parameters, but may involve the entire set of unknown parameters. Secondly, the choice of a particular parameter to fix and the value at which it is fixed are generally not clear.

If a range of allowable values or relationships between the parameters can be specified, from practical or theoretical considerations, they can be used as constraints on the parameter estimates. Such a procedure would require a constrained optimization technique. Including such parameter value constraints will most probably also reduce the convergence rate.

Rank deficient solutions

Without any of the above shortly described remedies, the parameter identifiability problems will usually appear as a difficulty with inverting the information matrix and obtaining accurate parameter estimates and error covariances. This numerical difficulty can be related to the spread in the eigenvalues of the information matrix. A perfect dependency among the parameters should (strictly speaking) result in a zero eigenvalue. However, round-off and other numerical errors prevent the matrix from being exactly singular. Therefore, all the eigenvalues will be nonzero with a spread between the smallest and the largest eigenvalue being many orders of magnitude. In such a case, a rank deficient solution for the inverse rather than a full rank solution might be better.

A rank deficient solution means that the inverse to the information matrix is computed leaving out one or more of the smallest eigenvalues. Each eigenvalue that is left out relates to a singular direction in parameter space. Therefore it indicates a combination of parameters that cannot be identified uniquely.

The eigenvalues of the information matrix are the dimensions of the uncertainty ellipsoid, associated with the parameters in parameter space. The smaller eigenvalues indicating a larger dimension and therefore more uncertainty.

There are two main consequences of a nearly singular information matrix:

- The information matrix $\mathbf{M}$ can be negative definite, resulting in a cost increase $\mathbf{J}(\hat{\boldsymbol{\theta}}^{i+1}) > \mathbf{J}(\hat{\boldsymbol{\theta}}^i)$ for the modified Newton-Raphson step.

- The modified Newton-Raphson algorithm step size $\Delta\hat{\boldsymbol{\theta}}$ in one or more directions can be large.

The second problem can be made plausible from the following. The inverse of the information matrix can be decomposed as:

$$\mathbf{M}^{-1} = \sum_{j=1}^{n_p} \frac{1}{\lambda_j} \mathbf{t}_j \mathbf{t}_j^T. \tag{5.46}$$

where λ_j and $\mathbf{t}_j$ are respectively the jth eigenvalue and jth eigenvector of the information matrix. The Modified Newton-Raphson step in the direction of $\mathbf{t}_j$ is found by combining

the previous expression with equation (5.44):

$$\Delta\hat{\boldsymbol{\theta}}_{\lambda_j} = -\frac{1}{\lambda_j}(\mathbf{t}_j^T \nabla_{\boldsymbol{\theta}}\mathbf{J})\mathbf{t}_j. \tag{5.47}$$

This step will be large for small λ_j, in a direction $\mathbf{t}_j$ for which little information is available. The parameter step $\Delta\hat{\boldsymbol{\theta}}$ is therefore dominated by bad information, resulting in a parameter vector update that does not approach the minimum of the cost function. There are several techniques for dealing with an ill-conditioned information matrix. Three possibilities associated with the Modified Newton-Raphson method are:

- Rank deficient method,

- Levenberg-Marquardt method,

- Bayes-like method.

The rank deficient method is based on the reduced-order inverse of the information matrix $\mathbf{M}$ using the singular value decomposition (SVD), see also [Rad97]:

$$\mathbf{M} = \mathbf{UST}^T \tag{5.48}$$

The reduced-order matrix inverse can than be determined from:

$$\mathbf{M}^{-1} = \mathbf{T}\begin{bmatrix} \frac{1}{\mu_1} & & & & & & \\ & \frac{1}{\mu_2} & & & & 0 & \\ & & \ddots & & & & \\ & & & \frac{1}{\mu_{n_p-m}} & & & \\ & & & & 0 & & \\ & 0 & & & & \ddots & \\ & & & & & & 0 \end{bmatrix}\mathbf{U}^T \tag{5.49}$$

$$= \sum_{j=1}^{n_p-m} \frac{1}{\mu_j}\mathbf{t}_j\mathbf{u}_j^T, \tag{5.50}$$

where $\mathbf{t}_j$ and $\mathbf{u}_j$ are the jth columns of respectively the matrices $\mathbf{T}$ and $\mathbf{U}$. The singular values μ_j are arranged from the largest to the smallest in magnitude:

$$\mu_1 > \mu_2 > \cdots > \mu_{n_p-m} > \cdots > \mu_{n_p} \tag{5.51}$$

The terms associated with the smallest m singular values are dropped in computing the matrix inverse. Each eigenvalue which is left out relates to a singular direction in parameter space. Therefore it indicates a combination of parameters that cannot be identified uniquely. The rank deficient solution fixes combinations of parameters corresponding to nearly zero eigenvalues. Consequently, it reduces the dimension of the space in which the set of parameter values that minimize the cost function are sought. It is important to

realize, however, that at each iteration the values for all the specified unknown parameters are assigned updated estimates.

In reference [Kle06] the following criterion is presented to drop any singular value for which:

$$\frac{\mu_j}{\mu_{max}} < N\varepsilon, \tag{5.52}$$

where N is the number of data points and ε is the computing precision.

It gives the inverse of the matrix $\mathbf{M}$ with the rank reduced from n_p to $n_p - m$. The inverse determined through a SVD is called pseudo-inverse and is usually indicated by $\mathbf{M}^+$ in literature. Here when it is written $\mathbf{M}^{-1}$, the reduced-order pseudo-inverse, calculated using equation (5.49), is meant in case of a rank deficient matrix $\mathbf{M}$.

The number of singular values to be neglected depends on which order rank deficient solution produces a parameter step resulting in a set of parameters with the lowest associated cost. The procedure can also be the following. Starting from some minimal number of singular values, a reduced rank inverse is computed. The parameter step is determined and the associated cost evaluated. One more singular value is then added and the procedure repeated. This is done until all the singular values (up until the rank of $\mathbf{M}$ has been reached) are added in, with the last inverse thus being a full rank inverse. The same procedure, starting from a minimum number of eigenvalues and progressing to the full rank is repeated every iteration. This procedure will later in this thesis be referred to as 'minimum search'.

This procedure is necessary if the information matrix does not have full rank, because now there are multiple answers $\Delta\hat{\boldsymbol{\theta}}^i$ to the minimization problem. Of all these possible answers, it is checked which one would give the smallest value of the cost function $\mathbf{J}(\hat{\boldsymbol{\theta}}^{i+1})$. That value for $\Delta\hat{\boldsymbol{\theta}}^i$ is than taken for this iteration step, the others are not stored. This is an approach with a considerable computational impact, but it proved to give the best convergence characteristics in the problems studied here. The problem is that there is no good rule or strategy known yet, which singular values should be skipped. It is certainly reasonable to search for 'breaks' in the singular values and count all singular values of about the same magnitude as either all zero or all nonzero. In an automized routine, the above proposed procedure seemed to work best.

In reference [Ste73] a comparison of results is presented between the rank deficient solution, the fixing parameters and the a priori weighting technique for a three state model. It is shown there that the rank deficient solution gives the best estimates.

The Levenberg-Marquardt method augments the information matrix ($\mathbf{M}^{-1} = (\mathbf{M}_0 + k\mathbf{A})^{-1}$, where the matrix $\mathbf{M}_0$ is the original information matrix) to improve its conditioning and thereby produce a more reasonable inverse. More information on this method can be found in references [Kle06], [Lou05] and [Nie99].

The Bayes-like method improves the conditioning of the information matrix by combining the measured data with prior estimates of some or all of the unknown parameters in

the model. A weighting technique is performed using the confidence of certain parameters. More details on this method can be found in [Kle06].

The rank deficient method was described here most detailed. The estimates obtained from all three techniques just mentioned will be biased. However, in practical cases, the bias is small compared with the inaccuracies that would have been introduced if M was nearly singular and nothing was done to regularize the estimation.

In some cases, the information matrix M is nearly singular only at certain points in the progression toward a solution using the Modified Newton-Raphson method. In those cases, the methods described earlier can be used temporarily to get past the difficult points. It can than be omitted as the sequence of parameter estimates approaches the solution.

The rank deficiency method is easy to use in this way. To implement the approach, the inverse of the information matrix is always calculated using the singular value decomposition. The singular value ratios are checked against the criterion, see equation (5.52), or multiple directions are 'scanned' by the procedure described above. If any singular values are too small, their corresponding terms are dropped from the inverse using equation (5.49) and the Modified Newton-Raphson method proceeds in the usual way. This approach is a simple method for addressing the near-singularity of the information matrix and works well in practice.

5.5   Numerical methods

The emphasis in this section is on the most common numerical difficulties encountered when implementing the minimization procedure from the previous sections on a digital system. A good reference on this topic is [Den96] that deals with numerical methods for unconstrained optimization and nonlinear equations for algorithms that are all based on Newton's method. Many problems with simple constraints, such as bounds on the variables, can be solved by unconstrained algorithms, because the constraints are satisfied by the unconstrained minimizer.

It is stated in reference [Den96], that the typical size of a nonlinear problem to be solved, amounts only two to thirty variables, where even two-variable problems can be difficult to solve. Intermediate problems are those with fifteen to fifty variables. Problems with fifty or more variables are large problems in this field. Unless they are only mildly nonlinear, or there is a good starting guess, it is stated that there is no good chance of solving them economically.

Furthermore, it is important to have an algorithm that works effectively in the absence of analytic derivatives. It is often the case that analytic derivatives are not readily available although the function is several times continuously differentiable.

A third aspect is that many nonlinear problems are quite expensive to solve. Either because an expensive nonlinear function is evaluated repeatedly or because the task is to solve many related problems.

Many real problems are poorly scaled, meaning that the sizes of the variables differ greatly. For example, one variable may always be in the range 10^6 to 10^7 and another in

the range 1 to 10. It is stated in reference [Den96] that most of the work in this field did not pay attention to the problem of scaling.

Section 5.5.1 describes some general aspects that should be considered when implementing the specific algorithm on a digital system. Section 5.5.2 describes the line searching method that is implemented to arrive at local convergence although the Newton step might be too large initially. Section 5.5.3 presents the method to numerically approximate the necessary gradients. Finally in section 5.5.4, the problem of poorly scaled problems will be addressed.

5.5.1   General aspects

The implications of storing real numbers to only a finite precision are important, but they can be summarized simply. First, since not every real number can be represented exactly on the computer, one can at best expect a solution to be as accurate as the computer precision. Second, depending on the computer and the compiler, the result of each intermediate arithmetic operation is either truncated or rounded to the accuracy of the machine. Thus the inaccuracy due to finite precision may accumulate and further diminish the accuracy of the results. Such errors are called round-off errors.

A consequence of the use of finite precision arithmetic and even more, of the iterative nature of the algorithm, is that no exact answers will be arrived at for most nonlinear problems. Therefore, often a measure is needed to determine how close a number x is to another number y. The concept that is used most often is that of the relative error in y as an approximation to a nonzero x:

$$\frac{|x - y|}{|x|} \leq \sqrt{\varepsilon}, \tag{5.53}$$

where ε denotes the machine epsilon (precision). Another effect of finite precision arithmetic is that certain aspects of the algorithm, such as stopping criteria, will depend on the machine precision.

In many cases, the supplier of a nonlinear problem knows from practical considerations that it has a solution and either that the solution is unique or that a solution in a particular region is desired. Therefore, the determination of the existence or uniqueness of solutions is usually not the primary concern in practice.

The resulting method is designed to converge to a *local* minimizer of a nonlinear functional or some solution of a system of nonlinear equations, from almost any starting point. It is practically impossible to know if you are at the global minimum of a function. Therefore this optimization algorithm can at best locate one local minimum.

The error at each iteration of Newton's method will be approximately the square of the previous error, see [Den96] for the mathematical proof. Thus if the initial guess is good enough, the error will decrease and eventually decrease rapidly. This pattern is known as local q-quadratic convergence. If the initial guess is not good enough, Newton's method will diverge. Therefore, Newton's method is useful for its fast local convergence, but it

needs to be incorporated into a more robust method that will be successful from farther starting points.

Although the Newton step may actually cause an increase in the value of the (cost) function, its direction will always be one in which the function value decreases initially. Thus, if the Newton step does not produce a decrease in the cost function, a reasonable strategy is to backtrack from $\hat{\boldsymbol{\theta}}^{i+1}$ to $\hat{\boldsymbol{\theta}}^i$, until one finds a point for which $\mathbf{J}(\hat{\boldsymbol{\theta}}^{i+1}) < \mathbf{J}(\hat{\boldsymbol{\theta}}^i)$. This is exactly how the line searching procedure is implemented, see also section 5.5.2. Starting from the Newton step, the parameter step $\Delta\hat{\boldsymbol{\theta}}^i$ is halved that often until $\mathbf{J}(\hat{\boldsymbol{\theta}}^{i+1}) < \mathbf{J}(\hat{\boldsymbol{\theta}}^i)$. This implementation is an example of a hybrid algorithm. One that attempts to combine global convergence and fast local convergence by first trying the Newton step at each iteration. However, always insisting that the iteration decreases some measure of the closeness to a solution. Such a hybrid mechanism is the key to practical success in solving multivariable nonlinear problems.

5.5.2   Line searching

In the Modified Newton-Raphson (or Gauss-Newton) method, the second order gradient of the cost function is approximated by the Fisher information matrix. If this matrix is positive definite, then the Newton direction will be a descent direction. Therefore the information matrix is coerced to be positive definite if it is not already. Because the resultant Newton direction will be a descent direction for the actual problem, it is guaranteed that for sufficiently small steps in the Newton direction, the function value will be decreased.

The Modified Newton-Raphson method leads to fast convergence near the minimum, where the cost function is quadratic. However, in the region far from the minimum this algorithm points in the right direction, but does not necessarily give a smaller value of the cost function $\mathbf{J}$.

Therefore an option for line searching is implemented, to find a least value of the Likelihood function along a line made from $\mathbf{J}(\hat{\boldsymbol{\theta}}^i)$ to $\mathbf{J}(\hat{\boldsymbol{\theta}}^{i+1})$. The scalar $0 < \alpha^i < 1$ in equations (5.31) and (5.44) is chosen such that after being multiplied with $\Delta\hat{\boldsymbol{\theta}}$, it results in a smaller value of the cost function $\mathbf{J}$. The optimization method becomes the Gauss-Newton algorithm with line searching option:

$$\hat{\boldsymbol{\theta}}^{i+1} = \hat{\boldsymbol{\theta}}^i + \alpha^i \Delta\hat{\boldsymbol{\theta}}^i \tag{5.54}$$

More information on the line searching method can be found in references [Spe70], [Sto83] and [Den96].

A minimum step length is defined in the algorithm, that is used to test for convergence. If the cost function $\mathbf{J}(\hat{\boldsymbol{\theta}}^{i+1})$ is not yet smaller then that from the previous step: $\mathbf{J}(\hat{\boldsymbol{\theta}}^{i+1})$ but the stepsize is smaller then the minimal stepsize, then the line search is terminated, since convergence would be detected at the end of the current iteration anyway. A maximum allowable step length is also declared to prevent excessively long steps that might occur due to a nearly singular information matrix.

This section dealt with the problem of finding an acceptable step length in a given direction of search. The underlying assumptions were that the direction would be the Newton direction and that the full Newton step would always be the first trial step. The resulting backtracking (by line search) algorithm incorporates these assumptions to attempt global convergence without sacrificing the local convergence properties of the Newton method, clearly the goal of any global strategy.

There are also some techniques that shorten the step length and also vary the direction. For more information on these techniques, one is referred to [Den96].

5.5.3   Calculation of the sensitivity matrix

It was shown in section 5.3.2 in equations (5.38) and (5.43) that in order to determine the parameter update, one needs to know the output sensitivities $\frac{\partial \mathbf{y}}{\partial \boldsymbol{\theta}}$. These derivatives are not always analytically available. In this section, the formulas are presented that are used to approximate these derivatives by finite differences.

For a multivariable function $\mathbf{F}(x)$ the jth column of the Jacobian is approximated by the forward difference:

$$\mathbf{A}_{.j} = \frac{\mathbf{F}(x + he_j) - \mathbf{F}(x)}{h}, \tag{5.55}$$

where e_j denotes the jth unit vector. The error in this approximation of the gradient is $O(h)$, where it is referred to [Den96] for the mathematical proof.

Equation (5.55) might give the impression that one stepsize h is used in constructing all of A. However, finite precision arithmetic causes that a different stepsize should be used for each column of $\mathbf{A}$. Furthermore, a uniform stepsize could be disastrous if the components of x differ widely in magnitude.

The stepsize is chosen as follows, for the sensitivity with respect to the pth parameter at the ith iteration step, $\hat{\theta}_p^i$:

$$h = \sqrt{\varepsilon} \quad if \quad |\hat{\theta}_p^i| < 1, \tag{5.56}$$

$$h = |\hat{\theta}_p^i| \cdot \sqrt{\varepsilon} \quad if \quad |\hat{\theta}_p^i| > 1, \tag{5.57}$$

where ε denotes the machine precision. This stepsize takes the effects of finite precision arithmetic into consideration.

Notice also that finite difference approximation of the Jacobian requires n additional evaluations of the function $\mathbf{F}$. Therefore it can be relatively expensive if evaluation of $\mathbf{F}$ is expensive or n is large.

In some cases, finite precision arithmetic might require more accurate finite-difference approximation using the central difference approximation. This approximation requires twice as many evaluations of $\mathbf{F}$ as forward differences, which is not acceptable for the applications considered in this thesis.

The number of function evaluations might be reduced (compared to forward difference)

by using multidimensional secant methods. The approximation to the Jacobian is calculated using only function evaluations that have already been calculated. The approximation to the Jacobian thus involves no additional cost in function evaluations, however, at the cost of a reduction in convergence rate. More information on secant methods can be found in reference [Den96].

An alternative method in the approximation of the derivative is that using a complex step, see further [Mar00] and [Kim05]. The complex step method is basically just that, a finite difference approximation using a complex step ih instead of h. The approximation error can be shown to be of the same order of magnitude as with the central difference method. However, using the complex step method, there is no substractive cancellation error. Consequently, the stepsize can be made arbitrarily small (as long as it remains inside the numerical range for real numbers on the computer). The complex step method is tested for the applications presented in this thesis. For the cases considered here, it did not noticeably improve the results or the convergence rate. However, it is recognized to be quite an elegant method that is implemented relatively easy. Therefore, if the forward difference technique does not provide a sufficiently accurate approximation of the gradient, the complex step method can be tested whether it improves results.

The accuracy in the solution will be limited by the accuracy in the gradient approximation. Owing to the accuracy needed in the gradient approximation, it is also shown in reference [Den96] that there is no useful secant approximation to the gradient in minimization algorithms.
An additional operation that improves the accuracy of the finite difference approximation is also implemented. Before the approximated Jacobian is calculated with equation (5.55), the following calculation is performed:

$$\begin{aligned}
temp &= x_j + h_j, & \text{(5.58)} \\
h_j &= temp - x_j. & \text{(5.59)}
\end{aligned}$$

This operation should minimize the round-off error.

The stepsize is a compromise that balances the nonlinearity error caused by taking a too large step $|h|$ with the finite precision and function evaluation errors from allowing the step $|h|$ too small.

5.5.4 Scaling

Scaling is an issue that is peripheral to the basic mathematical considerations in the solution of the optimization problem, but essential to the computer solution of actual problems. The main question is: how to adjust for problems that are badly scaled in the sense that the dependent or independent variables are of widely differing magnitudes?

The variables can be scaled using a diagonal scaling matrix $\mathbf{D}$, such that all variables

have approximately the same range:

$$\hat{\mathbf{x}} = \mathbf{D}\mathbf{x}, \tag{5.60}$$

where $\mathbf{x}$ are the variables to be scaled and $\hat{\mathbf{x}}$ are the newly scaled variables. It can be shown that the Newton step is unaffected by this transformation. It is even possible to use dynamic scaling, in case some x_i vary by many orders of magnitude, but this has not been included in the algorithm.

When solving systems of nonlinear equations, where the component functions differ in sizes, problems can occur. The Newton step is again independent of this scaling. However, the optimization requires a decrease in some norm. Therefore, it is clear that if the units of two component functions are widely different, the smaller component function will be virtually ignored. The algorithm also uses a positive diagonal scaling matrix on the dependent variable to prevent this. The scaling matrices can easily be set to identity matrices (if necessary) to keep the original scaling of the variables.

5.6   Simple example with a nonsingular information matrix

In this section a simple model is presented to show the principal features of the algorithm. The model is kept as simple as possible in order to provide maximum insight. The model is a linear state space model with two degrees of freedom. The output sensitivities can be determined analytically for this example and the results can be compared with those from the numerical approximation.

5.6.1   Measurement data

The measurement data in this example will be generated using the 'real' idealized model and adding measurement (gaussian) noise.

The dynamic equations of this linear model are:

$$\dot{\mathbf{x}} = \mathbf{A}\mathbf{x} + \mathbf{B}\mathbf{u} \tag{5.61}$$
$$\mathbf{z} = \mathbf{C}\mathbf{x} + \mathbf{D}\mathbf{u} + \mathbf{v}, \tag{5.62}$$

where:

$$\mathbf{A} = \begin{bmatrix} 0 & 1 \\ 0 & 0 \end{bmatrix}, \mathbf{B} = \begin{bmatrix} 0 \\ 0.01 \end{bmatrix} \tag{5.63}$$

$$\mathbf{C} = \begin{bmatrix} 1 & 0 \\ 0 & 1 \end{bmatrix}, \mathbf{D} = \begin{bmatrix} 0 & 0 \\ 0 & 0 \end{bmatrix}, \tag{5.64}$$

and $\mathbf{v}$ is gaussian noise with zero mean and standard deviation of 0.01, see figure (5.1). Notice that the matrix $\mathbf{C}$ is an identity matrix and $\mathbf{D}$ is a zero matrix. Consequently, the
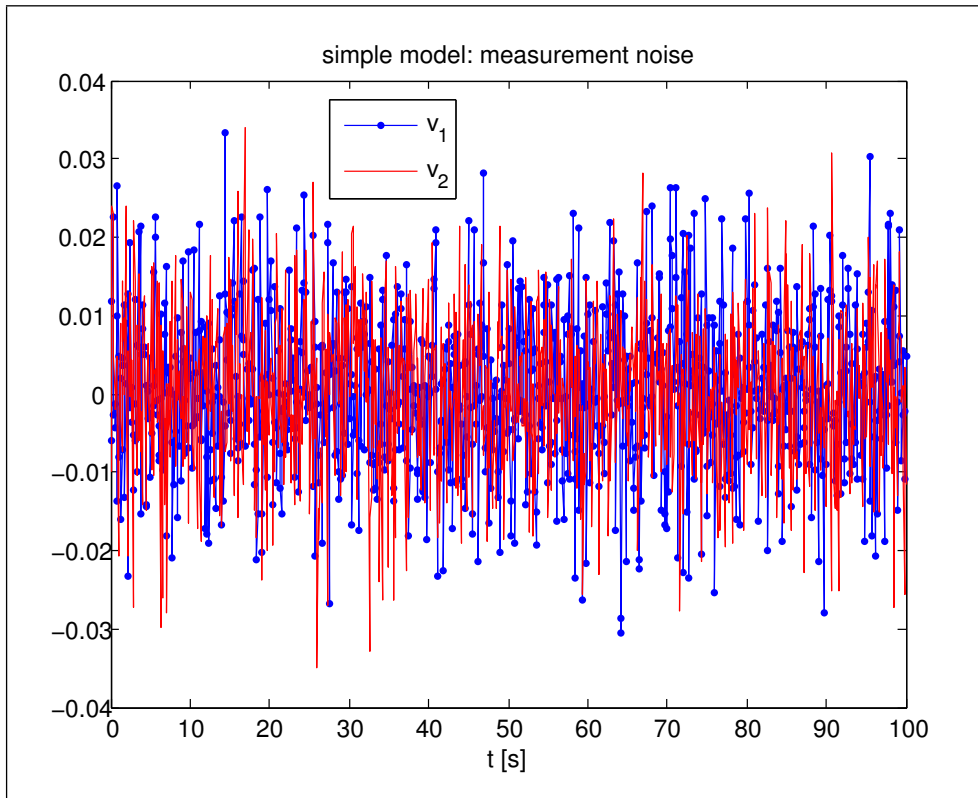
Figure 5.1: Measurement noise (gaussian) with zero mean and standard deviation 0.01

measurement vector is equal to just the state vector plus the measurement noise.

The number of samples N is 1000 taken at a sample time of 0.1. The input signal is as given in figure (5.2), the initial state vector is $[0\ 0]^T$. In this figure the time history of the states are also plotted. See figure (5.3) for the time histories of the output of the ideal model (blue line) and the measured data (red line).

5.6.2 Identification

In this section, two parameters of the model will be estimated using only the measurement data of the previous section. Of course, in this simple case, the 'real' values of the parameters are known. Therefore it can be checked very easily whether it converges to the right solution.

The same model structure is used, where at this point only two parameters θ_1 and θ_2 will be estimated.

$$\mathbf{A} = \begin{bmatrix} 0 & \theta_1 \\ 0 & 0 \end{bmatrix}, \mathbf{B} = \begin{bmatrix} 0 \\ \theta_2 \end{bmatrix}, \mathbf{C} = \begin{bmatrix} 1 & 0 \\ 0 & 1 \end{bmatrix}, \mathbf{D} = \begin{bmatrix} 0 & 0 \\ 0 & 0 \end{bmatrix}. \tag{5.65}$$
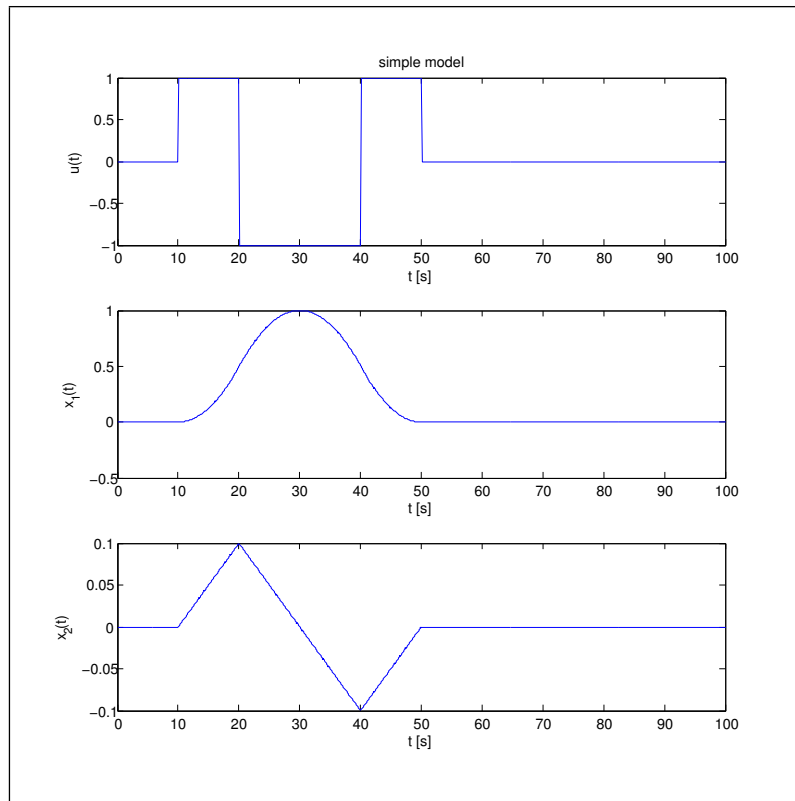
Figure 5.2: *Time histories of input and state of the simple example.*
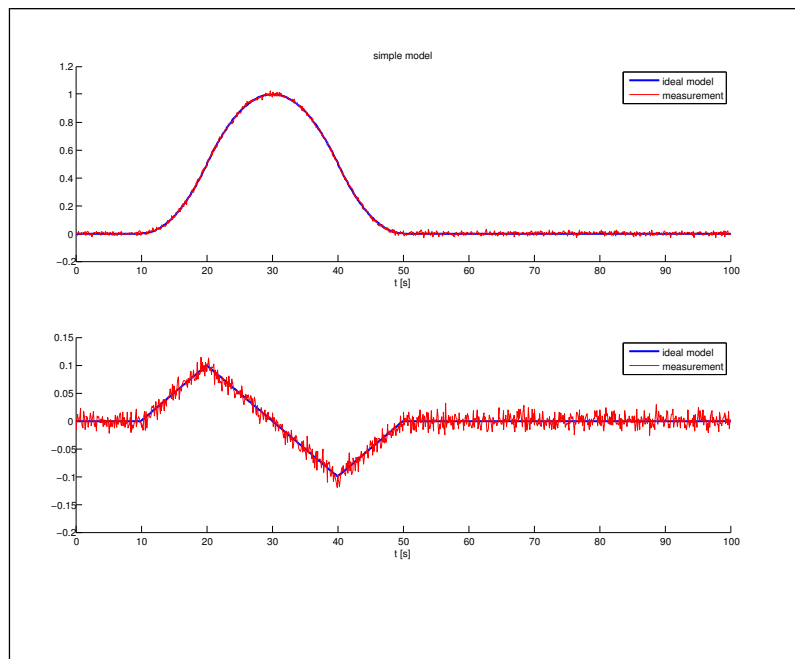
Figure 5.3: *Time histories of the output of the ideal simple example and that with added measurement noise. See figure (D.18) in the appendix for the full color image.*

The initial values of the parameters to be estimated are:

$$\hat{\boldsymbol{\theta}}_0 = \begin{bmatrix} 10 \\ 0.10 \end{bmatrix} \tag{5.66}$$

In figure (5.4) the output vector of this initial model is plotted together with the measured data. Obviously, there is a significant difference.

After 2 iterations, one gets the following values for the parameter estimates, using a fully analytical algorithm with analytical derivatives:

$$\hat{\boldsymbol{\theta}}_2 = \begin{bmatrix} 1.0011141473 \\ 0.0099852063 \end{bmatrix} \approx \theta = \begin{bmatrix} 1 \\ 0.01 \end{bmatrix} \tag{5.67}$$

Using the 'regular' algorithm with the numerical approximation to the gradient, one gets:

$$\hat{\boldsymbol{\theta}}_2 = \begin{bmatrix} 1.0014724702 \\ 0.0099816617 \end{bmatrix} \approx \theta = \begin{bmatrix} 1 \\ 0.01 \end{bmatrix} \tag{5.68}$$

In figure (5.5) the output vector of this model (after 2 iterations) is plotted together with the measured data. The system is completely identifiable. The difference between the estimated model and the measurements corresponds exactly with the added noise.
This was a very simple example. The system is completely identifiable. The Fisher information matrix is non-singular and convergence is reached after two updates in the parameters.
The algorithm recognized the nonsingular information matrix and determined the parameter update by using a regular inverse of the Fisher information matrix. The algorithm is also tested using a full rank pseudo inverse from a singular value decomposition. As expected, this leads to comparable results.

Obviously, the algorithm still has to be tested for a singular Fisher information matrix. In order to do this, the simple example can just be extended to contain one or multiple linear dependencies in the parameters that are to be estimated. This example will be presented in the next section.

5.7   Simple example with a singular information matrix

The example used in this section, is a modification of the example from the previous section. The input signal and the gaussian noise are kept the same.

5.7.1   Measurement data

The measurement data in this example will be generated using the 'real' idealized model and adding measurement (gaussian) noise and measurement biases.
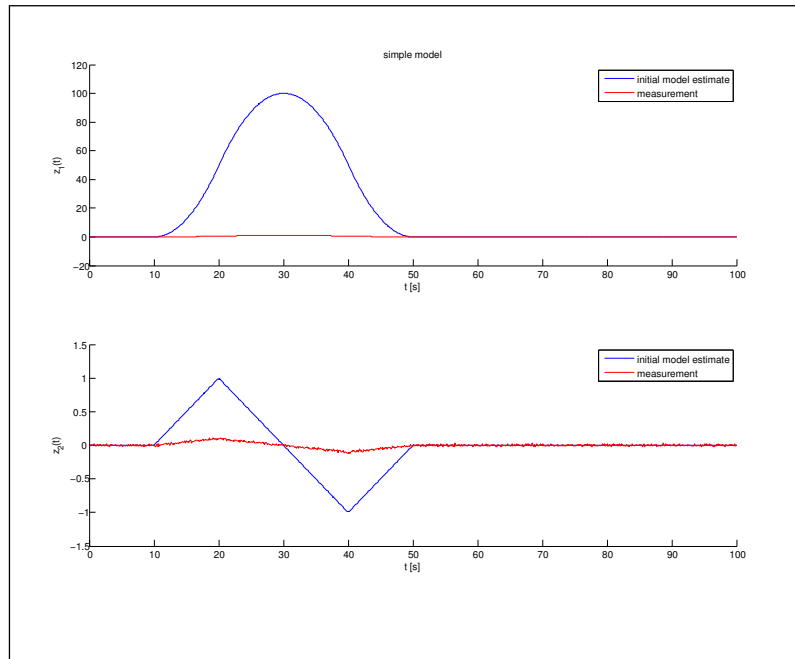
Figure 5.4: *Time histories of the output of the initial estimated model compared with the measurements for the simple example with a nonsingular information matrix. See figure (D.19) in the appendix for the full color image.*
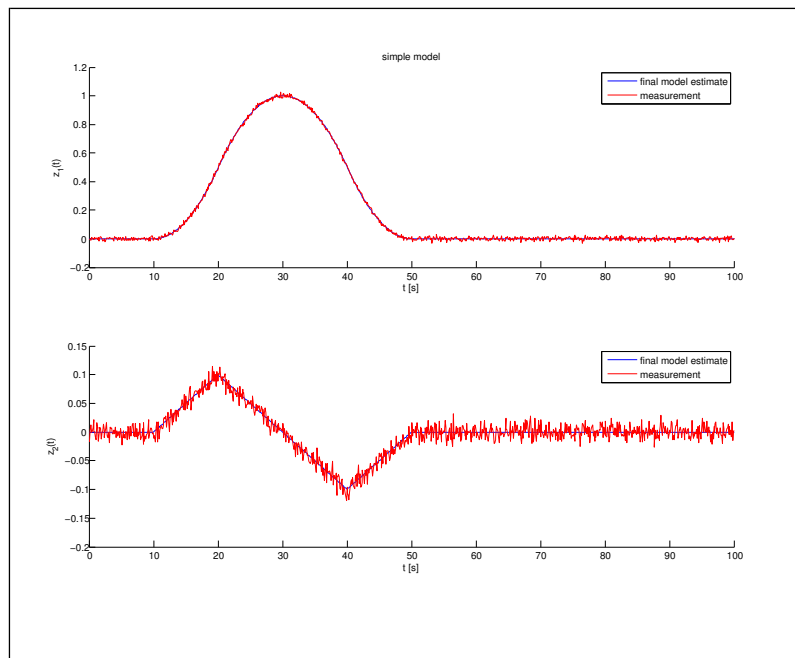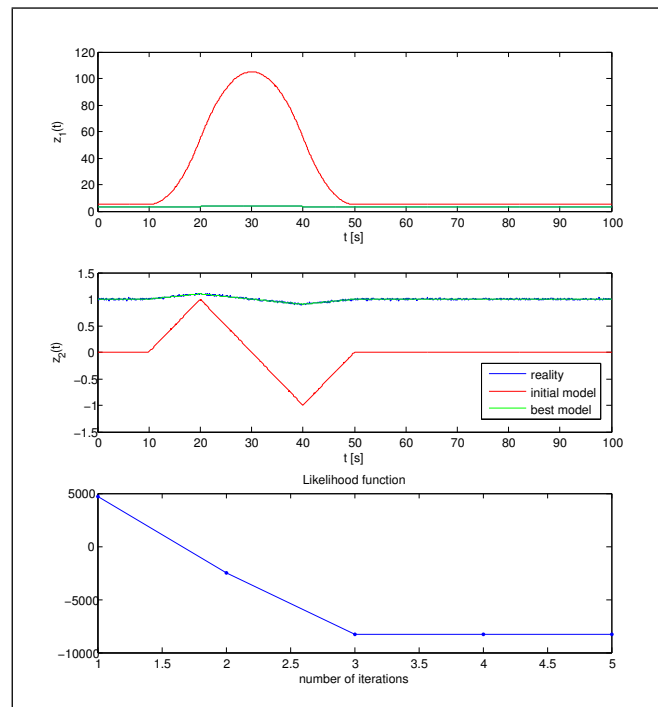

Figure 5.5: *Time histories of the output of the estimated model after 2 iterations compared with the measurements for the simple example with a nonsingular information matrix. See figure (D.20) in the appendix for the full color image.*

The dynamic equations of this linear model are:

$$\dot{\mathbf{x}} = \mathbf{A}\mathbf{x} + \mathbf{B}\mathbf{u} \tag{5.69}$$

$$\mathbf{z} = \mathbf{C}\mathbf{x} + \mathbf{D}\mathbf{u} + \mathbf{b} + \mathbf{v}, \tag{5.70}$$

where:

$$\mathbf{A} = \begin{bmatrix} 0 & 1 \\ 0 & 0 \end{bmatrix}, \mathbf{B} = \begin{bmatrix} 0 \\ 0.01 \end{bmatrix}, \mathbf{C} = \begin{bmatrix} 1 & 0 \\ 0 & 1 \end{bmatrix}, \mathbf{D} = \begin{bmatrix} 0 & 0 \\ 0 & 0 \end{bmatrix}, \mathbf{b} = \begin{bmatrix} 1 \\ 1 \end{bmatrix} \tag{5.71}$$

and $\mathbf{v}$ is gaussian noise with zero mean and standard deviation of 0.01, see figure (5.1) and $\mathbf{b}$ are biases on the measurements.

The number of samples N is again 1000 taken at a sample time of 0.1. The initial state vector is now $[2\ 0]^T$.

5.7.2   Identification

In this section, five parameters of the model will be estimated using only the measurement data of the previous section. Of course, in this simple case, the 'real' values of the parameters are known. Therefore it can be checked very easily whether it converges to the right solution.

The same model structure is used, where at this point five parameters θ_i for $i = 1 \ldots 5$ will be estimated.

$$\mathbf{A} = \begin{bmatrix} 0 & \theta_1 \\ 0 & 0 \end{bmatrix}, \mathbf{B} = \begin{bmatrix} 0 \\ \theta_2 \end{bmatrix}, \mathbf{C} = \begin{bmatrix} 1 & 0 \\ 0 & 1 \end{bmatrix}, \mathbf{D} = \begin{bmatrix} 0 & 0 \\ 0 & 0 \end{bmatrix}, \mathbf{b} = \begin{bmatrix} \theta_3 \\ \theta_4 \end{bmatrix}, \mathbf{x_0} = \begin{bmatrix} \theta_5 \\ 0 \end{bmatrix}. \tag{5.72}$$

The initial values of the parameters to be estimated are:

$$\hat{\boldsymbol{\theta}}_0 = \begin{bmatrix} 10 \\ 0.10 \\ 2 \\ 0 \\ 3 \end{bmatrix} \tag{5.73}$$

It can be derived from the state equations that there is a linear dependency between the third and the fifth parameter. It can be shown that the following dependency holds:

$$\theta_3 + \theta_5 = \hat{\theta}_3 + \hat{\theta}_5 \tag{5.74}$$

As a result of the singular information matrix, there are now multiple solutions to the minimization problem.

In figure (5.6) the output vector of this initial model is plotted together with the measured data. Obviously, there is a significant difference.

After 3 iterations (that is 2 parameter updates) the minimum has basically been reached, see also figure (5.6), showing the Likelihood function as a function of the iteration steps. After 5 iterations one gets the following results:

$$\hat{\boldsymbol{\theta}}_5 = \begin{bmatrix} 1.0036224015 \\ 0.0099673041 \\ 0.9997458060 \\ 1.0000159790 \\ 1.9997458609 \end{bmatrix} \approx \theta = \begin{bmatrix} 1 \\ 0.01 \\ 1 \\ 1 \\ 2 \end{bmatrix} \tag{5.75}$$

In figure (5.6) the output vector of the initial model and that after 5 iterations have been plotted together with the measured data, see figure (5.7) that zooms in on the measurements. Figure (5.8) shows the innovation of the estimation, which is clearly unbiased. The difference between the estimated model and the measurements corresponds again very well with the added gaussian noise.

The standard deviation is determined from the (pseudo) inverse of the Fisher information matrix, see further section 6.10:

$$\sigma_\theta = \begin{bmatrix} 0.0083159 \\ 8.2949 \cdot 10^{-5} \\ 0.00018577 \\ 0.00030289 \\ 0.00018577 \end{bmatrix} . \tag{5.76}$$

The order of magnitude of these values comply with those of the errors in the estimated parameters:

$$\varepsilon = \theta - \hat{\theta}_5 = \begin{bmatrix} -0.0036224 \\ 3.2696 \cdot 10^{-5} \\ 0.00025419 \\ -1.5979 \cdot 10^{-5} \\ 0.00025414 \end{bmatrix} , \tag{5.77}$$

meaning that the estimation is also efficient.

This example had identifiability problems due to the linear dependence in the parameters and consequently a singular information matrix. Although, using the rank deficient solution leads to very good results at a very fast convergence, the minimum is basically reached after 2 parameter updates.

The algorithm recognized the singular information matrix and determined the parameter update by using a reduced order pseudo-inverse of the Fisher information matrix. The algorithm tried for this small case all directions up to the full rank (4) of the (5 x 5) information matrix.

Obviously, these good results give confidence in the rank-deficient algorithm, but there

is a catch. For this rank-deficient problem, there are, many possible solutions due to the linear dependency in the parameters. The solution that will be found is the one closest to the choice of initial parameters. In practice, this will not really pose a problem as the desired or acceptable solution, will be the one closest to the initial set of parameters.

Furthermore, it was mentioned in section 5.5.1 that the algorithm converges to a local minimizer, from almost every starting point. For the rank-deficient problem, there are, however, many local minima that do not have to correspond to a global minimum. Finding a global minimum cannot be guaranteed by the algorithm.
It is stated in [Den96] that this is a very difficult problem that has not been as extensively studied or as successfully solved as that of finding a local minimum.
This is certainly a limitation of the algorithm. As long as the initial parameter estimates are close enough to the real values and the modelling structure represents the real behavior close enough, than convergence to the real parameters or at least a good correspondence in the output will be achieved.
The following two examples, will show that only minimal changes can already lead to poor results.

Modification 1

The third parameter used to describe the real model is changed from 1 to 4:

$$\theta = \begin{bmatrix} 1 \\ 0.01 \\ \mathbf{4} \\ 1 \\ 2 \end{bmatrix} \tag{5.78}$$

everything else is kept the same. The results of the optimization are plotted in figures (5.9) and (5.10). Now there are at least 5 iterations necessary (instead of 3). Furthermore, it can be seen in figure (5.10) that the correspondence for the second component of the output vector ($\hat{z}_2$) is poor. The parameter estimate also does not correspond to the 'real' parameters:

$$\hat{\boldsymbol{\theta}}_5 = \begin{bmatrix} 10.002023609 \\ 0.0010013264 \\ 2.4999224815 \\ 1.0005381005 \\ 3.4999224845 \end{bmatrix} \neq \theta = \begin{bmatrix} 1 \\ 0.01 \\ 4 \\ 1 \\ 2 \end{bmatrix} \tag{5.79}$$

Although, it can be seen that the third and the fifth parameters are in compliance with equation (5.74). This is an excellent example of the model converging to some local minimum, but not one that gives satisfying results. The results are definitely better then those from the initial model, but it could be better.

Modification 2

This time the fourth parameter, used to describe the real model, is changed from 1 to 4:

$$\theta = \begin{bmatrix} 1 \\ 0.01 \\ 1 \\ \mathbf{4} \\ 2 \end{bmatrix} \tag{5.80}$$

everything else is kept the same.

The results of the optimization are plotted in figures (5.11) and (5.12). There are at least 4 iterations necessary to arrive at a minimum. It can be seen in figure (5.12) that again the correspondence for the second component of the output vector ($\hat{z}_2$) is poor. The parameter estimate is quite good for parameters 3 to 5, but poor for the first two:

$$\hat{\boldsymbol{\theta}}_5 = \begin{bmatrix} 9.9736596948 \\ 0.0010021070 \\ 1.0001425253 \\ 3.9998498199 \\ 2.0001425253 \end{bmatrix} \neq \theta = \begin{bmatrix} 1 \\ 0.01 \\ 1 \\ 4 \\ 2 \end{bmatrix} \tag{5.81}$$

This is another example of the model converging to some local minimum, but not one that gives really satisfying results. The results are definitely better then those from the initial model, but again it could be better.

If the initial estimate of the first parameter is chosen to be 1.5 instead of 10, then the solution converges to the 'correct' values in four iterations:

$$\hat{\boldsymbol{\theta}}_4 = \begin{bmatrix} 0.9867100501 \\ 0.0101345478 \\ 0.9999619424 \\ 4.0002630906 \\ 1.9999619404 \end{bmatrix} \approx \theta = \begin{bmatrix} 1 \\ 0.01 \\ 1 \\ 4 \\ 2 \end{bmatrix} \tag{5.82}$$

Obviously, excellent correspondence with the measurements has now been reached, correspondence is similar to that in figure (5.7) and therefore the plots are omitted.

From this last modification it can be seen that if the initial estimates are chosen close enough to the 'real' parameters, excellent results are obtained. If the initial model is too far away from the 'truth', one of the multiple possible solutions is found, due to the linear dependency in the parameters, that does not have to be close to the desired parameters. Recall that this does not really pose a problem in practice, because the desired solution of the values of the parameters will be that which is closest to the initial values. In addition, the range of desired values can be prescribed by setting boundary values.

Figure 5.6: *Time histories of the output of the initial model and the final estimation compared with the measurements for the simple example with a singular information matrix. See figure (D.21) in the appendix for the full color image.*
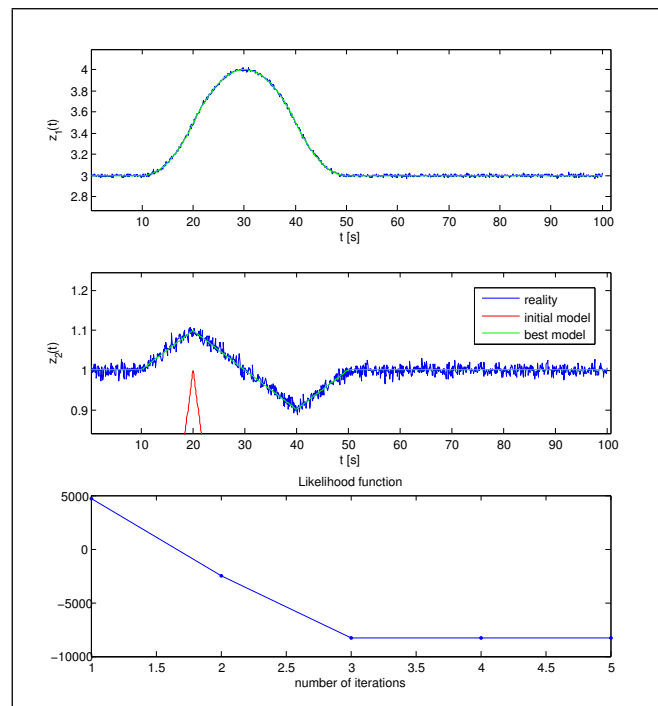
Figure 5.7: *Time histories of the output of the initial model and the final estimation compared with the measurements, zoomed in on the measurements for the simple example with a singular information matrix. See figure (D.22) in the appendix for the full color image.*
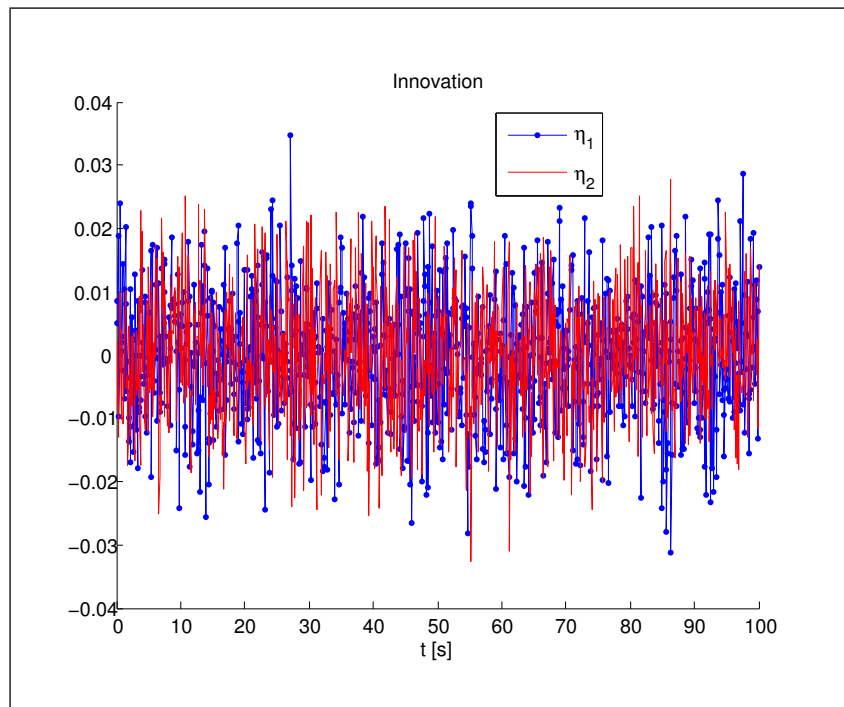
Figure 5.8: *Innovation plotted versus time, for the estimation after 5 iterations (simple example with a singular information matrix).*
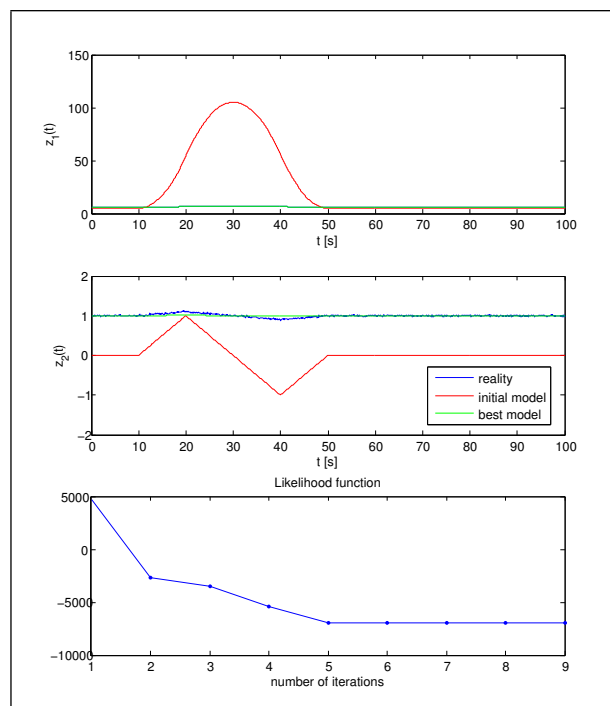
Figure 5.9: *Modification 1: Time histories of the output of the initial model and the final estimation compared with the measurements for the simple example with a singular information matrix. See figure (D.23) in the appendix for the full color image.*
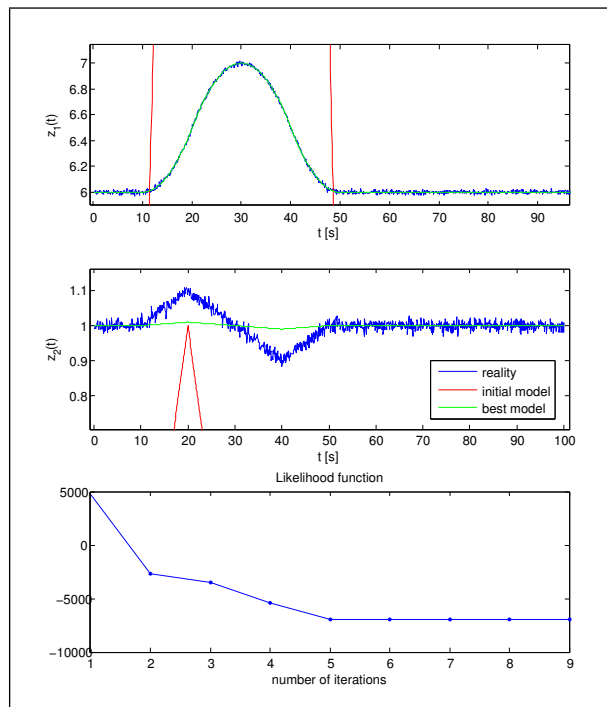
Figure 5.10: *Modification 1: Time histories of the output of the initial model and the final estimation compared with the measurements, zoomed in on the measurements for the simple example with a singular information matrix. See figure (D.24) in the appendix for the full color image.*
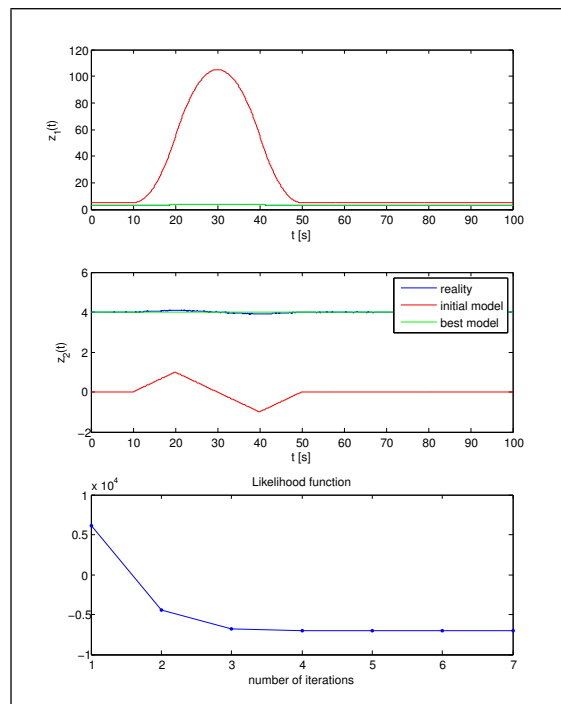
Figure 5.11: *Modification 2: Time histories of the output of the initial model and the final estimation compared with the measurements for the simple example with a singular information matrix. See figure (D.25) in the appendix for the full color image.*
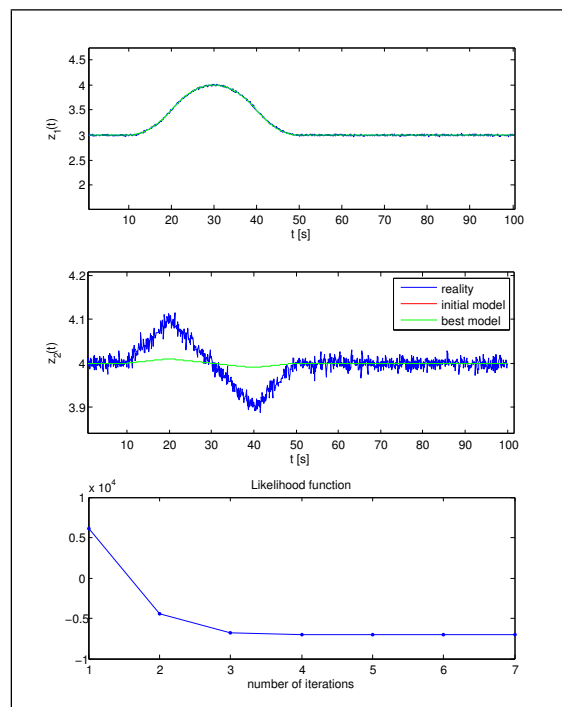
Figure 5.12: *Modification 2: Time histories of the output of the initial model and the final estimation compared with the measurements, zoomed in on the measurements for the simple example with a singular information matrix. See figure (D.26) in the appendix for the full color image.*

Identification of the flight loads monitoring model

The accuracy of parameter estimates is directly dependent on the quality of the flight measured data. Hence, high accuracy measurements of control inputs and of motion variables are a prerequisite for successful application of the modern methods of flight vehicle system identification.

Therefore, in section 6.1 a general overview of the flight test instrumentation system is given. Section 6.2 describes the loads measurement by strain gauges in specific. The details of the flight loads monitoring model are presented in section 6.3. This model is the basic model that is used in the several identification examples of section 6.4 to 6.8.

For clarity reasons, section 6.9 presents a summary of the identification examples. Model validation is the topic of section 6.10, where it will be dealt with issues related to the process of determining the correctness, accuracy, adequacy and applicability of the identified model.

6.1 General flight test instrumentation

Flight test instrumentation is the equipment concerned with the recording and monitoring of the motion and the condition of the experimental aircraft. It can monitor various parameters from the temperatures of specific components to the speed of the engines. This is often displayed in the cockpit or cabin to allow the aircrew to monitor the aircraft in flight, and is usually recorded on digital or magnetic media to allow the data to be interpreted later. Digital storage media like a solid state recorder that use flash memory cards have the advantage that they have no moving parts. This considerably enhances reliability and reduces the required maintenance compared to magnetic tape recorders.

The main components of the instrumentation system are:

159

- a data management system, storing information about the configuration of the instrumentation into a database,

- an airborne measurement system, containing a data acquisition unit, a state recorder, a telemetry transmitter, etc.

- a ground-based data processing system.

The data acquisition equipment sometimes has to be connected directly to aircraft systems. Consequently, safety aspects become an important issue and certification is necessary.

The focus in the present work lies on the loads measurements gathered during loads specific flight tests, see chapter 2 for more information on the loads environment. In order to be able to reconstruct the specific motion and response of the aircraft during a certain interval of these flight tests, several other important quantities have to be measured and recorded as well. The relevant quantities are:

- Air Data

    - static and dynamic pressure,

    - Indicated Airspeed (IAS), True airspeed (TAS),

    - total temperature and static air temperature,

    - angle of attack and angle of sideslip by a wind vane,

    - pressure altitude,

- Flight path data

    - attitude angles: roll, pitch, yaw, from a strapdown IRS (Inertial Reference System) or from the INS (Inertial Navigation System[1]),

    - ground speed,

    - translational accelerations,

    - rotational rates[2],

    - position (INS and GPS),

- Control data

    - rudder deflection,

    - aileron deflection,

    - elevator deflection,

    - tail plane deflection,

---

[1]An integral unit providing measurements of translational accelerations and rotational rates and those of attitude angles. The INS is sometimes called IMU (inertial measuring unit)

[2]The aerodynamic model from section 4.4 comprises contributions due to rotational rates

- spoiler deflection,

- slat/flap settings,

- engine data

  - fan speed,

  - other relevant engine settings necessary for accurate thrust prediction (the quantities that are needed are engine model specific, see also section 4.6. Examples of other important quantities that provide information about the status and performance of the engine are: fuel flow, engine pressure variation (EPR) and inter-turbine temperature, (ITT)),

- mass condition

  - loading plan (before flight),

  - fuel distribution.

This list can or should be further extended, depending on the specific application (aircraft, engine type, exact purpose of the flight test, etc.) and its corresponding requirements. In [Kli06] a general approach for developing a flight test instrumentation system is described, with applications for an F-16 and for helicopters such as Apache, Chinook and Cougar.

Some other aspects, related to data recording also affect data analysis. These are mentioned here, without going into details.

1. In case dynamic response is of primary importance, it needs to be ascertained that raw data from the INS is available, because some INS incorporate low pass filters.

2. The measurement of attitude angles are mostly provided by the INS, usually through internal integration of measured angular rates.

3. The minimum sampling rate, that is the rate at which data is sampled and recorded, should be twice the frequency of interest according to reference [Jat06]. In general, the data is sampled at a much higher frequency. In reference [Jat06]. it is stated that a sampling frequency of 20-25 HZ is usually sufficient for rigid body aerodynamic model estimation. For an extended model comprising rigid body and structural modes, a higher sampling rate is necessary.

4. The anti-aliasing filter for all measurements should have the same cut-off frequency, so that all signals will have the same time delays introduced by such filters.

5. Recording of raw data is usually preferable.

6. In addition to data acquisition and recording, data synchronisation is a very important aspect to be considered. In processing the measurement data it is very important to use the values of the quantities valid for the same instant in time. It is not a trivial task to enforce the exact simultaneous measurement of multiple

measuring devices/systems. Alternatively, a quantity can be measured and stored together with information on the time instant of the measurement, such that it is possible to perform a synchronisation in a post-process.

7. It is recommended to have immediate data processing of the most important aspects either onboard or ground-based by a telemetry link. This gives opportunity to modify the tests or to repair or make corrections to the measuring equipment. The later it is discovered that all or some of the measurements are incomplete or incorrect, the more difficult it gets to redo these tests, if not practically impossible or at least extremely expensive.

8. All sensors should be calibrated in laboratory and in situ as far as possible.

9. Data reduction should be avoided at the time of recording. Once the information is lost due to data compression in the recording, it can not be recovered.

Most of the parameters mentioned above are part of the mandatory flight recorder parameter acquisition required by the regulatory agencies. These parameters are recorded by the Flight Data Acquisition and Management System (FDAMS) or an equivalent system that is onboard of every commercial transport aircraft. This mandatory flight recorder parameter acquisition was initially regulated to aid in incident investigation. The regulations continue to increase the quantity and quality of this recorded flight data to help to further improve investigations. Furthermore, this recorded data does help the airlines in their maintenance programs to increase safety and reduce costs. It is also used in post-flight monitoring to determine the adherence to procedures and the exceedance of limits.

In the next section the instrumentation is described that is needed specifically for the loads measurements by strain gauges which is not (yet) part of the 'standard' parameter acquisition.

6.2   Loads measurement by strain gauges

Knowledge on the mechanical stress inside the material of the structure is important to evaluate the exposure of the material to loading. Direct measurement of mechanical stresses is practically impossible during operating conditions. A practical method to determine the material stresses experimentally is based on the discovery done by Robert Hooke in 1678. He discovered a relationship between material stress and the resulting deformation. This deformation, called 'strain', appears at the surface of the object. Consequently, it is accessible for measurement.
In the beginning, these measurements were performed mechanically using complicated constructions. These measuring devices had only limited application, see further [Hof87]. Their limitation to static measurements is their strongest limitation.

From about 1935, people got aware in this context of the effect published already in 1843 by Charles Wheatstone. The effect that is meant is that of the change in resistance of an electric conductor through the influence of mechanic loading. It took over 80 years

until this phenomenon was used technically. One of its reasons is that the change in resistance of a wire loaded by tension is very small. The development of amplifiers first established the necessary premises.

Around 1938, two people, Edward E. Simmons and Arthur Claude Ruge, independently developed the idea further to use this effect for measuring purposes, see reference [Hof87]. The actual 'electric resistance-strain gauge with bonded grid' [3] as it is known now, was invented by Arthur Claude Ruge of the Institute for Seismology from the Massachusetts Institute of Technology. He developed it to enable the measurement of the loading due to vibrations from simulated earthquakes on very thin-walled watertanks. The existing strain measurement devices could not be used for these very thin-walled models. Ruge used a thin resistance wire glued as meander on top of a piece of thin tissue paper, which is the so-called carrier foil. He studied the characteristics of this formation by gluing it to a bending beam and comparing it with familiar strain measurement devices. He found good correspondence and a linear relation between the strain and the signal over the complete measurement range for both positive as negative strains, as well as a good stability characteristic of the point of origin.

The biggest innovation in this, was to glue the resistance wire on a carrier foil. Consequently, an independent measurement device, that can be handled freely, was developed that could be glued to any surface of interest. It is very thin and light-weight. It needs no clamping force and creates practically no retroaction, such that it can be used for measurements on thin objects as well. The first prototypes of the strain gauge showed already superior behavior compared to all till then familiar strain measurement devices.

There are several types of strain gauges:

- metallic strain gauges, see figure 6.1 for a typical buildup of a bonded metallic strain gauge produced by chemical etching,

- semiconductor strain gauges (more sensitive than metallic strain gauges),

- vacuum-metallised strain gauges ,

- capacitance strain gauges (developed for usage at high temperatures up until 800 degrees Celcius),

- piezo-electric strain gauges (See reference [Sir00] for a comparison between piezo-electric strain gauges and conventional foil strain gauges. It is shown there that piezo-electric strain gauges have promising characteristics for smart structural sensing applications. Furthermore, it is also stated in reference [Sir00] that it is not advisable to use these sensors to measure strain levels more that the order of 150 microstrain. This is a consequence from nonlinearities and change in material properties with stress that affect the accuracy of the calibration.),

- strain-optical strain gauges (never attained practical value and not available anymore).

---

[3]in german: elektrische Widerstands-Dehnungsmessstreifen mit gebundenem Gitter
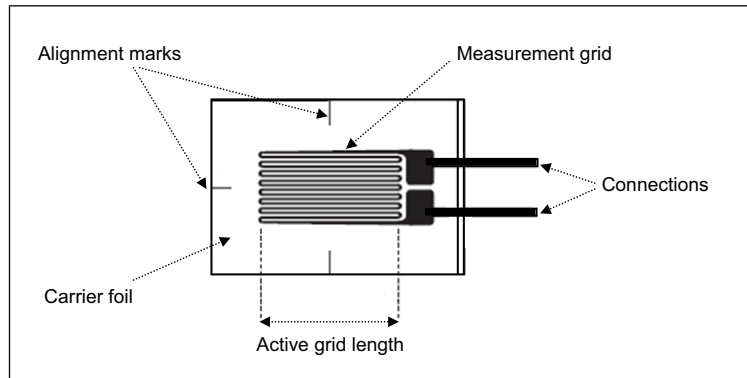
Figure 6.1: *Typical buildup of a bonded metallic strain gauge produced by chemical etching.*

- Mechanic strain gauges (data can be analysed after the measurements only).

The metallic strain gauges and semiconductor strain gauges are two kinds of so-called electric resistance strain gauges. Here only such electric resistance strain gauges will be considered. For more information on the other types of strain gauges one is referred to [Hof87].

6.2.1   Working principle of a strain gauge

The measurement of strain by a strain gauge requires a lossless transfer between the strain of the object of interest and that of the strain gauge. This necessitates a close connection between the strain gauge and the object. This close connection can best be achieved by special glues. Other types of bonding, like spot welding or ceramic bonding are used for special applications in the steel industry or at high temperatures.
In most cases only the surface of an object is accessible for measurement. Internal measurement of solid parts are only possible, if the strain gauges are encapsulated and already embedded during the production of the solid.
The transferred strain from the object to the strain gauge causes a measurable change of their electric resistance. This change in resistance is partly due to deformation of the conductor, partly due to the change in specific resistance σ of its material due to structural changes.
The change in resistance of a metallic strain gauge can be written as:

$$\frac{dR}{R_0} = \varepsilon(1 + 2\nu) + \frac{d\sigma}{\sigma} \tag{6.1}$$

where R is the electric resistance, ε is the strain and ν is the Poisson ratio. The first term on the right handside of this equation is the geometric part. The second term describes the part from the structural changes of the material.

The change in electric resistance for semiconductor strain gauges is, contrarily to metallic strain gauges, mostly due to differences in mobility of the electrons. The geometric portion is only a fraction (less then 2 %) of the total change in resistance. Here only metallic strain gauges will be considered, because these were applied in the present tests.
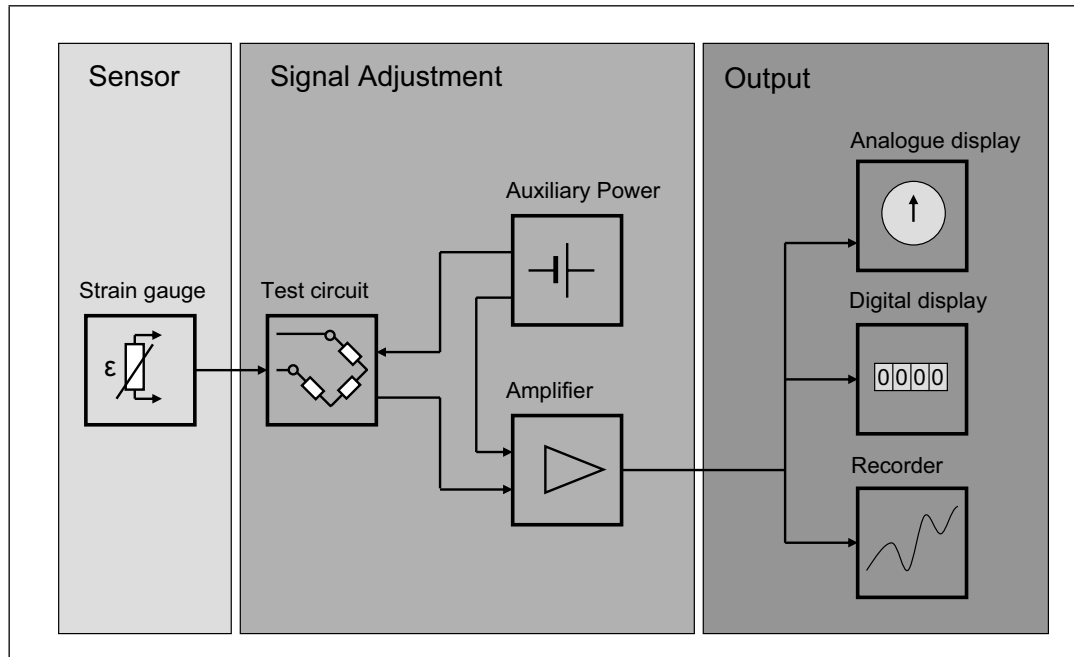
Figure 6.2: *Schematic overview of the inevitable parts of the measurement chain. This measurement chain is used in the measurement of strains by strain gauges.*

6.2.2 Measurement chain

The strains that are to be measured with the strain gauges are usually very small. Consequently, the changes in resistance will be very small and will not be measurable directly anymore by an Ohmmeter for example. This necessitates the strain gauge to be incorporated in a measurement chain, see figure (6.2). This measurement chain enables the exact determination of the change in resistance of the strain gauge.

The first part of the measurement chain is the strain gauge. The strain gauge transforms the mechanical strain into a change of electric resistance. The second part of the measurement chain is a test circuit (here a Wheatstone bridge) of which the strain gauge is a branch. Both the strain gauge as the test circuit are passive members of the measurement chain. Energy must be supplied to get a usable signal. This energy is taken from a separate source. Usually, a constant voltage is taken, occasionally a constant current.

The third member of the measurement chain is an amplifier. It amplifies the output voltage from the Wheatstone bridge to a sufficiently large signal (voltage or current) for the indicating instrument.

The fourth member of the measurement chain is the display. It transforms the output signal of the amplifier to a form perceivable by human sense organs. This could be the deflection of a needle (analogue) or by digital numbers on a display. If a time varying strain (a dynamic process) has to be measured, recording devices must be used instead of displays.

This is only a schematic overview of the inevitable parts of the measurement chain. In practice, this can be extended with extra devices, like filters, peak value detection, etc.

6.2.3 Factors of influence

Environmental circumstances like high pressures or magnetic fields have an influence on the behavior of strain gauges. A description of the influence from environmental impacts like high pressures, vacuum conditions, radiation, magnetic fields on strain gauges can be found in reference [Kli06]. In the following, the influences from temperature and humidity are presented. Also in reference [Kli06] a more extensive discussion on these factors of influence can be found.

Temperature

Strain gauges are used to determine mechanical loading by measuring the strain. However, strain can also occur in the absence of mechanical forces, namely when heating/cooling the object. Every object changes its dimensions when its temperature changes. This change in dimensions due to temperature induces no mechanical stress, if:

1. free expansion or contraction of the object is not hampered,

2. the object has a uniform temperature.

The resulting strain is called heat strain, contrarily to mechanical strain. As soon as the heat strain is hampered, stresses occur in the material. The amount of strain per Kelvin depends on the material and on the temperature. Two aspects are important when considering the influence of temperature on the quality of the measurement: the temperature level and the variation in temperature during the measurement. Changes in temperature affect mostly the point of origin of the measurement value of the strain gauge. This error can be limited to an acceptable amount by selecting self-compensating strain gauges or by applying an adequate compensation method.

An example of such a compensation method is presented in reference [Wel80]. Here a method is described that improves the temperature stability of semiconductor strain gauge transducers that can also be used in case of metallic foil strain gauges. It is a compensation method that uses active linear circuits to correct for both zero offset and sensitivity changes. The temperature compensation in [Wel80] is achieved by an additional circuit containing four amplifiers with variable gain. By suitable adjustment, the gain of these amplifiers automatically correct for the temperature induced zero offset and sensitivity changes in the transducer bridge.

There are many different types of strain gauges. It depends on the application and its specific requirements which type would be most optimal to use. If a direct current amplifier is connected to the strain gauge, it is best to use a strain gauge with a high resistance, fed using a high voltage. This improves the amplifier induced zero drift. On the other hand do high resistance closed measuring circuits more easily pick up interfering impulses when compared to those with low resistance. This would lead easily to measurement errors, if no efficient shielding is used.

The sensitivity of a strain gauge is indicated with a k-factor, which is defined as:

$$k = \frac{\Delta R / R_0}{\varepsilon},$$
(6.2)

The value of the k-factor is characteristic for the complete assembly of the strain gauge. The value of the k-factor is dependent on the temperature.

Strain gauges should react only by a change in resistance due to strain in their 'active' direction. If (small) changes in resistance occur due to strains across the active direction, the strain gauge is called cross-sensitive. The cross sensitivity q of a strain gauge is defined by:

$$q = \frac{k_q}{k_l},$$
(6.3)

where k_q is the strain sensitivity perpendicular to the direction of measurement and k_l is the sensitivity in the direction of measurement, see also equation (6.2). The geometry of the measurement grid of a strain gauge is designed such that the cross sensitivity will have a very small value. Other considerations, however, influence the design of the strain gauge as well, such that this is not always possible.

Thermal shift

At constant mechanical loading, the signal of the strain gauge can vary due to changes in temperature. This is called the thermal shift of a strain gauge. A thermal shift is a reversible process. It disappears as soon as the original temperature condition is obtained again.

If the object of interest experiences a variation in temperature in addition to the mechanical loading, the resulting strain is the sum of mechanical strain and thermal strain. The thermal portion is the error contained in the measured value of the strain. This error can be avoided or eliminated by using self-compensating strain gauges or by application of compensation methods as was already mentioned above.

In self-compensating strain gauges, one uses the effect that the temperature coefficient of the electric resistance of the material of the measurement grid can be changed by changes in the alloy or by heat treatment. The strain gauge is adjusted to the thermal strain of the object of interest.

The thermal shift of a strain gauge depends on the shape of the surface to which it is bonded. Applications in which the measuring grid of the strain gauge has a curvature in its active direction, have a different thermal shift compared to those that are planar. The influence from this curvature gets smaller, the more similar the thermal strain coefficients of the material of the object and that of the glue and the carrier of the strain gauge are. Self-compensating strain gauges should be used on planar surfaces. On curved surfaces their compensating effect gets incomplete.

Thermal drift

Thermal drift is not to be confused with thermal shift. Thermal drift arises mainly by structural changes and oxidation or corrosion of the grid material. It can also occur due to relaxation of the strain gauge or its glue due to longer heat exposure. Thermal drift is dependent on time and temperature and causes irreversible changes in the point of origin of the strain gauge. Thermal drift only appears as an error in absolute measurements. It can be avoided by using a Wheatstone bridge.

Humidity

Humidity is similar to temperature a main cause for instable strain gauges. Changes in humidity during a measurement cause uncontrollable changes in the point of origin. This error appears especially in absolute measurements, it sometimes also contributes to changes in sensitivity.

6.2.4   Wheatstone bridge

Figure (6.3) shows an electric diagram of a Wheatstone bridge, named after its inventor Sir Charles Wheatstone (1802-1875). The resistances R_1 to R_4 build the four branches of the Wheatstone bridge. U_B is the feeding voltage, U_A is the output voltage or measuring signal.
The voltage over the two branches R_1, R_2 and R_3, R_4 is partitioned corresponding to the magnitude of the resistances R_1 to R_4. The output voltage can be calculated as:

$$U_A = U_B \left(\frac{R_1 + \Delta R_1}{R_1 + \Delta R_1 + R_2 + \Delta R_2} - \frac{R_4 + \Delta R_4}{R_3 + \Delta R_3 + R_4 + \Delta R_4} \right) \qquad (6.4)$$

For strain gauge measurements, it is required for a Wheatstone bridge that resistance R_1 is equal to R_2 and that R_3 is equal to R_4. Neglecting terms with $\Delta R_X \cdot \Delta R_Y$, it can be derived that:

$$\frac{U_A}{U_B} = \frac{k}{4} (\varepsilon_1 - \varepsilon_2 + \varepsilon_3 - \varepsilon_4) \qquad (6.5)$$

The displayed strain ε_d can be written as:

$$\varepsilon_d = \frac{4}{k} \cdot \frac{U_A}{U_B} = \varepsilon_1 - \varepsilon_2 + \varepsilon_3 - \varepsilon_4. \qquad (6.6)$$

In these equations it is assumed that all resistances of the Wheatstone bridge R_1 to R_4 change. This is not the case if only part of the branches are equipped with strain gauges and the others with complementary resistances. To distinguish between them, these bridges are called: quarter bridges, half bridges, full bridges depending on the number of strain gauges in the circuit.
The compensation principle of the Wheatstone bridge is that disturbances that influence both neighboring branches of the Wheatstone bridge, have a different sign and thus diminish or even cancel each other in the output voltage.
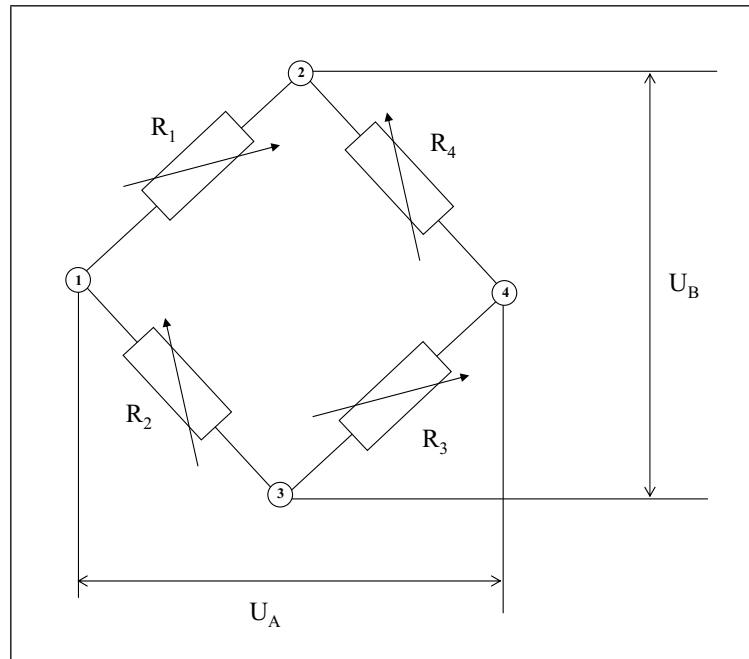
Figure 6.3: *Electric diagram of a Wheatstone bridge, where U_A is the output voltage, U_B is the feeding voltage, R_i is the resistance of branch i where $i = 1 \ldots 4$.*

6.2.5   Calibration of measuring system

The calibration of a single strain gauge that is used to measure the local stress is quite straightforward. First, the zero shift is determined. That is, if the object is unloaded the displayed value should be zero. Obviously, the object and its surroundings should experience no temperature variations as these would give rise to thermal stresses. Next, the object is loaded with a known load, that produces known stresses. Then the amplification factor of the amplifier is correspondingly adjusted.

In the present investigation, structural loads, such as shear force[4], bending moment and

---

[4]These shear forces are not to be confused with the shear stress τ

code:	component:	η [-]:	shear:	bending:	torsion:
1-2	WR, WL	0.11	x	x	x
4-5	WR	0.18	x	x	x
10-12	WR	0.37	x	x	x
20-21	WR, WL	0.55	x (WR)	x (WR, WL)	x (WR)
28-29	WR	0.74	x	x	x
37-38	WR	0.95	-	x	-
WLT	winglet	1.00	-	x	-

Table 6.1: *The six wing loads stations and the loads station at the winglet root and their location. (WR: wing right ; WL: wing left)*

torsion along structural components, are measured using strain gauges. There are six so-called loads stations on the right wing, two on the left wing and one at the right winglet root, see table (6.1). Contrarily to the measurement of local stresses, the selection and calibration of the strain gauges then gets more complicated or less straightforward. Although the use of a strain gauge for loads measurement is in some respect similar to its use in stress determination, a somewhat different approach is required since now strain is to be used as a means of obtaining information about the loads.

In flight research the loads of primary interest are generally those on wing or tail surfaces. In order to simplify the exposition of the procedure, descriptions are generally given in terms of a cantilever structure such as a wing or tail. However, the methods can be used with other structures as well.

Consider the measurement of the integrated bending moment along the wing structure. This is not a local load/stress, but more the integrated loading from the wing tip to the span position of concern, thus one value along the total chord length of this spanwise position. Such a structural load can generally not be measured by a single strain gauge, but should be determined from a combination of multiple strain gauges. The optimal number of strain gauges and their positions can be determined from a loads calibration procedure. Notice, that this kind of calibration comprises much more then just the determination of the zero shift and amplification factor mentioned at the beginning of this section.

A second difficulty stems from the fact that the aircraft structure is not loaded under one discrete force/moment, but by distributed gravitational loads, external pressure distributions, etc. There are many possible loading conditions. Each of these loading conditions have a contribution to the stress as measured locally. These stresses are the sum of stresses from torsional loads, bending loads, et cetera. It is very difficult to determine which portion was caused by which load.

In one measurement method, a series of point loads is applied to the structure. The loads equations are then derived via a least squares curve fitting algorithm using the strain gauge responses to the applied loads. An example of such a method that is used often in praxis, is the method developed by T.H. Skopinski, W.S. Aiken and W.B. Huston in 1954, see reference [Sko54]. In this method the parameters of the so-called Skopinski-equations (loads equations) are determined in the calibration procedure. However, the structure is usually highly instrumented with strain gauges and the number and selection of gauges used in the loads equation can be problematic. In reference [Nel94] an improved technique is presented that uses a genetic algorithm to choose the strain gauges used in the loads equations. The performance of this genetic algorithm is also compared with that of the so-called T-value technique and the Best Step Down technique, see [Nel94] for more information on these methods.

In experimental flight tests, it is frequently necessary to measure the shear force, torsion and bending moments on various portions of a vehicles structure, such as an aircraft wing. The strain gauges are placed strategically throughout the structure to ensure that all load paths are covered and to build in redundancy in case of gauge failure. The last aspect is quite important because strain gauges become relatively inaccessible once they are placed in the aircraft. It is necessary to locate the gauges at positions where the stress

levels will be adequate to obtain good sensitivity and simultaneously be away from areas of local stress concentrations. Ideally, the gauges are placed at a position such that a shear bridge would respond only to shear force, a moment bridge only to moment and so forth. Generally, it is only possible in an elementary truss type of beam that locations can be found where such a simple relation between load and strain exists.

Before the recorded outputs of selected strain gauges can be used to determine the applied loads, a ground calibration test must be done. Usually not all strain gauges are used in flight.
The ground calibration test consists of applying known loads to specific locations on the structure and recording the output from all the strain gauges. Least squares fitting of the ground test data from selected gauges results in a calibration equation. This equation is used to compute the in-flight loads from the recorded gauge readings.
Further important issues that should be addressed in the ground calibration test, are where to place the calibration loads and how many to use to represent in-flight loads. It is vital that the calibration loads be representative of in-flight loads to the best available knowledge.

In reference [Lok04] a parametric study is presented of various aircraft wing-load test features that affect the quality of the resultant derived shear force, bending moment and torque strain gauge load equations. The effect on the accuracy of the derived strain gauge equation has been compared for: single point loading compared with distributed loading, variation in applied test load magnitude and number of applied load cases. The object of study in reference [Lok04] has been an extensive wing-load calibration test of the (Active Aeroelastic Wing) F/A-18 aircraft. It was shown that the distributed-loading approach generally yields superior results when compared to those derived from a single-point loading approach. This can mainly be explained by the much higher total net load produced in the distributed loading cases than in the single-point loading cases. In the single-point loading cases, only a small amount of the load envelope can be exercised by the loading. This is a typical limiting factor of single-point loading. When loads are introduced to the test structure through surface-contact load pads, there is often a surface peak pressure limit, as imposed by local skin bending or substructure-crushing considerations.
The effect of load magnitude was also studied separately and was found to be significant. However, in the test a peak of 70% design limit load was applied, where it was found that already 50% of design limit loads would have given similar results. Although two dozen of distributed-load cases were available, it was also shown that only 6 diverse distributed-load cases would already lead to satisfactory equations.

6.3   Flight loads monitoring model

The measurements used in this thesis stem from flight test manoeuvres that consisted of normal cruise flights followed by coordinated turns with a slowly increasing roll angle.

It may be assumed that these flight conditions are quasi-steady. It may also be assumed that the state of the aircraft can be derived from the flight test measurements. The biggest uncertainty is expected to be contained in the parameters of the aerodynamic model and any physical effects that are not captured by the present model.

The main unknown that also has to be simultaneously reconstructed from the measurements is the deformation of the aircraft and therefore also the deformation induced loads. The prediction of the deformation of the aircraft and the corresponding deformation induced loads depend on the values of the parameters of the (aerodynamic) model. The equations of motion of the flexible aircraft will be solved for the deformation of the airframe in the following.

The dynamic equations of motion for the flexible aircraft can be written in terms of generalized coordinates as, compare with equation (4.67):

$$\mathbf{M}_{HH} \cdot \ddot{\mathbf{q}}_H + \mathbf{C}_{HH} \cdot \dot{\mathbf{q}}_H + \mathbf{K}_{HH} \cdot \mathbf{q}_H = \mathbf{F}_H = \mathbf{F}_{aero} + \mathbf{F}_{thrust}, \tag{6.7}$$

where $\mathbf{q}_H$ are the modal coordinates. This modal reduction is performed for the statically (Guyan) condensed aircraft model instead of the full model, explaining the notational difference between equations (4.67) and (6.7). See section 4.2 for a detailed description of these model reduction methods.

The modes can be divided into rigid body modes $\mathbf{q}_B$ (in general the first six modes, i.e. the three translational and the three rotational modes):

$$\mathbf{q}_B = \begin{bmatrix} x \\ y \\ z \\ \phi_x \\ \phi_y \\ \phi_z \end{bmatrix}, \tag{6.8}$$

and flexible modes $\mathbf{q}_F$. The modal coordinates of the rigid body modes are known from flight test measurements. In order to be able to solve for the modal coordinates of the flexible modes, the equations of motion can be partitioned as:

$$\begin{bmatrix} \mathbf{M}_{BB} & \mathbf{M}_{BF} \\ \mathbf{M}_{FB} & \mathbf{M}_{FF} \end{bmatrix} \begin{bmatrix} \ddot{\mathbf{q}}_B \\ \ddot{\mathbf{q}}_F \end{bmatrix} + \begin{bmatrix} \mathbf{C}_{BB} & \mathbf{C}_{BF} \\ \mathbf{C}_{FB} & \mathbf{C}_{FF} \end{bmatrix} \begin{bmatrix} \dot{\mathbf{q}}_B \\ \dot{\mathbf{q}}_F \end{bmatrix} + \begin{bmatrix} \mathbf{K}_{BB} & \mathbf{K}_{BF} \\ \mathbf{K}_{FB} & \mathbf{K}_{FF} \end{bmatrix} \begin{bmatrix} \mathbf{q}_B \\ \mathbf{q}_F \end{bmatrix} = \begin{bmatrix} \mathbf{F}_B \\ \mathbf{F}_F \end{bmatrix}. \tag{6.9}$$

Recall from section 4.3 that the mean axes system decouples the equations of motion such that the rigid body motion and the flexible motion of the aircraft are coupled only through the generalized external forces, or:

$$\begin{bmatrix} \mathbf{M}_{BB} & \mathbf{0} \\ \mathbf{0} & \mathbf{M}_{FF} \end{bmatrix} \begin{bmatrix} \ddot{\mathbf{q}}_B \\ \ddot{\mathbf{q}}_F \end{bmatrix} + \begin{bmatrix} \mathbf{C}_{BB} & \mathbf{0} \\ \mathbf{0} & \mathbf{C}_{FF} \end{bmatrix} \begin{bmatrix} \dot{\mathbf{q}}_B \\ \dot{\mathbf{q}}_F \end{bmatrix} + \begin{bmatrix} \mathbf{K}_{BB} & \mathbf{0} \\ \mathbf{0} & \mathbf{K}_{FF} \end{bmatrix} \begin{bmatrix} \mathbf{q}_B \\ \mathbf{q}_F \end{bmatrix} = \begin{bmatrix} \mathbf{F}_B \\ \mathbf{F}_F \end{bmatrix} \tag{6.10}$$

Notice that:

$$\begin{bmatrix} \mathbf{F}_B \\ \mathbf{F}_F \end{bmatrix} = \mathbf{\Phi}_{g1H}^T \mathbf{F}_{g1} = \mathbf{F}_H, \tag{6.11}$$

where $\mathbf{F}_{g1}$ are the external forces in physical coordinates and $\mathbf{F}_H$ are the generalized external forces. See [Res05] for the influence of inertial coupling on the equations of motion.

The rigid body motion can be solved for using equations (4.227) to (4.232), while accounting for the unknown deformation induced aerodynamic loads. This is possible only when equations (4.227) to (4.232) and the flexible equation:

$$\mathbf{M}_{FF}\ddot{\mathbf{q}}_F + \mathbf{C}_{FF}\dot{\mathbf{q}}_F + \mathbf{K}_{FF}\mathbf{q}_F = \mathbf{\Phi}_{g1F}^T \mathbf{F}_{g1}, \tag{6.12}$$

are simultaneously solved for.

Recall, that it may be assumed that the state of the aircraft can be derived from the flight test measurements. Meaning at this point, that the rigid body motion is estimated from the flight test measurements. The advantage is that no errors are introduced due to integration of the equations of motion for the rigid body.
The flight test data that were available to the author were not the raw measurements, but these were data generated in a post-process from the raw measurements by the people that supported the flight tests. The flight test data contains data for example for the true airspeed, the angle of attack and the angle of sideslip, but not directly for the speed components: u, v, w. In this case, the vector $[u \quad v \quad w]^T$ can be determined from the flight test data for the true airspeed, the angle of attack and the angle of sideslip:

$$\begin{bmatrix} u \\ v \\ w \end{bmatrix} = \begin{bmatrix} V_{TAS} \cdot \cos\alpha \cos\beta \\ V_{TAS} \cdot \sin\beta \\ V_{TAS} \cdot \sin\alpha \cos\beta \end{bmatrix} \tag{6.13}$$

This is needed here due to the specific data delivery, as mentioned above. The angle of attack is actually often derived from the measurement of the pitch angle and the horizontal and vertical speeds, as it is difficult to measure the angle of attack directly. This was just an example, see reference [Mul99] for an overview of different approaches to the solution of the flight path reconstruction problem from the raw measurement data with emphasis on Kalman filter/smoother and Maximum Likelihood methods.

The components of vector $[p \quad q \quad r]^T$ can be measured directly in flight and were also part of the delivered flight test data.

The acceleration vector can be determined from the equations of motion (4.227) to (4.230) to be:

$$\begin{bmatrix} a_X \\ a_Y \\ a_Z \end{bmatrix} = \begin{bmatrix} \dot{u} \\ \dot{v} \\ \dot{w} \end{bmatrix} + \begin{bmatrix} u \\ v \\ w \end{bmatrix} \times \begin{bmatrix} p \\ q \\ r \end{bmatrix} + \mathbf{L}_{BE} \cdot \begin{bmatrix} 0 \\ 0 \\ g \end{bmatrix} \tag{6.14}$$

where a_X, a_Y, a_Z denote the specific aerodynamic forces with respect to the mean axis system. Specific forces are the variables measured by 'ideal' accelerometers in the body's

centre of gravity. Under the assumption of a quasi steady flight condition, the time derivative of the vector $[u \quad v \quad w]^T$ is assumed to be zero in equation (6.14). The components of the transformation matrix $\mathbf{L}_{BE}$ are determined from the measured Euler-angles (ϕ, θ and ψ). The gravitational acceleration g is assumed to have the constant value of $9.80665 m/s^2$. Notice that the acceleration vector in equation (6.14) is now completely defined in terms of measured quantities.

The components of the acceleration can thus be reconstructed from the measured quantities: u, v, w, p, q, r, ϕ, θ, ψ. However, these components of the acceleration are also directly available from the flight test data. The identification of the FLM model presented in this section uses the direct data for the rigid body acceleration (specific force).

Next, equation (6.12) is used to determine the corresponding deformation of the aircraft. Furthermore, because quasi-steady manoeuvres are considered, it can be assumed that $\ddot{\mathbf{q}}_F$ and $\dot{\mathbf{q}}_F$ are null-vectors. The equation then simplifies to:

$$\mathbf{K}_{FF}\mathbf{q}_F = \mathbf{\Phi}_{g1F}^T \mathbf{F}_{g1}, \tag{6.15}$$

where the difficulty is embedded in the accurate determination of the external forces. Notice that the coupling with the rigid body motion is contained in this equation through the generalized external forces. These generalized external forces also contain the deformation induced aerodynamic loads, as presented in equations (4.234) and (4.235). The deformation of the aircraft can now be solved from:

$$\mathbf{K}_{FF}\mathbf{q}_F = \mathbf{\Phi}_{g1F}^T (\mathbf{F}_{g1,x_R} + \mathbf{F}_{g1,\delta} + \mathbf{F}_{g1,x_F} + \mathbf{F}_{g1,thrust}), \tag{6.16}$$

where the aerodynamic forces due to rigid body motion and control surface deflection are calculated after transformation of equation (4.240) and (4.244) from the aerodynamic to the structural physical coordinates, see also equation (4.287), and after multiplication with the dynamic pressure:

$$\mathbf{F}_{g1,x_R} + \mathbf{F}_{g1,\delta} = q \cdot \mathbf{G}_{kg1}^T \cdot (\mathbf{Q}_{kx_R}\mathbf{x}_R + \mathbf{Q}_{k\delta}\boldsymbol{\delta}). \tag{6.17}$$

In section 4.4.5 it was shown that the panel pressure due to deformation (change in panel downwash) is described by equation (4.265). The change in panel downwash from equation (4.265) can be described as a function of the flexible modal coordinates $\mathbf{q}_F$:

$$\Delta \mathbf{w}_J = \mathbf{D}_{jk} \cdot \mathbf{G}_{kg1} \cdot \mathbf{\Phi}_{g1F} \cdot \mathbf{q}_F, \tag{6.18}$$

see further section 4.5. The aerodynamic loads distribution induced by the flexible deformation of the airframe then can be calculated with:

$$\mathbf{F}_{g1,x_F} = q \cdot \mathbf{G}_{kg1}^T \cdot \mathbf{S}_{kj} \cdot \mathbf{Q}_{jj} \cdot \mathcal{R} \cdot \mathbf{D}_{jk} \cdot \mathbf{G}_{kg1} \cdot \mathbf{\Phi}_{g1F} \cdot \mathbf{q}_F, \tag{6.19}$$

If the matrix $\mathcal{R}$ is just the identity matrix, then the above equation for the flexibility effects simply resembles pure linear vortex lattice. Aerodynamic nonlinearities due to airframe flexibility can be captured as soon as the matrix $\mathcal{R}$ is not a constant matrix anymore, but a more complicated function of, for example, local deformation.

The thrust of each engine is determined using the thrust model of section 4.6 together with the measured fan speed of each engine. These thrust forces are splined onto the structural nodes by the following equation:

$$\mathbf{F}_{g1,thrust} = \mathbf{G}_{pg1}^T \cdot \begin{bmatrix} T_{E1} \\ T_{E2} \\ T_{E3} \\ T_{E4} \end{bmatrix} \tag{6.20}$$

Equation (6.16) has to be solved for the deformation $\mathbf{q}_F$ explicitly, where it should be noticed that the deformation also appears on the right hand side through equation (6.19).

The following expression can be derived if all contributions not dependant onto the deformation are summarized in $\mathbf{F}_{g1}^*$:

$$\left\{ \mathbf{K}_{FF} - q \cdot \mathbf{\Phi}_{g1F}^T \cdot \mathbf{T}_{kg1}^T \cdot \mathbf{S}_{kj} \cdot \mathbf{Q}_{jj} \cdot \mathcal{R} \cdot \mathbf{D}_{jk} \cdot \mathbf{T}_{kg1} \cdot \mathbf{\Phi}_{g1F} \right\} \mathbf{q}_F = \mathbf{\Phi}_{g1F} \cdot \mathbf{F}_{g1}^* \tag{6.21}$$

Now introducing the matrices:

$$\mathbf{Q}_{Fj} = \mathbf{\Phi}_{g1F}^T \cdot \mathbf{T}_{kg1}^T \cdot \mathbf{S}_{kj} \cdot \mathbf{Q}_{jj} \tag{6.22}$$
$$\mathbf{D}_{jF} = \mathbf{D}_{jk} \cdot \mathbf{T}_{kg1} \cdot \mathbf{\Phi}_{g1F}, \tag{6.23}$$

this can be written as:

$$\left\{ \mathbf{K}_{FF} - q \cdot \mathbf{Q}_{Fj} \cdot \mathcal{R} \cdot \mathbf{D}_{jF} \right\} \mathbf{q}_F = \mathbf{\Phi}_{g1F} \cdot \mathbf{F}_{g1}^* \tag{6.24}$$

This equation can be solved for the deformation as:

$$\mathbf{q}_F = \left\{ \mathbf{K}_{FF} - q \cdot \mathbf{Q}_{Fj} \cdot \mathcal{R} \cdot \mathbf{D}_{jF} \right\}^{-1} \cdot \left(\mathbf{\Phi}_{g1F} \cdot \mathbf{F}_{g1}^* \right) \tag{6.25}$$

Notice that the deformation is calculated based on the external forces that are estimated from the aerodynamic and thrust models with the measured states, control surface deflections and fan speed of the engines as input.

After having solved for the deformation of the aircraft in the generalized coordinates, the elastic nodal forces can be reconstructed from these generalized coordinates by the Force Summation Method:

$$\mathbf{F}_{g1}^{el} = \mathbf{F}_{g1} - \mathbf{M}_{g1g1} \cdot \mathbf{\Phi}_{g1H} \cdot \ddot{\mathbf{q}}_H - \mathbf{C}_{g1g1} \cdot \mathbf{\Phi}_{g1H} \cdot \dot{\mathbf{q}}_H \tag{6.26}$$

See references [Kar93] and [Res03] for more information on the Force Summation Method. In reference [Res03] different methods are compared with each other to determine loads from deformations. The following methods were compared: Mode Displacement Method, Force Summation Method, Mode Acceleration Method, Modal Truncation Augmentation Method, Residual Vector Method and the Fictitious Mass Method.

Notice that because a static aero-elastic problem is solved, the inertia and damping effects of the flexible modes could be neglected. However, also remark at this point that the inertial forces due to the angular speed of the aircraft are included.

6.4   Identification of theoretical model

In this section, simulated measurement data will be used to check the algorithm described in chapter 5 for a model that has a loads representative size and complexity. The advantage of generating simulated measurement data is obviously the exact knowledge of the 'real' system. The number of parameters that are to be identified is kept as small as possible to provide maximum insight.

The flight loads monitoring model of which the main aspects are described in section 6.3, is used. The matrix $\mathcal{R}$ in equation (6.19) is assumed to be a unity matrix throughout this section. Recall that if the matrix $\mathcal{R}$ is assumed to be a constant matrix, the flexibility effects are linearly accounted for.

The changes in model parameters will be done for the elements in the matrix describing the distributions on the aerodynamic grid, $\mathbf{Q}_{kx_R}$, instead of $\mathbf{Q}_{g1x_R}$ in equation (6.17), see further section 6.4.1. It is chosen for varying $\mathbf{Q}_{kx_R}$ because it is easier to modify the corresponding data in a physically meaningful sense. The elements of matrix $\mathbf{Q}_{kx_R}$ are defined on the aerodynamic k-grid and the corresponding lift and moment distributions can be derived quite directly from them. The aerodynamic load distribution splined onto the structural grid, cannot really be interpreted physically anymore. Therefore, it provides more insight to modify the aerodynamic data of the model directly on the aerodynamic grid.
Additionally, in the present model, the matrices $\mathbf{Q}_{kx_R}$ and $\mathbf{Q}_{g1x_R}$ cannot be transformed into each other only by the use of the spline matrix T_{kg1}. Going from $\mathbf{Q}_{kx_R}$ to $\mathbf{Q}_{g1x_R}$ a transformation of all elements is to be performed (while accounting for local reference frames at each grid point) from the aerodynamic reference frame into body axis.

The aerodynamic forces due to rigid body motion and control surface deflection are calculated using the equation, similar to equations (4.240) and (4.244):

$$\mathbf{F}^*_{g1,x_R} + \mathbf{F}_{g1,\delta} = q \cdot \left[f_1(\mathbf{Q}^*_{g1x_R}, \mathbf{x}_R) + f_2(\mathbf{Q}_{g1\delta}, \boldsymbol{\delta}) \right], \tag{6.27}$$

where f_1 and f_2 are nonlinear functions dependent on the aerodynamic database transformed already to the structural $g1$-grid and the state and input vectors, $\mathbf{x}_R$ and $\boldsymbol{\delta}$ respectively.
In this section, the aerodynamic distributions on the wings and winglets will be varied. To this end, the load distributions on these components will be calculated slightly different. The aerodynamic forces due to the angle of attack and the null distribution on the

wing and winglet are accounted for by:

$$\mathbf{F}_{g1_c, x_{Ri}} = q \cdot \mathbf{T}_{kg1}^T \cdot \mathbf{Q}_{k_c x_{Ri}} \cdot \mathbf{x}_{Ri}. \tag{6.28}$$

where the subscript i in $\mathbf{x}_{Ri}$ denotes that the elements 1 and α are accounted for in the state vector. The subscript c denotes the subset of corrected components (here wings and winglets). Obviously, the force contributions given by equation (6.28) have to be set to zero in matrix $\mathbf{Q}_{g1x_R}$ in equation (6.27) not to account for them twice, denoted by $\mathbf{Q}_{g1x_R}^*$. The aerodynamic load distribution due to rigid body motion is then:

$$\mathbf{F}_{g1_{x_R}} = \mathbf{F}_{g1, x_R}^* + \mathbf{F}_{g1, \delta} + \mathbf{F}_{g1_c, x_{Ri}}, \tag{6.29}$$

6.4.1   Model adjustments to artificially generate measurement data

In this section, the output vector will be determined for the modified model. This output vector will be the artificially generated measurement data used in the identification of the parameters in the next section.

The drag, lift and moment distributions contained in the matrix $\mathbf{Q}_{k_c x_{Ri}}$ are adjusted for the wing and winglets in equation (6.28):

$$\mathbf{Q}_{k_{winglet} x_{Ri}}^m = \theta_1 \cdot \mathbf{Q}_{k_{winglet} x_{Ri}} \tag{6.30}$$

$$\mathbf{Q}_{k_{wing} x_{Ri}}^m = \theta_2 \cdot \mathbf{Q}_{k_{wing} x_{Ri}} \tag{6.31}$$

$$\mathbf{Q}_{k_c x_{Ri}}^m = \begin{bmatrix} \mathbf{Q}_{k_{wing} x_{Ri}}^m \\ \mathbf{Q}_{k_{winglet} x_{Ri}}^m \end{bmatrix}, \tag{6.32}$$

where the superscript m indicates that these matrices are used to simulate the measurement data and:

$$\boldsymbol{\theta} = \begin{bmatrix} 1.5 \\ 1.2 \end{bmatrix}, \tag{6.33}$$

which means for the present example, the simultaneous adjustment of 792 model parameters.

The resulting wing loads can now be determined by feeding the modified flight loads monitoring model with time varying state and input vectors, see figure (6.4) and (6.5) respectively. The output of the flexible aircraft with modified rigid body aerodynamics can be found in figures (6.8) and (6.9) exemplarily for two load outputs. The output of the other 19 loads are omitted for clarity reasons. This output (all 21 load outputs) will be the artificially generated measurement data, just called measurement data in the remainder of this section.

6.4.2   Identification of parameters

It is known from the previous section, that the measurement data was generated with:

$$\boldsymbol{\theta} = \begin{bmatrix} 1.5 \\ 1.2 \end{bmatrix}, \tag{6.34}$$
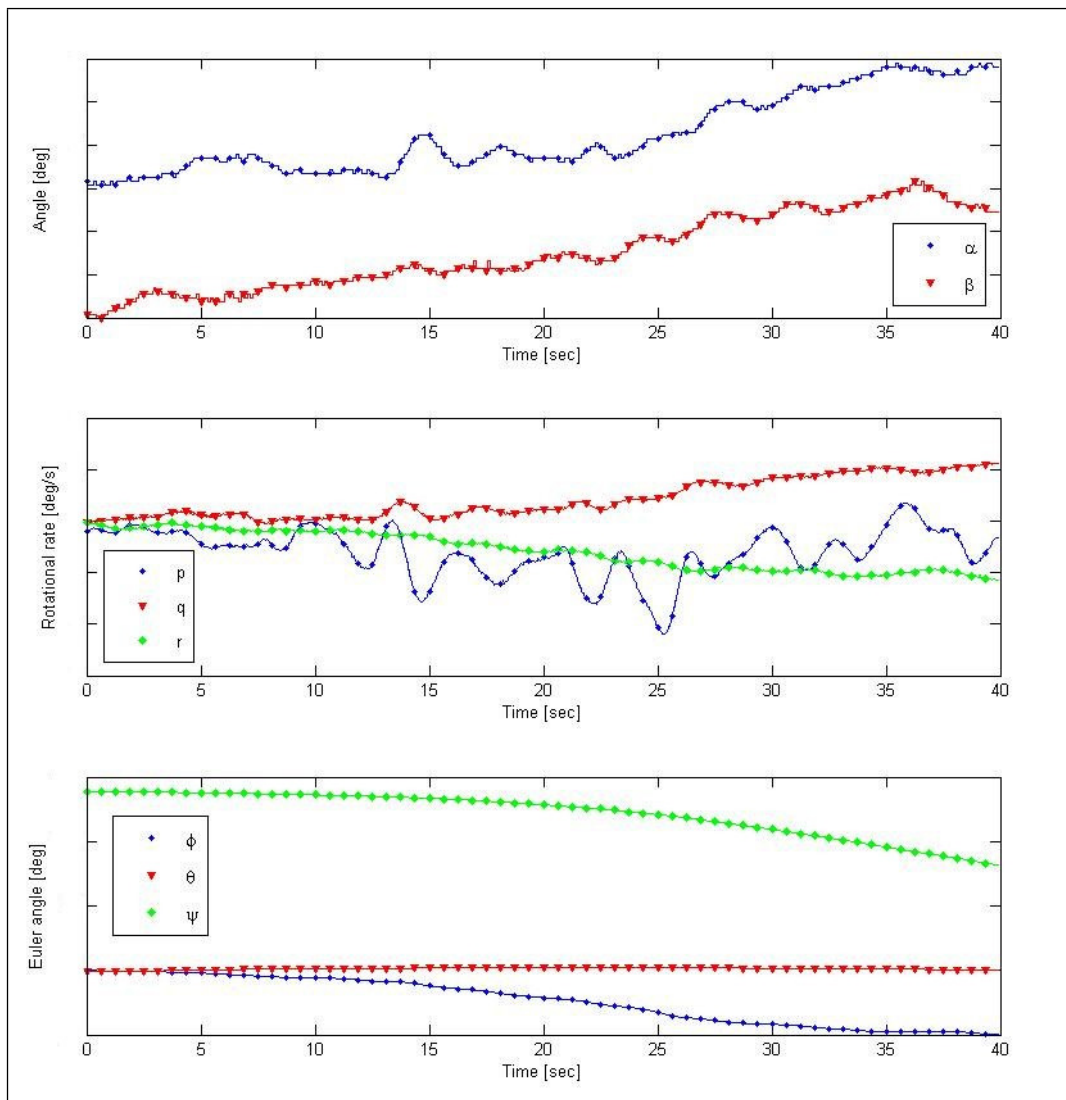
Figure 6.4: *Time history of the state variables that are input to the flight loads model and the Euler angles .*
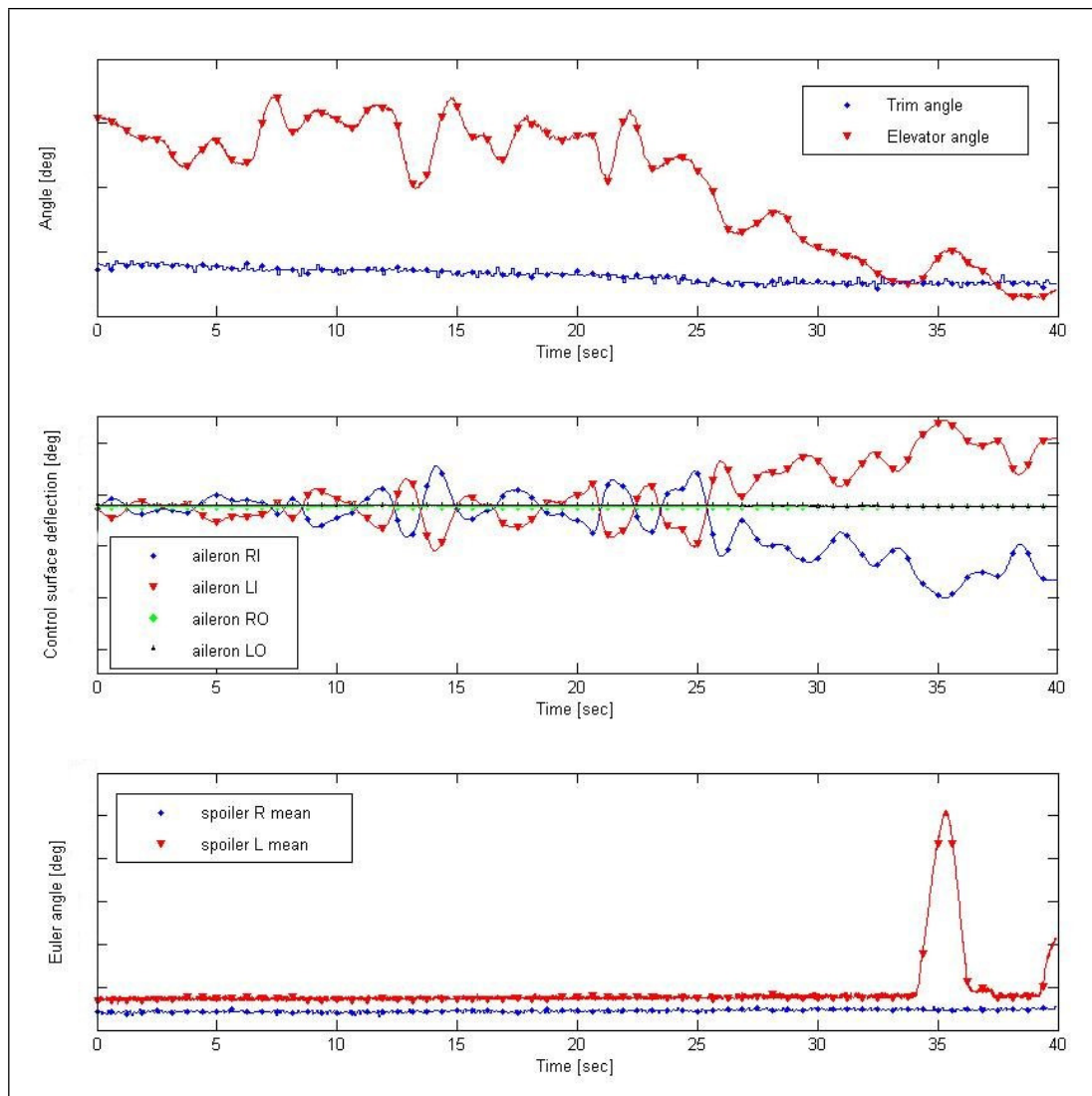
Figure 6.5: *Time history of the control surface deflections that are input to the flight loads model.*

It will be investigated here if and how fast the algorithm is able to identify these two parameters starting from the initial estimate:

$$\hat{\boldsymbol{\theta}} = \begin{bmatrix} 1 \\ 1 \end{bmatrix}, \tag{6.35}$$

An important issue in parameter identification is the choice of the parameters. The number of parameters should be as little as possible, while not restricting the model too much. Obviously, in this case it is known that the 'real' model can be predicted exactly by the correct adjustment of the two specific parameters only. Any different choice of parameters will be less ideal. In this example it will be looked at the performance of the algorithm for the ideal situation where the choice of parameters has been done appropriately. In section 6.7, the more complicated problem is dealt with, where the 'real' system and its parameters are not known and thus the ideal choice of parameters is not known.

The bounds on the parameters are set to:

$$\begin{bmatrix} -2 \\ -2 \end{bmatrix} < \hat{\boldsymbol{\theta}} < \begin{bmatrix} 2 \\ 2 \end{bmatrix}, \tag{6.36}$$

The calculated loads are scaled based on the measured loads for the first time step. This scaling is necessary in the identification procedure, because the order of magnitude of the absolute loads level at the stations is very different. If the relative error for each station should be minimised and not the absolute errors, this scaling of the output vector should be done. It additionally reduces numerical difficulties for the algorithm.

The choice of parameters is so good that the information matrix is not rank deficient and thus the parameter update can be calculated using a regular inverse of the information matrix by equation (5.44). For this problem a rank deficient solution procedure is not needed.

The algorithm needs only one step to arrive at its final solution:

$$\hat{\theta}_1 = \begin{bmatrix} 1.49999999706181 \\ 1.19999999923341 \end{bmatrix} \approx \begin{bmatrix} 1.50 \\ 1.20 \end{bmatrix} \tag{6.37}$$

As one can see, the match between the 'real' and the estimated parameters is extremely good. The error in the parameter estimation amounts less then $1 \cdot 10^{-8}$ for both parameters. In figure (6.6) and (6.7) some of the modified distributions are plotted. Figure (6.6) shows the gradient distributions with respect to the angle of attack along the wing, for the initial model, the final model and the 'real' values. The same is done in figure (6.7) for the winglet. The shape of the distribution has not been modified in this identification. Notice that with a good choice of model, parameters and boundary conditions, the shape of the distributions might as well be changed. However, extreme caution has to be taken as the risk of arriving at a non-physical model is very high at an apparently perfect match of the output vectors.

The output corresponds exactly with the measurement data, the results for two loads

stations can be found in figures (6.8) and (6.9). The results for the other loads stations are similar and are therefore omitted. Refer to table 6.1 for the location of the loads stations.

The negative Likelihood function from equation (5.35) had the value -104194.5 for the initial estimate and it approaches $-\infty$ for the final estimate. The Likelihood function can approach $-\infty$, if some diagonal elements of the matrix $\mathbf{R}$ get zero. This can happen, when there is no (gaussian) noise present on the measurement signal. For example if the noise has been removed from the measurement data by applying filters. In this investigation additional gaussian noise could have been added to the measurement data. In that case, the matrix $\mathbf{R}$ would have had no zero diagonal elements and the negative Likelihood function would have remained finite. However, the real measurement data used in this thesis is already filtered. The absence of measurement noise is a larger challenge for the numerical procedure of the algorithm and better comparable to the actual identification that will be performed in section 6.7 with the real measurement data. Therefore it is chosen not to artificially add noise in this section to the measurement vector.
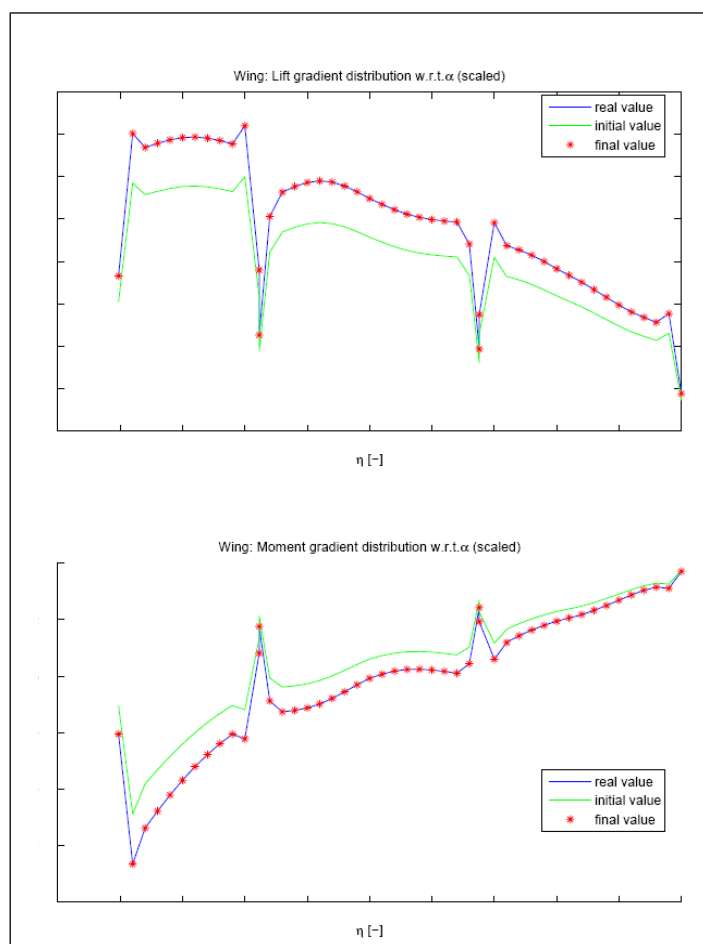
Figure 6.6: *Estimated distributions along the wing compared with 'real' distributions.*
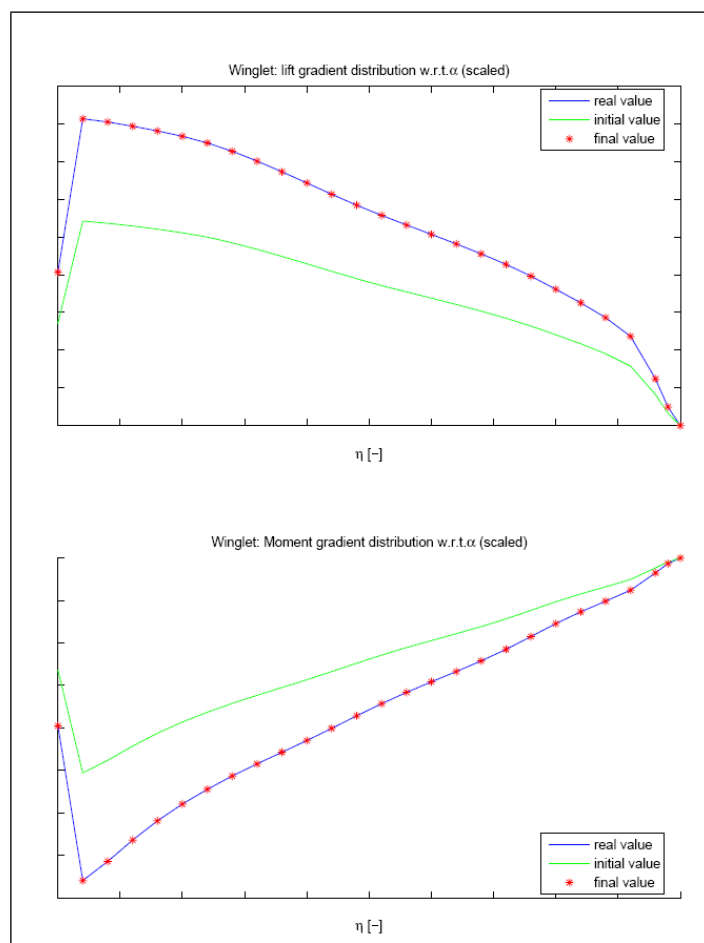
Figure 6.7: *Estimated distributions along the winglet compared with 'real' distributions.*
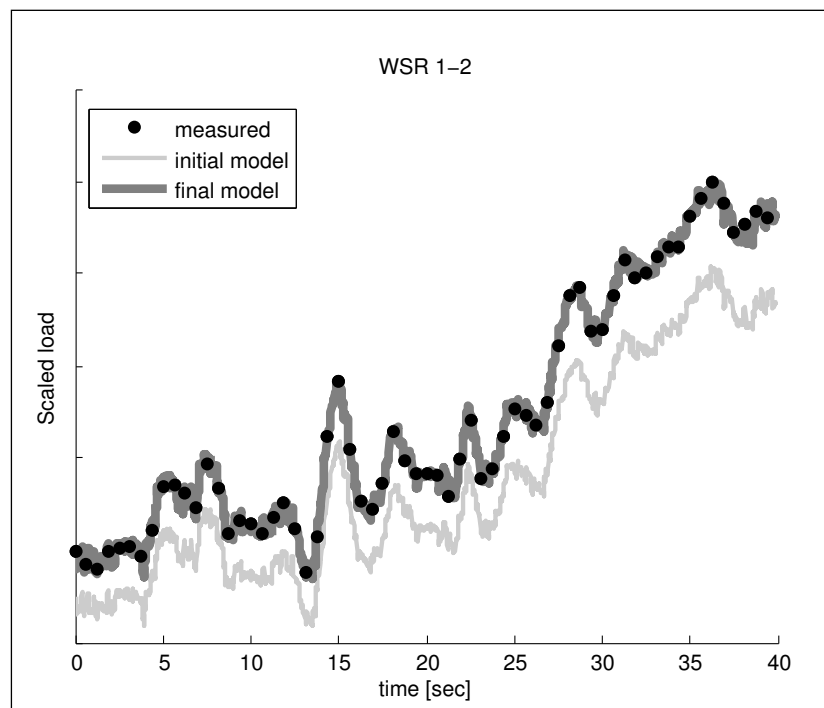
Figure 6.8: *Normalized shear force on the right wing vs. time for wing station 1 (the identification of the theoretical model).*
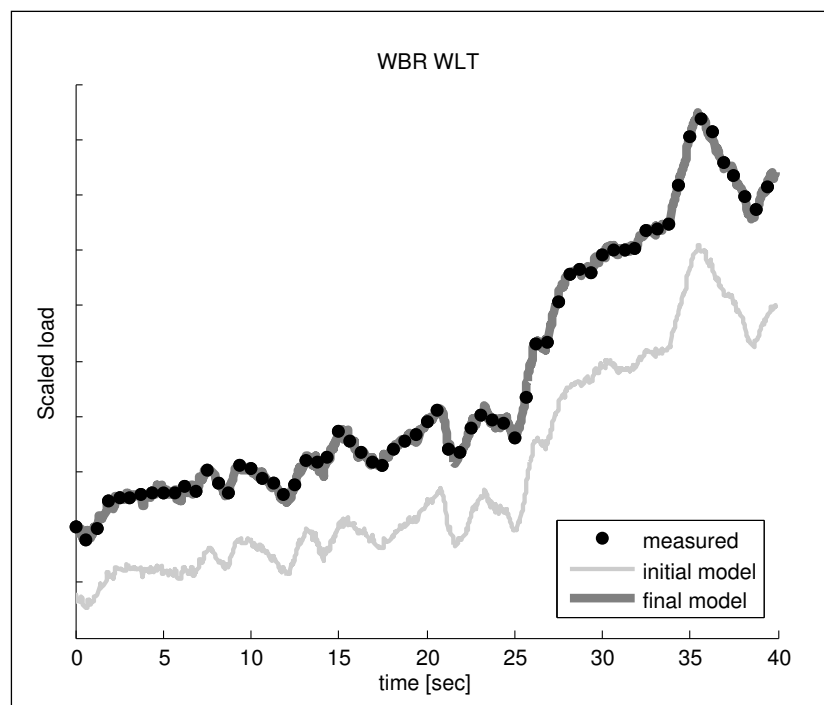
Figure 6.9: *Normalized winglet root bending moment vs. time (the identification of the theoretical model).*

6.5   Identification of flexibility effects

6.5.1   Methods to account for flexible effects

The algorithm of chapter 5 has mainly been developed to enable identification of possible nonlinear flexible aerodynamic effects.

The flight loads monitoring model of which the main aspects have already been described in section 6.3 is used. If the matrix $\mathcal{R}$ in equation (6.19) is a constant matrix, see the method 1 presented in this section, the flexible effects are linearly accounted for. Method 2 and method 3 will present the methods to account for nonlinear effects, where the matrix $\mathcal{R}$ no longer has constant coefficients. The aerodynamic forces induced by the airframe deformation are estimated using a model based on vortex lattice, see section 4.5.

Method 1: LINFLEX

The matrix $\mathcal{R}$ is determined from:

$$\mathcal{R} = diag(\mathbf{C}_f \cdot \mathbf{b}_f) \tag{6.38}$$

where the matrix $\mathbf{C}_f$ contains 2 shape functions per 'section' or 'strip' and the vector $\mathbf{b}_f$ is a vector with 2 corresponding constant parameters (per strip).

Method 1 is the method already presented in chapter 4, where $\mathbf{b}_f$ is a vector with constant elements, see section 4.4.4. It accounts for the flexibility effect based on linear aerodynamics.

Method 2

In method 2, the elements of $\mathbf{b}_f$ are a function of local angle of attack. A database is generated of $\mathbf{b}_f$ for each strip and 'alpha-region'. The local angle of attack is determined from the rigid body global angle of attack plus the deformation induced angle of attack. For each strip the current alpha-region is determined and the corresponding parameters $\mathbf{b}_f$ are selected.

The deformation induced angle of attack is also a function of the parameter vector $\mathbf{b}_f$, making it a coupled problem. In addition, the number of parameters that are to be identified would be very large. This method therefore requires substantial computational effort, which cannot be maintained in practice.

Method 3

Method 3 tries to capture the effects of Method 2 at considerably reduced computational effort. The idea is to derive the nonlinear parameter vector independent from the unknown deformation, while still accounting for an estimated level of deformation. This

can be done by writing the parameter vector as a function of the loads level:

$$\mathbf{b}_f(t) = \begin{bmatrix} \mathbf{a}_0 & \mathbf{a}_1 & \mathbf{a}_2 \end{bmatrix} \cdot \begin{bmatrix} 1 \\ N_Z(t) \\ N_Z^2(t) \end{bmatrix}, \qquad (6.39)$$

where the vector $\mathbf{a}_0$ is equal to $\mathbf{b}_f$ from method 1. The vectors $\mathbf{a}_1$ and $\mathbf{a}_2$ account for local nonlinear effects, depending on the loads level. The loads level N_Z is known from the flight test measurements.

However, we now have a vector $\mathbf{b}_f$ that is a function of time. Consequently, the deformation cannot be calculated at once for all time steps. The matrix equation has to be solved for each time step separately. For the current problem, this takes about 3 seconds per time step.

This is still much faster compared to method 2. In comparison with method 1 (linear flexibility), the computational effort is increased by a very large amount. A calculation for a representative time interval with Method 1 took a couple of minutes, where Method 2 requires over 2 hours.

Furthermore, the number of parameters is now three times the number of parameters from Method 1. Here lies exactly the problem of this method. For each iteration step (that is parameter update step), the computation of the sensitivity matrix requires a coupled loads computation for each parameter for each time step. For a time interval of 2555 time steps (which is only 40 seconds with a sampling rate of 64 Hz) and for three times 156 parameters[5] to identify, the time required for the evaluation of only 1 sensitivity matrix would amount:

$$3 \cdot 2555 \cdot 3 \cdot 156 = 3587220 \; sec \equiv 966.45 \; hours \equiv 41.5 \; days. \qquad (6.40)$$

The computational time needed for one iteration step linearly increases with the length of the time interval.

The addition of 'free' parameters to identify bias on the measurements, would not significantly increase the required computational time, because their output sensitivities are known analytically.

With or without measurement bias, *the time required using this method is way beyond acceptable and thus alternatives have to be found!*.

6.5.2   Discussion of results

In the previous section, three methods were presented to account for flexibility effects. Method 2 and 3 were modelling procedures to account for nonlinear flexibility effects, where method 1 accounts for it linearly. It was shown that method 2 and 3 could not be used here, because of the high computational effort involved.

---

[5]Already a subset of the total number of parameters. Here, 156 corresponds to correcting the parameters of only the wing and winglet. The number of parameters has already been reduced compared to the full number of variables (panels) from the vortex lattice method assuming shape functions (Birnbaum distributions).

Unfortunately, it is therefore not possible yet to do the identification of the nonlinear flexibility effects on a model of this size and complexity. Therefore, in this practical application of identification of parameters for a flight loads monitoring model, method 1 will be used.

The vortex lattice model of the complete aircraft, used in this study, consists of 2076 panels. Trying to identify each panel pressure would imply a highly overparametrization. The number of free variables has to be reduced considerably, while maintaining the highest possible level of detail. The 'only' parameters that will be set 'free' in the identification procedure, will be the parameters corresponding to the wing and winglets. These components are obviously mostly influenced by flexibility effects, as they experience the biggest deformations/displacements.

The wings and winglets are composed of 780 panels (excluding pods and pylons). Practical experience has shown good results when assuming shape functions in the chordwise direction, see also section 4.4.4, to further reduce the number of variables.

The number of variables has now been reduced to 156 to describe the load distributions on the left and right wing and winglet stations, having two free variables per station.

In addition, each component of the measurement vector $\mathbf{z}$, is expected to comprise a measurement bias. The measurement vector contains the data from 21 loads measurements. This brings the total amount of parameters to be identified at 177.

It was already mentioned in section 5.5, that problems with fifty or more variables are large problems in this field. Unless they are only mildly nonlinear, or there is a good starting guess, it is stated that there is no good chance of solving them economically.

With these statements in mind, the problem addressed here, having 177 free parameters can thus be considered as quite a large problem.

Notice, that such a large problem already occurs, while only accounting for a linear flexibility effect in a nonlinear system by using method 1. This also shows that in order to enable identification of aerodynamic nonlinear flexibility effects in the future, the following issues have to be addressed:

- find an alternative method to method 2 and 3 to significantly reduce the number of free variables,

- make the algorithm that solves the nonlinear coupled system for the deformation of the aircraft more efficient.

- increase the available computational power from a hardware perspective.

Comparison of initial model with measurements

At first, the results from the initial model are compared with the measurements, see the figures in appendix D. All 21 load outputs are accounted for in this identification, however for clarity reasons, the results are again only presented for 4 loads. At this point, it is only looked at the red and blue lines corresponding to the initial model and to the

measurements respectively.

Figure (D.27) is a representative example that shows a large discrepancy indicating the possibility of a significant bias for that loads measurement. This figure also shows that the shape of the curves are quite similar, making a pure shift quite plausible. This can also be said when looking for example at the scaled integrated shear load at the righthand wing station 3, and also for most of the other loads, but not all results are printed here as already mentioned before.

Therefore as a first test, the parameters of the initial model were maintained, however, a measurement bias is estimated based mainly on these observations.

Comparison of initial model plus initial bias with measurements

As an initial estimate for the bias, the mean difference between the measurements and the initial model is taken. The resulting estimate for the measurement vector is indicated using green in the figures in appendix D.

Comparison of the results show already very good correspondence for most of the loads measurements. This can be seen exemplarily when comparing the green and blue lines in figures (D.27) and (D.28) for respectively the integrated shear load at the righthand wing at wing station 4 and the integrated bending moment at the righthand wing station 5. These two figures are representative for all of the other loads, except for the integrated bending moment at the righthand wing station 6 and that at the winglet root, which will be considered below.

The bias determined here is also compared with those values determined from a reference on ground analysis of the loads stations. The reference on ground shift analysis is not very accurate due to the small loads level (even different in sign) on the ground. This contrarily to the high loads level in flight for which the loads stations are or should be calibrated.

The values for the bias have, however, the same order of magnitude. This confirms the observation that it could actually be mainly measurement bias and not a modelling discrepancy.

However, now it is looked at the integrated bending moment at the righthand wing station 6 and that at the winglet root, see respectively figures (D.29) and (D.30). It can be seen, when comparing the green and blue lines in these figures, that the discrepancy in the results cannot be explained fully by a 'pure' shift of the output of the initial model. Therefore it should be investigated whether a parametric adaptation can improve results especially for these 2 outer wing loads. In the following section, the Maximum Likelihood identification will be performed with and without initial bias and the results will be compared.

Comparison of estimated models with measurements

In this section, the results from the identification procedure using the Maximum Likelihood method will be presented.

Alternative:	MLM 1	MLM 2	MLM 3	MLM 4
Initial bias:	no	no	yes	yes
Search procedure:	full rank	minimum search	full rank	minimum search
$J(\hat{\boldsymbol{\theta}}^0)$	-8525.9398	-8525.9398	-111572.0850	-111572.0850
$J(\hat{\boldsymbol{\theta}}^1)$	-8832.4697	-116712.0875	-111773.0882	-115153.0008
$J(\hat{\boldsymbol{\theta}}^2)$	-9456.5935		-111858.3829	
$J(\hat{\boldsymbol{\theta}}^3)$	-10161.9113		-112192.6141	
$J(\hat{\boldsymbol{\theta}}^4)$			-112296.6514	
$J(\hat{\boldsymbol{\theta}}^5)$			-112373.7663	
$J(\hat{\boldsymbol{\theta}}^6)$			-112385.9719	
$J(\hat{\boldsymbol{\theta}}^7)$			-112392.4941	
$J(\hat{\boldsymbol{\theta}}^8)$			-112396.1912	

Table 6.2: Overview of alternatives tried in the Maximum Likelihood identification of the loads model.

It was already mentioned in section 5.5.1 that the identification algorithm will converge to a *local* minimizer of the Likelihood function. Therefore, different starting points and searching methods are tested, to find the smallest minimum at least from the alternatives considered. The four alternatives, for which the value of the Likelihood function at each iteration will be presented here for comparison, are called: "MLM 1", "MLM 2", "MLM 3", "MLM 4". See table 6.2 for an overview of the differences between these alternatives and the results for the Likelihood function at the iteration steps.
For all four alternatives a rank deficient method was necessary. The two alternatives in the rank deficient searching procedure are

- 'full rank': the number of singular values included in the determination of the pseudo-inverse of the Fisher matrix was taken equal to the rank of this matrix.

- 'minimum search': Multiple pseudo-inverses of the Fisher matrix are determined taking into account a prescribed minimal number of singular values (here 10) and adding one singular value at the time up to the full rank of this matrix. Each pseudo-inverse leads to a different search direction. In a second step, that direction that gives the smallest Likelihood function is maintained

It can be easily seen from table 6.2 that the alternative "MLM 2" gives the best estimate (smallest Likelihood function) of these four alternatives. Furthermore, it can be seen from this table that the 'minimum search' method required only one iteration step to converge to a local minimum for both alternatives ("MLM 2" and "MLM 4"). The 'full rank' search needed 3 iterations to converge for "MLM 1" and eight steps for "MLM 3". The 'minimum search' method has higher computational costs for one iteration step, but it needs less steps to converge. Here, the 'minimum search' method leads to the fastest convergence.

One can also see from table 6.2 that the initial Likelihood function assuming no ini-

nr.	$\hat{\mathbf{b}}$	$\hat{\mathbf{b}}_2$
1	0.1402	0.0871
2	1.1625	1.1670
3	0.4641	0.4202
4	0.5600	0.4944
5	-0.0230	-0.1563
6	0.3913	0.3336
7	0.5496	0.5065
8	0.1699	0.0745
9	0.3401	0.2531
10	0.1469	0.0046
11	0.9635	0.8375
12	1.3523	1.1670
13	1.3587	1.3449
14	0.7939	0.8091
15	3.1836	3.0567
16	-1.3240	-1.1892
17	0.3780	0.4680
18	1.4234	1.4218
19	0.2361	0.2404
20	0.2123	0.2180
21	0.9438	0.9438

Table 6.3: Comparison of biases. The initial bias $\hat{\mathbf{b}}$ is the mean difference between the initial model and the measurements, this is not the initial bias used in "MLM 2"!. Bias $\hat{\mathbf{b}}_2$ is the best estimate for the bias attained with "MLM 2" assuming no initial bias.

tial bias is much larger compared to the value for "MLM 3" and "MLM 4", assuming initial bias. However, although "MLM 2" starts at a worse estimate, it converges to the best estimate.

The initial bias for "MLM 3" and "MLM 4", was set to the mean difference between the measurements and the initial model, as described in section 6.5.2, where the initial bias for the bending moment of the winglet root was set to zero.

In table 6.3, the bias determined in 6.5.2 is compared with the estimated bias from "MLM 2". Most values are comparable, also confirming the observation from section 6.5.2 that most discrepancy seems to stem from measurement biases. The results from "MLM 2" are also plotted in figures (D.27) to (D.30) that can be found in appendix D. The output vector $\hat{\mathbf{y}}$ of the estimated model is plotted in magenta. The output vector plus the bias (estimated measurement vector $\hat{\mathbf{z}}$) is plotted in black.

The differences between the red and magenta, show the differences due to the first 156 (model) parameters. The shift magenta to black shows the shift due to the last 21 parameters for the measurement bias.

It is interesting to see that the black curves from the best estimate plus bias, arrived at

using "MLM 2" starting from assuming no bias, lie practically on top of the curves just shifted by the mean value of the difference from section 6.5.2.

Unfortunately, no better compliance could be reached between the components of the measurement vector (blue) and those of the estimated measurement vector (black). Recall from the previous section that especially for the integrated bending moments at the outer wing and winglet stations, see also figures (D.29) and (D.30), it was investigated whether the parametric adaptation might improve the results. As can be clearly seen from the figures (D.29) and (D.30), this is not the case.

This might be due to errors in the fixed parameters of the model, for example those describing the rigid body aerodynamics. Another explanation might be that the phenomena observed in the measurements are not captured by the equations describing this model.

Recall, that one of the assumptions of this model was that the description and data for the rigid body aerodynamic effects are correct. In the following section, it will be investigated using the results from highly sophisticated Reynolds Averaged Navier-Stokes simulations, whether dropping this assumption might lead to better results.

6.6   Study of static aero-elastics

The measurement data used in this thesis stem from a project that summarized several proposed new wing technologies and validated their improvement possibilities in flight. Aim of the programme was the proof of concept and in-flight validation of mature wing technologies for future transport aircraft application. The out-come of the project was to draw the technologies, individually and in combination to a maximum benefit at new aircraft environments to be defined.

For flight-testing, a large transport aircraft served as test bed equipped with an extensive amount of sensors, markers, cameras and gauges. In the flight test campaigns, objective has been the individual testing of selected technologies and recording aerodynamic performance, structural loads, aero-elastics and other relevant system data.

The present investigation was initiated after the first flight test measurements and the first analyses were performed for the aircraft equipped with large winglets[6]. Some unexpected differences between measurements and simulations are present, see also section 6.5, that are further investigated here.

In this thesis, the aerodynamics is studied mainly at the wing and winglet for static aeroelastic purposes. The results from coupled CFD-CSD simulations are compared with flight test measurements to determine the credibility of these simulations.

Furthermore, CFD calculations were also performed for the aircraft in fixed shape for a complete alpha sweep. The results from these calculations are compared with the corresponding data from the original aerodynamic database[7]. This database is not complete for all outer wing and winglet aspects.

---

[6]one of the technologies that have been tested
[7]Database determined from wind tunnel measurements

The structure of this section is as follows. More detailed information on the procedure of the aero-elastic solver can be found in section 6.6.1. The determination of the current propulsive forces is done using the thrust model from section 4.6. In section 6.6.2 the post-process of the CFD-data is described in order to make them useful for loads applications. A description of the aircraft geometry used for the investigation can be found in section 6.6.3. The discussion of results can be found in section 6.6.4. Finally, the conclusions are drawn in section 6.6.5.

6.6.1 Description of the aeroelastic solver

The aeroelastic (CFD-CSD[8]) simulations were performed in close cooperation with the Institute of Aerodynamics and Gasdynamics (IAG) of the University of Stuttgart. The simulations are highly accurate steady Reynolds-Averaged Navier-Stokes (RANS) simulations of the trimmed flexible aircraft. For the aeroelastic computations the CFD-solver FLOWer and a reduced order condensed structural model are loosely coupled. Loads and deformation transfer between two non-coinciding aerodynamic and structural meshes is based on a beam spline method, see reference [Rod01].
For every coupling step, an automated procedure generates structured meshes for the aerodynamic solver that are a combination of:

- fully block-structured grids with one-to-one connections,

- overlapping grids based on the Chimera-technique.

FLOWer is iteratively linked to the calculation of the aeroelastic deformations along with an inner trim cycle to calculate the steady aerodynamics of the flexible aircraft. It includes nonlinear transonic and viscous flow effects.

It is a free flight model in that none of the nodes are fixed, i.e. the model has all six degrees of freedom for every node. It features not only the elastic eigenmodes, but also the modes of the rigid body motion. A modal synthesis was performed to split these modes and to obtain a nonsingular stiffness matrix for the elastic eigenmodes. For the elastic analysis of this free-flying aircraft, an equilibrium state of all external forces (a trimmed state) should be reached beforehand. This in order to ensure that no resulting force acts on the center of gravity, which was a prerequisite to separate the elastic eigenmodes from the rigid body motion of the system. More information on the trim implementation can be found in [Kön07].
The static structural analysis is then performed to solve for the unknown deformation using a constant stiffness matrix. The loads vector is multiplied directly inside the aeroelastic module with the inverse of the stiffness matrix. In this way, it is not needed to couple 'outside' with a separate structural solver.
The CFD-solver is FLOWer/eLSA (finite volume RANS, second order). The spatial discretization is performed using a central differencing scheme after Jameson. The integrating in time is performed using fourth order explicit Runge-Kutta. The turbulence model

---

[8]Computational Fluid Dynamics - Computational Structural Dynamics

was LEA k-omega two equations model, fully turbulent flow. The computational structural dynamics (CSD), or FEM solver used in the pre-processing phase is MSC.Nastran.

6.6.2 Postprocessing of the CFD data

In order to enable the data handling of the output from the CFD calculations, an interface to Matlab had to be developed. The output of the CFD-solver contains the pressure coefficients on the surface of the aircraft and optionally the full field data (velocity vectors describing the flow in the volume grid that surrounds the aircraft). The size of such data-files is very large and are in this case provided in Tecplot-format. In order to use the information extracted from the CFD-data in the loads modelling environment and for comparison with the aerodynamic database for loads, the CFD-output is reduced to two dimensional data. Differently stated, the pressure distribution on the wing is integrated in chordwise direction to get the two dimensional force (normal and axial force) and moment distributions along the span.

Starting from a Tecplot-database, the following steps are automatically performed:

1. The first step of the procedure:

   (a) loads the Tecplot-database,

   (b) deselects the components that are not of direct interest,

   (c) makes slices/cuts at the prescribed positions:

       i. Here, eight cuts exactly at the same spanwise coordinates as those of the pressure belts installed on the test aircraft. There are six pressure belts on the wing and two on the winglet at representative locations.

       ii. Additional cuts to arrive at accurate spanwise distributions

   (d) exports the data at the slices in structured format to an ASCII-file.

2. The ASCII-files are then loaded by Matlab,

3. A procedure is run to determine:

   (a) an ordered chain of grid points that constitutes the shape of the airfoil,

   (b) double grid points from overlapping surfaces and other spurious points that are being neglected,

   (c) which points belong to the upper/lower side of the airfoil.

4. The resulting pressure and skin friction distributions over the upper and lower side of the lifting surfaces are then integrated (in the local airfoil reference frame) to arrive at the local normal and axial force and moment coefficients, according to

[And91]:

$$c_n(\eta_i) \quad = \quad \frac{1}{c} \int_0^c \Big(C_{p,l}(x, y, \eta_i) - C_{p,u}(x, y, \eta_i) \Big) dx +$$

$$+ \frac{1}{c} \int_0^c \Big(c_{f,u}(x, y, \eta_i) \frac{dy_u}{dx} + c_{f,l}(x, y, \eta_i) \frac{dy_l}{dx} \Big) dx \qquad (6.41)$$

$$c_a(\eta_i) \quad = \quad \frac{1}{c} \int_0^c \Big(C_{p,u}(x, y, \eta_i) \frac{dy_u}{dx} - C_{p,l}(x, y, \eta_i) \frac{dy_l}{dx} \Big) dx +$$

$$+ \frac{1}{c} \int_0^c \Big(c_{f,u}(x, y, \eta_i) + c_{f,l}(x, y, \eta_i) \Big) dx \qquad (6.42)$$

$$c_{m_{LE}}(\eta_i) \quad = \quad \frac{1}{c^2} \int_0^c \Big(C_{p,u}(x, y, \eta_i) - C_{p,l}(x, y, \eta_i) \Big) \cdot x \cdot dx +$$

$$- \frac{1}{c^2} \int_0^c \Big(c_{f,u}(x, y, \eta_i) \frac{dy_u}{dx} + c_{f,l}(x, y, \eta_i) \frac{dy_l}{dx} \Big) \cdot x \cdot dx +$$

$$+ \frac{1}{c^2} \int_0^c \Big(C_{p,u}(x, y, \eta_i) \frac{dy_u}{dx} + c_{f,u}(x, y, \eta_i) \Big) \cdot y_u \cdot dx +$$

$$+ \frac{1}{c^2} \int_0^c \Big(-C_{p,l}(x, y, \eta_i) \frac{dy_l}{dx} + c_{f,l}(x, y, \eta_i) \Big) \cdot y_l \cdot dx \qquad (6.43)$$

These equations can also be expressed in dimensionless coordinates as follows:

$$c_n(\eta_i) \quad = \quad \int_0^1 \Big(C_{p,l}(\xi, \zeta, \eta_i) - C_{p,u}(\xi, \zeta, \eta_i) \Big) d\xi +$$

$$+ \int_0^1 \Big(c_{f,u}(\xi, \zeta, \eta_i) \frac{d\zeta_u}{d\xi} + c_{f,l}(\xi, \zeta, \eta_i) \frac{d\zeta_l}{d\xi} \Big) d\xi \qquad (6.44)$$

$$c_a(\eta_i) \quad = \quad \int_0^1 \Big(C_{p,u}(\xi, \zeta, \eta_i) \frac{d\zeta_u}{d\xi} - C_{p,l}(\xi, \zeta, \eta_i) \frac{d\zeta_l}{d\xi} \Big) d\xi +$$

$$+ \int_0^1 \Big(c_{f,u}(\xi, \zeta, \eta_i) + c_{f,l}(\xi, \zeta, \eta_i) \Big) d\xi \qquad (6.45)$$

$$
\begin{aligned}
c_{m_{LE}}(\eta_i) \quad = \quad & \int_0^1 \Big(C_{p,u}(\xi,\zeta,\eta_i) - C_{p,l}(\xi,\zeta,\eta_i) \Big) \cdot \xi \cdot d\xi + \\
& - \int_0^1 \left(c_{f,u}(\xi,\zeta,\eta_i) \frac{d\zeta_u}{d\xi} + c_{f,l}(\xi,\zeta,\eta_i) \frac{d\zeta_l}{d\xi} \right) \cdot \xi \cdot d\xi + \\
& + \int_0^1 \left(C_{p,u}(\xi,\zeta,\eta_i) \frac{d\zeta_u}{d\xi} + c_{f,u}(\xi,\zeta,\eta_i) \right) \cdot \zeta_u \cdot d\xi + \\
& + \int_0^1 \left(-C_{p,l}(\xi,\zeta,\eta_i) \frac{d\zeta_l}{d\xi} + c_{f,l}(\xi,\zeta,\eta_i) \right) \cdot \zeta_l \cdot d\xi,
\end{aligned} \tag{6.46}
$$

where ξ and ζ are the dimensionless coordinates in the airfoil reference frame defined by $\xi = \frac{x}{c}$ and $\zeta = \frac{y}{c}$ respectively and η_i denotes the ith spanwise station. Notice that the moment coefficient is taken with respect to the leading edge (LE) of the airfoil.

6.6.3   Aircraft geometry

The aircraft studied is a large transport aircraft equipped with large winglets. The geometry of the large winglet and the wing tip were taken from a full-scale CATIA surface model.

The winglets were derived directly from tunnel model geometry. The winglet has a negative toe angle, meaning with toe out. No aeroelastic corrections to toe and cant angles have been made for this winglet. Also available were a CATIA V4 pre-jig wing envelope. This includes a representation of a slat. This 'pre-jig' state for the aircraft is the planar spar state used as a basis for wing component design. Alternatively stated, the aircraft reference geometry of the aerodynamic model is in quasi-flight shape. It means that it was actually in jig-shape but with wing twist from 1g flight shape superimposed.
The surfaces in the CATIA models do not define the extent of the geometry. This is due in large part to the nature of the surface quality of the Master Geometry tip surfaces. It is a combination of faces and boundary curves that define the winglet geometry in both cases. Some care is required in the interpretation of the required external envelope. Outside of the bounds imposed by the modifications, the Master Geometry tip surfaces define the external envelope.

The CATIA model used here defines the external geometric lines that were intended to act as a basis for manufacture for the Large winglet.

The geometry used in the RANS-simulations is as depicted in pink (reference) in figure (6.10). Notice that the surfaces of pods, pylons and other details like flap-track fairings are not included in the analysis. In section 6.6.3 it is described how the contribution in loads from the pods and pylons are accounted for.
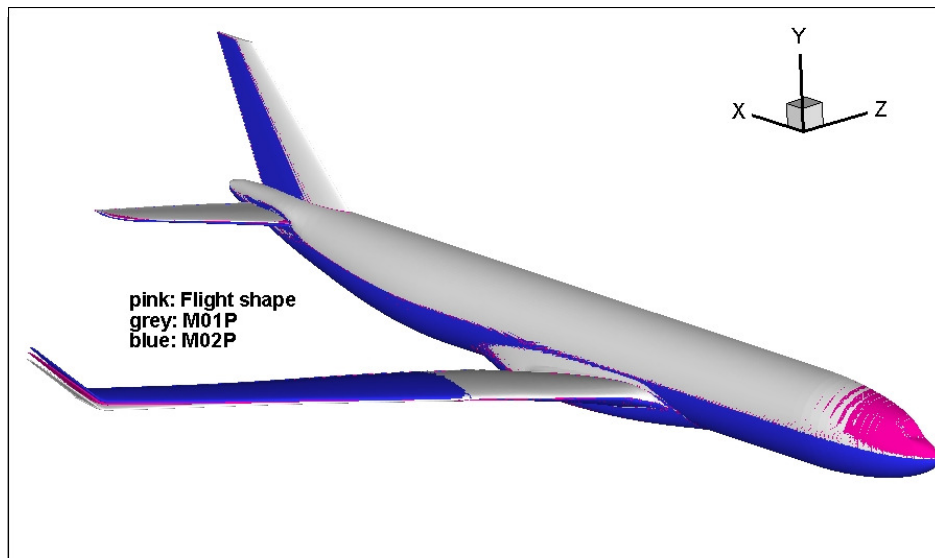
Figure 6.10: *Geometry of aircraft used in coupled CFD-CSD simulations. The deformed geometry is drawn for the two cases considered (M01P and M02P) together with the reference geometry.*
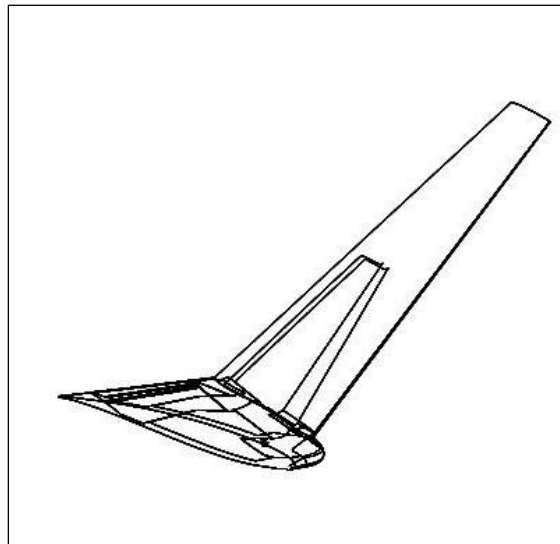
Figure 6.11: *Depicted are the wing tip together with the standard winglet and the large winglet for comparison.*

Aerodynamic Loads on the pods and pylons

It was not possible within the timeframe of this investigation to include the aerodynamic surfaces of the pods and pylons into the aerodynamic model. However, because the coupled RANS-CSD calculations are relative calculations with respect to the flight shape reference condition, it was proven to be of negligible influence.
The difference in direct lift and moment on the pods-pylons were estimated using data from the aerodynamic database and applied directly to the structural model (similar as with thrust). The influence on the shape of the aircraft was minimal. The resulting pressure distributions on the wing and winglet were then compared. No significant differences were found for the analysis including the effects from direct lift and moment compared to that where this was neglected.
Consequently, the absence of the aerodynamic surfaces of the pods and pylons does not pose a problem for the credibility of the analysis.

Structural model

The condensed stiffness matrices were input for the MSC.Nastran analysis to extract the stiffness and mass matrices that are used in the Flight loads monitoring model. The structural model is build up using three separate stiffness matrices. The first stiffness matrix is that for the total aircraft excluding the winglets. To get this stiffness matrix, a condensation of the detailed discretised full model is performed, see figure (6.12), including the landing gear attachment points to enable also ground calculations. This stiffness matrix contains no winglets. The large winglets, have their 'own' stiffness matrices that are additionally included in the model.
The complete stiffness matrix that is used in the coupling with the CFD-calculation is written out during the above described Nastran analysis using a so-called DMAP-alter.

Mass model

A structural analysis (MSC.Nastran) is used to build the mass matrix from the mass model. This mass matrix is written out during the Nastran analysis by a so called 'DMAP-alter'. The mass models were generated using the loading plan of the specific flight and the current fuel distribution for the specific time instant during flight test.

The fuel control and monitoring system is designed to give accurate indications in cruising condition. During manoeuvres, there can be significant (lateral) accelerations or bank angles that influence the accuracy of the indicated amounts of fuel in the single tanks. The fuel redistributes inside the tanks and the fuel surface is no longer level. The position of the fuel sensors then has a significant influence on the accuracy of the indication. For the manoeuvres considered in this report, this is expected to be of no significant influence. In the mass model, the fuel tanks are therefore filled assuming a level fuel surface.

Some load cases were calculated with different mass conditions to check the sensitivity of the analysis to the uncertainties in the fuel distribution. It was found that it suffices to use the indication of the fuel distribution during the cruise flight condition that directly

Figure 6.12: *Full (structural) model of the aircraft.*

precedes the steady coordinated turn under investigation. The advantage is that the fuel control and monitoring system is most accurate in such a level condition. Furthermore, during the two to four minutes of the manoeuvre, the amount of fuel burned is found to be negligible for this loads investigation.

6.6.4   Results

The results from the CFD-CSD calculations will now be compared with flight test pressure measurements. A flexible analysis (CFD-CSD) was performed as well as a pure CFD analysis. Input for the simulations were Mach number, free stream air density, static air pressure, Reynolds number and the desired load factor (N_Z) for the trim condition. These conditions obviously matched the corresponding flight conditions of the pressure measurements under consideration.

The results from the **flexible** analysis are presented here for a representative cruise condition (M01P) and a significant $> 1g$ condition (M02P) at the same Mach number.

The **rigid** analysis was performed for an alpha-sweep using FLOWer for a representative alpha region in steps of 1 degree. The shape of the aircraft remains the reference shape (quasi-flight shape) during the whole alpha-sweep. The general flight condition is similar to the flexible case M01P.

Pressure distribution methods permit the determination of aerodynamic loads in flight without corrections for inertia effects. The pressure measurement installations must how-

ever be very complete in order to obtain accurate load data. The time of installation and data reduction might be very lengthly. Therefore, the general use of pressure distribution methods in the measurement of loads on aircraft in flight is avoided, except when specific detailed load-distribution data are desired. A comparison of wing loads measured in flight on a fighter-type aircraft by strain gauge and pressure distribution methods has been performed in reference [Aik49]. Here, the comparison with the pressure measurements can be seen as spot checking the CFD-CSD results. If the comparison is good for those checks, the detailed distributed data from the CFD-CSD results can then be used to determine the complete load distributions. These results can then again be checked with the loads measurements. The information contained in the pressure and loads measurements only is too little such that they can be combined straight away. The CFD-CSD calculations might provide the missing link between the two. However, it is obvious that the CFD-CSD calculations must be of high quality to describe the real phenomenon accurate enough.

Flexible analysis

The aerodynamic geometry of the aircraft, used for the simulations is as depicted in figure (6.10). The pink shape corresponds to the geometry for the reference condition. The deformations of the airframe are calculated with respect to this condition.
The grey shape of the aircraft depicts the deformation for the cruise condition that is considered in the flexible analysis (case M01P). This flight condition corresponds to a lighter aircraft flying at a smaller Mach number compared to the reference condition (the pink shape). This explains the smaller deformation at the wing tip compared with the pink reference. The deformed state of the aircraft depicted in blue corresponds to the same flight condition as the grey shape. The aircraft depicted in the blue shape is, however, trimmed at a higher load factor. As can be seen in figure (6.10), the largest absolute upward deformations at the wing tip, occur for the 'blue' M02P case.

The aerodynamic geometry did not include flap-track fairings, pylons or pods. However, all structural mass is accounted for. Furthermore, an estimated thrust [9] and direct lift and moment contributions from the engines, estimated from the aerodynamic database, are applied to the structural model as direct loads. This seems to be a very rough estimation, considering the accurateness of the aerodynamic solver. Although, comparison of the results from CFD-CSD simulations that were performed with and without these contributions due to direct loads from the engines, showed that the differences in the deformation and pressure distributions at the specific stations are negligible.

Figure (6.13) shows the pressure distribution on the surface of the wing and winglet for the cruise condition (referred to as M01P). Figures (6.14) and (6.15) show the chordwise pressure distributions at the spanwise stations at which pressure measurements from flight test were available. The correspondence with the pressure measurements is pretty good. The largest differences occur for the two winglet stations. Unfortunately, the

---

[9]Estimated using a thrust model as described in section 4.6

winglet stations had a relatively small number of data points. First of all, due to the smaller size of the winglet (compared to the wing), the amount of flight test instrumentation is limited. Furthermore, it is more difficult to get stabilized conditions at the winglet, necessary for accurate pressure measurements, due to flexibility effects and the complicated flow field with large gradients in flow variables at the wing tip.

The differences for the outer wing stations could be explained by a slightly different deformation/geometry of the wing due to flexibility effects compared to reality. This could be caused by a structural model that is a little bit too weak.

The local lift (and moment) coefficient can be calculated from the chordwise pressure distributions by integration of the pressure coefficient along the upper and lower surface, see also reference [And89]. It can be directly seen from figures (6.14) and (6.15) that the lift coefficient from the flight test pressure measurements is lower for the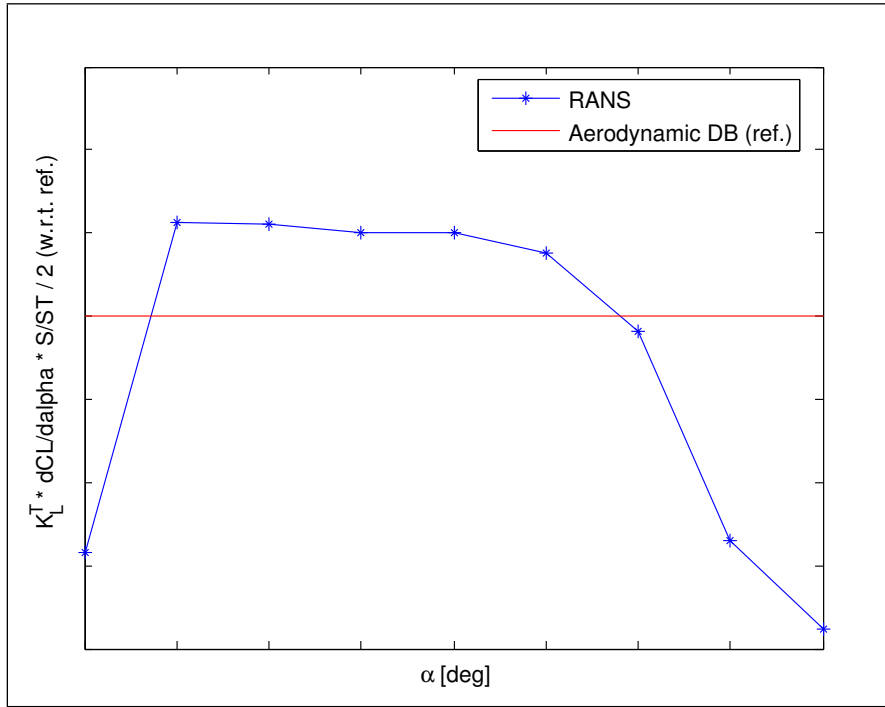 two winglet stations compared with the CFD-CSD simulations. Furthermore, the chordwise distributions of the most outer winglet station shows a higher after loading than the simulation, meaning that the pressure measurement indicates a higher nose down pitch for the winglet then the simulation. Keep in mind, however, that the integral values of the measured pressures distributions at the winglet have limited accuracy, because of the relatively low amount of data points.

Obviously, from a loads perspective, it is very interesting to compare the CFD-CSD simulations with flight test pressure measurements at the highest achievable load factors. The problem is that in order to accurately measure the pressure distributions a stabilized flight condition is necessary over a certain time interval. Measurements for these more extreme flight conditions were therefore not available in this case.

In addition, due to this certain time interval necessary to record the data from all the pressure holes and the unsteady flow phenomena occurring especially in the proximity of the wing tips (due to the tip vortices), it is questionable whether such a measurement procedure can lead to trustworthy distributions. Furthermore, there are no commercial flow solvers available yet that give trustworthy solutions beyond flow separation (if they converge at all!).

Rigid analysis

A rigid analysis has been performed for comparison of the CFD-results with the rigid data from the aerodynamic database. The data from this aerodynamic database is given in jig-shape for this aircraft model. The aerodynamic geometry of the aircraft, used for the simulations is as depicted by the pink shape in figure (6.10), although without horizontal tail. The pink shape corresponds to the geometry for the reference condition (flight shape).

Thus there is a difference in reference geometry. Therefore, only the gradient-effects will be considered. The absolute values are not directly comparable and this comparison is therefore omitted.

The flight conditions for case M01P (representative cruise condition) are taken for the alpha-sweep in the rigid analysis.
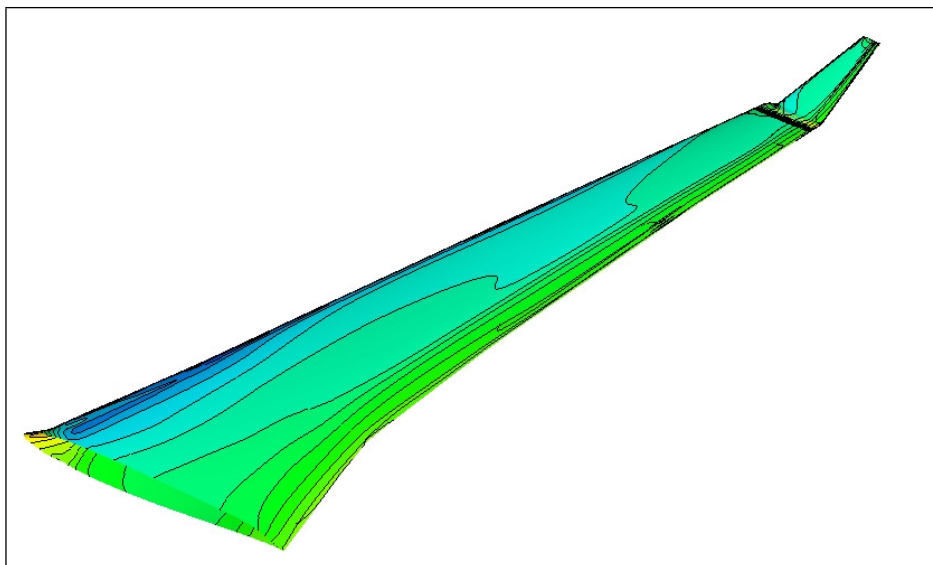
Figure 6.13: *Pressure distributions from coupled CFD-CSD simulations of the total aircraft plotted only for the wing and winglet (case: M01P).*
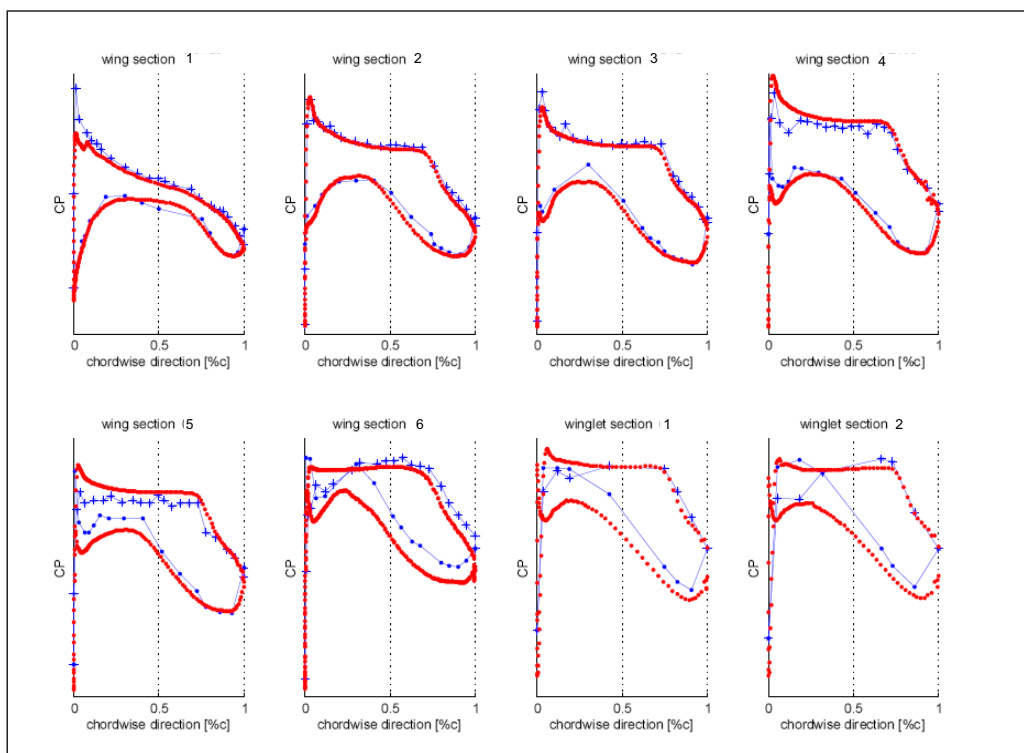
Figure 6.14: *Chordwise pressure distributions from coupled CFD-CSD simulations (red) compared with flight test measurements (blue) for the cruise condition M01P. Wing(let) section 1 corresponds to the most inboard wing(let) section.*
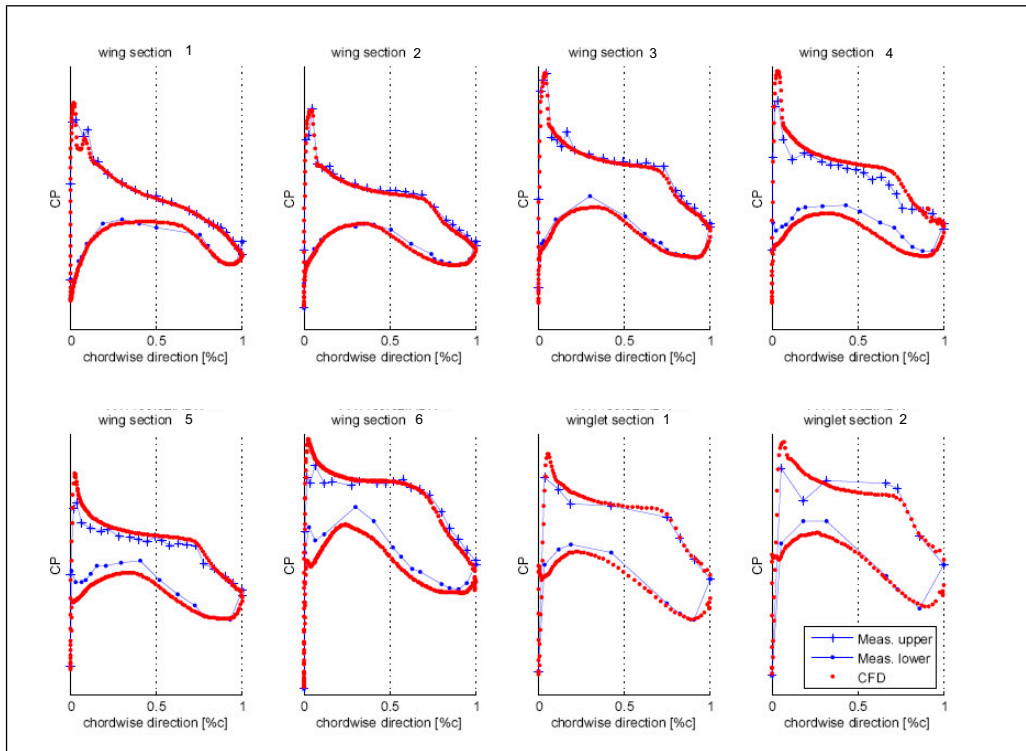
Figure 6.15: *Chordwise pressure distributions from coupled CFD-CSD simulations (red) compared with flight test measurements (blue) for the loads representative condition M02P ($>$ 1g). Wing(let) section 1 corresponds to the most inboard wing(let) section.*

The spanwise results for local lift and moment distributions for the alpha-sweep are depicted in figure (6.16). For the highest plotted alpha, it can be seen from the local lift and moment distributions for the wing, that there is flow separation. Notice, that the simulation had very bad convergence characteristics at this angle of attack due to this flow separation. Therefore, the results at this incidence angle have to be considered with caution. At a higher angle of attack, no convergence was reached.

Global winglet results

In the present study of the outer wing loads, the comparison at the winglet is of main importance. Due to the increasing differences at the winglet for increasing load factors between loads simulations and flight test, it is expected that the assumed alpha-gradient (from the aerodynamic database) will be too small compared with the CFD-results. Notice, that in section 6.6.4 the flexible CFD-CSD results were shown to be comparable with the flight test measurements. Therefore, it is expected that the gradients determined by a rigid CFD-analysis will be close to the 'real' values.

In the aerodynamic database, the direct wing tip fence lift is described by:

$$C_L^T = C_{L0}^T + K_L^T \cdot \frac{dC_L}{d\alpha}\big|_{WFP}(\alpha - \alpha_0) \qquad (6.47)$$

In order to be comparable with the CFD-data, the following quantity is taken for comparison:

$$K_L^T \cdot \frac{dC_L}{d\alpha}\big|_{WFP} \cdot \frac{S}{S^T} \cdot \frac{1}{2} \tag{6.48}$$

At the representative Mach number, this quantity has the following value according to the aerodynamic database:

$$K_L^T \cdot \frac{dC_L}{d\alpha}\big|_{WFP} \cdot \frac{S}{S^T} \cdot \frac{1}{2} = K_{ref} \tag{6.49}$$

The same quantity is determined for the RANS-simulations by integration over the winglet of the change in local lift coefficient at each alpha and transformation from the direction normal to the winglet surface to the direction perpendicular to the freestream and scaled with K_{ref}:

$$K_L^T \cdot \frac{dC_L}{d\alpha} \cdot \frac{S}{S^T} \cdot \frac{1}{2} \cdot \frac{1}{K_{ref}} = \int_0^1 \frac{dc_l}{d\alpha} \cdot \frac{l}{l_g} d\eta \cdot \sin(40.7 \cdot \frac{\pi}{180}) \cdot \frac{1}{K_{ref}} \tag{6.50}$$

The results are plotted in figure (6.17) together with the constant (w.r.t. alpha) value from the aerodynamic database, from equation (6.49).

The value plotted at $alpha_i$ has been determined from the difference in results from $alpha_i$ and $alpha_i + 1°$. Recall that the values at the bounds of alpha thus have a large uncertainty because of the separated flow and the bad convergence of the solution.

Notice that the graph is not constant, but varies over alpha. For the alpha range depicted in the center of the graph, the quantity varies more or less linearly. The specific quantity from equation (6.48), ranges around one more or less discrete value.

The difference between these varying RANS-results and the constant value (1) from the aerodynamic database can be seen very clearly from figure (6.17). In the moderate incidence angle range depicted in the center of figure (6.17), the RANS-results give larger values for the specific quantity.

Local wing/winglet results

In addition to the comparison of the integrated results at the winglet, the local gradients are also studied for the wing and the winglet. Two representative plots can be found in appendix A in figures (A.1) and (A.2) for the wing and winglet respectively.

The aerodynamic database, describing the rigid aerodynamic effects, gives constant values for the local gradients. This assumption is quite good along the wing up until $\eta \approx 0.5$. For the outer wing and especially for the winglet, there is a quite strong variation over alpha.

The green lines in the figures correspond to a linear fit that has been performed over the interval of the incidence angle that has the highest confidence. The linear fit gives a relatively good representation of the variation over angle of attack. It is therefore recommended to describe the gradient for the local lift on wing and winglets by a linear function. The actual function for local lift then becomes a second order function.
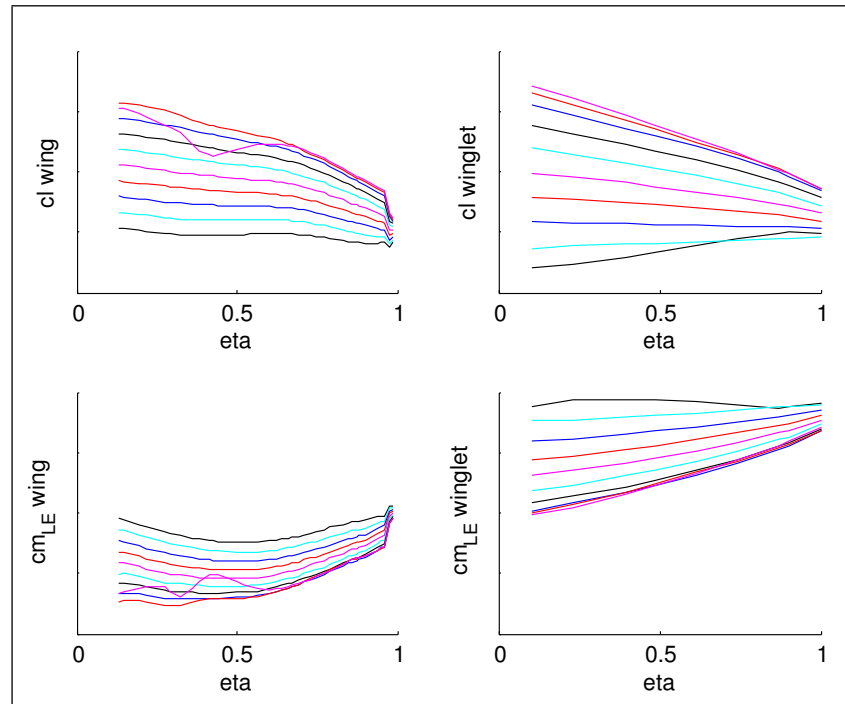
Figure 6.16: *Spanwise pressure distributions for an alpha-sweep. Data extracted from rigid analysis (CFD).*

This approach has been tested within the flight loads model. The static aerodynamic loads were thus described by a second order function instead of a linear function. A detailed description of this process and its results, will be presented in section 6.7.

6.6.5 Conclusion

1. The flexible CFD-CSD analysis showed pretty good correspondence with the pressure measurements from flight test.

   (a) The largest differences occur for the two winglet stations. This might be explained by the relatively small number of data points (pressure holes) for the winglet. Furthermore, it is more difficult to get stabilized conditions at the winglet, necessary for accurate pressure measurements, due to flexibility effects and the complicated flow field with large gradients in flow variables at the wing tip. These are in principle uncertainties on the side of the pressure measurements.

   (b) The differences for the outer wing stations could be explained by a slightly different deformation/geometry of the wing due to flexibility effects compared to reality. This could arise from uncertainties within the structural model.

   (c) The lift coefficient from flight test pressure measurements is lower for the two winglet stations compared with the CFD-CSD simulations.

Figure 6.17: *Integrated load on winglet (alpha-Gradient) scaled with its value from aerodynamic database.*

    (d) The chordwise distributions of the most outer winglet station shows a higher aft loading than the simulation. This means that the pressure measurement indicates a higher nose down pitch for the winglet then the simulation. However, the integral values of the measured pressure distributions at the winglet have limited accuracy, because of the relatively low amount of data points.

2. The rigid CFD analysis showed poor correspondence with the rigid aerodynamic data from the aerodynamic database.

    (a) The quantity:

$$K_L^T \cdot \frac{dC_L}{d\alpha}\big|_{WFP} \cdot \frac{S}{S^T} \cdot \frac{1}{2} \cdot \frac{1}{K_{ref}} \qquad (6.51)$$

is used for comparison of the gradient of the winglet total lift coefficient with respect to alpha. This quantity was shown to be larger in comparison with its value K_{ref} from the aerodynamic database.

    (b) The RANS-results showed a variation of this quantity around a constant value for the medium range of angle of attack. This in contrast to the value 1 from the aerodynamic database which is a constant (w.r.t. alpha) at this typical Mach Number.

    (c) Up until $\eta = 0.5$ on the wing, the assumption of a constant alpha-gradient for the local lift coefficient is quite good.

(d) For the outer wing and especially for the winglet, there is a quite strong variation over alpha. This variation can be relatively good represented by a linear function. It is therefore recommended to describe the gradient for the local lift on wing and winglets by a linear function.

6.7   Identification of nonlinear rigid effects: NL-rigid

It was shown in the previous section, that according to highly sophisticated CFD calculations, the gradient for the local lift on the wing and winglets with respect to the angle of attack can be approximated by linear functions. Consequently, the distributions due to the angle of attack become second order functions of the incidence angle. This in contrast to the assumption of constant gradients or switching between so-called regions. The flight loads monitoring model of which the main aspects are described in section 6.3, is again used. The modifications performed here are thus variations on that model. Further information on details of the modelling can be found in chapter 4.

6.7.1   Aerodynamic model

It was seen in section 6.5, that modifications in the aerodynamic modelling of the flexibility effects have been dissatisfactory. The modelling was either too complicated (would need too much computational resources) or was not able to describe the observed phenomena satisfactory. Together with the conclusions from section 6.6, the previous assumption of correct rigid body aerodynamics has been dropped here.
In this section, the matrix $\mathcal{R}$ from equation (6.19) is assumed to be a unity matrix. Recall that if the matrix $\mathcal{R}$ is assumed to be a constant matrix, the flexibility effects are linearly accounted for. Here it will thus be assumed that the aerodynamic contribution due to airframe flexibility is correct or at least the possible error is assumed to be insignificant. It will be investigated here, whether it is possible to describe the specific phenomenon under this assumption.

The focus in this section will be on modifying the calculation of the load distributions on the wing and winglets due to incidence from the rigid body motion, compare with equation (6.28):

$$\mathbf{F}_{g1_c, x_m} = q \cdot \mathbf{T}_{kg1}^T \cdot f_3(\mathbf{Q}_{k_c x_m} \mathbf{x}_m), \tag{6.52}$$

where the function f_3 describes an additional transformation from aerodynamic axes to body axes and a second order effect is included:

$$\mathbf{x}_m = \begin{bmatrix} 1 \\ \alpha \\ \alpha^2 \end{bmatrix} \tag{6.53}$$

The other aerodynamic forces due to rigid body motion and control surface deflection are again calculated using equation (6.27):

$$\mathbf{F}^*_{g1,x_R} + \mathbf{F}_{g1,\delta} = q \cdot \left[f_1(\mathbf{Q}^*_{g1x_R}, \mathbf{x}_R) + f_2(\mathbf{Q}_{g1\delta}, \boldsymbol{\delta}) \right],$$

The aerodynamic load distribution due to rigid body motion is then, recall equation (6.29):

$$\mathbf{F}_{g1_{x_R}} = \mathbf{F}^*_{g1,x_R} + \mathbf{F}_{g1,\delta} + \mathbf{F}_{g1_c,x_m},$$

One could assume that the same distributions are contained in matrix $\mathbf{Q}_{k_c x_m}$ as the 'original' model and that the second order effect is just added. However, there are some complications. In the present model, the matrices $\mathbf{Q}_{kx_R}$ and $\mathbf{Q}_{g1x_R}$ cannot be transformed into each other only by the use of the spline matrix T_{kg1}. Going from $\mathbf{Q}_{kx_R}$ to $\mathbf{Q}_{g1x_R}$ requires a transformation of all elements (while accounting for local reference frames at each grid point) from the aerodynamic reference frame into body axis. Furthermore, the drag distribution is accounted for separately and applied directly to the structural $g1$-grid. The drag distributions are determined such that the total amount of drag corresponds to the drag polar for the total aircraft (without horizontal stabilizer) as can be derived from the aerodynamic database. The modelling pre-process is thus different when taking $\mathbf{Q}_{kx_R}$ instead of $\mathbf{Q}_{g1x_R}$, but obviously both should lead to the same results. Therefore, an additional step is included to guarantee that the results from the initial guess of the new model are comparable with those from the original model. The additional features of the new model are then used to improve results. These improvements are only useful if it can be determined which improvements are caused by which effects. Alternatively stated, by deselecting principally additional features of the new model, one should be able to generate similar/equal results as with the original model to be able to draw conclusions with respect to the original model.

Therefore, it has to be investigated whether the new model that uses $\mathbf{Q}_{kx_R}$ can describe the specific effects comparable to the description by the original model that uses $\mathbf{Q}_{g1x_R}$. It is investigated first whether the procedure that uses the matrix $\mathbf{Q}_{kx_R}$, derived from the aerodynamic database, combined with the previously mentioned transformation from aerodynamic axes to body axes together with the specific implementation of drag, can be used to reconstruct exactly the same as when using $\mathbf{Q}_{g1x_R}$ directly. This requires the use of the expression:

$$\mathbf{F}_{k,x_R} = q \cdot f_4(\mathbf{Q}_{kx_R}, \mathbf{x}_R) \tag{6.54}$$

where f_4 is a piece-wise linear function dependent on the formulation in the aerodynamic database that was used to generate it. This formulation allows the use of a nonlinear function f_4 as well. The disadvantage by the description as in equation (6.54) is that it is computationally inefficient, which is very critical for simulations in the field of loads analysis. Notice that only one loads loop already involves $10 \cdot 10^3$ to $20 \cdot 10^3$ load cases to cover the whole flight envelope for all possible mass cases. The description from equation (6.54) requires a matrix interpolation for/at each angle of attack. Therefore, it is

additionally advantageous to use the modelling alternative as proposed here in equations (6.52) and (6.53).

An exact match could be achieved by using the formulation based on equation (6.54) compared to that by using the original model that uses $\mathbf{Q}_{g1x_R}$. Now, it should be investigated whether similar results can be achieved with the formulation from equation (6.52).

The difficulty with the formulation from equation (6.52) is that the distributions that are contained in the matrix $\mathbf{Q}_{k_c x_m}$ are unknown. To minimize possible differences due to only the different formulation of the specific effects, it is chosen to change as little as possible and thus use the 'hybrid' formulation as was already proposed in equation (6.54). It is expected that the phenomenon observed during flight test could be mainly described by modifications of the aerodynamic load contributions on the wings and winglets due to incidence. The practical desire is to keep the changes as minimal as possible but obviously with maximum effect.

The problem that remains is to determine meaningful null-, α- and α^2-distributions for the wing and winglets for distributed drag, lift and pitching moments, which means 18 distributions in total. As an initial guess, the null- and α-gradient distributions are taken from the aerodynamic database at an angle of attack of one degree. Each of these distributions ($\mathbf{d_a}$) can be superimposed with a linear function dependent on the spanwise positions along the component, such that:

$$\mathbf{d_l} = \boldsymbol{\eta} \cdot p_1 + p_2, \tag{6.55}$$

$$\mathbf{d_{tot}} = p_3 \cdot (\mathbf{d_a} + \mathbf{d_l}). \tag{6.56}$$

This approach guarantees physically meaningful distributions (comparable to those from the aerodynamic database), that each can be slightly modified by using 3 parameters for each effect and component to get for example more or less outboard loading.

The distributions for the α^2-effect are chosen to be equal to those for the α-effect, but each with their own 3 free parameters to allow for adjustments in shape and magnitude. In total this amounts to 54 free parameters that are to be adequately chosen.

Assuming no shape adjustments, thus for all effects p_1 and p_2 are initially set to zero, and furthermore $p_3 = 1$ for the null and α-effects and $p_3 = -2$ for the α^2-effect, leads to very good results. The identification algorithm from chapter 5 was used to optimise the 54 parameters that describe the distributions contained in the matrix $\mathbf{Q}_{k_c x_m}$ such that the forces on the structural $g1$-set, that can be determined from equation (6.52), are as close as possible to those determined based on the original formulation with the matrix $\mathbf{Q}_{g1_c x_R}$. The optimization did not find a significant parameter improvement for this model. Therefore it is chosen to take the initial set of parameters. A comparison of the lift coefficient versus angle of attack for the total aircraft without horizontal tailplane can be seen in figure (6.18). Equal correspondence is found for the distributions of local coefficients. The correspondence is assumed to be very well. Furthermore, because the functions describing the aerodynamic distributions are no longer piece-wise linear functions, the results might even become better, as the nonlinearities might be described more realistic with the new model. This will be investigated in the next section, where the new model is used in the flight test identification.
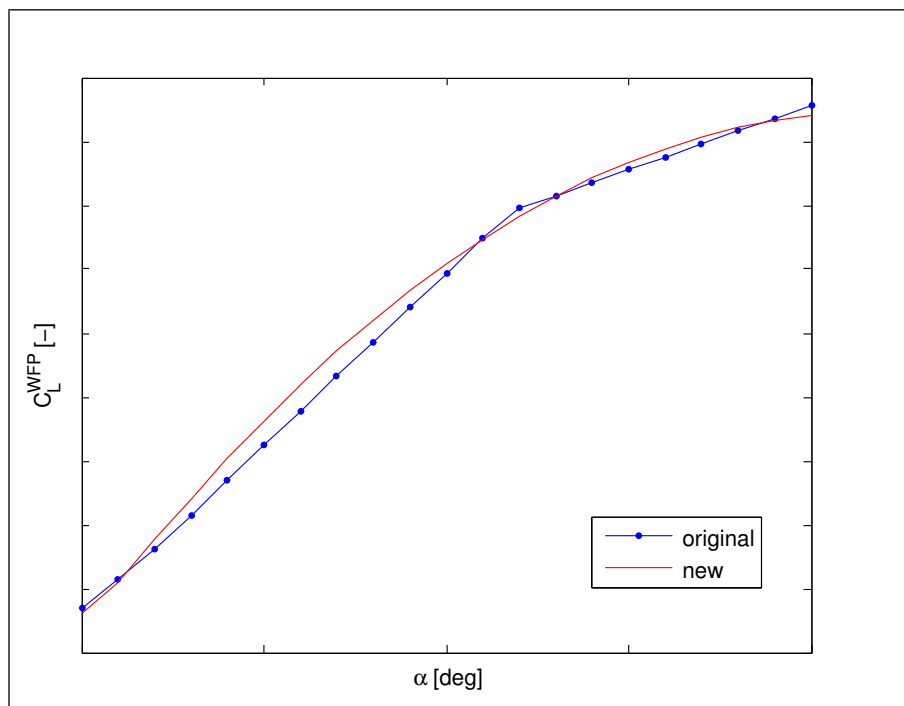
Figure 6.18: *Comparison of lift coefficients of total aircraft (without horizontal tailplane) using the original modelling to that using the new formulation given by equation (6.52).*

6.7.2 Flight test identification of parameters

The identification of the new model, presented in section 6.7.1, showes promising results straight away. However, the final procedure was found after several sessions of running the identification algorithm. It is quite an easy task for the algorithm to determine the values of a set of parameters such that a good match on the output vector is achieved, provided the model can potentially describe the desired phenomenon. However, in case of loads applications, which require consistent and distributed aircraft models, physically meaningful results have to be attained.

If no correct set of boundary conditions are chosen, it can be expected that the routine will come up with a nonphysical model. First of all, one has to choose adequate (upper and lower) boundaries for the parameters that are to be identified. The algorithm then controls the stepsize of the parameter update, while accounting for all prescribed boundary values. Secondly, a condition/equation should be present that controls the overall/total results as will be shown later in this section. Such an extra condition might narrow the searching path in a positive way, such that it will 'pass' local minima. This might improve the final result considerably, although starting from the same initial condition.

Furthermore, one should decide how much freedom in the model, in this case in the distributions, is needed and allowed. Too little freedom of the model might not lead to a good correspondence in the output vectors due to the large restrictions. Too much freedom might easily lead to nonphysical results that could be easily overseen in models of this size and complexity. This is a dangerous situation, because the model gives good predictions for the cases comparable to those for which the identification was done, but

might give completely erroneous results in all or many other cases one might want to predict with this model. It might even give completely wrong results for other stations or quantities, that were not part of the output vector.

Last but not least, symmetry conditions should always be imposed if possible. In the present case, there are significantly more loads stations on the right wing compared to the left. This would lead most probably to an asymmetric model, because there are not as many boundary conditions on the left as on the right wing. Furthermore, for the measurement stations that are available on both the left and right handside, it will not give exactly the same indicated (measured) values for the left and the right. This further would encourage asymmetries. In general it can be said that one should always be alert to include as much symmetry conditions as possible. It can minimize the required computational resources and the desired symmetry level of the model is guaranteed.

It should be checked whether the measurement data that is used for the identification is trustworthy and complies to the sign conventions. A visual check of a measurement signal might already be so convincing, that it can be concluded that a certain signal contains faulty data. This might be something like a trivial signal showing only bit-jumps. It is also recommended to check whether all signals have the sign that is to be expected. Otherwise, it might be necessary to change the sign of the data such that it complies again with the conventions. In general, the inclusion of faulty measurements will deteriorate the meaningfulness of the final results of the identification. In practically all applications, it is not wanted to finally being able to predict displayed (error contained) measurement values. The goal is to enable an accurate prediction of the actual quantity using the identified model. This actual local load is then used to determine the local stresses the structure has to sustain.

The measurement signals for loads measurements performed by strain gauges can contain drifts. In this case the magnitudes of the drifts are unknown and are difficult to estimate in advance with sufficient accuracy. Inclusion of the biases as parameters in the identification procedure can easily lead to erroneous and nonphysical results. A good meaning to circumvent this problem is to consider only relative changes with respect to a suitable 1g-cruise condition. Such suitable reference can be the stabilised cruise condition that precedes the specific manoeuvre. Assumptions on the drifts are then no longer required. It allows drifts to be present on the measurement data (under the restriction that these are constant during the time interval considered), without having negative impact on the identification results. At the end of the identification, the drifts on the measurements can be determined after comparison with the specific absolute values from the final model.

When considering the relative changes in the measurement data, an additional condition has to be included to guarantee an adequate overall loads level, again to prevent nonphysical results. A good means to control the overall loads level is by including the load factor N_Z as an extra boundary condition. This can be practically implemented by including N_Z as an element of the output vector.

This relative treatment of the measurement data combined with the overall control of the loads level by the N_Z-requirement are an excellent means to fully exploit the information contained in the measurement data while still preserving the model to stay physically possible.

θ_1	Parameter that scales simultaneously the null-distributions for drag, lift and pitching moment distributions on the winglets
θ_2	Parameter that scales simultaneously the null-distributions for drag, lift and pitching moment distributions on the wings
θ_3	Parameter that scales simultaneously the α-distributions for drag, lift and pitching moment distributions on the winglets
θ_4	Parameter that scales simultaneously the α-distributions for drag, lift and pitching moment distributions on the wings
θ_5	Parameter that scales simultaneously the α^2-distributions for drag, lift and pitching moment distributions on the winglets
θ_6	Parameter that scales simultaneously the α^2-distributions for drag, lift and pitching moment distributions on the wings

Table 6.4: *Description of the six free parameters that scale the specific distributions that are contained in the matrix $\mathbf{Q}_{k_c x_m}$, see also equation (6.52). These parameters are used in the identification of the nonlinear rigid effects in this section.*

The matrix $\mathbf{Q}_{k_c x_m}$ from equation (6.52) is used to start the identification based on the flight test measurements. Six free parameters are defined to be updated during this flight test identification. It is studied whether it is possible to describe the specific phenomena already with this limited number of free parameters. It is tried to stay as close as possible to the baseline model from a modelling philosophy viewpoint and with respect to its required input data, provided the final parameters stay within certain prescribed bounds. See table 6.4 for a description of the free parameters that will be used here. The initial and boundary values of these six free parameters are set to respectively:

$$\hat{\boldsymbol{\theta}}_0 = \begin{bmatrix} 1 \\ 1 \\ 1 \\ 1 \\ 1 \\ 1 \end{bmatrix}, \qquad \hat{\boldsymbol{\theta}}_{lower} = \begin{bmatrix} -4 \\ -4 \\ -4 \\ -4 \\ -2 \\ -2 \end{bmatrix}, \qquad \hat{\boldsymbol{\theta}}_{upper} = \begin{bmatrix} 4 \\ 4 \\ 4 \\ 4 \\ 2 \\ 2 \end{bmatrix}. \tag{6.57}$$

Additionally, the drag distributions on the complete aircraft are scaled corresponding to the total amount of drag determined from the drag polar of the aircraft (C_D as a function of $C_{L_{WFP}}^2$) based on the current amount of lift. This drag is then distributed along the components using a normalised drag distribution that is determined based on all three contributions from equation (6.29).

6.7.3 Discussion of results

In this section the results of the identification will be presented and discussed. Only two iterations steps were necessary to arrive at the final result. Table 6.5 shows the values of

$J(\hat{\boldsymbol{\theta}}_0)$	-48166.041
$J(\hat{\boldsymbol{\theta}}_1)$	-75175.815
$J(\hat{\boldsymbol{\theta}}_2)$	-76505.548

Table 6.5: *Values of the Negative Likelihood function during the identification of the loads model by modification of the rigid body aerodynamics.*
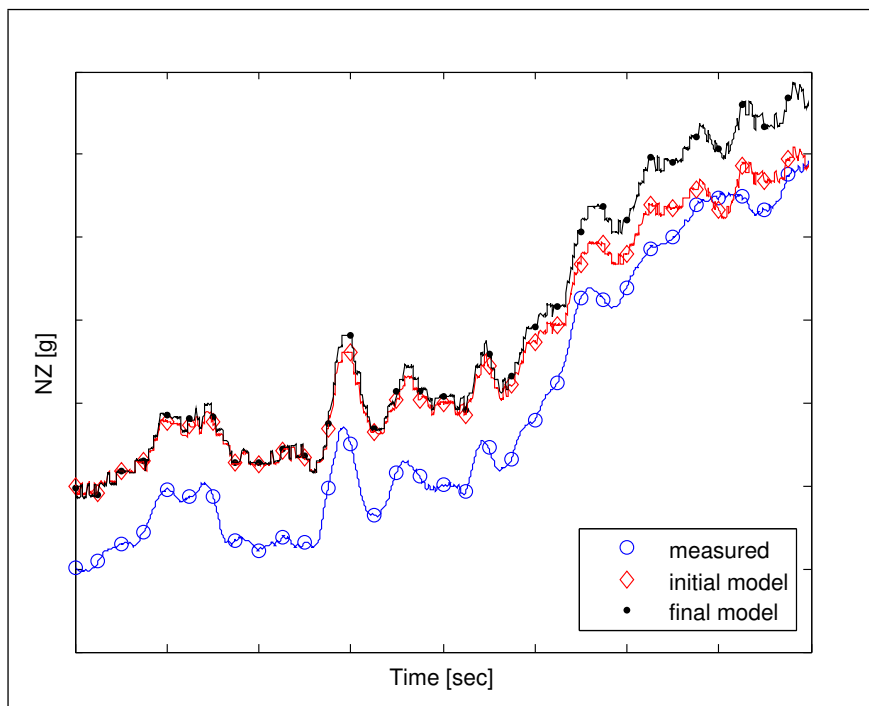
Figure 6.19: *Load factor in Z-direction versus time measurement compared to simulation with the initial and with final model, method "NL-rigid".*

the negative Likelihood function during these iteration steps. $J(\hat{\boldsymbol{\theta}}_0)$ indicates the value for the negative Likelihood function for the model using the initial values for the parameters. A relatively good estimate of the initial values of the parameters does not guarantee a better final result compared to a little bit worse start condition. It is definitely worth it, to improve the values of the parameters or the model itself to improve the starting condition. The initial values of this modified model can then be varied to investigate whether these variations lead to a better final result, the corresponding initial negative Likelihood function might or might not be smaller.

For clarity reasons, the results (values and plots) are only presented of that identification run that has lead to the best results. The insight and experience gained in running the different models and variations on them are tried to capture in words and presented when appropriate.

The 'best' results are in this respect not necessarily those with the smallest negative Likelihood function. The models were always checked afterwards in further detail for their physical meaning. For this aspect, it is difficult to capture all possible checks in advance of the identification, let alone to put them into a numerical criterion. Furthermore, it is not practicable to check everything due to the size and complexity of the model. A lot of engineering judgement and knowledge of the model is required to determine the most effective checks.

Values of the corresponding parameter vector during the identification of the loads model by modification of the rigid body aerodynamics:

$$
\hat{\boldsymbol{\theta}}_0 = \begin{bmatrix} 1 \\ 1 \\ 1 \\ 1 \\ 1 \\ 1 \end{bmatrix}, \qquad
\hat{\boldsymbol{\theta}}_1 = \begin{bmatrix} 0.2139591 \\ 0.9843337 \\ 3.0602078 \\ 0.9115758 \\ 1.7952409 \\ -0.9653210 \end{bmatrix}, \qquad
\hat{\boldsymbol{\theta}}_2 = \begin{bmatrix} 0.1270452 \\ 0.9828316 \\ 3.2988188 \\ 0.8995384 \\ 1.8348285 \\ -1.2082477 \end{bmatrix}. \qquad (6.58)
$$

These values show that if the α-gradient distributions on the winglet (scaled by element 3 and 5 of the parameter vector) are assumed to be considerably larger than 1, better correspondence results with the measurements.

Figure (6.19) shows the load factor in z-direction N_Z compared for the measurements, the initial model and the final model for the time interval considered. As can be seen also from this figure, the time interval considered starts at a 1g cruise condition. Then the coordinated turn is gradually increased up to a representative loads level.

Recall, that an additional element on the output vector was added, N_Z, to control the overall loads level. If the overall loads level (total aircraft) would be too big or too small for the initial model, this would be corrected if possible during the iterations. Here, the correspondence in N_Z is not that bad for the initial model, as can be seen in figure (6.19). In this case, apparently, the algorithm could not find a means to improve correspondence in N_Z without deteriorating the correspondence for the other elements of the output vector. At the beginning of the specific time interval, the load factor is exaggerated by a small amount. The relative increase in load factor over this time interval is less then measured as can be seen most clearly at the end of the time interval. On the contrary, the

final model shows a constant bias on the load factor as can be seen in figure (6.19). This constant bias for the final model is appreciated more, than the smaller relative increase that occurs for the initial model. The relative increase in load factor over the time interval is now described very well by the final model. The small difference is considered to be acceptable at this point. Moreover, this difference can be fully accounted for, if including a zero shift in the model for the N_Z sensor (or alternatively for the angle of attack).

Figures (6.20) to (6.23) show the results for the same 4 load measurements as presented in section 6.5. In each graph, the data is plotted from the baseline model, the initial model, the final model and obviously also the data from the measurements. Each figure contains two graphs. The upper of these three graphs is the most important, as it shows the scaled load relative to the 1g measurement at the starting point (the 1g-reference). The difference between this scaled load relative to its reference was input for the Maximum Likelihood procedure of the algorithm. The same data is plotted in the lower graph, however versus the load factor instead of time. This lower graph is plotted because it shows the behavior of the local load as a function of the overall load factor. In practically all cases, the upper graph (vs. time) provides more insight to the difference at each time step.

Comparison of local loads

The results will now be looked at in more detail. It is important to note at this point that there are uncertainties in the strain gauge measurements. These aspects cannot be influenced a-posteriori and therefore these are treated here as unknown disturbances.
All load outputs showed good to excellent correspondence, except for the integrated shear force on the righthand wing station 2. Because the rest of the load outputs gave that good results, the measurement of this specific shear force is assumed to be corrupt. See figures (6.20) to (6.23) for the same 4 load measurements as presented in section 6.5.

Figure (6.20) shows the scaled shear force on the right wing at the fourth wing station. The correspondence is clearly better for the final model compared with the baseline and the initial model. The correspondence in the relative loads level is very well.
Figure (6.21) shows the scaled bending moment on the right wing at the fifth wing station. The correspondence is clearly better for the final model compared with the baseline and the initial model. The correspondence in the relative loads level is very well.
Figure (6.22) shows the scaled bending moment on the right wing at the sixth and most outboard wing station. The correspondence is again clearly better for the final model compared with the baseline and the initial model. The correspondence in the relative loads level is excellent for the final model. The correspondence in the relative loads level for the baseline and initial model were poor.
Figure (6.23) shows the scaled bending moment at the root of the right winglet. The correspondence is again clearly better for the final model compared with the baseline and the initial model. The correspondence in the relative loads level is excellent for the final model. The correspondence in the relative loads level for the baseline and initial model
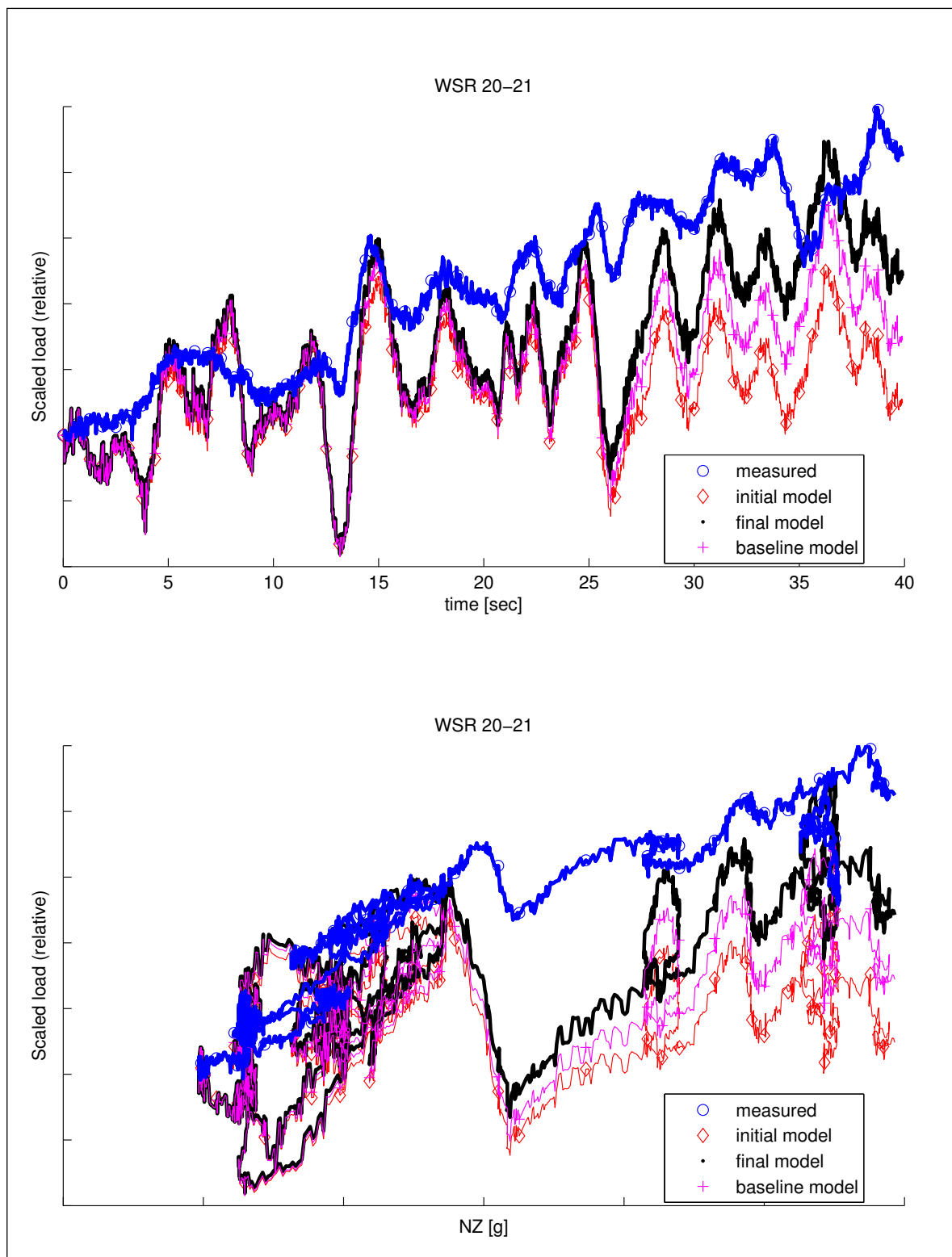
Figure 6.20: *Shear force (relative) on wing right vs. time and load factor respectively for wing station 4, method "NL-rigid".*
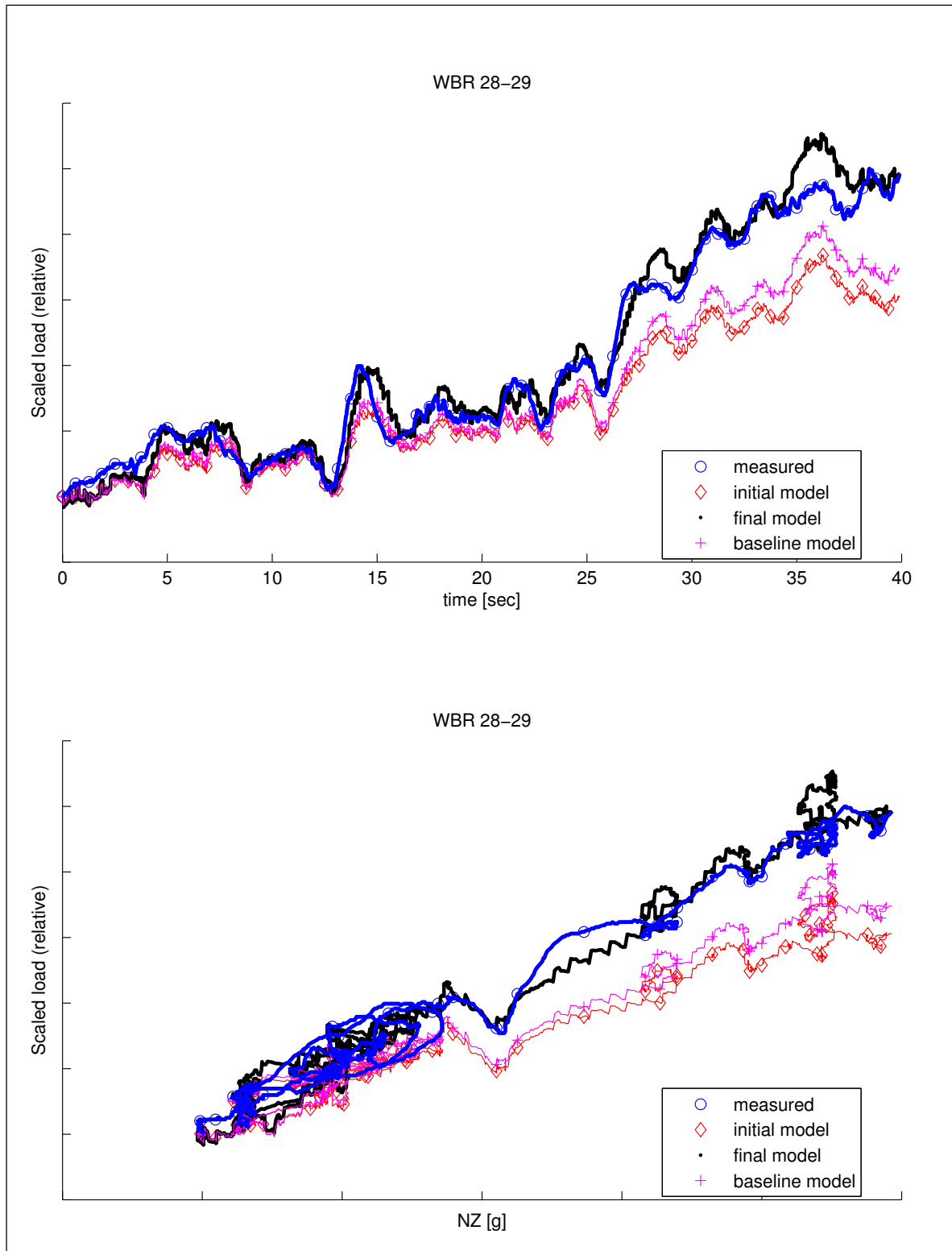
Figure 6.21: *Bending moment (relative) on wing right vs. time and load factor respectively for wing station 5, method "NL-rigid".*
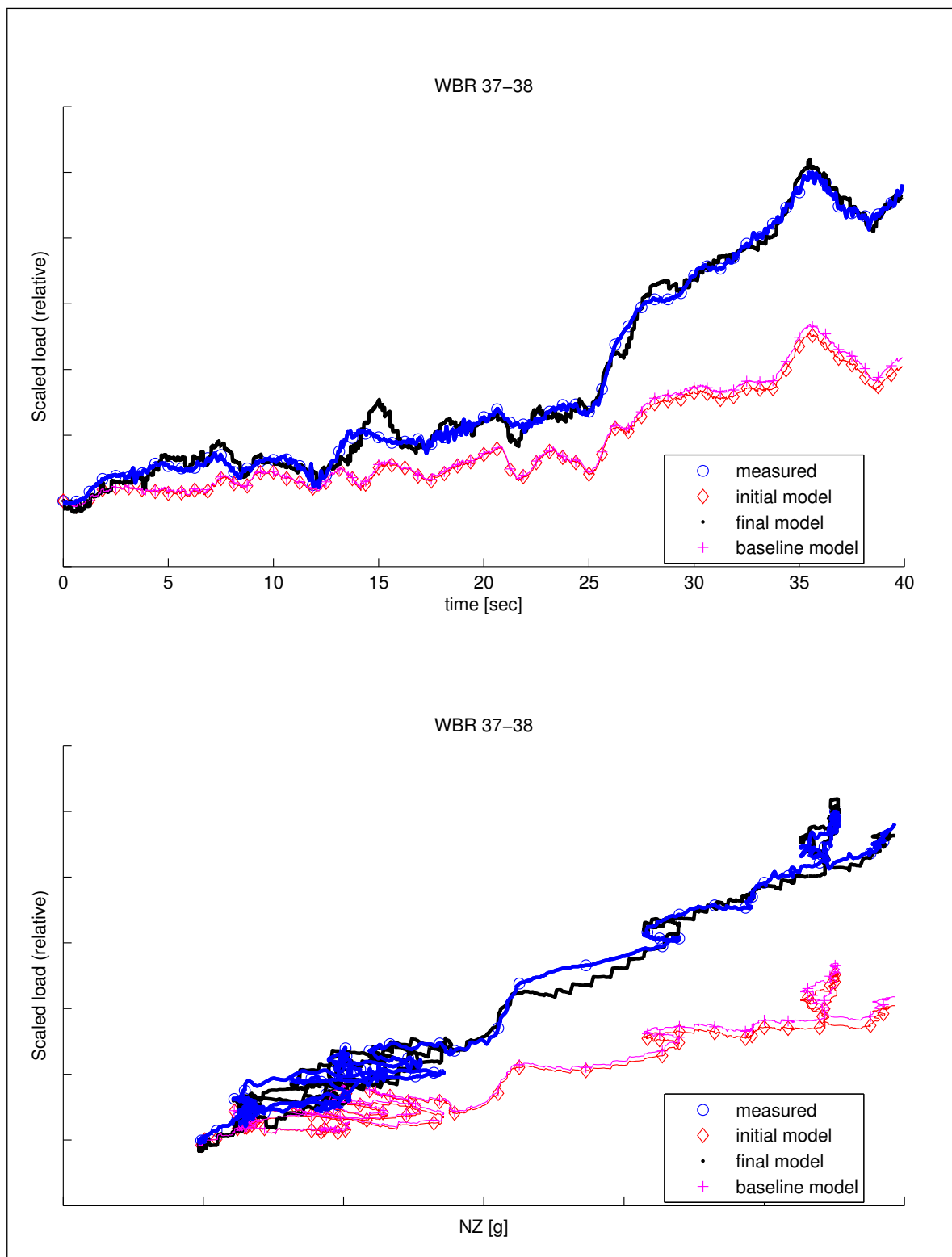
Figure 6.22: *Bending moment (relative) on wing right vs. time and load factor respectively for wing station 6, method "NL-rigid".*
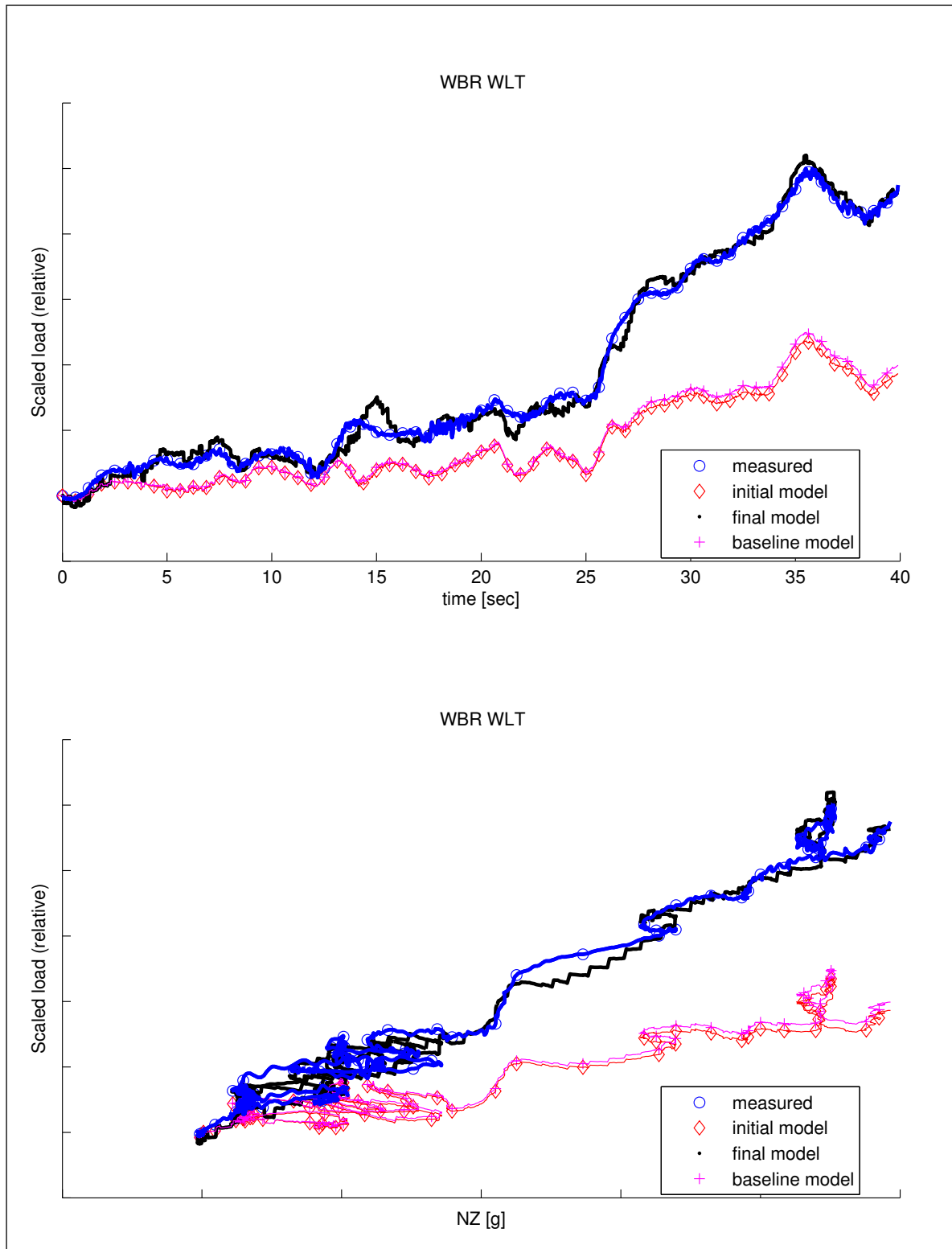
Figure 6.23: *Bending moment (relative) at winglet root vs. time and load factor respectively, righthand side, method "NL-rigid".*

were poor.

It can be concluded from these results that the correspondence on the outboard wing and for the winglet were excellent for the final model, where the initial and baseline model have shown to give poor results. On the more inboard part of the wing, the results of the final model have been very well in most cases. In any case, the final model has not been significantly better or worse on the more inboard part of the wing compared to the baseline or initial model. It is a very nice result that the final model gives such an improvement in the area of main concern, where the baseline model has shown to produce poor results.

The final model that was determined by the identification procedure shows to give good to very good results on the output vector. Remaining discrepancies between the model and the measurement are acceptable and might stem from measurement inaccuracies of the loads and/or states. Now, it should be checked whether the aerodynamic distributions that were adjusted to arrive at this final model are still physically possible.

Verification of local aerodynamics of identified model

Here, it will be checked whether the modified aerodynamics is still physically meaningful. The local and distributed rigid aerodynamic input is compared for the baseline, initial and final models. It would involve too many figures, to show them all. Furthermore, they are very similar and therefore omitted. See figure (6.24) for a representative graph of the local lift force at a certain spanwise wing station as a function of angle of attack. The final model was identified based on data ranging in angle of attacks between 1.5 and 3 degrees. The plotted range in angle of attack is very large in this figure and unrealistic. It cannot be flown completely by the aircraft at this Mach number. It is the range that is used for practical reasons in the simulation. The aerodynamic database contains maximum lift coefficients (stall) and lift coefficients (with corresponding angle of attack) where buffeting occurs, which are accounted for separately in the simulation.

Notice, that due to the different modelling only the 'total' effect due to incidence should be compared. It is for example not meaningful to compare the null-effect distributions of the different models. It can be seen from figure (6.24) that the initial (parabolic) model is very close to the baseline model, showing that the parameters of this initial model are set correctly, which was one of the topics of section 6.7.1. It can be further seen, that the final model has a much larger local lift force slope. This is a little bit suspicious and further study is recommended. Therefore, it will be investigated in the next section whether the aerodynamic behavior determined with the Navier-Stokes calculations from section 6.6 gives comparable local results.

6.8   Identification of rigid effects using CFD-results

The model from the previous section is an elegant means to model the aerodynamic non-linearities at the high angles of attack. However, the range in angle of attack during the
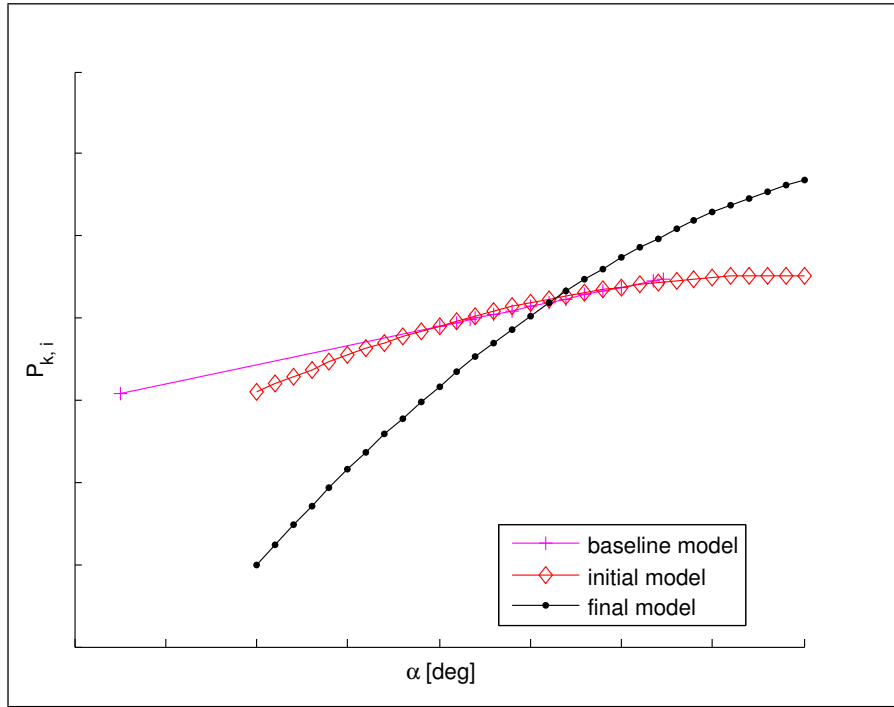
Figure 6.24: *Representative local lift force curve as a function of angle of attack on the aerodynamic k-grid, compared for the baseline model and for the initial and final NL-rigid models.*

specific manoeuvre (time interval) was limited to a small range of moderate angles of attack. In this range both the aerodynamic database and the CFD simulations predict a still more or less linear behavior. Therefore, the focus here will lie on the most optimal description of the aerodynamic behavior in this still linear region. As soon as the most optimal model (input data) has been found for this region, the model can also be extended for the higher angles of attack.

6.8.1 Model initialized with CFD derived input data

In this section, it will be investigated whether better correspondence with the flight loads measurements can be achieved when feeding the flight loads model from section 6.3 directly with the distributions determined from the Navier-Stokes calculations. The (non-linear) data from the CFD simulations is directly applied to the model, similar to the description by equation (6.54):

$$\mathbf{F}_{k,x_R} = q \cdot f_4(\mathbf{Q}_{kx_R}, \mathbf{x}_R)$$

where f_4 is a nonlinear function in this case. Recall, that such a formulation requires a matrix interpolation at each angle of attack, but with the advantage that no information is lost due to linearization.

It is again expected that the phenomenon observed during flight test can be mainly described by modifications of the aerodynamic load contributions on the wings and winglets

due to incidence. The aerodynamic distributions along the other components of the aircraft are described according to the baseline model. The aerodynamic load distribution due to rigid body motion is then again, recall equation (6.29):

$$\mathbf{F}_{g1_{x_R}} = \mathbf{F}^*_{g1,x_R} + \mathbf{F}_{g1,\delta} + \mathbf{F}_{g1_c,x_m},$$

The elements of the matrix $\mathbf{Q}_{kx_R}$ can be determined from the CFD-calculations as follows. First, equations (6.44) to (6.46) are used to determine the local force and moment distributions on the CFD-grid. Unfortunately, the skin friction values were not available for the rigid CFD-calculations (alpha-sweep). However, it was studied whether this contribution is significant for this specific loads purpose. The integration of all effects could be done for the results of the flexible CFD-CSM calculations, where all necessary information was available. It was found that the contribution from skin friction is significantly smaller and can be neglected for the loads applications considered in this report.

At this point it should be mentioned that, it is not a trivial task to determine drag contributions from CFD-calculations, see references [Dam99], [Gil99] and [Kro01] for further information. The integration of the distribution of the pressure and skin friction over the surface of the aircraft is called near field analysis in literature. This in contrast to a far field analysis where the integration is performed over a plane sufficiently far downstream of the aircraft.

The distributions from the CFD-data have to be interpolated to the aerodynamic k-grid of the flight loads model. The nodal force and moment distributions can then be determined from the interpolated force and moment distributions by:

$$\mathbf{Q}_{k_i x_R} = S_c \cdot c_{n_j} \cdot \frac{l_j}{l_g} \cdot \Delta\eta_i \tag{6.59}$$

$$\mathbf{Q}_{k_i x_R} = S_c \cdot c_{a_j} \cdot \frac{l_j}{l_g} \cdot \Delta\eta_i \tag{6.60}$$

$$\mathbf{Q}_{k_i x_R} = S_{c_i} \cdot c_{m_{LE_j}} \cdot \frac{l_j}{l_g} \cdot \Delta\eta_j, \tag{6.61}$$

where c_{n_j}, c_{a_j} and $c_{m_{LE_j}}$ denote the local values of c_n, c_a and $c_{m_{LE}}$ for the ith degree of freedom of the jth grid point corresponding to the aerodynamic k-set. S_c is the reference area of the corresponding component, l_j is the local chord and $\Delta\eta_j$ is the local stripwidth.

Notice, that these quantities are defined in body axis already. The nodal forces and moments can thus be mapped directly onto the aerodynamic grid, without any additional transformations.

The local normal force (F_{k,x_R}) for a certain (jth) aerodynamic grid point can be plotted versus the angle of attack, which is done in figure (6.25). This figure shows a comparison for the initial and final model from NL-rigid, see section 6.7, compared with the baseline model and the RANS-derived data for the local normal force. From this figure it can be seen that the normal force gradient with respect to the angle of attack is practically identical for the baseline model compared with the RANS-derived data. The curve for the final model is quite similar compared to the the baseline model and the RANS-derived

data. The absolute value of the normal force from the RANS-derived data is relatively close to that of the baseline model.

Figure (6.26) shows the same figure but now on the outer wing ($\eta = 0.94$). Not all figures are printed here, because this would involve too many figures. The differences in the absolute values on the outer wing are clearly larger when compared with those on the inner wing (as can be seen from comparison with the previous figure).

It can be seen that the gradients from the final model are comparable to those from the baseline model and from the RANS-derived data. This confirms that the identified normal force gradients for the final model are plausible along the wing. Clear differences can be observed in the absolute level between the baseline model, the final model and the RANS-derived data. It is described later in this section, where these differences stem from.

Similar observations can be done for the local moment, see figures (6.27) and (6.28). The main difference is that the local moment from the RANS-derived data shows a clear nonlinear behavior over the complete range of the angle of attack. The gradients with respect to the angle of attack for the local moment are similar for the final model and the baseline model. Figures (6.29) to (6.30) show respectively the local normal force and local pitching moment distributions at a fixed angle of attack of exemplarily 0 degrees. These figures show that the shape of the distributions are physically possible. There is a clear difference in absolute values as can be seen from these figures. Comparison of the correspondence in the overall load factor N_Z can provide a means to determine which level of absolute values corresponds most to the flight test measurements.

Similar comparisons of gradients and distributions can be performed for the winglets. See figure (6.31) for a plot of the local normal force versus the angle of attack for the aerodynamic grid point at the winglet root. It can be seen that the gradients of the baseline model and the initial model are quite similar as expected. The large gradients from the NL-rigid final model show to correspond well with the gradients determined from the RANS-analysis. This confirms that the aerodynamics as derived by the identification (NL-rigid) from section 6.7 are plausible and seem to correspond well with the RANS-data, see also figures (6.32) and (6.33) for a spanwise winglet station at $\eta = 0.84$ and for the local pitching moment at the winglet root respectively. Clear differences can be observed in the absolute level between the final model and the RANS-derived data. It is also described later in this section, where these differences stem from. Figures (6.34) to (6.38) show the distributions for the local normal force and pitching moment at a fixed angle of attack. Notice from figure (6.34) that for this angle of attack (-1 degree), the final model and the RANS-data are different in sign, when compared with the baseline and initial model. This is not the case for the other angles of attack. The main observation from these plots is that the shapes of the distributions are plausible. Comparison with the flight test data will have to show which of these aerodynamic input data leads to the best correspondence with the measurements.

The value of the negative Likelihood function can be determined for this model initialized with the RANS-data, see table 6.6. This value (-71063) for the Likelihood function is already pretty close to the final value (-76506) after model identification of the NL-

rigid model from section 6.7. This good agreement with the flight loads measurements for the initial model gives much confidence for identification of parameters based on this initial model. It should be noted that these results were generated after neglecting the axial forces from equation (6.45). The largest contribution stems obviously from the normal forces. An explanation for the fact, why the results get better after neglecting the axial terms, is still to be found. It might be due to the fact described below, however this cannot be proved to date.

Figure (6.39) shows the load factor in z-direction N_Z compared for the measurements, the initial model and the final model from section 6.7 and for the initial model from the RANS data (called just RANS from now on) for the time interval considered. Notice that no identification has been done yet for the model presented here. The correspondence in N_Z is not very well for the initial RANS model, as can be seen in figure (6.39). In this case, N_Z is too small for the initial model. This can be explained from the origin of the CFD-calculations. Unfortunately, the jig-shape geometry of the aircraft was not available. Recall from section 6.6 that the CFD-calculations are performed for the aircraft in 'quasi' flight shape. Due to the nose down twist of the outboard flexible wing, the outer wing produces less lift in 'quasi' flight shape compared to jig-shape for the same angle of attack. Keeping this drawback in mind, it is interesting to see what correspondence can still be achieved starting from this input data.

Figures (6.40) to (6.43) show the results for the 4 load outputs (of 21 in total), similarly as in sections 6.5 and 6.7, of the RANS model compared to the initial and final model from section 6.7 and the baseline model. Each figure contains as before the two graphs, where the upper graph is the most important. It shows the scaled load relative to the 1g measurement at the starting point (the 1g-reference).

The discussion of results will not be as exhaustive as in section 6.7 because the results can be interpreted similarly. Only the most significant differences are mentioned here.
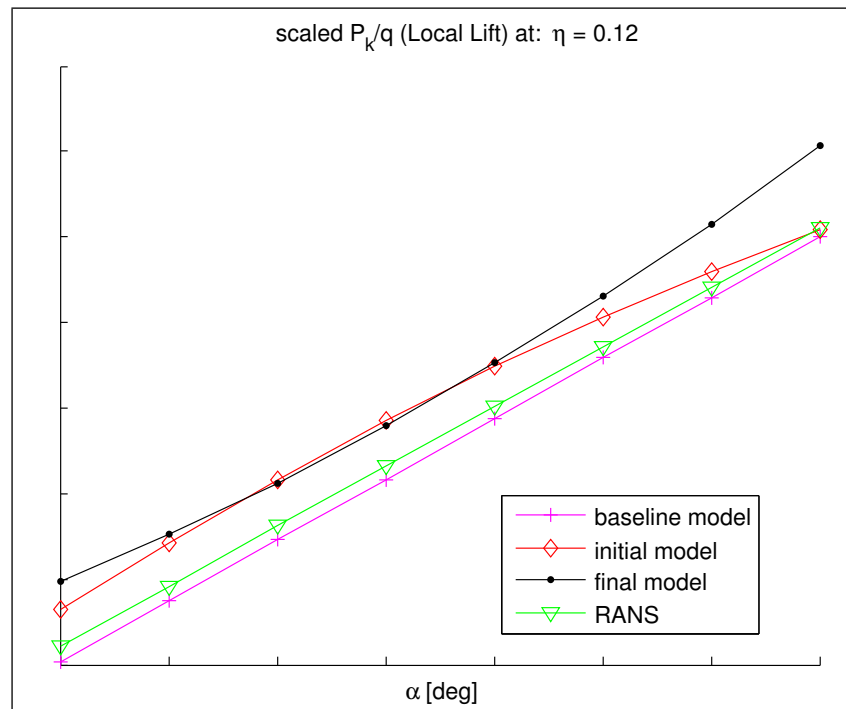
Figure 6.25: *Normal force ($\mathbf{P}_{k,x_R}$) for the jth aerodynamic wing grid point corresponding to $\eta = 0.12$. The initial and final model correspond to the NL-rigid model presented in section 6.7*
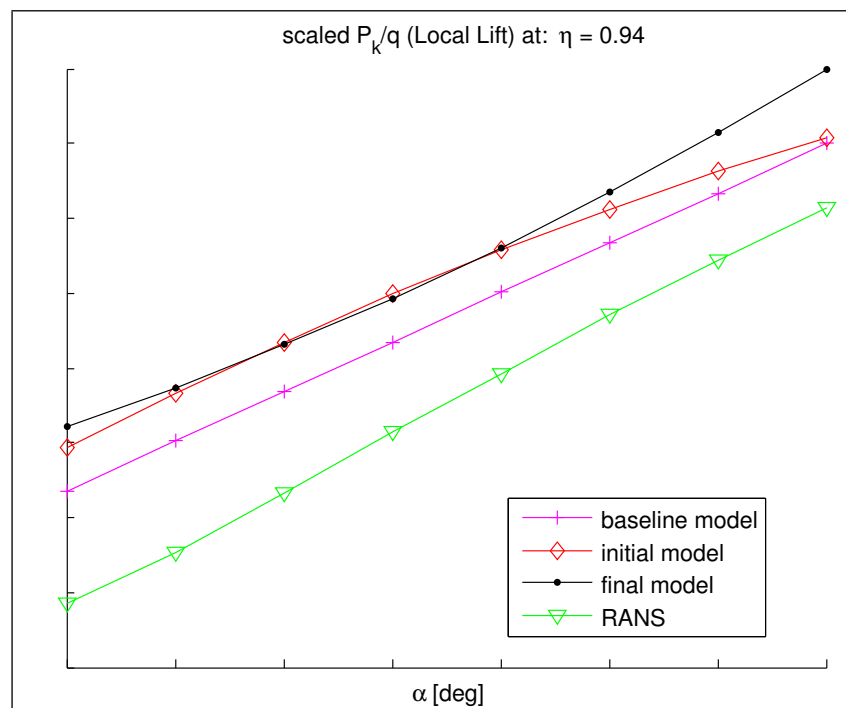
Figure 6.26: *Normal force ($\mathbf{P}_{k,x_R}$) for the jth aerodynamic wing grid point corresponding to $\eta = 0.94$. The initial and final model correspond to the NL-rigid model presented in section 6.7*
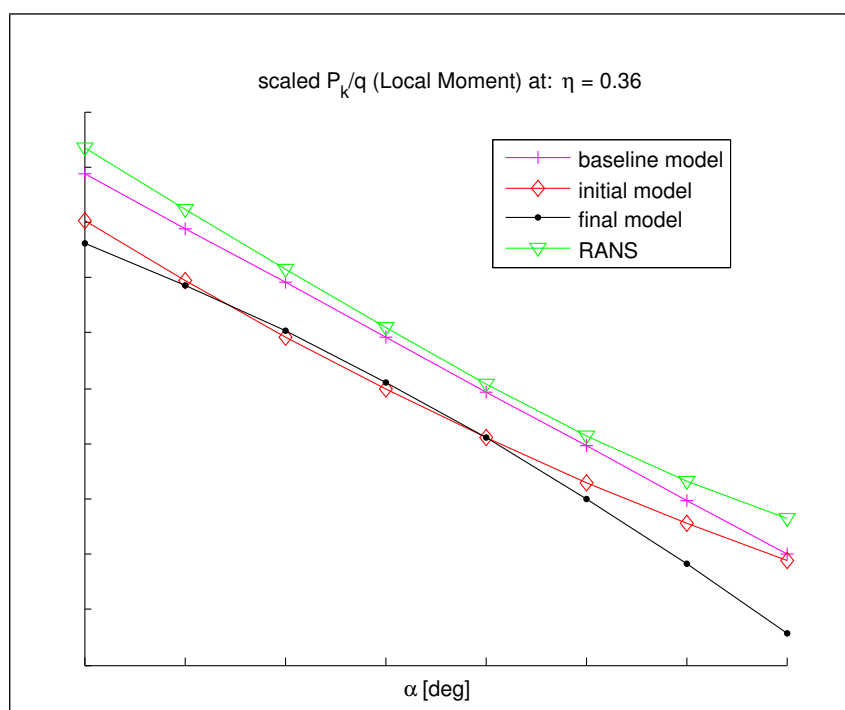
Figure 6.27: *Pitching moment* ($\mathbf{P}_{k,x_R}$) *for the jth aerodynamic wing grid point corresponding to* $\eta = 0.36$. *The initial and final model correspond to the NL-rigid model presented in section 6.7*
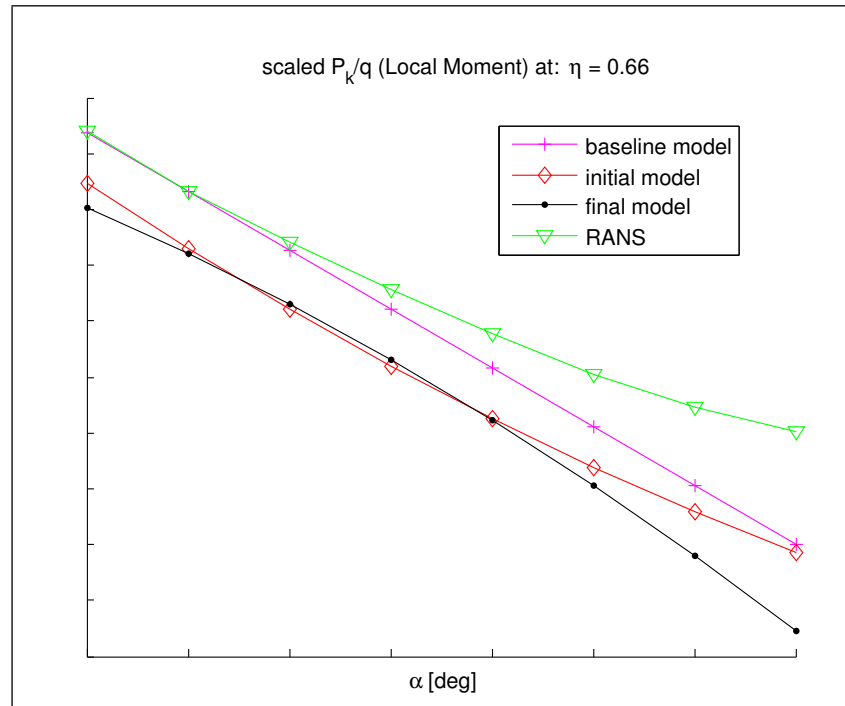
Figure 6.28: *Pitching moment ($\mathbf{P}_{k,x_R}$) for the jth aerodynamic wing grid point corresponding to $\eta = 0.66$. The initial and final model correspond to the NL-rigid model presented in section 6.7*
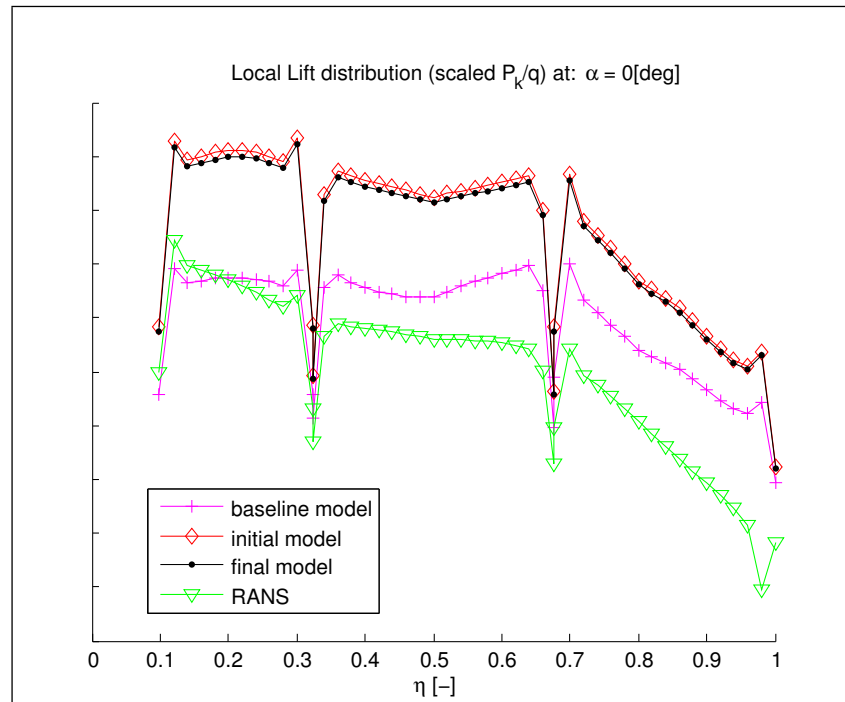
Figure 6.29: *Normal force distribution along the wing derived from $\mathbf{P}_{k,x_R}$ at an angle of attack of $\alpha = 0$ deg. The initial and final model correspond to the NL-rigid model presented in section 6.7*
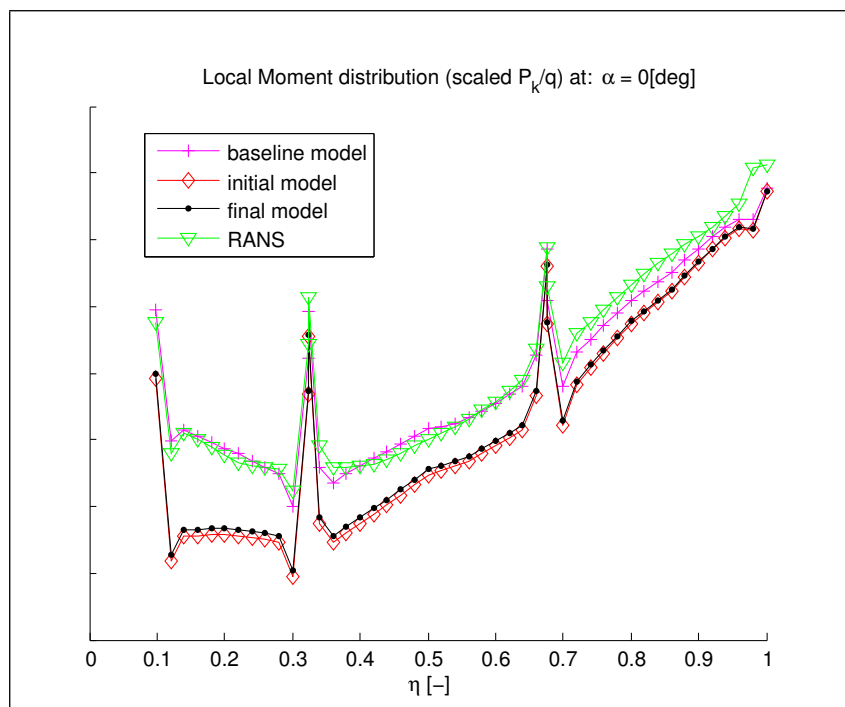
Figure 6.30: *Pitching moment distribution along the wing derived from $\mathbf{P}_{k,x_R}$ at an angle of attack of $\alpha = 0$ deg. The initial and final model correspond to the NL-rigid model presented in section 6.7*
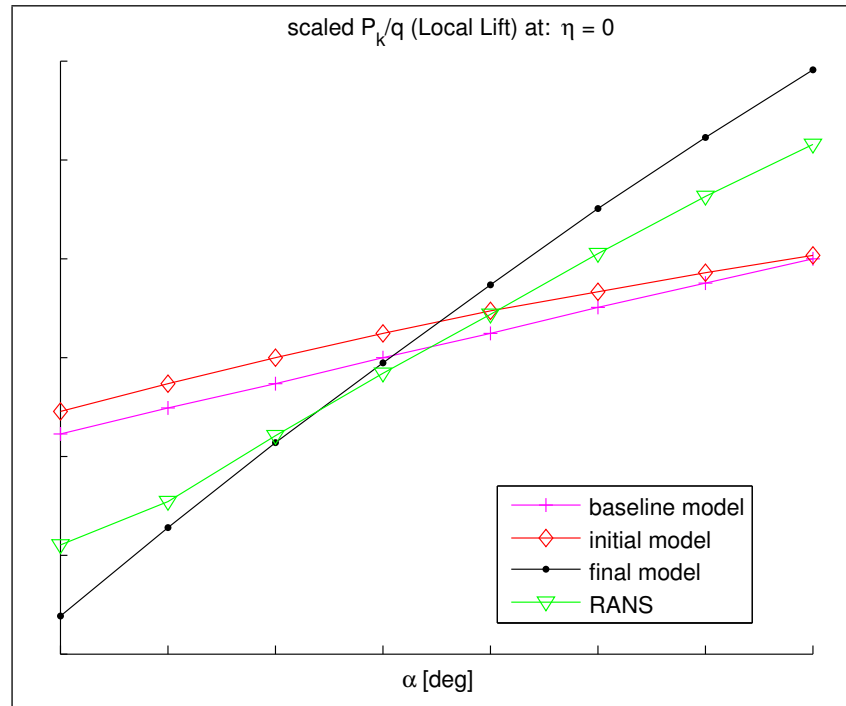
Figure 6.31: *Normal force ($\mathbf{P}_{k,x_R}$) for the jth aerodynamic winglet grid point corresponding to $\eta = 0$. The initial and final model correspond to the NL-rigid model presented in section 6.7*
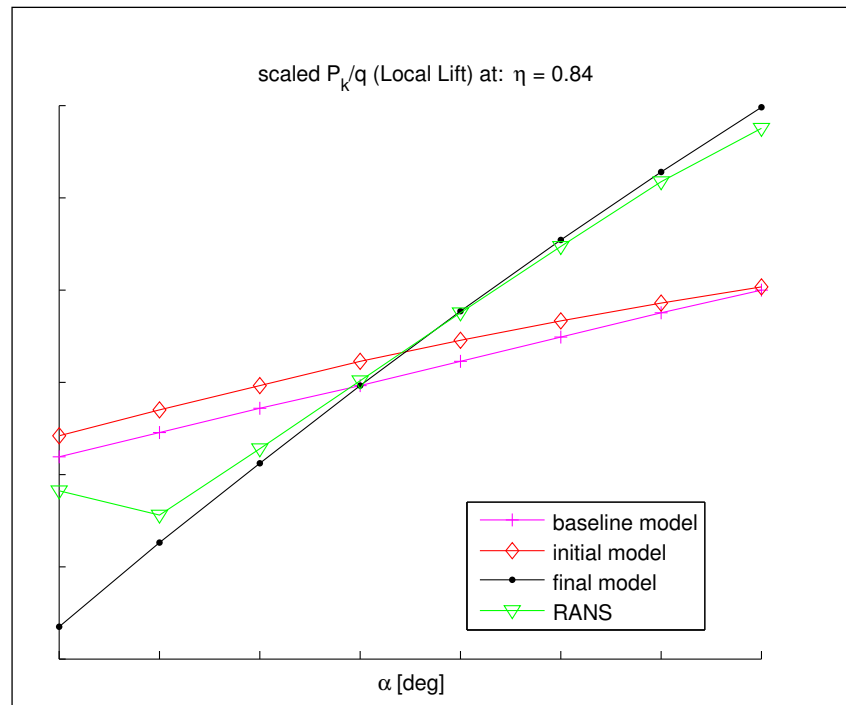
Figure 6.32: *Normal force ($\mathbf{P}_{k,x_R}$) for the jth aerodynamic winglet grid point corresponding to $\eta = 0.84$. The initial and final model correspond to the NL-rigid model presented in section 6.7*
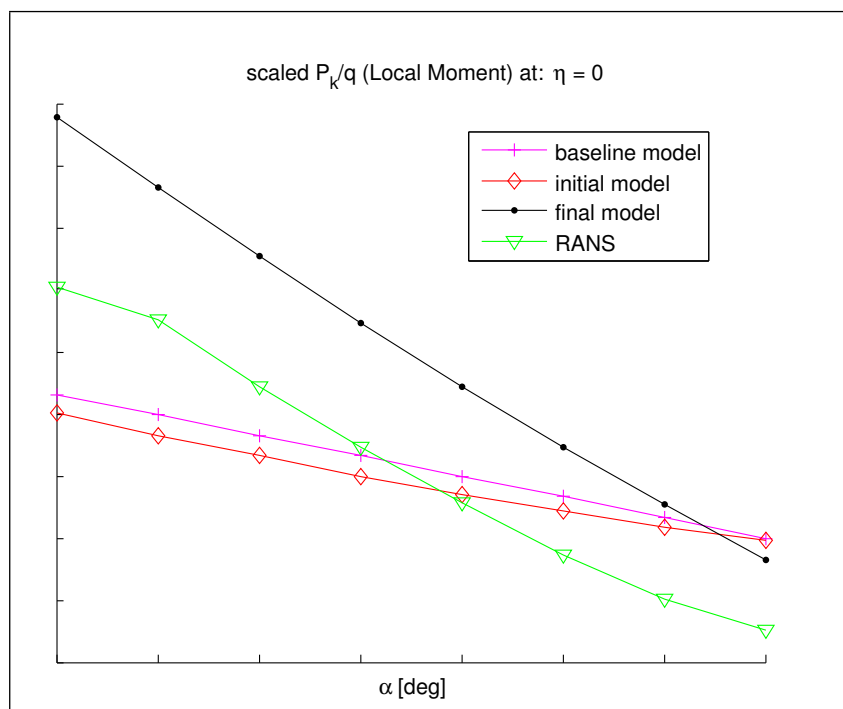
Figure 6.33: *Pitching moment ($\mathbf{P}_{k,x_R}$) for the jth aerodynamic winglet grid point corresponding to $\eta = 0$. The initial and final model correspond to the NL-rigid model presented in section 6.7*
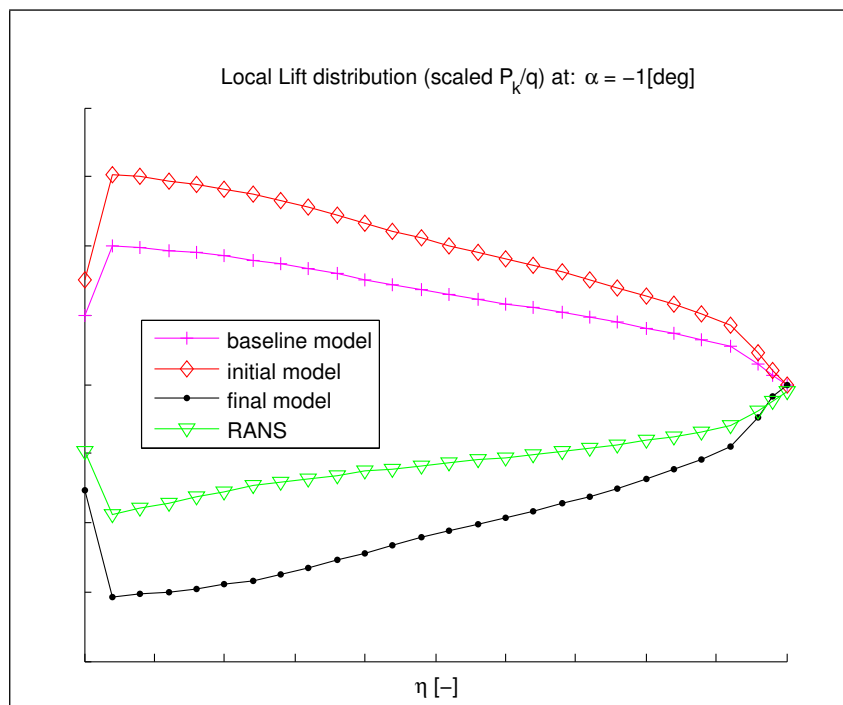
Figure 6.34: *Normal force distribution along the winglet derived from $\mathbf{P}_{k,x_R}$ at an angle of attack of $\alpha = -1$ deg. The initial and final model correspond to the NL-rigid model presented in section 6.7*
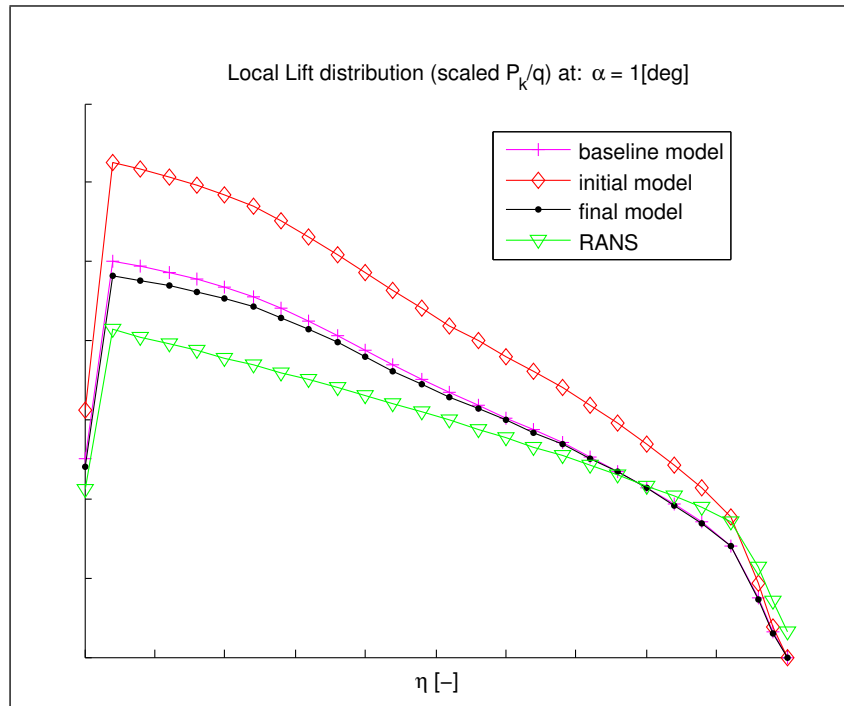
Figure 6.35: *Normal force distribution along the winglet derived from $\mathbf{P}_{k,x_R}$ at an angle of attack of $\alpha = 1$ deg. The initial and final model correspond to the NL-rigid model presented in section 6.7*
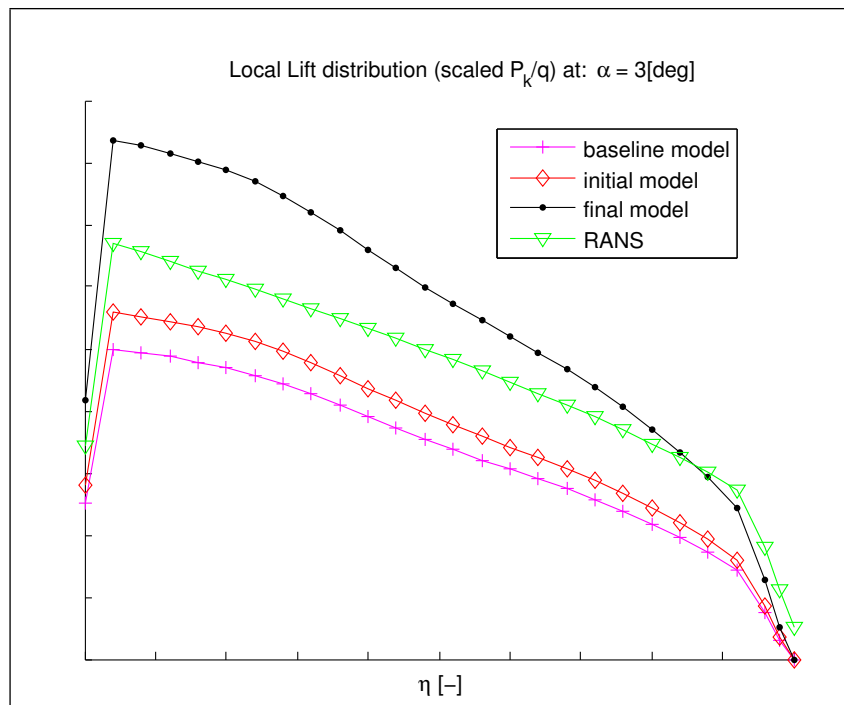
Figure 6.36: *Normal force distribution along the winglet derived from $\mathbf{P}_{k,x_R}$ at an angle of attack of $\alpha = 3$ deg. The initial and final model correspond to the NL-rigid model presented in section 6.7*
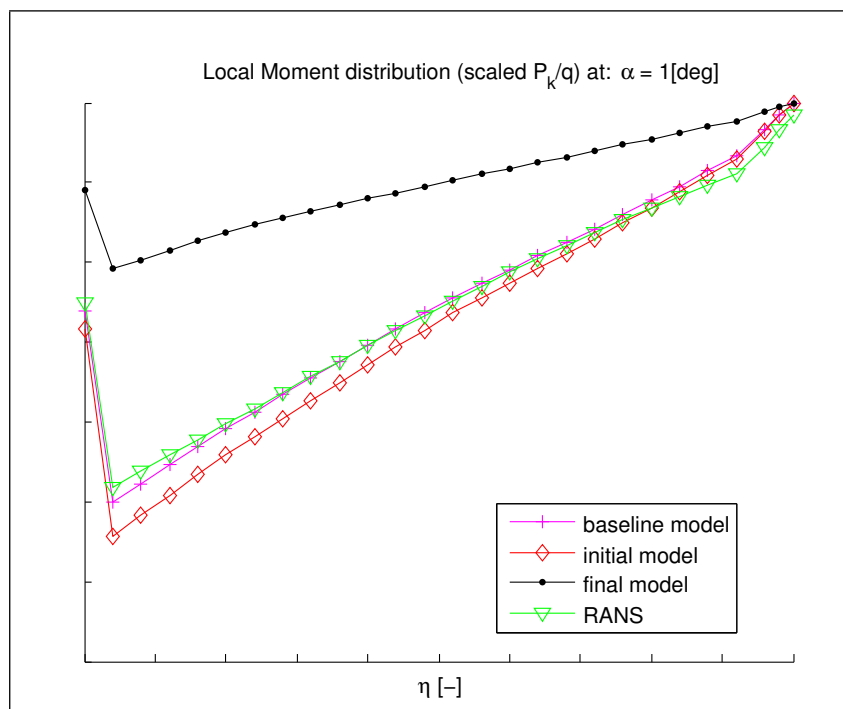
Figure 6.37: *Pitching moment distribution along the winglet derived from $\mathbf{P}_{k,x_R}$ at an angle of attack of $\alpha = 1$ deg. The initial and final model correspond to the NL-rigid model presented in section 6.7*
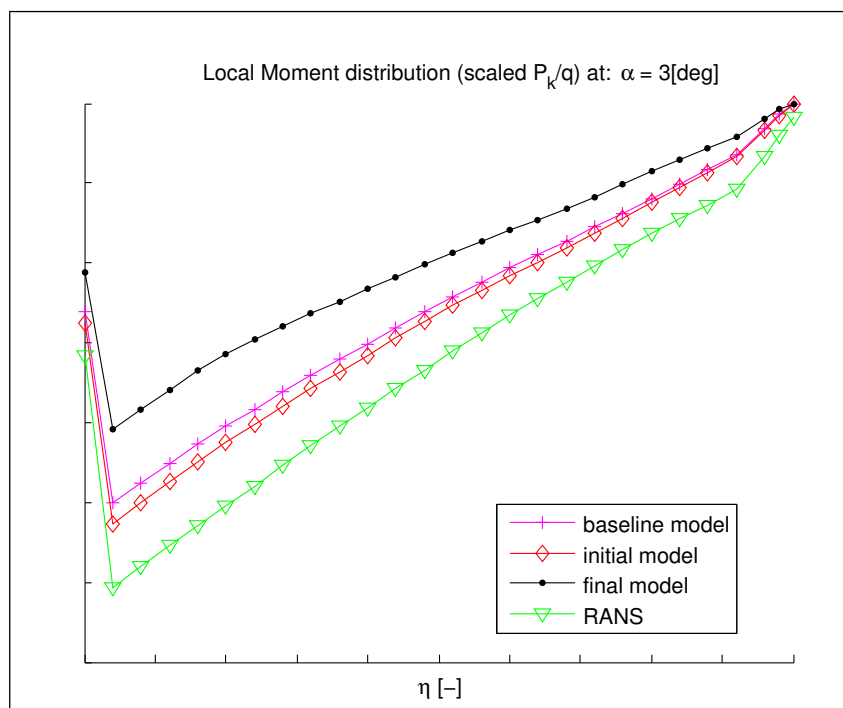
Figure 6.38: *Pitching moment distribution along the winglet derived from $\mathbf{P}_{k,x_R}$ at an angle of attack of $\alpha = 3$ deg. The initial and final model correspond to the NL-rigid model presented in section 6.7*
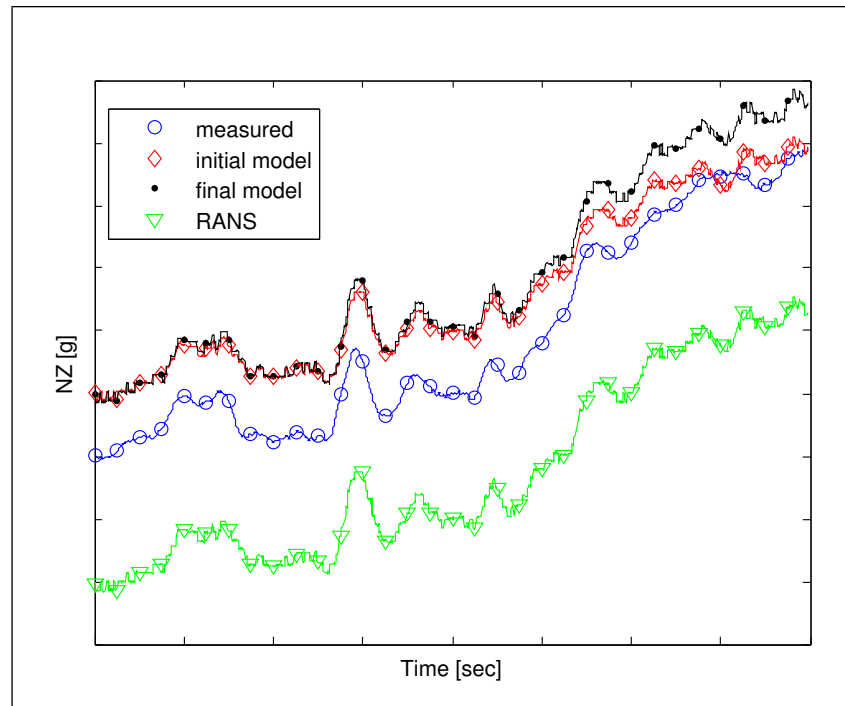
Figure 6.39: *Load factor in Z-direction versus time. The measurements are compared with the results from the initial and final NL-rigid model, presented in section 6.7, and with the results from the initial model based on the CFD data (called just RANS).*

$J(\hat{\boldsymbol{\theta}}_0)$	-71063

Table 6.6: *Value of the Negative Likelihood function of the loads model initialized by modification of the rigid body aerodynamics according to the data derived from CFD-calculations (RANS).*

Comparison of local loads

It can be seen from figure (6.40) and (6.41) that the local loads level lies below that of the baseline model for these two load outputs. This is true for practically all load outputs. This can be explained from the overall loads level that is too small for the RANS model. The positive exceptions are the winglet root bending and the bending at wing station 6, see figures (6.42) and (6.43) respectively, where the absolute loads level even corresponds extremely good for the winglet root bending, although this might be a coincidence. The relative loads level (upper graph) is predicted excellent for both of these stations.

It can be concluded from these results, that the overall correspondence is very similar to that of the final model of section 6.7, where the physical meaning of the input data is given by the trustworthy CFD-data. Recall, from section 6.6 that good correspondence was achieved between the flexible CFD-CSM calculations and the in flight pressure measurements.

Because of the missing flight-to-jig-correction of the CFD input data, it will be investigated in the following sections, whether the RANS-based model can be adjusted or modified further to get an even better model.
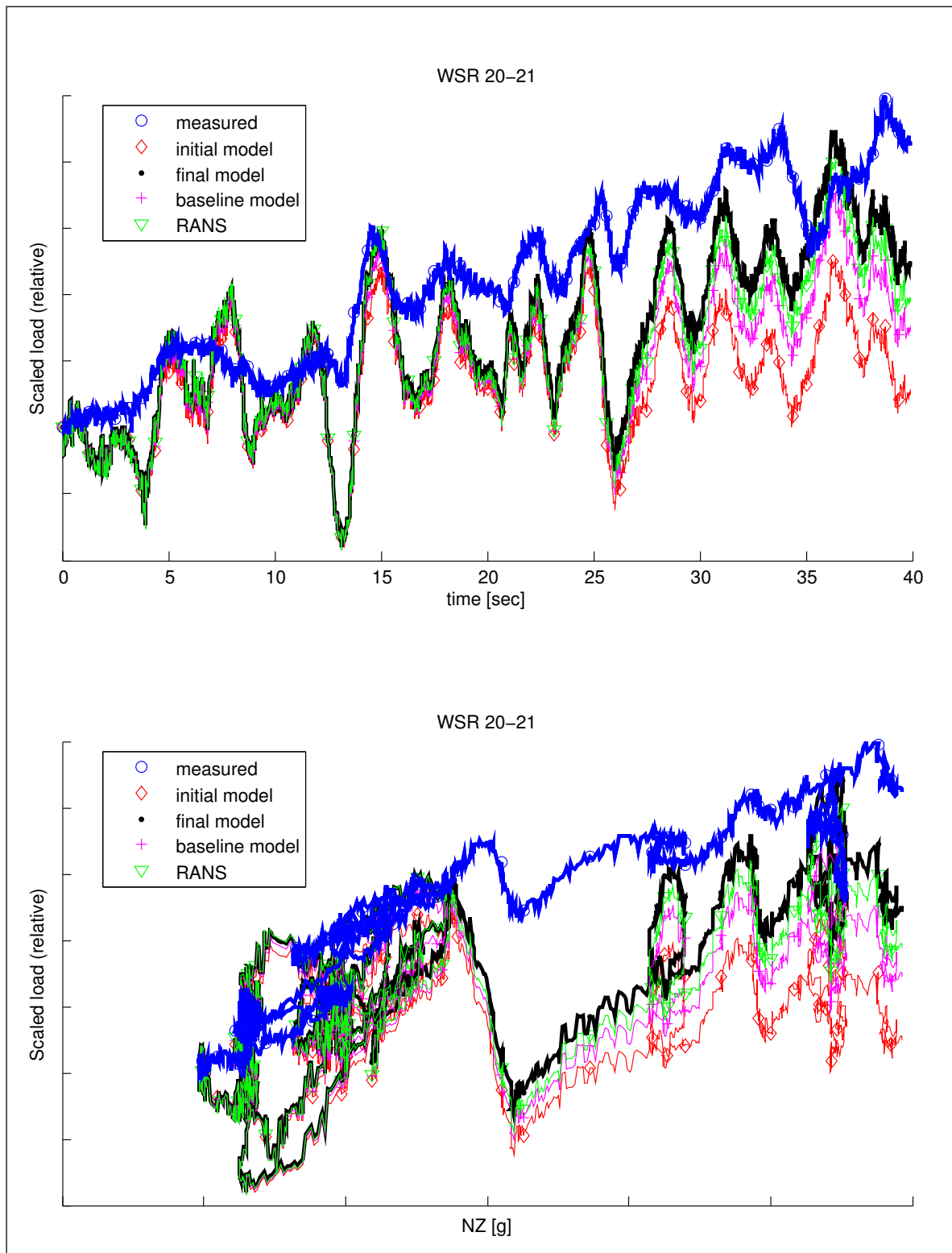
Figure 6.40: *Shear force (relative) on wing right vs. time and load factor respectively for wing station 4. The measurements are compared with the results from the initial and final NL-rigid model, presented in section 6.7, and with the results from the initial model based on the CFD data (called just RANS).*
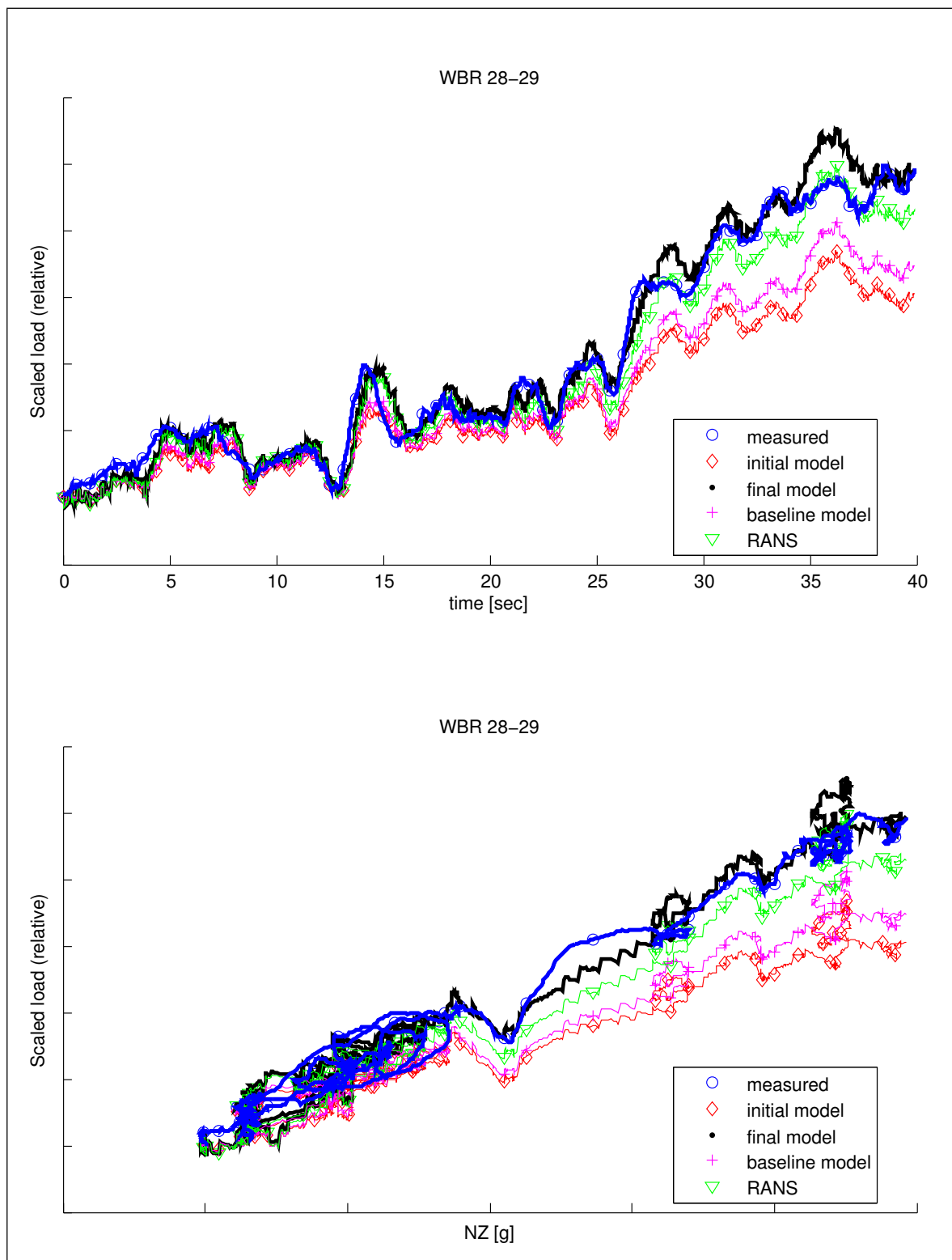
Figure 6.41: *Bending moment (relative) on wing right vs. time and load factor respectively for wing station 5. The measurements are compared with the results from the initial and final NL-rigid model, presented in section 6.7, and with the results from the initial model based on the CFD data (called just RANS).*
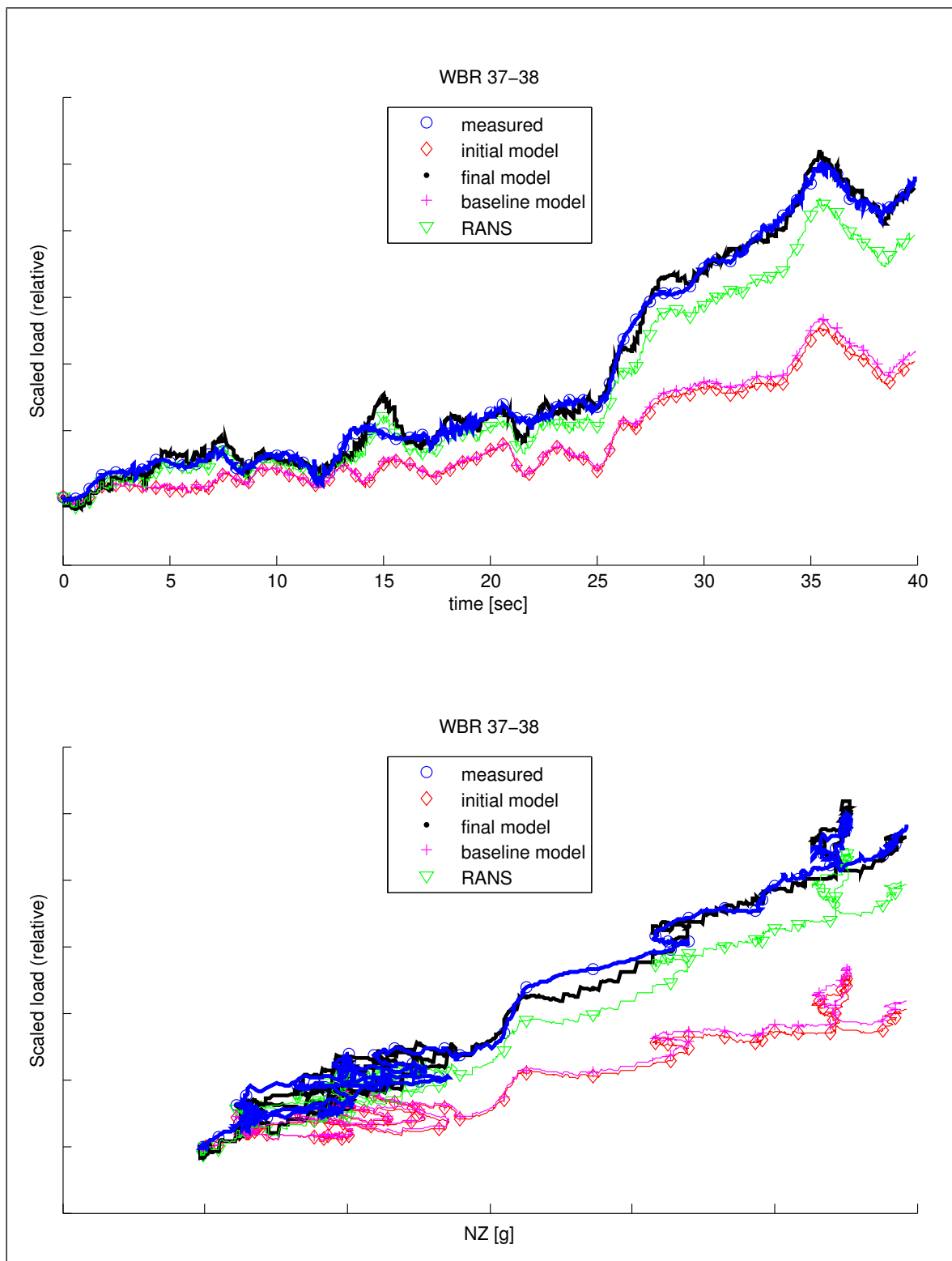
Figure 6.42: *Bending moment (relative) on wing right vs. time and load factor respectively for wing station 6. The measurements are compared with the results from the initial and final NL-rigid model, presented in section 6.7, and with the results from the initial model based on the CFD data (called just RANS).*
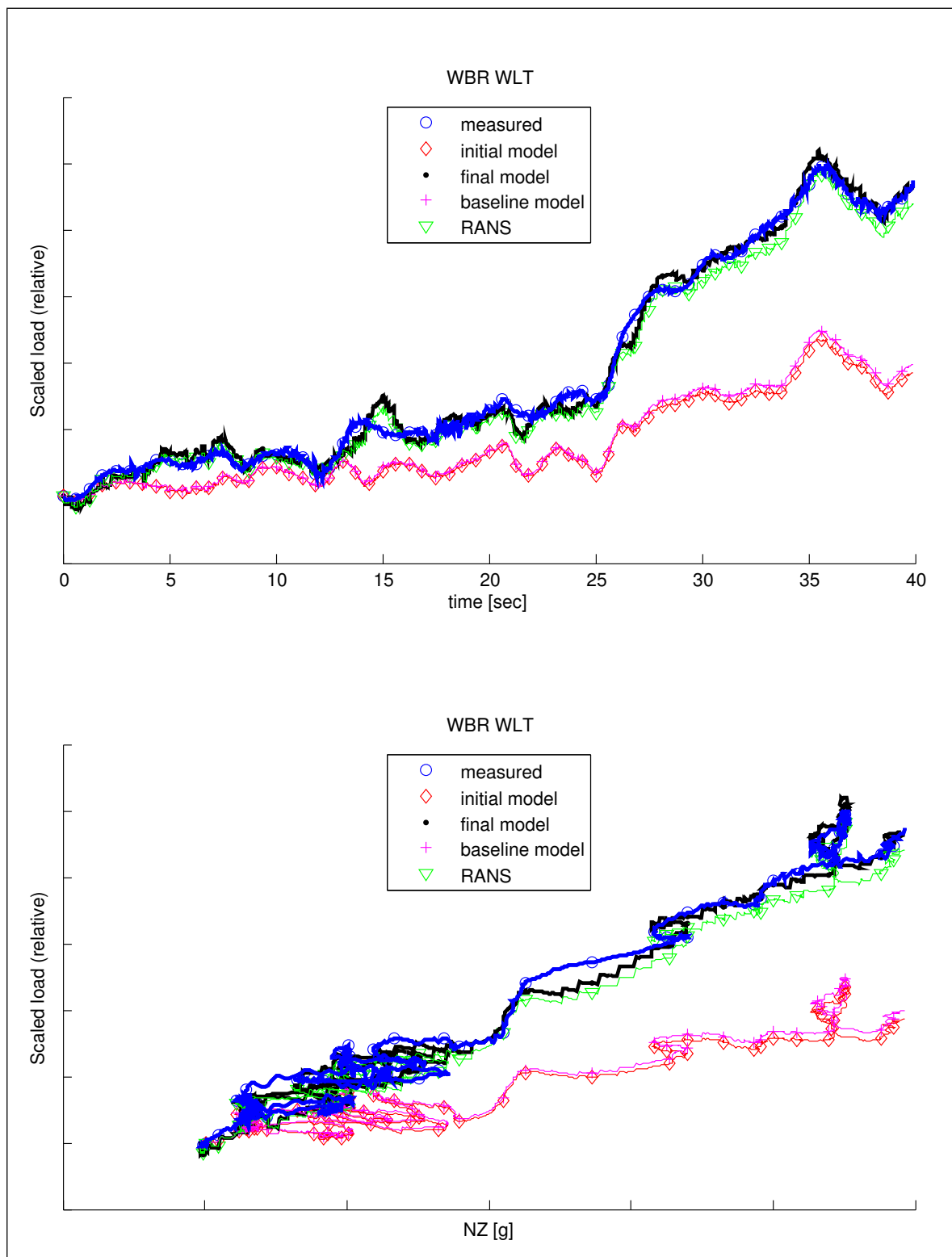
Figure 6.43: *Bending moment (relative) at winglet root vs. time and load factor respectively, righthand side. The measurements are compared with the results from the initial and final NL-rigid model, presented in section 6.7, and with the results from the initial model based on the CFD data (called just RANS).*

6.8.2   Identification of a hybrid model

The RANS-based model will be adjusted here to account for the flight-to-jig-correction that actually should be performed to the CFD-results. To this end, it is chosen for a 'hybrid' model. Hybrid in the sense that the null-distributions are taken from the baseline model (based on the usual aerodynamic database) and the gradient distributions for the angle of attack determined from the CFD-calculations. The null-distributions are defined for the jig-shape aircraft directly. The local gradient distributions for this range in angles of attack are practically the same for flight shape and jig shape. Recall that normally the flight-to-jig-correction involves only a correction of the null-distribution. Consequently, the hybrid model has the potential to take the best of both worlds. It will be investigated in this section whether the results from this model can match the expectations.

The gradient distributions for the angle of attack are determined from the CFD-calculations up until flow separation occurs. Over this range in angle of attack, the variation in the local gradients is very small and the mean value can be taken for each spanwise station. The aerodynamic model is now described in similarity to equation (6.52), by:

$$\mathbf{F}_{g1_c,x_m} = q \cdot \mathbf{T}_{kg1}^T \cdot \mathbf{Q}_{k_c x_m} \mathbf{x}_m, \tag{6.62}$$

where no additional transformation is performed from aerodynamic axes to body axes and without the second order effect, thus:

$$\mathbf{x}_m = \begin{bmatrix} 1 \\ \alpha \end{bmatrix} \tag{6.63}$$

As before, the aerodynamic distributions along the other components of the aircraft are described according to the baseline model. The aerodynamic load distribution due to rigid body motion is then again, recall equation (6.29):

$$\mathbf{F}_{g1_{x_R}} = \mathbf{F}_{g1,x_R}^* + \mathbf{F}_{g1,\delta} + \mathbf{F}_{g1_c,x_m},$$

The identification will be done setting all 396 variables describing the null and angle of attack gradients on the wings and winglets to free parameters. The determination of one sensitivity matrix (needed for each iteration step) then takes approximately one and a half hours.

The results from the initial hybrid model are a little bit worse compared to the RANS model. The value of the negative Likelihood function is now -70878, see table 6.7 compared to -71063 before. From the same table can be seen that a very low value for the negative Likelihood function could be found after two iterations. However, at the cost of a nonphysical model as will be shown later. Comparing the overall load factor from the RANS model in figure (6.39) with that of the initial hybrid model in figure (6.44) shows that the flight-to-jig-corrective adjustments show the desired result of an increase in overall load factor such that it gets closer to the measured value. The final hybrid model even shows an excellent agreement in the overall load factor. The detailed results for 4 specific load outputs are put in appendix B, because the final model concerns a nonphysical

$J(\hat{\boldsymbol{\theta}}_0)$	-70878
$J(\hat{\boldsymbol{\theta}}_1)$	-80501
$J(\hat{\boldsymbol{\theta}}_2)$	-84580

Table 6.7: *Values of the Negative Likelihood function during the identification of the loads model by modification of the rigid body aerodynamics.*

model. This can be seen directly from the corresponding null distributions, see figures (6.45), (6.47) and (6.49). The gradient distributions seem quite plausible, therefore the negative Likelihood function is determined for a model based on the null distributions from the baseline model, but having the gradients from the final hybrid model. The negative Likelihood function then has the value -79924, which is a pretty good result for a model that would still be possible from a physical point of view.

Due to this observation, the last model that will be investigated here, will have fixed null distributions (from the original aerodynamic database) but free gradients. This identification involves no further model adjustments, it involves only half of the free parameters from the previous identification of the hybrid model. This alternative identification will be called hybridII to prevent confusion. The results from that identification are presented in the next section.
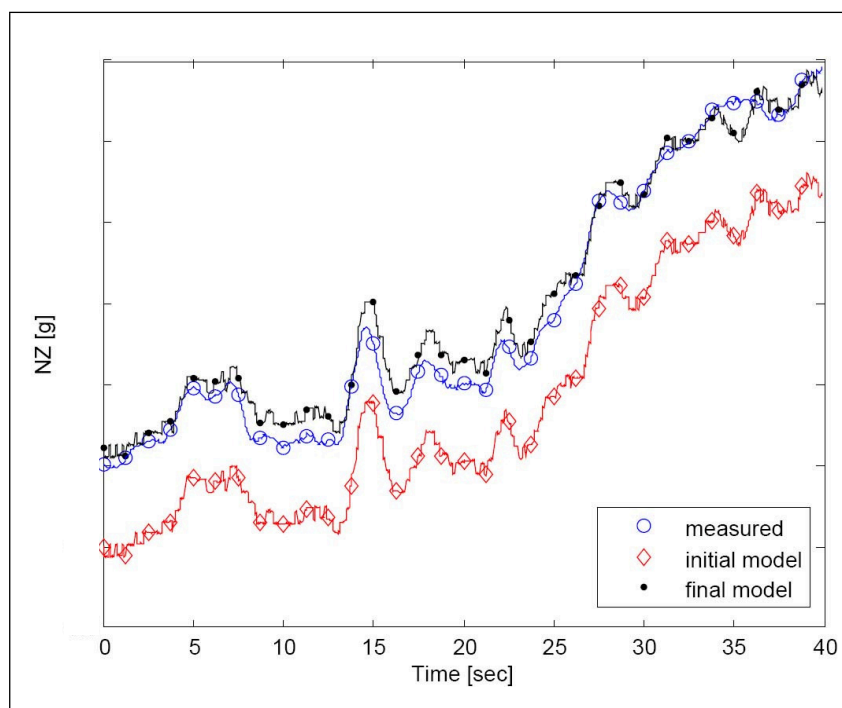
Figure 6.44: *Load factor in Z-direction versus time measurement compared to simulation with the initial and with final hybrid model.*
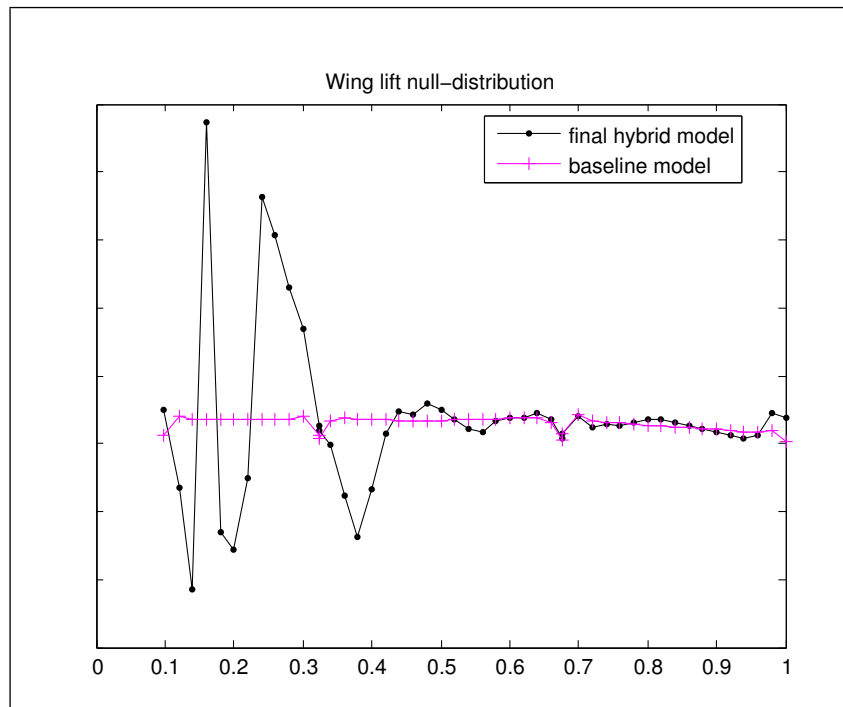
Figure 6.45: *Null distribution for lift along the wing according to the baseline and final hybrid model.*
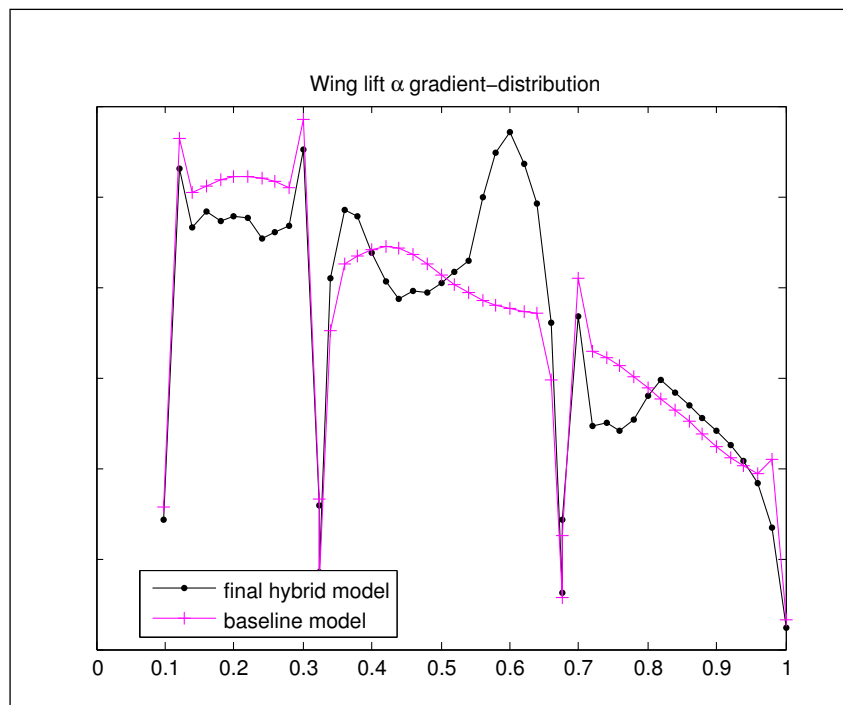
Figure 6.46: *Gradient distribution for lift w.r.t. angle of attack along the wing according to the baseline and final hybrid model.*
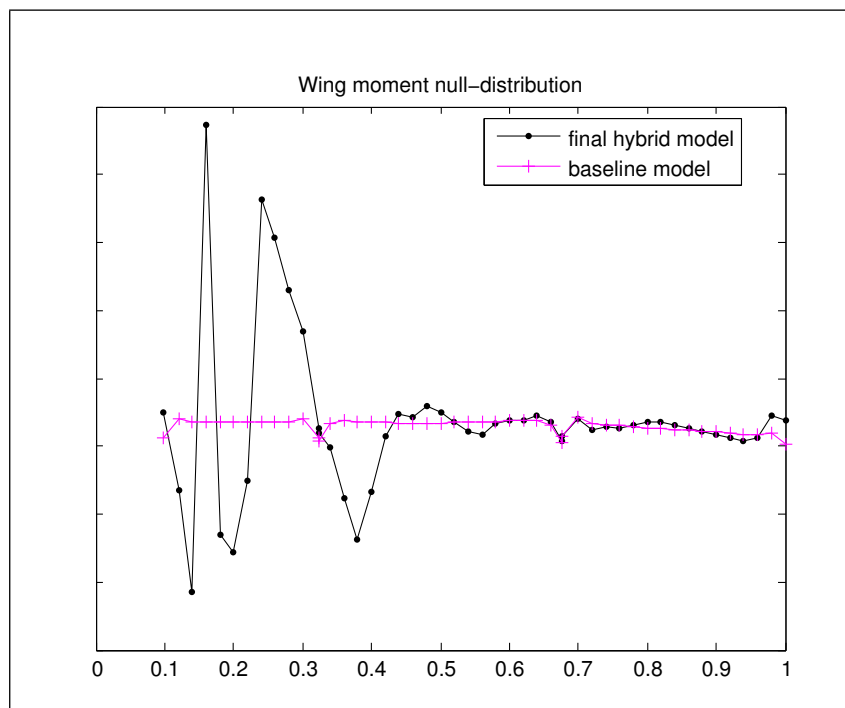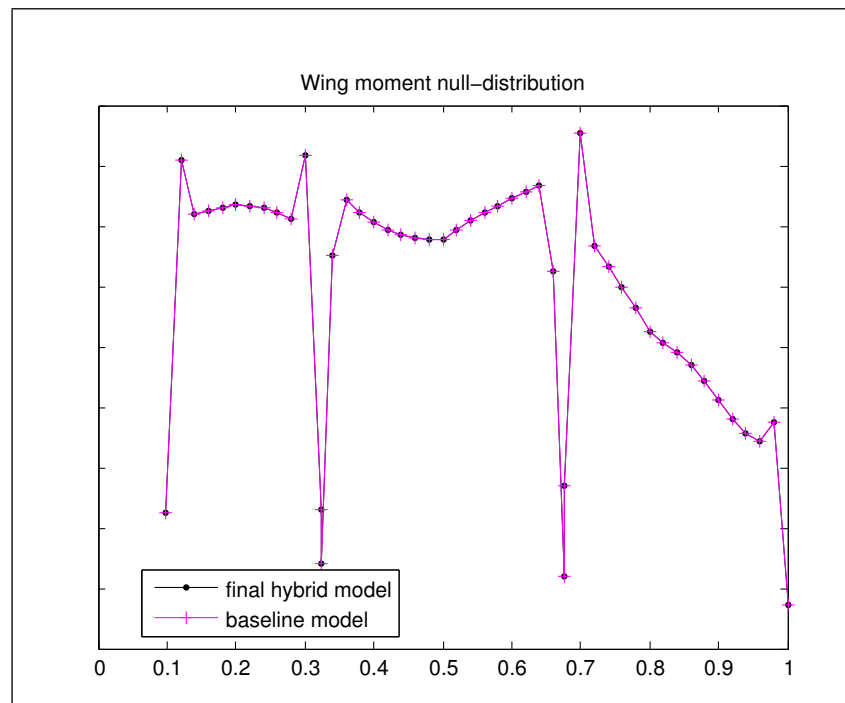
Figure 6.47: *Null distribution for moment along the wing according to the baseline and final hybrid model.*
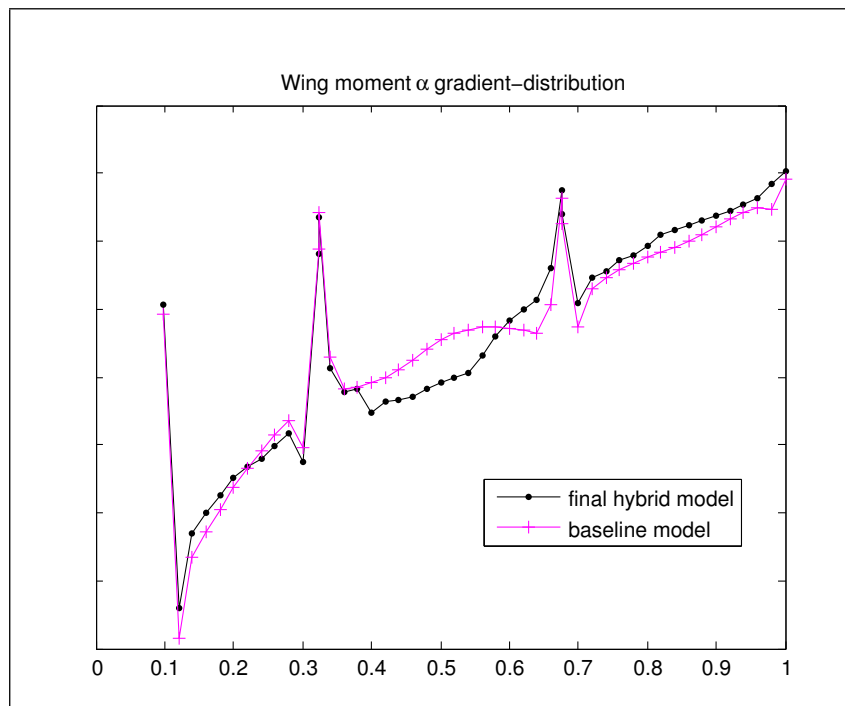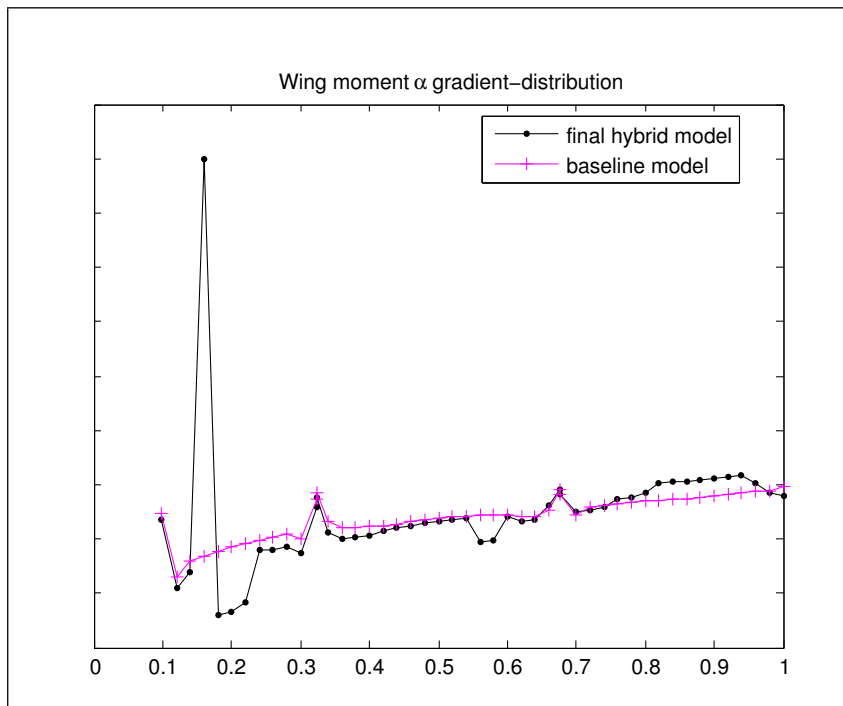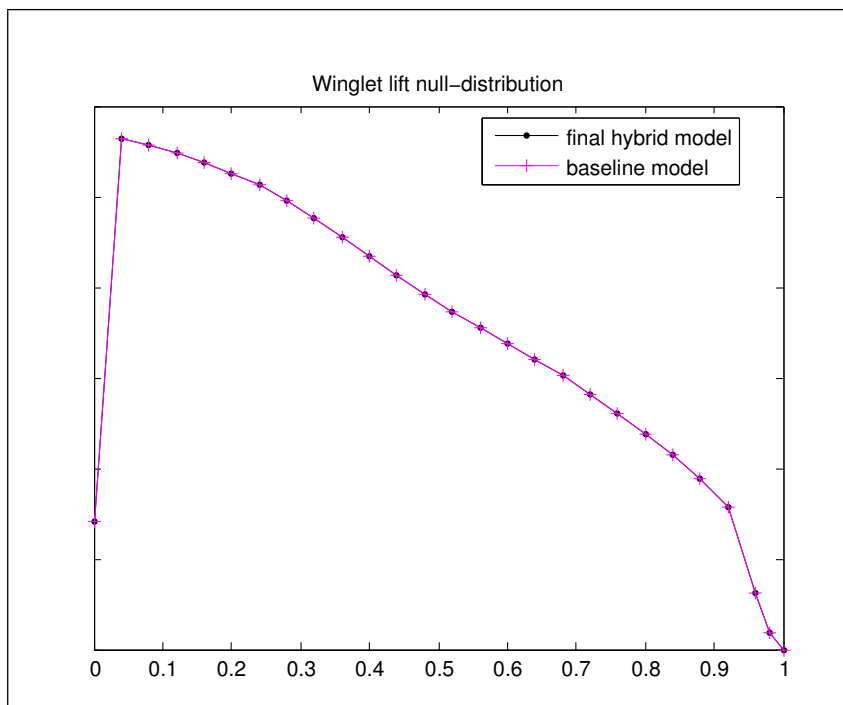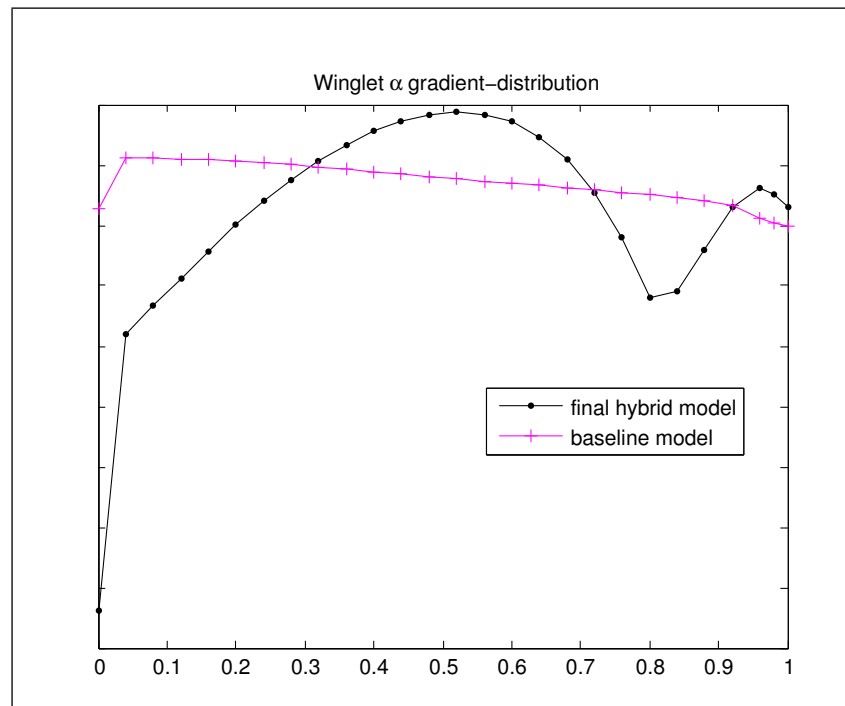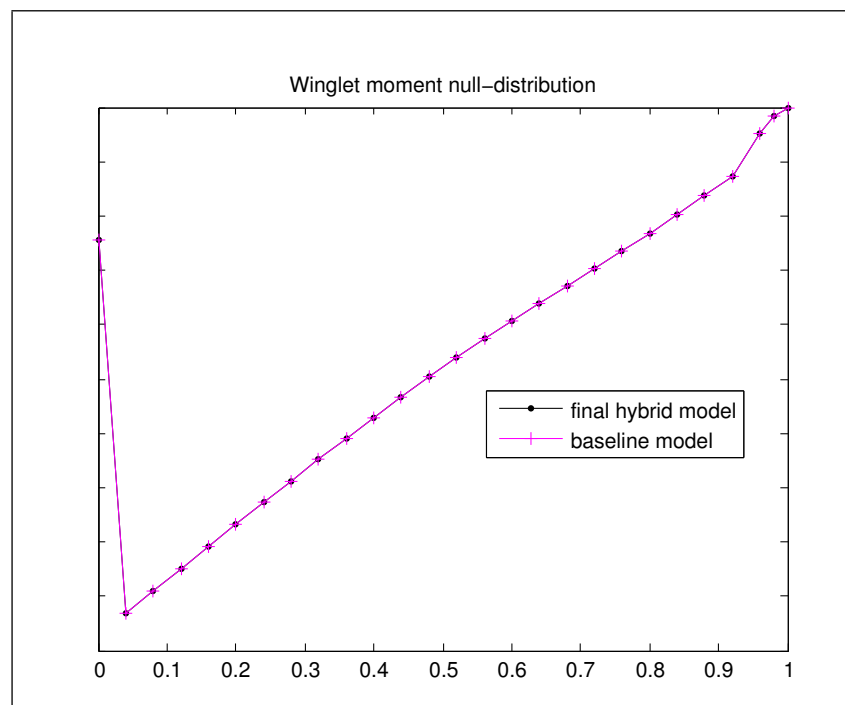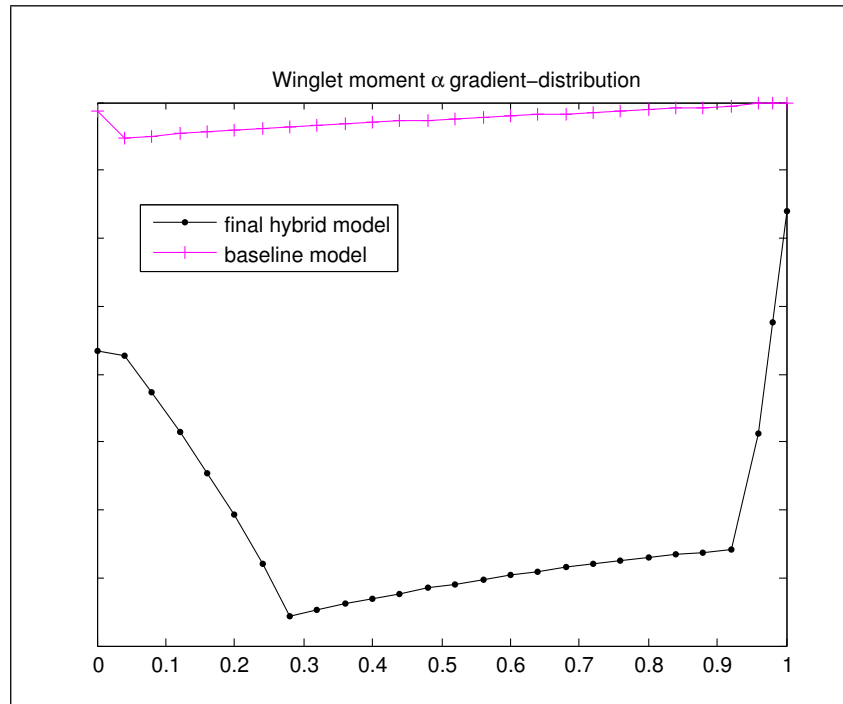

Figure 6.48: *Gradient distribution for moment w.r.t. angle of attack along the wing according to the baseline and final hybrid model.*
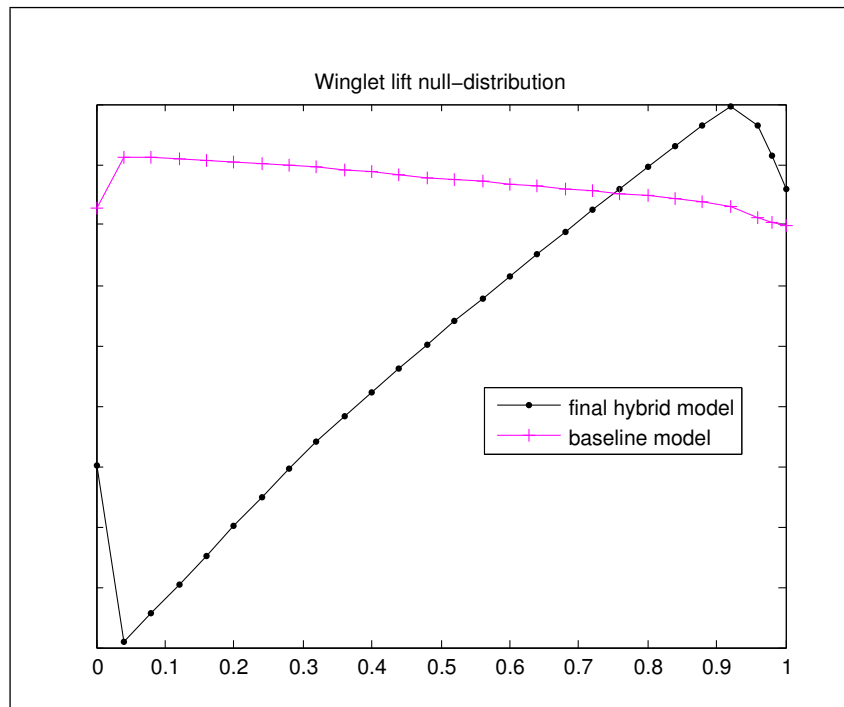
Figure 6.49: *Null distribution for lift along the winglet according to the baseline and final hybrid model.*
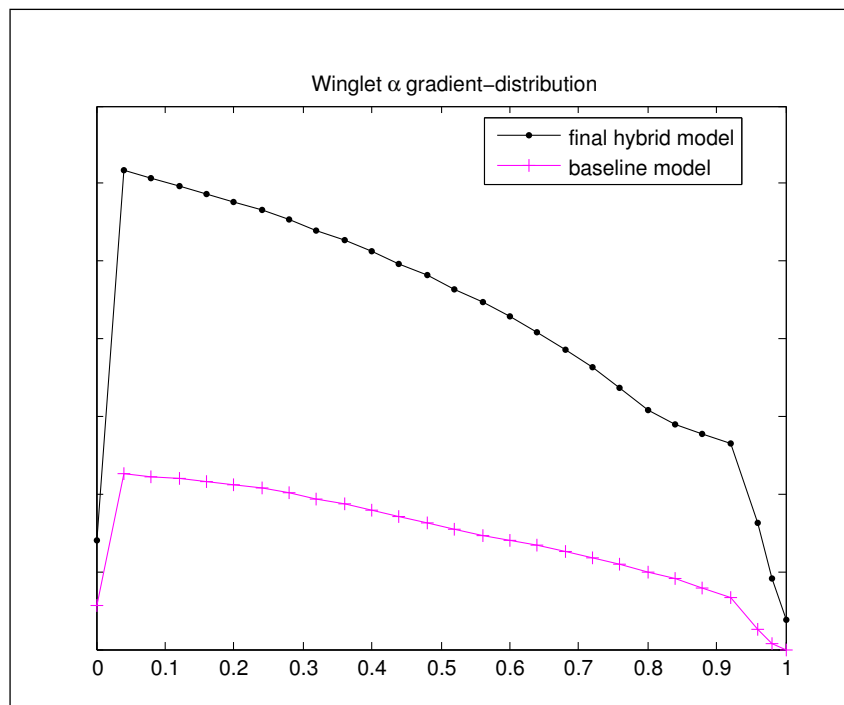
Figure 6.50: *Gradient distribution for lift w.r.t. angle of attack along the winglet according to the baseline and final hybrid model.*
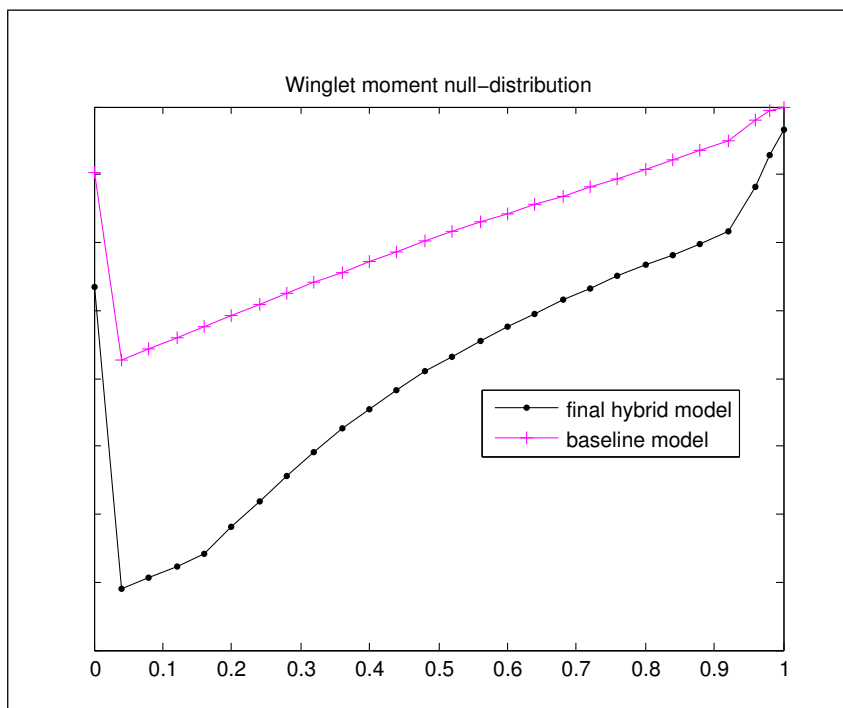
Figure 6.51: *Null distribution for moment along the winglet according to the baseline and final hybrid model.*
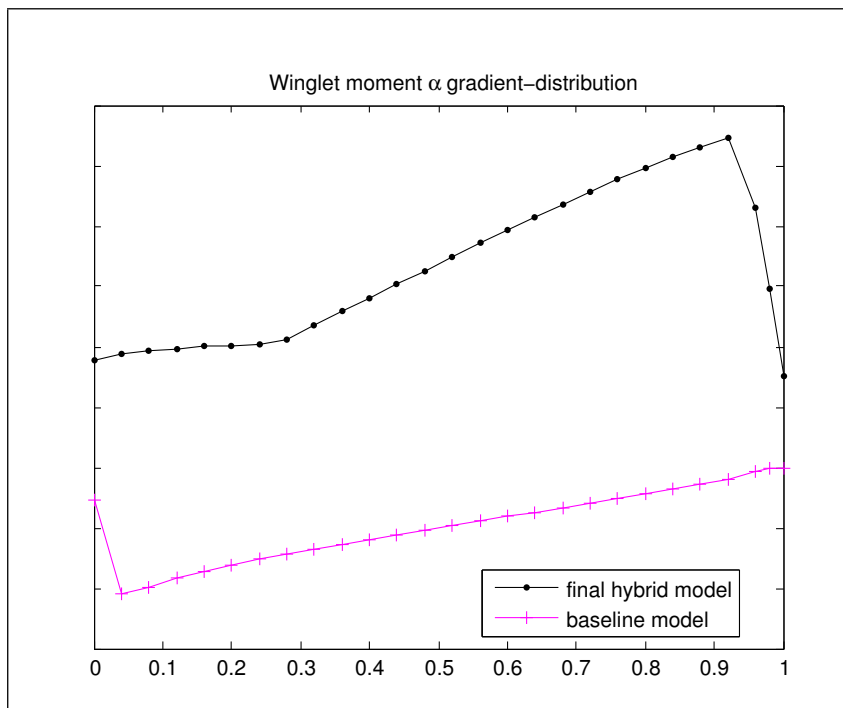
Figure 6.52: *Gradient distribution for moment w.r.t. angle of attack along the winglet according to the baseline and final hybrid model.*

$J(\hat{\boldsymbol{\theta}}_0)$	-70878
$J(\hat{\boldsymbol{\theta}}_1)$	-77160
$J(\hat{\boldsymbol{\theta}}_2)$	-83876
$J(\hat{\boldsymbol{\theta}}_3)$	-87343
$J(\hat{\boldsymbol{\theta}}_4)$	-87366

Table 6.8: *Values of the Negative Likelihood function during the identification (hybridII) of the loads model by modification of the rigid body aerodynamics.*

6.8.3   Alternative identification of the hybrid model: hybridII

In the previous section it was shown that setting all parameters free, that describe the null and gradient distributions for lift and moment along the wings and winglets, leads to a nonphysical model. It was shown that if the null-distribution is taken from the original baseline model and the plausible identified alpha gradient distributions are taken, a pretty good correspondence results (Negative Likelihood function value of -79924). In this section it will be investigated whether keeping the null distributions fixed from the beginning of the identification and setting only the variables of the gradient distributions free, will lead to better results.

The initial value of the negative Likelihood function is again -70878, see table 6.8. Notice, that the initial model has not been changed. From the same table can be seen that the lowest value for the negative Likelihood function was found: -87366. However, again at the cost of a nonphysical model as will be shown later.

Comparing the overall load factor from figure (6.53) shows similar agreement with the measured values compared to the curves in figure (6.44).

The detailed results for 4 specific load outputs are put again in the appendix, i.e. appendix C, because the final model concerns again a nonphysical model. This can be seen directly from all the corresponding gradient distributions, see figures (6.55), (6.57), (6.59) and (6.61). The null distributions are exactly those from the baseline model as can be seen from figures (6.54), (6.56), (6.58) and (6.60). This model is given no further attention as it is physically meaningless.
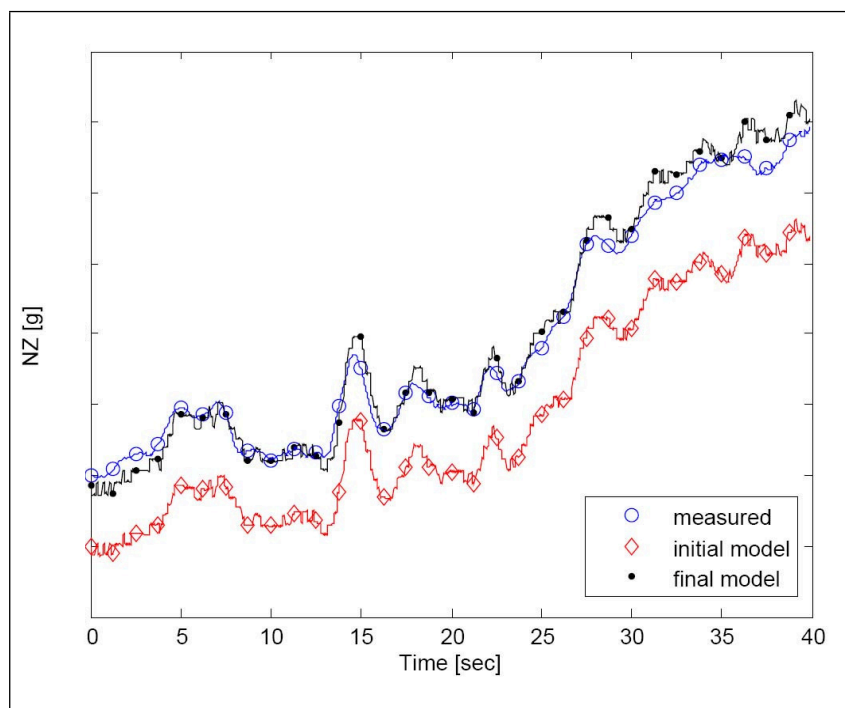
Figure 6.53: *Load factor in Z-direction versus time measurement compared to simulation with the initial and with final hybrid model (hybridII).*
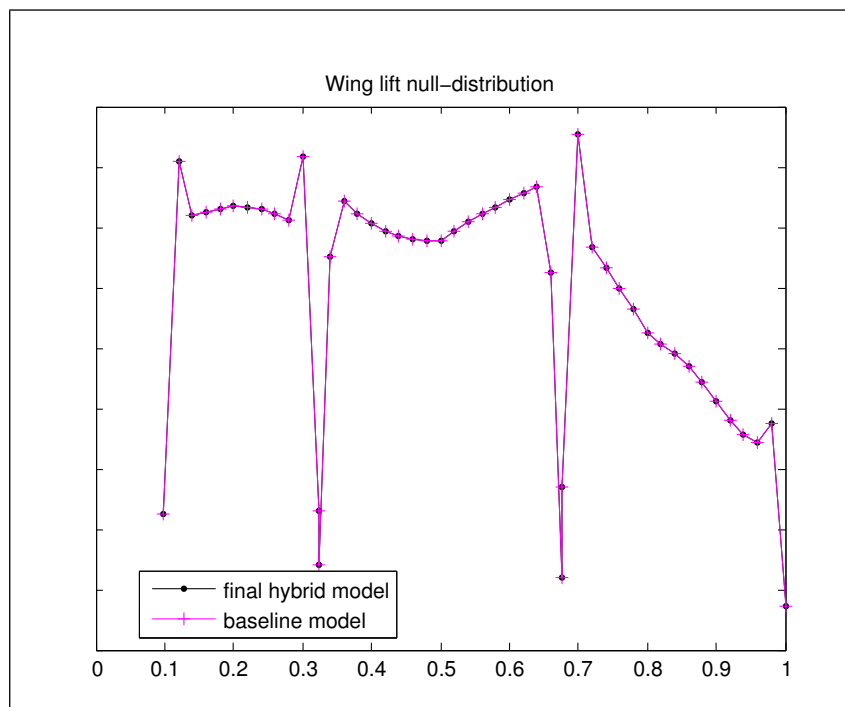
Figure 6.54: *Null distribution for lift along the wing according to the baseline and final hybridII model.*
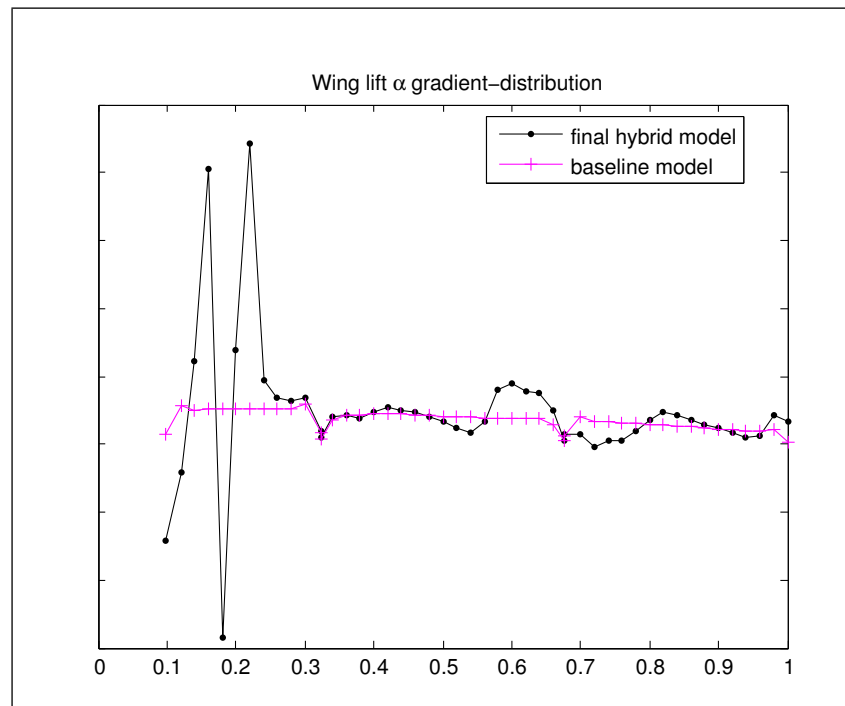
Figure 6.55: *Gradient distribution for lift w.r.t. angle of attack along the wing according to the baseline and final hybridII model.*

Figure 6.56: *Null distribution for moment along the wing according to the baseline and final hybridII model.*

Figure 6.57: *Gradient distribution for moment w.r.t. angle of attack along the wing according to the baseline and final hybridII model.*

Figure 6.58: *Null distribution for lift along the winglet according to the baseline and final hybridII model.*

Figure 6.59: *Gradient distribution for lift w.r.t. angle of attack along the winglet according to the baseline and final hybridII model.*

Figure 6.60: *Null distribution for moment along the winglet according to the baseline and final hybridII model.*

Figure 6.61: *Gradient distribution for moment w.r.t. angle of attack along the winglet according to the baseline and final hybridII model.*

6.8.4 Conclusion

It is obvious from the examples presented in section 6.8, that the initial models based on the aerodynamic data derived from RANS-calculations give already very good correspondence with the flight loads measurements $(J(\hat{\boldsymbol{\theta}}_0) \approx -70 \cdot 10^3)$. On the other hand, it was shown that further model adjustments determined from identification leads in almost all cases to non physical models.

The recommended model, that is the one that is physically probable and has relatively good correspondence with the flight loads measurements, will be the initial hybrid model based on the null distributions from the original aerodynamic database and the gradients determined from RANS-calculations. Although, this model gives a too small overall loads level compared to the measured value of N_Z, it is the most physical assumption on the aerodynamic input data. The flexible CFD-CSD calculations have shown to give good correspondence with the in flight pressure measurements. Consequently, a lot of confidence can be put onto the rigid CFD-calculations that were done here for an alpha sweep. The uncertainties in the loads measurements and the apparently conflicting measurement data for the different loads at the wing and winglet stations, make that no clear conclusions can be drawn about the 'real' biases on the measurement data. The best overall results are achieved by the NL-rigid model from section 6.7. This model could be optimised in an identification for a best fit to the flight test loads measurements, when considered relative to a corresponding reference condition.

It can further be recommended to perform the rigid alpha sweep CFD-calculations for the aircraft in jig-shape, as this is expected to give the most optimal model input data,

based on the experience gained here.

6.9   Summary of proposed models

To minimize the level of confusion, the most important aspects of the proposed alternative aerodynamic models are presented here.

1. Nonlinflex
   Assumes the correct description and data of the rigid body aerodynamics. Modifications to the model by the free parameters of the identification are only done to that part of the model that describes the aerodynamic loads due to flexibility of the airframe. Three alternative methods are proposed:

   (a) Method 1: LINFLEX

   $$\mathcal{R} = diag(\mathbf{C}_f \cdot \mathbf{b}_f) \tag{6.64}$$

   where the vector $\mathbf{b}_f$ is a constant vector. It accounts for the flexibility effect based on linear aerodynamics.

   (b) Method 2:
   In method 2, the elements of the vector $\mathbf{b}_f$ are a function of local angle of attack.

   $$\mathbf{b}_f = f(\boldsymbol{\alpha}_i) \tag{6.65}$$

   where the vector $\boldsymbol{\alpha}_i$ contains the local angles of attack due to the aircraft global angle of attack and the local deformation. It is possible to account for local nonlinear aerodynamic flexibility effects.

   (c) Method 3:
   In method 3, the elements of the vector $\mathbf{b}_f$ are a function of time. It reduces the computational effort when compared with method 2, although it is still possible to account for local nonlinear aerodynamic flexibility effects by using the measured overall load factor N_Z. Now:

   $$\mathbf{b}_f(t) = \begin{bmatrix} \mathbf{a}_0 & \mathbf{a}_1 & \mathbf{a}_2 \end{bmatrix} \cdot \begin{bmatrix} 1 \\ N_Z(t) \\ N_Z{}^2(t) \end{bmatrix} \tag{6.66}$$

Identification of the models from Method 2 & 3 involve a very high computational effort and therefore these models cannot yet be identified within an acceptable timeframe. Method 1 is computationally very efficient and can be used for identification. The drawback is that method 1 only accounts for flexibility effects based on linear aerodynamics. The identification of this model showed that the physical phenomena observed in the flight test measurements are not captured by this model.

2. NL-rigid
   The assumption of correct rigid body aerodynamics is been dropped from here on. The aerodynamic load distributions on the wings and winglets are described by equation (6.52):

   $$\mathbf{F}_{g1_c, x_m} = q \cdot \mathbf{T}_{kg1}^T \cdot f_3(\mathbf{Q}_{k_c x_m} \mathbf{x}_m),$$

   where the function f_3 describes an additional transformation from aerodynamic axes to body axes and a second order effect is included, equation (6.53):

   $$\mathbf{x}_m = \begin{bmatrix} 1 \\ \alpha \\ \alpha^2 \end{bmatrix}$$

   The relative local loads (gradients) can be correctly predicted by using this model. The absolute loads level was however a little bit larger when compared with the measurements of N_Z. The gradient distributions (for local lift and pitching moment) along the winglets are much larger compared with the baseline aerodynamics. The gradient distributions from this model are, however, comparable with those derived from RANS simulations.

3. RANS-model
   The aerodynamic distributions along the wing and winglet are determined from the RANS-simulations and directly fed into the model. The advantage is that all nonlinearities in the aerodynamics of the specific components are included. This model leads directly to very good correspondence with the flight test measurements. Because of the flight-to-jig discrepancy in this model, the resulting overall loads level was shown to be considerably smaller.

4. Hybrid I/II:
   Developed to include the flight-to-jig-correction that was not present in the RANS-model. It takes the Null-distributions along the wings and winglets from the original aerodynamic database, but the gradient distributions from the (mean) values derived from the RANS simulations.
   The results for the local loads for the initial model are a little bit worse when compared with the RANS-model. However, the absolute loads level is significantly improved, but still a little bit smaller compared with the measured values. The identification Hybrid I modified both the null and gradient distributions, where the identification Hybrid II modified only the gradient distributions. Both identification procedures lead to nonphysical models.

6.10   Model validation

In order to gain confidence in, or reject, a particular model, it is necessary to perform a model validation. Parameter estimation and model validation are integral parts of flight vehicle system identification. The main goal of parameter estimation is to determine the

model, given the system inputs and responses. The main task of model validation is to answer the question: "How do you know that you got the right answer (the identified model)?". In this section it will be dealt with issues related to the process of determining the correctness, accuracy, adequacy and applicability of the identified model.

Some model validation has already been performed in section 6.6 and 6.8 by comparing the input data and simulation results with the data derived from the highly sophisticated rigid and flexible RANS calculations. In a model validation it should be determined whether adequate correspondence exists between the computational results of the model and the actual data (if available) or other theoretical data.

Jategaonkar introduces in [Jat06] three subcategories for the different aspects of model validation:

- statistical properties of the estimates,

- residual analysis,

- model predictive quality.

It is of paramount importance to carefully check each of these aspects. This will be the topic of the following sections.

6.10.1 Statistical accuracy of parameter estimates

The statistical accuracy will now be determined of the estimates that have been obtained from the experimental data. In some sense the issue of accuracy of the estimates, belongs to the category of tests that are required to evaluate the model accuracy and validation.

It was presented in chapter 5 that the parameter covariance matrix of the Maximum Likelihood Method satisfies the Cramér-Rao inequality, see equation (5.45). It can be even shown that the Maximum Likelihood Estimator is asymptotically efficient in the sense of achieving the Cramér-Rao lower bound, see [Jat06]. The property of asymptotic efficiency implies that the Maximum Likelihood Estimator makes efficient use of the available data. This property is obviously very advantageous in practical applications. The Cramér-Rao lower bound indicates the theoretically maximum achievable accuracy of the estimates.

The parameter error covariance matrix $\mathbf{P}$ is given by the inverse of the Fisher information matrix $\mathbf{M}$, see also equation (5.45). The parameter error covariance matrix thus depends upon the model parameters $\boldsymbol{\theta}$, the data points being analysed N, and the covariance matrix of the residuals $\hat{\mathbf{R}}$ (i.e., on the measurement noise).

Since the information matrix is required in the optimisation of the cost function, the parameter error covariance matrix is automatically available. The diagonal elements of $\mathbf{P}$, which are the variances of the estimates, are indicators of the accuracy of the estimates. The standard deviation σ and correlation coefficients of the estimates can be readily obtained by:

$$\sigma_{\theta_i} = \sqrt{p_{ii}} \tag{6.67}$$

$$\rho_{\theta_i \theta_j} = \frac{p_{ij}}{\sqrt{p_{ii}p_{jj}}}, \tag{6.68}$$

where i is the index for the parameter. The relative standard deviation as a percentage is simply given by $100 \cdot \frac{\sigma_{\theta_i}}{\theta_i}$. The correlation coefficients are a measure of the statistical dependence between the parameters and obtained from the off-diagonal elements of $\mathbf{P}$. The estimates are statistically more accurate the smaller the standard deviations and the smaller the correlation coefficients.

The Gauss-Newton method (or alternatively Levenberg-Marquardt method) delivers information on the statistical accuracy of the estimates as a by-product. This is, besides the fast convergence, one of the advantages of this method when compared with other optimisation methods such as Powell's, Jacob's, simplex or subplex, see further reference [Jat06].

Equations (6.67) and (6.68) principally provide an easy way to obtain theoretical information about the accuracy of the estimates and correlation among them. However, in practical applications this is a more complex issue and not without ambiguities. The standard deviations obtained from equation (6.67) are found to be too optimistic in practice. The cause for this discrepancy has been traced to colored residuals, see further [Jat06]. In [Jat06] an ad hoc approach of a fudge factor f_f is presented to obtain a realistic estimate of the errors. It is common practice to use a fudge factor of typically 5 to 10. This is an approach that is based on experience. It attempts to bridge the gap between theory (assumption of independent noise samples) and practice (white noise is a mathematical assumption and residual spectra are seldom white). The autocorrelation function and the power spectral density of the residuals are statistical measures to check for whiteness. However, noise statistics is of secondary importance, where the primary goal is to determine a model that is sufficiently close to reality and with good predictive capability.

One would expect the scatter in the estimates of a particular derivative from the same model and from repeated experiments to agree with a band resulting from the standard deviations that are corrected through a fudge factor. Unfortunately, this is not always the case. The scatter in the estimates is then larger than the standard deviations. There exists no theoretical means to overcome this discrepancy. This should be kept in mind while interpreting these statistical accuracies.

Similar can be said with respect to the correlation coefficients. Correlation coefficients greater than 0.9 require some attention. Those greater than 0.95 can be considered to be almost linearly dependent. However, the actual magnitude of these numbers may vary from application to application. Unfortunately, the above numbers are not true in all cases. It is possible that estimates are encountered that are plausible and in the expected range, but the correlation coefficients were larger than the threshold indicated above or even close to 1.

6.10.2   Residual Analysis

Residual analysis is a statistical approach to judge the quality of the fit. In the following, the goodness of fit and Theil's inequality coefficient will be considered.

Goodness of fit

The value of the cost function is a measure of the model fit. In this thesis, the negative likelihood function was used as the cost function.

Although it is the most direct way to evaluate the model quality, there are some practical difficulties associated with the evaluation of the numerical values. In general, the cost function should be small. However, the value of the cost function depends on the number of system outputs and the amount of noise in the data analysed. It also depends upon the units of the variables being weighed in the cost function. Therefore, the absolute value alone does not yield any clues to the quality of the model fit. Consequently, there is no criterion available that would allow a direct comparison of different models. Goodness of fit can not be seen as a criterion. It is a necessary but not a sufficient condition. A perfect fit of one or more experiments is likely to result in good predicting capabilities for other data, but it does not guarantee perfect prediction capability.

Theil's inequality coefficient

Theil's inequality coefficient provides another form of output statistics for the overall fit. It provides a little more insight into the correlation between two time series, compared with the goodness of fit in terms of the residuals. In this case, the two time series are the measured aircraft responses z and the model predicted responses y. Theil's inequality coefficient for each of the output variables is defined as:

$$U_i = \frac{\sqrt{\frac{1}{N} \sum_{k=1}^{N} [z_i(t_k) - y_i(t_k)]^2}}{\sqrt{\frac{1}{N} \sum_{k=1}^{N} [z_i(t_k)]^2} + \sqrt{\frac{1}{N} \sum_{k=1}^{N} [y_i(t_k)]^2}}, \qquad i = 1, 2, \ldots, n_y, \qquad (6.69)$$

where z is the measurement vector, y the model output vector and N is the total number of data points. This equation provides n_y separate Theil's inequality coefficients U_i, corresponding to the n_y outputs. A single measure for the overall fit can also be defined, called multiple Theil's inequality coefficient. This quantity is then based on the fit errors in the multiple pairs of time series. It is, however, preferable to treat the inequality coefficients separately, because it aids in locating outputs that are matched better and those which are not. In statistical terminology, it represents the ratio of the root mean square fit error and the root mean square values of the measured and estimated signals summed together. From equation (6.69), it can be seen that U is a normalised index, bounded within the closed interval between zero and unity. This normalisation is the main advantage of this procedure over the goodness of fit. A perfect fit is implied by $U = 0$ (case of equality) and $U = 1$ corresponds to the case of maximum inequality. When two time series are significantly different, the value of U will be close to 1. Therefore, Theil's inequality provides insight into the validity of the predicted responses. The acceptable value of U depends on the application. Although, as a rule of thumb, a value in the range 0.25 to 0.3 indicates in general a good agreement.

Theil also decomposed the fit error between the two time series, $[z_i - y_i]$, in terms of

bias, variance and covariance proportions:

$$U_i^M = \frac{(\bar{z}_i - \bar{y}_i)^2}{\frac{1}{N}\sum_{k=1}^{N}[z_i(t_k) - y_i(t_k)]^2}, \tag{6.70}$$

$$U_i^S = \frac{(\sigma_{z_i} - \sigma_{y_i})^2}{\frac{1}{N}\sum_{k=1}^{N}[z_i(t_k) - y_i(t_k)]^2}, \tag{6.71}$$

$$U_i^C = \frac{2(1 - \rho_i)\sigma_{z_i}\sigma_{y_i}}{\frac{1}{N}\sum_{k=1}^{N}[z_i(t_k) - y_i(t_k)]^2}, \tag{6.72}$$

where as before the index i ($i = 1, \ldots, n_y$) refers to the ith output variable, $\bar{z}_i$ and $\bar{y}_i$ denote the corresponding mean values, σ and ρ respectively the standard deviations and correlation coefficient of the two time series z and y. These are given by:

$$\sigma_{z_i} = \sqrt{\frac{1}{N}\sum_{k=1}^{N}[z_i(t_k) - \bar{z}_i]^2}, \tag{6.73}$$

$$\sigma_{y_i} = \sqrt{\frac{1}{N}\sum_{k=1}^{N}[y_i(t_k) - \bar{y}_i]^2}, \tag{6.74}$$

$$\rho = \frac{1}{\sigma_{z_i}\sigma_{y_i}}\frac{1}{N}\sum_{k=1}^{N}[z_i(t_k) - \bar{z}_i][y_i(t_k) - \bar{y}_i]. \tag{6.75}$$

The three proportions (U_i^M, U_i^S, U_i^C) defined in equations (6.70) to (6.72), are again treated separately for each output variable.

The bias proportion U_i^M is a measure of the systematic error in the identified model. The variance proportion U_i^S represents the model's ability to duplicate the variability in the true system. The covariance proportion U_i^C is also called a measure of nonsystematic error. The above decomposition provides insight into the causes of fit error. In an ideal case, the bias and the variance proportions should be zero or they should at least be very small. The covariance proportion should be close to 1. It is stated in [Jat06] that the sum of the three proportions turn out to be 1. Large values of U_i^M and U_i^S are typically above 0.1 and indicate the need for a model update.

6.10.3   Model plausibility and model predictive capability

It is advisable to check the plausibility of the estimates from the physics of the dynamical system. A good response match can be achieved by a overparameterized model, but it will not necessarily give a good system representation. The plausibility of the estimated parameters can be most directly checked by comparison with estimates obtained from other sources, for example from CFD calculations or from aerodynamic databases derived from wind tunnel measurements. The estimates can also be checked and interpreted from physical understanding of the system under investigation.

The final test for an identified model is to check the model predictive capability using complementary flight test data, that is, flight maneuvers not used in the estimation. This step provides increased confidence in the identified model. More detailed information on the aspects of model validation can be found in reference [Jat06].

6.10.4   Numerical validation of the NL-rigid model

This section presents the results of the statistical analysis of the NL-rigid model, that was identified in section 6.7.

First of all, the standard deviation can be determined directly from the Fisher information matrix, see equation (6.67). The results are presented in table 6.9. It can be seen that the standard deviation is the biggest $\approx 12\%$ for the fifth parameter.
The correlation coefficients can be determined according to equation (6.68), see table 6.10 for the results. The elements on the diagonal are equal to one by definition, the off-diagonal terms should be less then 0.9. It was already mentioned in section 6.10.1 that off-diagonal terms larger then 0.9 require some attention. The first, third and fifth parameters show large values of correlation coefficients as well as the combination of parameters 4 and 6. Recall that the results might still be plausible, although attention is required.

The value of the negative Likelihood function was used as the main criterion for the optimisation algorithm. This value is a measure of the goodness of fit of the model, see further 6.7.3.

Theil's inequality coefficient has been determined according to equation (6.69) and the results can be found in table 6.11. Recall that a value in the range 0.25 to 0.3 indicates in general a good agreement. Output variables 14, 16 and 18 show coefficients in the range between 0.3 and 0.4, which indicates an acceptable agreement. Except for the first two variables, all other output variables show values below 0.3 implying a good to very good agreement.
The values of the bias, variance and covariance proportions, U_i^M, U_i^S and U_i^C respectively, are also presented in table 6.11. The bias proportion is a measure of the systematic error in the identified model. Its values should be very small, preferably below 0.1. As can be seen from the values from the bias proportion, the identified model still provides a potential area for systematic model improvements. The values of the variance proportion are smaller and thus a bit better. Recall that the variance proportion represents the model's ability to duplicate the variability in the true system. The covariance proportion should be close to one, which is not the case for 13 of the 21 output variables. This can be mainly contributed to the large values of the bias proportion for the corresponding output variables.

i	σ_{θ_i}	$100 \cdot \frac{\sigma_{\theta_i}}{\theta_i}$	$f_f \cdot \sigma_{\theta_i}$
1	0.0088185	6.9412	0.066138
2	0.00059724	0.060767	0.0044793
3	0.034531	1.0468	0.25898
4	0.0026744	0.29731	0.020058
5	0.22224	12.112	1.6668
6	0.025588	-2.1178	0.19191

Table 6.9: *Standard deviation of the NL-rigid parameter estimates, where a typical fudge factor of $f_f = 7.5$ is taken.*

$\rho_{\theta_i\theta_j}$	$j=1$	$j=2$	$j=3$	$j=4$	$j=5$	$j=6$
$i=1$	1	-0.28512	-0.98892	0.35725	-0.96151	0.22469
$i=2$	-0.28512	1	0.30476	-0.6953	0.2968	-0.45486
$i=3$	-0.98892	0.30476	1	-0.35725	0.99073	-0.21795
$i=4$	0.35725	-0.6953	-0.35725	1	-0.33746	0.93925
$i=5$	-0.96151	0.2968	0.99073	-0.33746	1	-0.1978
$i=6$	0.22469	-0.45486	-0.21795	0.93925	-0.1978	1

Table 6.10: *Correlation coefficients of the NL-rigid parameter estimates.*

output nr.	U_i	U_i^M	U_i^S	U_i^C
1	0.57928	0.5902	0.086442	0.32336
2	0.80917	0.56439	0.42056	0.015051
3	0.11783	0.065878	0.0057454	0.92838
4	0.27284	0.55509	0.0021096	0.4428
5	0.10285	0.12851	0.060705	0.81079
6	0.1402	0.27806	8.2423e-005	0.72186
7	0.11962	0.016751	0.011689	0.97156
8	0.12054	0.017868	0.10261	0.87953
9	0.11894	0.11848	0.23903	0.64249
10	0.054312	0.061932	0.21176	0.72631
11	0.031204	0.0049476	0.01405	0.981
12	0.030727	1.9729e-006	0.034867	0.96513
13	0.28941	0.7325	0.14881	0.1187
14	0.31616	0.12356	1.5962e-006	0.87643
15	0.11555	0.079521	0.23097	0.68951
16	0.33665	0.30235	0.34093	0.35672
17	0.28852	0.39665	0.57042	0.032933
18	0.39252	0.64096	0.066836	0.2922
19	0.18514	0.29872	0.0032537	0.69803
20	0.13643	0.11518	0.031976	0.85284
21	0.039095	0.97748	0.0012019	0.021315

Table 6.11: *Theil's inequality coefficients of the NL-rigid parameter estimates.*

6.10.5   Predictive capability of the NL-rigid model

In general, if the identification of the model is performed using the maximum amount of available flight data, it can be expected that this automatically leads to a model with adequate fidelity. In this section complementary flight data is used to check the model predictive capability. That is, flight data is taken that was not used in the estimation of the model parameters. Good performance of the model for these 'unknown' time intervals can obviously increase the confidence in the identified model significantly.

Here, it is chosen to test the identified model using the data from an loads relevant adjacent time interval. This implies comparable flight conditions, such that the model can be expected to perform well. The specific time interval is loads relevant, as the bank angle during the specific coordinated turn was increased even further compared to the data that was used for identification. This test will show whether the model provides meaningful predictions even for this significantly higher loads case.

The time interval starts, where the data from the previous chapters has ended, see for example figure (6.19). See figure (6.62) for the similar graph of the load factor N_Z plotted versus time for the specific time interval considered here. It can be seen from this figure that the model provides a very good prediction for the total loads at the highest loads level. At the smaller N_Z levels, the prediction is considerably larger then the measurement, but it is more important to be accurate at the highest loads levels because these will drive the structural design. Figures (6.63) to (6.66) show the results as in previous sections for four representative local loads. In general, it can be said that the prediction of the local loads for the 21 loads stations on the wing and winglet is very good using the identified model from NL-rigid. The relative shear force on the right wing at wing section 4 is presented in figure (6.63). It can be seen from this figure that there are some differences between the model and the measurements, but these are acceptable. Similar can be said for the bending moment on the right wing at the fifth and the sixth wing station and on the winglet, which are shown in respectively figure (6.64), (6.65) and (6.66). At the highest loads level, the simulation provides conservative predictions that are sufficiently accurate, which is desirable from a loads perspective. At the lowest loads level, some differences can be observed. These differences are considered to be less important, because they will not drive the design.
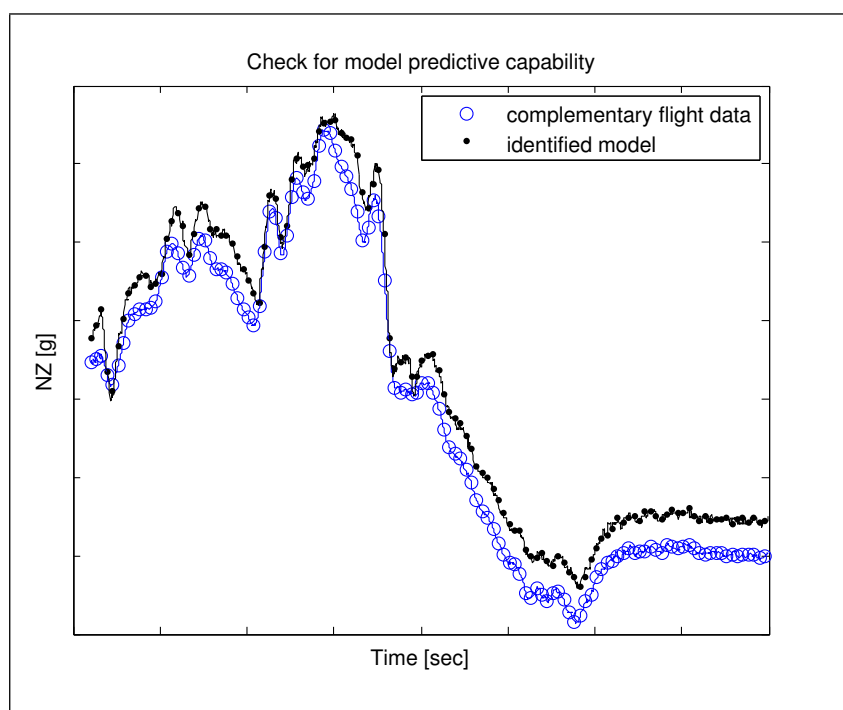
Figure 6.62: *Load factor in Z-direction versus time complementary flight data compared to simulation with the identified model from NL-rigid.*
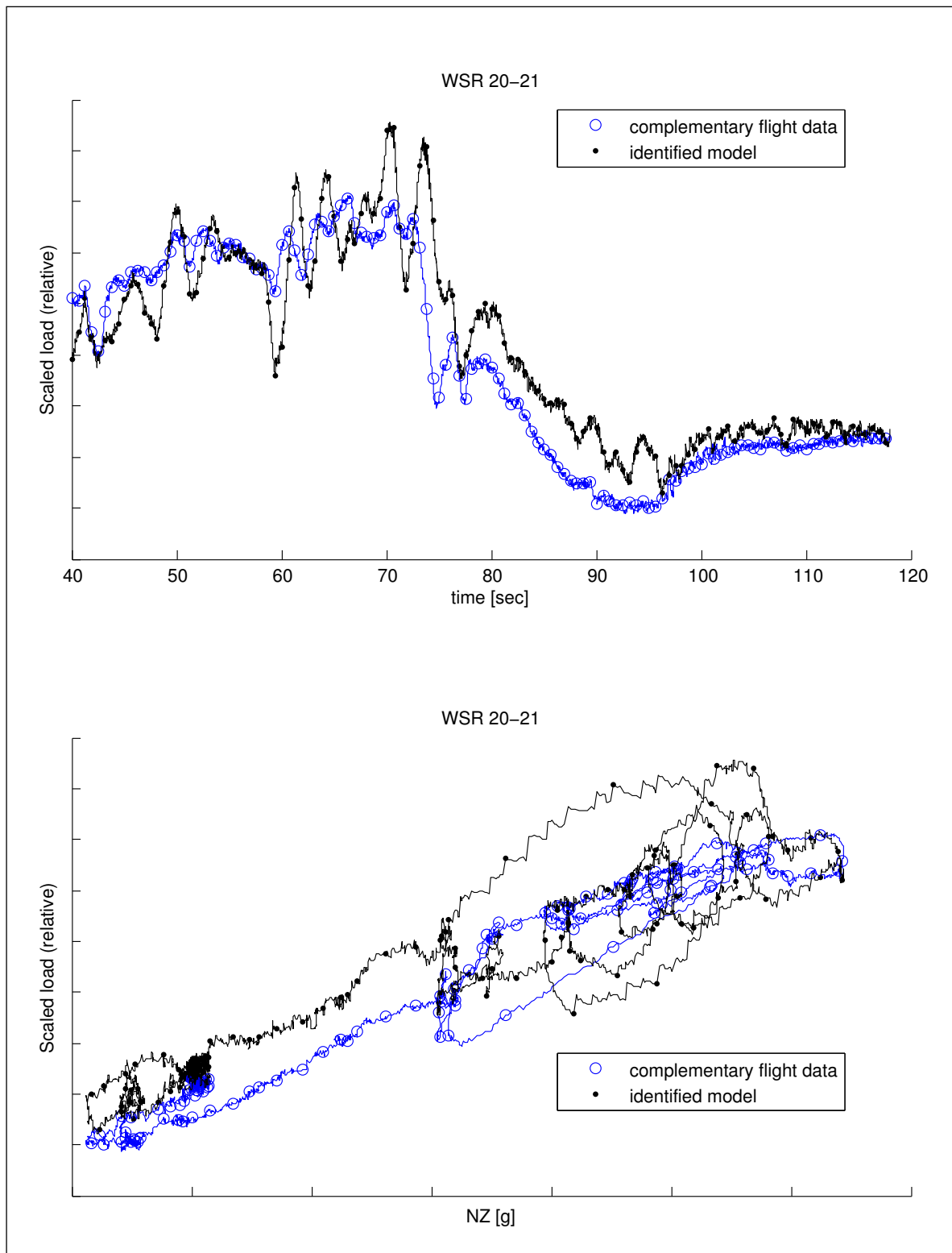
Figure 6.63: *Shear force (relative) on wing right vs. time and load factor respectively for wing station 4. Complementary flight data is compared to simulation with the identified model from NL-rigid.*
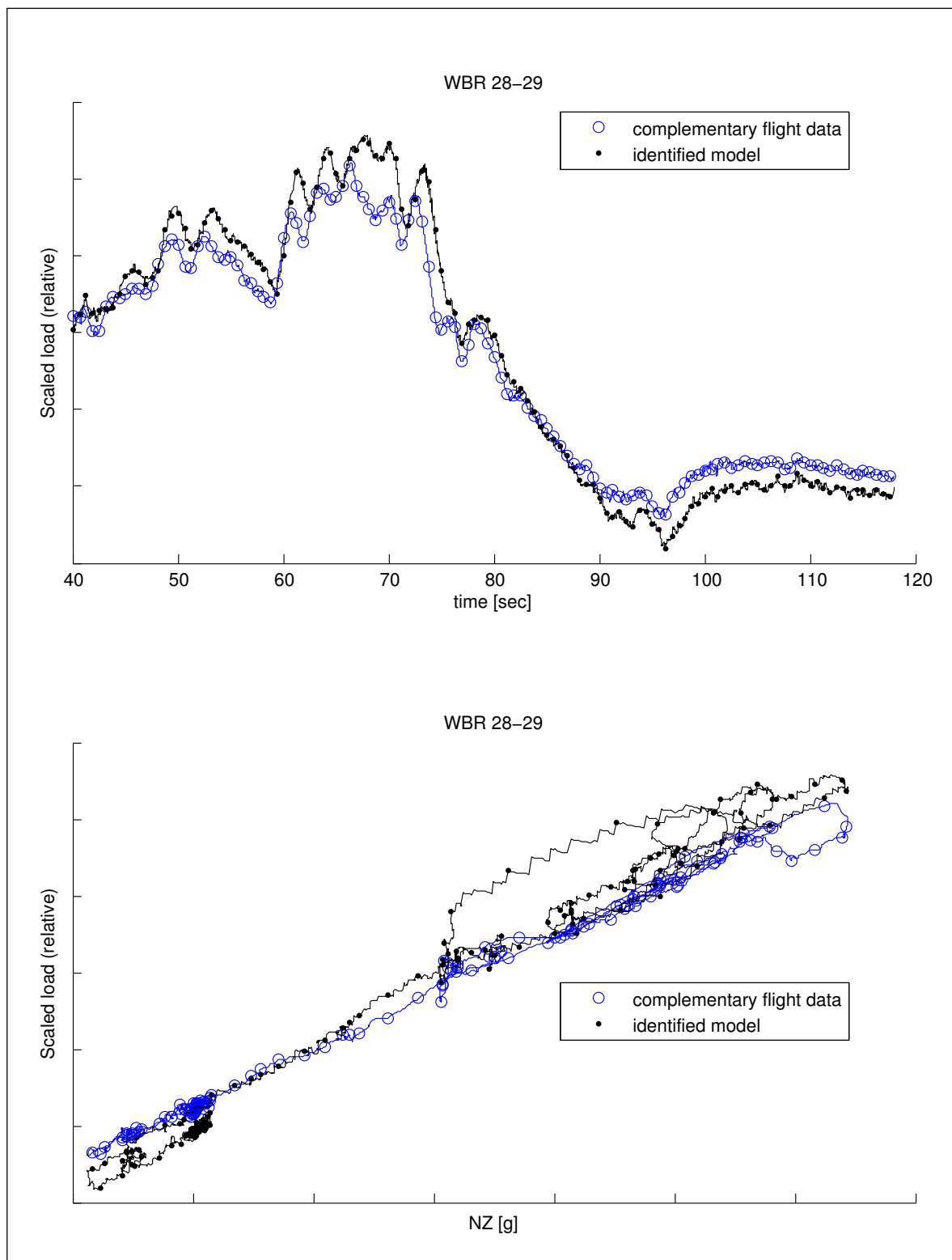
Figure 6.64: *Bending moment (relative) on wing right vs. time and load factor respectively for wing station 5. Complementary flight data is compared to simulation with the identified model from NL-rigid.*
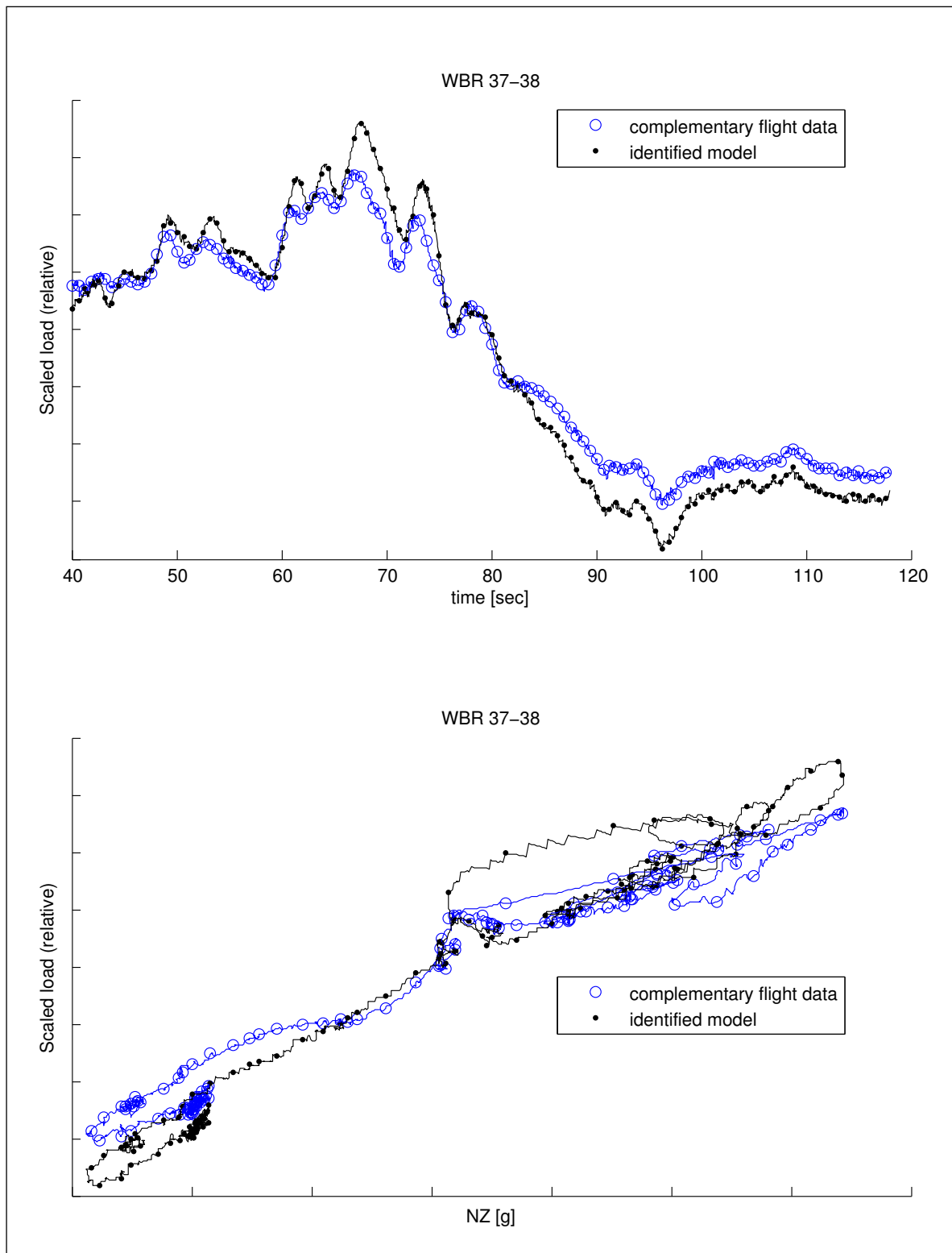
Figure 6.65: *Bending moment (relative) on wing right vs. time and load factor respectively for wing station 6. Complementary flight data is compared to simulation with the identified model from NL-rigid.*
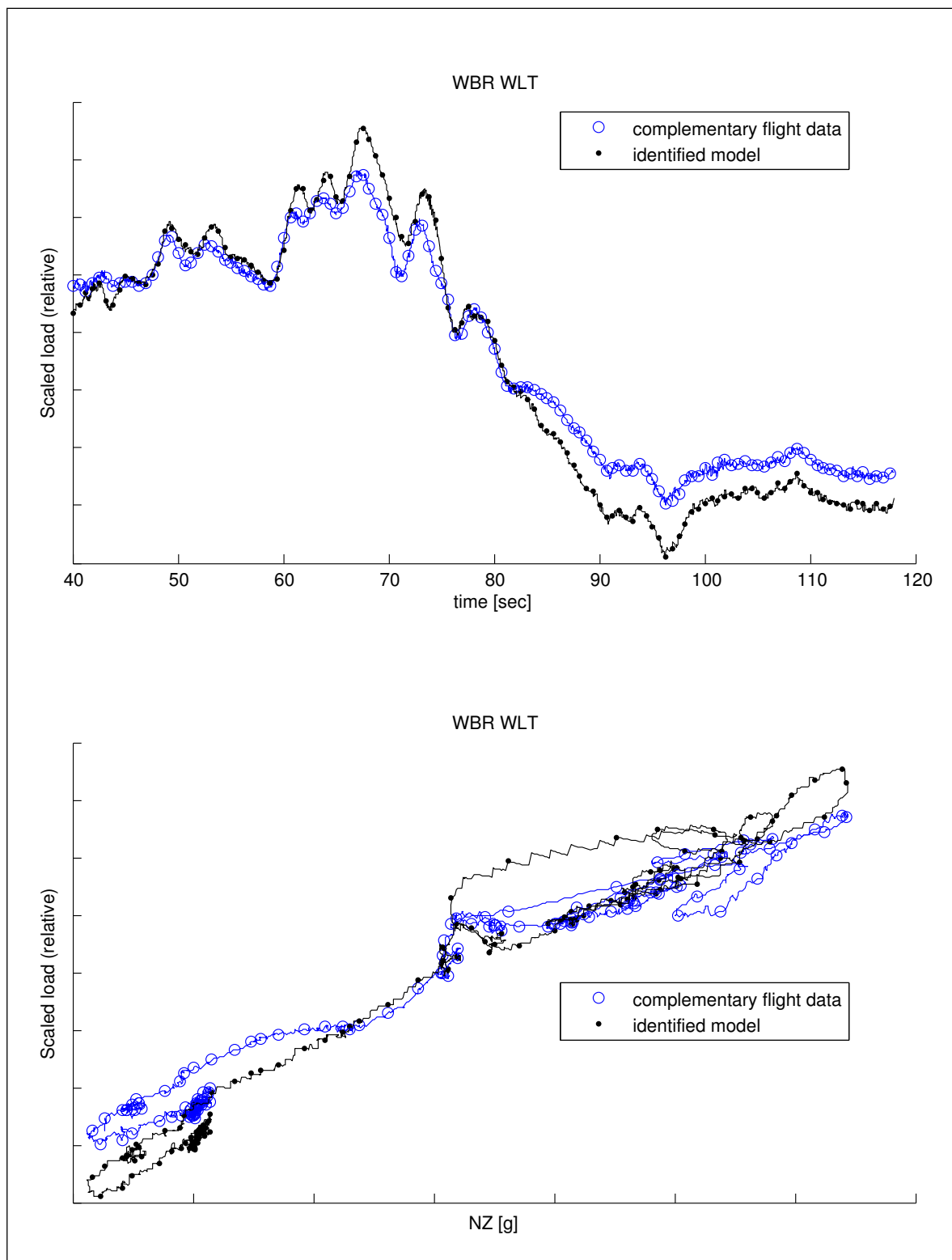
Figure 6.66: *Bending moment (relative) at winglet root vs. time and load factor respectively, righthand side. Complementary flight data is compared to simulation with the identified model from NL-rigid.*

Chapter 7

Conclusions

This chapter presents the conclusions of this thesis. The conclusions are categorized into: general conclusions, conclusions about the optimisation algorithm, about the measurements and concerning the identification of the flight loads monitoring model in specific.

1. General:

    (a) Flight test measurements have shown that flexibility effects of the airframe have to be taken into account when predicting the (aerodynamic) loads on the winglet. Obviously, the largest contribution stems from the flexibility of the wing.

    (b) Wing tip devices can be compared with each other by using the resulting Wing Root Bending Moment as a means to quantify the influence of a tip device with respect to loads. For the trade-off between two alternatives in an early design phase this is a good parameter to predict the structural (weight) impact of these devices. However, when the design decision is made, a more detailed analysis is required to address the loads along the whole span to enable a safe and efficient wing design.

2. The optimisation algorithm:

    (a) An algorithm is developed that is able to identify the parameters in a non-linear coupled aero-elastic manoeuvre loads model. The algorithm is based on the Maximum Likelihood method which is capable of solving even rank-deficient problems.

    (b) The success of the identification of a specific model, strongly depends on the structure of the model and the assumed initial values. The model must be sophisticated enough to capture/describe the phenomena contained in the measurements, however simple/small enough to enable its identification with the available computational resources.

263

(c) The algorithm developed converges for all investigated cases from any starting point to a local minimum. For rank-deficient problems there are, however, many solutions corresponding to to a local minimum. Furthermore, there is no guarantee that the algorithm will locate the global minimum.

(d) As long as the initial parameter estimates are close enough to the real values and the modelling structure represents the real behavior of the system close enough, then convergence to the real parameters or at least a good correspondence in the output will be achieved.

(e) For rank-deficient problems considered here, the 'minimum search' method has led to the fastest convergence. It requires a higher computational effort per iteration step, but it needs a considerably smaller number of iteration steps and leads to the best results.

(f) The theoretical identification (based on simulated measurements, where the 'real' system is known) of a loads representative model, has shown that with the correct assumption of parameters and boundary values, the optimisation algorithm is capable to arrive at very good results within only one iteration step. In case the structure of the model, the free parameters and their boundary values are chosen appropriately, the algorithm based on the Maximum Likelihood Method is very efficient and accurate in finding the actual values of the parameters. The match between the 'real' and the estimated parameters was found to be extremely good. The error in the parameter estimation was less then $1 \cdot 10^{-8}$ for both parameters.

(g) The identification algorithm has mostly proven its value as a rapid and direct means to quantify model improvements.

3. Measurements:

(a) Aspects like temperature, humidity and creep can induce a drift in the indicated output value of a strain gauge. By comparing the loads measurements relative to an adequate reference, such possible disturbances can be practically excluded from the analysis. It was shown that such an adequate reference can be the stabilised cruise condition that precedes the specific manoeuvre.

(b) A loads calibration is difficult and definitely not as straightforward as with a local stress analysis.

(c) The relative treatment of the loads measurement plus the addition of the overall loads factor N_Z as an optimization criterion are an excellent means to fully exploit the information contained in the measurement data while still preserving the model to stay physically probable. Unknown drifts are allowed to be present on the measurement data, because this procedure can prevent the possible negative influence of drifts on the identification results.

4. Identification of the flight loads monitoring model:

   (a) Modifying the modelling of flexibility effects:

      i. Due to the very high computational effort involved, it was found to be impossible at this moment to identify for nonlinear flexibility effects on a model of this size and complexity.

      ii. The identification of just linear flexibility effects (LINFLEX) shows significant differences between the estimated model and the measurement data. This can be the result of errors in the apriori fixed parameters and/or because of physical phenomena not captured by the model.

      iii. The identification accounting for linear flexibility effects (LINFLEX) showed that most of the discrepancies seem to stem from drifts on the loads measurements.

      iv. The values of the estimated drift from the best estimate from the identification of flexibility effects using method LINFLEX as part of the Flight Loads Monitoring model are comparable to the mean difference between the initial model and the measurements. Most differences seem to stem from drifts. These drifts are of the same order of magnitude as those determined from a reference on ground analysis of the loads stations. However, this model together with such drifts can still not explain the high load increase observed on the outer wing and winglet as a function of the load factor N_Z. Further investigation of the phenomenon on the outer wing proved to be necessary.

   (b) Modifying the modelling of rigid aerodynamic effects:

      i. Steady Reynolds-Averaged Navier-Stokes simulations of the trimmed flexible aircraft showed pretty good correspondence in the chordwise pressure distributions compared with flight test measurements. The lift coefficient derived from flight test pressure measurements is lower for the two winglet stations compared with the CFD-CSD simulations. The pressure measurement for the winglet stations also show a higher after loading (higher nose down pitch) compared to the simulation. On the other hand, the integral values of the measured pressure distributions at the winglet have limited accuracy, because of the relatively small number of data points.

      ii. The nonlinear model describing the rigid aerodynamics (called NL-rigid) presented in chapter 6.7 is an elegant method, that is capable of describing the specific phenomena at the outboard wing and winglet. The gradients in local lift become high on the outboard wing but these are comparable or similar to those derived from CFD-calculations. For the time interval considered, the range in angle of attack is limited. In this region, both the CFD-calculations as well as the original aerodynamic database predict still linear behavior. Therefore, for the time interval considered, the description of aerodynamic nonlinearities is insignificant for the description of the observed phenomena.

iii. The model based on the CFD-calculations (called RANS-model) shows immediately very good correspondence with flight test. The gradients on the outboard wing and winglet for example for local lift are considerably larger when compared with the baseline aerodynamics. However, the overall loads level is too small for the RANS model, due to the missing flight-to-jig-correction of the CFD input data.

iv. The CFD (RANS) calculations were performed for the aircraft geometry in quasi flight shape. The aerodynamic model input should be for the jig-shape aircraft. Methods were presented to account for this difference, although it is recommended to perform the specific rigid CFD-calculations for a jig shaped geometry and to use that as model input.

v. Further optimization of the CFD-based models has lead to distributions for the wings and winglets, which are physically improbable. This encourages the conclusion that the remaining differences might stem from disturbances on the measurements.

vi. No convincing means has been found to describe all measured *absolute* loads simultaneously with sufficient accuracy by a model that is physically probable. The NL-rigid model could be optimised in an identification for a best fit to the flight test loads measurements, when considered relative to a corresponding reference condition.

Chapter 8

Recommendations

In order to enable identification of nonlinear flexibility effects in the future or to improve results in general, the following recommendations can be given:

1. The optimization procedure could be performed using multiple parallel computers. The implementation of an automated parallelization scheme as well as an increase of the available computational power for each computer would decrease the required time to solve a certain problem.

2. The algorithm developed in this thesis assumes that system input is completely known and that there is no process noise in the system. This is the assumption typical for an output error method. The algorithm could be extended to include process noise in the procedure of Maximum Likelihood. Consequently, the state of the system also has to be estimated with the use of an Extended Kalman filter for a nonlinear system.

3. In investigating in-flight (winglet) loads, it is recommended to get detailed information in advance about the status of the flight test instrumentation (calibration results, accuracies, system architecture, etc.), either by documentation or recalibration.

4. It is difficult to reconstruct or detect any sources of disturbances by looking at Terabytes of recorded data and by reading the flight logs. Therefore, it is further recommended to be present during the aircraft preparations to know the exact status, condition, loading plan of the aircraft and during the flight test to be able to notice any anomalies during the flight.

5. The CFD-calculations should be performed for the case of an alpha sweep for a rigid aircraft in jig-shape (instead of 'quasi' flight shape), as this is expected to

give the most optimal model input data, based on the experience gained with the CFD based RANS-model and with the hybrid models.

Alpha-gradient plots from rigid analysis
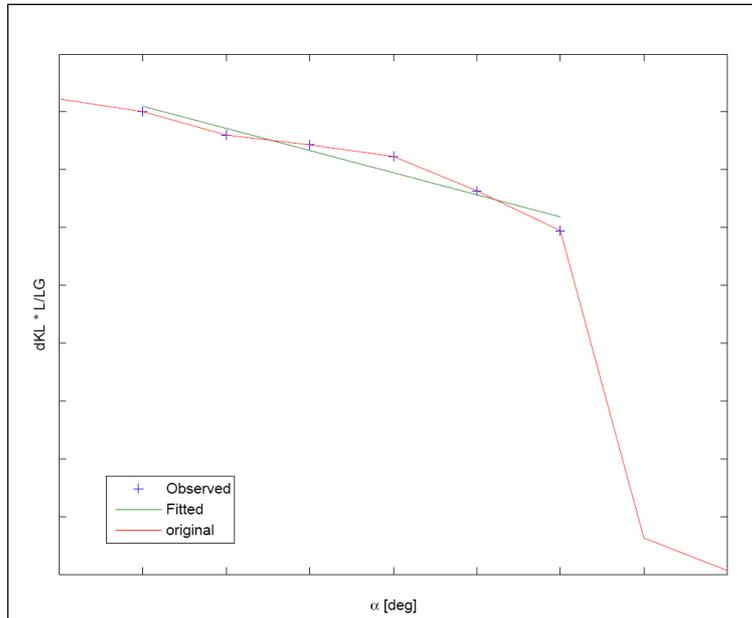
Figure A.1: *Local alpha-gradient at representative wing station.*
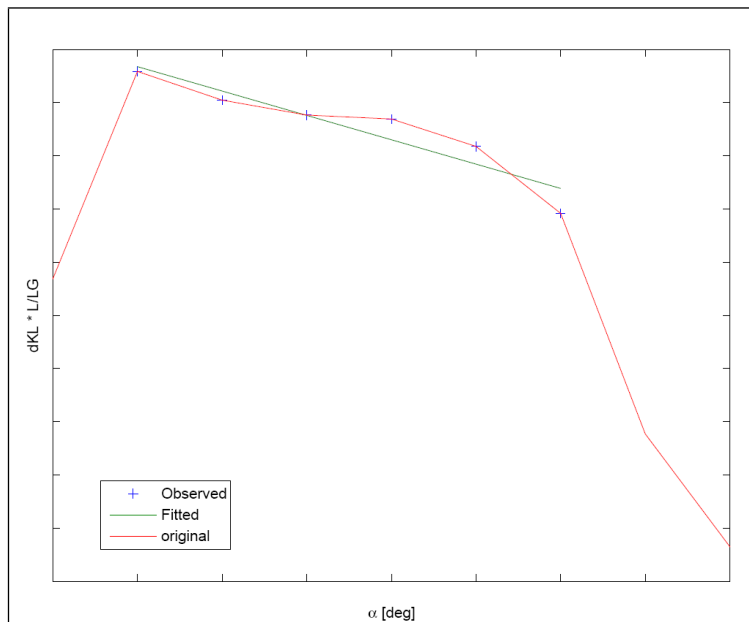
Figure A.2: *Local alpha-gradient at representative winglet station.*

Results hybrid model
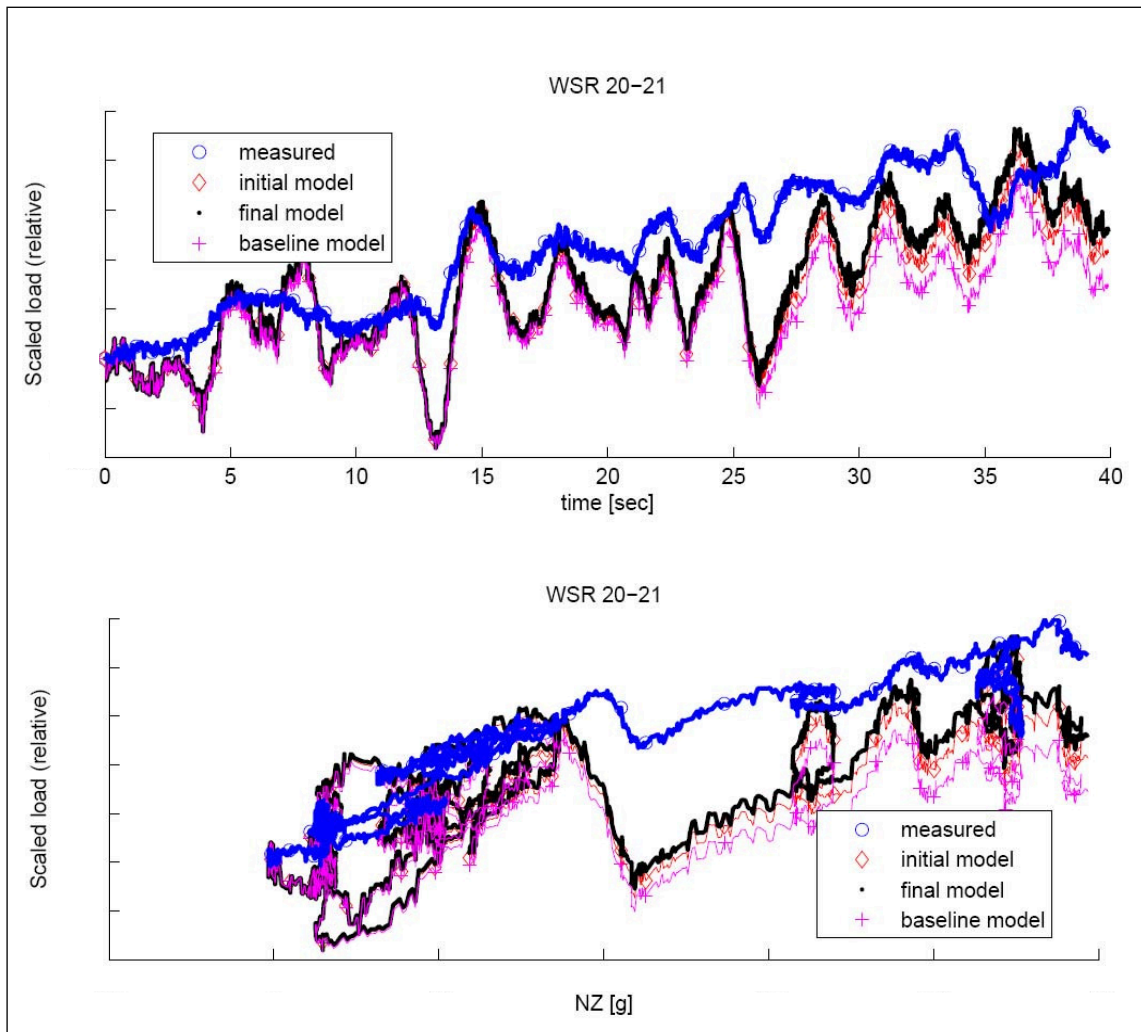
Figure B.1: *Shear force (relative) on wing right vs. time and load factor respectively for wing station 4, method "Hybrid".*
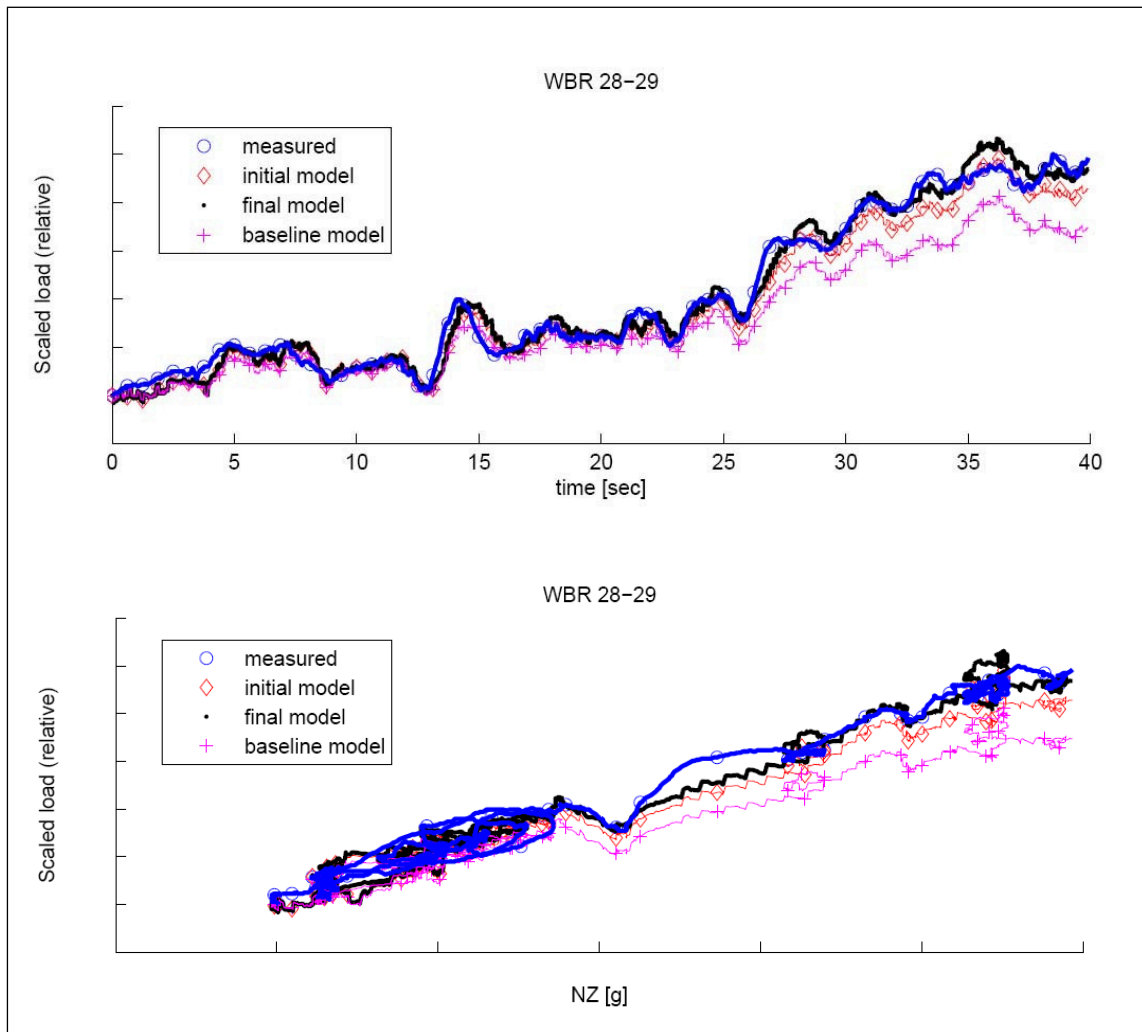
Figure B.2: *Bending moment (relative) on wing right vs. time and load factor respectively for wing station 5, method "Hybrid".*
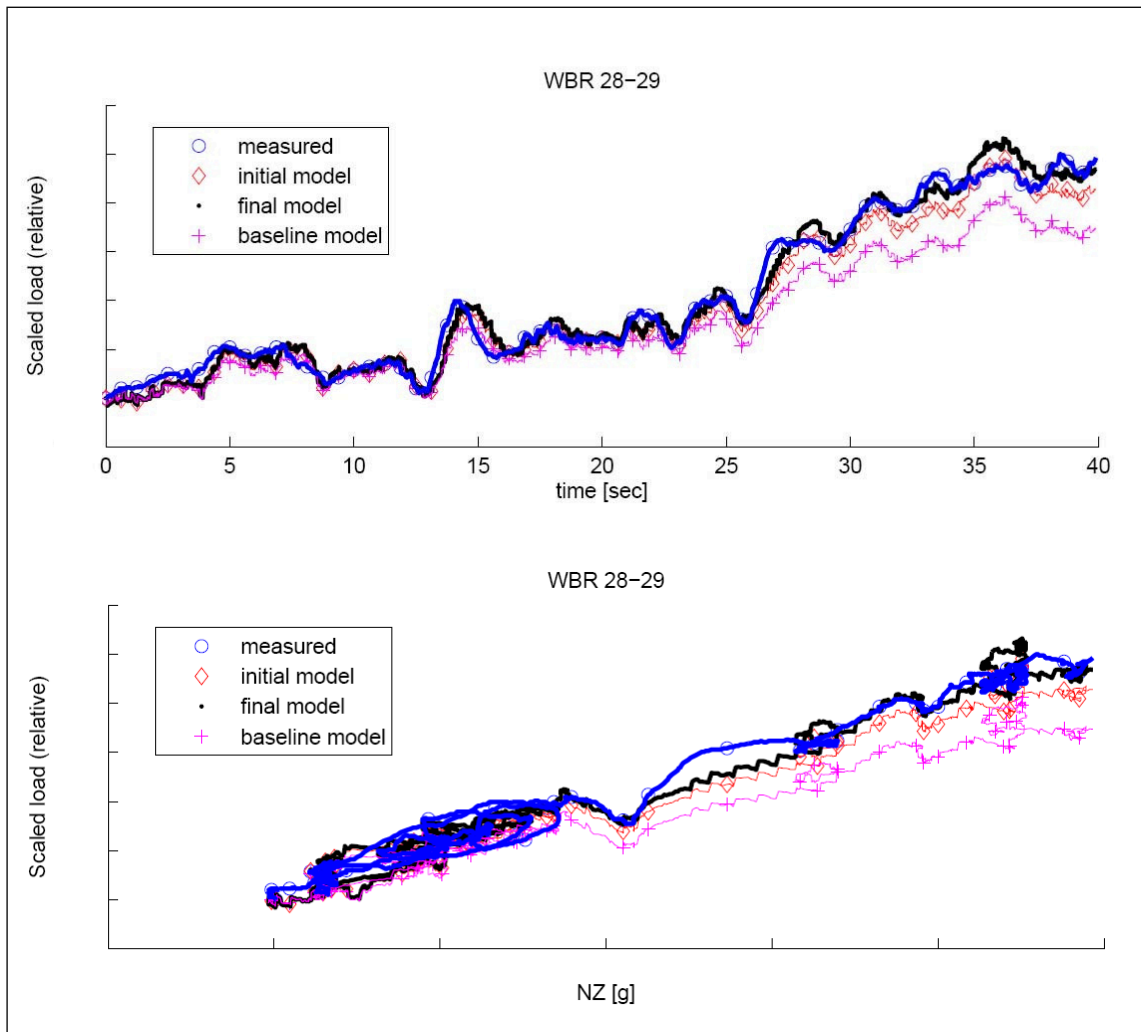
Figure B.3: *Bending moment (relative) on wing right vs. time and load factor respectively for wing station 6, method "Hybrid".*
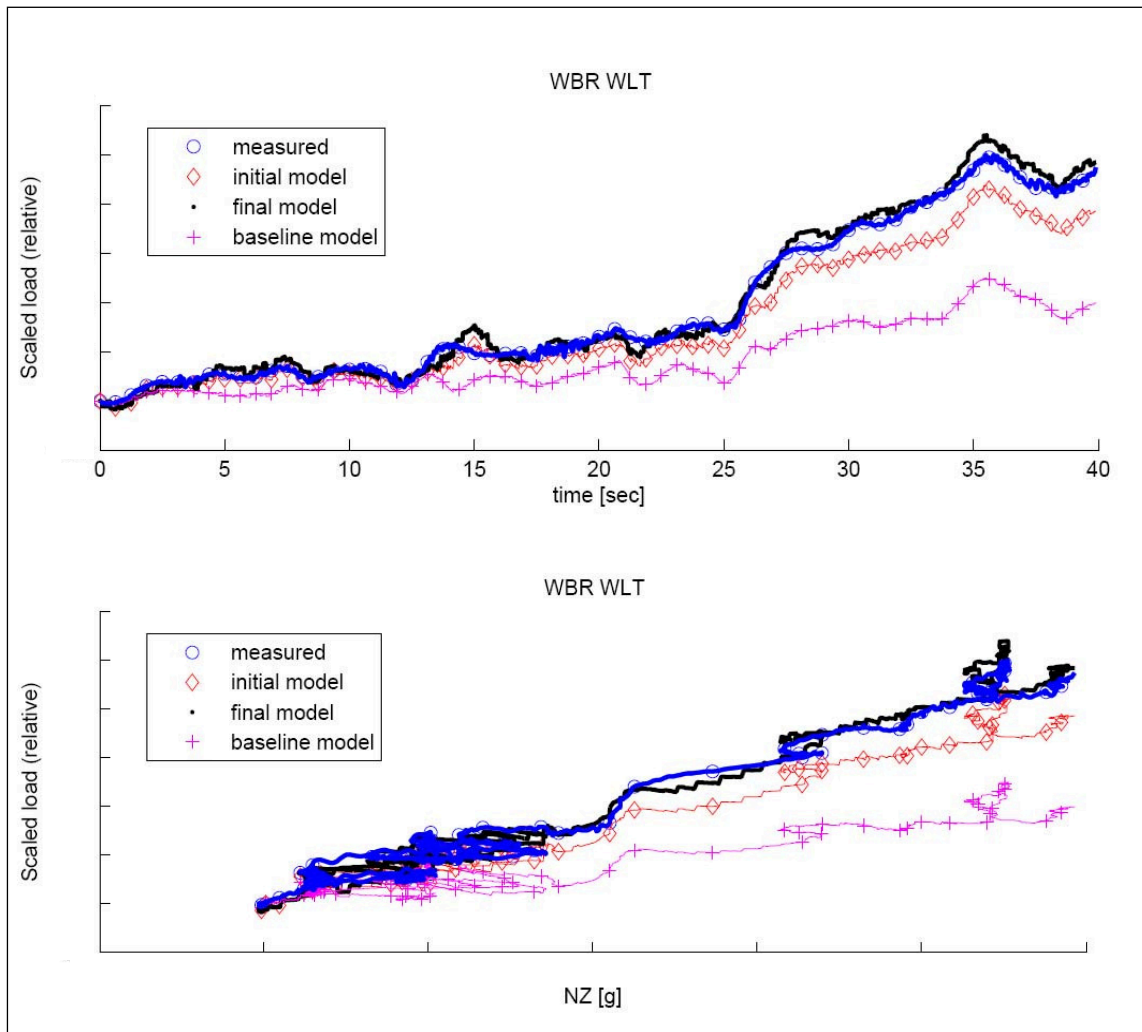
Figure B.4: *Bending moment (relative) at winglet root vs. time and load factor respectively, righthand side, method "Hybrid".*

C

Results hybridII model
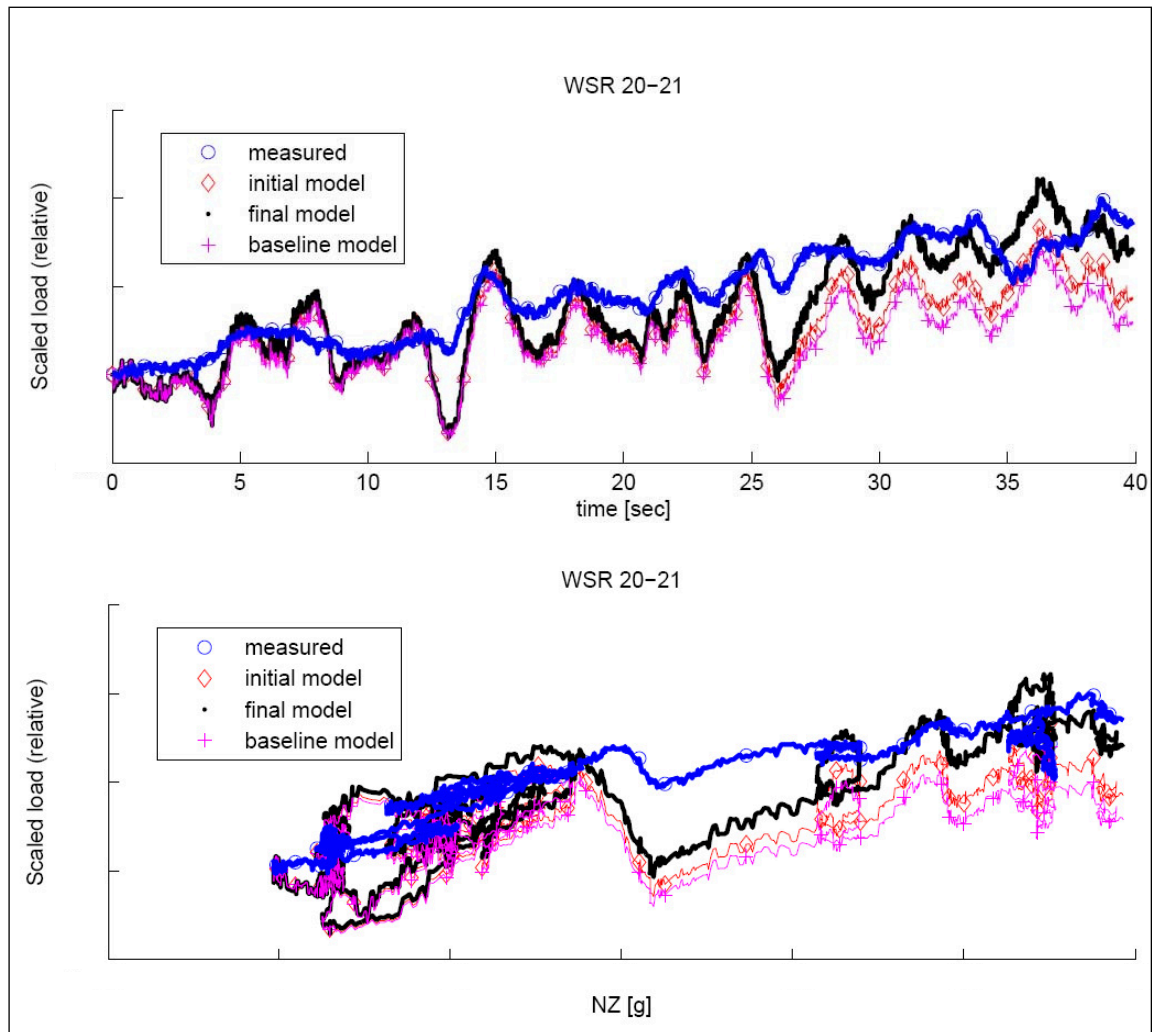
Figure C.1: *Shear force (relative) on wing right vs. time and load factor respectively for wing station 4, method "HybridII".*
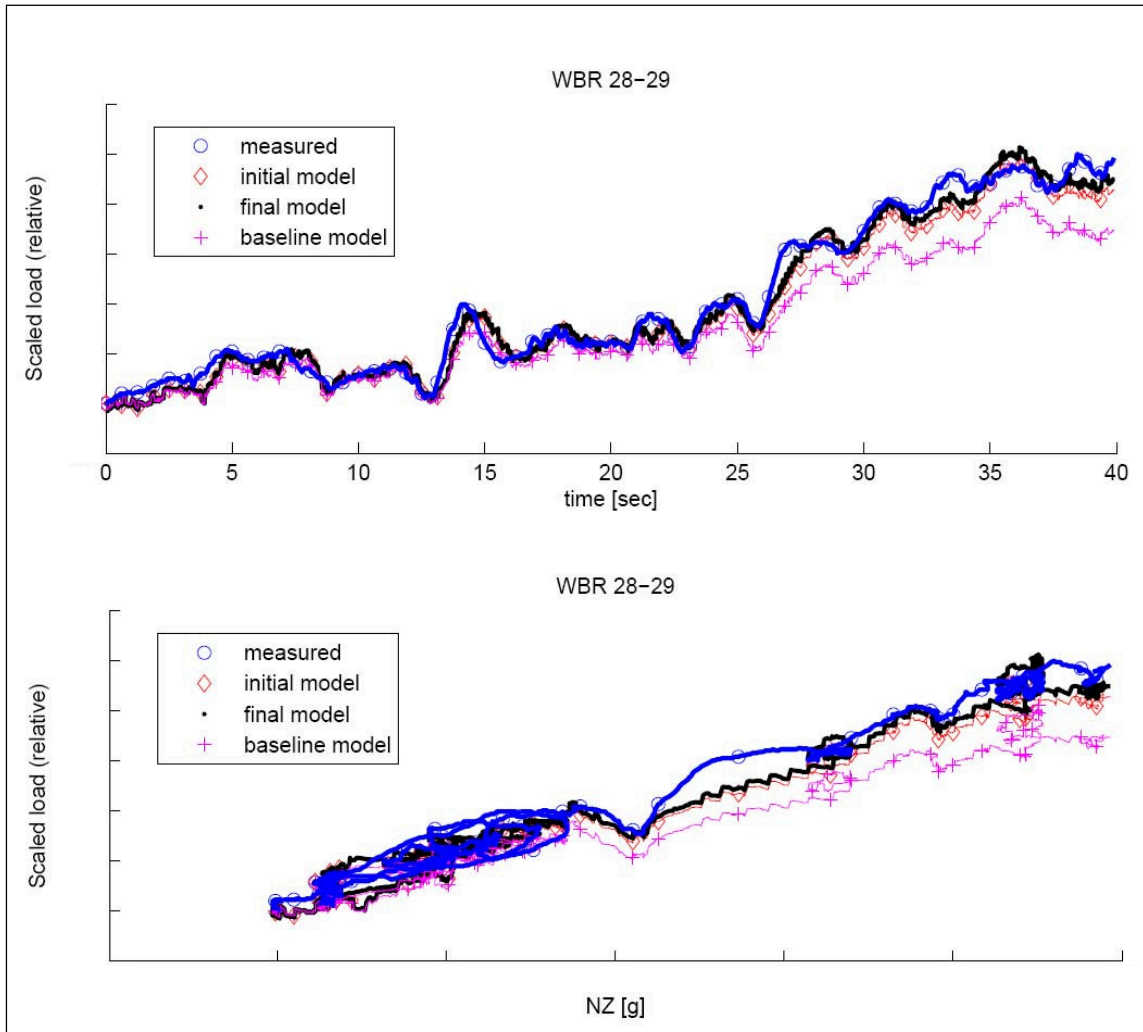
Figure C.2: *Bending moment (relative) on wing right vs. time and load factor respectively for wing station 5, method "HybridII".*
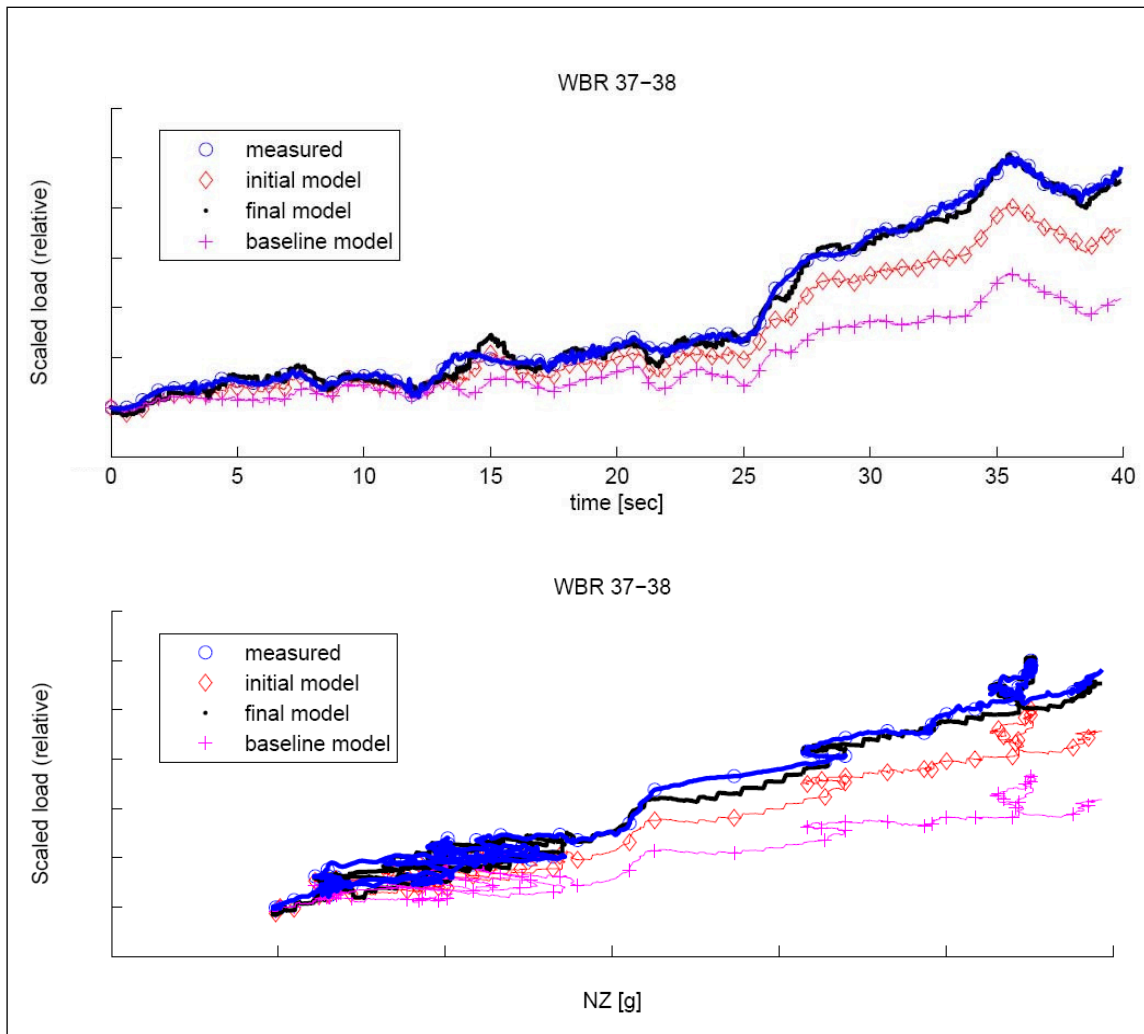
Figure C.3: *Bending moment (relative) on wing right vs. time and load factor respectively for wing station 6, method "HybridII".*
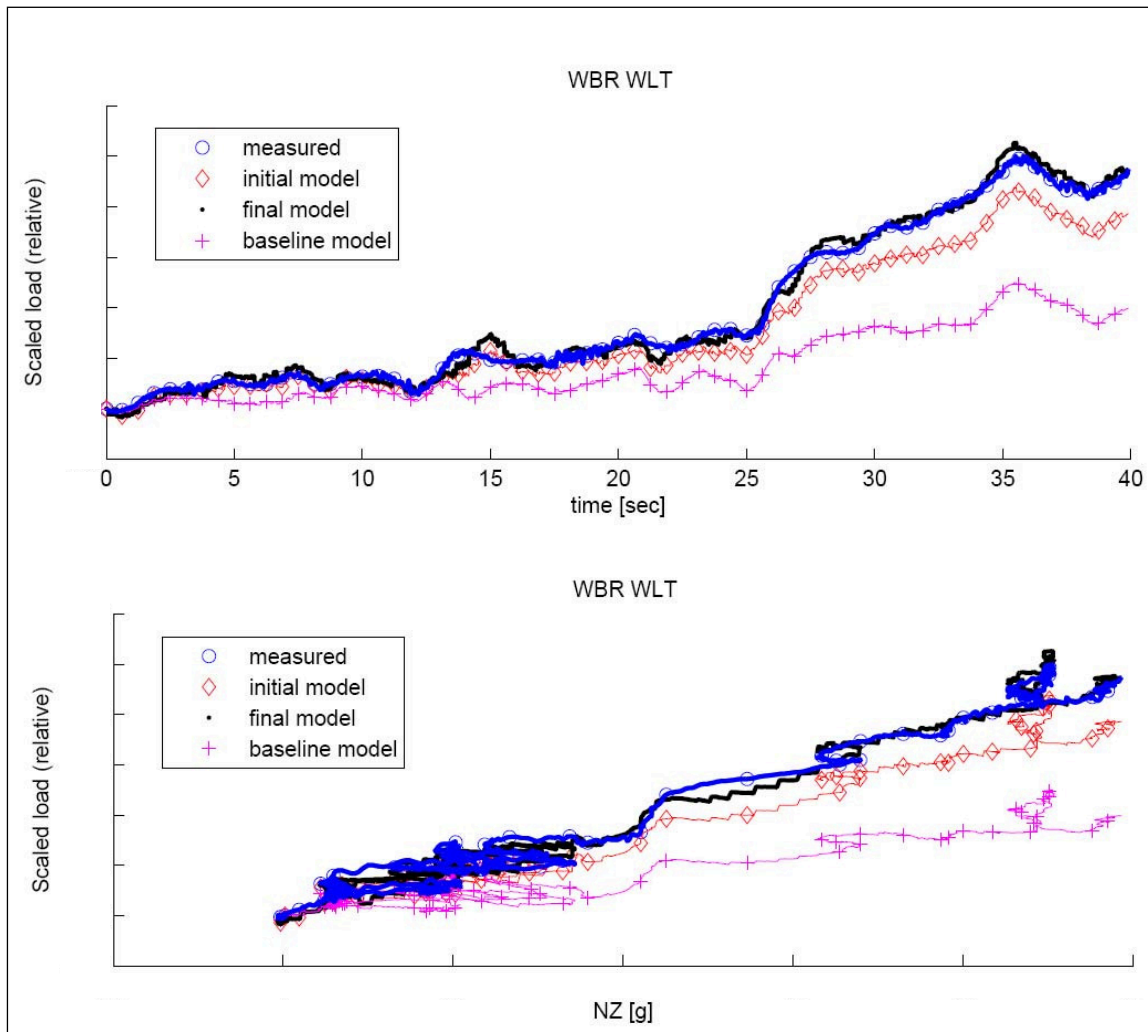
Figure C.4: *Bending moment (relative) at winglet root vs. time and load factor respectively, righthand side, method "HybridII".*

D

Full color pictures
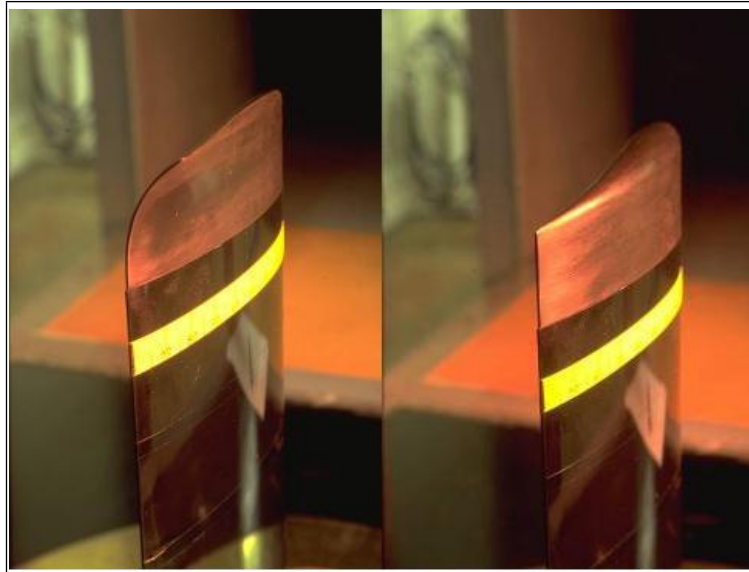
Figure D.1: A wind tunnel model of a wing with a Hoerner tip on the left. For comparison, the same wing with a round tip on the right. Photo by Antonio Filippone. Equivalent to figure (3.4).

Figure D.2: Conventional winglet of an Airbus A340-541. Photo by Fabian Gysel. Equivalent to figure (3.7).

Figure D.3: *Shark fin tip on a HPH 304 S sailplane. Photo by Tim Mara. Equivalent to figure (3.9).*

Figure D.4: *Wing Tip Fences on the Airbus A380. Photo by Thomas Wirtenberger. Equivalent to figure (3.10).*
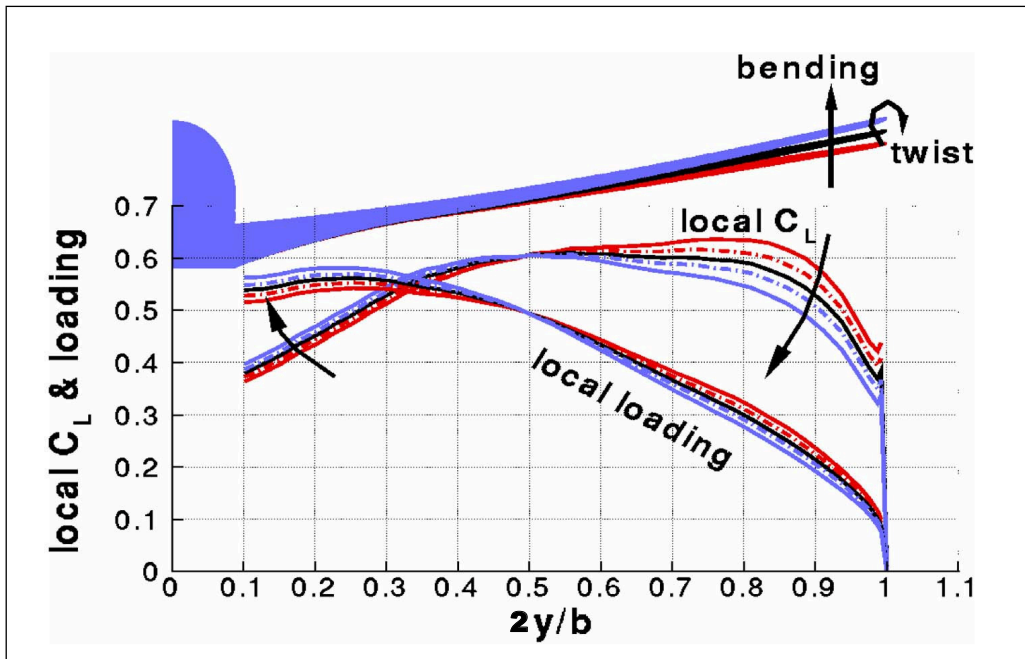
Figure D.5: Clean wing - Loads variations along the span at cruise as a function of twist. Arrows indicate nose down twist. The wing tip variation is ± 1 degree in comparison to the reference. Black = reference, blue = nose down and red = nose up. Image by Jean-Luc Hantrais-Gervois, see also reference [HG06]. Equivalent to figure (3.14).
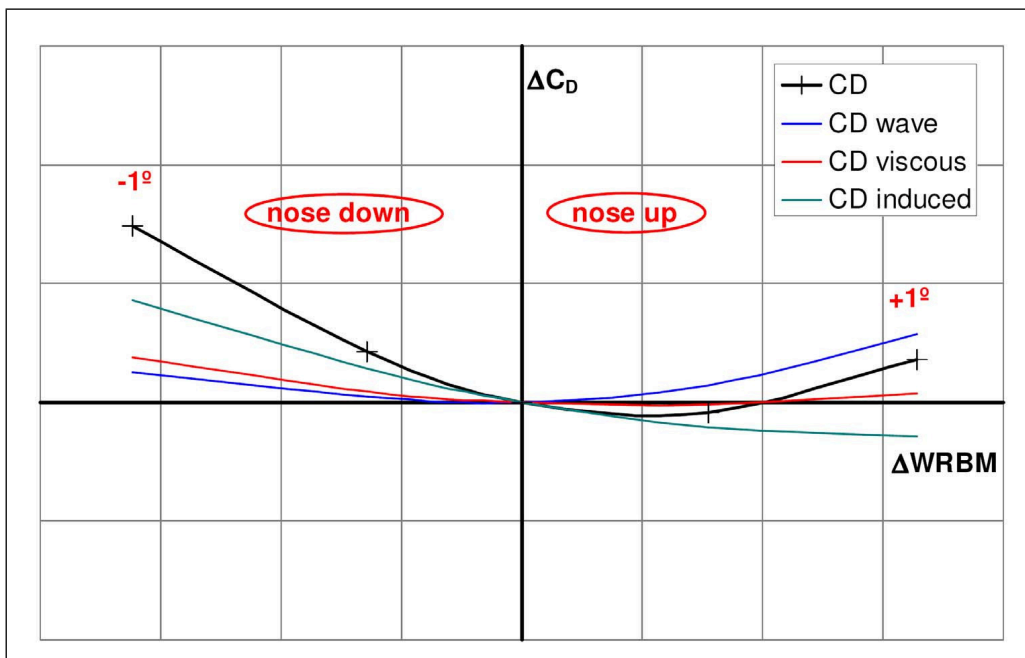
*Figure D.6:* Clean wing - Drag and WRBM increments to the reference flight shape at cruise as a function of twist. The wing tip variation is ± 1 degree in comparison to the reference. Image by Jean-Luc Hantrais-Gervois, see also reference [HG06]. Equivalent to figure (3.15).
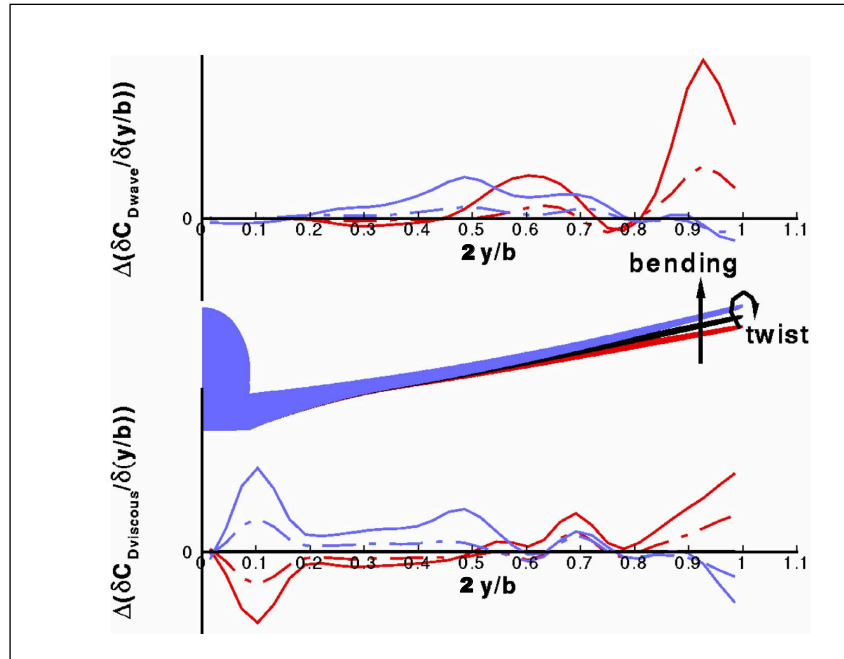
Figure D.7: *Clean wing - Drag increments to the reference flight shape at cruise over span as a function of twist.The wing tip variation is ± 1 degree in comparison to the reference. Blue = nose down and red = nose up. Image by Jean-Luc Hantrais-Gervois, see also reference [HG06]. Equivalent to figure (3.16).*
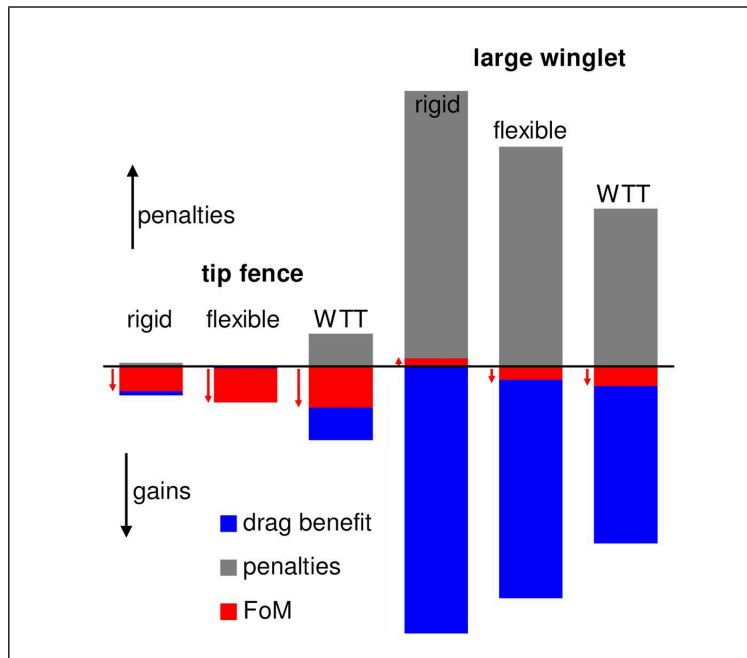
Figure D.8: *Comparison of the rigid and flexible assessments of a tip fence and a large winglet in comparison with a reference Küchemann tip. The penalties include structural, weight and industrial trade-off considerations. Image by Jean-Luc Hantrais-Gervois, see also reference [HG06]. Equivalent to figure (D.8).*
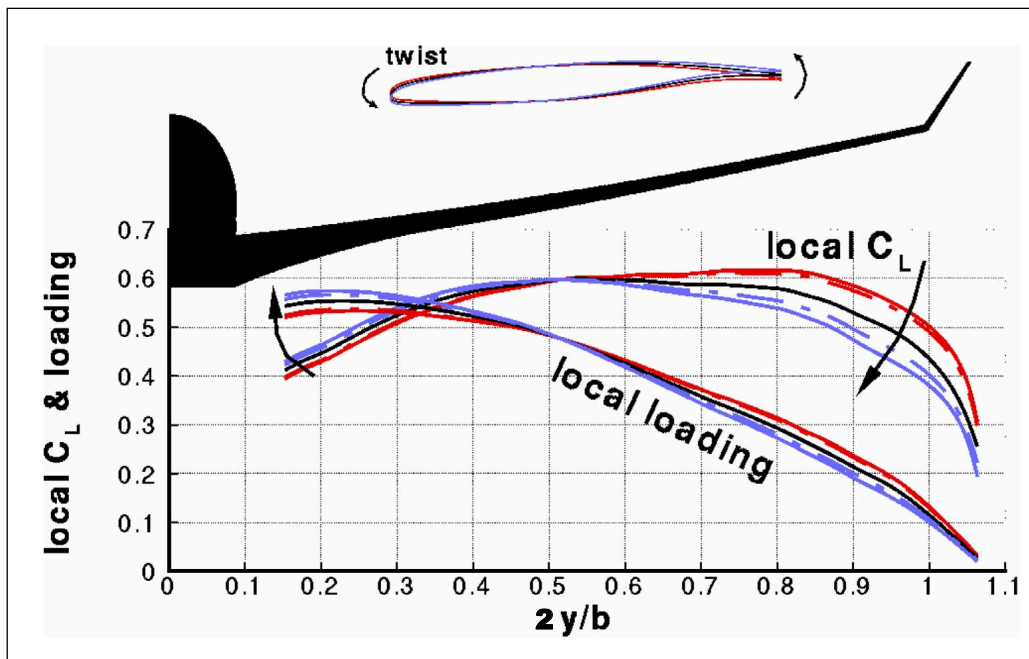
Figure D.9: *Wing plus large winglet - Loads variations along the span at cruise as a function of twist. Arrows indicate nose down twist. The wing tip variation is ± 1 degree in comparison to the reference. Black = reference, blue = nose down and red = nose up. Image by Jean-Luc Hantrais-Gervois, see also reference [HG06]. Equivalent to figure (3.19).*
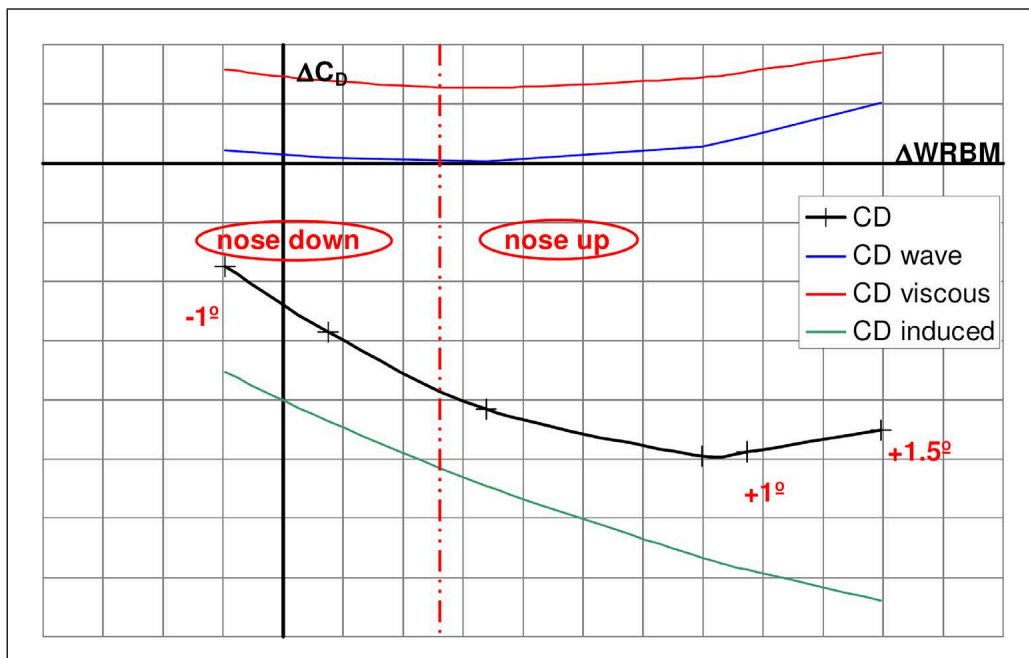
Figure D.10: *Wing plus large winglet - Drag and WRBM increments to the reference clean flight shape at cruise as a function of twist. The wing tip variation is +1.5/-1 degree in comparison to the reference equipped with the large winglet (dash-dot red line). Image by Jean-Luc Hantrais-Gervois, see also reference [HG06]. Equivalent to figure (3.20).*
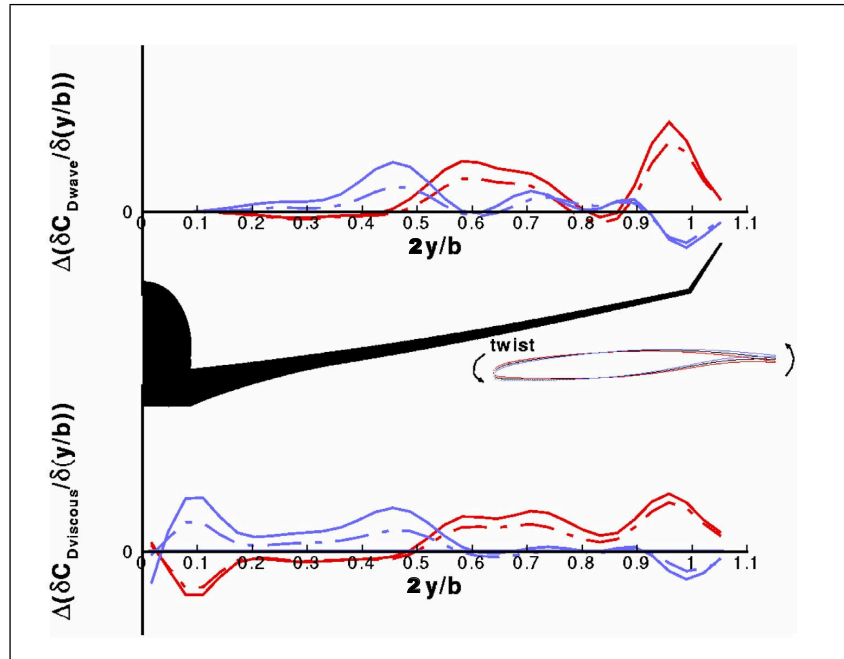
**Figure D.11:** *Wing plus large winglet - Drag increments to the reference flight shape at cruise over span as a function of twist. The wing tip variation is ± 1 degree in comparison to the reference equipped with the large winglet. Blue = nose down and red = nose up. Image by Jean-Luc Hantrais-Gervois, see also reference [HG06]. Equivalent to figure (3.21).*
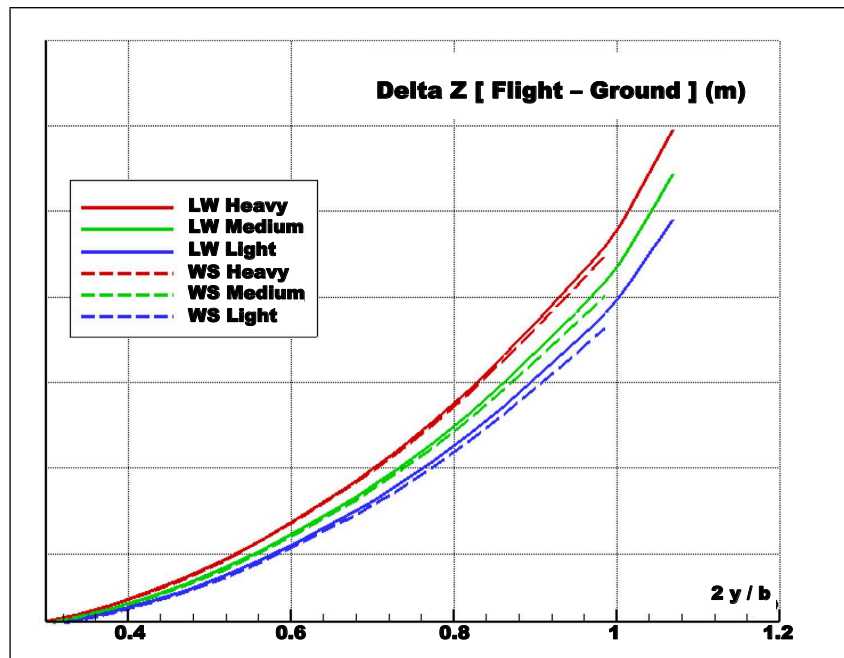
Figure D.12: *Comparison of vertical bending deformations with a weight evolution for both winglets. Image by Jean-Luc Hantrais-Gervois, see also reference [HG06]. Equivalent to figure (3.22).*
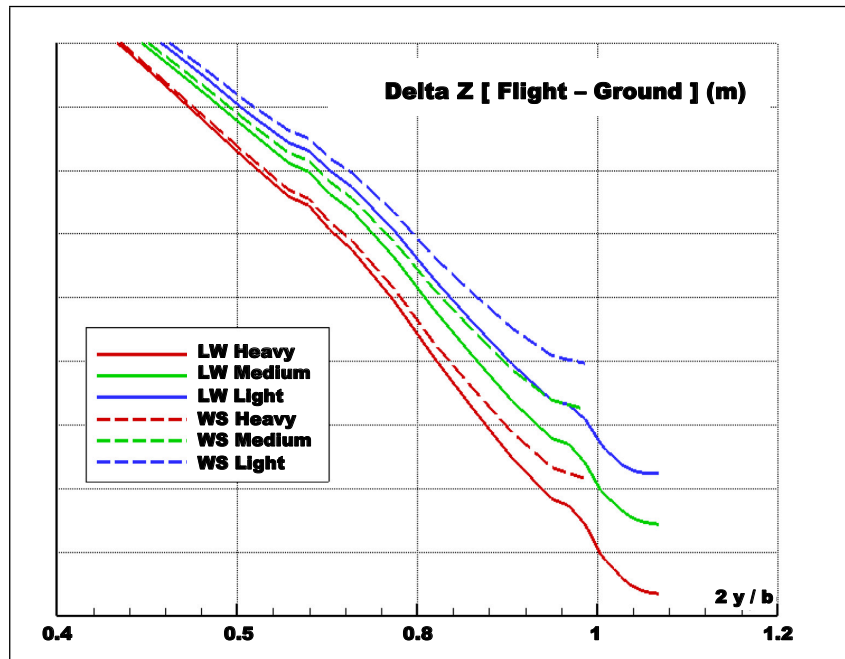
Figure D.13: *Comparison of twist deformations with a weight evolution for both winglets. Image by Jean-Luc Hantrais-Gervois, see also reference [HG06]. Equivalent to figure (3.23).*
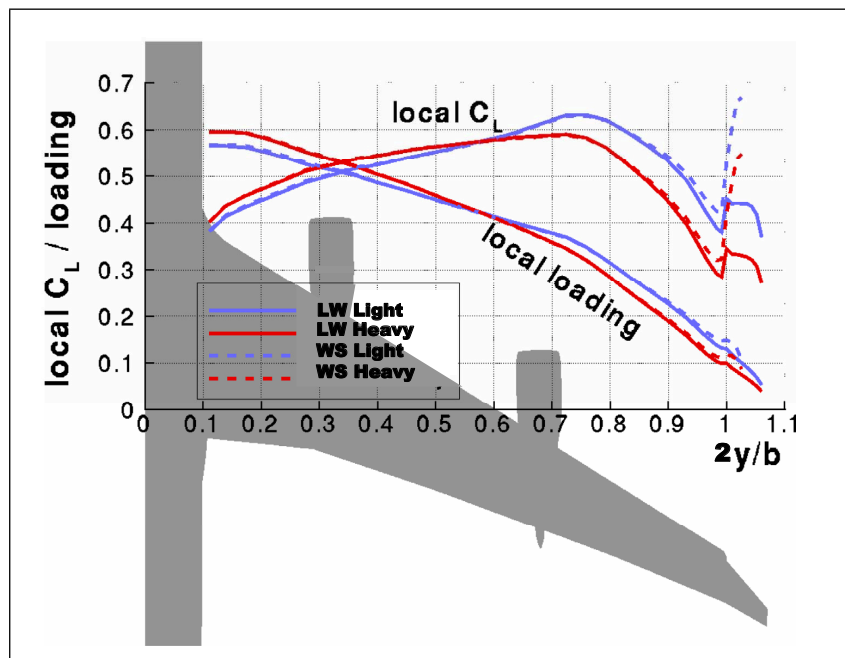
Figure D.14: *Large winglet and standard winglet span loadings for two weights. Image by Jean-Luc Hantrais-Gervois, see also reference [HG06]. Equivalent to figure (3.24).*
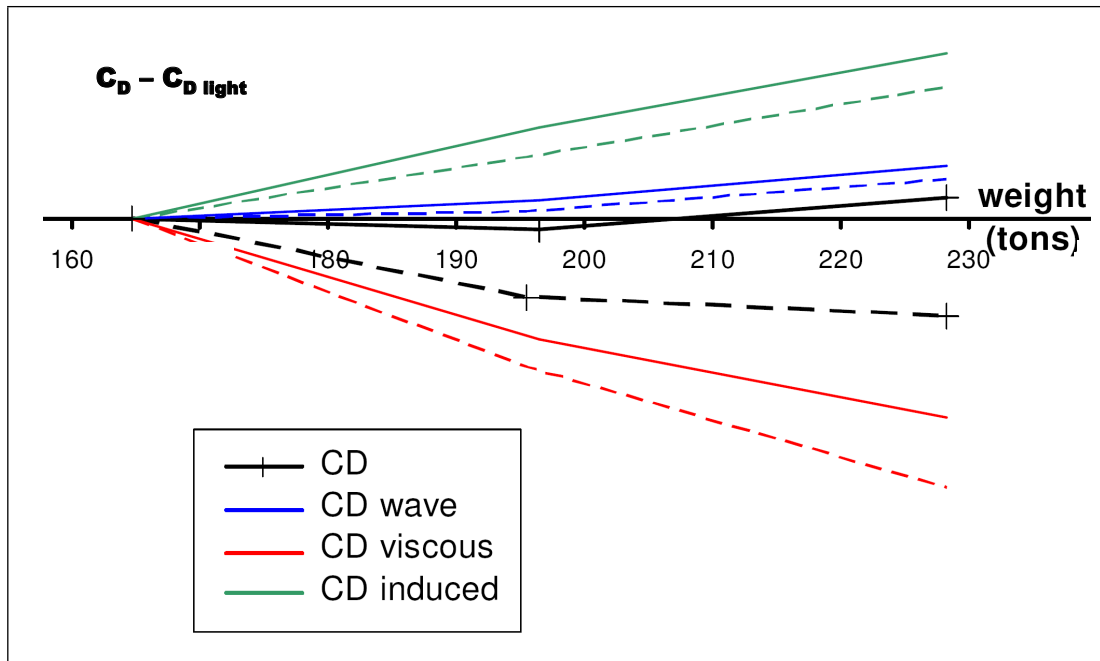
Figure D.15: *Large winglet (solid lines) and standard winglet (dashed lines) drag evolutions over weight. Image by Jean-Luc Hantrais-Gervois, see also reference [HG06]. Equivalent to figure (3.25).*
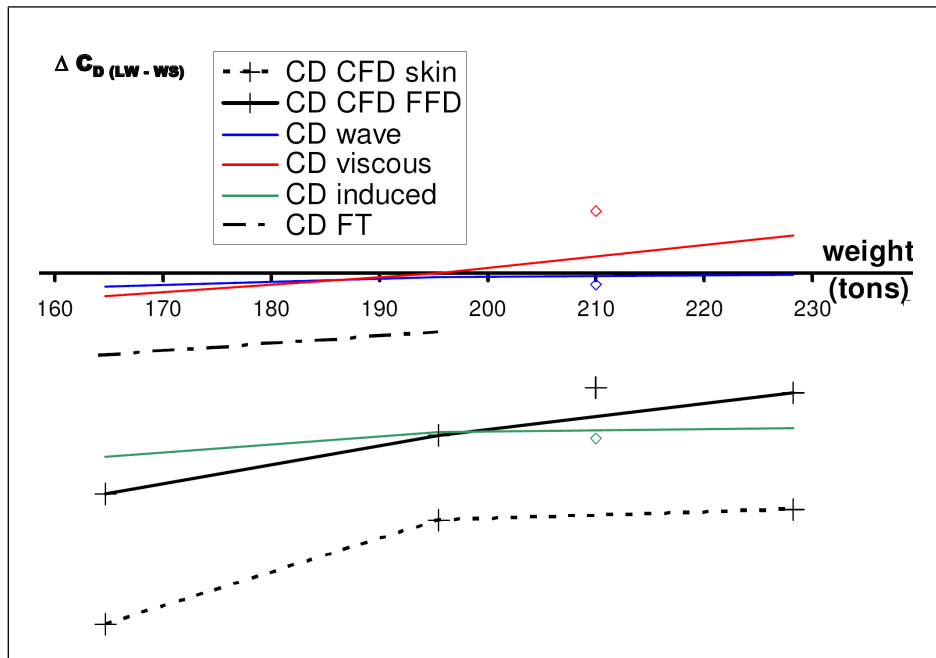
Figure D.16: *Large winglet drag gains in comparison to the standard winglet as a function of weight. The rigid predictions are indicated in empty symbols. Image by Jean-Luc Hantrais-Gervois, see also reference [HG06]. Equivalent to figure (3.26).*
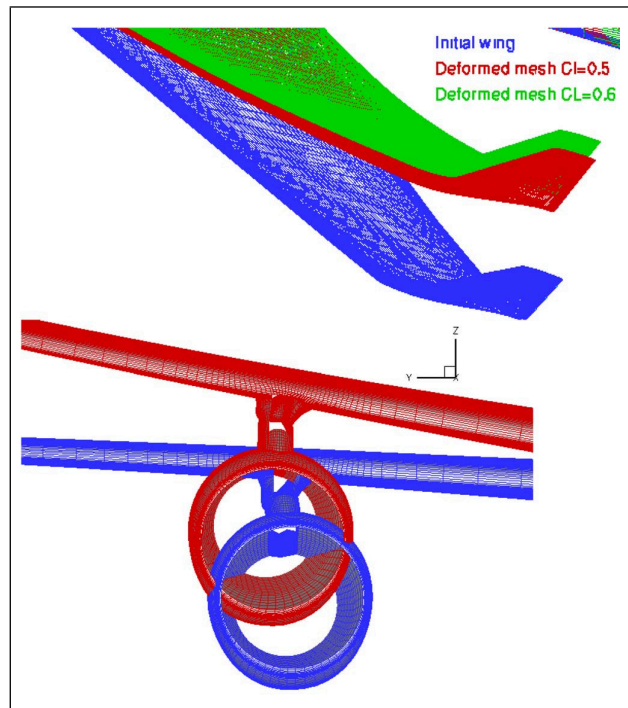
Figure D.17: *Examples of mesh deformation. Image by Jean-Luc Hantrais-Gervois, see also reference [HG06]. Equivalent to figure (3.28).*
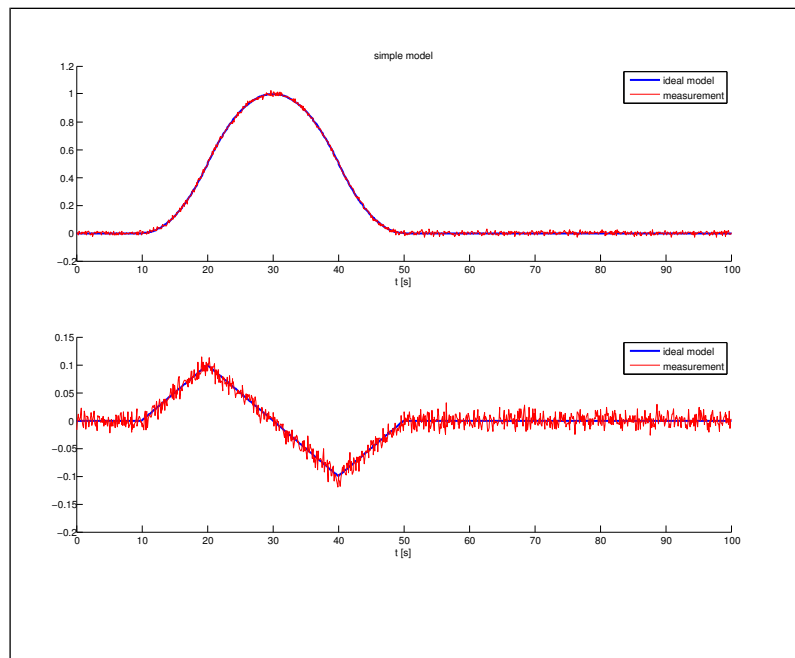
Figure D.18: *Time histories of the output of the ideal simple example and that with added measurement noise. Equivalent to figure (5.3).*
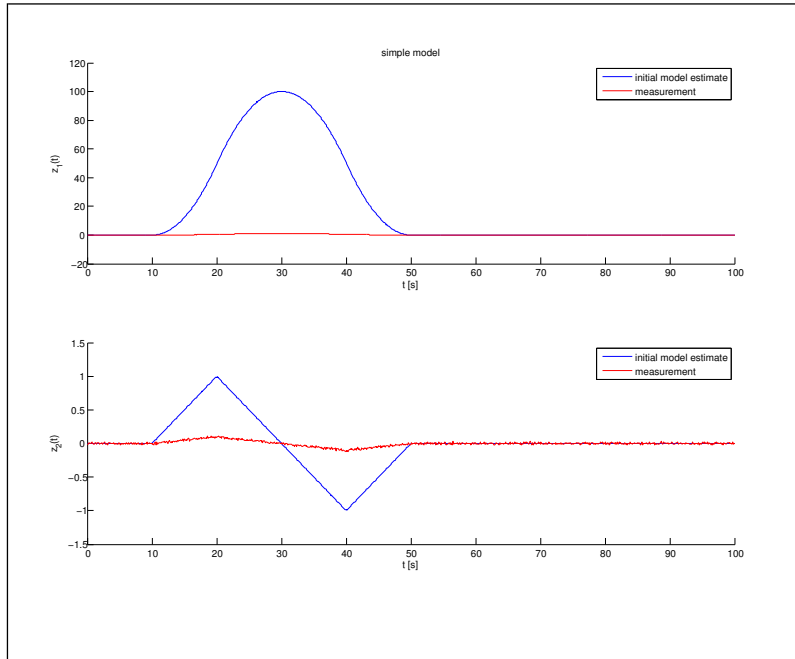
Figure D.19: *Time histories of the output of the initial estimated model compared with the measurements for the simple example with a nonsingular information matrix. Equivalent to figure (5.4).*
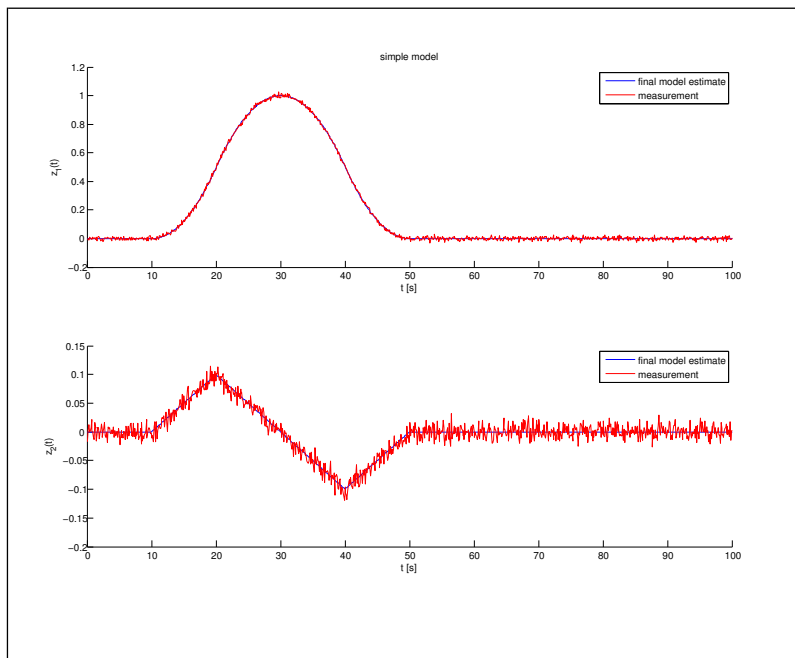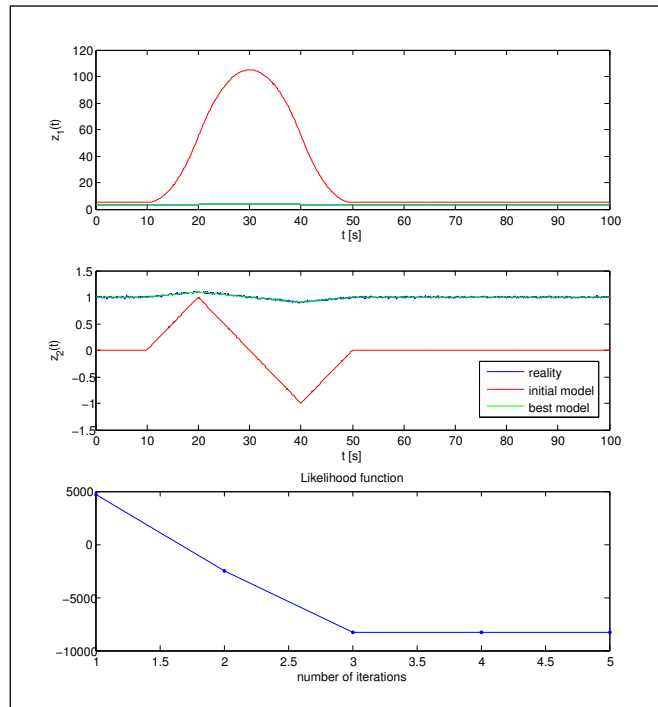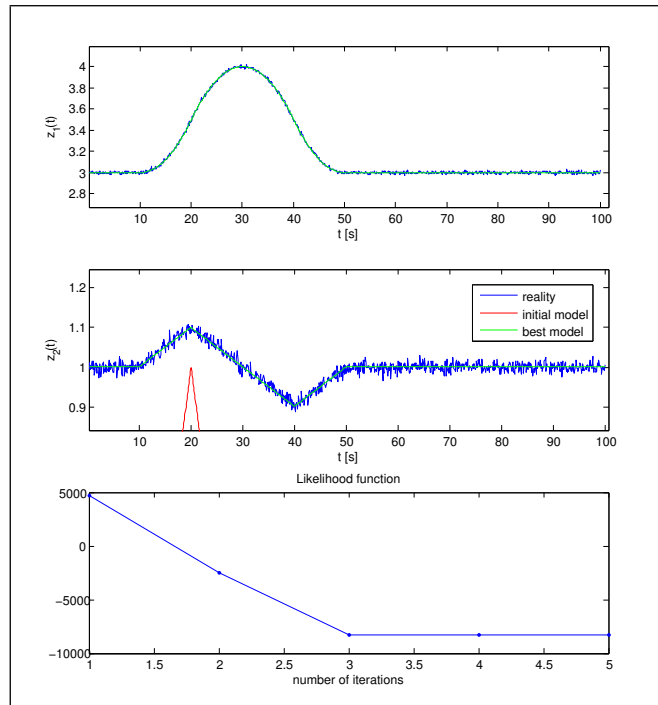

Figure D.20: *Time histories of the output of the estimated model after 2 iterations compared with the measurements for the simple example with a nonsingular information matrix. Equivalent to figure (5.5).*

Figure D.21: *Time histories of the output of the initial model and the final estimation compared with the measurements for the simple example with a singular information matrix. Equivalent to figure (5.6).*

Figure D.22: *Time histories of the output of the initial model and the final estimation compared with the measurements, zoomed in on the measurements for the simple example with a singular information matrix. Equivalent to figure (5.7).*
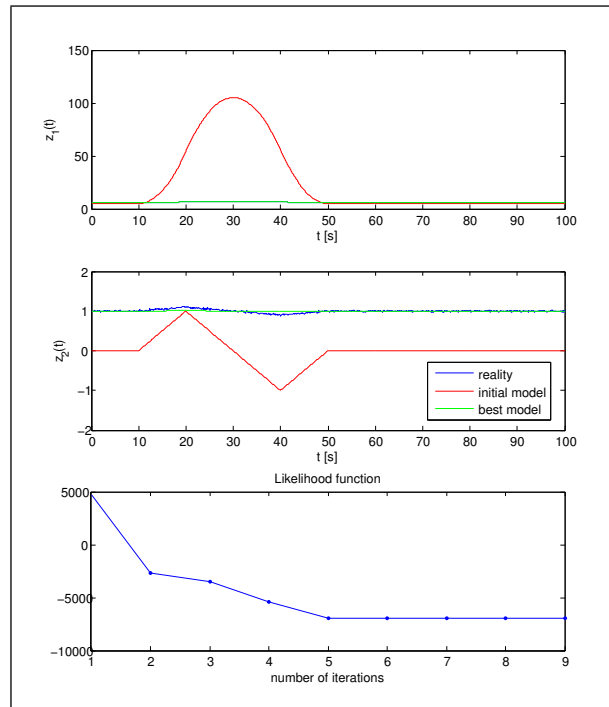
Figure D.23: Modification 1: Time histories of the output of the initial model and the final estimation compared with the measurements for the simple example with a singular information matrix. Equivalent to figure (5.9).
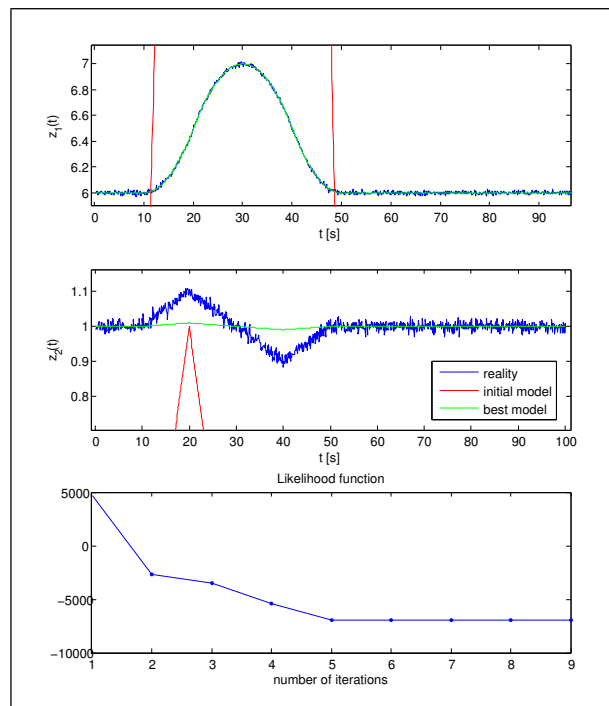

Figure D.24: Modification 1: Time histories of the output of the initial model and the final estimation compared with the measurements, zoomed in on the measurements for the simple example with a singular information matrix. Equivalent to figure (5.10).
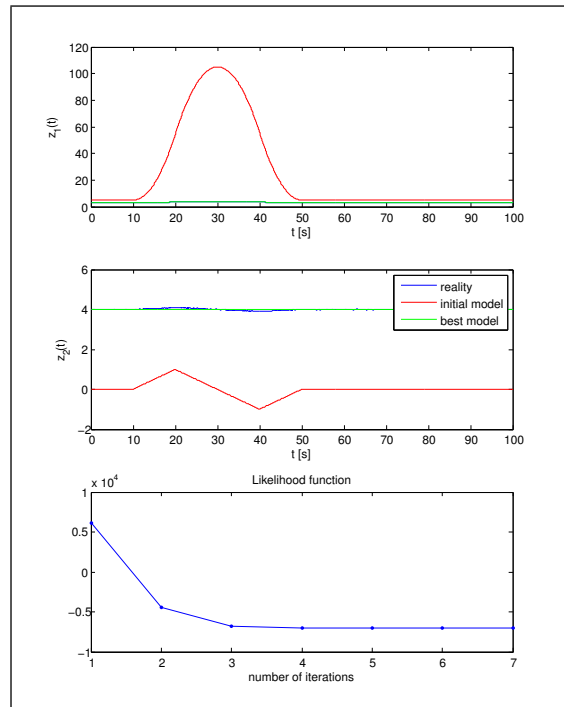
Figure D.25: *Modification 2: Time histories of the output of the initial model and the final estimation compared with the measurements for the simple example with a singular information matrix. Equivalent to figure (5.11).*
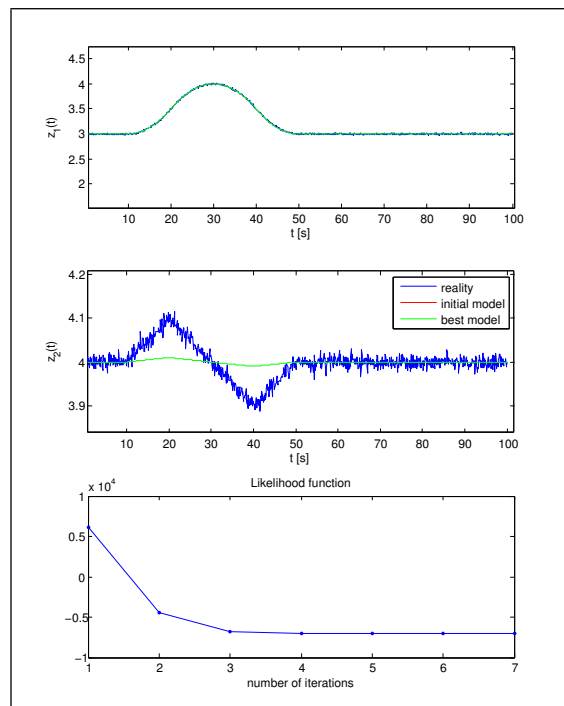

Figure D.26: *Modification 2: Time histories of the output of the initial model and the final estimation compared with the measurements, zoomed in on the measurements for the simple example with a singular information matrix. Equivalent to figure (5.12).*
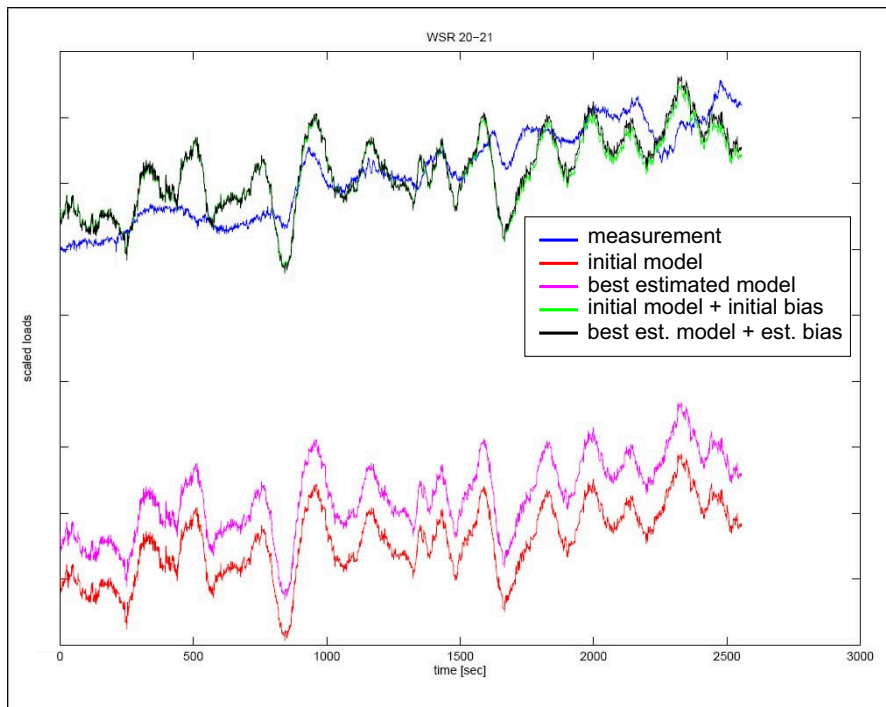
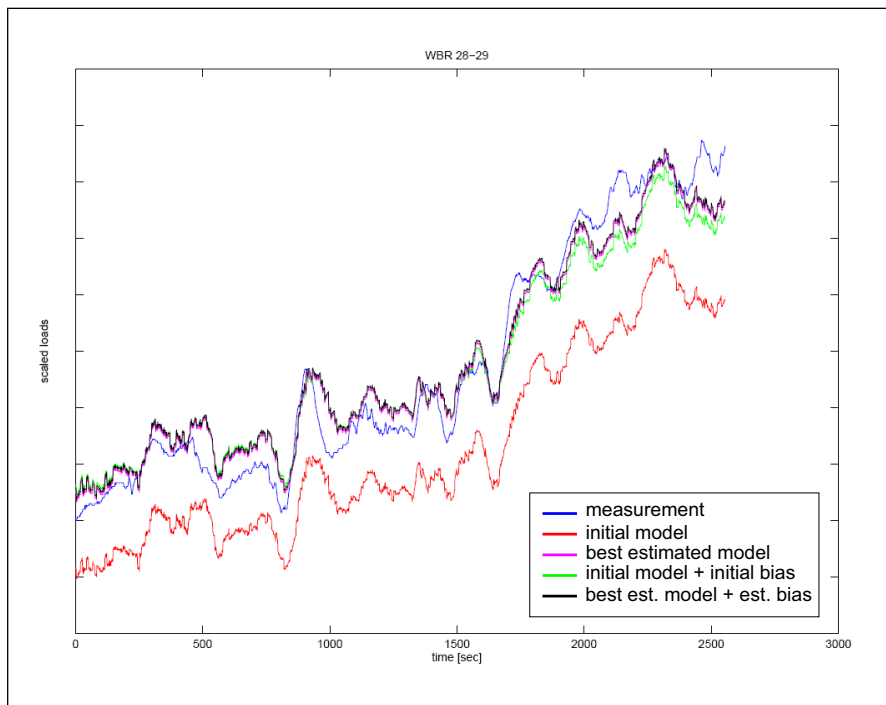**Figure D.27:** *Scaled integrated shear load at righthand wing station 4, by method "LINFLEX"*

Figure D.28: *Scaled integrated bending moment at righthand wing station 5, by method "LIN-FLEX"*
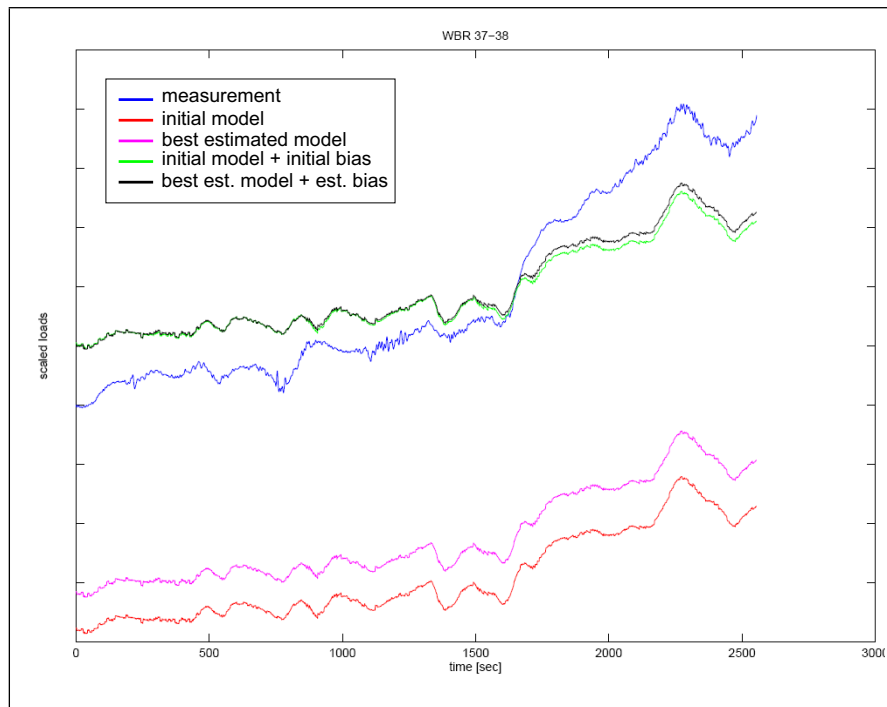
Figure D.29: *Scaled integrated bending moment at righthand wing station 6, by method "LIN-FLEX"*
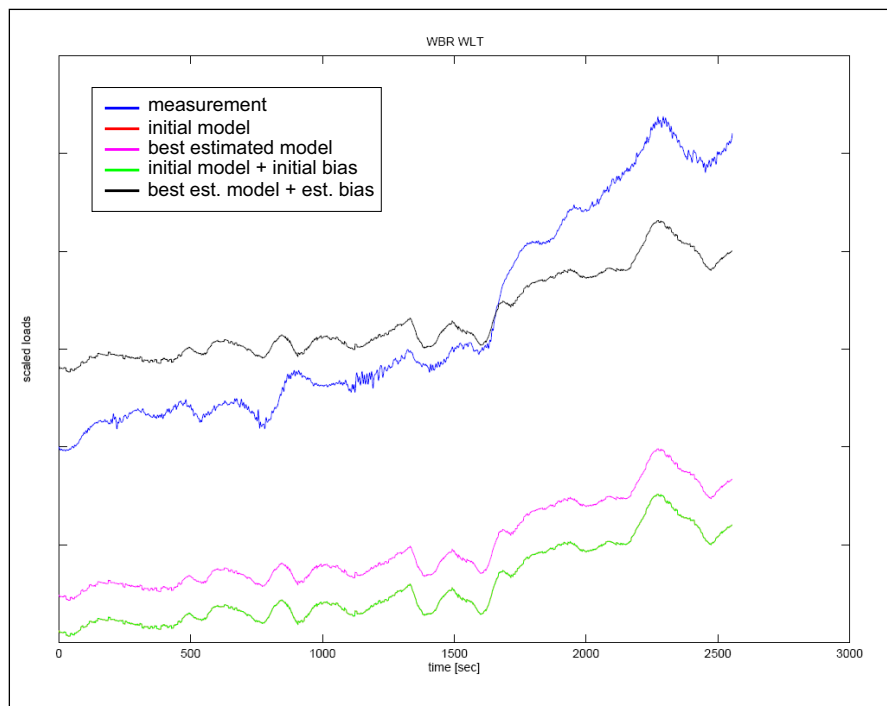

Figure D.30: *Scaled integrated bending moment at righthand winglet root, by method "LINFLEX"*

Samenvatting

De ontwikkelingen in de numerieke berekeningsalgorithmen en in de computer-hardware gaan steeds sneller. Dit maakt de toepassing van steeds geavanceerdere methoden mogelijk. Zo worden ook steeds nauwkeurigere voorspellingen mogelijk bij de bepaling van de belastingen op vliegtuigconstructies. Bovendien wordt er bij het ontwerp van vliegtuigconstructies een hogere mate aan elasticiteit getolereerd, waardoor deze duidelijk lichter geconstrueerd kunnen worden. De vliegtuigen van de toekomst kunnen groter worden. Desondanks kunnen betere prestaties en minder massa worden bereikt. De prestatie van het vliegtuig kan nog verder worden verbeterd door het gebruik van winglets of door andere toevoegingen aan het uiteinde van de vleugel.

De steeds groter wordende flexibiliteit in combinatie met de grotere afmetingen kunnen leiden tot significante verplaatsingen van de constructie. Door deze grotere verplaatsingen wordt de interactie tussen de aerodynamica en de structuurmechanica steeds belangrijker. Doordat de winglets aan het uiteinden van de vleugels zijn geplaatst, worden hun aerodynamische prestaties duidelijk beinvloed door de bewegingen van de elastische vleugel.

Uiteraard moet een veilig en betrouwbaar gebruik van het vliegtuig worden gegarandeerd en bewezen door middel van geschikte ontwerp-berekeningen. Dit wordt gecontroleerd door middel van de regelgeving, die is opgesteld door de Luchtvaartauthoriteiten. De certificatie van verkeersvliegtuigen is uitsluitend mogelijk als het ontwerp voldoet aan deze Luchtwaardigheidsvoorschriften. In de Luchtwaardigheidsvoorschriften ('Certification Specifications', CS) van de Europese Luchtvaartauthoriteiten ('European Aviation Safety Agency', EASA) is het volgende voorschrift opgenomen:

'Indien de verplaatsingen onder belaste toestand ervoor zorgen dat de verdeling van de externe of interne belastingen significant worden veranderd, dan moet met deze herverdeling rekening worden gehouden'.[1].

Het doel van dit proefschrift is een algorithme te ontwikkelen, waarmee het mogelijk is om elastische effecten op de buitenvleugel te identificeren binnen de context van be-

---

[1] Vrij vertaald uit CS 25.301(c): 'if deflections under load would significantly change the distribution of external or internal loads, this redistribution must be taken into account.'

lastingsbepaling tijdens manoeuvres, gebaseerd op de Maximum Likelihood Methode. Het grote verschil met de benaderingen van bestaande publicaties is dat de modellen in dit proefschrift baseren op verdeelde lokale data, in plaats van op het netto effect op de vliegprestaties. Doordat dit veroorzaakt dat de grootte van de specifieke modellen veel groter moet zijn, wordt het mogelijk om met de geidentificeerde modellen een veel gedetailleerdere interpretatie van de geobserveerde toe- of afname in de prestaties van het winglet te maken.

Als eerste is onderzocht hoe een winglet of alternatieve toevoegingen aan het uiteinde van de vleugel werken. Er zijn veel referenties die de aerodynamische prestatie van deze alternatieven in het algemeen maar ook van winglets in het bijzonder onderzoeken. Deze onderzoeken vergelijken over het algemeen de verbetering in de luchtweerstand die met de verschillende alternatieven kunnen worden behaald. Deze onderzoeken zijn vrijwel allemaal gebaseerd op wind tunnel metingen, of pure aerodynamische analyse's (CFD) en dus geldig voor een star vliegtuig. Deze studie's zijn erg belangrijk voor het verkrijgen van inzicht in de ingewikkelde stroming rond het uiteinde van de vleugel. Met behulp van dit inzicht kunnen nog sneller efficientere ontwerpen worden ontwikkeld. Echter hebben vliegproeven uitgewezen dat rekening moet worden gehouden met de elasticiteit van de constructie voor de bepaling van het belastingsniveau van het winglet.
Als tweede stap is het model voor de belastingsbepaling tijdens manoeuvres opgebouwd. Een algorithme is ontwikkeld, dat in staat is om de parameters in zo'n niet-lineair gekoppeld aero-elastisch model te identificeren. Dit algorithme is gebaseerd op de Maximum Likelihood Methode, dat zelfs oplossingen vindt in het geval van een singuliere informatiematrix. Het algorithme is getest met behulp van allereerst een eenvoudig 2 vrijheidsgraden model. Ten tweede is het algorithme getest met behulp van gesimuleerde meetdata, verkregen via een kleine modificatie in het belastingen observatie model. In beide gevallen is het 'werkelijke' systeem bekend. Hierdoor is het mogelijk het algorithme op zijn efficientie en juistheid te controlleren. Uiteindelijk, is de identificatie procedure toegepast op een praktijk relevant probleem, gebruik makend van echte vliegproefdata. De identificatie procedure met behulp van deze vliegproefdata is vijfmaal uitgevoerd waarbij de aanpassingen zijn gedaan binnen de modellering van de aerodynamische effecten voor de vleugels en winglets.

De mate van succes bij de identificatie van een specifiek model is sterk afhankelijk van de modelstructuur en de aangenomen beginwaarden voor de modelparameters. Het model moet geavanceerd genoeg zijn om de fenomenen, die aanwezig zijn in de meetdata, te kunnen beschrijven. Het moet echter ook eenvoudig/klein genoeg zijn, om het probleem met de voorhandene resourcen te kunnen identificeren. Het is gebleken dat het op dit moment praktisch nog niet mogelijk was om niet-lineaire aerodynamische elasticiteitseffecten te identificeren voor een model van deze grote en complexiteit, simpelweg door de benodigde grote rekencapaciteit.
De identificatie van het model, dat slechts rekening houdt met lineaire elasticiteitseffecten, laat echter zien dat er significante verschillen aanwezig zijn tussen het geschatte model en de metingen. Dit kan worden veroorzaakt door onjuiste apriori waarden voor de constante parameters en/of omdat niet alle aanwezige fenomenen in voldoende mate

worden beschreven door het model. Dit lineaire model kan de grote belastingstoename ten gevolge van de belastingsfactor, die opgetreden is aan de buitenvleugel en het winglet, niet verklaren. Dit maakt een uitgebreider onderzoek van dit fenomeen voor de buitenvleugel noodzakelijk.

Resultaten uit stationaire RANS[2] simulaties van het getrimde elastische vliegtuig tonen een vrij goede overeenkomst in de drukprofielen vergeleken met drukmetingen tijdens vliegproeven. De lift-coëfficiënt bepaald uit de drukmetingen is echter lager voor de twee stations van het winglet vergeleken met de CFD-CSD[3] simulaties. De drukmetingen aan het winglet tonen tevens een hoger resulterend moment (dat een neerwaarts draaiende beweging van de winglet neus veroorzaakt) vergeleken met de simulatie. Ann de andere kant moet rekening worden gehouden met het feit dat de geintegreerde waarde van de gemeten drukprofielen een beperkte nauwkeurigheid hebben, vanwege het relatief geringe aantal waarden.

CFD simulaties zijn vervolgens gebruikt om de aerodynamische belastingsverdeling voor een vleugel met winglet gedetailleerder te onderzoeken met behulp van een starre analyse voor meerdere invalshoeken. Het model 'NL-rigid' is ontwikkeld om de niet-lineaire starre aerodynamische effecten te beschrijven. Dit model kon worden geoptimaliseerd met de identificatieprocedure, waardoor de beste overeenstemming met de vliegproefdata verkregen werd. In dit model is het opvallend dat met name de locale gradiënten voor de winglets met betrekking tot the invalshoek duidelijk groter zijn, vergeleken met de waarden volgens de originele aerodynamische databank. Deze geidentificeerde gradiënten zijn vergeleken met de waarden volgens de CFD-simulaties en blijken hiermee goed overeen te komen.

De aerodynamische data verkregen uit de CFD-simulaties is ook direct ingevoerd in het belastingen observatie model. De resultaten verkregen aan de hand van de beginwaarden van dit model (RANS-model genoemd) vertonen een goede overeenstemming met de vliegproefdata. Verdere optimalisatie van dit model was niet mogelijk zonder dat aerodynamische verdelingen resulteren die fysiek gezien onwaarschijnlijk zijn.

Er zijn twee 'hybride' identificaties uitgevoerd. Deze baseerden op hetzelfde hybride model (een combinatie uitgaande van de originele aerodynamische data en die verkregen uit de CFD-simulaties), dat is ontwikkeld om het RANS-model te corrigeren voor de 'flight-to-jig'-discrepantie die nog aanwezig was in de ingangsdata. Het verschil tussen deze twee hybride identificaties was slechts de keuze van de vrije parameters. Het globale belastingsniveau werd duidelijk verbeterd door middel van het hybride model, vergeleken met de resultaten van het RANS-model. Verdere optimalisatie van dit model was niet mogelijk zonder het verkrijgen van fysiek onwaarschijnlijke aerodynamische verdelingen voor de vleugels en winglets.

Het is gebleken, dat het identificatie algorithme uit dit proefschrift heel goed kan worden gebruikt om moduleringsverbeteringen direct tijdens de ontwikkeling te kwantificeren. Tevens kan dit algorithme natuurlijk worden gebruikt bij het identificeren van de meest optimale waarden voor de vrije parameters van het betreffende model.

---

[2]Reynolds-Averaged Navier-Stokes

[3]CFD-CSM: Computational Fluid Dynamics - Computational Structural Mechanics

Bibliography

[Aik49]   W. Aiken and D. Howard. A comparison of wing loads measured in flight on a fighter-type airplane by strain-gage and pressure-distribution methods. Tech. Rep. NACA-TN-1967, NACA, November 1949.

[And89]   J. Anderson, Jr. *Introduction to Flight*. McGraw-Hill Series in Aeronautical and Aerospace Engineering. McGraw-Hill, 3rd edn., 1989.

[And91]   J. Anderson, Jr. *Fundamentals of Aerodynamics*. McGraw-Hill, 2nd edn., 1991.

[Bar81]   M. Barber and D. Selegan. Kc-135 winglet program review. (NASA CP 2211), September 1981. Proceedings of a symposium held at Dryden Flight Research Center.

[But87]   C. Buttrill, T. Zeiler, and P. Arbuckle. Nonlinear simulation of a flexible aircraft in maneuvering flight. (AIAA 87-2501):pp. 122–133, 1987.

[Chu87]   Q. Chu. *Maximum Likelihood parameter identification of flexible spacecraft*. Ph.D. thesis, Delft University of Technology, 1987.

[Coi00]   R. Coimbra and F. Catalano. An experimental study on wing tip devices for agricultural aircraft. 2000.

[Dam83]   C. van Dam. Analysis of nonplanar wing-tip-mounted lifting surfaces on low-speed airplanes. (NASA CR 3684), 1983.

[Dam99]   C. van Dam. Recent experience with different methods of drag prediction. *Progress in Aerospace Sciences*, vol. 35:pp. 751–798, 1999.

[Dam05]   H. Damveld and J. Mulder. Influence of instationary aerodynamics and trimming on the dynamics of an aeroelastic aircraft. (AIAA 2005-6334), August 2005.

303

[Den96] J. Dennis, Jr. and R. Schnabel. *Numerical Methods for Unconstrained Optimization and Nonlinear Equations*. SIAM, 1996.

[Eyk79] P. Eykhoff. *System Identification: Parameter and State Estimation*. J. W. Arrowsmith Ltd., 1979.

[Gil99] M. Giles and R. Cummings. Wake integration for three-dimensional flowfield computations: Theoretical development. *Journal of Aircraft*, vol. 36(2):pp. 357–365, 1999.

[Gro72] R. Grove, R. Bowles, and S. Mayhew. A procedure for estimating stability and control parameters from flight test data by using maximum likelihood methods employing a real-time digital system. (NASA TN D-6735), May 1972.

[HG06] J.-L. Hantrais-Gervois and M. Rapin. Aerodynamic and structural behaviour of a wing equipped with a winglet at cruise. (AIAA 2006-1489), January 2006.

[Hof87] K. Hoffmann. *Eine Einführung in die Technik des Messens mit Dehnungsmeßstreifen*. Hottinger Baldwin Messtechnik GmbH, 1987.

[Hof03] J. Hofstee, T. Kier, C. Cerulli, and G. Looye. A variable, fully flexible dynamic response tool for special investigations (varloads). June 2003.

[Ish76] K. Ishimitsu. Aerodynamic design and analysis of winglets. (AIAA 76-940), september 1976.

[Jat06] R. Jategaonkar. *Flight vehicle system identification: A time domain methodology*. American Institute of Aeronautics and Astronautics, Inc., 2006.

[Kar93] M. Karpel and E. Presente. Structural dynamic loads in response to impulsive excitation. Tech. rep., Technion - Israel Institute of Technology, Haifa, Israel, 1993.

[Kie07] T. Kier, G. Looye, M. Scharpenberg, and M. Reijerkerk. Process, methods and tools for flexible aircraft flight dynamics model integration. *International Forum on Aeroelasticity and Structural Dynamics (IFASD)*, 2007.

[Kim05] J. Kim, D. Bates, and I. Postlethwaite. Nonlinear robust performance analysis using complex-step gradient approximation. 2005.

[Kle06] V. Klein. *Aircraft System Identification: Theory and Practice*. AIAA Education Series, 2006.

[Kli06] J. Klijn. Development of flight test instrumentation: an evolutionary approach. Tech. Rep. NLR-TP-2006-407, National Aerospace Laboratory NLR, July 2006.

[Kön07] B. König, M. Pätzold, T. Lutz, and E. Kramer. Shock control bumps on flexible and trimmed transport aircraft in transonic flow, 2007.

[Kro01] I. Kroo. Drag due to lift: Concepts for prediction and reduction. *Annu Rev Fluid Mechanics*, vol. 33:pp. 587–617, 2001.

[Liv03] E. Livne. Future of airplane aeroelasticity. *Journal of Aircraft*, vol. 40(6):pp. 1066–1092, 2003.

[Lok04] W. Lokos and R. Stauf. Strain-gage loads calibration parametric study. Tech. Rep. NASA-TM-2004-212853, NASA, August 2004.

[Loo99] G. Looye. Integrated flight mechanics and aeroelastic aircraft modeling using object-oriented modeling techniques. *AIAA*, vol. 99-4192, 1999.

[Loo05] G. Looye. Integration of rigid and aeroelastic aircraft models using the residualised model method. 2005.

[Loo08] G. Looye. *An integrated approach to aircraft modelling and flight control law design*. Ph.D. thesis, TU Delft, 2008.

[Lou05] M. Lourakis. A brief description of the levenberg-marquardt algorithm implemented by levmar. February 2005.

[Mar00] J. Martins, I. Kroo, and J. Alonso. An automated method for sensitivity analysis using complex variables. (AIAA-2000-0689), 2000.

[Mul86] J. Mulder. *Design and evaluation of dynamic flight test manoeuvres*. Ph.D. thesis, TU Delft, 1986.

[Mul99] J. Mulder, Q. Chu, J. Sridhar, J. Breeman, and M. Laban. Non-linear aircraft flight path reconstruction review and new advances. *Progress in Aerospace Sciences*, vol. 35:pp. 673–726, 1999.

[Myk02] L. Myklebust and B. Skallerud. Model reduction methods for flexible structures. *15th Nordic Seminar on Computational Mechanics*, 18-19 Oct 2002.

[Nel94] S. A. Nelson. Strain gage selection in loads equations using a genetic algorithm. Tech. Rep. NASA CR 4597, NASA, 1994.

[Nie99] H. Nielsen. Damping parameter in marquardt's method. (Technical Report: IMM-REP-1999-05), 1999.

[Qu04] Z.-Q. Qu. *Model order reduction techniques: with applications in finite element analysis*. London: Springer-Verlag, 2004.

[Rad97] L. Rade and B. Westergren. *Springers Mathematische Formeln: Taschenbuch für Ingenieure, Naturwissenschaftler, Wirtschaftswissenschaftler*. Springer, 2nd edn., 1997.

[Ren04] J. Reneaux. Overview on drag reduction technologies for civil transport aircraft. July 2004.

[Res03] C. Reschke. *Berechnung dynamischer Lasten bei elastischen Strukturen*. Master's thesis, Universität Stuttgart, January 2003.

[Res05] C. Reschke. Flight loads analysis with inertailly coupled equations of motion. (AIAA 2005-6026), August 2005.

[Rod71] W. Rodden, J. Giesing, and T. Kalman. New developments and applications of the subsonic doublet-lattice method for nonplanar configurations. 1971.

[Rod01] W. Rodden and E. Johnson. *MSC.NASTRAN V68 Aeroelastic Analysis User's Guide*. The MacNeal-Schwendler Corporation, 2001.

[Sch97] J. Schuler.   *Flugregelung und aktive Schwingungsdämpfung für flexible Großraumflugzeuge*. Ph.D. thesis, Universität Stuttgart, 1997.

[Sir00] J. Sirohi and I. Chopra.   Fundamental understanding of piezoelectric strain sensors. *Journal of Intelligent Material Systems and Structures*, vol. 11:pp. 246–257, April 2000.

[Sko54] T. Skopinski, W. Aiken, and W. Huston. Calibration of strain-gage installations in aircraft structures for the measurement of flight loads. Tech. Rep. NACA Report 1178, 1954.

[Spe70] C. Speedy, R. Brown, and G. Goodwin. *Control theory: Identification and optimum control*. Oliver & Boyd, 1970.

[Squ05] G. Squeglia. Introduction to loads requirements and computation course. Supaero/ENSICA, 2005.

[Ste73] D. Stepner and R. Mehra.   Maximum likelihood identification and optimal input design for identifying aircraft stability and control derivatives. (NASA CR-2200), March 1973.

[Sto83] J. Stoer. *Einführung in die Numerische Mathematik I*. Springer-Verlag, 4th edn., 1983.

[Teu03] P. Teufel. *Böenmodellierung und Lastabminderung für ein flexibles Flugzeug*. Ph.D. thesis, Universität Stuttgart, 2003.

[Was86] M. Waszak and D. Schmidt. On the flight dynamics of aeroelastic vehicles. *AIAA*, vol. 86-2077:pp. 120–133, 1986.

[Was87] M. Waszak, J. Davidson, and D. Schmidt.   A simulation study of the flight dynamics of elastic aircraft. *NASA CR 4102*, 1987.

[Was88] M. Waszak and D. Schmidt. Flight dynamics of aeroelastic vehicles. *Journal of Aircraft*, vol. 25(NO. 6), June 1988.

[Wel80] B. Welsh and C. Pyne. A method to improve the temperature stability of semiconductor strain gauge transducers. *Journal of Physics*, vol. 13:pp. 816–818, February 1980.

[Wel04] G. Welch and G. Bishop. An introduction to the kalman filter. April 2004.

[Whi76] R. Whitcomb. A design approach and selected wind-tunnel results at high subsonic speeds for wing-tip mounted winglets. (NASA TN D-8260), July 1976.

Curriculum Vitae

Marianne Jacoba Reijerkerk was born on June 15th, 1980, in Hanau, Germany. From 1992 to 1998 she attended the 'Insula College' in Dordrecht where she obtained the Atheneum certificate.

In 1998 she started her studies at the Delft University of Technology, Faculty of Aerospace Engineering. In August 1999 she obtained her Propedeuse (Cum Laude). In January, 2004, at the Disciplinary Group for Aerodynamics, she obtained the M.Sc. degree in Aerospace Engineering for her study on flexible aircraft modelling with structural and aerodynamic non-linearities. This research was conducted at Airbus Deutschland GmbH in Hamburg under the supervision of Prof.dr.ir. P.G. Bakker and Dr.ir.drs. H. Bijl.

In February, 2004, she started working as a Young scientist (Ph.D.-candidate) within an 'Industrie Patenschaft' between DLR Oberpfaffenhofen, Institute of Robotics and Mechatronics located in Weßling, Germany and Airbus Loads & Aeroelastics domain in Hamburg, Germany. Here she has performed aero-elastic research on the outer wing and winglet loads of a large transport aircraft using measured wind tunnel and flight test data in combination with different simulation environments. This thesis is based on the results from these investigations.